Building Minimal Spindles

Reconstituting spindle positioning in synthetic cells

Building Minimal Spindles

Reconstituting spindle positioning in synthetic cells

Dissertation

for the purpose of obtaining the degree of doctor
at Delft University of Technology
by the authority of the Rector Magnificus, prof. dr. ir. T.H.J.J. van der Hagen,
Chair of the Board for Doctorates
to be defended publicly on Friday 12, September 2025 at 12:30 o'clock

by

Yash Kiran JAWALE

Master of Science,
Indian Institute of Science Education and Research Pune, India,
born in Jalgaon, India.

This dissertation has been approved by the promotors.

Composition of the doctoral committee:

Rector Magnificus	chairperson
Prof. dr. A. M. Dogterom	TU Delft, NL (*promotor*)
Dr. ir. L. Laan	TU Delft, NL (*promotor*)
Independent members:	
Prof. dr. T. Surrey	CRG, Spain
Prof. dr. A. P. Liu	U. of Michigan, USA
Dr. P. Gayathri	IISER Pune, India
Prof. dr. M. E. Tanenbaum	TU Delft / Hubrecht Inst., NL
Prof. dr. G. H. Koenderink	TU Delft, NL
Prof. dr. ir. P. A. S. Daran-Lapujade	TU Delft, NL *(reserve member)*

This research was supported by the "BaSyC - Building a Synthetic Cell" Gravitation grant (024.003.019) from OCW and NWO.

Keywords: Microtubules, Centrosomes, Asters, Spindle, Synthetic cells, Droplets, Liposomes, cDICE, dsGUV, Nucleus, Actin cortex, ParM, Optogenetics

Cover by: Yash (tech support by Nemo & rendered on Yuchang's MacBook)

Front & Back: A swirling, puzzle-piece spindle emerging over a sketched blueprint, capturing the beauty and chaos of building life's machinery piece-by-piece. & A scientist in the lab bridges concept to reality, building a minimal spindle as ideas converge.

Printed by: Gildeprint

ISBN/EAN: (print) 978-94-6384-833-6 (digital) 978-94-6518-103-5

The copies of this dissertation are available at

Electronic & Digital	https://repository.tudelft.nl/
Data	https://data.4tu.nl/

To
my parents, my sister
(and a part of my brain)

Yash

Contents

A digital version of this thesis, featuring interactive elements and animations, is available at: `https://repository.tudelft.nl` and `https://research.tudelft.nl`

Summary

It all started with the Big Bang, the birth of the universe. Life eventually emerged, somewhere along the way. Yet we still do not fully understand how, let alone why it continues to sustain. For instance, how does a cell, the fundamental unit of life, known so far to be composed of basic biomolecules, carry out several complex cellular processes? Cells may take different sizes, shapes, forms, functions, and timescales, but they all generate energy, grow and divide. They even adapt when needed be, to keep propagating life.

This brings us to several questions. Do we understand the basics of life yet? How can we know more? Assuming we know enough, can we build life again? If we were to do so, building it as per our will this time would still seem like a remote possibility. In Chapter 1, we take a closer look at these questions. We know that a cell needs to maintain metabolism, grow its membrane, replicate its genetic information and separate it into two equal halves, and divide. We know most of the key components involved by now. Several of these processes involve the cytoskeleton in some form or the other. The constant turnover and remodelling of the cytoskeleton contributes to the mechanisms underlying these processes. Here, we choose to focus on the DNA segregation machinery. Microtubules, a key player of the cytoskeleton, does most of the heavy lifting, literally and figuratively. It helps assemble the spindle, with the help of which the DNA is aligned and later segregated. Microtubules provide the framework for other proteins to interact, while generating force to position the spindle and pull the DNA apart. This phenomenon serves as our motivation to investigate further about the microtubules and their role in DNA segregation.

There are two ways to study these processes currently, you either dismantle the components out one by one, also known as the 'top-down' approach, or you assemble the components one by one, also known as the 'bottom-up' approach. The aim is to check how the behaviour of the system changes in response to the addition or deletion of these components. We picked the latter, where you create a container and encapsulate these components together to see if they work as expected. So, in Chapter 2, we explored different ways to make multiple types of containers that resemble a cell, and multiple ways to modify them. No one method fits all the required criteria to make a membrane similar to the cellular membrane, but each method has its own strengths and limitations. While droplets are the easiest to work with, the emulsion transfer based methods are most compatible with cellular conditions.

So, in Chapter 3, we first focused on understanding more about continuous droplet interface crossing encapsulation (cDICE), one of the methods used for forming containers. We built a high-speed imaging setup to see how vesicles are formed. We saw that vesicle-sized droplets are rarely formed at the initial step, and at the last step, there appears to be a size-selective crossing at the interface to transform

droplets into vesicles. Furthermore, the prospective contents of the vesicles potentially affect the formation of membrane.

In Chapter 4, we attempted to encapsulate tubulin within the vesicles, as a first step towards rebuilding a mitotic spindle, a part of the cell. However, given that the tubulin is a challenging protein to work with, and requires very specific conditions, we had limited success in our attempt despite previous reports that encapsulation is possible under very specific conditions. We used cDICE as well as other methods to encapsulate tubulin within vesicles, but with little positive outcomes. Direct observations of tubulin interacting with the membrane revealed, that it disrupts the membrane. Although we are yet to gain sufficient clarity, we know that this interaction hindered our efforts at assembling the spindle in a 3D cell-like confinement.

So, we switched containers and moved to emulsion droplets. In Chapter 5, we focused on reconstituting basic components inside the droplets. The idea was to first characterize the encapsulation of individual components and later increase the complexity of the reconstitution by adding more components one after another. We characterized parts of cellular processes involving singular components, including aster formation, nucleus positioning and actin cortex formation. Later, we combined them to see how they influence each other in a confinement. We also explored ways to externally regulate them. Next, in Chapter 6, we reattempted to build the spindle, but this time in a droplet. We first rebuilt a basic mitotic spindle inside a droplet by combining different components like multiple asters, motor proteins, and crosslinkers, as described earlier. With the aim of increasing the complexity of our reconstitution, we then decided to mimic the asymmetric positioning of the spindle observed in the first cell division of the *Caenorhabditis elegans* embryo. For this, we introduced an optogenetic tool, iLID, to modulate dynein, the motor component present on the cell membrane. While we found iLID to work on bilayer membranes, it had photo-activation issues inside the droplets. This limited our efforts to reposition the minimally reconstituted spindle asymmetrically in the confinement. Assembling a mitotic spindle is a pretty challenging task.

Having faced difficulties trying to build a complex eukaryotic spindle, we thought of taking a step back, looking at the bigger picture and using our learnings into building something simpler. We asked, knowing the basics of individual components, can we not just build the whole cell, but only with minimal components, and from scratch? Already, efforts are made towards building a minimal synthetic cell. In Chapter 7, we contribute to the synthetic cell with our understanding of the cytoskeleton, and designed a minimal spindle for DNA segregation. First, we reconstituted ParMRC, a bacterial DNA partitioning system *in vitro*. It is a simpler system, with only three components. Next, we attempted to externally regulate it using iLID. We modified the adaptor protein, ParR to make it photoactivatable. While individual components functioned normally, the system as a whole is not functional yet. The design needs further fine-tuning.

Lastly, in Chapter 8, we summarise and discuss our findings and the challenges we faced during the assembly of the two different DNA segregation machineries, at different levels of complexity, and potential ways to try to mitigate them. Attempting to build a part of the cell or even the synthetic cell in a minimal form from scratch,

seems like an ambitious goal. Even though such a reconstituted system may only mimic some properties of the natural cell, it helps in gaining new fundamental insights. My work improves our understanding about how lipids form membranes, how this may be disrupted by membrane-tubulin interactions, and how to keep interacting cytoskeletal proteins functional while maintaining lipid membranes, the component that separates living from non-living.

Samenvatting

Het begon allemaal met de oerknal, de geboorte van het universum. Uiteindelijk ontstond ergens ook het leven. Nog steeds weten we niet precies hoe, laat staan waarom het blijft overleven. Bijvoorbeeld, hoe voert een cel, de fundamentele eenheid van het leven — bestaand slechts uit eenvoudige biomoleculen — verschillende complexe cellulaire processen uit? Cellen komen voor in verschillende maten, vormen, functies en leven op verschillende tijdschalen, maar ze hebben altijd het volgende gemeen: ze groeien, ze genereren energie en ze delen. Ze passen zich zelfs aan de omgeving aan, indien nodig, om zo het leven te blijven voortzetten.

Dit roept verschillende vragen op: Begrijpen we ondertussen de basisprincipes van het leven? Hoe kunnen we er meer over te weten komen? In de veronderstelling dat we het leven goed genoeg begrijpen, kunnen we het dan ook maken? Op dit moment lijkt het bouwen van leven naar ons eigen ontwerp nog een verre mogelijkheid. In hoofdstuk 1 gaan we dieper in op deze vragen. We weten dat een cel zijn metabolisme in stand moet houden, zijn membraan moet groeien, zijn genetische informatie moet dupliceren, in twee gelijke delen moet splitsen en uiteindelijk zichzelf moet delen. We kennen inmiddels de meeste componenten die hierbij betrokken zijn, en veel van deze processen omvatten in de een of andere vorm het cytoskelet. Er vindt een constante omzetting en her-modellering plaats van het cytoskelet, dat onderliggend is aan deze processen. In dit hoofdstuk leggen we de focus op DNA-segregatie machinerie. Microtubuli, een van de belangrijkste spelers van het cytoskelet, doen letterlijk en figuurlijk het zwaarste werk, en helpen bij het samenstellen van de spoelfiguur waarop het DNA wordt uitgelijnd en later wordt gescheiden. Microtubuli vormen het cellulaire skelet waaraan vele andere eiwitten binden, en het genereert zelf krachten om de spoelfiguur te positioneren en om aan het DNA te trekken. Deze centrale rol is de basis voor onze motivatie om de mechanistische rol van microtubuli in DNA segregatie nader te onderzoeken.

Er zijn twee benadering om deze processen te onderzoeken: ofwel haalt men de componenten van de cel één voor één uit het complete systeem (bekend als de 'top-down' methode), of men bouwt het systeem op door componenten één voor één toe te voegen (bekend als de 'bottom-up' methode). Het doel is het bestuderen hoe het gedrag van het systeem veranderd door het toevoegen of verwijderen van deze individuele componenten. Wij kozen voor de laatste benadering, waarbij men de verschillende componenten inkapselt in een begrensd volume om te zien of ze zich gedragen zoals men verwacht. Aldus onderzochten we in hoofdstuk 2 verschillende manieren om diverse soorten containers te maken die lijken op een cel en verschillende methodes om deze containers te modificeren. Er niet één enkele methode die voldoet aan alle vereiste criteria om een membraan te maken dat precies lijkt op het celmembraan, maar elke methode heeft zo zijn eigen sterke en zwakke punten.

Hoewel druppeltjes ('droplets' in het hoofdstuk) het gemakkelijkst zijn om mee te werken, zijn de op emulsie-overdracht gebaseerde methoden het meest compatibel met cellulaire omstandigheden.

Dus in hoofdstuk 3 richten we ons eerst op het beter begrijpen van een dergelijke methode van containervorming, namelijk continue druppelinterface-kruising-encapsulatie (cDICE). We bouwden een high-speed imaging-opstelling om te zien hoe vesikels worden gevormd. Daarmee zagen we dat druppeltjes ter grootte van een vesikel maar zelden worden gevormd in de eerste stap, en dat er in de laatste stap op de interface een grootte-selectieve kruising lijkt te zijn om druppeltjes om te zetten in vesikels. Daarnaast beïnvloedt ook de inhoud van het vesikel de membraanvorming.

In hoofdstuk 4 probeerdenwe tubuline eiwitten in vesikels te encapsuleren, als een eerste stap naar het herbouwen van een spoelfiguur, een cruciaal deel van de cel. We werden er snel aan herinnerd dat tubuline een uitdagend eiwit is om mee te werken en dat het zeer specifieke omstandigheden vereist. Ondanks het feit dat de literatuur stelt dat encapsulatie mogelijk is onder specifieke omstandigheden, zagen we zeer beperkt succes met tubuline-encapsulatie in vesikels. We probeerden niet alleen de cDICE, maar verschillende andere methoden om tubuline in vesikels te encapsuleren, maar zonder succesvolle resultaten. Directe observaties van tubuline-interacties met membranen onthulden dat tubuline het membraan verstoort. We weten nog niet precies hoe, maar dit belemmerde onze pogingen om de spoelfiguur in 3D cel-achtige opsluiting te assembleren.

Dus we pauzeerden het werk aan de containers, en gingen over op emulsiedruppels. In hoofdstuk 5, concentreerden we ons op het reconstrueren van basiscomponenten in de druppels. Het idee was om eerst de inkapseling van individuele (losse) componenten te karakteriseren, en om later de complexiteit van de reconstitutie te vergroten door meer componenten één voor één toe te voegen. We karakteriseerden eerst (delen van) cellulaire processen waarbij enkelvoudige componenten betrokken waren, zoals astervorming, positionering van de kern en vorming van de actinecortex. Later combineerden we ze om te zien hoe ze elkaar beïnvloeden tijdens opsluiting, en onderzochten we ook manieren om ze extern te reguleren. Vervolgens, in hoofdstuk 6, probeerden we opnieuw de spoelfiguur te bouwen, maar dit keer in een druppel. We slaagden er in om een minimalistische spoelfiguur in een druppel te reconstrueren door verschillende componenten te combineren, zoals meerdere asters, motor-eiwitten en cross-linkers, zoals eerder beschreven. Vervolgens wilden we de complexiteit van onze reconstitutie verder vergroten, dus besloten we om de asymmetrische positionering van de spoel na te bootsen die werd waargenomen in de eerste celdeling van het Caenorhabditis elegans embryo. Hiervoor introduceerden we een optogenetisch hulpmiddel, de zogenaamde "improved light-induced dimer (iLID)", om het motor-eiwit dat dat aanwezig is op de celmembraan (dyneïne) te moduleren. De iLID had echter problemen met licht-activatie in de druppels, terwijl het wel werkte op de dubbellaagse membranen. Dit beperkte onze inspanningen om de minimale spoelfiguur asymmetrisch te herpositioneren in de opsluiting. Het reconstitueren van een mitotische spoel blijkt dus een behoorlijk uitdagende taak.

Omdat we problemen hadden met het bouwen van een complexe eukaryotische

spoelfiguur, besloten we om een stap terug te doen, naar het grotere geheel te kijken en onze kennis te gebruiken om iets eenvoudigers te bouwen. Zouden we, met de basisprincipes van individuele componenten, niet gewoon een hele cel vanaf nul kunnen opbouwen met alleen de minimale vereiste componenten? Al geruime tijd worden er pogingen gedaan om een minimale synthetische cel te bouwen. In hoofdstuk 7 besloten we om met onze expertise van het cytoskelet bij te dragen aan een dergelijke synthetische cel, door een minimale spoelfiguur te ontwerpen voor DNA-segregatie. We hebben eerst in vitro het bacteriële DNA-partitiesysteem 'ParMRC' gereconstitueerd. Het 'ParMRC' is een van de eenvoudigste systemen voor DNA-partitie en heeft slechts drie componenten. Later probeerden we externe controle erover te krijgen met behulp van de hierboven genoemde optogenetische tool iLID, door het adaptor-eiwit ParR licht-activeerbaar te maken. Hoewel wildtype componenten normaal functioneren, is de licht-activeerbare variant als geheel nog niet functioneel. Het ontwerp moet dus nog verder worden verfijnd.

Ten slotte vatten we in hoofdstuk 8 de uitdagingen samen die we tegenkwamen tijdens de assemblage van twee verschillende DNA-segregatiemachines, op verschillende complexiteit-niveaus, en bespreken we mogelijke manieren om deze uitdagingen aan te pakken. De poging om een deel van de cel of zelfs de synthetische cel in een minimale vorm vanaf nul te bouwen, lijkt een vergezochte taak. Hoewel een dergelijk gereconstitueerd systeem slechts enkele eigenschappen van een natuurlijk cel zal kunnen nabootsen, zal het ons toch helpen om tot nieuwe fundamentele inzichten te komen. Mijn werk draagt bij aan ons begrip van de manier waarop lipiden membranen vormen, hoe deze formatie verstoord wordt door membraan-tubuline interacties, en hoe men interacterende cytoskelet-eiwitten functioneel kan houden in de aanwezigheid van lipidemembranen — het component wat het leven van het niet-leven scheidt.

सारांश

ब्रम्हांडाची उत्पत्ती ही महास्फोटापासून (बीग बँग) सुरू झाली. या सर्व कालक्रमणामध्ये कुठे तरी कसे तरी जीवन उदयास आले. तरीही आपल्याला अजून पर्यंत पूर्णपणे समजलेले नाही की ते कसे झाले आणि ते सतत कायम का टिकून आहे? उदाहरणार्थ जीवनाचे मूलभूत एकक पेशी जे मूलभूत जैवरेणुंनी (बायोमॉलिक्युल्स) बनलेले असल्याचे आतापर्यंत ज्ञात आहे, ती अनेक किचकट गुंतागुंतीच्या पेशीय प्रक्रिया कशा पार पाडते? पेशींचे आकार, स्वरूप, कार्ये आणि कालमर्यादा भिन्न असू शकतात, परंतू त्या सर्व उर्जा निर्माण करतात, वाढतात आणि विभाजित होतात. जीवनाचा प्रसार चालू ठेवण्यासाठी आवश्यकते नुसार त्या परिस्थितीशी जुळवून घेतात.

यामुळे आपल्याला अनेक प्रश्न पडतात. आपल्याला अजूनही जीवनाची मूलभूत तत्वे समजली आहेत का? आपण अधिक कसे जाणून घेऊ शकतो? आपल्याला पुरेशे ज्ञान आहे असे गृहित धरले तर आपण पुन्हा जीवन निर्माण करू शकतो का? जर आपल्याला यावेळी असे निर्माण करायचे असेल तेही आपल्या ईच्छेनुसार तर त्याची अजूनही दुर्गम शक्यता वाटते. अध्याय १ मध्ये आपण या प्रश्नांचा बारकाईने अभ्यास करू. आपल्याला माहित आहे की पेशीला चयापचय राखणे, तीचे पेशी पटल वाढवणे, तीची अनुवंशिक माहिती प्रतिकृती करणे ती दोन समान भागांमध्ये वेगळी करणे आणि विभाजीत होणे आवश्यक आहे. आतापर्यंत आपल्याला त्यात समाविष्ट असलेले बहुतेक प्रमुख घटक माहित आहे. या अनेक प्रक्रियांमध्ये पेशीकंकाळ (सायटोस्केलेटन) कोणत्या ना कोणत्या स्वरूपात सामील आहे. पेशीकंकाळची सतत उलाढाल आणि पुनर्रचना या प्रक्रियांच्या अंतर्गत असलेल्या यंत्रणेत योगदान देते. येथे आपण डी.एन.ए. विलगीकरण यंत्रणेवर लक्ष केंद्रित करण्याचे निवडले आहे. सूक्ष्मनलिका (मायक्रोट्युब्यूल) पेशीकंकाळचा एक मुख्य घटक, शाब्दिक आणि लाक्षणिक रीत्या सर्वात मोठा भार उचलते व तर्कुतंतु (स्पींडल) जुळणी करण्यास मदत करते. ज्याच्या मदतीने डी.एन.ए. संरेखित होतो आणि नंतर विलगीकृत होतो. सूक्ष्मनलिका इतर प्रथिनांच्या परस्पर क्रियेसाठी आधारभुत संरचना प्रदान करतात, तसेच तर्कुतंतुला स्थिती देण्यासाठी आणि डी.एन.ए. ला वेगळे खेचण्यासाठी शक्ति प्रदान करतात. हा घटनाक्रम सूक्ष्मनलिका आणि डी.एन.ए. विलगीकरणा मधील त्यांची भूमिका याबद्दल पुढील संशोधन करण्यासाठी आमची प्रेरणा म्हणून काम करतो.

सध्या या प्रकियांवर अभ्यास करण्याचे दोन मार्ग आहेत, एक तर घटकांना एक-एक करून काढून टाकणे ज्याला 'टॉप-डाऊन' (top-down) दृष्टीकोन म्हणतात, किंवा घटक एक-एक करून एकत्र करता, ज्याला 'बॉटम-अप' (bottom-up) दृष्टीकोन म्हणतात. या घटकांच्या जोडणी किंवा काढणीच्या प्रतिसादात प्रणालीचे वर्तन कसे बदलते हे तपासणे हा यामागचा उद्देश आहे. आम्ही दुसरा मार्ग निवडला, जिथे तुम्ही एक पात्र तयार करता आणि त्यात हे घटक एकत्र आवरणीकृत (एन्कॅप्सुलेट) करता हे पाहण्यासाठी की ते अपेक्षित कार्य करतात की नाही म्हणून अध्याय २ मध्ये आम्ही पेशी सारखे दिसणारे अनेक प्रकारचे पात्र बनवण्याचे विविध मार्ग आणि त्यांच्या परिवर्तनाचे अनेक मार्ग शोधले पेशींच्या पेशीपटला सारखे पेशीपटल बनवण्यासाठी कोणतीही एक पध्दत सर्व आवश्यक निकषांना पूर्ण करत नाही, परंतू प्रत्येक पद्धतीची स्वतःची बलस्थाने आणि मर्यादा आहेत. थेंबांसह (ड्रॉपलेट) काम करणे सर्वात सोपे असले तरी, इमल्शन ट्रान्सफर आधारीत पद्धती पेशींच्या परीस्थितीशी सर्वाधिक सुसंगत आहेत.

म्हणून अध्याय ३ मध्ये आम्ही प्रथम पात्र तयार करण्यासाठी वापरल्या जाणा-या पद्धतींमध्ये एक

असलेल्या कंटीन्युअस ड्रॉपलेट इंटरफेस क्रॉसिंग एन्कॅप्सुलेशन (cDICE) बद्दल अधिक समजून घेण्यावर लक्ष केंद्रित केल. पुटिका कशा तयार होतात हे पाहण्यासाठी आम्ही एक उच्चगती चित्रीकरणाची मांडणी तयार केली. आम्ही पाहिले की पुटिकांच्या आकाराचे थेंब सुरूवातीच्या टप्प्यात थेंबांना पुटिकांमध्ये रूपांतरीत करण्यासाठी इंटरफेसवर आकार निवडक क्रॉसिंग असल्याचे दिसून येते. या व्यतिरिक्त पुटिकांमधील अपेक्षित घटक पेशीपटलाच्या निर्मितीवर संभाव्य परिणाम करू शकतात.

अध्याय ४ मध्ये आम्ही पेशीचा एक भाग असलेल्या माइटोटिक स्पिंडलची पुनर्बांधणी करण्याच्या दिशेने पहिले पाऊल म्हणून, पुटिकांमध्ये ट्युब्युलिन आवरणीकृत करण्याचा प्रयत्न केला. तथापि ट्युब्युलिन हे काम करण्यासाठी एक आव्हानात्मक प्रथिन आहे आणि त्यासाठी अतिशय विशिष्ट परिस्थितीची आवश्यकता असते हे लक्षात घेता, पूर्वीच्या अहवालानुसार, अतिशय विशिष्ट परिस्थितीत आवरणीकरण शक्य आहे, तरीही आम्हाला आमच्या प्रयत्नात मर्यादित यश मिळाले. पुटिकांमध्ये ट्युब्युलिन आवरणीकृत करण्यासाठी आम्ही cDICE तसेच इतर पद्धती वापरल्या, परंतु त्याचे सकारात्मक परिणाम कमी मिळाले. ट्युब्युलिनच्या पेशी पटलासह परस्पर क्रियांचे थेट निरिक्षण दर्शविते की ते पेशीपटलाला विस्कळित करते. जरी आम्हाला अद्याप पुरेशी स्पष्टता मिळाली नसली तरी, आम्हाला माहित आहे की या परस्पर क्रियांमुळे त्री आयामी (थ्री डी) पेशी सारख्या बंदिस्त परिस्थितीत तर्कुतंतुंना एकत्र जोडण्याच्या आमच्या प्रयत्नांना अडथळा निर्माण झाला.

म्हणून आम्ही पात्र बदलले आणि इमल्शन थेंबांकडे वळलो. अध्याय ५ मध्ये आम्ही थेंबांच्या आत मूलभूत घटकांची पुनर्रचना करण्यावर लक्ष केंद्रित केले. प्रथम वैयक्तिक घटकांच्या आवरणीकरणाचे वैशिष्ट्यीकरण करणे आणि नंतर एका मागून एक अधिक घटक जोडून पुनर्रचनेची गुंतागुंती वाढवणे ही कल्पना होती. आम्ही एकल घटकांशी संबंधित पेशीय प्रक्रियांचे भाग वैशिष्ट्यीकृत केले, ज्यात ॲस्टर निर्मिती केंद्रकाची (न्युक्लिअस) स्थिती आणि ॲक्टिन कॉर्टेक्सची निर्मिती यांचा समावेश आहे. नंतर आम्ही त्यांना एकत्र केले जेणे करून बंदिस्त परिस्थितीत ते एकमेकांवर कसे प्रभाव टाकतात ते पाहता येईल. आम्ही त्यांना बाह्यरीत्या नियंत्रित करण्याचे मार्ग देखील शोधले. पुढील अध्याय ६ मध्ये आम्ही तर्कुतंतू बांधण्याचा पुन्हा प्रयत्न केला, पण यावेळी थेंबांमध्ये आम्ही आधी वर्णन केल्याप्रमाणे अनेक ॲस्टर, मोटर प्रथिने आणि क्रॉसलिंकर सारख्या वेगवेगळया घटकांना एकत्र थेंबाच्या आत एक मूलभूत माइटोटिक तर्कुतंतू पुन्हा तयार केला. आमच्या पुनर्रचनेची गुंतागुंती वाढवण्याच्या उद्देशाने आम्ही नंतर कॅनोरहॅब्डायटिस एलिगन्स गर्भाच्या पहिल्या पेशी विभाजनात आढळलेल्या तर्कुतंतूच्या असममित स्थितीची नक्कल करण्याचा निर्णय घेतला. आम्ही पेशीपटलावर उपस्थित असलेल्या डायनेन, मोटर घटकांमध्ये नियंत्रित करण्यासाठी प्रकाश जैवीक साधन, इम्प्रूव्ह्ड लाईट-इंड्यूस्ड डाइमर (iLID) सादर केले. आम्हाला आढळले की व्दिस्तरीय पेशी पटलावर iLID काम करते. परंतु थेंबांच्या आत प्रकाश क्रियाशीलतेच्या समस्यांचा सामना करावा लागला. यामुळे कमीत कमी पुनर्रचित तर्कुतंतुला असममितपणे बंदिस्त परिस्थितीत पुनर्रस्थित करण्याचे आमचे प्रयत्न मर्यादित झाले. माइटोटिक तर्कुतंतू एकत्र करणे हे एक अत्यंत आव्हानात्मक कार्य आहे.

गुंतागुंतीचे युकॅरियोटिक तर्कुतंतू तयार करण्याच्या प्रयत्नात अडचणींचा सामना केल्यानंतर, आम्ही एक पाऊल मागे घेण्याचा विचार केला, व्यापक दृष्टिकोन ठेवला आणि आमच्या शिकलेल्या गोष्टींना वापरून काही सोपे तयार करण्याचा विचार केला. आम्ही विचारले, वैयक्तिक घटकांच्या मूलभूत गोष्टी समजून घेतल्यास, आपण संपूर्ण पेशी केवळ किमान घटकांसह आणि अगदी सुरूवातीपासूनच तयार करू शकतो का? या पूर्वीच किमान कृत्रिम पेशी तयार करण्यासाठी प्रयत्न केले जात आहेत. अध्याय ७ मध्ये आम्ही पेशी कंकालच्या आमच्या समजूतीसह कृत्रिम पेशींमध्ये योगदान देतो आणि डी.एन.ए. पृथक्करणासाठी किमान तर्कुतंतूची योजना करतो. प्रथम आम्ही ParMRC, एक जीवाणु डी.एन.ए. विभाजन प्रणालीची इन विट्रो पुनर्रचना केली ही एक सोपी प्रणाली आहे. ज्यामध्ये फक्त तीन घटक आहेत. पुढे आम्ही iLID वापरून बाह्यरित्या त्याचे नियमन करण्याचा प्रयत्न केला. आम्ही जुळणी करणारा प्रथिन, ParR मध्ये सुधारणा करून ते प्रकाश सक्रियक्षम बनवले. वैयक्तिक घटक सामान्यपणे

कार्य करत असले तरी संपूर्ण प्रणाली अद्याप कार्यरत नाही. सदर योजनेला आणखी बारीक सारीक समायोजनाची आवश्यकता आहे.

शेवटी अध्याय ८ मध्ये आम्ही आमच्या निष्कर्षांचा सारांश आणि दोन वेगवेगळया डी.एन.ए. पृथक्करण यंत्रांच्या जोडणी दरम्यान आम्हाला आलेल्या आव्हानांचा, गुंतागुंतीच्या वेगवेगळया स्तरांवर आणि त्यांना कमी करण्याचा प्रयत्न करण्याचे संभाव्य मार्ग यांचा सारांश व चर्चा करतो. किमान स्वरूपात पेशीचा एक भाग किंवा कृत्रिम पेशी अगदी सुरूवातीपासुन तयार करण्याचा प्रयत्न करणे हे एक महत्वाकांक्षी ध्येय वाटते. जरी अशी पुनर्रचित प्रणाली नैसर्गिक पेशींच्या फक्त काही गुणधर्माची नक्कल करू शकते. तरीही ती नवीन मूलभूत अंतर्दृष्टी मिळविण्यास मदत करते. माझे काम मेदापासून पेशीपटल कसे बनते, हे पेशीपटल ट्युब्युलिनच्या परस्पर क्रियांमुळे कसे विस्कळित होऊ शकते, आणि मेद पेशीपटल — सजीवांना निर्जीवांपासून वेगळा करणारा घटक, ला टिकवून ठेवण्यासाठी परस्पर क्रियांन्वयीत पेशीकंकालीय प्रथिनांना कार्यशील कसे ठेवायचे या बद्दल आपल्या समजुतीमध्ये सुधारणा करते.

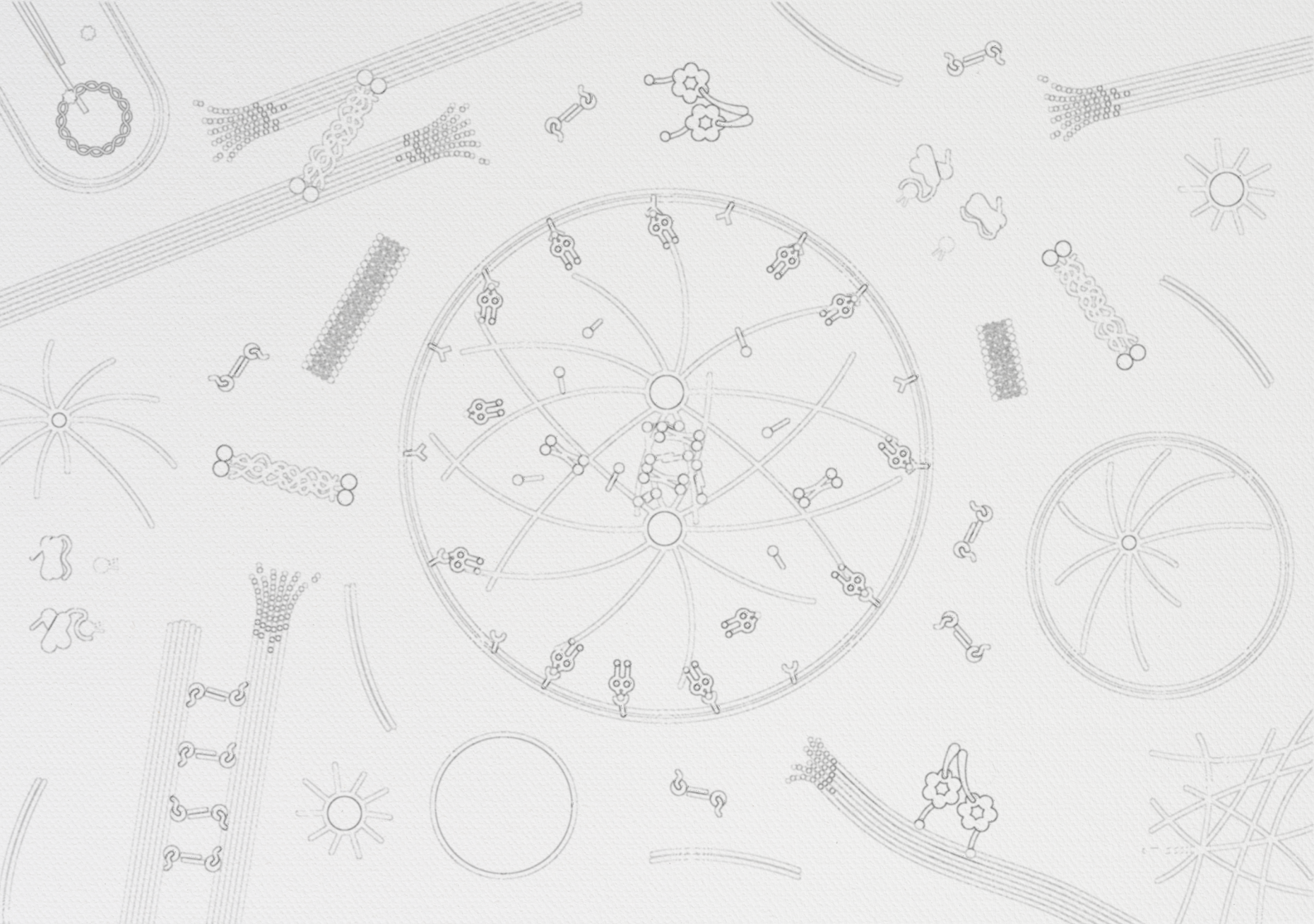

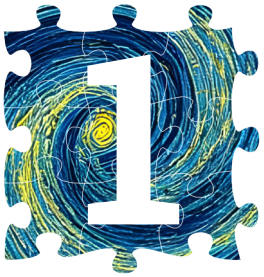

Introduction

Ship of theseus.
Reap what you sow.

The cell is the fundamental unit of life, which performs various processes essential to growth, division and survival. Despite being the foundation of life, a cell is composed of smaller, non-living components. This brings us to a question: What truly gives rise to life? Here, we provide a general overview of the cytoskeletal components, their properties, and their role in cytoskeleton remodelling during cellular processes, with a focus on microtubule and aster-based nuclear and spindle positioning. We describe the two strategies, top-down and bottom-up, used to study these cellular processes and lay the foundations of this work, explaining our overall motivation for investigating asymmetric spindle positioning. We also discuss the motivation for creating a synthetic cell and a synthetic spindle. Finally, a chapter-wise outline of this thesis is provided.

The cell

Life and the universe are unarguably the two most complex mysteries for humans to solve. Despite major scientific advancements, open questions remains on the origin of the universe and that of life. What is so unique about life form on earth? Are they the only ones in the universe? "Where is everybody?" asks the Fermi paradox [1]. Attempts have been made to potentially explain the paradox [2, 3], but what is life? While there is precise definition, there exist several debatable ones[1] [5]. "Life is a self-sustained chemical system capable of undergoing Darwinian evolution"[2] is one of the examples. The fundamental unit of life is a cell (Fig. 1.1). A biologist's view on a cell can be something that grows, divides and responds to its environment [7]. While a physicist would like to say, it's a only bag of proteins that keeps evading thermodynamic decay and remains out of equilibrium [8, 9].

1.1 Cellular processes

Life at the cellular level is quite robust. Cells pass on genetic information to daughter cells, maintain cellular metabolism and replicate to ensure their survival. Cells perform several processes like transport, signaling, migration and division [11]. They adapt to their environment and evolve over time. This resilience emerges from a complex, interconnected network of biochemical signaling pathways. These pathways are a part of different cellular processes. The interconnected pathways provide for redundancy in the system. At the mechanical core of this signaling network lies the cytoskeleton, that plays an important role in cellular function. Alterations in the interaction between signaling pathways and the cytoskeleton are known to disrupt cellular function, potentially leading to various disease states [12].

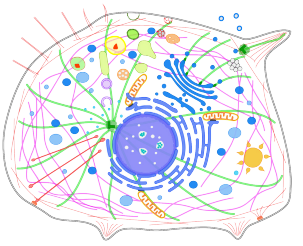

Figure 1.1: **What is a cell?** A eukaryotic cell with a collection/organization of proteins in a lipid bilayer membrane (adapted from SwissBioPics [10]). [ ]

1.1.1 The cytoskeleton

The cytoskeleton is a complex and dynamic network of protein filaments that extend across the cytoplasm of eukaryotic cells [13, §16]. This network helps cells to maintain their structural integrity, drives cellular mobility, and allows for cell polarization and differentiation. It's ability to rapidly remodel itself enables cells to respond to stimuli and maintain homeostasis. The cytoskeleton consists of three main types of filaments: actin filaments (AFs) (review [14, 15]), intermediate filaments (IFs) (review [16, 17]), and microtubules (MTs) (review [18, 19]). Each filament-type has its own set of binding and crosslinking proteins. These components play an important role in various critical cellular processes.

[1] The 132 definitions of life [4].
[2] Definitions by Horowitz & Miller [6], frequently used by NASA.

Microtubules

MTs are composed of **heterodimers** of α- and β- tubulin (55 kDa each) [20] (Fig. 1.2). These heterodimers assemble head-to-tail into slightly curved protofilaments. Predominantly *in vivo*, **thirteen** such protofilaments associate laterally, straightening to form a hollow cylinder, a 'tubule', with diameter⌀ **25 nm** (inner diameter 14 nm) and length ranging from ∼1 µm to ∼100 µm [21]. In an MT lattice[3], typically the distance between heterodimers within the protofilament (height) is ∼81.7 Å (81.2–84.5 Å), the distance between protofilaments (width) is ∼53.1 Å, and the depth is ∼47.4 Å [22–24]. MTs are rigid polymers with persistence lengths of 4.2 ± 0.3–6.6 ± 0.9 mm [25–27]. The number of protofilaments in MTs spontaneously assembled *in vitro* vary between 9 and 16, with majority having 14 protofilaments [28, 29]. A 13 protofilament MT forms a B-type lattice with a left-handed 3-start helix **seam**. The protofilaments are straight, with no helical pitch and the monomers in the protofilaments have α to α and β to β lateral interactions, except at the seam [30, 31].

Tubulins need cytosolic chaperonin CCT (TriC, TCP1, or Ct-cpn60) for its proper **folding** [32] along with other cofactors (see review [33])[4,5]. This results in formation of α/β-tubulin heterodimer, with GDP bound β-tubulin (at exchangeable or E-site) [36] and GTP bound α-tubulin (at non-exchangeable or N-site), which remains non-hydrolyzable [37]. Hence, tubulin is purified as α/β-tubulin heterodimer [38].

The protofilaments are polar due to the asymmetry of the tubulin heterodimer, which exposes β-tubulin (with a hydrolyzable nucleotide) at one end of the protofilament creating a fast-growing **plus end** and α-tubulin at the other end creating a slow-growing **minus end**. MTs show '**dynamic instability**' [40, 41], wherein they stochastically switch between phases of **growth** and **shrinkage**. The change from growing state to shrinking state is called a '**catastrophe**' and that from shrinking state to growing state is called a '**rescue**'. A third state, called a 'pause', is rarely observed and not fully understood. Dynamic instability is characterized by rates of growth and shrinkage, and frequencies of catastrophe[6] and rescue[7].

GTP-tubulin association rate depends on tubulin concentration and temperature[8] [44], and is constant during growth and shrinkage, being greater at the plus end of an MT than at the minus end. This GTP is hydrolysed soon after polymerization into GDP·P_i and subsequently, the P_i is released. On the other hand, the GDP-tubulin disassociation rate differs vastly (∼500 x) during growth and shrinkage and is not concentration-dependent [45]. Upon **GTP hydrolysis**, tubulin undergoes a change in conformation, straight (0–5° bend) to curved (10–12° bend) [46, 47], and expanded

[3] Dimensions of tubulin heterodimer have variations based to the tubulin nucleotide-state, tubulin isotypes, lattice type, and interactions with MAPs. Furthermore, the structural data lacks the information about the disordered surface loops and tails. Mentioned dimensions are based of the PDB 6DPV, a 13-3 undecorated GDP MT from wild boar.

[4] Therefore, bacterial expression of tubulin is not possible and tubulin is purified from brain. Recently, protocols for insect-cell expression of genetically modified tubulin have been developed [34, 35]

[5] Chaperones and cofactors interact with tubulin with its hydrophobic patches during heterodimer formation and ensure structural integrity in an aqueous environment.

[6] The rate of switching from a growing to a shrinking state.

[7] The rate of switching from a shrinking to a growing state.

[8] Tubulin adapts according to the organism's body temperature or environment to optimize the polymerization rate [42, 43].

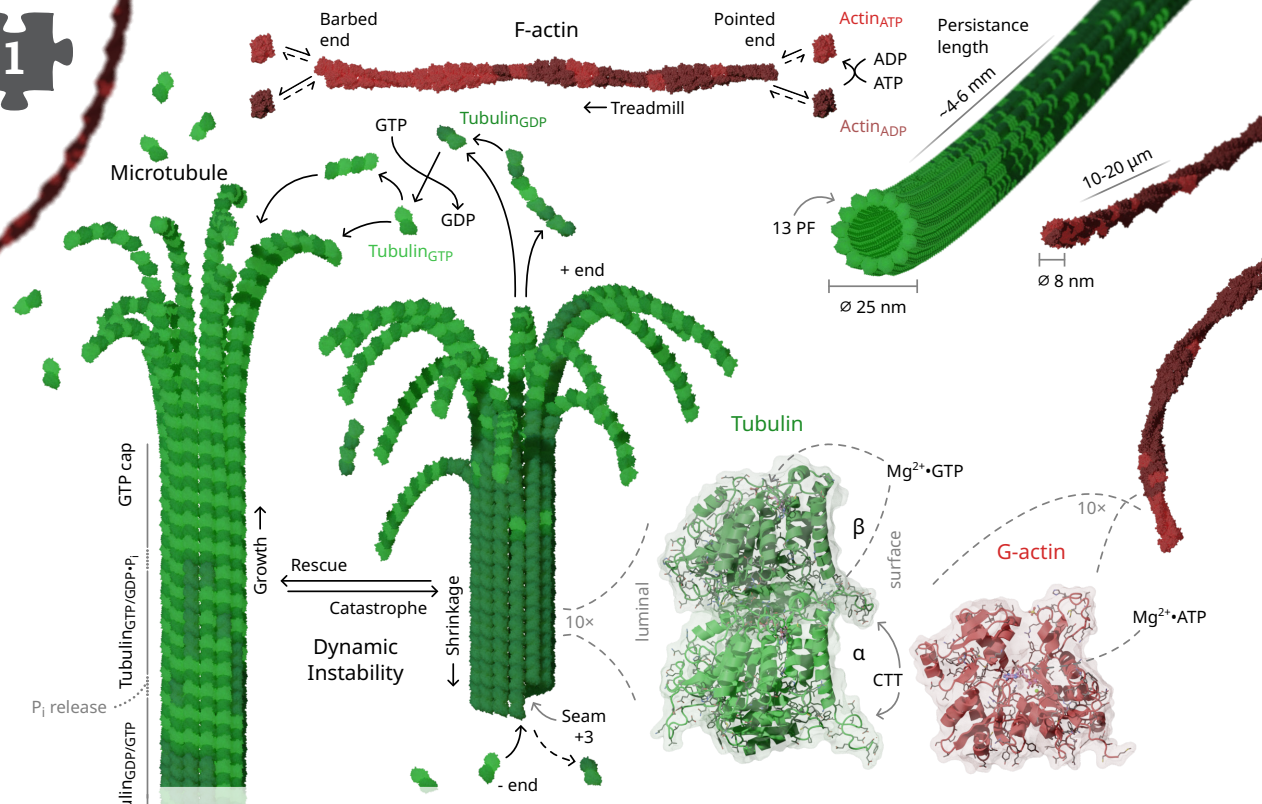

Figure 1.2: **Cytoskeleton and its dynamics.** (Top) Actin filament treadmilling, actin monomers added at barbed (plus) end and removed from pointed (minus) end at same rate. (Left) MT dynamic instability. MTs grow with the addition of GTP dimers. The GTP dimer-rich region at plus end is called a 'GTP cap', which prevents catastrophe. GTP in β-tubulin hydrolyses slowly. The polymerizing MT undergoes catastrophe and starts depolymerizing and during a rescue, the shrinking MT starts growing again. The helical pitch of protofilaments creates a mis-match of 1.5 dimers, called a 'seam'. (Right middle) Structure of actin monomer (PDB 5MVY) and tubulin heterodimer (a modified PDB 3J6E) with α- and β-tubulin. (Right bottom) Cross-section view of MT (⌀ 25 nm, 13 protofilaments) and actin (⌀ 8 nm). Image rendered in Blender [39]. [ ]

((4.210 ± 0.012) nm) to compact ((4.100 ± 0.002) nm) [48, 49]. This leads to lateral weakening and longitudinal reinforcement, which creates strain in MT lattice, as it is energetically unfavourable. This explains the **crown**, sheets, tapered, or zipping appearance of protofilaments in a polymerizing state and the **horns**, peeling, unzipping, or blunt ends in a depolymerizing state [50, 51]. The depolymerized curved oligomers of GDP-tubulin tend to form rings [47, 50, 52]. GTP hydrolysis is required for dynamic instability [53] but not for MT polymerization.

The delay between the GTP hydrolysis after addition of the tubulin dimer leads to the formation of so-called **GTP cap** at the growing end [54]. The cap is hypothesized to stabilize the growing end and prevent catastrophe. The quantitative evidence of

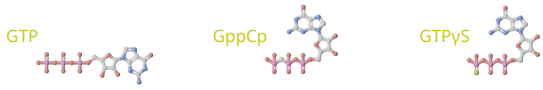

the long postulated GTP cap have been recently demonstrated [55], with the end-binding (EB) protein's ability to bind GTP-tubulin [56, 57]. While GTP cap can be long, but the minimum size of cap at the MT end required for stabilization is still not clear, ranges from monolayer cap (i.e. one GTP-tubulin per protofilament) [58–60], <40 subunits [61] to 700–750 subunits [62, 63]. The MT length distributions also become linearly dependent on tubulin concentration. In bulk, they show steady state, but individual MTs exhibit constant fluctuation as a result of dynamic instability. MTs can be stabilized with a GTP analog (GTPγS, non-hydrolyzable) [64], a GTP mimic (GMPCPP, very slowly hydrolyzable) [65], chemicals (such as taxol) [66], mutant tubulin (E254D, non-catalysing) [55] or with stabilizer MAPs (TOG-domain) [67]. Certain drugs also affect MT dynamics: *Paclitaxel* (binds taxane site[9]; e.g. docetaxel) to stabilize polymerized MTs, *Colchicine* (binds to colchicine domain), and *Vinca* alkaloids (binds to vinca domain; e.g. vinblastine) suppress MT dynamics at low concentrations and depolymerize MT at high concentrations [70].

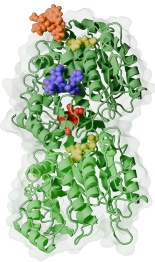

There are five main families, the α-, β-, γ-, δ-, and ε-tubulins [71]. Tubulins have differential expression of alternative genes and different functional roles [72, 73]. α/β-tubulin heterodimer polymerizes into MTs, γ-tubulin helps nucleate MTs, and δ-, and ε-tubulins are associated with centrioles and have diverse organisms specific roles. Human genome contains nine genes (**isotypes**) each for α- and β-tubulins [74]. These tubulin isotypes are highly conserved across most eukaryotes. The ζ-tubulin, the sixth tubulin family, lost in evolution, found in very few eukaryotes (not present in humans), and thought to have a similar role to that of a δ-tubulin [75].

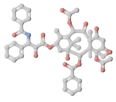
Paclitaxel

The C-terminal of α- (10–12 a a) and β-tubulin (16–22 a a) is negatively charged, very acidic and highly disordered [76, 77]. These tails (E-hooks) are located on the outer surface of MTs (every 4 nm longitudinally, and 5 nm laterally)[10] and act as key regulators for interaction of many MT-binding proteins (MTBPs) or MT-associated proteins (MAPs)s. As opposed to the conserved amino acid sequence of the tubulin body (80–95 %), the tails have sequence variations (∼50 %). Another level of variety comes from the **posttranslational modifications** (PTMs) of tubulin, mostly on the tails. The tail is subjected to PTMs like phosphorylation, detyrosination (/re-tyrosination), glutamylation, and glycylation[11], and the tubulin body to additional PTMs like acetylation, methylation, palmitoylation, ubiquitylation, phosphorylation, and polyamination (see reviews [78, 79]). Tyrosination, glutamylation and glycylation are performed by a family of enzymes, tubulin tyrosine ligase (TTL) and similar tubulin tyrosine ligase-like (TTLL). And the modifications from TTL and TTLLs are removed by carboxypeptidases (CCPs). Detyrosination is performed by vasohibin (VASH), and acetylation[12] by acetyltransferase (TAT). PTMs have shown to affect the biochemical, physical, mechanical, polymerization (nucleation, dynamics, and stability), and MAP-related properties of MTs. The combination of differential expression of tubulin isotypes together with an extensive number of possible combinations of

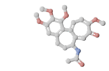
Colchicine

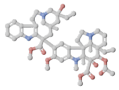
Vinblastine

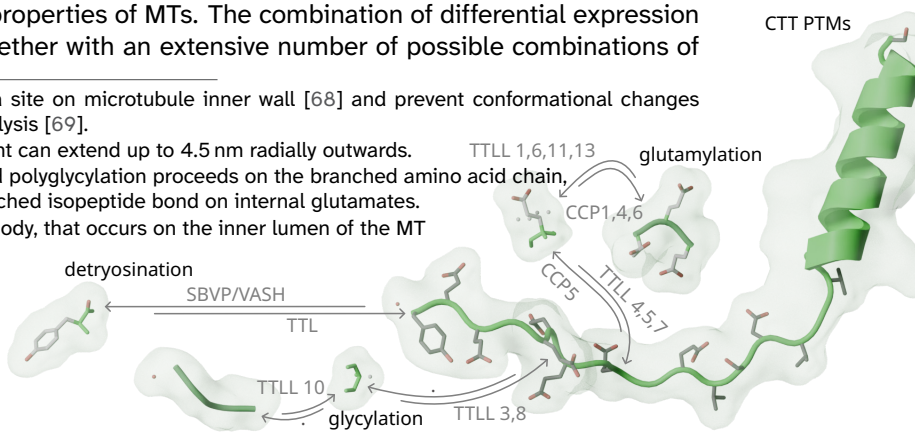

[9] Paclitaxel drugs bind at a site on microtubule inner wall [68] and prevent conformational changes arising due to GTP hydrolysis [69].

[10] The tails when fully straight can extend up to 4.5 nm radially outwards.

[11] The polyglutamylation and polyglycylation proceeds on the branched amino acid chain, formed through a γ-branched isopeptide bond on internal glutamates.

[12] Only PTM on the tubulin body, that occurs on the inner lumen of the MT

PTMs reconstitutes the **tubulin code** [80]. Even slight perturbations to PTMs on MTs affects cell physiology and lead to various motility and neuronal diseases.

Critical to the polymerization dynamics is the nucleation of the MTs. **Nucleation** from pure tubulin is an energetically unfavourable and highly cooperative process. It is nucleation rate (τ) limiting and depends on tubulin concentration (C), $\frac{1}{\tau} \propto C^{12\pm2}$ [81–83]. Basics of MT nucleation and polymerization can be explained even with a simple model for single polymer [84, §4][85]. The model explains, **critical concentration** for polymerization (C^*_{poly}) — at which the rate of association and dissociation are the same, and critical nucleus size (N) — subunits required to assemble stable nucleus, but fails to explain, critical concentration for nucleation (C^*_{nuc}) — at which nucleus is likely to be formed. Spontaneous formation of MT is rare unless tubulin concentration is very high. Typically C^*_{nuc} is ∼20 µM for *de novo* **spontaneous nucleation**, but C^*_{poly} is only ∼1 µM for the elongation from existing MT seed (for mammalian tubulin [83, 86]). Following complex models explore MT properties, like multistep nucleation [87], accretion-based nucleation [88], and bound-unbound growth [89, 90], and simulations (molecular dynamics, Brownian, Monte-Carlo) for individual MT dynamics [91–93]. The nucleation barrier can be lowered with use of chemicals (e.g. GMPCPP [65]), small molecule crowding (e.g. glycerol [94]) and stabilizing drugs (e.g. Taxol [66]).

MT assembly can be aided with a **template** (a stable scaffold for assembly) or a non-template (facilitate longitudinal or lateral subunit interactions with MAPs) based nucleation (see [95]). Centrosomes are the microtubule organising centres (MTOCs), the primary source of MTs, in the cells. Majority of MTs emerging from the centrosomes originate from several γ-tubulin ring complexes (**γTuRC**), each of which has a lock-washer-shaped structure, and is present in the pericentriolar material (PCM) [96, 97]. γTuRC, an asymmetric left-handed spiral, is composed of 14 γ-tubulin small complex (γTuSC or spokes). Each γTuSC contains a copy of γ-tubulin and one of five γ-tubulin complex proteins (GCP, GCP2–6). α-tubulin has more affinity for γ-tubulin than β-tubulin. This helps in MT nucleation by favouring dimer assembly on the template. These γTuSCs assemble on γTuSC receptors (e.g. CDK5RAP2) complex (see [98]). The γTuRC also has luminal MOZART[13] (Mzt1), for targeting γTuRC at MTOC, and actin, for positioning γTuRC on MTs, and NEDD1 on the outside, which acts as an adaptor for the Augmin complex (HAUS). Augmin complex recruits γTuRC on sides of preformed MTs, and creates branch nucleation point [99]. γTuRC is a 14-subunit complex, but interestingly nucleates 13 protofilament MTs. Recently, the γTuRC conformational change from open to closed state, where the first and the last γTuSC in the helix overlaps and create a 13 γ-tubulin template with 3-start seam, was discovered, explaining the high nucleation efficiency of 13 protofilament MTs from γTuRC [100–102]. CAMSAP[14], in absence of CDK5RAP2, can bind to partially close γTuRC and facilitate the release of γTuRC capped MTs [103]. The critical concentration for nucleation from a template is lowed, $C^*_{template} >\sim 6$ µM [86]. Nucleus assembly is still unfavourable on a template but less than spontaneous.

[13] Mitotic spindle organizing protein associated with a ring of γ-tubulin
[14] Calmodulin-regulated spectrin-associated protein

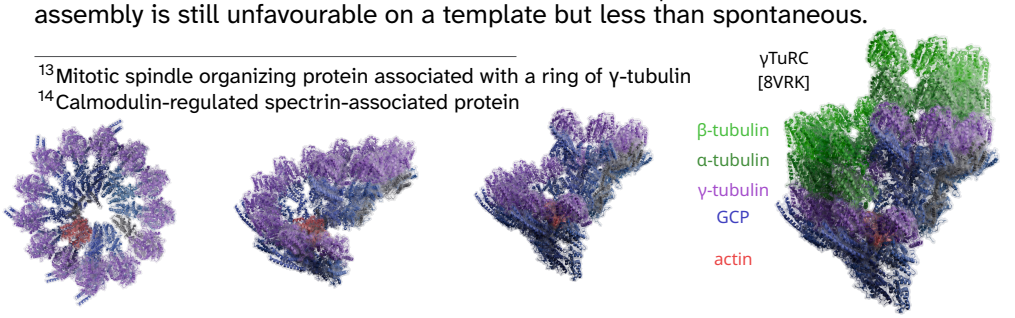

Non-templated pathways include MAPs like MT polymerases of XMAP215 family proteins (with TOG[15] domains) which promote longitudinal elongation, promoting spontaneous nucleation, accelerating growth, while synergizing with γTuRC [86, 104–106], MT suppressors such as TPX2[16], which stabilize MT ends and aid nucleation by stabilizing nucleus intermediates [107], and CLASP[17] and CAMSAP which also work together or independent of γTuRC (see [67]).

In conclusion, the dynamic nature of microtubules is central to their function in the cell. Understanding the mechanisms underlying microtubule dynamics provides insights into various cellular processes.

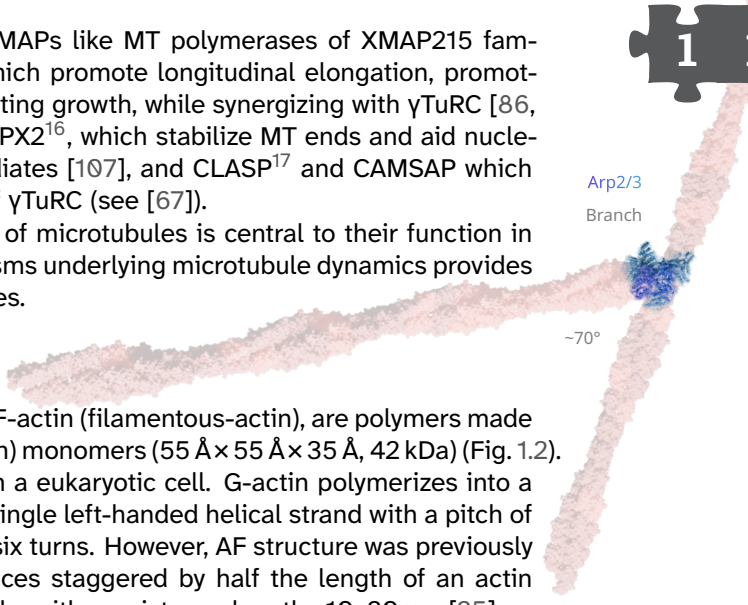

Actin filaments

AFs also known as microfilaments or F-actin (filamentous-actin), are polymers made of G-actin (monomeric-/globular-actin) monomers (55 Å × 55 Å × 35 Å, 42 kDa) (Fig. 1.2). Actin is the most abundant protein in a eukaryotic cell. G-actin polymerizes into a **5–9 nm** wide thread, consisting of a single left-handed helical strand with a pitch of 13 G-actin subunits, repeating every six turns. However, AF structure was previously interpreted as two right-handed helices staggered by half the length of an actin monomer[18] [108–110]. AFs are flexible, with persistence lengths 10–20 µm [25].

There are three main **isoforms** of actin, α-actin (3 genes, one each for skeletal, cardiac, and smooth muscle cells), β-actin (one gene, non-muscle cells), and γ-actin (2 genes, one each for smooth and non-muscle cells). Actin is highly conserved (375 a a), and the isoforms only differ in a few amino acids at the N-terminus [111, 112]. Actin undergoes **PTMs** likes methylation (skeletal α-actin), N-terminus acetylation, cleavage and re-acetylation.

Actin[19] is a globular protein, with a deep medial cleft, and is classified into subdomains 1–4. ATP binds in the cleft. Upon incorporation of actin monomers in the filament, G-actin (globular) transition into F-actin (flat) [114]. The actin domains, subunits 1 and 2, undergo a propeller-twist (12–13°) that stimulates the ATPase activity of F-actin. After the hydrolysis and P_i release, the link between domains weakens, making ADP F-actin less stable than ADP G-actin[20]. Thus, the actin filament is readily disassembled.

Actin polymerizes spontaneously in the presence of monovalent or divalent ions. Polymerization can be explained with simple model. Although the polymerization process is nucleation-rate limited (as that of tubulin), the actin nucleus size (N) 3–4 is much smaller compared to tubulin [84, 85]. AFs are polar, with a fast-growing **barbed end**, and a slow-growing **pointed end** due to the structure of the G-actin monomer subunit. Above a critical concentration (C^*_{poly}), AFs grow at both the barbed end (0.12 µM) and the pointed end (0.62 µM), maintaining sufficient ATP-

[15] Tumor overexpressed gene
[16] TPX2 (Targeting protein for Xklp2); kinesin-like protein
[17] CLIP-associated protein; Clip-like proteins
[18] The –166.6° twist per molecule being close to 180°, the structure appears like two slowly turning right-handed strands.
[19] Actin is purified from rabbit skeletal muscle acetone powder [113].
[20] F-actin is flatter than G-actin.

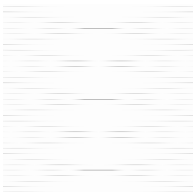
Ideal actin diffraction pattern (FFT)

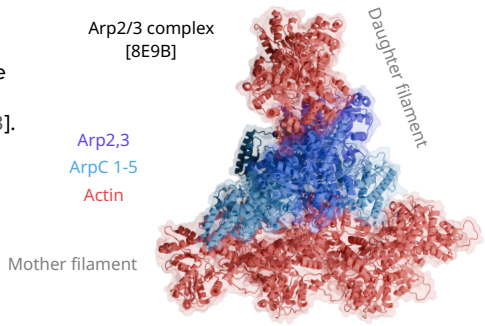

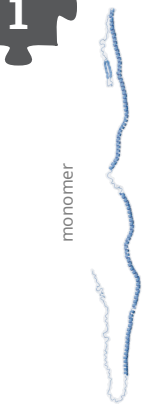

bound G-actin monomers at both ends [115]. While below that concentration, ATP to ADP hydrolysis catches with new monomer addition at the slow-growing pointed end, causing the actin to depolymerize. Interestingly, at the 'critical concentration', the barbed end grows at the same speed at which the pointed end is shrinking. This is known as **treadmilling** of filaments[21].

Actin dynamics is influenced by small molecules, such as phalloidin (stabilizes by preventing depolymerization [117]), cytochalasin D (inhibits both further association and dissociation of monomers by binding to the barbed end), and latrunculin A and B (inhibit polymerization by binding in the cleft [118]).

Actin polymerization is aided by nucleation proteins. Arp[22]2/3 complex blocks the pointed end of actin filament and nucleates filaments that elongate from barbed ends. Nucleation is facilitated by stabilizing polymerization intermediates. The newly branched actin is rigid and stable, and at a relatively constant (70 ± 7)° angle [119]. The Arp2/3 complex is recruited by verprolin-cofilin-acidic (VCA) and needs activation by cofactors (such as WAVE[23]), while formins create unbranched actin filaments, by stabilizing actin dimers. Further, α-actinin cross-links two actin filaments.

Intermediate filaments

IFs are double-helical filaments with diameter **~10 nm**, and as their name suggests, have a size intermediate to that of MTs and AFs. IFs form 58 nm long and 16 nm wide unit-length filaments (**ULFs**). Each ULF is composed of eight tetramers, and each tetramer is composed of two antiparallel dimers. IFs are apolar or nonpolar, due to the antiparallel tetramers. Unlike AFs and MTs, which are composed of a few isoforms, the IFs have a large genetic variation (67 human genes) [120]. However, the basic subunit of IFs has conserved length and hydrophobic patches. The monomer follows a **tripartite** organization with a central α-helical rod domain flanked by non-α-helical domains on either ends. They are classified into five major **classes** - I (e.g. keratins a), II (e.g. keratins b), III (e.g. vimentin), IV (e.g. neuro filaments), and V (e.g. lamins) and an orphan class (see review [17]). IFs also undergo **PTMs**, particularly phosphorylation, glycosylation, sumoylation, and acetylation.

IFs are nucleotide independent and undergo self-assembly. Their growth rate is limited by slow longitudinal association[24] of ULFs. IFs subunits are in equilibrium with the polymer[25]. They are flexible, extremely stable, and form a mesh network. This gives rise to viscoelastic properties, which provides cells and nuclei with mechanical support, and resistance to extracellular stress. Different IFs have cell-specific roles, organelle (e.g. nucleus, mitochondria) positioning and membrane trafficking. In case of external stress, they also regulate a cell's ability to grow, divide, migrate or apoptosis (see review [16]).

[21] Slow turnover <1 subunit/s in cells [116].
[22] actin-related protein
[23] WASp family verprolin homologous protein; Wiskott-Aldrich syndrome protein
[24] Order of magnitude of days.
[25] Rate of one out of 200 tetramers per hour

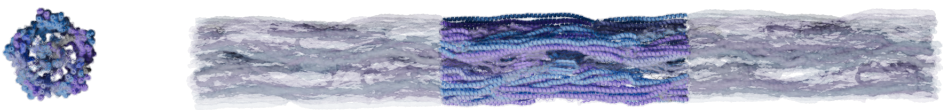

Motors and Associated proteins

Many proteins bind cytoskeleton filaments and are associated with them, and are therefore called MT-associated proteins/MT-binding proteins (MAPs/MTBPs), actin-related proteins/actin-binding proteins (ARPs/ABPs) and associated proteins (APs) for respective IFs. These proteins regulate filament dynamics and organization, and even have certain cell-specific roles, thus playing an important role in cellular functioning. Imbalances in the levels of these proteins disrupt the physiological state and cause pathologies (see [121]).

MAPs are broadly classified as stabilizers, destabilizers, capping, and cross-linkers [18]. Stabilizers promote polymerization and some examples are EB1–3, CLIPs, NDC80 (also grouped as MT plus end tracking proteins (+TIPs)), and XMAP215, CLASP, STOP, and doublecortin (see [122]). Destabilizers increase overall dimer dissociation, and stathmin is one such MAP. These also include severing proteins such as, katanin, spastin, fidgetin, which cut MTs (see [123]). Capping MAPs are usually associated with minus ends and include γTuRC and CAMSAPs, while MAP65 (Ase1/PRC1) is an example of bundler or cross-linker [124]. Integrators like Tau, MAP2, MAP4 coat MT lattice [125].

ABPs include the following classes: Profilin family proteins (bind and cap G-actin and prevent assembly), cofilin family proteins (induce depolymerization), gelsolin family proteins (sever actin filaments), and cross-linkers like fimbrin and filamin (see [14]).

Motors are the other interesting class of APs. Three superfamilies of motor proteins can enable directed movement and generate forces: Kinesin and dynein motors on MTs and myosin motors on AFs. Kinesin and myosin are ATPases[26], whereas dynein is an AAA ATPase (see [126]).

Different cytoskeletal filaments often interact and work together in various cellular processes, and their dynamics and function is tightly integrated. This is known as cytoskeletal **crosstalk**, and is facilitated by a set of associated proteins (mostly +TIP MAPs and capping ABPs), which are specialized and cell-specific. This crosstalk coordinates actin-MT crosslinking, MT guidance, MT stabilization, MT anchoring, MT growth barrier, AF nucleation, spindle positioning and orientation, and regulates cell migration, division, polarization, axon growth, specification, and maintenance (see [127, 128]).

1.1.2 Cytoskeletal remodelling

During various cellular processes, the cytoskeleton of the cell undergoes extensive remodelling, often changing the shape and size of the cell. During these changes, MT network transforms the most at the global cellular level, even though the actin network may have more turnover, but the changes are mostly confined locally. Aster formation and positioning accounts for most of this MT network reorganization and requires significant amount of force with precious control and coordination.

[26] Share a common ancestor related to GTPases.

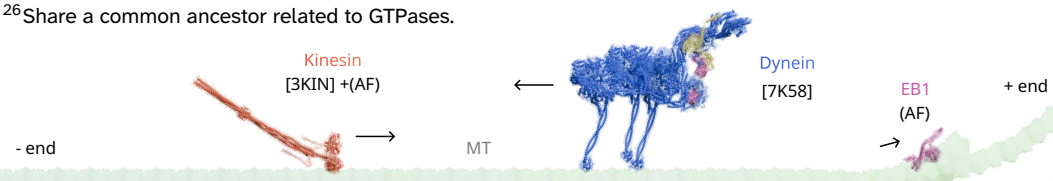

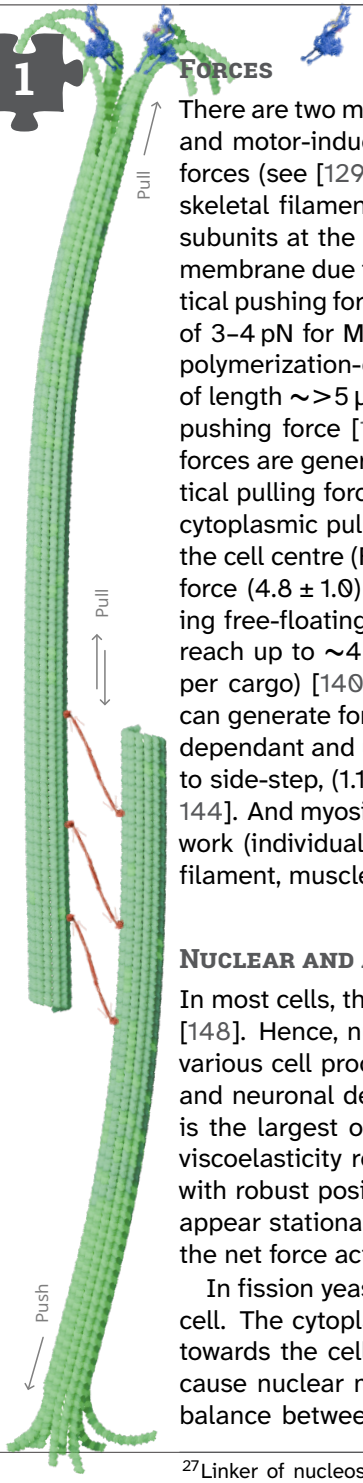

Forces

There are two main sources of cytoskeletal forces in the cell — polymerization forces and motor-induced forces. These forces can be classified as pushing and pulling forces (see [129]). Pushing forces are polymerization forces, generated when cytoskeletal filaments hit the membrane and keep growing with continual addition of subunits at the tip as a result of frequent gaps formed in-between the tip and the membrane due to thermal fluctuations (Brownian ratchet model), also known as cortical pushing force (Fig. 1.3). *In vitro* experiments have demonstrated pushing forces of 3–4 pN for MTs [26, 130–132], and $\ll$1 pN ($\sim$0.035–0.06 pN) for actin [133], by polymerization-driven growth against a barrier. This force is length-dependent; MTs of length $\sim>5$ µm buckle under this force, rendering them ineffective in generating pushing force [134, 135]. Motors can generate different types of forces. Pulling forces are generated by transport of dynein on MTs. This force is also known as cortical pulling force when MT ends are captured by membrane-bound dynein, and as cytoplasmic pulling force when cargoes are transported on MTs by dynein towards the cell centre (Fig. 1.3). *In vitro* experiments have demonstrated dynein generating force (4.8 ± 1.0) pN by pulling MTs [136–138], and $\sim$0.9 pN force due to drag during free-floating transport assay in a viscous environment [139]. These forces can reach up to $\sim$4 pN *in vivo* cargo transport (which involves multiple dynein motors per cargo) [140]. Kinesin superfamily of motor proteins, with their vast diversity, can generate forces ranging from $\lesssim$0 pN to 5–6 pN [141, 142]. These forces are ATP dependant and usually occur in anti-parallel MTs overlaps. Kinesins are also known to side-step, (1.1 ± 0.2)°, and generate rotational torque upto $\sim$(32 ± 15) pNnm [143, 144]. And myosin generates contractile forces of $\sim$1–2 pN in a crosslinked actin network (individual, non-muscle) [145, 146] and $\sim$10.5–17 pN in sarcomeres (myosin-filament, muscles) [147].

Nuclear and aster positioning

In most cells, the nucleus and the MTOC (centrosome) are usually linked by LINC[27] [148]. Hence, nuclear movement coincides with aster assembly and positioning in various cell processes involving morphogenetic events like embryogenesis, retinal and neuronal development, and epithelia and muscle cell formation. The nucleus is the largest organelle and requires significant force to move it, as cytoplasmic viscoelasticity resists large movements. Yet, nuclear positioning is highly precise with robust positioning mechanisms. In migratory cells, although the nucleus may appear stationary, it is constantly moving in the direction of cellular movement, as the net force acting on it is zero [149].

In fission yeast, the interphase nucleus is actively positioned in the middle of the cell. The cytoplasmic MTs form anti parallel bundles with their plus ends growing towards the cell poles [150, 151]. These MT bundles exert pushing forces, which cause nuclear movement, but centering of the nucleus is achieved as a result of balance between pushing forces from opposite poles [152, 153]. The balance is

[27] Linker of nucleoskeleton and cytoskeleton (LINC) complexes composed of KASH and SUN protein bridges.

also regulated by MAPs like Ase1 (PRC1), Tip1 (CLIP170) and Mal3 (EB3).

In budding yeast, the nucleus is moved into the bud neck. MTs originate from the MTOC and are tracked into the bud on polarized actin cables [154]. The MTs off load dynein on the membrane at the cortex in the bud [155], and this dynein generates pulling forces required for nuclear oscillation and positioning [156] [157].

In eggs and embryos of metazoans like worm, fly, frog and mouse, pronuclei apposition or migrate, eventually meeting and fusing in the middle of the cell. Centering of the male pronucleus requires MTs to polymerize from its MTOC, which exert cortical pushing force [158] or cytoplasmic pulling force [159, 160]. On the other hand, the female pronucleus is transported on the aster by dynein towards the male pronucleus for fusion [161]. These mechanisms are classified into two types: 'MTOC-dependent nuclear positioning' and 'nuclear tracking along microtubules' respectively [162]. The nucleus remains in the centre until DNA segregation and cell division, due to the balance of forces generated by motor and MT polymerization dynamics, to facilitate the formation of two equal blastomeres. At times, in early embryos and stem cells, the nucleus position asymmetrically, aiding developmental changes in daughter cells.

Asymmetric positioning of the nucleus also occurs in syncytial systems, multinucleated non-dividing cells, such as skeletal muscle cells, fly embryos, worm hypodermis, slime mould, and filamentous fungi, where several nuclei get positioned at the cell periphery (see [166]). In *Drosophila*, the early embryo undergoes multiple rapid nuclear division without cytokinesis. These nuclei are positioned equidistantly and require both actin and microtubules [167]. Astral MTs generate optimal separ-

Figure 1.3: **Nucleus and spindle positioning.** (bottom) Schematic of ♂*C. elegans* (Image adapted from J. J. Froehlich, CC BY-SA 4.0). (left) Pronuclear migration, nuclear centering, and asymmetric spindle positioning during *C. elegans* embryo first cell division (Tubulin, MTs, asters, and DNA, chromosomes, nucleus). Movie adapted from [163]. [ ] (right) Different pushing and pulling forces involved in the nucleus and spindle positioning, and biophysical parameters (boxes) influencing them. (Schematic adapted from [164], based on [165].)

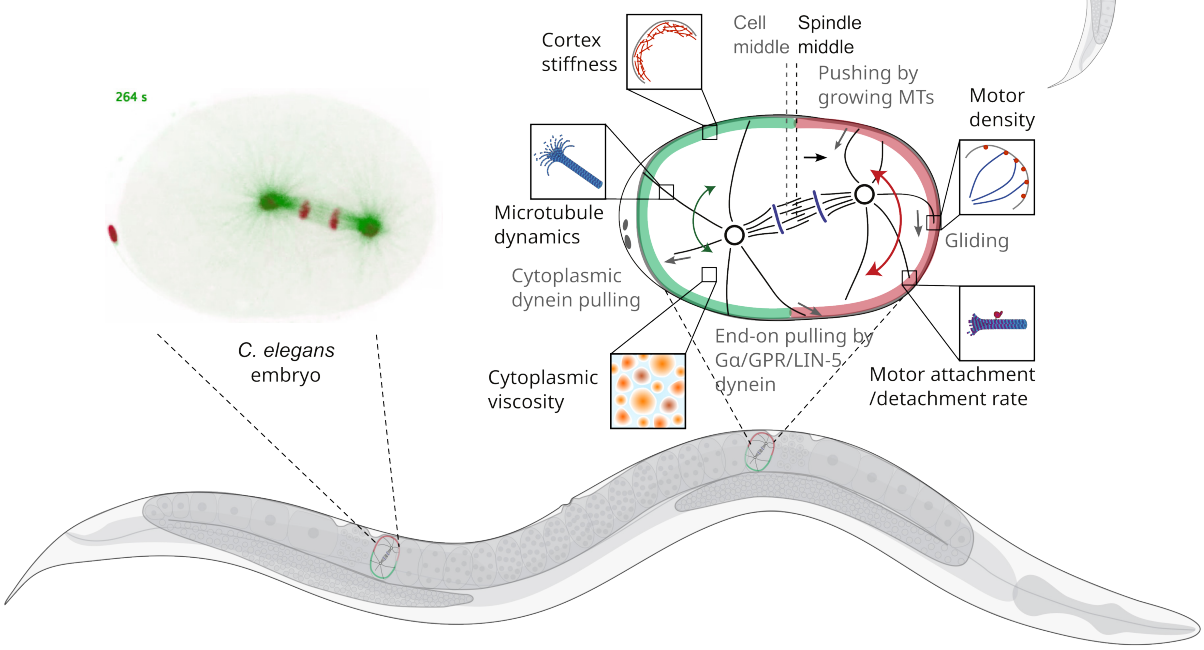

ation between neighbouring sister nuclei by repelling each other and with cytoplasmic pulling forces [168], independent of cell cortex, to prevent fusion. Further, actin forms a cap (enclosure) around each nucleus to confine them [169]. Although nuclear positioning mechanisms in eggs and embryos are species- and cell-specific, similarities can be seen across them. Overall, nuclear positioning plays a crucial role in development, and positioning abnormalities may lead to disease.

Spindle positioning

Spindle assembly and positioning follows nuclear positioning in most above-mentioned cases of dividing cells. The mitotic spindle is self-organized [170] and has three primary roles — (1) assemble and orient the spindle (Hertwig's rule [171]), (2) align chromosomes to form metaphase plate, and (3) segregate chromosomes, while maintaining spindle size [172]. Centrosomes (MTOCs) and chromosomes are the main organizers of the mitotic spindle. The mitotic spindle is assembled from MTs originating from centrosomes (MTOCs, the eventual poles of the spindle), while some MTs also originate from kinetochores and within the spindle (see [173–175]). MTs emerging from the centrosomes are called interpolar MTs (I-MTs) if they create an antiparallel overlap with MTs from opposing poles and make the central spindle, or astral MTs (A-MTs) if they extend away from the poles towards the cell membrane. MTs emerging from the kinetochores of chromosomes are called K-MTs (bundles of K-MTs called as K-fibres [176]). K-MTs help capture and align chromosomes on spindle midplane and later segregate them [177]. Segregation of chromosomes towards the poles also involves MT pulling forces generated by depolymerizing K-MTs at the kinetochore (reverse Brownian ratchet [178]). Forces generated at single kinetochore ranges around ∼5–6 pN/MT[179]. A-MTs help in spindle orientation and positioning [180]. I-MTs stabilize the spindle in the metaphase and help in pole separation in anaphase [173]. The central spindle overlap is mainly organized by MAPs like Eg5[28] [181], PRC1[29] [182], spindlin, and CPC[30] [183]. The overlap also helps in coordinating the positioning of the division plane (actomyosin contractile ring) during the cytokinesis [127]. Many MAPs including motors, help assemble the spindle and segregate chromosomes by regulating MT dynamics [184]. Furthermore, cell size and shape influence spindle positioning [185].

Similar to nuclear positioning, spindle positioning also depends on the forces generated by MTs. For fission yeast cells (∼5 µm), the nucleus and the spindle can be positioned simply by pushing forces. However, cell size varies by orders of magnitude from budding yeast (∼5 µm) to frog embryo (∼1200 µm). In smaller cells (∼<100 µm), MTs from asters can grow and reach the cortex to exert pushing forces. On the other hand, in large cells, pushing forces become inefficient, either due to buckling of long MTs ($F \propto \frac{1}{l^2}$) [26, 134, 135] or the inability of MTs to reach the cortex. Despite this, spindle is symmetrically positioned in sea urchin embryo (∼120 µm), and Xenopus embryo (∼1200 µm), and asymmetrically positioned in budding yeast

[28] A homotetrameric kinesin 5, also KIF11
[29] Protein regulator of cytokinesis 1 / MAP65 / Ase1 (abnormal spindle elongation 1)
[30] Chromosome passenger complex

(∼5 µm) [186], *Caenorhabditis elegans* embryo (∼50 µm), and Drosophila embryo (∼500 µm) [187]. So, it is suggested that larger cells rely on MT pulling forces, either cytoplasmic [188] or cortical. This poses the question, how does the spindle find the centre of the cell? [189]. The spindle operates in a state of dynamic equilibrium, with forces being continuously generated and balanced. A push-pull model is proposed for a coordinated balance of forces to ensure proper spindle positioning [190]. A general theory for the positioning mechanics of asters in confined geometries has been developed and it helps understand force balance in various different cellular circumstances [191].

The first division of *C. elegans* embryo is a well-studied model (Fig. 1.3). It is known that the embryo gets rapidly polarized after fertilization, and PAR[31] proteins are responsible for this cell polarity [192]. Perturbing PAR proteins disrupts asymmetric spindle positioning [193]. Also, dynein is critical for spindle dynamics [160]. Grill et al. [194] showed clear evidence for cortical pulling forces in *C. elegans*, and presence of asymmetric distribution of force generating complexes (FGC) at the cortex [195]. FGC contains G-protein signaling receptor proteins Gα, GPR-1/2 (LGN), LIN-5 (NuMA) [196] and dynein (which is recruited to the cortex directly or indirectly via NuMA) [197, 198]. Dynein binds the A-MTs in an end-on configuration and generate pulling forces by minus end-directed transport and MT depolymerization [136, 199]. The PAR domains remodel actomyosin cytoskeleton and redistribute the FGC, with more FGC density on the posterior side. This results in more net cortical pulling force from the posterior pole, and eventual posterior displacement of the spindle, leading to asymmetric cell division.

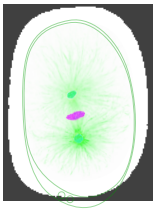

The spindle length increases as chromosomes are separated during anaphase [200]. This is governed by the crosslinking proteins, Eg5 and PRC1 (Ase1), which regulated the overlap between antiparallel MTs in the central spindle. Eg5 can bundle and slide across antiparallel MTs to increase the overlap [201, 202]. The magnitude of pushing force generated by Eg5 is proportional to the length of the overlap [203]. Ase1 is a passive diffusible that also cross-links antiparallel MTs but decreases the overlap overtime. It acts as compressible gas, increasing entropic forces as it is compacted in smaller overlaps [204]. Even though force per molecule is 0.1–0.2 pN [205], with enough molecules, a force of few pN can be generated, enough to resist Eg5 motors. It also prevents a complete breakdown of sliding overlap [206].

Recently, Garzon-Coral et al. [158] made precise measurement of forces in spindle positioning using magnetic tweezers, ∼100 pN was required to displace a spindle pole [158]. Pushing forces acting on the spindle arise from ∼200 A-MTs. It is also argued that in subsequent cell division, spindle positioning is mainly due to cortical pushing, while cortical pulling and cytoplasmic pulling interfere and oppose it. The *C. elegans* first cell division mechanism is more complex, wherein the spindle exhibits rocking oscillatory motion while it is segregating chromosomes. This motion varies in frequency and amplitude in both lateral and longitudinal axes across different worm species [207]. Also, the cytoplasmic viscosity changes ∼6 x across species, affecting the cytoplasmic pulling [208]. Other cytoskeletal components and upstream regulatory pathway, along with the shape of the embryo, control the

[31] for partitioning defective proteins

Spindle and the cell (embryo) (scale x500)

Xenopus Drosophila Sea urchin *C. elegans* Budding yeast

precise dynamic of the spindle. This helps us understand some underlying force generating mechanisms in spindle positioning.

Acentrosomal spindle can also be self-organized around chromosomes. Chromosomes release Ras-related nuclear protein (RCC1), which activates RanGTP-ase and nucleators, creating a gradient of spindle assembly factors (SAFs), and generating numerous MTs. Along with MAPs and motors like Eg5 and dynein, these MTs can form a spindle with pole-focusing (see [209]).

The mitotic spindle, with its complex architecture and dynamic nature, is central to the process of cell division. Understanding its structure, dynamics, and regulation provides insights into the fundamental mechanisms of cell division and has implications for diseases in which cell division is dysregulated.

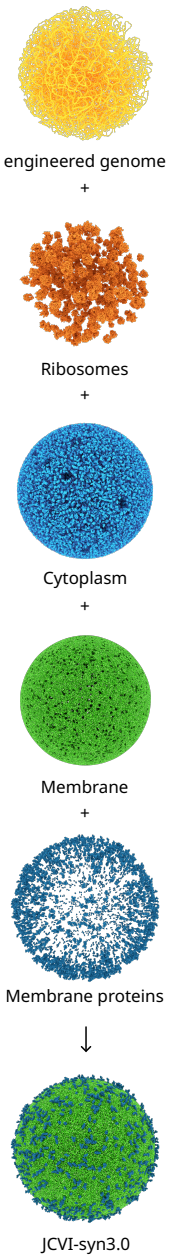

1.2 Approaches

A cell is a small, but complex entity, with thousands of genes, and performs various functions. Scientists are curious to know how the cell (the first cell, or even the protocell) was created, the underlying mechanisms of each function, and the fundamental role of each protein. To understand the cell, the following two approaches are followed [210].

1.2.1 Top down

One way to answer this question is to dissect the system one molecule at a time. It has traditionally been used in cell biology. A single gene in the cell is perturbed, either removed by knock-out/deletion, knock-down/RNAi-silencing, mutation or added to rescue (in knock-out/down), over-expressed, to characterize its physiological function. (Co-)purifying proteins associated with the gene helps to identify their interactions. This is a common approach traditionally used in *in vivo* cell biology experiments and is called the '**Top-down**' approach (see [211]). Many important proteins and cellular functions were discovered using this approach. This method is also incorporated with orthogonal spatio temporal control, like optogenetics and auxin-inducible degron (AID) system. However, with this approach, understanding of the system is often limited to a qualitative level.

With the rise of synthetic biology in the last decade, a new focus on minimal genome has emerged. It is a quest to create the ultimate efficient organism. Instead of removing a single gene, the genome is stripped down to the absolute minimum number of genes. The idea is to remove the redundancies and reduce the complexity, to create an organism that can be completely characterized (Fig. 1.4). This will improve its engineerability, increase biosynthetic capacity and allow for refunctionalization [212]. It is like taking the top-down approach further down. Genome reduction with traditional methods has yielded limited but promising results.[32] *Escherichia coli* (MG1655) genome (4.64 Mb), in which the function of only ∼48.9 % genes is known, has been reduced to 3.26 Mb (Δ16 strain, with slow growth and

[32] Attempts also made on *Bacillus subtilis*, *Streptomyces avermitilis* and *Schizosaccharomyces pombe* genome.

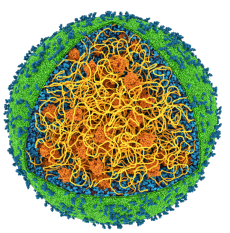

abnormal shape [213]) and smallest to 2.83 Mb (Δ33a strain, sensitive to oxidative stress [214]). With modern DNA synthesis and ligation, genomes can be synthesized from scratch. Starting with a genome from bacteria with the smallest genome (525 genes), *Mycoplasma genitalium*, a minimal synthetic functional genome (with predicted minimum 375 genes) was synthesized and transplanted in *Mycoplasma mycoides*, JCVI-syn1.0 (*Mycoplasma laboratorium*) was created [215]. Recent strains JCVI-syn3.0 (473 genes) and JCVI-syn3A (493 genes), with optimized genome for physiology, still have ∼20 % genes of unknown function. Further, JCVI-syn3.0+126 requires additional 7 ftsZ related genes to fix cell size and division defects [216]. This still has three times more genes compared to the proposed theoretical minimum of 151 genes [217].

This points towards our current limitation in understanding of the genome and cellular processes. Also, the understanding of the system remains limited.

1.2.2 Bottom up

The other way to answer the question is to build life from scratch [218, 219]. Individual proteins involved in complex processes are studied in isolation (or with a few other proteins). Single molecule *in vitro* experiments with purified proteins help dissect the exact role of each protein. This approach is called the '**Bottom-up**' approach [211]. Using techniques like single-molecule imaging, optical tweezers, and

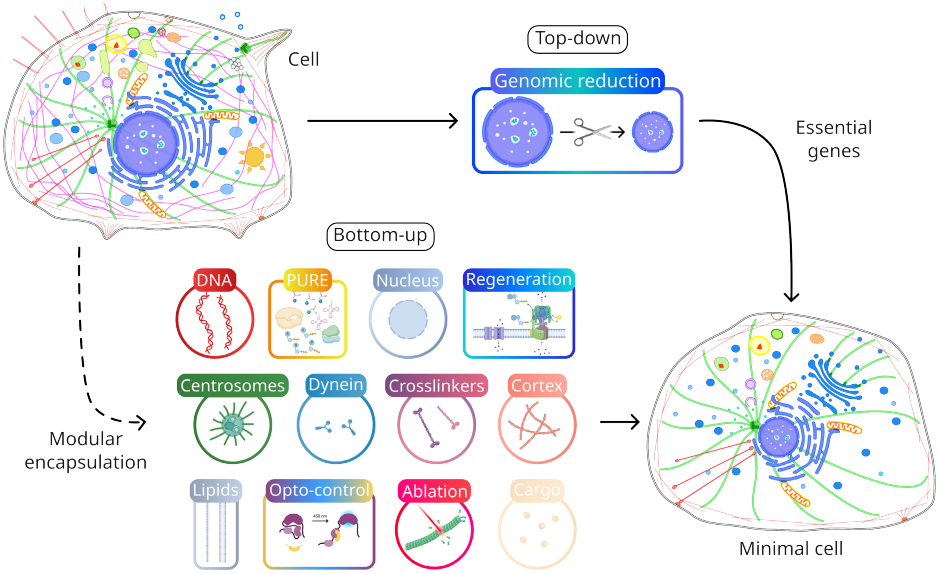

Figure 1.4: **Building a minimal cell.** Understanding cell and cellular processes with minimal cell using either Top-down or Bottom-up approach. [| click on interactive buttons] (Images adapted from SwissBioPics [10] and partially created with BioRender.com)

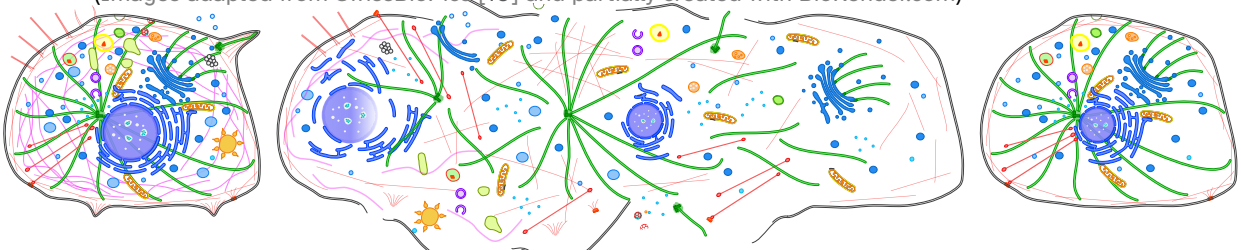

AFM[33], properties of many important proteins were studied in this approach.

In vitro bulk reconstitutions offer precise quantitative and mechanistic understanding of individual proteins or a few proteins together, but their role at the system level remains unclear. Will confining a minimal set of proteins in a 3D container such as the lipid bilayer membrane of a cell lead to emergence of more complex properties and self organization? This can help build up the complexity of bottom-up reconstitution. Compartmentalization due to encapsulation is proposed to help build complex dynamic out of equilibrium system [220], but it comes with limitations. As all known life-forms have some form of phospholipid coating [221], here, we would like to define this class of experiments as '*in artificio*'[34]. It means mimicking cellular environment, chemically and physically. With a set of purified proteins (or even multiple interacting proteins) of choice or even expressed *de novo* in the IVTT system[35], can be encapsulated to create a custom synthetic minimal cell that mimics any cellular process (Fig. 1.4). The use of unnatural (e.g. chimeric) components (DNA, protein, lipids[36]) along with tools for direct and indirect manipulation like optogenetics, magnetic tweezers, laser ablation, could potentially help to gain better control and understanding of the system. However, encapsulation is challenging, especially with lipid bilayers.

Since the last few decades, with the rise of synthetic biology, a new focus on modularity has emerged. Instead of a single gene, modules (i.e. operons or networks) with multiple genes are studied with increasing complexity. It is like building the bottom a step further up. Genes, considered as fundamental unit of information in life, bio-bricks [224], are swapped (like Lego pieces) or mixed across species with the aim of not only getting fundamental insights by building upon existing systems, but also creating new functionalities. Since these are mostly expressed *in vivo* or cell-free extracts, one should consider interaction and influence from other cellular components, and preferably use IVTT systems like PURE [225] (Fig. 1.4). Several new gene circuits have been developed to regulate and modulate organisms [226]. Synthetic biology has its challenges, but also lots of potential for further innovation [227].

Both top-down and bottom-up approaches focus on developing methods for building and manipulating life, but the end goal is to understand, engineer, and program life.

1.3 Reconstituting a spindle

Here, we focus on the bottom-up approach to understand aster positioning and spindle assembly, since the basics of spindle positioning have been well studied with the basic top-down approach, and for advanced top-down approach, a eukaryotic

[33] Atomic Force Microscopy

[34] Not *in vivo*, since proteins are not inside their natural environment i.e. cell, and not *in vitro*, as they are not completely outside (cell), but in an artificial cell-like confinement.

[35] A minimal *in vitro* transcription-translation system of known composition.

[36] Bio-compatible synthetic components (e.g. synthetic chemical polymers [222, 223]) have been developed too.

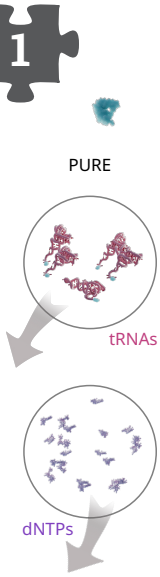

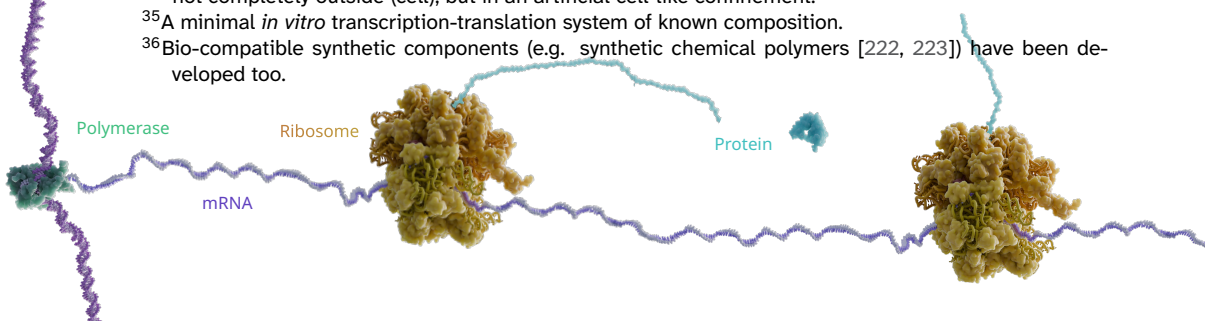

system with a minimal genome for spindle characterization has not been developed yet.

1.3.1 Towards building a spindle

The foundation of a complex, dynamic, functional mitotic spindle reconstitution has been in the works since decades. Individual components have been characterized and reconstituted *in vitro* in geometries with increasing dimensionality [228].

In a typical *in vitro* reconstitution of MT dynamics assay in flow chambers[37], MTs have infinite space to grow in principle. Therefore, experiments with artificial 1D barriers[38,39] were designed to confine the growth of free MTs [60]. MTs were nucleated from MT seeds attached to the glass surface. MTs grow and encounter the barrier, if the MT keeps growing it eventually buckle and bends, and if MT growth is stalled, it cannot exert enough pushing force [60, 131]. These MTs eventually shrink as they experience increased catastrophe frequency [131, 231]. Dynein is known to walk processively on MT towards the minus end, and generate force ∼(4.8 ± 1.0) pN [138]. The (end-on) cortical interaction between dynein and MTs were reconstituted in 1D barriers. Dynein was recruited on gold barriers with biotin-thiol chemistry [229, 230, 232]. The MT end is captured by dynein: it inhibits its growth and triggers MT catastrophe, generating force (2.0 ± 1.4) pN [136]. Depolymerizing MTs are shown to generate ∼5 pN force [233].

Next, experiments were designed to observe the interaction of arrays of MTs, e.g. aster (MTOCs), with the 2D confinement, square chambers[40]. MT asters (22 µM tubulin) were nucleated from purified centrosomes[41]. Dynein was similarly attached to gold barrier and the chamber was sealed with a thin PDMS lid. In the absence of dynein, the MTs from asters grow against the walls, create pushing forces, bend and buckle, and eventually get off-centre. In the presence of dynein at the walls (i.e. artificial cortex), MTs from the aster get trapped and position the aster in the centre of the chamber [136, 229].

Since cells are 3D objects, experiments of aster positioning were developed in 3D confinement including water-in-oil droplets[42]. Droplets were generated using a microfluidic device[43]. MT asters (34 µM tubulin) were nucleated from centrosomes. Dynein was recruited to the lipid cortex of the droplet with biotin-streptavidin biochemistry. In the absence of dynein, MTs grow long and reach the cortex, and eventually buckle and push the aster towards the cortex. In the presence of dynein at the cortex, MTs from the aster are equally pulled from all sides, and the aster positions itself in the centre of the droplet [228].

[37] Chamber size: 2 cm L × 2 mm W × 0.1 mm H

[38] Silicon oxide (SiO_2) barriers ∼100–250 nm high, with carbide (SiC) overhang cap ∼1 µm long.

[39] Multilayer barriers of gold (Au) ∼150 nm sandwich between chromium (Cr) and chromium or silicon oxide (SiO_2) overhang cap[229, 230].

[40] Chamber size: 10–15 µm × 10–15 µm × ∼2.5–2.7 mm H. Multilayer barriers of gold (Au) sandwich between chromium (Cr) and chromium or silicon oxide (SiO_2) overhang cap[136].

[41] Purified centrosomes from human lymphoblastic KE37 cell lines [234].

[42] Droplets with surfactant stabilized lipid monolayer. Droplet size: 15–20 µm

[43] T-junction: 12.5 µm. Device cast of PDMS. [235]

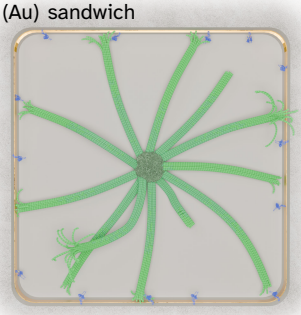

Some researchers also observed MT dynamics in confinement, in the presence of other cytoskeletal proteins. MTs and motors (kinesin) confined in pseudo-3D microwells can self-organize into different forms — vortices, asters, or bundles based on relative MT-motor concentrations [236]. Also, MTs and motors (kinesin-14) confined in 3D droplets can self-organize into different forms — cortex, ring-bundle, or even asters bundles based on relative MT-motor concentrations [237, 238]. Interaction of actin with aster MTs, through actin-MT cytolinkers, was also demonstrated in 3D droplets [239].

1.3.2 Asymmetric spindle positioning

A basic mitotic spindle can be assembled and positioned in 3D droplets. [235]. It involves two asters, dynein at the cortex, and kinesin and crosslinker in mid-spindle. The two asters, repelling each other and being pulling by cortical dynein, position slightly away from the cortex. The kinesin-5 and Ase1 create interpolar connection with antiparallel overlap. This mitotic spindle-like arrangement is positioned symmetrically in the centre of the droplet. It is a result of counterbalance between the aster repulsive and kinesin-5 pushing forces, and cortical and Ase1 meditated pulling forces.

As described earlier (Sec. 1.1.2), in a *C. elegans* embryo, the first cell division

Figure 1.5: **Project conceptualization.** Sketch of asymmetric spindle positioning project idea. [ ]

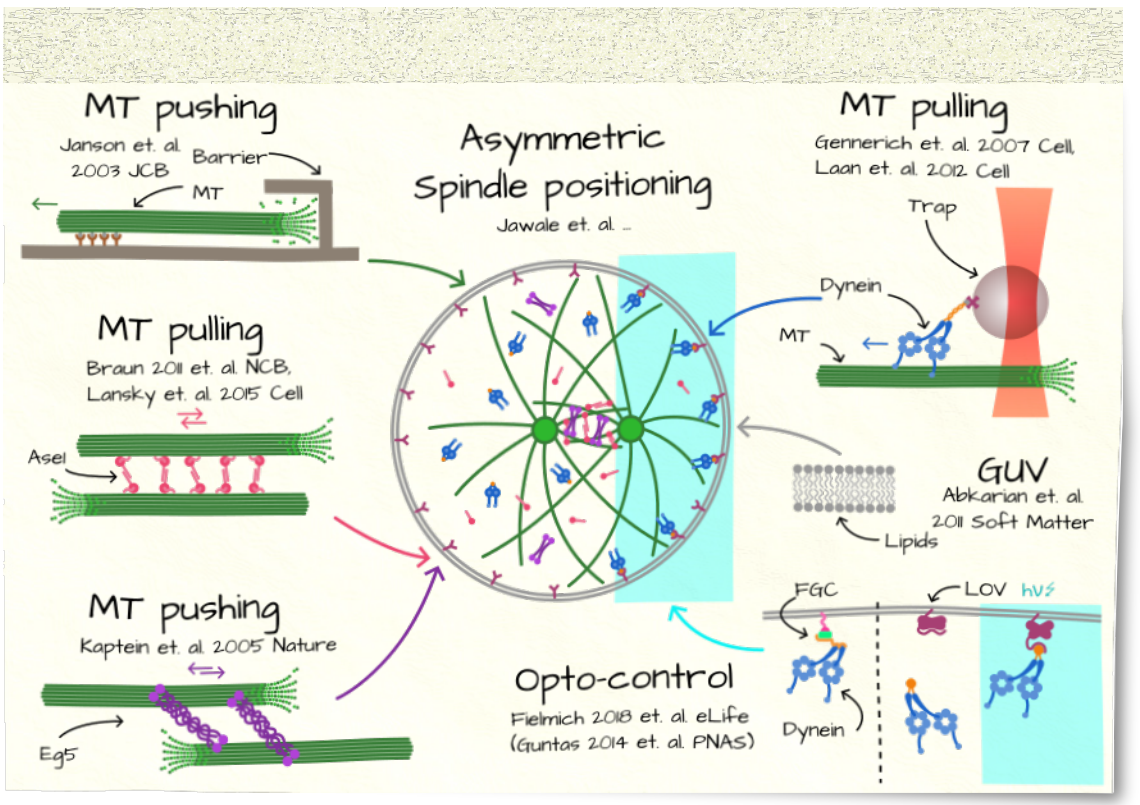

results in uneven daughter cells as a result of asymmetric spindle positioning. In this thesis, we attempt to reconstitute asymmetric spindle positioning in 3D confinement to recapture the spindle dynamics from the *C. elegans* first cell division (Fig. 1.5). It will increase the complexity of the above-mentioned minimal mitotic spindle reconstitution, further advancing the foundation towards eventually building a complex, dynamic mitotic spindle with features. This minimal spindle assembly and positioning assay would potentially be without cellular feedback, redundancies, and regulation, and will provide precise control on the environment while testing hypotheses and models generated from top-down *in vivo* work, and may provide better insights for understanding the underlying mechanisms.

The current minimal mitotic spindle is confined in a water-in-oil lipid monolayer droplet. Droplets have very high surface tension. Therefore, it is very difficult to deform their default spherical shape. Also, a droplet is a closed system. Changing the confinement container to liposomes, a lipid bilayer membrane vesicle, will help it make more cell-like. Furthermore, the *C. elegans* embryo is slightly elongated, which defines the natural axis for asymmetric spindle orientation and off-centering. Modulating the shape of confinement with cylindrical microfluidic trap helps to break the spherical symmetry. The crucial event responsible for posterior spindle displacement is the uneven distribution of dynein (force generating complex) at the cortex. An external control on dynein localization is required. Optogenetics tools like light-induced dimerization (iLID) [240] have been shown to provide spatiotemporal control over *in vivo* protein localization [241]. Fielmich et al. [163] demonstrated the use of optogenetics tools to create artificial asymmetric dynein distribution in *C. elegans* embryos. LIN-5, the only component of the FGC is required to achieve asymmetric spindle positioning. We design a similar iLID-based optogenetic system to facilitate asymmetric localization of dynein at the cortex in our experiments. We assume this would be potentially sufficient to recapture the displacement of the spindle away from the centre in our in vitro minimal reconstitution (Fig. 1.5).

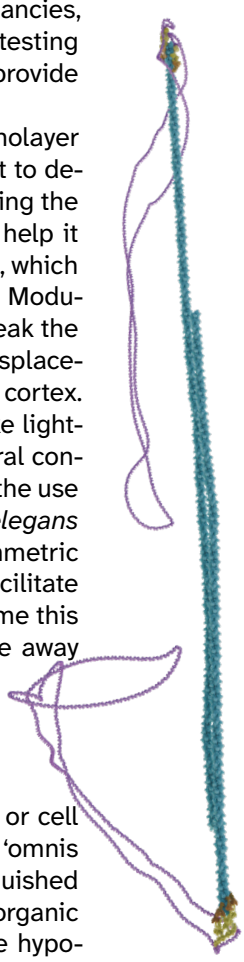

Minimal spindle

1.4 Minimal spindle for a synthetic cell

We started talking about cell (**??**). If not 'what', maybe 'how'? How did life or cell originate? It was believed cells comes from cells based on Virchow [242] 'omnis cellula e cellula', we know that now as well, but back then, that strictly distinguished living (organic) matter from non-living (non-organic). It was first shown that organic matter (urea) can be created from non-organic matter [243], leading to the hypothesis of chemical origins of life. Later, Miller [244] demonstrated the synthesis of building blocks of life from inorganic chemicals under conditions of the early earth [245]. This supported the Oparin-Haldane conjecture of primordial soup [246, 247], and idea of chemical origins of life. Giving rise to multiple models, including the RNA world, compartmentalistic approach, and enzyme-free metabolism [248].

Considering the limitations[44] of time, using similar principles, can be build a living object with non-living parts? Can we put together a simple mix of biological

[44] Inability to express and assemble ribosomes *in vitro* — the quintessential component for protein synthesis, just one of the example of the limitation.

components to self-organize into a minimal cell? [217]. If we understand the system and parts of the system, we should be able to build a synthetic cell[45]. A synthetic cell based on a natural cell requires a lipid membrane (boundary), central dogma (DNA⇄RNA⟶Protein, information transfer), and a metabolism (energy production) [249]. It should be able to perform the following cellular processes — DNA processing, cell fuelling, and cell division (Fig. 1.6). The above systems need to be modular, and integrated with each other spatiotemporally. Building a synthetic cell from scratch will allow us greater control, while potentially providing deeper insights and a better understanding of cellular functions.

Here, our focus is on developing a cell division module for the minimal synthetic cell. With overall understanding of DNA segregation and cell division mechanisms across various organisms, we design a minimal spindle compliant with the characteristics of a synthetic cell.

1.5 Thesis outline

In this chapter, we briefly discussed the cell and cellular processes, with a general overview of the cytoskeleton and its role in the remodelling underlying these cellular processes. The scope of this thesis falls under biophysics and synthetic biology domains, wherein I describe my work towards reconstitution of the DNA segregation machinery, with the aim of improving our understanding of it. For DNA segregation in the context of eukaryotic cells, the focus is on *in vitro* reconstituting an asymmetrically positioning mitotic spindle in terms of its biophysical properties, whereas in the context of a synthetic cell, the focus is on designing a minimal DNA segregation module as a proof-of-concept from a bottom-up synthetic biology point of view.

Compartmentalization is essential for both projects. We need encapsulation tech-

Figure 1.6: **Syncell.** Building a Synthetic Cell (BaSyC) with DNA processing, cell fueling, and cell division (Artist: Graham Johnson). [ ]

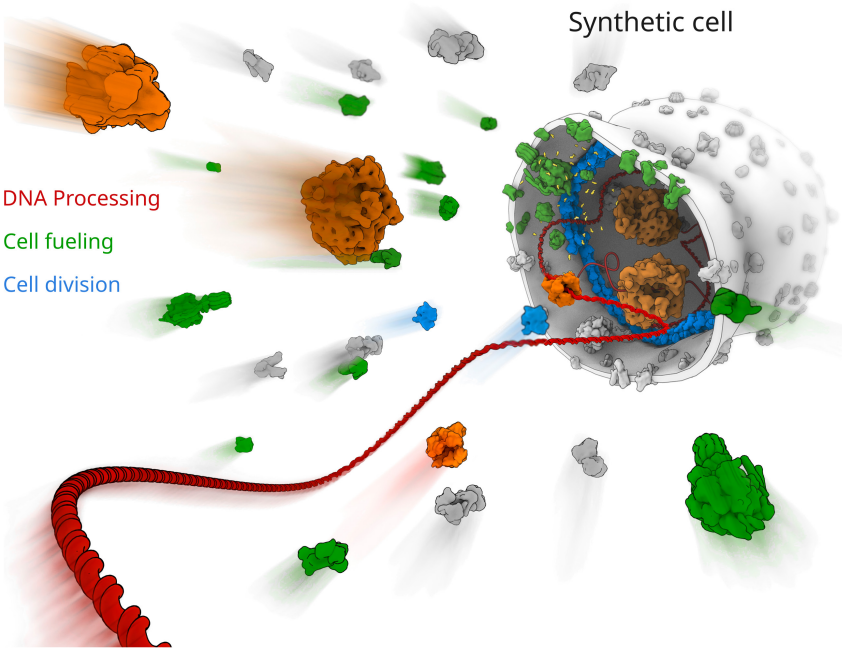

niques to create containers depending on the requirements of the system. In Chapter 2, we explore various methods to form containers, across different types of containers such as droplets and vesicles. Making the container is only the first step; ways of modulation of these containers are also crucial for eventual control. So, we also investigate the tools required for altering container content and its shape. We observe different advantages and disadvantages in the various encapsulation methods, no one method fits all the possible criteria. The eventual choice varies on a case-by-case basis. But in general, droplets are easiest to make, and cDICE is ideal for most GUV scenarios.

Of the many encapsulation methods we test, we explore one specific method named, cDICE, details of which are in Chapter 3. We are interested in optimizing the method for a better yield of the vesicles for our cytoskeletal system. We perform high-speed imaging of vesicle formation in the cDICE setup, and discover variations in the underlying vesicle formation process as well as size-selective crossing at the second oil-water interface. We study the effects of interactions of proteins with the organic phase, and explore trade-offs of varying certain parameters from the original protocol.

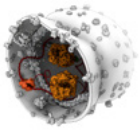

Next, being aware of potentially negative interactions of protein with the lipids, in Chapter 4, we attempt to encapsulate tubulin, the cytoskeletal component required for aster formation and positioning. We use various methods with different approaches to vesicle formation, in our attempts to successfully encapsulate tubulin. None of the methods seems sufficiently promising for tubulin encapsulation in vesicles and very few vesicles are seen with tubulin. Subsequently, a more direct observation of negative tubulin-lipid interactions provides evidence for the ineffectiveness of these encapsulation techniques. We observe that tubulin disrupts the lipid bilayer, even though the underlying mechanism for such destructive interactions remains unclear.

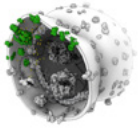

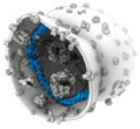

We then shift focus from vesicles to droplets for tubulin-based encapsulations. In Chapter 5, we characterize MTOCs for aster formation and build up the complexity of the 3D *in vitro* aster-based reconstitutions. We introduce two novel components, the nucleus (mimicked by a bead), and the actin cortex (as discussed in Sec. 1.1.2), to investigate their influence on aster positioning. Interestingly, the bead and the aster exhibit co-localization, and this contributes to centring of the aster. Co-encapsulation and co-polymerization of actin and tubulin for aster positioning in the presence of an actin cortex requires meticulous optimization, of which first results are reported.

Continuing to increase the complexity of the reconstitutions, in Chapter 6, we build on previous efforts of reconstituting the dynein-driven bipolar spindle positioning [250] to reconstitute asymmetric spindle positioning (Sec. 1.3.2). As a start, we replicate and compare results with previous work. Next, we attempt the incorporation of optogenetic tools for spatiotemporal control of dynein in droplets. We engineered molecular opto-control over the recruitment of dynein to the droplet interface, but so far with no success for photo-activation.

Further, in Chapter 7, we present a perspective on a minimal DNA segregation

[45] "What I cannot create, I do not understand" — Richard Feynman

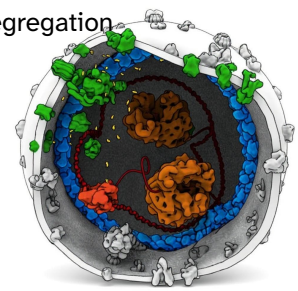

module for the synthetic cell. Instead of a complex *C. elegans* spindle, it is based on a much simpler bacterial DNA segregation system, ParMRC. We introduce optogenetic control for spatiotemporal control of segregation, and ensure that it follows the basic requirements of the synthetic cell, such as compatibility with PURE-based gene expression. In this promising work-in-progress, we demonstrate the functionality of individual opto-ParR components, but the system requires further optimization to achieve light-responsive DNA segregation.

Finally, in Chapter 8, we summarize the main findings and discuss the remaining challenges as well as possible future research avenues, not only for successful reconstitution of asymmetric spindle positioning, but also for the minimal synthetic segrosome.

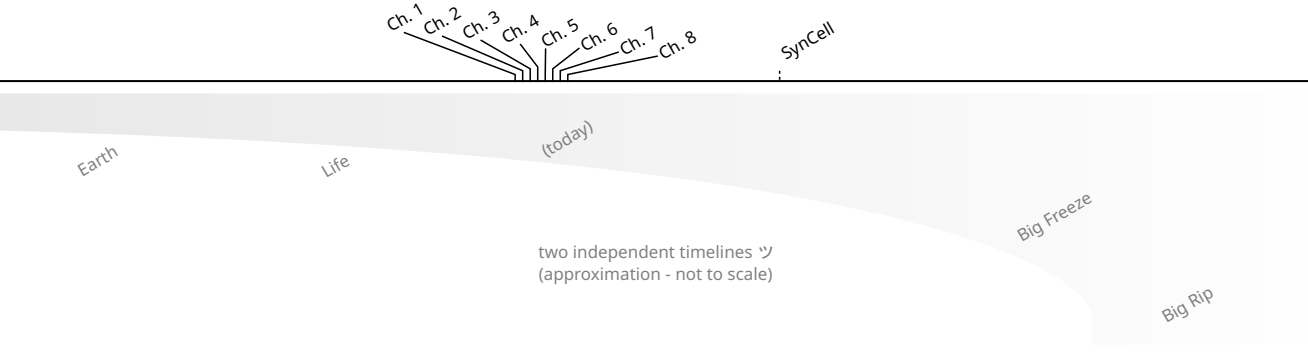
Ch. 1
Ch. 2
Ch. 3
Ch. 4
Ch. 5
Ch. 6
Ch. 7
Ch. 8
SynCell
Earth
Life
(today)
Big Freeze
Big Rip
two independent timelines ツ
(approximation - not to scale)

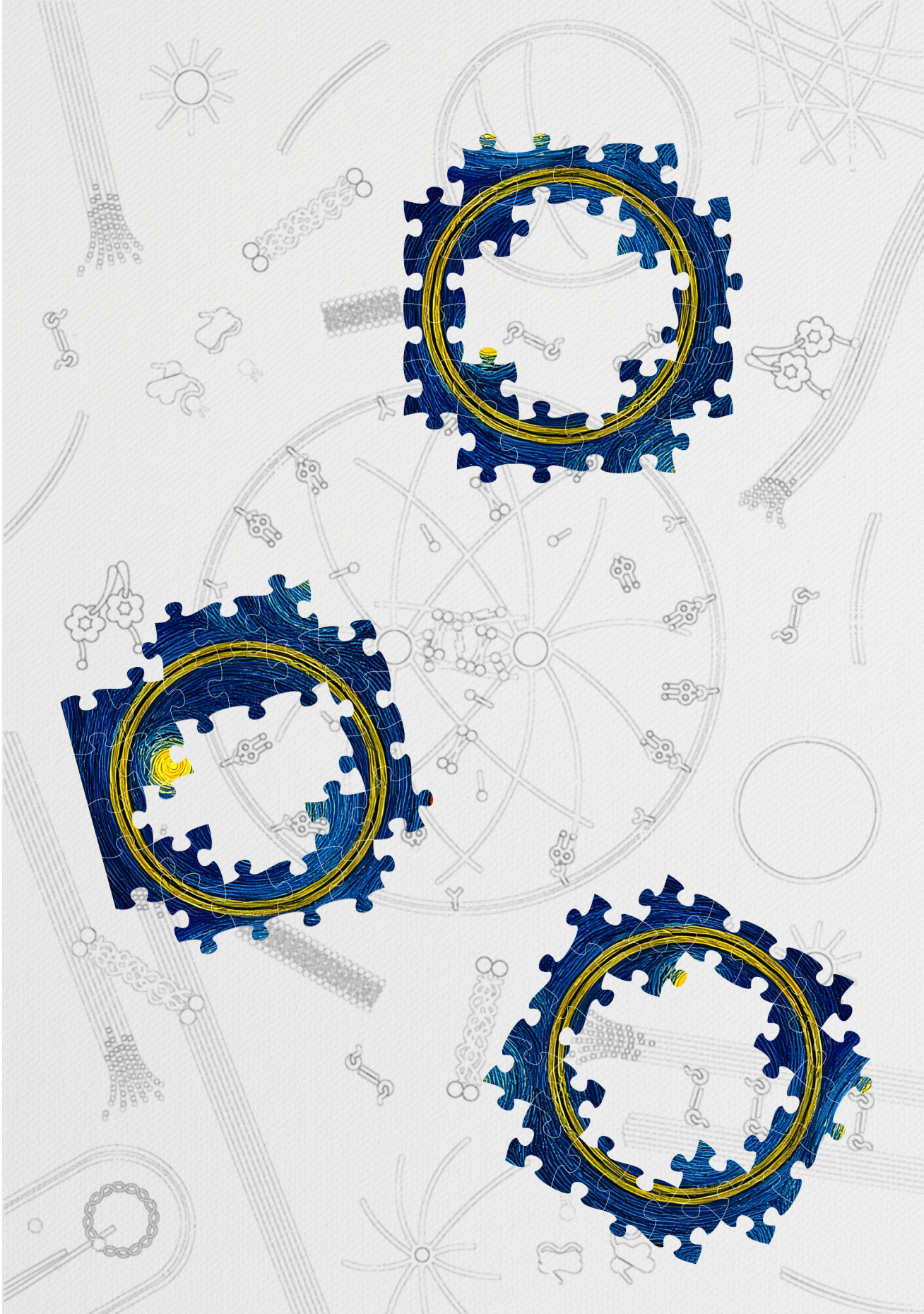

Containers maketh SynCell

Walk a mile in someone else's shoes.
Old wine in new bottles.
Horses for courses.

Cells are compartmentalized, active biological components separated from the surrounding environment. So, the encapsulation of components in a cell-like container is a crucial aspect of synthetic cell research. Droplets and vesicles are the two basic types of such containers. Various encapsulation techniques have been developed to create synthetic cell-like environments. Each has its strengths and limitations, along with varying requirements for equipment and skill set. No one method fits all situations. Here we test different encapsulation techniques and evaluate them based on their reproducibility, quality, and quantity of containers while maintaining the functional requirements of synthetic cell experiments. We find droplets are easiest to work with, while emulsion transfer based methods like cDICE (continuous Droplet Interface Crossing Encapsulation) are ideal for most types of encapsulation. Further, these methods can be combined with additional techniques to overcome some of their limitations.

This chapter includes vesicle formation experiments performed with, Chang Chen (Siddharth Deshpande lab, WUR, Netherlands) for Octanol-assisted Liposomes Assembly (OLA), and Martin Schröeter and Jacqueline De Lora (Joachim P. Spatz lab, MPI-MR, Germany) for droplet stabilized Giant Unilamellar Vesicle (dsGUV) and pico-injection.

2

2.1 Introduction

The field of synthetic cells has grown substantially during the last decade [251–255]. An integral part of synthetic cell experiments are the containers used to encapsulate synthetic cell components (as discussed in Ch. 1). These containers can be simple droplets or cell-membrane mimicking giant unilamellar vesicles (GUVs). Such containers have been extensively used in the past. Simple vesicles were for example used to study membrane properties [256, 257], *in vitro* systems like cytoskeletal proteins have been encapsulated in vesicles [258–260], and whole frog egg extracts have for example been encapsulated in droplets [261, 262]. In recent years, many vesicle formation techniques have been developed, focusing on the quality of the membrane and improving lipid incorporation and protein encapsulations (see [263], reviews [264–266]).

2.1.1 Droplets versus vesicles

Containers for synthetic cells need to be able to encapsulate water-soluble cellular components. While cells have a huge range of size (∼1–100 µm), synthetic cells are intended to be ∼5–20 µm, considering imaging limitations and ease of manufacturing and handling them.

Droplets

The water-in-oil droplets are one such container that is relatively simple and easy to work with. Droplets can be generated by the simple pipetting method or advanced microfluidic systems, which offer better size control. They are typically created from lipid-oil dispersions made in mineral oil[1]. The lipids dissolved in the oil populate on the water-oil interface of the droplets in the emulsion. The lipids, being a diverse class of molecules [267], with hydrophobic tails and hydrophilic heads, act as surfactant to stabilize the droplet emulsion. Hence, droplets just have one layer of lipids at the oil-water interface. However, to ensure complete coverage of the interface requires a very high concentration of lipids; hence, synthetic surfactants like Span 80 are used additionally to stabilize the emulsion[2] [268]. This can however be problematic for membrane interacting proteins, as only a monolayer of lipids is present at the oil-water interface, in addition to high amounts of surfactants. Droplets are very stable due to stabilization by artificial surfactants. They have very high interfacial tension (compared to vesicles) and act as hard to deform rigid containers[3]. Due to these properties, droplets have a very high yield (owing to efficient formation and high stability) and are compatible (not severely affected by) with dif-

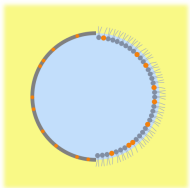

Droplet with lipid monolayer in oil.

[1] Typically, light mineral oil (less dense, less viscous, smaller hydrocarbon chains) is preferred over heavy mineral oil.

[2] Most surfactants such as Span 80 and even lipids are usually dissolved in oil. However, at times, some water-soluble surfactants such as Tween 20 are also used to aid stabilization.

[3] Droplets are practically impossible to deform by cytoskeletal components but actually easy to deform using external physical forces such as microfluidic confinement or aspiration.

ferent buffers and can encapsulate complex protein mixtures. However, droplets are typically considered as closed systems, with very limited exchange due to very low solubilities of the two phases in each other.

Vesicles

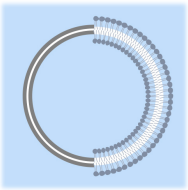

GUV with lipid bilayer in water.

Vesicle (also called as liposome or giant unilamellar vesicle (GUV)) is another container, which is the most natural and closest substitute to a cell membrane. A vesicle has a lipid bilayer as opposed to a lipid monolayer in a droplet. It has two aqueous phases separated by a lipid membrane. This makes vesicles more difficult to work with due to the fragile and delicate nature of the lipid bilayer. However, the bilayer membrane offers flexibility, fluidity, elasticity, active and passive permeability, and better bio-compatibility. The majority of the vesicle formation techniques can be classified into two groups: swelling-based and emulsion transfer-based. Swelling-based methods are generally easy to set up and quick to perform, but the yield can vary a lot depending on the surface[4]. Lipids are dried on a surface to form thin films. Later hydration with an aqueous solution results in spontaneous swelling of lipid layers, which tend to break off into spherical vesicles[5]. Emulsion transfer-based methods are a bit more complicated but offer better yield and encapsulation. They typically use lipid-oil dispersions made with different oil compositions[6]. A water-in-oil emulsion, just like droplets, is formed using various different ways. Then the droplets are forced into another oil-water interface using forces of gravity [269], centrifugation [270, 271] or fluid flow [272]. This causes the lipid monolayer droplet to acquire another lipid layer, resulting in the formation of bilayer vesicles. Sugar (sucrose and glucose) solutions are used to create density differences between the different solutions while retaining matching osmolarity. Vesicles are however delicate. The osmotic balance needs to be maintained, otherwise they can either deflate and shrink or burst when trying to expand.

2.1.2 Evaluating vesicle formation methods

New ways for vesicle production are constantly being developed. One of the reasons for this is that no one method fits all different types of reconstitution and encapsulation. To assess their applicability, each method should be evaluated for the following features: GUV size control, GUV yield, buffer compatibility, protein compatibility, protein encapsulation composition and efficiency[7], bilayer quality, lipid compatibility and composition, and technical complexity. As explained to some extent below,

[4] Just glass has a very poor yield, aided usually by applying an electric field or having a porous support like a gel.

[5] Spherical vesicles have the lowest surface-to-volume ratio shape, but vesicles can also have excess surface area that deviates from a spherical shape.

[6] Oils such as light mineral oil and silicon oil together with solvents like chloroform and decane help tune the lipid solubility and aggregate sizes.

[7] Comparing the initial protein compositions and concentrations in the IA solutions with that of vesicles' lumen (for individual vesicles).

each method has its strengths and weakness. Table 2.1 provides a schematic overview of different commonly used vesicle formation methods that can help to select a preferred technique, depending on basic features of the reconstitution such as — protein mix and membrane composition. Note that other methods can often also be made to work with custom optimizations or with involving additional steps.

Note: This chapter is not intended as a comprehensive review of all available techniques. Systematically testing all parameters across different methods under controlled conditions and statistically comparing the outcomes would be a substantial undertaking in itself. Rather, it provides an overview of our experiences in reproducing and establishing published protocols, as well as the technical challenges encountered across different approaches. As each technique has its own advantages and trade-offs — and given the notable lack of detailed comparative studies — I share here my impressions and working preferences, with the aim of helping others navigate similar decisions. This should be regarded as a **Perspective**, offering insight rather than quantitative evaluation.

Technique		Size	Protein		Membrane		
			Composition	Trans-membrane	Quality	Cholesterol	Asymmetry
Swelling	Electro-formation	✗	✗	○	●	●	✗
	Gel	✗			✗	○	✗
	Bead	✗	○		○	○	✗
Emulsion	cDICE	○	●			○	●
	OLA	●	●			○	
	Inverted Emulsion		●	○		○	●
	DSSF	○	●			○	
Other	dsGUV	○	●	●	●		

Table 2.1: **Vesicle techniques — quick preferences.** A quick overview of preferences for different vesicle formation technique. Key — ● ideal/preferred, ○ works, ○ not ideal, ✗ avoid. [cDICE — continuous Droplet Interface Crossing Encapsulation; OLA — Octanol-assisted Liposomes Assembly; DSSF — Droplet Shooting and Size Filtration; dsGUV — droplet stabilized Giant Unilamellar Vesicle]

Swelling-based methods are recommended for their bilayer quality, with electroformation [273] being considered as the gold standard. The lipid bilayer is usually solvent free, except in case of gel-assisted swelling, where residues of agarose/PVA gel are observed in the membrane [274]. This makes these GUVs ideal for studying membrane properties like elasticity, permeability, and lipid diffusion and organization. A disadvantage is that the size of GUVs cannot be controlled with swelling-based approaches. Also, electroformation becomes increasing challenging when high salt or physiological salt condition buffers are used. The protocol that is normally quick ($\leq$1 h), needs to be performed under harsh conditions (e.g. longer

period of time, high frequency), and yield is drastically reduced [275]. This makes it not ideal for encapsulation, as especially purified proteins start to degrade. Bead-assisted swelling on the other hand is readily compatible with high-salt buffers, proteins, and even *in vitro* transcription/translation (IVTT: TXTL, PUREfrex®), but is not preferred in case of complex reconstitutions with many proteins, as maintenance of encapsulation stoichiometry cannot be ensured. Swelling-based methods are compatible with most types of lipids (charged, natural, synthetic, cholesterol). Only these methods, and especially electroformation, have been shown to successfully incorporate cholesterol, with the vesicle lipid composition matching that of the original lipid composition [276]. However, more complex membrane architectures like leaflet asymmetry cannot be achieved with swelling-based methods.

Emulsion transfer-based methods are preferred when encapsulating complex protein solutions. They have good encapsulation efficiency and can maintain the stoichiometry of the proteins in the aqueous solution. Buffer compatibility is not a major issue, since the outer aqueous solution is generally a sugar solution. The osmotic pressure of the outer aqueous solution can be adjusted to that of buffer, to prevent any osmotic shock to the vesicles. After GUV formation, the outer aqueous sugar solution can be diluted with concentrated buffer to restore the ionic composition and minimize the flow of small ions and molecules across the vesicle bilayer. Emulsion transfer-based methods depend on density differences between inner and outer aqueous solutions. These density differences are generated with high concentrations of sugars (sucrose/glucose) and reagents such as OptiPrep™ , Poloxamer 188 (P188), glycerol, and dextran. At high concentrations these reagents start interfering with protein function. Emulsion transfer-based methods are slightly more involved compared to swelling-based methods in terms of preparation and instrumentation required. Once set up, these can have comparable yields of vesicles. While exact comparison of the yield is not possible[8], emulsion transfer requires a significantly higher amount of lipids[9], with higher concentrations and large volumes of lipid-oil dispersion solutions[10]. The size of the vesicles can be controlled, especially with microfluidic chip-based methods like Octanol-assisted Liposomes Assembly (OLA). With methods such as continuous Droplet Interface Crossing Encapsulation (cDICE) and droplet shooting and size filtration (DSSF), size control is more difficult as small capillaries which are good for control tend to get blocked easily, whereas the use of large diameter capillaries[11] affects the ability to control GUV size [277]. For emulsion transfer-based methods, the unilamellarity of lipid membranes has been demonstrated with functional α-hemolysin assays, but at the same time trace amount of oil residues are often observed. Most lipids are compatible with emulsion transfer-based methods, with a few exceptions in case of OLA and DSSF. It is possible to incorporate cholesterol in the membrane, but the emulsion transfer-based methods are the worst for capturing cholesterol in lipid ratio (<80 %) [276]. Vesicles

[8] In case of swelling, lipids in the dried lipid films are the limiting resource and swelling solution is in excess. And for emulsion transfer, the inner aqueous protein solution is limiting and lipids in LoD are in excess.

[9] swelling ∼50 µg and emulsion transfer ∼1.4 mg

[10] LoD ∼0.25 mM ∼3–5 mL

[11] ⌀ ∼100 µm vs ⌀ ∼5–20 µm

with asymmetric lipid leaflets can however be generated with cDICE and inverted emulsions, using multiple stacked LoD solutions [278].

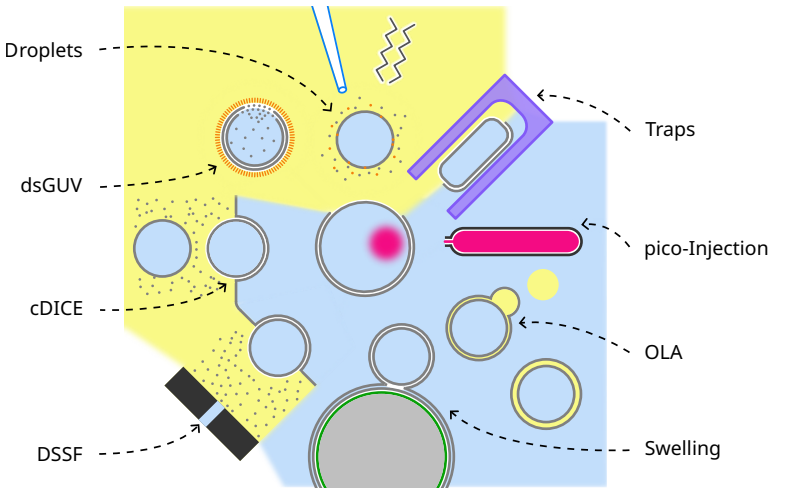

Figure 2.1: **Making containers.** Overview of different encapsulation techniques explored in this thesis for making (and modulating) droplets and vesicles. The colour-coded components are: oil, lipids, water, gel, bead, surfactant, pico-injector, and traps.

While most techniques fall under either the swelling- or emulsion transfer- based approach, droplet stabilized Giant Unilamellar Vesicle (dsGUV) [279, 280] is a recent method that uses a different approach of SUV fusion for GUV formation[12] which is worth exploring. It is a multi-modal method that can either be performed in bulk or with microfluidics. A high yield of vesicles is obtained and the size can be controlled using a microfluidic approach. It is widely compatible with different buffers, as it forms surfactant-stabilized droplets. Complex protein mixtures can be encapsulated while maintaining protein stoichiometry [279]. Since it uses SUVs, or proteoliposomes (preloaded with transmembrane proteins), to form the membrane, it is one of the best methods for reconstituting transmembrane proteins. It overcomes most of the limitations of previous methods in terms of membrane protein reconstitution (see review [282, §1]). The quality of lipid membranes is not affected since no solvents are used. The ability to incorporate cholesterol depends on the starting SUV composition, but asymmetric lipid leaflets are not possible with dsGUV. Formation of GUVs requires an additional optional step of releasing the GUVs from the droplet which provided a template for the membrane formation. This last step is difficult and has low efficiency.

In the remainder of this chapter, we discuss various techniques that we explored for encapsulating our proteins of interest (Fig. 2.1), and how each technique fared in our hands. During this process, we were interested in requirements like encapsulation of complex protein mixtures, maximizing vesicle yield and vesicle size control.

[12] Previously, SUV solution was subjected to freeze and thaw cycles to induce fusion into larger liposomes and entrap (encapsulate) the surrounding protein solution [281].

2.2 Droplet protocols

Water-in-Oil (W/O) emulsion droplets provide the simplest form of 3D confinement. Droplets have been successfully used to encapsulate cytoskeletal proteins [235, 238, 283]. The following sections provide a comprehensive overview of various droplet-generation methods. And see Sec. 2.6 for the detailed protocols.

2.2.1 Pipetting and dragging

A simple and easy way to generate droplets is by pipetting [239]. A protein containing inner aqueous (IA) solution is added to an Eppendorf tube containing a lipid-in-oil (LO) dispersion. The mix is pipetted up-and-down to create droplets (Fig. 2.2(a)). The experiment is very quick, can be performed in a few minutes and results in very high yield of droplets (Fig. 2.2(c)). Droplets can be made with as little as 0.5 µL of IA solution, very efficient in terms of protein utilization. No optimizations are required in the protocol, and it works most of the time. However, the manual step of pipetting up-and-down is a bit subjective and can lead to person-to-person variations. The droplets are formed by shear forces acting on the IA solution while entering and exiting the pipette tip. Droplets remain stable for few days. The yield and size depend on the pipette tip size and pipetting details. A smaller pipette tip leads to more and smaller droplets, and faster pipetting or more repetitions also leads to formation of many smaller droplets. The yield and size are inversely related, as the total amount of IA solution remains constant.

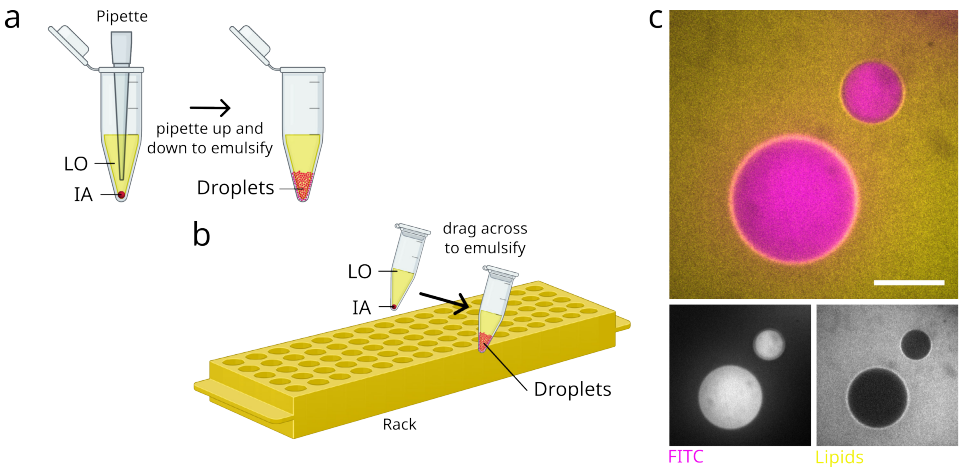

Figure 2.2: **Droplet formation with pipetting and dragging.** Schematics showing water-in-oil (W/O) emulsion droplets formed by, (a) pipetting up-and-down inner aqueous (IA) solution in lipid-in-oil (LO) dispersion and (b) dragging tube with IA solution in LO dispersion at a tilted angle over tube rack. The shear forces generated during (a) pipetting and (b) dragging lead to formation of droplets. Figures partially created in BioRender.com. (c) Droplets of varying sizes made by pipetting 1 µL IA — FITC (50 nM) in 40 µL LO — DOPC, Cy5-PE (0.025 n%). Scale bar — 20 µm.

We created a variant of this protocol, with slight modification. The Eppendorf tube containing the mix is dragged across an Eppendorf tube rack (Fig. 2.2(b)). Similar working principles and caveats apply, but the benefits are that also (very) small IA drops can be mixed into the LO dispersion and that all the IA droplets go through each mixing round. Also, shear force experienced by sensitive proteins are believed to be less compared to passing through a narrow pipette tip multiple times. Dragging across the longer side of the rack or dragging multiple times leads to formation of smaller droplets. In both protocol variants, the droplets follow a normal size distribution (Fig. 2.2(c)). So droplet size can be controlled to a certain extent, but no precise control or a tighter size distribution is possible. The protocol works with any physiological buffer conditions. Encapsulation of complex protein mixes is not an issue, and the stoichiometry as well as concentrations of various proteins are maintained. Most lipid interacting (not transmembrane) proteins function normally (with a few exceptions, see Ch. 4). One of the disadvantages of working with droplets is their high rigidity, so studying membrane deforming or cytoskeletal proteins might not yield similar results as compared to a flexible cell or vesicles. Droplets can be imaged in a simple (even non-cleaned, untreated glass) flow chamber. Traditionally, narrow PDMS wells, where droplets stack over each other, are used for observation ([239]). But even with confocal microscopy it becomes impossible to image droplets even one droplet layer above the glass surface, as already the imaging in top-half of droplet (near the glass) results in poor imaging quality compared to bottom-half due to loss of signal due to refractive index of surrounding oil. A flat geometry, such as a flow chamber, where droplets spread out in a single layer, is better suited for observation.

2.2.2 Microfluidic chip

Droplets can be produced in a more controlled way (compared to pipetting or dragging) with a microfluidic chip [228, 235]. The microfluidic chip (Fig. 2.3(a)) has inlets for protein-containing IA and LO solutions, an outlet for droplet collection, and a flow-focusing T-junction (Figs. 2.3(b) & 2.3(c)). A full detailed and scaled design of the chip is shown in Fig. 2.S1. The inlets have dust filters (concentric reducing circles pattern) to prevent any protein aggregates from passing into the chip. The IA and LO solutions are flown into the chip using a flow-controlled pressure pump. The flow of IA and LO solutions through the T-junction results in the formation of droplets (Figs. 2.3(c) & 2.3(d), Fig. 2.S5, Fig. 2.3(e)). The droplet generation on chip needs ∼15 min; however, the setup needs a lot of preparations and a certain level of experience[13] with the instruments to successfully generate droplets. The microfluidic chip needs to be manufactured, either in a cleanroom (requires access and training) or custom ordered commercially. A pressure flow controller is required. The PDMS device needs to be cast and assembled beforehand, at least a few days before the experiments[14].

[13] Priming/loading the tubes with solutions, proper connection of the tubing on the chip, setting up with sequential flow of solutions, optimizing the pressures/flow-rates for droplet formation, and tuning size and frequency.

[14] A freshly assembled device by plasma bonding has a hydrophilic surface, not suitable for oil solutions.

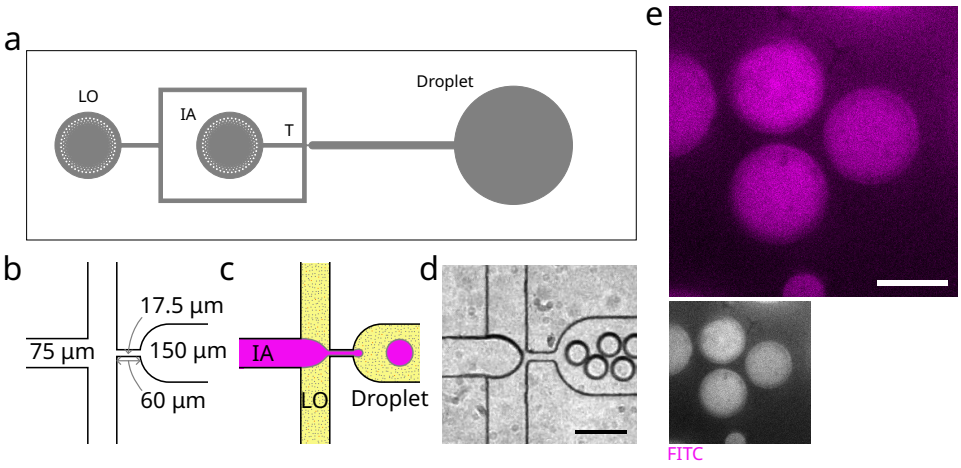

Figure 2.3: **Droplet formation with a microfluidic chip.** Water-in-oil (W/O) emulsion droplets formed using a microfluidic chip. (a) Schematic of the device with inlets for inner aqueous (IA) solution and lipid-in-oil (LO) dispersion with a filter, a flow focusing T-junction, and outlet for droplets (scaled, for detailed design see Fig. 2.S1). Details of the T-junction, (b) dimensions, (c) droplet formation schematic with IA and LO solutions, and (d) a bright-field image (scale bar — 10 µm). See Fig. 2.S5 for movie. (e) Droplets of uniform sizes made with IA — FITC (50 nM) and LO — DOPC using a microfluidic chip. Precise size control is possible by controlling the IA and OA solution flow rates. Scale bar — 20 µm.

The protocol is straight forward and does not need many optimizations. However, there are tricks, like avoiding wetting certain parts of the T-junction with the LO solution, and the ratio of flow rates of IA and LO solutions that needs to be specified in the protocol. While the dimensions of the T-junction in principle regulate the size of droplets formed on the microfluidic chip, an unoptimized flow rate ratio can vastly affect the size, homogeneity, consistency, and frequency of droplet formation. The main advantage of using a microfluidic chip over pipetting or dragging is the uniform size distribution of droplets. Droplets still follow a normal size distribution, but there is much less variation. While ~10–50 µL of IA solution is required, it is a high-throughput method; droplets are produced at ~kHz frequency, and the yield is high. Droplets made with a microfluidic chip are also compatible with most proteins and work for complex protein mixtures. However, one needs to be cautious and check if proteins are sticking to the tubing and walls of the PDMS channels. Use of PTFE tubing is recommended to prevent sticking.

2.3 Vesicle protocols

Vesicles, cell-mimics, are also often used to encapsulate cytoskeletal proteins [284–288]. This has become increasingly prevalent in recent years as a result of the development of more bio-compatible vesicle production techniques. Vesicles with vary-

ing lipid composition [289], charged lipids [278, 285], sterols [278, 290], asymmetric leaflets [290–292], phase-separated domains [278, 293], and transmembrane proteins [294] can also be produced. A regular flow chamber can be used as the observation chamber[15]. The following sections provide a comprehensive overview of various vesicle-generation methods we explored. And see Sec. 2.6 for the detailed protocols.

2.3.1 Gel- and bead-assisted swelling

A simple and easy way to generate vesicles is by using swelling-based methods such as gel-assisted swelling [295] or bead swelling [296, 297]. In gel-assisted swelling, sucrose containing polyvinyl alcohol (PVA) solution is spread over a glass surface, excess solution is drained, and the glass is baked to form PVA gel[16]. Lipids of desired composition in chloroform are spread over the PVA gel with a Hamilton glass syringe needle and dried under vacuum to form thin lipid films (Fig. 2.4(b)). The protein-containing IA solution is added on top of the dried lipid films, and the films spontaneously start swelling. Vesicles bud off the swelling lipid film (Fig. 2.4(d)). The swelling experiment is easy and quick (∼1–2 min) but needs some preparation. The PVA-coated glass can be made in advance, but dried lipid films should be freshly made just before the swelling. After swelling, most vesicles remain attached to the surface (Fig. 2.4(d)) and can be washed off with excess IA solution. One of the drawbacks of swelling methods is that the inside and outside solutions are the same. This is not ideal to image proteins inside the vesicle. The outside solution can be exchanged during the wash-off step or during dilution with the outer aqueous (OA) solution. Ideally, the OA solution should be isotonic (or $\sim +\Delta 10$–15 mOsm). The protocol is quite simple and does not even need sophisticated swelling and observation chambers ([295]). The tricks for spreading the gel, adding the lipid solution and vesicle collection should, however, be described in the protocol. The protocol does need optimization because the sucrose concentrations in PVA gel needs to be tweaked based on the salt concentration used to maintain the osmotic difference with IA solution. Vesicle yields inversely depend on the ionic strength of the buffer; membranes are solvent-free but can have traces of PVA. There is, however, no size control. Swelling-based vesicles are ideal for studying the physical properties of the membrane. That being said, generally the encapsulation efficiency seems not very good; it only works for low concentrations of proteins, and it is difficult to encapsulate protein mixtures with fixed stoichiometry or larger or complexes of proteins. Gel-assisted swelling is typically compatible with *in vitro* reconstitution buffers and diverse lipids. Swelling is one of the best methods to incorporate sterols into the vesicles.

[15] The glass surface needs to be cleaned and passivated with BSA or κ-casein to prevent sticking and bursting of vesicles on the glass surface.

[16] Often sugars (Saccharides) are placed under the lipid film during the drying phase. This helps during hydration, as sugars increase the osmotic difference across the lipid film and facilitate osmosis of water across the different lipid layers, making them swell faster [298].

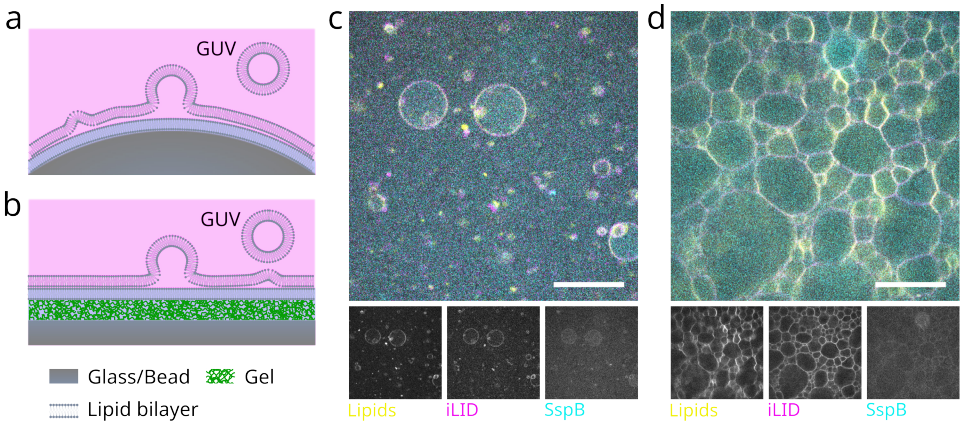

Figure 2.4: **Vesicle formation with swelling.** Schematics of vesicle formation with, (a) bead swelling and (b) gel-assisted swelling on glass. A PVA gel (5 %w/v) is deposited on the glass surface. Lipid films are dried on glass beads (with rhamnose 100 mM) or on the PVA gel (with sucrose 50 mM). GUVs are formed by hydration of lipid films with protein in MRB80 buffer. Vesicles formed with (c) bead swelling, IA — YFP-LactC2-iLID[17] (2 µM), SspB-mOrg[18] (2.25 µM) and LO — DOPC, DOPE (35.6 n%), DOPS (11.5 n%), Cardiolipin (2.1 n%), PEG-biotin (1 n%), and Cy5-PE (0.5 n%) and (d) gel-assisted swelling, IA — YFP-LactC2-iLID (2 µM) and SspB-mOrg (2.25 µM), sucrose (50 mM) and LO — DOPC, DOPS (30 n%), and Cy5-PE (0.5 n%) (vesicles attached on glass surface). LactC2-iLID localizes to the membrane (DOPS). Scale bar — 20 µm.

In case of bead swelling, lipids with rhamnose (sugar) are directly dried on the glass bead surface (Fig. 2.4(a)) under rotating vacuum. The lipid-coated beads are incubated with IA solution for ∼0.5–2 h, with constant or occasional shaking. A series of freeze-and-thaw (freeze with liquid nitrogen and thaw on ice) cycles are performed to promote fusion of SUV (formed on the lipid-coated bead surface) into GUVs and also to promote encapsulation through membrane pores formed during temperature cycling. Similar to gel swelling, the excess IA solution needs to be diluted or exchanged with OA solution by GUV pelleting. This results in vesicles (Fig. 2.4(c)) with a diameter of (8.23 ± 3.49) µm (Fig. 2.S2(a)). The experiment is slightly involved and needs preparation of lipid-coated beads. But the lipid-coated beads can be stored under Argon at 4 °C for months (it is recommended to vacuum dry for ∼0.5 h, just before use). The protocol does not need any optimization. Vesicle yield is good, but there is no control on size. The encapsulation efficiency and lipid compatibility of bead swelling is comparable to that of gel-assisted swelling. Bead

[17] YFP-LactC2-iLID — A component of the optogenetic switch protein pair, here as an placeholder and representing membrane-bound proteins for testing membranes in vesicle formation. See Ch. 6 for more details on optogenetic tool, iLID-SspB.

[18] SspB-mOrg — Another component of the optogenetic switch protein pair, here as an placeholder and representing cytosolic proteins for testing encapsulation during vesicle formation. See Ch. 6 for more details. SspB binds to iLID up to photoactivation with blue light.

swelling is very efficient in terms of the lipids used to produce vesicles, due to the very high surface area coated with lipid films.

2.3.2 cDICE and eDICE

The continuous Droplet Interface Crossing Encapsulation (cDICE) [271, 277, 299] and a variant, emulsion Droplet Interface Crossing Encapsulation (eDICE) [288, 300] are emulsion-based vesicle formation techniques. The setup basically consists of a spinning chamber, with an outer layer of outer aqueous (OA) solution and an inner layer of lipid-in-oil (LO) dispersion. In both cases, droplets are first produced and then spun through an interface, but in the case of cDICE, droplets are made by injecting the protein-containing inner aqueous (IA) solution into the LO dispersion with the help of a capillary (Fig. 2.5(a)), whereas in the case of eDICE, a previously made emulsion of IA-in-LO droplets is injected through the central aperture hole with the help of a pipette tip (Fig. 2.5(a)). The IA solution coming out of capillary forms droplets. Then these droplets travel outwards in the spinning chamber due to centrifugal forces. The droplets acquire a first layer of lipids in the LO dispersion; and crossing the LO-OA interface, they acquire another lipid layer for a bi-layer vesicle (cDICE Fig. 2.5(c), eDICE Fig. 2.5(d)). Establishing the cDICE or

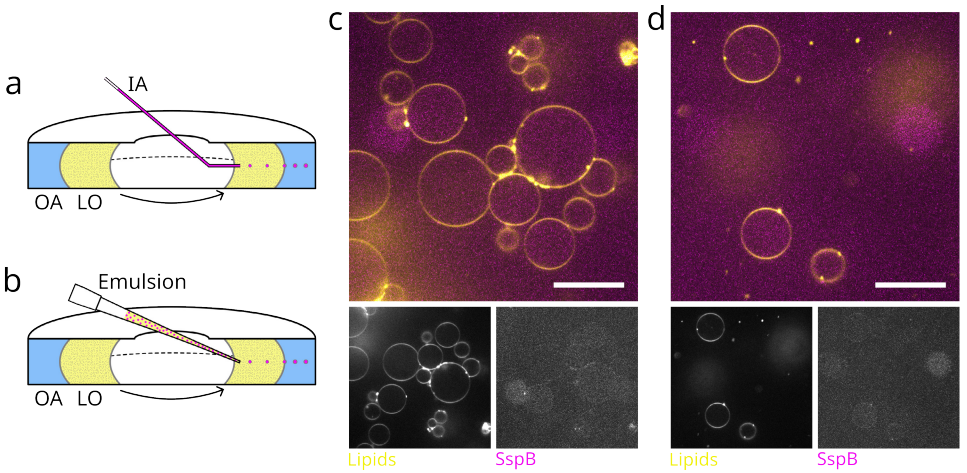

Figure 2.5: **Vesicle formation with DICE.** Schematics of vesicle formation with, (a) cDICE and (b) eDICE. A rotating chamber contains layers (out-in) of outer aqueous (OA) solution and lipid-in-oil (LO) dispersion. The inner aqueous (IA) solution is injected with a capillary from the centre in (a) cDICE, while a pre-made IA-in-LO emulsion is pipetted from the centre in (b) eDICE. Vesicles formed with (c) cDICE using a ⌀ 100 µm capillary and (d) eDICE. In both cases, IA — SspB-Ch (0.5 µM), OptiPrep (18.5 %w/v), LO — DOPC, PEG2000-PE (0.01 n%), and Cy5-PE (0.1 n%), and OA — glucose (∼ +Δ15–20 mOsmol). Scale bar — 20 µm.

eDICE setup requires a significant amount of time and effort[19]. The chamber can be 3D printed or made by gluing two Petri dishes together. The spinning rotor can be made using a custom stepper motor and controller or by modifying a table-top centrifuge or magnetic stirrer. The capillary with the required diameter needs to be pulled, cut, and bent, or custom pre-manufactured capillaries can be bought. Capillaries need to be surface-treated to prevent protein sticking. A fresh LO dispersion needs to be made in a humidity-controlled glovebox. The IA-in-LO emulsion for eDICE needs to be made fresh by dragging the tube over an Eppendorf rack just before the experiment and used quickly, as no strong surfactant is present to stabilize the droplets. Experiments require ∼10–15 min. The protocol can require optimization, and some experience[20] along with an in-person demo helps. This is because many finer details in the various steps of the protocol can be performed with slight variations.

The protocol should provide justification for the choice of parameter values, as this helps with troubleshooting and optimization. These protocols can have a very good yield of vesicles (although this depends on the physiological conditions and even the proteins in the IA solution, see Ch. 4). The original cDICE [271] protocol shows vesicle size control by varying the capillary diameter, but working with a small diameter (⌀ 5–20 µm) capillary is tricky as they are prone to clogging with proteins even after surface treatment. The use of a larger diameter (⌀ 100 µm) [277] leads to formation of vesicles of diameter (10.54 ± 0.71) µm (Fig. 2.S2(b)). Control over vesicle size is thus lost (for more details, see Ch. 3). The DICE methods are known for their encapsulation efficiency (cDICE 47.1 %, eDICE 93.3 % [288]) and their ability to maintain complex protein stoichiometry during encapsulation and to encapsulate large protein complexes. The IA solution needs to be dense compared to the OA solution, in order for droplets to travel beyond the LO-OA interface. This is typically achieved by the addition OptiPrep (which is incompatible with some proteins) or sucrose to the IA solution. Emulsion-based DICE methods remain a top choice for encapsulating many protein systems, despite initial learning curve and troubleshooting. Some modifications to the chamber design, i.e. a wide chamber with a wider central aperture hole (Fig. 2.S3(b)) have been reported [300] compared to the original chamber (Fig. 2.S3(a)) [271] to improve vesicle yield. We also tried variants of the modified design, i.e. a thinner chamber (Fig. 2.S3(c)) and a larger chamber (Fig. 2.S3(d)) but had no success with vesicle formation. We further explored, in detail, the process of vesicle formation in cDICE and addressed some issues during vesicle formation in Ch. 3.

2.3.3 OLA

Octanol-assisted Liposome Assembly (OLA) is a microfluidic chip-based variant of emulsion-based vesicle formation [301]. With the replacement of oil with alcohol (1-octanol) in OLA as the lipid dispersion media, it is generally accepted that there is

[19] There exist numerous ways to assemble the cDICE setup, design the chamber and manufacture it, and ways to inject the IA solution. Each resulting in slight variations in yield.

[20] Quickness required for injecting eDICE droplet emulsion; handling of the chamber while decanting the LO and OA solutions; collecting vesicles from the bottom.

no residual oil in the leaflets of the lipid membrane. The microfluidic chip has inlets for protein-containing inner aqueous (IA) solution, lipid-in-octanol (LO) solution, and outer aqueous (OA) solution, outlets for vesicle collection and drainage for octanol drops (Fig. 2.6(a)). The water-in-octanol-in-water (W/O/W) double emulsion droplets are generated at a 6-way junction (Figs. 2.6(b) & 4.5(b)), in which octanol quickly collects on one side of the droplets (Fig. 2.S6). Then octanol spontaneously forms a pocket on the droplet which eventually breaks off, leading to the formation of a vesicle (Fig. 2.6(d)). The octanol droplets are lighter than the IA and OA solutions and

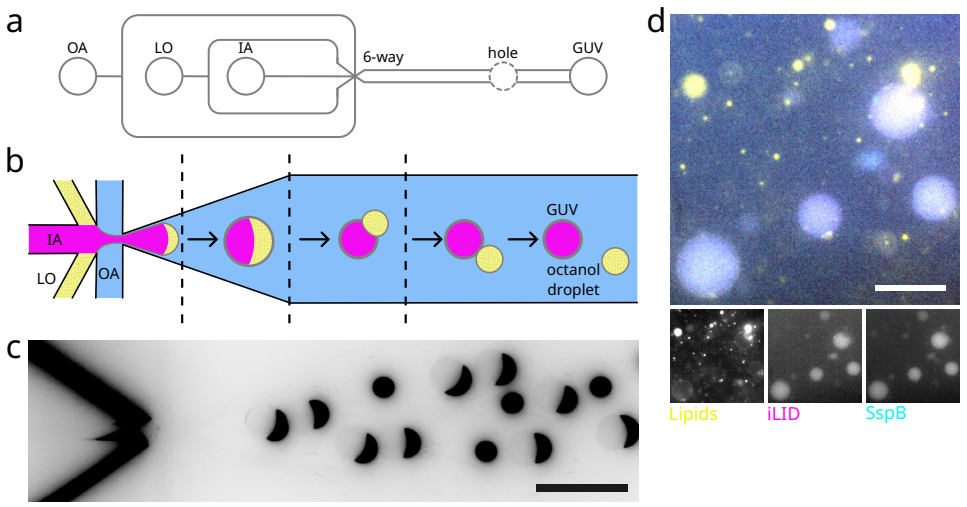

Figure 2.6: **Vesicle formation with OLA.** (a) Schematic of the OLA microfluidic chip with inlets for outer aqueous (OA) solution, lipid-in-octanol (LO) dispersion, and inner aqueous (IA) solution, outlets for octanol droplet drainage (hole) and GUVs, and a flow focusing 6-way junction. (b) (Zoomed schematic of 6-way junction) IA solution, LO dispersion, and OA solution at the 6-way junction form water-in-octanol-in-water (W/O/W) droplets. Octanol spontaneously collects to form a pocket in-between lipid leaflets and eventually breaks off as an octanol droplet, leading to formation of a vesicle. (c) Fluorescence image (LO dispersion, inverted LUT) shows the process of W/O/W droplet formation at the 6-way junction and subsequent transitioning into octanol pockets and vesicles (scale bar — 100 µm). See Fig. 2.S6 for movie. (d) Vesicles formed with OLA, IA — YFP-LactC2-iLID (0.5 µM) and SspB-mOrg (0.56 µM), LO — DOPC and Cy5-PE, and OA. YFP-LactC2-iLID does not localise to the membrane in the absence of DOPS. Scale bar — 20 µm.

can thus be separated at the exit hole in the chip. Setting up the OLA method takes time, similar to droplet production with microfluidic chips. Flow pressure pumps are required, microfluidic chips need to be manufactured or bought, and the PDMS devices need to be cast and assembled. An additional step of hydrophilic coating of the post-junction channel with PVA is crucial for the working of the method. Coating is tricky and requires experience, as asymmetric or too much coating beyond the junction will result in no formation of W/O/W droplets. Tricks like hydrophilic coating

until just a semicircle behind the 6-way junction are important. The PDMS devices, once assembled and coated, can be stored for a few weeks. With the pre-experiment setup done, the experiment itself just takes about ∼15 min.

All microfluidic protocols should provide range estimates for the IA, LO, and OA solution flow rates ideal for the used chip dimensions, as this affects the vesicle production frequency and size. Then the only optimization steps are PVA coating and fine-tuning the flow rates. If all parameters are optimal, as with all microfluidic-based methods, the vesicle yield is high and size can be controlled. OLA has no issues with encapsulation efficiency and is in principle expected to be compatible with large proteins and complex protein encapsulations. The method works well with physiological conditions, as the IA and OA solutions can be made with the same buffer. Working with a 6-way junction can be tricky as it needs balancing flow rates of three different solutions. Hence, an alternative with 2 consecutive 3-way T-junctions has been proposed [272], also with an additional serpentine loop design to promote removal of residual octanol droplets. One of the issues working with OLA is the requirement of a high amount of density and viscosity agents (glycerol, dextran) in the IA and OA solutions. This leaves very little space for the addition of proteins of interest in the IA solution.

2.3.4 DSSF

The droplet shooting and size filtration (DSSF) method is an emulsion-based method for vesicle formation that combines principles of microfluidics and centrifugation-based emulsion transfer in a novel geometry. It uses a single glass capillary holder made of plastic discs held in place using micro-screws, fitted in an Eppendorf tube [302]. A variation of the original DSSF design replaces the complicated holder assembly with a custom designed two-part capillary holder, which can be 3D printed [303]. Another high-throughput variant of DSSF replaces the single capillary design with a glass disc with a micro-channel array (MiCA) [304] which also requires a custom holder. The MiCA is made by fusing many tiny solid glass capillaries (6.2 µm) with a few centrally placed hollow glass capillaries in a hexagonal pattern. The final MiCA disc is obtained by dicing fused capillaries. This fabrication requires high-grade industrial machinery.

We designed our own alternative MiCA for DSSF, with discs made out of silicon wafers with 7 centrally etched holes in a hexagonal pattern. The disc is 3 mm wide, and holes with diameter ⌀ 5–20 µm are arranged in a 300 µm wide hexagonal pattern (Fig. 2.7(a) right, Fig. 2.S4(c)). The disc needs a hydrophobic coating for proper droplet formation. The disc is assembled in a custom plastic holder with a cap, along with a rubber O-ring to prevent leakage of protein-containing (IA) solution (Fig. 2.7(a) middle). The adaptor is placed on a PCR tube containing layers of lipid-in-oil (LO) dispersion and OA solution (Fig. 2.7(a) left; see also photo of disc, adaptor parts along with swing rotor centrifuge tube and centrifuge tube adaptor in Fig. 2.S4(a)). The DSSF method uses the shear forces of a narrow opening to form droplets, similar to the microfluidic chip, and the centrifugal force for the droplets to travel across LO and OA solutions, similar to cDICE. This is a simplified cDICE geometry with fewer moving parts, where the IA solution, the capillary, the LO dispersion, and the OA

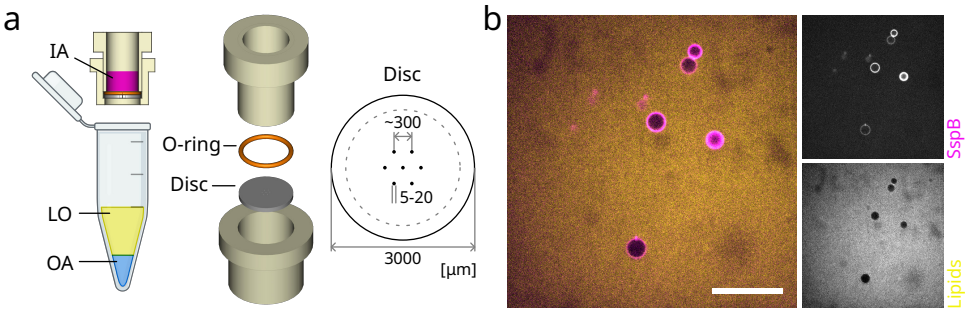

Figure 2.7: **Droplet and vesicle formation with DSSF.** (a) (left) Schematic of our DSSF assembly. Inner aqueous (IA) solution exits the assembly from the disc holes, forming drops due to the centrifugal force. The drops fly in through the tube, pass the lipid-in-oil (LO) solution and the outer aqueous (OA) solution in the tube to form vesicles, or only the LO solution to form W/O droplets. Figure partially created in BioRender.com. (middle) A split view of the DSSF assembly: the O-ring and disc are sandwiched in-between a cap and holder (a photo of the whole DSSF assembly and the swing-rotor tube adaptor is shown in Fig. 2.S4(a)). (right) Schematic of the DSSF disc (⌀ 3 mm), with 7 holes (⌀ 5–20 µm) arranged in a hexagonal pattern (300 µm) (image of the silicon wafer disc is shown in Fig. 2.S4(c)). (b) Droplets made with a 10 µm DSSF disc, IA — SspB-mCh (1.58 µM) and LO — DOPC and Cy5-PE (0.025 n%). With unexpected localisation of SspB-mCh at the droplet interface. (Vesicles made with DSSF are shown in Fig. 2.S4(b)). Scale bar — 20 µm.

solution all are stationary in the local frame of reference while the whole assembly is spinning. The droplets are generated through the disc, in the device itself, instead of pre-formed droplets like in the case of inverse emulsion or eDICE. The protocol becomes quick and straightforward once the main droplet-generating component (whether a capillary, MiCA, or disc) and its holders are fabricated.

Similar optimizations to cDICE, such as balancing the solution osmolarity, are needed. The centrifugation speed and duration vary from device to device[21]. Also, the quantities of LO and OA solutions used vary. The DSSF method can work with tiny amounts of IA solution (≤0.5 µL) and has been shown to have good yields [302]. The size of the vesicles can be tuned with the size of the holes in the disc. We, however, did not manage to form any vesicles using this method. Even after trying many optimization steps, we only saw lipid aggregates or very tiny vesicles (Fig. 2.S4(b)). We tested DSSF for droplet formation as an intermediate step in vesicle formation and we did see droplets (Fig. 2.7(b)) formed with our silicon disc. The yield of droplets is high (Fig. 2.S4(d)) and comparable to published yields [304]. In our troubleshooting efforts, we tried replicating the original DSSF with capillary using our custom 3D printed holder (Fig. 2.S4(e)) but with no success. Taking advantage of a visit during a conference[22], we also tried the holder from Venero et al. [303] (an improved

[21] Across various reports, the protocol parameters seemed empirically determined based on what seems to be working.

[22] SynCell 2022 conference, The Hague

injection-moulded holder (Fig. 2.S4(f))), again with no success in vesicle formation[23].

We did not put in further efforts for optimizing this method. The encapsulation of complex protein solutions is in principle expected to not be an issue. However, one of the issues with the DSSF method is that the droplets travel through air from the tip of the capillary or the bottom of the disc until they reach the LO dispersion. The water from the IA solution can evaporate, leading to concentration changes, and the proteins can interact with air at the water-air interface. An example of this can be seen in Fig. 2.7(b), where protein from the IA solution is found stuck at the interface. A solution for the evaporation issue is to submerge the tip of the capillary in the LO dispersion or make contact of the bottom of the disc with the LO dispersion [305].

2.3.5 dsGUV

Up till now, we explored vesicle formation based on either swelling or emulsion transfer. The droplet-stabilized Giant Unilamellar Vesicle (dsGUV) method [279] is a different class of method for vesicle formation, based on SUV fusion. The method can be implemented in a microfluidic chip [279, 306] or even in bulk with agitation, like droplet pipetting or dragging [280]. The underlying working principle of the dsGUV method is based on charge-mediated fusion of small unilamellar vesicles (SUVs) on a charged surface of a surfactant-stabilized droplet. dsGUV formation is in principle similar to SLB formation but inside a 3D droplet shell. The lipid-containing aqueous (LA) solution and surfactant-in-oil (SO) dispersion form droplets due to shear forces either at the T-junction or in Eppendorf tubes. The SO solution contains PFPE-PEG-PFPE, a click tri-block surfactant (cTS), and Krytox, a modified-PFPE surfactant with a negative charged head group, dissolved in fluorinated HFE oil. The LO solution contains proteins of interest and pre-made SUVs. The divalent Magnesium (Mg^{2+}) ions from the aqueous buffer bind to the Krytox on the charged surface of the droplet stabilized by cTS. The SUVs from the LO solution burst when coming in contact with Mg^{2+} ions and spread on the droplet inner surface, forming a supported lipid bilayer (SLB, Fig. 2.8(a)). An SLB covering the entire surface of the droplet results in the formation of a vesicle (Fig. 2.8(b)) on the inner surface of the droplet. This process is quite spontaneous, but to ensure entire coverage of the surface, it is recommended to incubate the dsGUVs overnight (∼12 h), or a minimum of 0.5–1 h.

The method is simple. Bulk droplet production takes only a few minutes, and the microfluidic approach requires ∼15–30 min (excluding the PDMS device casting, assembly, and coating). The reagents required are, however, not common and, at times, can be difficult to acquire. For most of the proteins, the protocol works well and needs no optimizations. The yield is high, comparable to other microfluidic methods, and similar size control can be achieved. Encapsulation of complex protein solutions also works as expected, even under physiological buffer conditions. Lipid-interacting proteins work just fine even in the presence of the surfactant droplet supporting the GUV. The only issue is the GUV cannot be deformed with droplet stabilization present. To solve this issue, the GUVs can be released into an aqueous

[23]This DSSF experiment was tried in our laboratory together with the first author of Venero et al. [303]

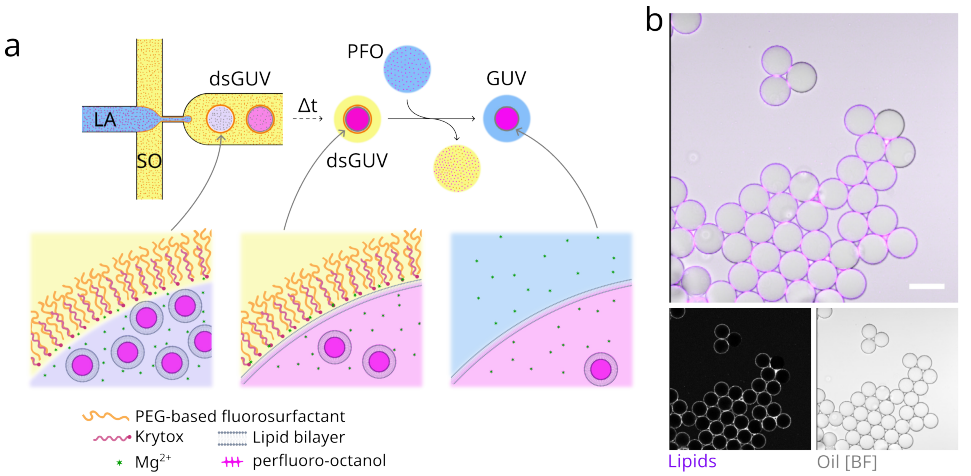

Figure 2.8: **Vesicle formation with dsGUV.** (a) Schematic showing formation of a W/O droplet in a microfluidic chip at the T-junction with lipid containing aqueous (LA) solution and surfactant-in-oil (SO) dispersion. Overtime, the W/O droplet transforms into a dsGUV. The matured vesicle (GUV) is released with the help of an aqueous perfluoro-1-octanol (PFO) solution and the surfactant-in-oil dispersion is washed off. (bottom-left) W/O droplet interface — PEG-based fluoro-surfactant, click tri-block surfactant (cTS), and Krytox stabilize the W/O emulsion. (bottom-middle) Formation of dsGUV - SUVs in the LA solution burst, release their inner aqueous solution, and form a lipid bilayer on the Krytox and Magnesium (Mg^{2+}) ions complex at the droplet interface (bottom-right) The GUV with s lipid bilayer covering the entire droplet interface is released by destabilizing the surfactant layer with a PFO solution. (b) Vesicles formed with dsGUV, SUV — DOPC, PEG2000-PE (4 n%) and AF488-PE (0.5 n%), and SO. Bright-field image of dsGUVs in oil (vesicles are not released, but still have a surfactant layer). Scale bar — 20 µm.

environment by washing off the surfactant layer with a perfluoro-1-octanol (PFO) solution. The GUV release with PFO can sometimes be tricky, leading to decreased yield. A modification of dsGUV protocol simplifies the GUV release step to simple centrifugation [307]. It replaces the surfactants (cTS and Krytox) with fluorinated silica nanoparticles (FNPs), which acts as an active Pickering emulsions to stabilize the droplets.

2.4 Container modification

Droplets and vesicles provide good 3D confinement for encapsulated proteins. These containers are usually spherical, closed, and of fixed size. The ability to change these properties, by modifying the container and the content inside, opens up new possibilities. Additional components can be added via pico-injection [308]. The shape can be adjusted with microfluidic traps [309] and micropipette aspiration [310]. The size can be modulated with osmotic shock [311] or increased by the addition of extra

lipids (SUVs) [312]. Containers can even be mechanically forced to undergo fission [313, 314] or fusion [315]. Here we describe a couple of techniques that we tried, relating to the overall focus of this thesis.

2.4.1 PICO-INJECTION

Pico-injection is a powerful technique that provides a way to modify the contents of the container in a precise and sequential way [308]. It is compatible with both droplets and vesicles. The microfluidic chip used for this has a primary channel for containers. The channel with the component to be injected connects to the primary channel orthogonally with a T-junction (Fig. 2.9(a)). A pair of electrodes is present opposite to the T-junction across the primary channel. A strong oscillating electric field focusing at the T-junction is applied with the help of the electrodes to induce pico-injection. We used pico-injection to add our protein of interest to empty preformed vesicles made with dsGUV [279].

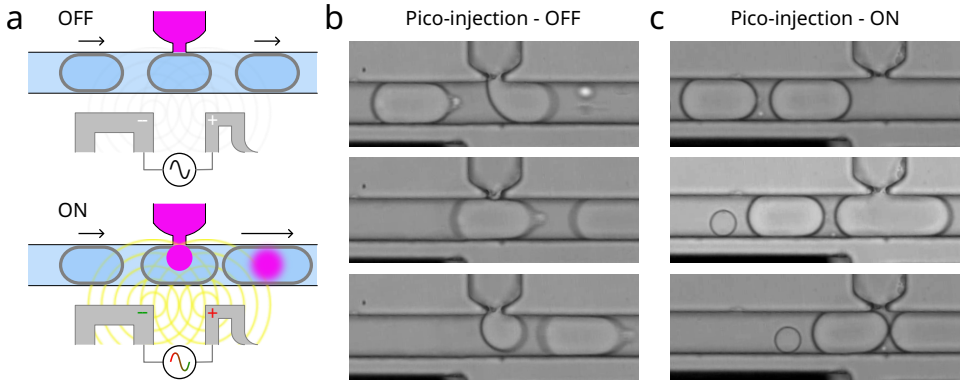

Figure 2.9: **Pico-injection of vesicles.** (a) Schematics showing the pico-injection technology. Shown is a T-junction with pre-made vesicles (dsGUVs) flowing along a horizontal channel, and a perpendicular/vertical channel with narrow opening which contains the protein of interest solution. A pair of electrodes is present on the opposite side of the T-junction. (top) OFF scenario — vesicles pass the T-junction unaffected. (bottom) ON scenario — an electric field (0–1000 V, 20 000 Hz) is applied at the T-junction with the help of the electrodes. The electric field disrupts the droplet interface and membrane as the dsGUVs pass the T-junction and triggers the pico-injection. The protein solution gets injected in to the dsGUVs. (b) OFF scenario (top) dsGUV approaching the T-junction (some protein solution leaks into the horizontal channel due to negative flow pressure). (middle) Protein solution cannot enter the dsGUV. (bottom) dsGUV passes by the T-junction unaffected. The size of the dsGUV is the same before and after passing the T-junction. (c) ON scenario (top) dsGUVs approaching the T-junction. (middle) Protein solution being injected into the first dsGUV. The size of the dsGUV increases. (bottom) Pico-injection stops when the first dsGUV has passed by the T-junction. Following dsGUVs will also get injected as they pass by the T-junction. All images are bright-field, captured with a high-speed camera. The black edge at the bottom-left is one of the (negative) electrodes. See Fig. 2.S7 for movies.

When no electric field is applied, the vesicles pass by the T-junction, with no protein solution being injected into them (Fig. 2.9(a) top, Figs. 2.S7 & 2.9(b)). The size (with length as a proxy for volume) of the vesicle before and after crossing the T-junction remains the same. At times, some protein solution leaks from the T-junction as it is also under pressure. This is not an issue, as this solution does not contain lipids. It does not form any droplets and is diluted in the background solution. The flow rates need to be tuned such that the interface between fluids from the primary and injection channels remains maintained at the T-junction.

When a strong oscillating electric field is applied, the protein solution from the injection channel gets added to the passing vesicles (Fig. 2.9(a) bottom). The size of the vesicles can be seen increasing as they pass by the T-junction (Figs. 2.S7 & 2.9(c)). The amount of solution that can be injected ranges from femtolitres to picolitres, depending on the flow pressure applied on the injection channel. It also depends on the size of the vesicle, as bigger (longer) vesicles have more contact time at the T-junction. The injection stops as soon as the vesicle exits the T-junction. The newly injected solution can, at times, be seen even in the bright-field images as a blob. The injected protein solutions usually have a slightly higher optical density and viscosity, and do not immediately mix with the rest of the vesicle volume. The majority of the vesicles passing the T-junction get injected.

The pico-injection protocol is comparable to other microfluidic protocols in terms of complexity and experience required. Preparations similar to microfluidic methods are required: making the chip, casting PDMS, assembling and coating the devices. Plus the additional step of filling in the electrodes with liquid solder, a low melting temperature metal alloy. However, the technique requires special hardware, an oscilloscope, for generating a high-frequency alternating electric field, and a high-voltage amplifier capable of amplifying the electric field. An electric field that is always on works fine, but an advanced setup where a vesicle passing the T-junction triggers the electric field can also be implemented for precise control.

2.4.2 Shape control

Droplets and vesicles are spherical, while cells come in various shapes. Hence, it would be nice for a synthetic cell, droplet, or vesicle to also take different shapes. This can be achieved with the help of microfluidic traps of different shapes, like discs and tubes. Such shape modulation has been shown for droplets [309]. Here, we demonstrate the application of this technique to vesicles.

This method also uses microfluidic devices. The device contains multiple repeats of the traps, arranged in parallel rows with half a row offset per column, to maximize the chances of a vesicle getting trapped. The individual tubular trap that we used consists of two long parallel walls with a funnel opening at the front and narrow drainage channels at the back (Fig. 2.10(a)). The vesicle entering the trap gets transformed from a sphere into a long tubular cylinder (Fig. 2.10(b)). The vesicle needs to be osmotically deflated to increase its chances of getting trapped without bursting. No such measures are required for trapping droplets.

The shape modulation with microfluidic traps is comparable to other microfluidic protocols in terms of complexity and experience required. Preparations similar to

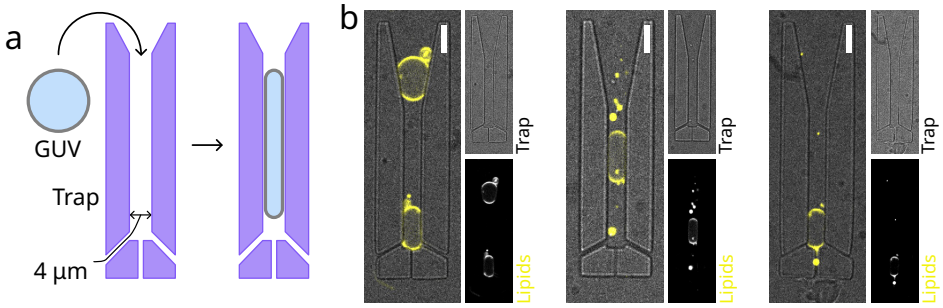

Figure 2.10: **Shape modulation of vesicles.** Vesicles tend to keep a spherical shape, but the shape of (osmotically deflated) vesicles can be changed using microfluidic traps. (a) Schematic of a tubular trap (cross-section width 4 µm and height ~4 µm). A spherical vesicle that is flown into trap transforms into a tubular vesicle. (b) Images of vesicles which become elongated after getting trapped into tubular microfluidic traps. Scale bar — 5 µm.

microfluidic methods are required: making the chip, casting PDMS, assembling and coating the devices. As a simple variant of shape-modulating traps, large traps or baskets can be used to just hold the vesicle for long-term observations without any shape modulation.

2.5 Discussion

We explored several techniques for the production of synthetic cell containers. The goal was to identify techniques that give a high yield of containers along with size control, which can also handle complex encapsulations in a consistent and reliable manner. As a preliminary evaluation, we tested container production with just the buffer or, at times, with a simple protein, SspB.

Droplets made by pipetting and dragging are the easiest and fastest way to make containers and encapsulate proteins in 3D. While droplets made with microfluidics offer better control over size, this comes at a cost of more time and effort. The inability to deform and the presence of only a lipid monolayer remain the biggest drawbacks of the droplets.

In the case of vesicles, the swelling-based approach is the fastest and easiest way to make vesicles. However, protein encapsulation is not ideal. Among the various emulsion transfer-based techniques, cDICE and OLA remain the most effective and optimal methods for generating vesicles when encapsulating proteins. Both cDICE and eDICE require special hardware, where skipping the use of a capillary can simplify the protocol at the cost of size control. Note, however, that vesicle collection from a tilted chamber is a learning experience. OLA does produce a high yield of vesicles with size control but requires optimizing and knowing ideal flow rates of the solutions. The success of OLA is also tightly related to the quality of coating of the PDMS devices, especially near the T-junction. Even a small deviation or error in coating can result in failure. Both, cDICE and OLA, come with some nuances that a

user needs to discover with experience or can only pick up by seeing an in-person demonstration. Often these minor details and optimizations are intentionally or unintentionally left out of the written protocols. DSSF, despite seemingly a fairly simple and straight-forward method, failed to make vesicles in our hands. Even trying different DSSF variants and their optimizations just led to poor droplet production but no successful vesicle formation. We think better hydrophobic surface treatment of the MiCA disc can improve inefficient droplet formation.

The fusion-based method, dsGUV, seems just as good as emulsion-based methods like cDICE and OLA. Vesicles can be made as easily as droplets just by shaking when there is no need for size control. Some reagents are, however, uncommon, with limited availability, and some reagents need to be custom synthesized.

Table 2.1 highlights the point that no one method fits all the purposes, but generally swelling-based methods are ideal for membrane characterization and emulsion transfer-based methods are ideal for encapsulating proteins. The dsGUV method also shows great promise as an alternative approach for protein encapsulation. Here our focus remained limited to container yield and size control, but how would encapsulating more complex proteins, especially cytoskeletal proteins, affects these techniques will be important for our purposes (see Ch. 4). While successful attempts have been made to encapsulate cytoskeletal proteins (see review [316]), it is interesting to test some of these methods in more detail and evaluate their efficacy, given how many optimization steps are already required to form containers solely with buffers and simple proteins.

New methods for the production of containers are constantly being developed to overcome current limitations. In general, better attention should be given to the documentation of protocols. Initial efforts have been made to create a standardized template[24] for data collection across labs in order to formulate a generic vesicle production protocol. Providing detailed explanations for each step as well as the reason for chosen values of parameters in those steps is important. Even mentioning that a certain value of a parameter is empirical and has no particular reason helps in better understanding a method. Ideally, alternatives for reagents and instruments from different vendors should also be suggested. Or at least an explanation for the choice of a current one should be given so that alternatives can be identified appropriately. For example, in the case of most emulsion transfer methods, why does the outer aqueous solution need to be a sugar solution in deionized water instead of a buffer? In cDICE, why is a particular ratio of silicon oil to mineral oil used for the lipid-oil dispersion? In DSSF, why are there contrasting values across protocols, such as short high-speed vs. long low-speed centrifugation? In dsGUV, why use specifically HFE7500 oil or an cTS with PEG 1500? For the cDICE protocol (see Methods Sec. 2.6), we have tried to provide such detail based on our experiences. Also, efforts should be made during method development to make sure it is compatible with basic minimal biological systems. Not necessarily with testing

[24] [personal communications] Together with Eugenia Romantseva (Build-a-Cell; National Institute of Standards and Technology, Maryland, USA) and James Hindley (fabriCELL; Imperial College London, London, UK), as a part of 'Metrics for containers' working group, during the satellite Build-a-Cell workshop #10, following the SynCell 2023 conference, Minneapolis.

with proteins, but at least with buffers with physiological salt conditions, and not just limiting the demonstration to a proof-of-principle with a sugar solution in deionized water.

The use of supplementary techniques like pico-injection or microfluidic shape modulation can be used to overcome some limitations of primary container formation methods. These can allow for subsequent encapsulation of complex protein mixes while keeping steps of vesicle formation simple or have the ability to make non-spherical containers.

Method development taking into consideration the practical biological applications; providing detailed protocols with detailed explanations for each step, all parameter values; and choice of reagents will significantly help the end-user to reproduce the protocols and make informed choices for optimization steps if required. This will undoubtedly facilitate more complex *in vitro* reconstitutions of protein systems and advance our goal of building a synthetic cell with a bottom-up approach.

2.6 Material and Methods

2.6.1 Materials

Chemicals Chemicals were purchased from Merck (Merck Life Science NV, Netherlands), unless otherwise stated: Mineral oil (M5904 Sigma), Silicone oil (viscosity 5 cSt, 25 °C, 317667 Sigma), Span® 80 (S6760 Sigma), Fluorescein 5-isothiocyanate (FITC), Silicone Elastomers RTV615 (PDMS, RTV615 Momemtive, Lubribond), 1,4-Piperazinediethanesulfonic acid, Piperazine-1,4-bis(2-ethanesulfonic acid), Piperazine-N,N'-bis(2-ethanesulfonic acid) (PIPES, P6757 Sigma), magnesium chloride ($MgCl_2$, M8266), ethylene glycol-bis(2-aminoethylether)-N,N,N',N'-tetraacetic acid (EGTA, E3889 Sigma), potassium hydroxide (KOH, 221473 Sigma), κ-casein (C0406 Sigma), Molykote high-vacuum silicone grease (vacuum grease, Z273554 Sigma), Parafilm® (P7793 Sigma), Chloroform (102447 Supelco), OptiPrep™ (D1556 Sigma) 1H,1H,2H,2H-Perfluoro-1-octanol (PFO, 370533 Sigma) .

Lipids All lipids were purchased from Avanti Research (Merck Life Science NV, Netherlands): 1,2-di-(9Z-octadecenoyl)-sn-glycero-3-phosphocholine (DOPC, 850375C), 1,2-di-(9Z-octadecenoyl)-sn-glycero-3-phospho-L-serine (sodium salt) (DOPS, 840035C), 1,2-di-(9Z-octadecenoyl)-sn-glycero-3-phosphoethanolamine (DOPE, 850725C), 1,1',2,2'-tetra-(9Z-octadecenoyl) cardiolipin (sodium salt) (Cardiolipin, 710335C), 1,2-distearoyl-sn-glycero-3-phosphoethanolamine-N-[biotinyl(polyethylene glycol)-2000] (ammonium salt) (DSPE-PEG(2000)-Biotin 880129C), 1,2-distearoyl-sn-glycero-3-phosphoethanolamine-N-[methoxy(polyethylene glycol)-2000] (ammonium salt) (PEG(2000)-PE 880120C), 1,2-dioleoyl-sn-glycero-3-phosphoethanolamine-N-(Cyanine 5) (Cy5-PE, 810335C), ATTO 488 1,2-dioleoyl-sn-glycero-3-phosphoethanolamine (AF488-PE, AD 488-161, ATTO TEC GmbH Siegen, DE).

All lipids were stored under argon in amber glass vials ND9 (548-0030A, VWR Avantor), with caps (548-8002A, VWR Avantor) sealed with Parafilm and stored at −20 °C. Lipids were handled in a fume hood with glass syringes (700RN series, Hamilton®).

BUFFERS AND PROTEINS MRB80 buffer was composed of 80 mM PIPES, 4 mM $MgCl_2$, and 1 mM EGTA. pH 6.8 was adjusted with KOH solution (initially, with KOH pellets). 5 x and 1 x buffer stocks were made, filter sterilized (Whatman™ 0.2–0.45 µm) and stored at –20 °C. MRB80 buffer was used in all experiments, unless otherwise stated.

Oxygen scavenger (OX) mix was composed of 200 µg mL^{-1} catalase, 400 µg mL^{-1} glucose oxidase, and 4 mM DTT in MRB80. 50 x stock was made and stored at –20 °C.

All protein mixes were made on ice (4 °C), unless otherwise stated.

General conditions for protein purification from *Escherichia coli* — Relevant plasmids were transformed into *Escherichia coli* ER2566 cells (New England Biolabs, *fhuA2 lacZ::T7 gene1 [lon] ompT gal sulA11 R(mcr73::miniTn10–Tet^S)2 [dcm] R(zgb-210::Tn10–Tet^S) endA1 Δ(mcrC-mrr)114::IS10*) containing a Rosetta™2 plasmid (Novagen), and selected on LB agar media supplemented with 34 µg mL^{-1} chloramphenicol and either 100 µg mL^{-1} ampicillin or 50 µg mL^{-1} kanamycin. For expression, overnight pre-cultures were diluted 1:100 into 1–4 L prewarmed LB or TB with fresh antibiotics and cultures were grown in baffled flasks shaking at 200 rpm at 37 °C until the OD_{600} reached ∼0.6. Expression was induced by IPTG and either performed for 2–3 h at 37 °C, or (following a 30 min incubation on ice) overnight at 18 °C. Cells were harvested by centrifugation (10 min, 4000 rpm, JLA8.1000 rotor), washed in 50 mL PBS, and lysed using a French Press (CF1 Constant Systems) at 20 kpsi, 4 °C. Unbroken cells, debris, and aggregates were pelleted in a Ti45 rotor (30 min, 40 000 rpm, 4 °C). Affinity purification was typically performed with either Talon® Superflow™ (Cytiva GE28-9575-02), HisPur™ Ni-NTA Resin (Thermo Fisher 88222), cOmplete™ His-Tag Purification Resin (Roche 5893682001), amylose resin (New England Biolabs E8022S) or Glutathione Superflow Agarose (Thermo Fisher 25237). Prior to size exclusion chromatography (on a Superdex 75 or 200 Increase 10/300 column), proteins were concentrated using a MWCO 10 kDa Vivaspin centrifugal concentrator (Sigma Z614610).

YFP-LactC2-iLID — A maltose binding protein (MBP) fusion construct encoding MBP-3C-YFP-L_1-C2-L_2-iLID was synthesized and cloned into pMAL-c5X by Genscript (pED48), where 3C represents the recognition site LEVLFQGP for human rhinovirus protease 3C, YFP the monomeric yellow fluorescent protein mEYFP [317], L_1 the short linker sequence SGLRS, C2 the phosphatidylserine-binding domain of bovine lactadherin (residues 270–427 from Uniprot Q95114), L_2 the long linker sequence GSGSGSEAAAKEAAAKEAAAKGSGSGS, and iLID and improved light-induced dimerization domain [240]. The protein was expressed overnight at 18 °C in terrific broth medium, purified using amylose resin (New England Biolabs E8022S) in PBS supplemented with 10 mM EDTA, 0.1 % $Tween_{20}$ and 250 mM NaCl. MBP was cleaved off with homemade 3C protease and the final buffer used for size exclusion chromatography was 20 mM HEPES/NaOH pH7.5 (room temperature), 200 mM NaCl, 5 %w/v glycerol.

pED48 | MBP 3C YFP L_1 C2 L_2 iLID

```
  1 MKIEEGKLVI WINGDKGYNG LAEVGKKFEK DTGIKVTVEH
```

```
  41 PDKLEEKFPQ VAATGDGPDI IFWAHDRFGG YAQSGLLAEI
  81 TPDKAFQDKL YPFTWDAVRY NGKLIAYPIA VEALSLIYNK
 121 DLLPNPPKTW EEIPALDKEL KAKGKSALMF NLQEPYFTWP
 161 LIAADGGYAF KYENGKYDIK DVGVDNAGAK AGLTFLVDLI
 201 KNKHMNADTD YSIAEAAFNK GETAMTINGP WAWSNIDTSK
 241 VNYGVTVLPT FKGQPSKPFV GVLSAGINAA SPNKELAKEF
 281 LENYLLTDEG LEAVNKDKPL GAVALKSYEE ELVKDPRIAA
 321 TMENAQKGEI MPNIPQMSAF WYAVRTAVIN AASGRQTVDE
 361 ALKDAQTNSS SNNNNNNNNN NLGIEGRISH MSMGGRDIVD
 401 GSDYDIPTTL EVLFQGPKLG GMVSKGEELF TGVVPILVEL
 441 DGDVNGHKFS VSGEGEGDAT YGKLTLKFIC TTGKLPVPWP
 481 TLVTTFGYGL QCFARYPDHM KQHDFFKSAM PEGYVQERTI
 521 FFKDDGNYKT RAEVKFEGDT LVNRIELKGI DFKEDGNILG
 561 HKLEYNYNSH NVYIMADKQK NGIKVNFKIR HNIEDGSVQL
 601 ADHYQQNTPI GDGPVLLPDN HYLSYQSKLS KDPNEKRDHM
 641 VLLEFVTAAG ITLGMDELYK SGLRSCTEPL GLKDNTIPNK
 681 QITASSYYKT WGLSAFSWFP YYARLDNQGK FNAWTAQTNS
 721 ASEWLQIDLG SQKRVTGIIT QGARDFGHIQ YVAAYRVAYG
 761 DDGVTWTEYK DPGASESKIF PGNMDNNSHK KNIFETPFQA
 801 RFVRIQPVAW HNRITLRVEL LGCGSGSGSE AAAKEAAAKE
 841 AAAKGSGSGS LATTLERIEK NFVITDPRLP DNPIIFASDS
 881 FLQLTEYSRE EILGRNCRFL QGPETDRATV RKIRDAIDNQ
 921 TEVTVQLINY TKSGKKFWNV FHLQPMRDYK GDVQYFIGVQ
 961 LDGTERLHGA AEREAVCLIK KTAFQIAEAA NDENYF
```

SspB-nano-mOrg, **SspB-mCh** — Opto-protein SspB variants (with mOrange and mCherry) were purified in-house as described in Guntas et al. [240].

SAMPLE PREPARATION The glass slides were cleaned by 30 min sonication cycles in KOH (optional), 5 %v/v Hellmanex™ III (Z805939 Hellma), and deionised (Milli-Q®) water. Glass coverslips were cleaned in acid Piranha solution (sulfuric acid : chilled 30 % hydrogen peroxide, ratio 3:1) for 10 min (protocol based on [318]). Piranha treatment was followed by rinsing and 15 min sonication (Ultrasonics™ CPX-952-238R Branson) in deionised water. Coverslips are stored under deionised water. Samples were imaged on #1 glass coverslips (24x24 Epredia, VWR) and glass slides (126x76 Epredia, VWR). Flow chambers were created with coverslip and glass slide separated by two layers of parafilm (height ∼200 µm, chamber volume ∼50–150 µL). Parafilm was adhered to glass surfaces by heating briefly on a hotplate. During the incubation period, flow chambers were kept in a dark and moist environment (aluminum foil wrapped petri-dish, with wet tissue papers).

Droplets and GUVs were transferred with a cut-off 200 µL pipette tip to prevent further shear induced breakage. Droplets were imaged in PDMS wells or in flow chambers. PDMS wells were created with ∼5 mm thick PDMS slab with holes made with ∼2 mm biopsy punches, adhered on a glass coverslip. GUVs were imaged in flow chambers. Flow chambers were washed with MRB80 buffer, passivated with

κ-casein (0.5 mg mL^{-1}, 10 min), and washed with OA solution. After flowing in GUV solution, flow chambers were sealed with vacuum grease to prevent evaporation.

IMAGE ACQUISITION AND DATA ANALYSIS Samples were observed on a Nikon ECLIPSE Ti-E inverted microscope with a spinning disk confocal head (CSU-W1-T2 Yokogawa, Japan), ring-TIRF unit (iLas 3 GATACA Systems, Paris) with 405 nm (100 mW), 488 nm (150 mW), 561 nm (100 mW), 642 nm (110 mW) laser lines and a quad filter cube (TRF89901 Chroma), 355 nm (400 ps, 2 kW) UV ablation pulse laser, dual EM-CCD cameras (Evolve512 Photometrics), 100 x objective (CFI APO TIRF 100XC oil 1.49 NA, Nikon), and 100 x objective (CFI S Fluor 100XS oil 0.5–1.3 NA, Nikon) for UV ablation. The final magnification was 6.25 pixel/µm. The objectives were heated (22–30 °C, if required) with a custom 3D printed metal collar and a custom water heater and pump (AMOLF).

The microscope setup was controlled with MetaMorph software (v7.10.4 Molecular Devices, LLC.). The images were acquired with 0.5–1 s frame time and ∼100 ms exposure per channel. The images were analysed using FIJI ImageJ [319]. Data was processed using Python (v3.8.x Anaconda, LLC.), unless otherwise indicated.

2.6.2 Protocol

Droplets

Protein mix A 500 µL mix (IA) of 50 nM FITC in MRB80.

Lipid-in-oil (LO) dispersion Lipid solution of 99.993 75 n% (molar percentages) DOPC and 0.006 25 n% Cy5-PE was made in chloroform. Lipids were dried under a gentle N_2 gas stream in a screw cap glass vial and dessicated under vacuum for 2 h. Mineral oil and 0.6 %v/v Span 80™ (0.6–2 %v/v) were added to make lipid concentration of 0.625 mg mL^{-1}. The dried lipid film and oil solution was sonicated in water-bath sonicator (Ultrasonics™ CPX-952-238R Branson) for 30 min. The glass vial threads were wrapped with Teflon tape, and the closed cap was sealed with a Parafilm. The LO solution was stored at 4 °C and used for up to 1–2 weeks.

FORMATION Pipetting and dragging — Droplets were formed based on the protocol described in Vendel et al. [239]. 0.5–1 µL protein mix was added to 40–50 µL LO solution in a micro centrifuge tube (0.5 mL Eppendorf). Droplets were made by either pipetting up and down 20–40 times with a 10 µL pipette or by dragging the tube over the tube rack (short or long side) 5–10 times. The droplets were allowed to settle in the tube for ∼5 min and retrieved from the bottom of the tube with a cut-off 200 µL pipette tip.

Microfluidic chip — Droplets were formed based on the protocol described in Vleugel et al. [235]. The microfluidic chip was connected to solution reservoirs with PEEK or FEP tubing (211508-10 ID 1 mm; 211582-3 ID 0.5 mm) and flow was regulated with a pressure controller pump (MFCS™ -EZ 1000 mbar Fluigent, Paris). The pump was controlled by MAESFLO software (v3.3.1 Fluigent, Paris). The formation of droplets (size and frequency) was controlled with regulating aqueous and LO solution flow rates (∼1:4 pressure ratio).

The chip moulds were fabricated from silicon wafers (J14059 Siegert Wafers GmbH) either with SU-8 soft/optical lithography (described in [235]) or with a DRIE

Bosch process (deep reactive ion etching, described in [320]) with ICP (inductive coupled plasma) on PlasmaPro 100 Estrelas (Oxford Instruments), using SF6/C4F8 gasses and photo-resist mask (ARN4400). The silicon moulds were treated with Trichloro(1H,1H,2H,2H-perfluorooctyl)silane (448931 Sigma) for 2–24 h under roughing pump vacuum in an inert (with Argon gas) environment to prevent adhesion of PDMS to the wafer.

The chip devices were made with PDMS. The PDMS pre-polymers were mixed in 10:1 ratio and vacuum degassed for ∼30 min. PDMS was poured on to the silicon wafer and vacuum degassed again for ∼30 min. Glass coverslips were either coated with PDMS using a spin coater (Spin 150i Polos) or pressed in PDMS against a blank silicon wafer to create a minimal PDMS layer. The PDMS was cured by baking in an oven (E 28 Binder) at 100 °C for 1 h. The PDMS microfluidic device moulds were cut using razor blades and inlets holes were created using biopsy punches. The PDMS devices and PDMS coated glass coverslip were activated by Oxygen plasma treatment (50 W, 30 s, Plasma Prep III SPI) before bonding. Assembled devices can be further heated for ∼15–30 min.

GUV

Bead swelling

PROTEIN MIX A 20 µL mix (IA) of 1 mM Trolox, 0.5 mg mL^{-1} κ-casein, 1 x OX, 2 µM YFP-LactC2-iLID, 2.25 µM SspB-mOrg, 50 mM KCl, and 50 mM glucose (added at last) was made in MRB80.

LIPID COATED BEADS Lipid solution (2.543 µmol) of 62.3 n% DOPC, 35.6 n% DOPE, 2.1 n% Cardiolipin, 1 n% DSPE-PEG-biotin, and 0.5 n% Cy5-PE was made in chloroform in a 10 mL round-bottom flask. Flushed (wash syringe) with additional chloroform (2 x volume of lipids). Rhamnose (100 mM in methanol) was added to make chloroform:methanol ratio 2.5:1. 600 mg of glass beads (∼200–300 µm) were added. The mixture was dried with a rotary evaporator (200 mbar, 50 rpm, 2–3 h). Dried lipid coated beads were recovered with a small spatula and split into 6 micro centrifuge tubes. Beads are further dried overnight in a vacuum desiccator. Tubes were flushed with argon, sealed with parafilm, and stored at –20 °C.

FORMATION GUVs were formed based on the protocol described in [296, 297]. Some (∼10–25 mg) lipid coated were taken in a fresh micro centrifuge tube and IA (swelling protein mix) solution was added. GUVs were allowed to swell on ice (with frequent rocking) or on a rotor (∼10 rpm) in the cold room for 2 h. 4 freeze-thaw cycles, freezing in liquid N_2 and thawing on ice, were performed. The mixture can be diluted (2.5–10 x) with buffer to reduce protein (IA) concentration on the outside of GUVs.

Flow chambers were functionalized with BSA:BSA-Biotin (0.666 mg mL^{-1}, 10 min) and Neutravidin (1 mg mL^{-1}, 10 min) to attach GUVs at the glass surface. Each step of functionalization incubation was followed with MRB80 washes.

Gel swelling

PROTEIN MIX A 100–200 µL mix (IA) of 1 mM Trolox, 0.5 mg mL^{-1} κ-casein, 1 x OX, 2 µM YFP-LactC2-iLID, 2.25 µM SspB-mOrg, 50 mM KCl, 50 mM glucose (added at last), and 50 mM sucrose was made in MRB80.

LIPID COATED COVERSLIP Lipid solution (1 mg mL^{-1}) of 69.5 n% DOPC, 30 n% DOPS, and 0.5 n% Cy5-PE was made in chloroform. 100 µL of PVA solution (5 %w/v, 200 mM sucrose) was spread on an O_2 plasma cleaned (20 W, 30 s) coverslip by tilting until all area was covered. Excess PVA solution was absorbed with a tissue paper (from one corner). The coverslip was baked in an oven (100–120 °C, 30 min) to dry the PVA gel. Lipid solution (10 µL per coverslip) was added and spread on PVA coated coverslip with the help of a syringe needle shaft (until most of the chloroform was evaporated). The coverslip was dried in a vacuum desiccator for 30 min.

FORMATION GUVs were formed based on the protocol described in [295]. 100–200 µL of IA solution was added to a lipid coated PVA coverslip and spread around. The GUVs were allowed to swell for ∼5–10 min. The swelled GUVs were collected in a micro centrifuge tube from one corner of a tilted coverslip. The coverslip was washed with additional ∼200 µL OA solution (50 mM glucose in MRB80) to aid removal of GUVs from the PVA gel surface and also to dilute the protein (IA) concentration outside the GUVs (in OA solution).

cDICE and eDICE

PROTEIN MIX A 40–200 µL mix (IA) of 0.5 µM SspB-Ch and 18.5 %w/v[25] OptiPrep™ was made in MRB80[26]. A 1000 µL solution (OA) of glucose in deionised water. The osmolarity of IA was measured (∼272 mOsmol) with a freezing point osmometer (OSMOMAT® 3000, Gonotec GmbH) and the osmolarity of the OA solution was adjusted with glucose (∼290 mOsmol; ∼ +Δ15–20 mOsmol[27]).

LO SOLUTION Lipid solution (1.728 µmoles) of 99.89 n% DOPC, 0.01 n% PEG-2k-PE[28], and 0.1 n% Cy5-PE was made in chloroform in a glass vial (10000782 Fisherbrand, Thermo). Lipids were dried under a gentle N_2 gas stream in a glass vial (with threads wrapped in a Teflon tape[29]) and dessicated under vacuum for 30 min.

The glass vial was transferred into a glovebox[30]. The dried lipid were first resuspended in 415 µL (6 % of final volume) chloroform (or n-decane:chloroform) solu-

[25] [Arbitrary] higher density difference in IA and OA results in better GUV yield, as low as 6.5 %w/v shown to considerable GUV yield.

[26] Since significantly high volume (∼20 %v) of density medium reagent (OptiPrep™ or glucose) are added, use of 5 x stock of MRB80 buffer (instead of 1 x buffer stock to make up solution volume) allows for maintaining the buffer composition.

[27] [Arbitrary] Osmolarity of OA should be slightly higher than IA so that GUVs are slightly deflated, and the bilayer does not have a high membrane tension.

[28] Addition of a small fraction of PEGylated lipids results in better GUV yield, the PEG chain is suspected to prevent interaction of GUV membranes, sticky GUVs, and bursting. Presence of a higher fraction of PEGylated lipids starts to adversely affect the GUV yield.

[29] Teflon tape creates a better air-seal between vial and its cap, preventing moisture to enter the vial.

[30] Inert N_2 environment, <1 % humidity, promotes better yield.

tion[31]. Silicone oil and mineral oil were combined in 4:1 ratio[32] and mixed vigorously by vortexing. Under continuous gentle vortexing, 6.5 mL (94 % of final volume) of oil mixture was slowly added to the dissolved lipid-chloroform solution in the vial. This resulted in 0.25 mM[33] LO concentration. The vial was capped and sealed with parafilm[34]. The sealed vial was immediately vigorously vortexed for 30 s in the glovebox and then removed from the glovebox.

The LO solution was again vigorously vortexed for 2 min and sonicated in an ice (double boiler[35]) bath for 15 min. LO solution was immediately used for GUV preparation but can be stored at 4 °C to be used on the same day.

FORMATION cDICE — GUVs were formed based on the protocol described in [271, 277]. Also read Ch. 3 for more details. GUV formation was performed at room temperature ((24 ± 1) °C) in a humidity (RH 10–20 %) controlled room. We used a home-built spinning chamber setup and 3D-printed chamber[36] described in [277]. The chamber was placed on the rotor and set to spin at 1900 rpm[37]. 700 µL of OA solution and ∼5.5 mL of LO solution were added consecutively. The (5–20 µm) glass capillaries (as described in Abkarian et al. [271]) were used initially. These capillaries were formed in two steps. First, a glass capillary (EC130-0016 Harvard Apparatus, US) was pulled in to two fine capillaries using a laser-heated pipette puller (P-2000 Sutter Instruments Co.) with settings: Heat 450, Filament 4, Velocity 50, Delay 255, and Pull 150. The pulled end of capillaries were cut to diameters of desired opening using a microforge (MF-900 Narishige). However, later the 100 µm[38] capillary (fused silica tube[39] TSP-100375) was used. The capillaries were connected to a syringe filled with protein-less IA solution. The syringe was mounted on the syringe pump (PHD ULTRA™ Harvard Apparatus, US). The IA solution was pulled in from the capillary. The capillary was mounted on the setup and inserted into the spinning chamber from the central opening at the top, just as to insert the capillary tip[40] inside the LO solution. The IA solution was injected at 10 µL min^{-1}[41]

[31] Lipids have lower solubility in n-decane compared to chloroform, which results in bigger lipid aggregates in LO solution eventually. This affects lipid adsorption at the water-oil interface during droplet's flight in LO solution. Even 10–20 % n-decane shows significantly better yield, with slight lipid aggregates and irregularities. With higher n-decane percentage, it becomes difficult to completely resuspend dried lipids.

[32] [Arbitrary] Lipids have lower solubility in silicone oil compared to minieral oil. The ratio of the oils can be tweaked. This also affects the size of lipid aggregates in the LO solution.

[33] 0.1–2 mM Lower LO concentration is preferred for better lipid adsorption, but complete water-oil surface coverage of lipid is limited by droplet's time-of-flight in LO solution.

[34] To further improve the air-seal of the glass vial, for water-bath sonication later.

[35] Lipids are temperature sensitive (T_M melting temperature), and sonication generates heat. A dual glass beaker setup, with ice filled in between them, acts as a heat sink.

[36] [Arbitrary] Chamber size can be customized, but it's effect on other interdependent parameter (e.g. time of flight) needs to be taken into account.

[37] [Arbitrary] Can be changed, but it's effect on other interdependent parameter (e.g. IA solution density, LO concentration, Bond number) needs to be taken into account.

[38] Small diameter (5–20 µm) capillaries provide better control over GUV size but are prone to clogging with proteins.

[39] Polyimide coating provides hydrophobic surface and removes the need for silanization and optical glue.

[40] Capillary tip should be parallel to the ground and orthogonal to the LO solution interface.

[41] [Arbitrary] 10–50 µL min^{-1} Low flow rate is preferred. Higher flow rate can lead to jetting and high-back

Few minutes after the IA solution was completely injected, the spinning chamber was slowly stopped[42]. The chamber was tilted (45–90°) slowly, along with slowly removing the majority of the LO solution (to prevent overflow from the central hole, after tilting). GUVs were allowed to settle down and concentrate at the bottom for ∼10 min and retrieved (∼1.33 x IA solution volume) from the bottom of the chamber with a cut-off 200 µL pipette tip.

eDICE — GUVs were formed based on the protocol described in [288, 300]. The protocol was similar to cDICE, but no use of capillary for droplet formation. Instead, IA-LO droplet emulsion was created by dragging[43]. Only ∼5 mL of LO solution was added to the spinning chamber, and the rest 1 mL LO solution was added to a 2 mL micro centrifuge tube. The ∼25 µL IA solution was added to the LO solution tube. Emulsions were made by dragging the tube over the tube rack (short or long side) 5–10[44] times. The emulsion was immediately[45] added into the spinning chamber and setup was allowed to spin for 3 min. The chamber was stopped slowly and GUVs are recovered in a similar manner as in the cDICE protocol.

OLA

PROTEIN MIX A 80 µL mix (IA) of 1 mM Trolox, 0.5 mg mL^{-1} κ-casein, 1 x OX, 0.5 µM YFP-LactC2-iLID, 0.56 µM SspB-mOrg, 50 mM KCl, 15 % glycerol, 5 mM dextran (6000 MW) and 50 mM glucose (added at last) was made in MRB80 (5 x). A 100 µL solution (OA) of 15 % glycerol, and 5 % F68 surfactant was made in MRB80 (5 x).

LIPID-OCTANOL SOLUTION Lipid mix of 99.9 n% DOPC, and 0.1 n% Cy5-PE was made in chloroform. LO solution (80 µL, 5 mg mL^{-1}) was made of 4 µL lipid mix and 76 µL 1-octanol.

FORMATION GUVs were formed based on the protocol described in [301, 321]. The microfluidic device was connected to the pressure pump with tubing. Pressure was applied to the IA (∼100 mbar), LO (∼100 mbar), and OA (∼200 mbar) solution channels. Once the device is filled with OA untill the exit hole, pressure was reduced to 100 mbar. Air bubbles from the channel and junction were removed by temporarily increasing the LO and IA pressure to 200 mbar consecutively. Once all air bubbles were removed, pressures in all channels were reduced to 50 mbar. The LO channel pressure was gradually increased (+0.1–1 mbar) to optimize GUV formation at the junction.

The chip moulds were made on silicone wafers with SU-8 photoresist (described in [321]). The chip devices were made with PDMS. The PDMS microfluidic device moulds were cut and assembled on PDMS coated coverslips (as described above in Microfluidic droplet formation Sec. 2.6). The exit channel after the junction in the microfluidic device was made hydrophilic by treating it with PVA solution (5 %w/v,

pressure, depending on capillary diameter.

[42] Sudden stop can create turbulent flow, which can damage GUVs.

[43] This results in larger spread in droplet sizes, and eventually in GUV sizes, compared to capillary made droplets in cDICE.

[44] [Arbitrary] more number of dragging leads to overall smaller droplets

[45] IA-LO W/O droplet emulsion is unstable and starts merging, as it does not contain any artificial surfactant (apart from lipids) e.g. Span 80

5 min). No region before or including the 6-way junction should be rendered hydrophilic, as it would affect W/O/W emulsion formation.

Samples were observed on a Nikon-Ti2-Eclipse microscope with a pE-300ultra illumination system, and a Prime BSI Express sCMOS camera.

DSSF

PROTEIN MIX A 200 µL mix (IA) of 1.58 µM SspB-mCh was made in MRB80. A 1000 µL solution (OA) of glucose in deionised water (osmolarity adjusted, as described above in cDICE protein mix Sec. 2.6).
LO SOLUTION LO solution of 99.975 n% DOPC, and 0.025 n% Cy5-PE was made (as described above in cDICE LO solution Sec. 2.6).
FORMATION Droplets and GUVs were formed based on the protocol described in [302, 304]. The 30 µL OA and 170 µL LO for GUVs and 170 µL LO only for droplets were layered into a micro centrifuge tube. The DSSF setup (cup, holder, and O-ring) was assembled with a DSSF disc[46]. The assembly was mounted on the micro centrifuge tube. 20 µL IA solution was added on the DSSF disc. The tube was centrifuged at 1600 g for 3 min and/or at 13 000 g for 7 min. The droplets and GUVs were retrieved from the bottom of the tube with a cut-off 200 µL pipette tip.

dsGUV

PROTEIN MIX MRB80 buffer.
SO SOLUTION SUVs of lipid composition, 95.5 n% DOPC, 4 n% PEG-2k-PE, and 0.5 n% AF488-PE, were generated by extrusion (as described in [322]). Lipids were mixed and dried under N_2 stream. Lipids were vacuum dried in desiccator for 1 h. Dried lipids were resuspended in MRB80 buffer by sonication for 1 h. The aqueous lipid solution was homogenized by extruding 11 times through 200 nm and 50 nm pore size polycarbonate filters (610006, 610003 Avanti) consecutively using an extruder (610000 Avanti). A lipid containing aqueous (LA) solution was made of 2 mM SUVs in MRB80.

Tri-block PFPE(7000 g mol^{-1})-PEG(1500 g mol^{-1})-PFPE(7000 g mol^{-1}) (cTS) surfactant were synthesized (as described in [323]). cTS were dissolved in FC-40 / HFE-7500 fluorinated oil (3M, USA). The 400 µL surfactant-in-oil (SO) solution was made of 2.5 mM cTS and 10 mM Krytox in HFE-7500 oil.
FORMATION dsGUVs were formed based on the protocol described in [279]. The microfluidic device was connected to the pressure pump with tubing. Pressure was applied to solution channels to generate the following flow rates, LA (∼120 µL h^{-1}), and SO (∼160 µL h^{-1}). Stable droplet creation was achieved at 1 kHz rate. dsGUVs were incubated on rollers for 30 min (or overnight, for better yeild) in a cold room.

GUVs were released from dsGUVs, if needed. First, 100 µL of dsGUVs were added in 2 mL micro centrifuge tube containing 1 mL of SO solution. Next, 100 µL of MRB80 buffer was layered on top. The surfactant droplets were destabilized by addition of 100 µL of 20 %v/v PFO in HFE-7500 oil. Then the tube was carefully tilted and slowly

[46] The cup and holder were made in-house by milling PTFE material. And the DSSF disc was made as described in Sec. 2.6, with an AZ® 12XT mask.

rotated until the emulsion was broken. GUVs were collected from the tube with a cut-off 200 µL pipette tip.

The chip moulds were made on silicone wafers with SU-8 photoresist (described in [279]). The chip devices were made with PDMS. The PDMS microfluidic device moulds were cut and assembled on PDMS coated coverslips (as described above in Microfluidic droplet formation Sec. 2.6). The channels were made hydrophobic by treating with Ombrello (5 min). The device was heated on a hot plate to dry and evaporate excess reagent.

Samples were observed on a Leica SP5 confocal microscope (Leica Microsystems, Germany) with an argon and a white light laser, and a 63x oil objective (HCX PL APO 63x/1.40-0.60; Leica Microsystems GmbH, Germany).

PICO-INJECTION

INJECTION Pico injection was performed based on the protocol described in [279]. The PDMS devices were assembled (as described above in dsGUV section, see Sec. 2.6). Electrodes were filled with Indalloy® 19 (51 % indium, 32.5 % bismuth, 16.5 % tin, T_M 60 °C). The PDMS device was heated on a hot plate (90 °C), the alloy metal wire melts and fills in the electrode channels due to capillary forces. External electrical cables (with stripped ends) were inserted in inlets of electrode channels. The alloy solidifies once the device is taken off the hot plate. The electric cable joint with PDMS device was secured with a UV curable glue.

The design of electrodes was based on Abate et al. [308]. Electric field (1 kHz, 250 V) was applied using a signal generator (HM 8150, HAMEG Germany) and an amplifier (623B-H-CE, TREK USA). The electric field destabilizes the lipid bilayer and allows for injection of solution. 1–100 pL of solution was injected depending on the applied pressure.

SHAPE CONTROL

TRAP GUVs trapping was based on the protocol described in [309]. The chip moulds were made on silicone wafers with DRIE (described in [309]). The chip devices were made with PDMS. The PDMS microfluidic device moulds were cut and assembled on PDMS coated coverslips (as described above in Microfluidic droplet formation Sec. 2.6). The PDMS device was made hydrophilic by treating it with PVA solution (5 %w/v, 5 min) and excess PVA was removed from channels by vacuum (negative pressure) at the outlet. The device was baked in an oven (80 °C, 20 min) to completely dry the PVA gel.

GUVs were slightly deflated osmotically. The microfluidic device was connected to the pressure pump with tubing (see Sec. 2.6). Pressure was applied to flow in the GUVs in the channel containing traps. Half-drop / staggered repeats of traps increases chances of entrapment of GUVs. Once trapped, the GUV slides into the trap and changes shape.

2.7 Data Availability

All data used in the dissertation are available as a collection via 4TU.ResearchData at DOI: 10.4121/1647ae32-1a2d-4c18-8ad8-3e81ba87ac6a [324], which includes source data for the images and plots for all the chapters.

2.8 Acknowledgements

We thank Eli van der Sluis and Anne Doerr for purifying proteins. We thank the following people for their help with introduction and troubleshooting with encapsulation techniques — Kim Vendel (Droplets); Renu Maan (Microfluidic droplets); Anne Doerr (Bead swelling); Lennard van Buren (Gel swelling); Federico Fanalista (cDICE and trapping). We thank Nemo Andrea for making the silicon wafer moulds for microfluidic droplet chip and DSSF chip. We thank Cees Dekker for kindly providing the silicon wafer for microfluidic traps. We thank Roland Dries for help with microscopy and setting up cDICE setup. We thank Thibaud van Eupen for help with initial cDICE imaging and testing chambers. We thank Dimitri de Roos for making DSSF adaptors.

2.9 Supplementary Information

2.9.1 Supplementary Figures

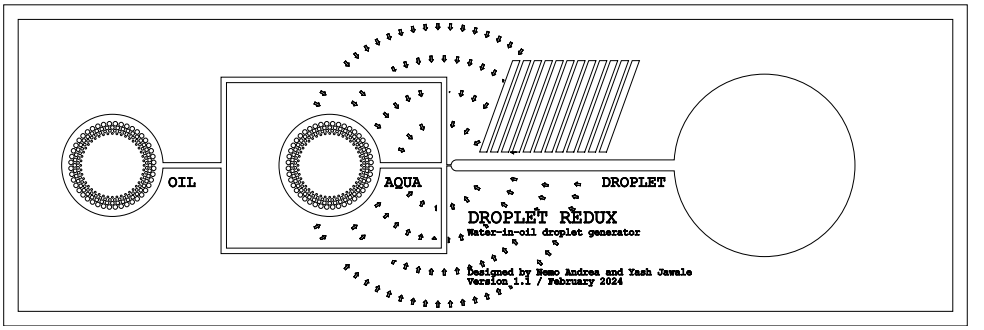

Figure 2.S1: **Microfluidic chip design.** Detailed scaled design for water-in-oil emulsion droplet formation (outer bounding box — height 4400 µm, width 13 000 µm). Inlets and outlet are labelled. Inlets have reducing circular filters for dust and protein aggregates. A cluster of arrows pointing towards a T-junction for easy navigation under microscope. A group of slanting lines helps with easy visual differentiation (with eye) of top and bottom surfaces on a PDMS device cast of the microfluidic chip.

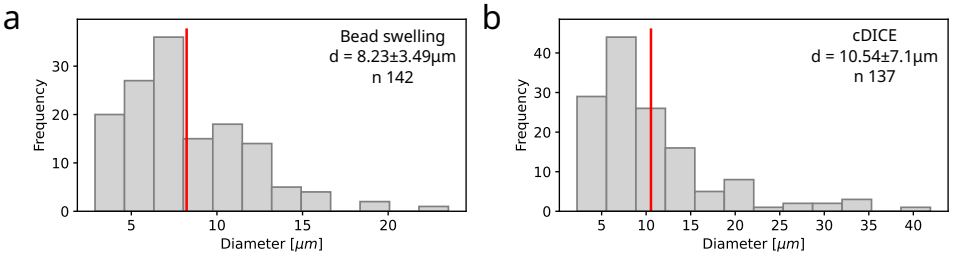

Figure 2.S2: **Vesicle size distribution.** The histogram of the sizes of vesicles made with, (a) bead swelling and (b) cDICE. The red line indicates the mean vesicle size. The number of histogram bins given by $\sqrt{n}$.

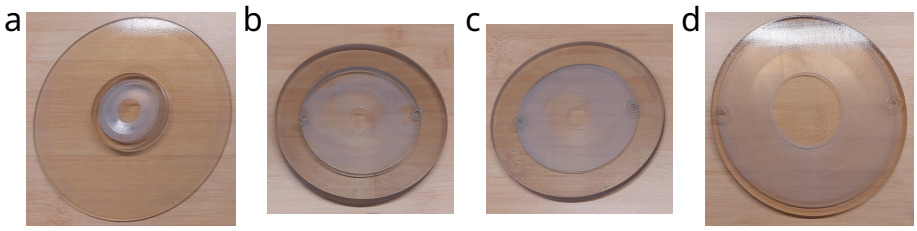

Figure 2.S3: **Variety of cDICE chambers.** Different sizes of 3D printed cDICE chambers, (a) original design [277] - $\varnothing_{chamber}$ 38 mm, h 7 mm, $\varnothing_{aperture}$ 17.5 mm (based on [271]), (b) design 1 - $\varnothing_{chamber}$ 90 mm, h 5 mm, $\varnothing_{aperture}$ 17.5 mm (partly inspired from [300]), (c) design 2 - $\varnothing_{chamber}$ 90 mm, h 2 mm, $\varnothing_{aperture}$ 17.5 mm (partly inspired from [300]), and (d) design 3 - $\varnothing_{chamber}$ 120 mm, h 2 mm, $\varnothing_{aperture}$ 47.5 mm. Chambers were 3D printed using a Objet260 Connex3 (Stratasys) printer (at AMOLF).

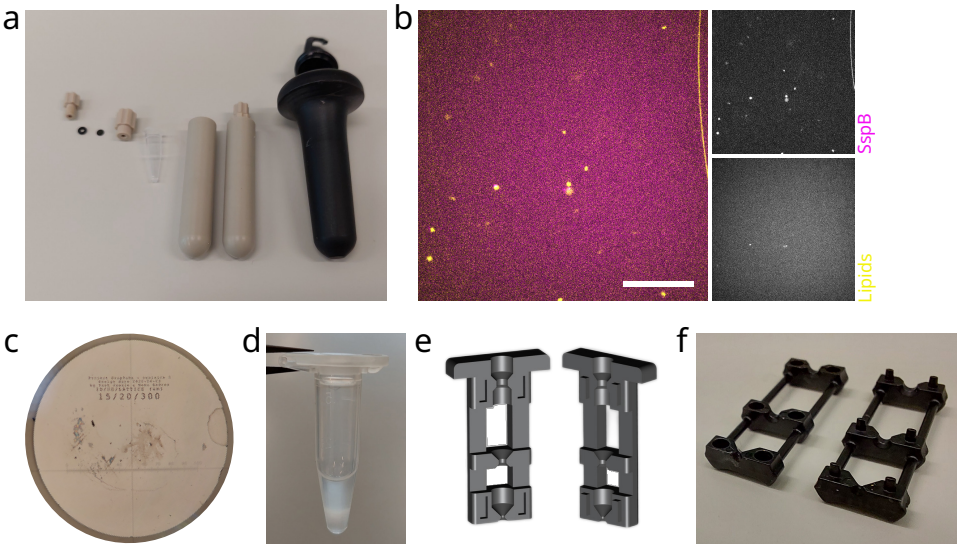

Figure 2.S4: **DSSF and variants.** (a) Photo of DSSF assembly (cap, O-ring, Si disc, holder), PCR tube, and swing rotor adaptor and swing rotor tube. (b) Vesicles made with 10 µm DSSF disc, IA — SspB-mCh (1.58 µM), LO — DOPC and Cy5-PE (0.025 n%), and OA. Vesicles seems very small, with almost no lipid signal (scale bar — 20 µm). (c) Image of silicon wafer disc with ⌀ 15 µm holes. (d) Photo of tube containing droplets (white, cloudy) formed with DSSF. (e) CAD model (used for 3D printing) of our custom DSSF variant, that uses single capillary for formation of droplets. (f) Injection model of DSCF [303], another DSSF variant, that uses single capillary for formation of droplets.

2.9.2 Supplementary Movies

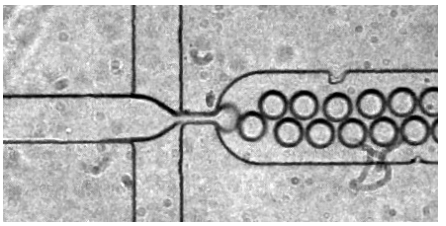

Figure 2.S5: **Droplet formation with a microfluidic chip.** Water in oil droplet formation at the T-junction (Fig. 2.3(a)) of a microfluidic chip. [ ]

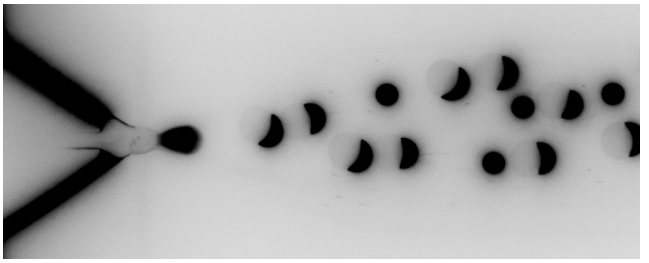

Figure 2.S6: **Vesicle formation with OLA.** Vesicle formation at 6-way junction on an OLA chip (Fig. 2.6(a)). [ ]

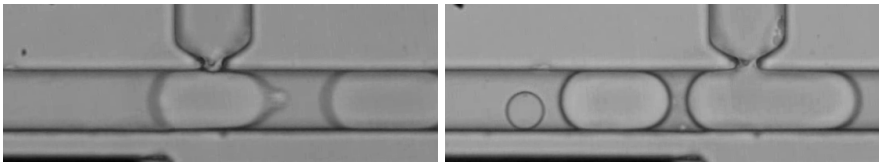

Figure 2.S7: **Pico-injection of vesicles.** Pico-injection of dsGUVs, (left) OFF scenario (Fig. 2.9(b)), and (right) ON scenario (Fig. 2.9(c)). [ ]

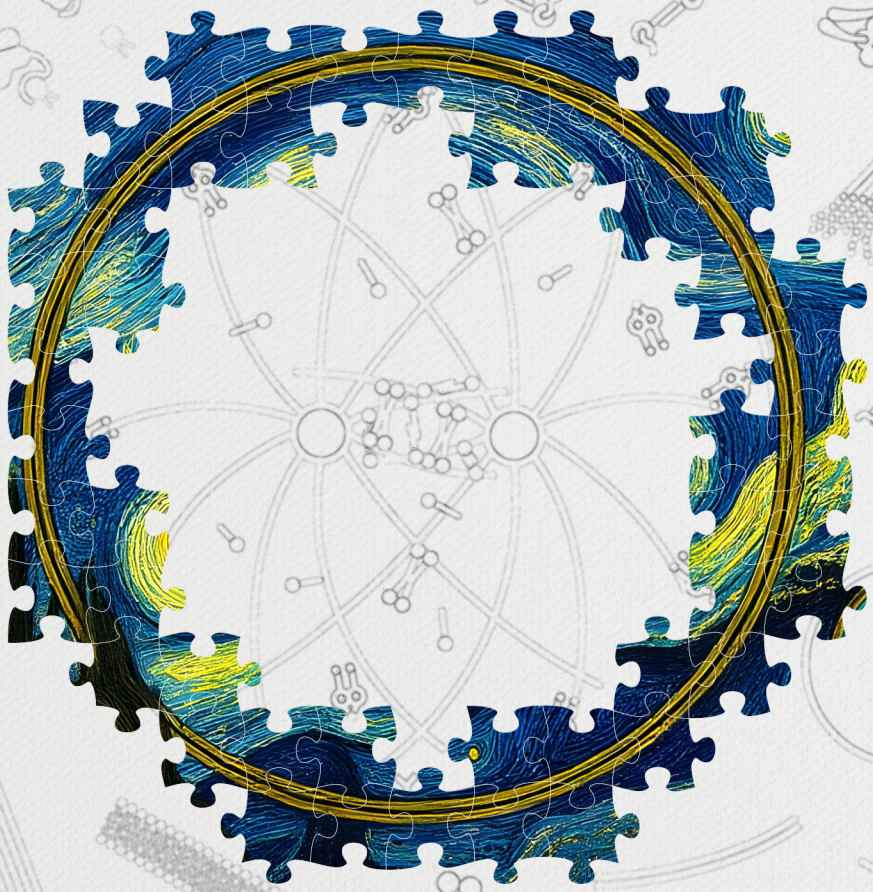

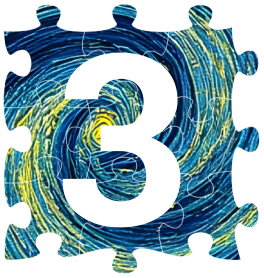

High-speed imaging of GUV formation in cDICE

Seeing is believing.
Pandora's box.

Giant unilamellar vesicles (GUVs) are widely used as in vitro model membranes in biophysics and as cell-sized containers in synthetic biology. Despite their ubiquitous use, there is no one-size-fits-all method for their production. Numerous methods have been developed to meet the demanding requirements of reproducibility, reliability, and high yield, while simultaneously achieving robust encapsulation. Emulsion-based methods are often praised for their apparent simplicity and good yields; hence, methods like continuous droplet interface crossing encapsulation (cDICE) that make use of this principle, have gained popularity. However, the underlying physical principles governing the formation of GUVs in cDICE and related methods remain poorly understood. To this end, we have developed a high-speed microscopy setup that allows us to visualize GUV formation in real-time. Our experiments reveal a complex droplet formation process occurring at the capillary orifice, generating >30 µm-sized droplets and only in some cases GUV-sized (∼15 µm) satellite droplets. According to existing theoretical models, the oil-water interface should allow for crossing of all droplets but based on our observations and scaling arguments on the fluid dynamics within the system, we find a size-selective crossing of GUV-sized droplets only. The origin of these droplet remains partly unclear; we hypothesize that some small GUVs might be formed from large droplets sitting at the second interface. Finally, we demonstrate that proteins in the inner solution affect GUV formation by increasing the viscosity and altering lipid adsorption kinetics. These results will not only contribute to a better understanding of GUV formation

This chapter has been published as High-speed imaging of giant unilamellar vesicle formation in cDICE, Lori Van de Cauter*, Yash K. Jawale*, Daniel Tam, Lucia Baldauf, Lennard van Buren, Gijsje H. Koenderink, Marileen Dogterom, and Kristina A. Ganzinger, *ACS Omega* 2024 9 (41), 42278-42288 DOI: 10.1021/acsomega.4c04825 [325] (* equal contribution)

processes in cDICE, but ultimately also aid the development of more reliable and efficient methods for GUV production.

3

3.1 Introduction

The quest to understand and manipulate the building blocks of life, including the countless interacting molecules and biochemical reactions making up cellular life, is a major aim of biophysics and synthetic biology [326]. One key tool in these fields are giant unilamellar vesicles (GUVs) as cell-sized, lipid bilayer-enclosed reaction compartments [263, 327]. Since their first description [328] in 1969, GUVs have proven to be a powerful and versatile tool as they can be directly observed using real-time microscopy and easily manipulated using biophysical tools, making them ideal in vitro model membrane systems [263, 329, 330]. More recently, GUVs have also been proposed as containers for a future synthetic cell [251, 265, 331, 332] and as reaction containers for chemistry and more complex cargo carriers in drug delivery [333, 334].

Despite the widespread research use of GUVs, there is still no one-size-fits-all method for their production [265]. Over the years, numerous methods have been developed to meet the demanding requirements of reproducibility, reliability, and high yield, while simultaneously achieving robust encapsulation. Historically, swelling-based methods (natural swelling [328], electroformation [273, 335–337], and gel-assisted swelling [295, 338–340]) have been used extensively for studying the biophysical properties of membranes. However, these easy-to-implement, high-yield methods offer poor control over encapsulation efficiency and the stoichiometry of encapsulated molecules. Thus, they only offer limited compatibility with establishing complex reconstituted systems. Emulsion-based techniques (water-in-oil droplets crossing an oil-water interface using gravity, centrifugation, microfluidic devices, or microfluidic jetting [301, 341–346]) on the other hand, offer more control over GUV content and enable experiments with complex encapsulated contents. Despite the potential cost of residual membrane impurities [265, 347, 348], emulsion-based methods have therefore gained popularity in recent years.

One method that particularly gained a lot of traction is called continuous droplet interface crossing encapsulation (cDICE) [271, 277, 278, 285, 349–351]. In cDICE, water-in-oil (w/o) droplets that are produced at a capillary orifice are continuously forced through an oil-water interface by centrifugal force in a rotating chamber, thereby forming a lipid bilayer and thus GUVs [271]. Recent optimization has made the method compatible with a wide range of biological systems, thereby offering control over encapsulated content, a high GUV yield, and straightforward implementation [277]. However, our understanding to which degree the encapsulated contents' complexity in cDICE can be extended, with respect to both physical properties (e.g. viscosity of encapsulated fluid) and physicochemical properties (e.g. which proteins and protein systems), remains limited. While many successes have been celebrated using cDICE, we still do not understand the underlying GUV formation process and how this affects the inherent variability in content encapsulation and yield seen in cDICE [265].

To gain a deeper understanding of GUV formation in cDICE, we have developed a high-speed microscopy setup that allows us to visualize the GUV formation process inside the rotating chamber in real-time. We focused on the capillary orifice, where initial droplet formation occurs, and on the oil-water interface, where droplets are converted into GUVs. Our experiments reveal a complex droplet formation process occurring at the capillary orifice, governing both the formation of larger droplets and, likely, satellite droplets of the size of typical cDICE GUVs (12 µm being the average diameter of GUVs formed with cDICE [277]) in some cases. The transfer of these droplets through the oil-water interface appears to exhibit selectivity toward GUV-sized droplets that may also be formed from large droplets at the second interface. We support these experimental observations with scaling arguments. Finally, we demonstrate that the addition of protein to the inner solution increases the viscosity and alters the kinetics of lipid adsorption, thereby significantly influencing the process of GUV formation.

3.2 Results

3.2.1 Design of an imaging setup to visualize droplet and GUV formation in cDICE

In the cDICE method, the initial step of GUV formation is the generation of droplets at a capillary orifice, which is inserted perpendicularly into the oil layer in the rotating chamber. In its original implementation, cDICE uses a capillary diameter of 2–25 µm to allow for tight control over GUV sizes [271]. However, we and others found such narrow capillaries to be very impractical when encapsulating protein solutions, as these capillaries are prone to rapid clogging, leading to highly irreproducible results. In our previous work, we showed that this issue can be circumvented by using wide capillaries with a diameter of 100 µm [277]. The flow regime is therefore significantly different from the original protocol [271], and one would not necessarily expect tight control over droplet sizes. Still, we found that these capillaries produced a surprisingly narrow size distribution of GUV sizes, roughly ten times smaller than the capillary orifice (∼10 µm vs ∼100 µm) [277].

To better understand how a large capillary orifice can still lead to such relatively monodispersed GUV size distribution in cDICE, we developed a high-speed microscopy setup to, for the first time, visualize the processes of droplet and GUV formation in cDICE in real-time (Fig. 3.1). We designed the setup so that the camera is suspended vertically above the cDICE apparatus, capturing the light of a light source located directly beneath the rotating chamber (see method section for a full description of the setup; Fig. 3.1(a)). This way, we are able to capture the process along the horizontal axis of the rotational chamber: from the capillary orifice, where initial droplet formation occurs (Fig. 3.1(b) i), to the oil-water interface, where droplets are converted into GUVs (Fig. 3.1(b) ii). Due to the high rotation speeds that are used in cDICE (∼1900 rpm), all processes happen on a very fast timescale, on the order of microseconds (10^{-6}–10^{-5} s). To obtain a sufficiently high time resolution, we therefore used fast cameras in combination with brief exposure times up to 1 µs, reaching frame rates up to 30 000 fps.

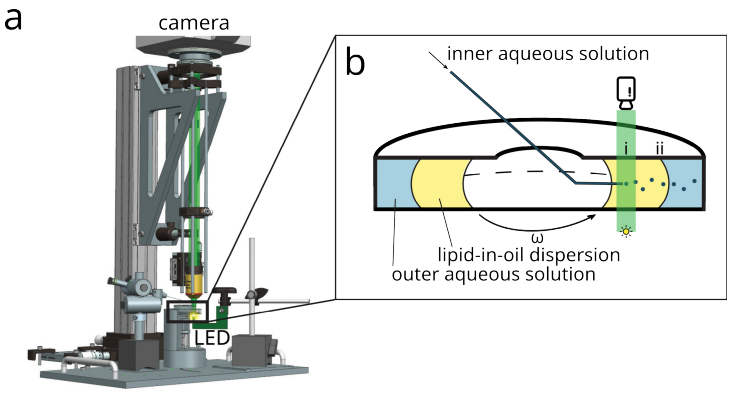

Figure 3.1: **Development of a high-speed imaging setup to visualize GUV formation in cDICE.** (a) The imaging setup consists of a high-speed camera suspended above the rotating chamber and an intense light source located directly below the rotating chamber. For an interactive 360° view of the setup, see method section. (b) In cDICE, (i) aqueous droplets are generated at the capillary orifice; subsequently travel outward through the lipid-in-oil dispersion; and finally (ii) traverse the oil-water interface, where droplets are converted into GUVs.

3.2.2 Droplet formation at the capillary orifice is governed by shear forces

When we focused our imaging setup on the capillary orifice at our default conditions for GUV production (100 µm diameter fused silica capillary, a rotation speed of 1900 rpm, and a flow rate through the capillary of 25 µL min^{-1}; see method section for further details), it immediately became clear that droplet formation under these conditions is a non-uniform, highly dynamic process with an irregular breakup pattern of a liquid filament into individual droplets (Fig. 3.2(a), Fig. 3.S7). Instead of the distinct droplet formation expected for low Reynolds numbers [271, 352], we observed fluid exiting the capillary forming a liquid filament, which often adhered to the capillary. Droplets breakup took place at the end of the liquid filament at a fast rate, with droplet sizes clearly larger than the average cDICE GUV ((68.6 ± 2.8) µm, approximately 2500 droplets per second).

Upon silanization of the capillary, we no longer observed the fluid adhering to the capillary, resulting in a more regular droplet breakup mechanism (Fig. 3.S1). This can likely be explained by an increased surface hydrophobicity upon silanization when compared to the default polyimide capillary coating surrounding the capillary and the uncoated cut tip cross-section with chipped coating edges, which results in less wetting of the capillary surfaces.

We observed a significant variability in the droplet breakup dynamics at the end of the liquid filament. Factors contributing to this variability include irregularities in the capillary orifices resulting from suboptimal cutting or capillary deterioration over sustained use, differences in capillary insertion angle, and the occasionally-observed presence of an air pocket at the base of the capillary (Figs. 3.2(a) & 3.2(c)).

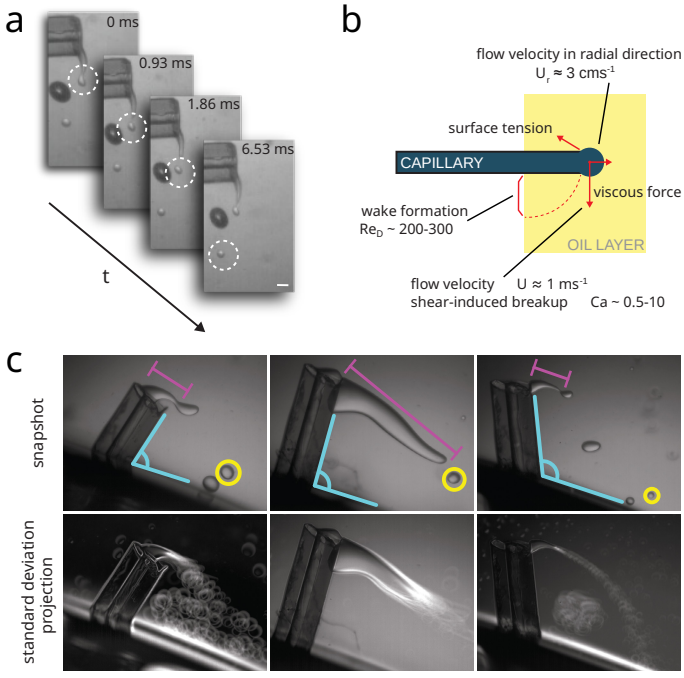

Figure 3.2: **Droplet formation at the capillary orifice is governed by shear forces.** (a) Microscopic image sequence capturing a droplet of PBS buffer with 18.5 %v/v OptiPrep™ being sheared off from the liquid stream at the capillary orifice at a rotation speed of 1900 rpm. Scale bar indicates 100 µm. (b) Illustration depicting the different forces acting at the capillary orifice: the capillary number ($\sim$ 0.5–10) indicates a shear-induced breakup mechanism, while the Reynolds number ($\sim$ 200–300) describes the wake formation behind the capillary. The shear velocity ($U \approx 1\,\mathrm{m\,s^{-1}}$) is larger than the flow velocity in the radial direction ($U_r \approx 3\,\mathrm{cm\,s^{-1}}$), further indicating droplet formation is shear-induced. (c) Microscopy images highlighting the high inter-experiment variability using same capillary in consecutive independent experiments. For identical experimental conditions, noticeable differences can be seen, e.g. in insertion angle, liquid filament, and droplet size. Bottom row: standard deviation stack projection of 100 frames (every 50$^{\mathrm{th}}$ frame of 5000 frames). White highlights indicate variations in movement, such as the occurrence of a droplet vortex in the wake of the capillary (left and right image) and the movements of the liquid filament end (left and middle).

Note that in all these cases, the experimental condition was indistinguishable by eye, and the differences only became apparent when visualizing droplet formation with our dedicated imaging setup.

To better understand the observed droplet breakup mechanisms, we turn to scaling arguments to rationalize our findings (Fig. 3.2(b)). Our video recordings (Fig. 3.S7) suggest that droplet breakup at the tip of the capillary is not due to inertial jetting, but instead is induced by viscous shear stresses. For droplets forming from a capillary of diameter D, inertial jetting is expected for flow rates larger than a critical flow rate scaling with $\sim \pi(D^3\gamma/2\rho_i)^{1/2}$, where $\rho_i \gtrapprox 1\,\mathrm{g\,mL^{-1}}$ denotes the density

of the inner solution (e.g. 1.0183 g mL^{-1} for MRB80 buffer with 1.75 %w/v sucrose) and γ is the interfacial tension between the dispersed and the continuous phases [352]. In our experiments, the flow rate through the capillary is 25 µL min^{-1}, which is significantly lower than the critical flow rate. This is consistent with our observation that droplets are indeed sheared off the capillary. Here, we must therefore consider the balance between surface tension and viscous forces characterized by the capillary number . is given by $= \mu U/\gamma$. The flow velocity U at the point of insertion of the capillary is $U = \Omega R_i$, where R_i is the distance between the capillary orifice and the center of rotation of the chamber and Ω is the rotation speed. With $R_i \sim 1$ cm, $\Omega \sim 1000$–2700 rpm, $\mu \sim 4 \times 10^{-3}$–$5 \times 10^{-3}$ kg m^{-1} s^{-1} and assuming an interfacial tension between the inner solution and the oil phase of $\gamma \sim 10^{-3}$–10^{-2} mN/m [277], the capillary number ranges between 0.5 and 10. Monodispersed droplets form at the tip of the capillary through a dripping mechanism for low values of the capillary number [271]. Within the higher range of reached in our experiments, droplets are therefore expected to deform and the break up mechanism to be unstable, in agreement with our observations.

cDICE experiments require high rotational speed ($\Omega > 1000$ rpm), producing flow instabilities in the wake of the static capillary inserted into the rotation chamber. Indeed, the Reynolds number, characteristic of the flow around the capillary, $_D = \rho UD/\mu$, yields values in the range of $_D \sim 200$–300, with $\rho \sim 0.934$ g mL^{-1} being the density of the lipid-in-oil dispersion. For $_D \geq 47$, periodic vortex shedding in the wake of a cylinder is expected [353], and for $_D \geq 150$, further three-dimensional instabilities are predicted [353], suggesting that the wake around the capillary will also affect droplet breakup. Indeed, we observe oscillations in droplet breakup, caused by the non-linear effects in the wake, and the inner solution adhering to the outer capillary surface. Additionally, we observed that the droplets did not immediately travel outward as expected, but rather initially exhibited an inward movement in the wake of the capillary and towards the center of the rotating chamber, before travelling outward. The larger diameter of the capillary leads to a larger capillary number and to a wake instability, which both contribute to a less stable droplet breakup and larger variation in droplet size compared to previous work [271].

3.2.3 Droplet size in contrast to GUV size, is dependent on the rotation speed

To explore factors that influence droplet breakup in cDICE, we next altered the rotation speed of the rotating chamber. As the rotation speed of the chamber increases, the flow velocity at the capillary orifice also increases and the viscous forces become stronger. This leads to the droplets being more likely to break up, resulting in smaller droplets. In line with this expectation, an increase in rotation speed to 2700 rpm resulted in smaller droplets formed at a higher frequency ((28.5 ± 8.7) µm and ~34 500 droplets per second; Fig. 3.3, Fig. 3.S8). Decreasing the rotation speed to 1000 rpm, the lowest speed at which oil and water layers maintain a vertical interface and GUVs can be produced, had the opposite effect, i.e. larger droplets formed at a lower frequency ((273 ± 41) µm and ~40 droplets per second; Fig. 3.3, Fig. 3.S9).

We can estimate the droplet size from a force balance between the surface tension force $\sim \pi D\gamma$ and the viscous force $\sim 6\pi\mu aU$, where D is the outer diameter of the capillary and a is the radius of the droplet [352]. The droplet size above which break up is expected, scales with the inverse of the capillary number $a/D \sim (6)^{-1}$, and we predict a droplet diameter of ~100 µm at 1900 rpm increasing to ~200 µm when the rotation rate is decreased to 1000 rpm. These scaling are consistent with the order of magnitude of our experimental measurements (Fig. 3.3). Droplet formation is thus shear-induced in a broad range of rotation speeds, encompassing both lower and higher speeds than the default of 1900 rpm. Our observation that droplet size is dependent on chamber rotation speed contrasts with the size distributions for GUVs obtained using these conditions: these distributions are all indistinguishable from one another and centered around 12 µm (Fig. 3.S2), thus 3–30-fold smaller in diameter than the produced droplets. Hence, a large number of the droplets formed at the capillary are not directly converted into GUVs.

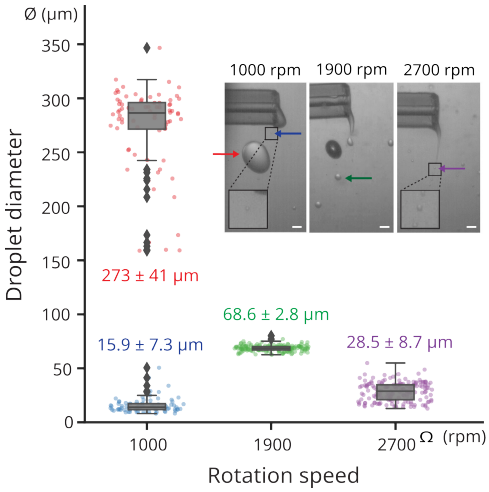

Figure 3.3: **Size distributions of droplets for different rotation speeds.** Box plots of droplet diameter ⌀ at rotation speeds Ω of 1000 rpm, 1900 rpm, and 2700 rpm (n = 148, 152, and 157, respectively, for N=1). Individual data points indicate single droplets and box plots indicate medians and quartiles, while outliers are marked with individual diamond shapes. A rotation speed of 1000 rpm resulted in two distinct droplet populations: large droplets of mean diameter ⌀ (273 ± 41) µm and satellite droplets of mean diameter ⌀ (15.9 ± 7.3) µm. A rotation speed of 1900 rpm resulted in the narrowest distribution, with a mean droplet diameter ⌀ of (68.6 ± 2.8) µm. 2700 rpm resulted in the smallest droplet sizes, with a mean diameter ⌀ of (28.5 ± 8.7) µm. Inset: representative field-of-views for the different rotation speeds indicating the formed droplets with arrows. Scale bars indicate 100 µm.

While a rotation speed Ω of 1900 rpm resulted in the narrowest droplet size distribution of all explored rotation speeds, interestingly, a rotation speed of 1000 rpm resulted in two distinct populations (Fig. 3.3): one primary population of droplets with a mean diameter ⌀ of (273 ± 41) µm and a secondary population consisting of smaller droplets with a mean diameter ⌀ of (15.9 ± 7.3) µm. Occasionally, the formation of large and small droplets was disrupted when e.g. a droplet merged with

the liquid stream or collided with the capillary. Inspecting the videos more closely, we found that the observed population of small droplets are satellite droplets, produced when a bigger droplet breaks off from the main liquid thread at the tip of the capillary (Fig. 3.S9). Such satellite droplets have previously been observed in many breakup configurations, from T-junctions to the breakup of droplets in pure shear [354]. While we did not observe any satellite formation for rotation speeds >1000 rpm, this may be due to our limited optical and temporal resolution: the satellite droplets observed for 1000 rpm (diameter ∼15 µm) were at the limits of our image resolution, droplets of any smaller diameter were too small to be identified and measured with sufficient certainty (see methods Sec. 3.4 for further details). It is therefore possible that satellite droplets of all sizes, within the size range of the final GUVs (1–20 µm), are also formed, but not detected by our imaging setup.

In addition to the small satellite droplets we observed at 1000 rpm, smaller droplets could theoretically also be formed when larger droplets break up due to shear forces generated in the flow by the rapid relative motion of the bottom wall of the rotational chamber with respect to the capillary. Droplets formed at the tip of the capillary are entrained by the flow in the rotation direction at a high velocity of $U \approx \Omega R_i \approx 1\,\mathrm{m\,s^{-1}}$ compared to the slow radial motion $U_r = (\rho_i - \rho_o)\, a^2 \Omega^2 R_i / \mu \approx 3\,\mathrm{cm\,s^{-1}}$, determined by the balance between centrifugal and viscous forces. These droplets therefore interact with the wake left behind the capillary for several rotations. In the wake, the characteristic shear rate ε scales with $\varepsilon \sim \Omega R_i / l$, where the characteristic length scale l for shear around the capillary will range between the outer diameter of the glass capillary ≈ 0.5 mm and the distance between the capillary and the bottom of the flow chamber ≈ 5 mm. One can define another capillary number as $_\varepsilon = \mu \varepsilon a / \gamma$, where a is the radius of the droplet [355, 356]. This number characterizes the relative magnitude of the viscous shear forces due to the shear rate ε and the surface tension forces. $_\varepsilon = 1$ corresponds to a condition where the smallest droplets cannot be further broken up by the shear [355, 356] and yields $a \sim \gamma / \mu\varepsilon$. Knowing $h \sim 0.5$ cm, we find that the interfacial tension of the monolayer at the inner solution/oil interface needs to be approximately $\gamma \sim 10^{-5}$–10^{-6} N/m to produce droplets of $a \sim 5$ µm, equivalent to the final GUV size. This value for an interfacial tension at an aqueous/oil interface is extremely low and not expected, even in presence of surfactants or lipids. For reference, the interfacial surface tension between two miscible liquids is of the order 10^{-6} N/m [357]. Hence, we conclude that it is unlikely GUV-sized droplets form by shear force-induced droplet breakup after droplet formation at the capillary orifice.

3.2.4 Protein in the inner solution affects viscosity and lipid adsorption

Next, we set out to study the effect of proteins on droplet formation at the capillary orifice. It is well known that encapsulation of more complex solute mixtures, such as proteins and their associated buffers, leads to a decreased yield and variable encapsulation efficiencies [277, 358]. For cDICE specifically, it has been reported that the yield decreased at high protein concentration [359], yet it is still unknown

why this is the case. We also noticed both protein- and buffer-dependent effects on yield and encapsulation efficiencies, with MRB80 buffer and tubulin both resulting in worse outcomes than G-buffer and actin (Fig. 3.S3). To better understand what may be causing this difference, we chose to investigate the effect of these proteins on droplet formation, additionally motivated by the widespread efforts for cytoskeletal reconstitution inside GUVs.

Upon addition of either protein, droplet breakup at the capillary orifice also occurred at the tip of the liquid stream exiting the capillary. However, the oscillations of the liquid stream in the wake of the capillary were significantly reduced (Fig. 3.4(a), Figs. 3.S10-3.S13). Remarkably, in the case of tubulin, the liquid stream displayed a tendency to adhere to the air-oil interface. To explain these observations, we characterized the inner solution. We looked into both the physical properties, i.e. dynamic viscosity as determined by bulk shear rheology, and physicochemical properties, specifically lipid adsorption rate determined from pendant drop tensiometry.

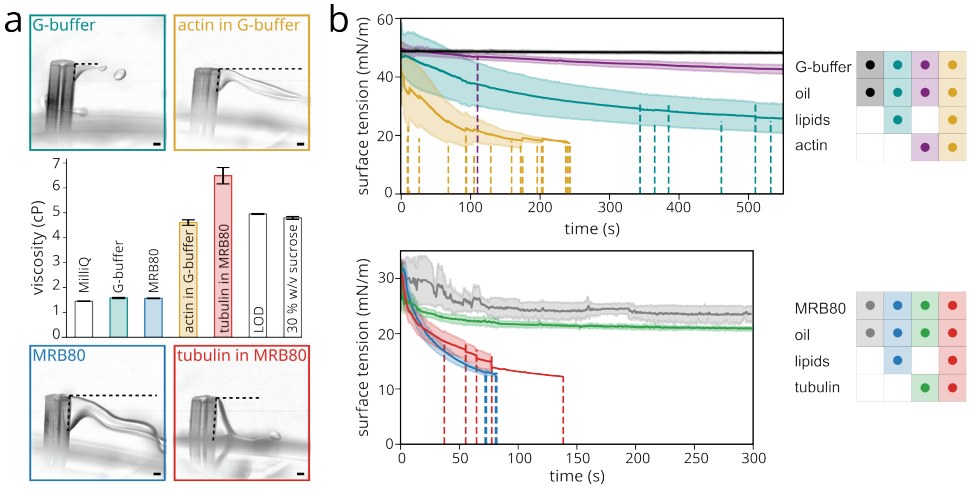

Figure 3.4: **Effect of protein on aqueous solution properties.** (a) Representative field-of-views of droplet formation at the capillary orifice for different buffer and protein solutions (actin 4 µM and tubulin 40 µM). Horizontal dotted lines indicate the liquid filament length just before the drop breaks off, while vertical dotted lines along the capillary indicate the extent of external capillary surface wetted by the aqueous solution. Images are background subtracted for better contrast. Scale bars indicate 100 um. Middle: Dynamic viscosity measured using a parallel plate rheometer for different buffers (G-buffer with 6.5 %v/v OptiPrep™, MRB80 with 1.75 %w/v sucrose) and protein solutions (actin 1 µM and tubulin 33.33 µM), along with water (MilliQ), lipid-in-oil dispersion (LOD) and 30 %w/v sucrose solution in MRB80 for reference. Error bars represent standard deviation. (b) Interfacial tension kinetics measured using pendant-drop tensiometry for different combinations of aqueous and oil solutions; G-buffer and actin 4 µM (top), and MRB80 and tubulin 33.33 µM (bottom). Solid lines represent the average values and the shaded region corresponds to standard deviation. The vertical dotted lines represent the event of falling of a drop and truncation of data.

In presence of actin and tubulin, the dynamic viscosity increased with respect to its accompanying buffer, G-buffer and MRB80 buffer respectively (Fig. 3.4(a)). For actin (1 µM in G-buffer, 6.5 %v/v OptiPrep™), an almost threefold increase from 1.58 cP to 4.61 cP was observed (Fig. 3.4(a), yellow bar), while for tubulin (33.33 µM in MRB80 buffer, 1.75 %v/v sucrose), the viscosity increased fourfold from 1.57 cP to 6.49 cP (Fig. 3.4(a), red bar). All solutions still exhibited Newtonian fluid behaviour. Important to note is that the used concentrations of added proteins remained within the micromolar range and are widely used in the field. Interestingly, the viscosity of the inner solution containing protein was similar to the viscosity of the continuous phase, i.e. the surrounding lipid-in-oil dispersion (Fig. 3.4(a), middle 'LOD' bar). The fragmentation of the liquid filament into droplets at the end of the capillary is the consequence of complex instabilities beyond the scope of this study. These mechanisms are significantly affected by the viscosity of the inner solution and the increased viscosity due to the added protein will dampen the flow dynamics in the liquid filament. This dissipation in the liquid stream can explain the decrease in the fluctuations observed in the liquid filament exiting the capillary (Fig. 3.4(a), Figs. 3.S10-3.S13). Moreover, previous studies on capillary breakup have reported the viscosity to affect the fragmentation pattern and the size distribution of satellite droplets significantly. In particular, the viscosity increase in a liquid filament has been associated with fewer and larger satellite droplets [360, 361]. Therefore, proteins included in the inner solution can have a significant impact in the size distribution of droplet formed at the capillary exit. Altogether, these results show a nuanced interplay between the physical properties of the encapsulation solution, varying with its composition even at low protein concentrations, and the fluid dynamic processes that govern droplet breakup.

To investigate how the addition of protein to the inner solution alters the physicochemical properties of the interface, we used pendant drop tensiometry [362] to study lipid monolayer formation in a controlled environment. We analyzed the lipid adsorption kinetics and interfacial tension dynamics of the water-oil interface for different encapsulation solutions, mimicking droplet formation at the capillary orifice. It has been shown that proteins spontaneously adsorb at the oil-water interface and their behaviour cannot unequivocally be attributed to a single protein property, with thermodynamic stability, structural properties, and concentration all being contributing factors [363, 364]. Particularly, actin has been shown to exhibit surface activity in a charge-dependent manner, influenced by both lipid and buffer composition, with a more pronounced effect observed for the filamentous form compared to actin monomers [365–367]. Tubulin (specially β-tubulin inserts amphipathic polymerizing interface into DOPE membrane) is also shown to interact with the lipid membranes [368, 369].

Upon adding 4 µM actin to the inner solution, a pronounced decline in interfacial tension was observed (Fig. 3.4(b), purple curve), with some droplets detaching before the end of the experiment (Fig. 3.4(b), dashed lines). This trend was consistent for tubulin (Fig. 3.4(b), green curve). To examine the roles of actin and tubulin as surface-active agents in the interfacial tension, we then compared the interfacial tension dynamics against a lipid-free oil dispersion. Both actin and tubulin had

only a marginal impact on interfacial tension when compared to the protein-free condition (Fig. 3.4(b), black curve vs purple curve and grey curve vs green curve). Interestingly, while actin and lipids individually at the interface exhibited slow kinetics, their combined presence displayed an accelerated decrease (Fig. 3.4(b), yellow curve), suggesting a synergistic effect beyond mere additivity. We found this effect could not be countered via electrostatic or steric repulsion (i.e. presence of charged or PEGylated lipids, respectively, Fig. 3.S4). These results imply that actin could, in line with previous research [365], quickly cover the surface of the droplets traversing the lipid-in-oil dispersion, potentially impeding lipid monolayer formation and/or monolayer zipping. However, the full extent of this synergistic effect is yet to be uncovered. Furthermore, these results underscore the importance of the compositions of both inner solution and lipid-in-oil dispersion, as both affect mono- and bilayer formation.

3.2.5 GUV FORMATION AT THE OIL-WATER INTERFACE SEEMS SIZE SELECTIVE

Droplet formation in cDICE occurs on extremely short timescales; for the default conditions (i.e. 1900 rpm, 25 µL min^{-1}), we observed droplets of approximately ∼ 70 µm in diameter being sheared off at a frequency of ∼ 2500 Hz. Theoretically, given a total encapsulation volume of 100 µL, > 500 000 droplets are formed during a single experiment. Interestingly, this number does not correspond to the final number of GUVs produced using cDICE, as reported in other publications (∼ 1000 GUVs [277]). Furthermore, if those droplets larger than the finally observed GUVs (i.e. non satellite droplets, ∼ 70 µm for the default conditions) do not subsequently shear to form smaller droplets as discussed above, these two observations together indicate a sub-optimal GUV formation process downstream, whereby most droplets do not convert into GUVs at the oil-water interface and potential additional hidden mechanisms generating smaller droplets.

To look more closely at droplet-to-GUV conversion into GUVs in cDICE, we imaged the oil-water interface where the final step of GUV formation in cDICE occurs: droplets transfer through the oil-water interface and two monolayers fuse together to form a bilayer (Fig. 3.5(a)). As postulated by Abkarian et al. [271], the two monolayers can also form a pore, thereby causing the droplet to burst, resulting in no GUV being formed. We note that when we collected GUVs in cDICE experiments, we observed that the outer solution after GUV generation also contained components of the inner solution, in agreement with the suggestion that a fraction of droplets burst at the oil-water interface.

In our experiments, we unfortunately did not observe a clear transfer of droplets through the interface nor bursting of droplets, possibly because resolving GUV-sized droplets at the interface was not feasible with the limited imaging contrast of standard bright field illumination. Instead, we made two other striking observations. First, we observed droplets several orders of magnitude larger than the typical size of GUVs which were stationary on the oil-water interface (Fig. 3.5(b), Figs. 3.S14 & 3.S15). These stationary droplets showed a decreased contrast on the

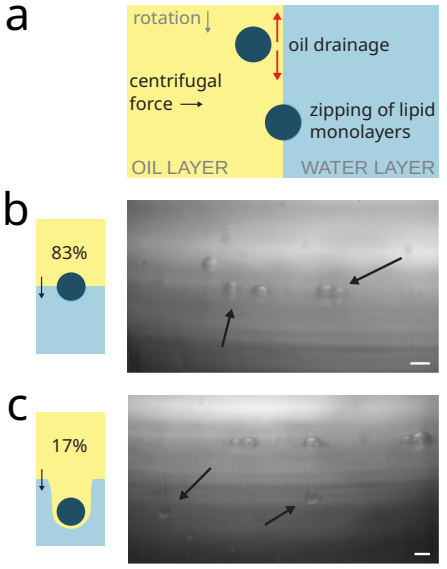

Figure 3.5: **Droplet transfer through the oil-water interface is suboptimal.** (a) The lipid-in-oil dispersion in between the approaching lipid monolayer-covered droplets and the oil-water interface needs to be drained for the two monolayers to zip together and successful GUV formation to occur. (b) When droplets are not fully covered by a lipid monolayer when reaching the oil-water interface, successful transfer cannot occur and instead, stationary, semi-transferred droplets are observed (83.3%, n=289). Scale bar indicates 100 µm. (c) When drainage of the oil layer between the approaching droplet and oil-water interface is insufficient, the formation of comet tails can be observed (16.7%, n=58): a droplet distorts the oil-water interface and drags the lipid-in-oil dispersion into the outer aqueous solution, hindering successful GUV formation. The Scale bar indicates 100 µm. Droplets (n=347) interacting with oil-water interface are counted every 5th frame for 50 frames.

side of the outer aqueous phase, suggesting partial transfer across the interface. Since the transfer time of a droplet to the oil-water interface is inversely proportional to the radius of the droplets squared [271], it is possible that the flight time of these larger droplets is too short for lipids to fully adsorb on the interface. Consequently, no zipping mechanism is possible, leading to these larger droplets crowding the interface, as we observed in our video recordings.

A second observation was the formation of comet tails (Fig. 3.5(c)): every 1 in 6th droplets (17%) coming at the oil-water interface, pass the interface dragging a tail of the oil solution into the outer aqueous solution, likely because the oil did not drain quickly enough and thus prevented monolayer fusion. Due to the difference in contrast with the outer aqueous phase, we infer that oil is still present between the part of the interface dragged into the outer phase and the droplet. The Bond number $= \Delta\rho a r^2 / \gamma$, where a is the acceleration and r the radius of droplet, represents the ratio of centrifugal force to surface tension force. For these large droplets, is on the order of 1, meaning they will deform the interface, as observed in our video recordings, and drag the oil phase into the outer aqueous phase. This results in the observed comet tail formation and no GUV formation from the droplets undergoing this process.

As we find that the addition of protein to our inner solution significantly alters the characteristics of the solution and affects droplet formation at the capillary orifice, we asked how the increased viscosity and altered lipid adsorption kinetics might impact the transfer of droplets through the oil-water interface. The accelerated lipid

adsorption due to the addition of protein does not lead to a decreased flight time of the droplets, but this mixed layer of lipids and proteins is not suitable for droplet transfer or monolayer zipping. On the other hand, the increased viscosity of the inner solution could influence the timescale of the drainage of the lubrication film, i.e. the lipid-in-oil dispersion in between the droplet and the oil-water interface, required for successful monolayer zipping. Furthermore, the increased viscosity could reduce the flow caused by Marangoni stresses, which play a role in facilitating the zipping process [271].

An approximate breakthrough condition for spherical objects of radius a to pass through an interface of interfacial tension γ is $(\rho_i - \rho_o)\,\Omega^2 R_o a^2 / \gamma \geq 3/2$, where R_o is the distance between the axis of rotation and the location of the oil-outer solution interface [370]. For small droplets of radius $a \sim 5\,\mu m$ to cross the interface, a low surface tension on the order of $\gamma \sim 10^{-6}$ N/m is required. Such low surface tension has been reported for lipid bilayers [371] and therefore if such small droplets are present in the oil phase, they can cross the interface to form GUVs. It should be emphasized that the breakthrough condition sets a criterion for the smallest droplet that can cross the interface. Any droplet larger than 10 µm in diameter would be expected to cross the interface as well and form larger GUVs. The fact that we do not observe GUVs of larger diameters than ~ 20 µm [277], but do observe large droplets at the oil-water interface, suggests that the upper size limit for GUV formation might be controlled by membrane zipping and/or lipid coverage of the droplet/interface. Insufficient lipid coverage could, for example, lead to droplet/GUV shrinkage during GUV forming until the lipid density to form a bilayer is reached, thereby resulting in smaller GUVs than originally produced droplets.

Comparing cDICE GUV size distributions to those obtained by eDICE, a recent adaptation of cDICE where the droplets are generated by vortexing, pipetting, or scraping, instead of a capillary, but transferred through a second interface in a rotational chamber, identical to cDICE. Interestingly, we noticed that the final GUV size distributions were similar for the two methods [288], despite vastly different droplet size distributions were used as a starting point (Fig. 3.S5). Furthermore, we found GUV sizes to be remarkably similar for different membrane compositions in eDICE (Fig. 3.S6). Taken together, these cDICE and eDICE results indicate a yet unknown mechanism for size-selectiveness of droplet and/or GUV formation at the oil-water interface that promotes the production of similarly-sized GUVs for a wide distribution of droplet sizes. For example, it is possible that GUVs form at the oil-water interface in cDICE and eDICE by pinching off from larger droplets sitting at the interface. While we did not observe any event like this, we would expect this process to happen on a length scale (and possible time scale) beyond the resolution of our imaging setup.

3.3 Conclusion

In summary, by designing and building a custom imaging setup to visualize droplet formation and droplet interface transfer in cDICE in real-time, we were able to, for the first time, collect direct in situ imaging data to further understand the underly-

ing mechanisms governing GUV formation in this technique. We found that droplet formation at the capillary orifice produced droplets that are much larger than the size of the final GUVs. For a capillary diameter of 100 µm, the formation of droplets in cDICE bears some similarities with the formation of droplets at T-junctions in microfluidics, a well-studied phenomenon [372, 373]. In such microfluidic channels, the geometric confinement provided by the channels leads to flow restrictions on the continuous phase at the origin of a squeezing pressure. This pressure promotes droplet break up at much smaller values of as compared to our experiments. However, there are similarities in the droplet formation regimes. For example, a decrease in droplet volume for increasing values of has been widely reported [372, 373]. These studies have also reported a transition from a breakup droplet formation mechanism for low values of to a dripping mechanism at higher , whereby a long liquid filament of the dispersed phase forms and droplets pinch off at the end of the filament. This is in contrast to the use of smaller capillary openings in the original cDICE implementation, in the range of 2–25 µm [271], where the smaller inner diameter of the capillary leads to smaller droplet sizes by a combination of smaller total interfacial force resisting the breakup of the droplet and a smaller Reynolds number. Only as a side process, smaller satellite droplets are being formed. Furthermore, we showed that the addition of protein to the inner solution increases its viscosity and changes interfacial tension dynamics, impacting droplet formation and likely also droplet interface transfer. Imaging of the oil-water interface revealed that droplet transfer is frequently stalled, large droplets remain stuck at the interface, and transfer exhibits a size-selectivity. This size-selectivity of droplet transfer to GUVs was further confirmed using eDICE, a variant of cDICE where no capillary is used, which yielded similar size distribution despite vastly different droplets as input. We think therefore that, in addition to small (satellite) droplets being able to cross the interface to form GUVs, GUVs could also be produced by pinching off from the larger droplets we observed sitting at the rotating oil-water interface. While we did not directly observe this route of GUV formation directly, we also would not expect that we would be able to resolve GUVs leaving from the interface with our imaging setup. Further studies are needed to further elucidate the effect of lipid composition, including cholesterol or charged lipids, and different proteins or protein mixes. We believe the presented results can be of interest not only for cDICE but to other emulsion-based GUV formation methods as well, as they suggest that GUVs do not just form as a simple conversion from droplets to GUVs at a second interface. Our study furthermore emphasizes the need for inter-disciplinary collaboration to fully grasp the intricacies of the processes involved in emulsion-based GUV production methods to develop even more reliable and efficient methods for GUV production. We hope this research will serve as a stepping stone for future research, enhancing emulsion-based GUV formation.

3.4 Material and Methods

Design and fabrication of the spinning device

The cDICE device was identical to Van de Cauter et al. [277]. An additional opening underneath the spinning chamber was created by removing part of the motor housing. This way, the light source could be placed directly below the spinning chamber to achieve transillumination. The design for the adjusted cDICE device is available on GitHub (GanzingerLab/cDICE_microscope).

Fabrication of spinning chambers

Transparent, cylindrical chambers, 35 mm in diameter and 10 mm in height, were made from two lids of Petri dishes (Falcon® REF 351008). To create a waterproof, closed chamber, the sides of the two lids were first sanded using sandpaper to create a rough surface after which they were glued together using a thin layer of optical glue (Norland Optical Adhesive 81). After curing of the glue using UV light, the side of the chamber was wrapped with a strip of Parafilm®. The chambers include a circular opening of 15 mm in diameter in the top to allow facile access to the solutions with the capillary.

General cDICE experimental workflow

While it is possible, and needed, to tweak various operational parameters to encapsulate a particular (non-)biological system in cDICE, we chose to use the parameters established in a recent optimization study by Van de Cauter et al. [277] as default conditions for cDICE. Specifically, we used a 100 µm diameter capillary, a rotation speed of 1900 rpm, and a flow rate through the capillary of 25 µL min^{-1}. For the lipid-in-oil dispersion, 18:1 1,2-dioleoyl-sn-glycero-3-phophocholine (DOPC) lipids were dispersed using chloroform in a 4:1 ratio silicon oil:mineral oil (silicon oil – viscosity 5 cst (25 °C), Sigma-Aldrich; mineral oil – BioReagent, Sigma-Aldrich). A fused silica capillary tubing with polyimide coating (TSP-100375, Molex LLC) was used to inject inner aqueous solutions. The general cDICE experimental workflow and preparation of lipid-in-oil dispersion was based on Van de Cauter et al. [277]. The following parameters differed: the volume of the outer solution was increased to 1.07 mL to account for the difference in dimensions between the 3D printed spinning chambers, as used in Van de Cauter et al. [277], and the Petri dish spinning chambers that were used for imaging experiments, as mentioned above. Room humidity was not controlled during imaging experiments and the chambers were spun for the entirety of the imaging experiments instead of a predetermined time. G-buffer (5 mM tris(hydroxymethyl)aminomethane hydrochloride (Tris-HCl) pH 7.8 and 0.1 mM calcium chloride ($CaCl_2$), 0.02 mM adenosine triphosphate (ATP) and 4 mM dithiothreitol (DTT)) with 18.5 %v/v OptiPrep™ was encapsulated in every experiment (to achieve a density difference between the inner and outer aqueous solution), unless specified otherwise. For experiments with silanized capillaries, the tip of the capillary was submerged for one minute in dichlorodimethylsilance (DMDCS) (40140, Sigma Aldrich), before removing excess with nitrogen gas.

Home-built imaging setup

The light of a single LED (Luxeon V2, 315lm@700mA; used without lens) or a Lumencor light engine (SOLA 6-LCR-SB) was collected by a 200 mm focal length achromatic lens (Thorlabs AC254-200-A-ML; lens mount: Thorlabs CXY1). The setup was equipped with a 4X or 10X objective (Nikon Plan Fluor 4x/0.13 PhL DL and Nikon Plan Fluor 10x/0.30 ∞/0.17 WD 16, respectively) that was mounted on a Z-stage (Thorlabs CT1; adapter: Thorlabs SM1A10). X/Y motion control was provided by two translational stages with a step size of 25 mm (Thorlabs PT1). Images were recorded using a high-speed camera (Kron Technologies Chronos 2.1-HD and Photron FASTCAM SA4) which was mounted on the setup using a custom-designed 3D printed construction. The full setup was mounted on a Thorlabs cage system that was mounted on a breadboard (Thorlabs MB1030/M) to easily move the full setup over the cDICE device. The full component list and design plans, including an interactive 3D model of the setup, can be found on GitHub (GanzingerLab/cDICE_microscope).

Droplet size analysis

Droplet size analysis was performed manually using the Fiji software [319]. The image pixel size was derived from three independent measurements of the capillary opening, accounting for capillary size uncertainty. Triplicate measurements were performed for a subset of each dataset to quantify the measurement error. For each droplet, we then measured both area and diameter, yielding two independent measurements of the droplet diameter with associated error calculated through error propagation. The large pixel size ((2.431 ± 0.105) µm) in comparison to the droplet size characterized, in combination with a measurement error of 2 µm, calculated from measuring a subset of data in triplicate, posed a limit on our analysis of smaller droplets. Additionally, the high speed of the process, resulting in motion blur and droplets quickly moving out of focus, as well as the limited contrast, caused by the small difference in refractive index between the droplets and the surrounding medium (1.333 for water vs 1.403 for silicone oil), makes it difficult to distinguish the droplets from the background in the video recordings. Data visualization was achieved through Python-generated plots. The frequency was estimated using the mean droplet size and the flow rate of the inner solution. Note that for the analysis of droplet size and frequency, we used video recordings in which the fluid tail did not adhere to the capillary surface (one experiment per condition).

Viscosity measurements

The dynamic viscosities of the solutions were measured on a Kinexus Malvern Pro rheometer. A stainless steel plate-plate geometry with 40 and 20 mm radius were used for buffer solutions and protein-containing solutions respectively. Viscosity was measured every 5 s as a function of shear rate with a 2 min logarithmic viscometry ramp from 0.5–100 s^{-1}. As expected for simple viscous liquid, viscosities for higher shear rate were constant. The values at 100 s^{-1} were used to calculate the reported viscosity of each solution. MRB80 buffers consists of 80 mM piperazine-N,N'-bis(2-ethanesulfonic acid) (PIPES) pH 6.8, 4 mM magnesium chloride ($MgCl_2$), and 1 mM

ethylene glycol-bis(β-aminoethyl ether)-N,N,N',N'-tetraacetic acid (EGTA).

Tensiometry measurements

The pendant drop measurements were performed using a DSA 30S drop shape analyser (Kruss, Germany) and analysed with the Kruss Advanced software. Experimental conditions for G-buffer and actin-containing solutions were as described in Van de Cauter et al. [277], while changes for MRB80 buffer and tubulin-containing solutions are described below. Initially a 2 µL droplet of aqueous solution is drawn in a lipid-in-oil dispersion containing glass cuvette (Hellma Analytics) and then volume of the droplet is adjusted to 8 µL using an automated dosing system from a hanging glass syringe with needle diameter of 0.313 mm (Hamilton). As soon as the droplet reached its final volume, the droplet was analysed (for 300 s at 25 fps for solutions containing tubulin and lipids and at 5 fps for rest of the solutions) by automatic contour detection and fitted with the Young-Laplace equation to yield the interfacial tension. The densities of lipid oil solution (0.8685 mg mL^{-1}), G-buffer with 18.5 %v/v OptiPrep™ (1.0574 mg mL^{-1}), and MRB80 with 1.75 %w/v Sucrose (1.0066 mg mL^{-1}) were used in the interfacial tension calculations. These densities were measured by weighing 1 mL of solution. For G-buffer with OptiPrep™, the density was estimated using the volume-weighted-mean. The surface tension values were smoothened with a rolling-mean of 1 s. Room humidity was not controlled. In several experiments, interfacial tension decreased very rapidly (abnormally), causing the droplets to detach as soon as they are formed. These measurements were discarded from analysis.

3.5 Data Availability

All data used in the article are available via 4TU.ResearchData at DOI: 10.4121/f86cd528-8bcc-4e76-b530-4e272516e4ec [374], which includes source data for the images and plots.

3.6 Acknowledgements

We thank Roy Hoitink for his contributions during the initial exploration of the imaging setup, SaFyre Reese for experimental help during parameter screening, and Irene Istúriz Petitjean for help with rheology experiments. We would also like to thank Dr. Arjen Jakobi for generously lending us the Chronos 2.1-HD camera, and Iliya Cerjak and Bob Krijger for technical help with the design of the imaging setup and the light source, respectively.

3.7 Supplementary Information

eDICE GUVs were prepared as described in Baldauf et al. [288]. Emulsion droplets were produced in an identical fashion to those produced in the intermediate GUV preparation step in eDICE, where we emulsified a disperse phase into 1 mL of oil

phase by mechanical agitation. To allow us to image the aqueous droplets in oil, we additionally dissolved 2 %v/v Span80 (Sigma Aldrich) in the oil phase to stabilize the interface [239]. This addition of surfactant was necessary to prevent the droplets from coalescing before or during the ∼30 min necessary for imaging, but it changes the interfacial properties and may thus have an impact on the droplet size distribution. The addition of extra surfactant has been shown to decrease the average size of emulsion droplets generated in turbulent flow [375], so our measurements likely underestimate the true size of droplets generated during the eDICE GUV formation process. Epifluorescence images of water-in-oil droplets and GUVs were acquired on an inverted Nikon Ti Eclipse microscope equipped with a 60x water immersion objective (CFI Plan Apochromat VC), a digital CMOS camera (Orca Flash 4.0), and an LED light source (Lumencor Spectra Pad X). Phase contrast images were acquired on the same Nikon Ti microscope.

Composition [n%]	Diameter [$\mu \pm \sigma$] (µm)	N	Imaged by
100 DOPC	10.08 ± 4.49	187	Phase contrast
100 EggPC	9.844 ± 4.89	108	Phase contrast
80:20 DOPC:cholesterol	10.88 ± 4.20	38	Phase contrast
95:5 DOPC:DGS-NTA(Ni)	9.522 ± 3.32	47	Widefield
95:5 DOPC:bioPE	11.68 ± 5.43	60	Widefield

Table 3.S1: **Lipid composition details for eDICE GUVs and size statistic.**

3.7.1 Supplementary Figures

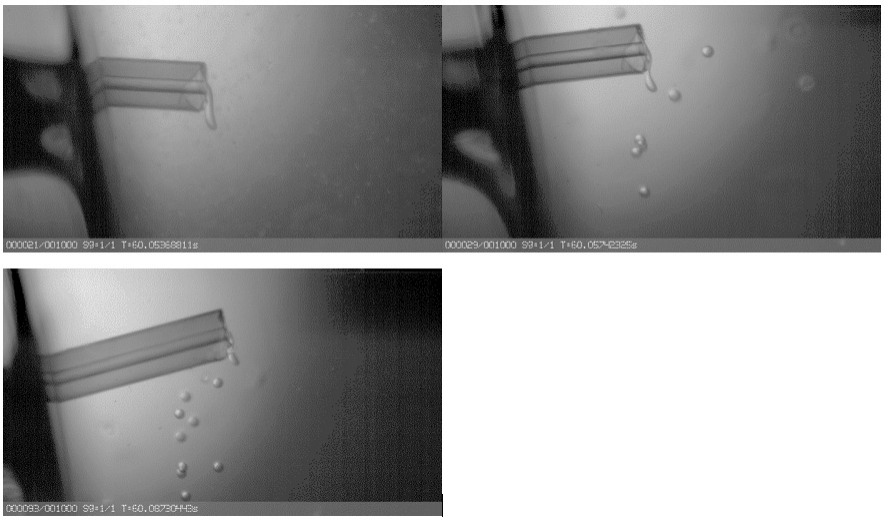

Figure 3.S1: **Silanization of the capillary prevented attachment of the liquid thread to the capillary.** Representative field-of-views, differences can be seen in insertion angle, -insertion depth, and capillary orifice (i.e. cut finish and coating chipping off). In all three cases, the capillary was silanized, and the liquid stream did not adhere to the capillary. The capillary was silanized using dichlorodimethylsilane (40140, Sigma Aldrich) by submerging the tip of the capillary for one minute, before removing excess with nitrogen gas. The capillary opening is 100 µm.

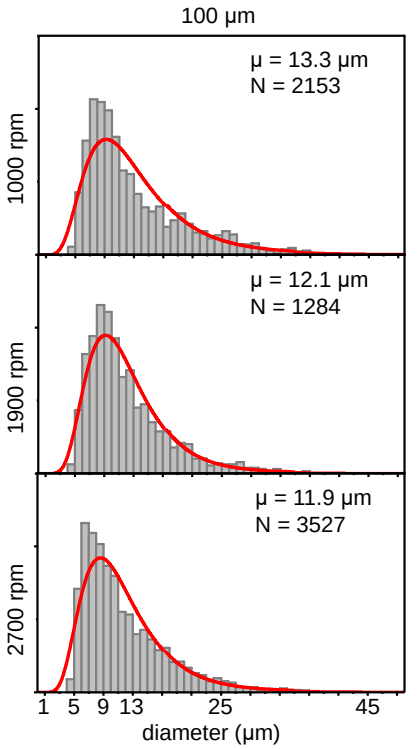

Figure 3.S2: **Size distributions of GUVs for different rotation speeds.** Size distribution of GUVs made at rotation speeds Ω of 1000 rpm, 1900 rpm, and 2700 rpm. The individual graphs represent pooled data for three experiments. The distributions are fitted to a log-normal function. Reprinted (adapted) with permission from Van de Cauter et al. [277].

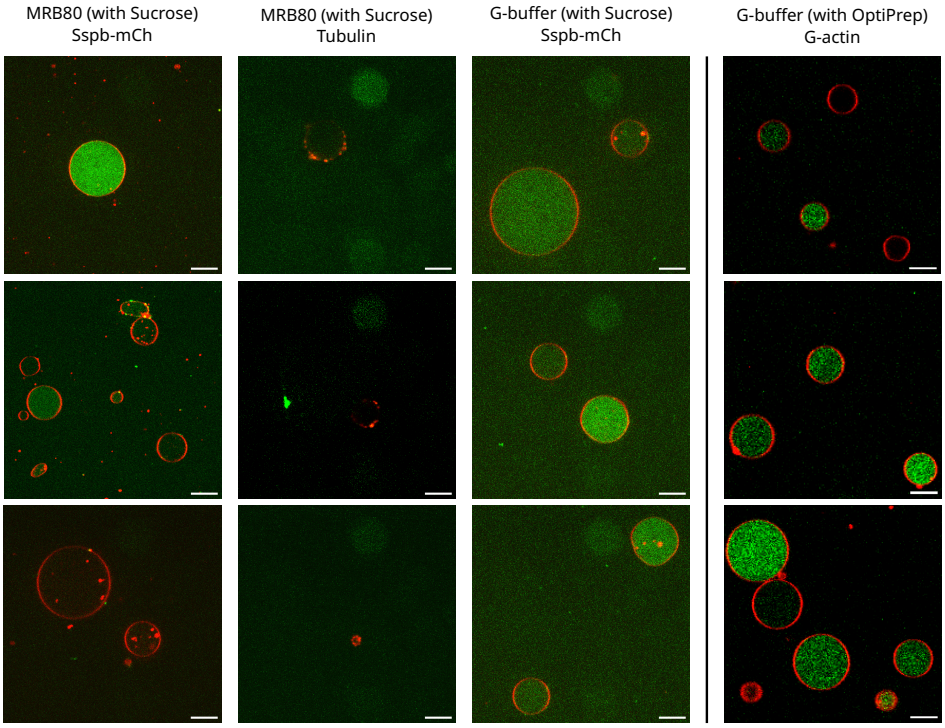

Figure 3.S3: **Variation in yield and encapsulations of GUVs for different inner aqueous solutions.** Representative field-of-views of GUVs made using cDICE, differences can be seen in yield and quality (encapsulation efficiency, membrane cleanliness) for different inner aqueous solutions (columns left to right) – SspB-mCherry in MRB80 buffer (with sucrose), tubulin in MRB80 buffer (with sucrose), SspB-mCherry in MRB80 buffer (with sucrose) and G-actin in G-buffer (with OptiPrep). GUVs (lipids – Cy5) are marked as red, and encapsulated proteins (SspB – mCherry, Tubulin – Rhodamine, Actin – Alexa Fluro 488) as green. SspB (stringent starvation protein B) is an adaptor protein which delivers ssrA-tagged proteins to ClpXP for degradation in *Escherichia coli*, here used as an alternative to cytoskeletal proteins (actin, tubulin). Scale – 10µm. The G-actin in G-buffer panel reprinted (adapted) with permission from Van de Cauter et al. [277].

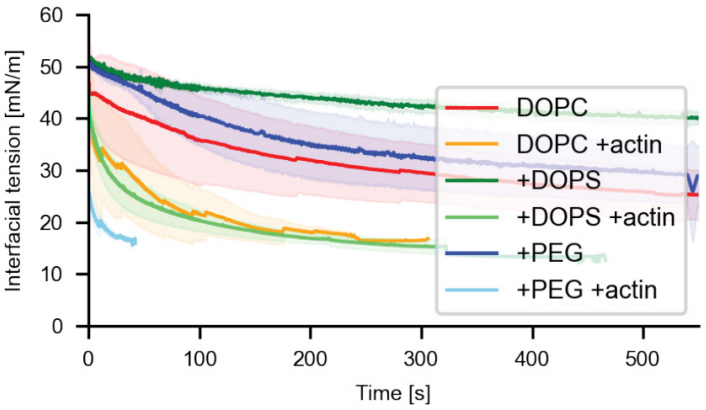

Figure 3.S4: **Interfacial tension evolution with and without actin using different lipid compositions.** Each curve represents the average over N measurements with the shaded region being the standard deviation. Only DOPC against inner aqueous solution (G-buffer with 18.5 %v/v OptiPrep™) without (red line, N=21) and with (orange line, N=19) 4.4 µM actin, DOPC with 20 % DOPS against inner aqueous solution without (dark green line, N=2) and with (light green line, N=3) 4.4 µM actin, and finally DOPC with 5 % PEG 2000 DOPE measured against inner aqueous solution without (dark blue line, N=3) and with 4.4 µM actin (light blue line, N=3). Total lipid concentration is 0.2 mg mL^{-1}.

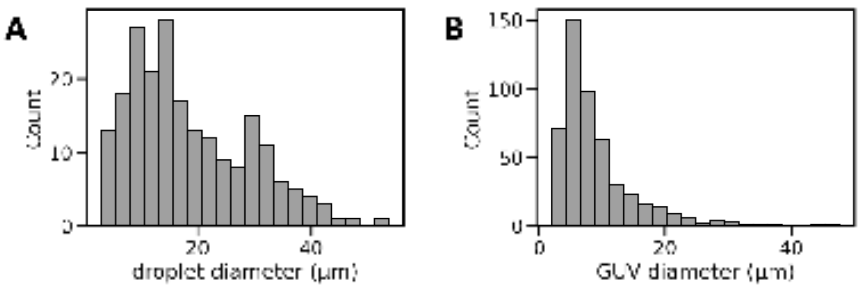

Figure 3.S5: **Size distribution of droplets and GUVs in eDICE.** (a) Histogram of the diameters of droplets generated in the first step of eDICE (N = 213 droplets from 2 separate experiments). Droplets contained 4.4 µM actin in F-buffer with 6.5 %v/v OptiPrep™ and were stabilized by surfactants in addition to lipids. (b) Histogram of GUV sizes generated by eDICE (N = 494 GUVs from 4 separate experiments).

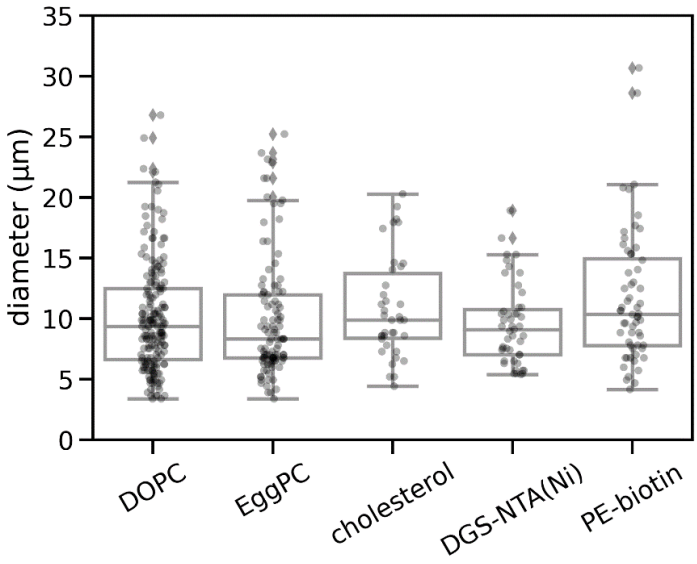

Figure 3.S6: **Size distribution for GUVs produced using eDICE with various membrane composition.** GUVs with different membrane composition produced by eDICE (see Tab. 3.S1; GUVs were prepared as described in Baldauf et al. [288]). The membranes for widefield imaging also contained 0.05 % Cy5-labeled lipids. GUVs with 5 % Biotin-PE in the membrane also encapsulated 0.88 µM Atto 488-conjugated streptavidin (Sigma Aldrich), all others are without encapsulated proteins. Sizes were measured manually in Fiji, fitting circles to max projections of a Z-stack. Box plots comparing the GUV sizes are displayed on the graph, the distributions are not statistically different (p=0.070 by one-way ANOVA). Epifluorescence images of GUVs were acquired on an inverted Nikon Ti Eclipse microscope equipped with a 60x water immersion objective (CFI Plan Apochromat VC), a digital CMOS camera (Orca Flash 4.0), and an LED light source (Lumencor Spectra Pad X). Phase contrast images were acquired on the same Nikon Ti microscope.

3.7.2 Supplementary Movies

Figure 3.S7: **Droplet formation at the capillary orifice at a rotation speed of 1900 rpm.** Video recordings of droplet formation at the 100 µm diameter fused silica capillary orifice at a rotation speed of 1900 rpm. The playback speed is 5 fps for a total of 50 frames. [partial, low-res]

Figure 3.S8: **Droplet formation at the capillary orifice at a rotation speed of 2700 rpm.** Video recordings of droplet formation at the 100 µm diameter fused silica capillary orifice at a rotation speed of 2700 rpm. The playback speed is 5 fps for a total of 50 frames. [partial, low-res]

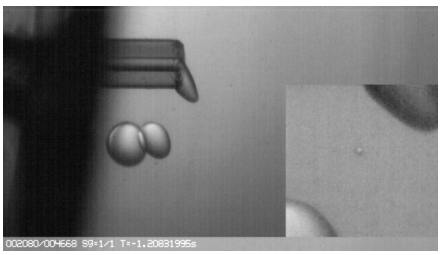

Figure 3.S9: **Droplet formation at the capillary orifice at a rotation speed of 1000 rpm.** Video recordings of droplet formation at the 100 µm diameter fused silica capillary orifice at a rotation speed of 1000 rpm. The playback speed is 5 fps for a total of 50 frames. The video has 3.5x zoom inset from region under the capillary for better visualization of the satellite droplets. An instance of satellite droplet can be seen from on-screen frame number 2080 for a few frames. [partial, low-res]

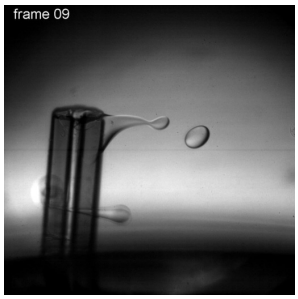

Figure 3.S10: **Droplet formation at the capillary orifice for G-buffer.** Video recordings of droplet formation at the 100 µm diameter fused silica capillary orifice with G-buffer as inner solution. The playback speed is 4 fps. [reduced, low-res]

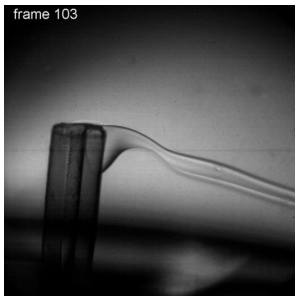

Figure 3.S11: **Droplet formation at the capillary orifice for actin in G-buffer.** Video recordings of droplet formation at the 100 µm diameter fused silica capillary orifice with actin in G-buffer as inner solution. The playback speed is 4 fps. [reduced, low-res]

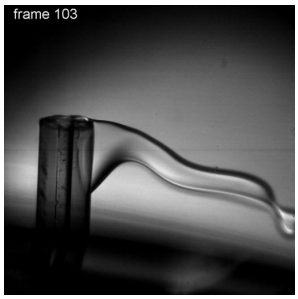

Figure 3.S12: **Droplet formation at the capillary orifice for MRB80 buffer.** Video recordings of droplet formation at the 100 µm diameter fused silica capillary orifice with MRB80 buffer as inner solution. The playback speed is 4 fps. [reduced, low-res]

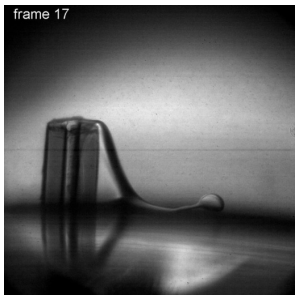

Figure 3.S13: **Droplet formation at the capillary orifice for tubulin in MRB80 buffer.** Video recordings of droplet formation at the 100 µm diameter fused silica capillary orifice with tubulin in MRB80 buffer as inner solution. The playback speed is 4 fps. [reduced, low-res]

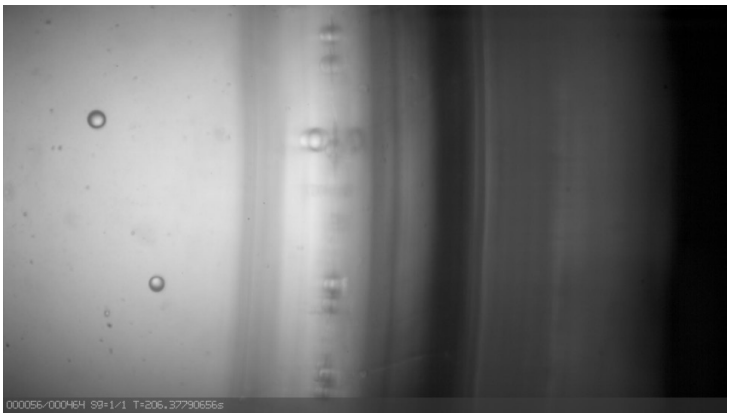

Figure 3.S14: **Oil-water interface.** Video recording of the oil-water interface. The playback speed is 4 fps for a total of 50 frames. [partial, low-res]

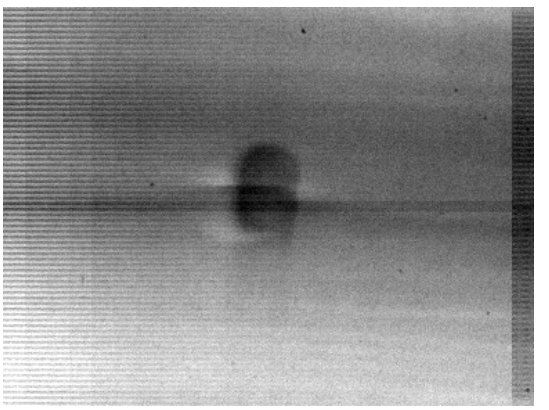

Figure 3.S15: **Droplet at oil-water interface.** Video recording of a droplet arriving and getting stuck at the oil-water interface. The frames from 30 000 fps (1 µs exposure) recording are manually selected to correspond to a path of a single tracked droplet. [ ]

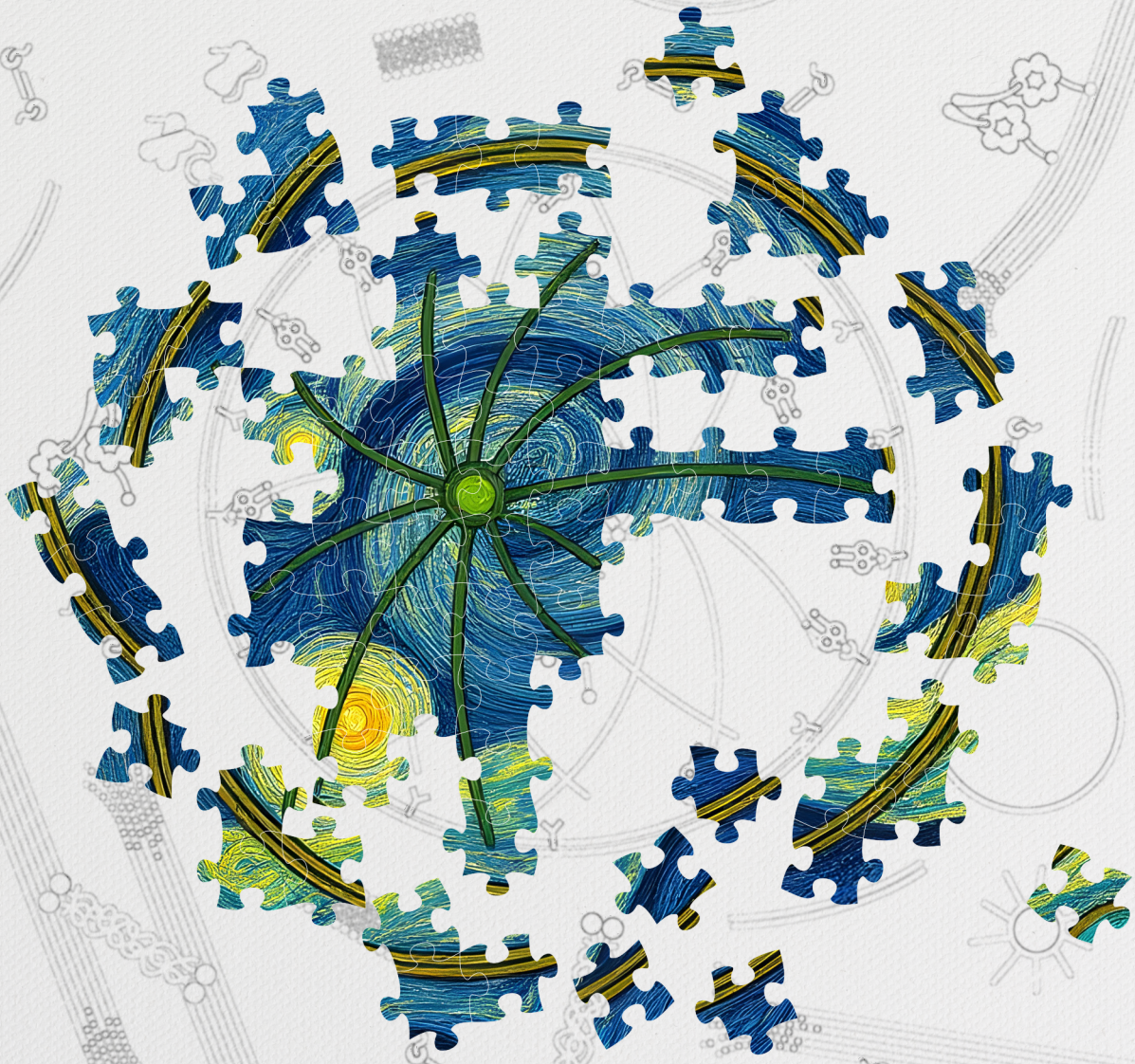

Tubulin interactions affect membrane formation

Midas Touch.
Occam's Razor.
Black Swan.

Tubulin is one of the most dynamic and abundant proteins in a eukaryotic cell. For it to function outside the cellular context, in vitro, tubulin has very specific requirements for its biochemical environment. This makes it a challenging protein to work with and has limited complex in vitro reconstitutions involving tubulin, especially for synthetic cell research. Attempts at tubulin encapsulation in vesicles have had limited success. Here, we have systematically explored tubulin encapsulation with different encapsulation methods, encompassing different bilayer formation approaches. We find similar limited success across methods, with one common observation: the presence of tubulin interferes with the lipid membrane formation and stability. Finally, with a novel membrane interaction assay, we show that tubulin destroys the simple lipid bilayer. The exact underlying mechanism remains to be discovered.

This chapter includes the tubulin reconstitution with different encapsulation methods performed with, Martin Schröeter and Jacqueline De Lora (Joachim P. Spatz lab, MPI-MR, Germany) for dsGUV and pico-injection, Chang Chen (Siddharth Deshpande lab, WUR, Netherlands) for OLA, Arash Yahyazadeh Shourabi (Marie-Eve Aubin-Tam lab, TUD, Netherlands) for FsLB, and Nicola De Franceschi (IMol, Poland) for some of the cDICE experiments.

4.1 Introduction

The mitotic apparatus of the cells has always fascinated biologists. Microtubules (MTs) were first observed in 60s in the mitotic spindle [376–378] and soon 'tubulin'[1] was later identified and isolated [380, 381]. It was only 15–20 years later that Mitchison & Kirschner [40] demonstrated the dynamic instability *in vitro* and Kirschner [382] demonstrated how it affects cell morphology. These works revived and created new interest in the field of tubulin cytoskeleton [383], which is still going on strong. Yet, we are still only 'scratching the surface of the tubulin'. The delay in the initial discoveries related to tubulin can be attributed to the fact that tubulin is a challenging protein to work with *in vitro*.

Tubulin needs very specific *in vitro* working conditions. Tubulin is temperature sensitive [384], MTs depolymerize in the cold ($T^* = 22\,°C$ [385]). Thermal cycling ages tubulin and affects its ability to polymerize [386]. Tubulin polymerization is concentration dependant and requires minimal critical concentration (CC) [387]. Calcium ions (Ca^{2+}), even in small quantities (∼6 uM), inhibit tubulin polymerization, and chelation with EGTA is essential [388]. Magnesium ions (Mg^{2+}) and GTP, are both essential as the Mg-GTP complex in required for tubulin polymerization [389]. Presence of other ions like Zinc (Zn^{2+}), or common buffer additives like glycerol adversely affects the tubulin polymerization and leads to non-functional tubulin polymorphism like sheets and rings [390–392]. Unlike most proteins, tubulin requires sulfonate buffers for *in vitro* polymerization, with PIPES inducing more vigorous polymerization compared to MES [393]. Furthermore, changes in pH and ionic strength of buffer also affect polymerization [394]. Although these conditions, barely resembles the cytoplasm.

The discovery of the structure of the tubulin dimer (1TUB [77], Fig. 4.1(a)), aided in comprehending some of the complex nature of tubulin. At neutral pH, tubulin is negatively charged. Basic surface electrostatic characterization reveals regions of positive and negative charges (Fig. 4.1(b)). The α/β-tubulin complex has the strongest attractive electrostatic attractions [395]. The tubulin heterodimer is thus very stable, has a very slow dissociation constant (K_d 10^{-11} M) and very long half-life (∼9.6 h) [396]. These charges play an important role in how tubulin monomers interact with each other and in MTs MAPs [395, 397]. Hydrophobicity screening the tubulin dimer surface reveals hydrophilic and hydrophobic patches (Fig. 4.1(c)) [398]. The tubulin dimer has two significant non-polar hydrophobic sites, one at the α/β-tubulin contact region and the other possibly at the polymerizing interface [399]. The C-terminal tails of both α-tubulin and β-tubulin (unstructured parts missing in the structure) also contribute significantly towards the overall negative charge of the tubulin and are also hydrophobic [397]. MAPs are known to interact with the MT lattice with the help of the C-terminal tails. Electrostatics play an integral role in these interactions, but hydrophobic interactions are important too [400].

Encapsulating tubulin in a 3D container, be it a droplet or a vesicle, for a synthetic cell reconstitution involves lipids. And lipids are amphipathic molecules with polar hydrophilic head group and non-polar hydrophobic tail (choline like DOPC,

[1] It could well have been, 'spactin', 'flactin', and 'tektin' [379], but the choice of 'tubulin' seems particularly apt.

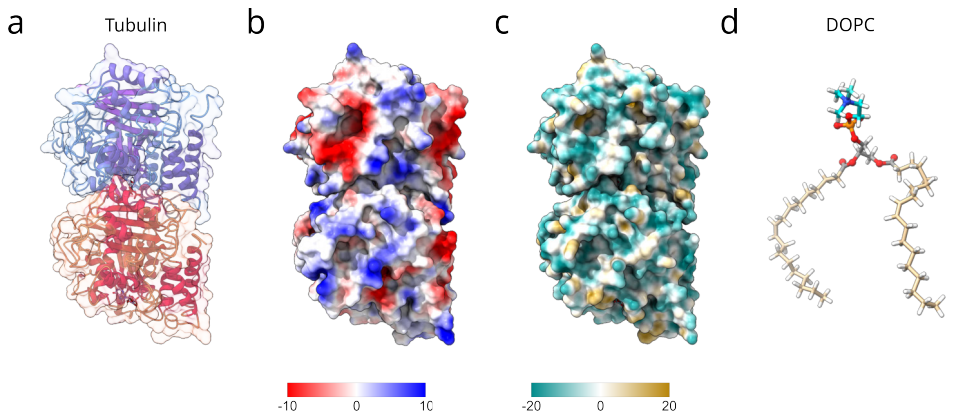

Figure 4.1: **Tubulin and lipid 3D structure.** (a) Tubulin alpha-beta dimer (PDB 1TUB), α-tubulin and β-tubulin, secondary structure in cartoon representation and a molecular surface shell. (b) (c) Molecular surface of tubulin with, (b) Coulombic electrostatic potential (ESP) (calculated with ABPS [401]) and (c) molecular hydrophobicity potential (MHP) (calculated using Kyte-Doolittle scale [402]). (d) 18:1(n-9)-18:1(n-9) PC (DOPC) lipid molecule (Stockholm lipids [403]) in ball-stick representation, with polar hydrophilic (choline (+ve), phosphate (-ve), glycerol) head group and non-polar hydrophobic (hydrocarbon) tail. Images rendered with ChimeraX [404]. [ ]

Fig. 4.1(d)). The polar hydrophilic head group can also have a charge, depending on the type of the lipid molecule (e.g. negative — serine like DOPS). With the hydrophobic and hydrophilic patches of tubulin, tubulin shows signs of being an amphipathic protein, and expect it to also interact lipids directly. Tubulin, especially α-tubulin's polymerization interface, is shown to interact with lipids, with a higher preference for DOPE compared to DOPC [369]. This indicates tubulin's interaction at the lipid membrane.

Simple tubulin encapsulation in vesicles is possible. Encapsulated tubulin can polymerize into MT, and can deform the vesicle or poke the vesicle to form ϕ shape or buckle in under tension [258–260, 405, 406]. Change in hydrostatic pressure can also affect the dynamics of the MT inside the vesicle [407]. In our attempts at encapsulating proteins with cDICE method, we see that proteins affect the vesicle formation and yield of GUVs is significantly reduced (see Ch. 3). Here, we explore further how tubulin is affecting vesicle formation. And try to encapsulate tubulin with different techniques, that use different approaches at membrane formation to dissect the tubulin-lipid interactions.

4.2 Results

4.2.1 Tubulin and aqueous solution affect each other.

Proteins with their associated buffers are known to affect the yield and encapsulation efficiency of GUVs [286, 358, 359], especially with higher protein concentrations in

case of cDICE. Vesicle formation is a complicated process, and exactly how protein affects this process is not fully understood. In order to gain insight into this, we, in Ch. 3, have shown that the presence of proteins changes the physical properties of aqueous solution like viscosity and surface tension. Proteins affect the adsorption kinetics of lipid at the water-oil interface, interfering with the monolayer formation. Here, we continued exploring the effect of proteins on other physical property of aqueous solutions.

The contact angle, i.e. the hydrophobicity, is in a way related to the surface tension given by Young's equation [408]. So extending our previous work on surface tension (Sec. 3.2.4), we chose to quantify the static drop contact angle in a simple experiment on a silicon wafer (Fig. 4.S1(a)). We did not observe any drastic change in contact angle, as in the case of viscosity. Water was the most hydrophilic, compared to proteins (tubulin 5–30 µM, actin 2 µM) and their buffers (Fig. 4.S1(b)). MRB80 was more hydrophobic than G-buffer. And addition or increasing protein concentration makes solution slightly more hydrophobic. The contact angle did not change much, but the interpretation of angle varies a lot depending on the different definitions of hydrophobicity [409]. The angle θ of (60.5500 ± 3.4895)° for tubulin (30 µM) is on the cut-off ($\theta > 65°$) for hydrophobicity proposed by Vogler [410] based on changes in hydrogen bonds and long-range interactions. In chapter Ch. 3, we see the protein solution sticking to hydrophobic walls of the capillary in cDICE. And during DSSF, the protein solution initial travels through air before coming in contact with the oil. This introduces third phase, capillary surface or air, in addition to aqueous protein mix and lipid-oil dispersion, creating a contact angle between the three phases. Hydrophobicity is in relation to water (over a surface in air), but most vesicle formation protocols use oil (non-wettable long hydrocarbon chains) as medium for lipid dispersion, so quantifying oleophobicity (contact angle of proteins with oils and surfaces) would be interesting. While it is clear that higher tubulin concentrations make solutions hydrophobic, more complex measurements like dynamic angle and angle hysteresis can potentially provide better insights [409]. Furthermore, implications of contact angle for protein solutions in a biological context are lacking. This can help to understand another interesting problem of protein wetting or protein liquid-liquid phase separation (LLPS) too.

The protein of interest affects the aqueous solution, but can other components of the solution have any effect on the protein itself. We investigated the effect of such component, OptiPrep™ , on tubulin. It is widely used for purification of cells from tissue cultures or organelles from cells [411]. OptiPrep™ [2] is known to only increase the density and viscosity of the solution without affecting other parameters like osmolality, pH, and ionic strength. Due to this property, it is convenient to use OptiPrep™ (18.5 %v/v) to increase density without affecting osmolality of IAS for emulsion transfer based GUV formation methods like cDICE [277], without worrying about yield of GUVs by maintaining osmolality of IAS and OAS with sucrose-glucose density contrast ($\Delta\rho$ =100 mM), as originally proposed in Abkarian et al. [271]. However, Baldauf et al. [288] have shown OptiPrep™ drastically affects the actin polymerization rate, attributed to reduced diffusion of actin monomers.

[2] solution of 60 % iodixanol in water

Hence, we tested tubulin dynamics in presence of OptiPrep™ . Absolutely no tubulin polymerization is seen, even with MT seeds, in standard cDICE IAS containing tubulin (40 µM) and OptiPrep™ (18.5 %v/v) (Fig. 4.S2(b)), while tubulin polymerises in MT dynamic assay mix (tubulin 40 µM and sucrose 1.75 %w/v). OptiPrep™ severely inhibits tubulin polymerization. We checked if this inhibition is similarly resulting from reduced diffusion of tubulin dimers, as for actin monomers. The diffusivity of tubulin dimers reduces with OptiPrep™ and other crowding agents like sucrose, PEG, and BSA compared to with just MRB80. It is affected most by OptiPrep™ and least by sucrose[3]. This decrease in diffusivity of tubulin dimers could have explained slower polymerization rate, but a complete suppression of polymerization by OptiPrep™ is indicative of some biochemical inhibition[4] of tubulin.

Hence, we had to switch back to using sucrose-glucose density gradient for balancing osmolalities of IAS and OAS for cDICE experiments. MRB80 buffer (80 mM PIPES) has high ionic strength compared to G-buffer (5 mM TrisHCl). So osmotically equivalent (∼275 mOsm/kg [5]) IAS with MRB80[6] has ∼4.5 x less sucrose compared to IAS with G-buffer[7]. Even the osmolality of just MRB80[8] is greater than the recommended value. This limits and reduces the IAS-OAS density contrast ($\Delta\rho$) for IAS with MRB80[9] against OAS with water[10]. This reduced density contrast affects droplet transfer at oil-water interface [271], thus partially reducing the yield of GUVs with cDICE.

4.2.2 Attempting tubulin encapsulation in GUV

Aware of the effect of proteins on most vesicle formation methods, leading to suboptimal yields, we tried the following methods to encapsulate tubulin in GUVs.

Swelling

We tried two swelling based approach, bead swelling and gel swelling. In case of bead-assisted swelling, the yield of GUVs reduces significantly when tubulin is present in aqueous solution. The encapsulation efficiency varies a lot. The size of vesicles is also reduced, and many smaller vesicles are seen. The vesicles have lipid aggregates and tend to stick to each other (Fig. 4.2(a)). Encapsulated tubulin showed no signs of polymerization. We even tried conditions, 30–50 µM tubulin and 7.5 %v/v glycerol,

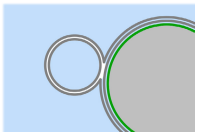

GUV swelling from gel/bead.

[3] Preliminary fluorescence correlation spectroscopy (FCS) data not shown. A similar effect was observed for actin [412, §4]

[4] One of the speculation is that it can form a coat (corona) around the tubulin surface that prevents interactions of the polymerization interface.

[5] recommended osmolality of IAS is 200 mOsm/kg by Abkarian et al. [271]

[6] 2.5 %v/v sucrose 2 M

[7] 22.5 %v/v sucrose 1 M

[8] ∼225 mOsm/kg

[9] ∼5 x lower | $\Delta\rho$(MRB80)∼0.000 578 mg mL^{-1} and $\Delta\rho$(G-buffer)∼0.002 95 mg mL^{-1}

[10] 27.5 %v/v glucose 1 M

as described previously by Kattan [413, §3] but with no success in tubulin polymerization with bead swelling.

Gel-assisted swelling is known for its quick and easy way to make GUVs with high yield. However, when we tried swelling lipid films on gel with tubulin containing aqueous solution, we saw very few vesicles. Of the few vesicles seen, the size of vesicles was also smaller compared to just MRB80 buffer vesicles. Interestingly, the quality of vesicles was not affected, the membranes were clean, without any lipid aggregates. The vesicles barely had any tubulin inside them compared to the swelling solution (Fig. 4.2(b)). The encapsulation efficiency was very low. We did not see any tubulin polymerization inside the vesicles. However, the tubulin outside in swelling solution, was active and polymerized into MTs (Fig. 4.2(b)). Lots of MT bundles were seen floating in the background. Gel swelling method is not known for good encapsulation efficiency and our results agree with it. The drastic decrease in the GUV yield is however surprising.

cDICE and eDICE

Next, we tried cDICE, and its' variant eDICE, for encapsulating tubulin in vesicles. cDICE is a widely used method in the field for GUV formation due to its ability to produced high yield of vesicles, with size control and better encapsulation efficiencies suited for complex protein reconstitutions [271, 277].

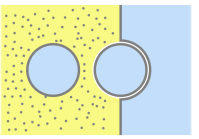

Droplet crossing oil-water interface forms GUV.

The first thing we notice trying to form vesicles with MRB80 buffer by cDICE was the significantly reduced yield. The yield was ~10 x lower compared to yield of vesicles with G-buffer. Although it is difficult to quantify the yield of vesicles quantitatively, the qualitative disparity was striking apparent. Similar decrease in yield was observed with vesicles with MRB80 buffer by inverse emulsion method[11]. The yield of GUVs with sucrose was a bit lower than with OptiPrep™ , as expected from Sec. 4.2.1.

The yield of vesicles was further affected based on the protein encapsulated inside the GUVs. For a simple, small protein like SspB, the yield of vesicles was not further affected (Fig. 4.3(b)). The sample was still crowded with GUVs even after 10 x dilution with OAS before imaging. But in case of encapsulating tubulin, the yield of vesicles drop severely, ~100 x decrease (Fig. 4.3(a)). The GUVs in the sample were sparingly observed, even without diluting the sample. The experiments were conducted consecutively on the same time, with same aqueous and lipid-oil solutions, and imaged with same conditions to maintain identical conditions and to try to quantify the difference in the yield of GUVs due to presence of tubulin. The size of GUVs was fairly consistent with just MRB80 buffer and also across protein samples. The quality of GUVs was also good with clean membranes and non-sticky vesicles, while some lipid aggregates were seen in case of tubulin encapsulation. Encapsulation efficiency varied across GUVs, but not much difference was observed across

[11] [personal communications] Independent observation by Andreas Fink, Ada Cavalcanti-Adam lab (Max Planck Institute for Medical Research, Heidelberg, Germany)

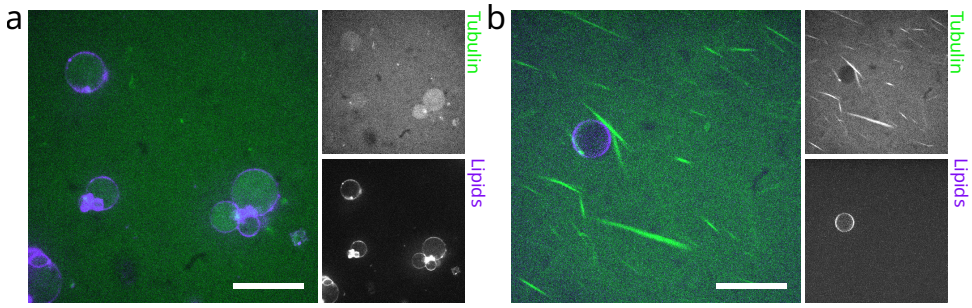

Figure 4.2: **Tubulin encapsulation with swelling techniques.** (a) GUVs formed using glass bead swelling. GUVs have lipid aggregates and clump together, and tubulin (40 µM) with MT seeds does not polymerise. (b) GUVs formed using gel swelling. Tubulin (40 µM) inside GUVs does not polymerise, while MT bundles seen outside. Scale bar — 20 µm.

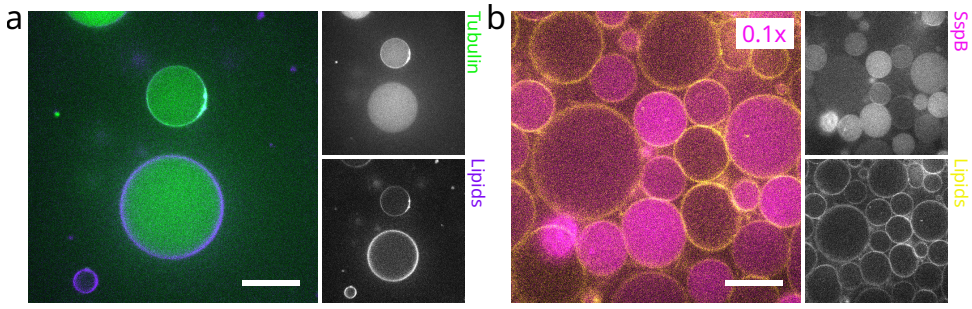

Figure 4.3: **Effect of proteins on cDICE GUV yield.** GUVs formed using cDICE consecutively under identical conditions, different proteins in IAS, with (a) tubulin (35 µM) and (b) SspB (1 µM). Yield of GUVs with tubulin was much lower compared to GUVs with SspB (even when diluted 10 x before imaging). Scale bar — 20 µm.

different protein samples. The proteins have not misbehaved, i.e. aggregating, or sticking to the cortex, and were present in the lumen. The tubulin was not expected to polymerise as the sample was kept at room temperature.

With the only handful of GUVs obtained with tubulin encapsulation by cDICE, we next tested if the tubulin can still polymerise into MTs inside the vesicles. Tubulin polymerization was promoted by heating the sample to ∼27–30 °C. If the vesicles had enough tubulin encapsulated, instead of polymerizing, it aggregates and forms artefacts (Fig. 4.4(a)). Artefacts range from puncta, 3D (non-physiological) filamentous shapes, sticky at the cortex, and sticky vesicles. Some vesicles did show tubulin signal in the lumen but did not polymerize, maybe due to lack of enough encapsulated tubulin concentration. So we tried to aid the polymerization by stabilizing filaments, promoting nucleation, and crowding agents. Addition of PEG-6000 and PEG-35000, as crowding agents to facilitate polymerization, also showed not ef-

fects on tubulin polymerization (Figs. 4.S4(e) & 4.S4(f)). The addition of taxol, an MT stabilizing drug, causes tubulin to go and stick to the cortex (Fig. 4.S4(c)). And with the addition of GMPCPP, a slowly hydrolysing analogue of GTP, there is also no polymerization of tubulin, and it goes to the cortex (Fig. 4.S4(d)). We added MT seeds, pre-nucleated MTs, to reduce and still no MTs (Figs. 4.S4(c) & 4.S4(d)). We see some filamentous structures, which also coated the MT seeds. While some of these conditions had OptiPrep™ , which drastically inhibits tubulin polymerization (as described earlier), we also tried with sucrose. Sucrose by itself has also been shown to slightly stabilize the MTs. Even with taxol in presence of sucrose, we did not see any polymerization, and tubulin still goes to the cortex and vesicles has lots of lipid aggregates sticking on the surface (Fig. 4.S4(a)). Lastly we also tried adding centrosomes (MTOCs), which make asters by growing hundreds of microtubules, but still no signs of tubulin polymerization (Fig. 4.S4(b)). During these optimizations, we also varied tubulin concentrations from 5–105 µM, lower ranges to minimize the effect of tubulin on GUVs and higher ranges to promote polymerization, but we did not observe any microtubules in vesicles. During trying to optimize tubulin encapsulation in vesicle with cDICE, we tried lots of different conditions with no success, many with zero yield (Tab. 4.S1).

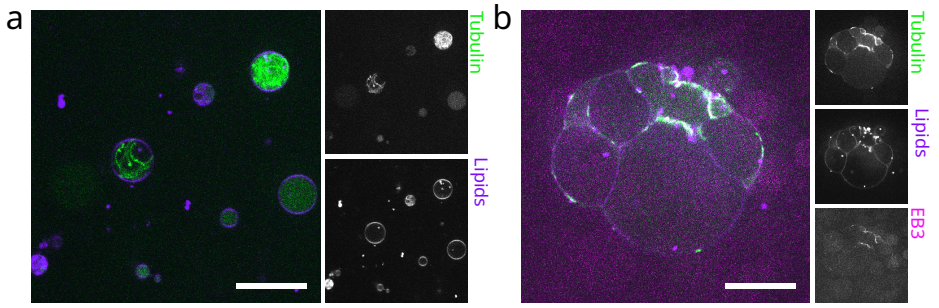

Figure 4.4: **Tubulin polymerization issues.** GUVs formed using, (a) cDICE with IAS — tubulin (40 µM) and OptiPrep™ (18.5 %v/v) and (b) eDICE with IAS — tubulin (105 µM), EB3 (200 nM) and Sucrose (1.75 %w/v). Images shown are representative of GUVs with various different tubulin and GUV artefacts. GUV yield is lower. Tubulin does not polymerise, aggregates, and forms artefacts. Lipid aggregates, possible remnants of GUVs, are seen. In case of eDICE, clusters of GUVs stuck together are seen. Scale bar — 20 µm.

It is also difficult to visualize single microtubules in 3D vesicles, as they move rapidly. We tried using secondary molecules as reporter MTs, EB3 (Fig. 4.4(b)), MAP7, and TUBright (a labelled peptide marker for tubulin [414]), but we do not see any signal, mostly due to absence of MTs. During optimization conditions, we also tried encapsulating tubulin with eDICE, a variant of cDICE, and we saw no polymerization with tubulin sticking to the cortex and at the contact sites between vesicles in a cluster (Fig. 4.4(b)). Furthermore, the vesicles from eDICE were very sticky. The clustering of droplet may have happen in the emulsion stage itself, as it lacks any strong stabilizing agents (e.g. Span80) and tubulin like to interfere with lipid ad-

sorption (shown in Sec. 3.2.4). But then these huge droplet clusters should not end up as vesicles due to size selectivity at water-oil interface (explained in Sec. 3.2.5). So the vesicles from eDICE, after formation, stick to each other and form clusters. Images shown are representative, different vesicles had different variations of artefacts and hardly any microtubules. Furthermore, inter-experiment variability is high, both in vesicle yield — which occasionally resulting in no vesicles, and in tubulin polymerization — which frequently produces artifacts.

Complications with GUV formation, encapsulation efficiency and polymerization issues seem to be very specific to the tubulin. So as a test, we quickly tried encapsulating another cytoskeletal protein, bacterial tubulin (bTubAB), an apparent homolog of eukaryotic tubulin. Encapsulating bTubAB in MRB80 with cDICE results in GUVs without any optimizations. We see bTubAB polymerizing into bacterial microtubule filaments (bMT) and even deform the vesicles (Fig. 4.S3). The yield is good, comparable to just MRB80 vesicles. Encapsulation efficiency is still fluctuating and size of GUVs is slightly smaller. Similar deformation of vesicles with expressed and polymerized bMT is shown with vesicles formed with bead swelling too [415].

OLA

Next, we tried OLA, which is also an emulsion transfer method but uses microfluidic chips and a different physico-chemistry approach for vesicle formation. After having problems with generating droplets of desired sized in cDICE, we hoped the microfluidic approach would help solve at least one of the previous issues and improve the vesicle yield.

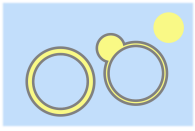

OLA GUV releasing octanol pocket.

After optimizing and adjusting the IA, LO, OA solutions flow rates for encapsulating tubulin with MRB80, we see water-octanol-water droplets emerging from the 6-way T-junction (Fig. 4.5(a)). But as soon as the octanol pockets start developing on the droplets, the droplets burst. This lead to spreading of tubulin in the post T-junction channel (Fig. 4.5(b)). The lipids may not have enough time to cover enough droplet surface, or maybe tubulin was again interfering with lipid adsorption on the octanol-water interface.

After sometime, even the formation of W/O/W droplets at the T-junction was interrupted and only an uninterrupted stream of LO solution was observed (Fig. 4.5(d)). The tubulin was seen spreading all across the post T-junction channel and a dense filamentous network appears. This network seemed to contain MTs nucleating from tubulin stuck to the microchannel surface. The growing super long MTs bend under the flow of the solutions. Also, in the region before the T-junction, in the IA channel, the tubulin signal seems to show filamentous structures (Fig. 4.5(c)). So in case of OLA, the tubulin started polymerizing into very long MTs, even before being encapsulated. This enhanced polymerization could possible be explained by the presence of crowding agents (5 mM dextran (MW 6000) and 15 %v/v glycerol) in the IA solution required for OLA. Therefore, even though tubulin was polymerizing in the OLA microfluidic chip, the method is not suitable as no stable vesicles are obtained at the end.

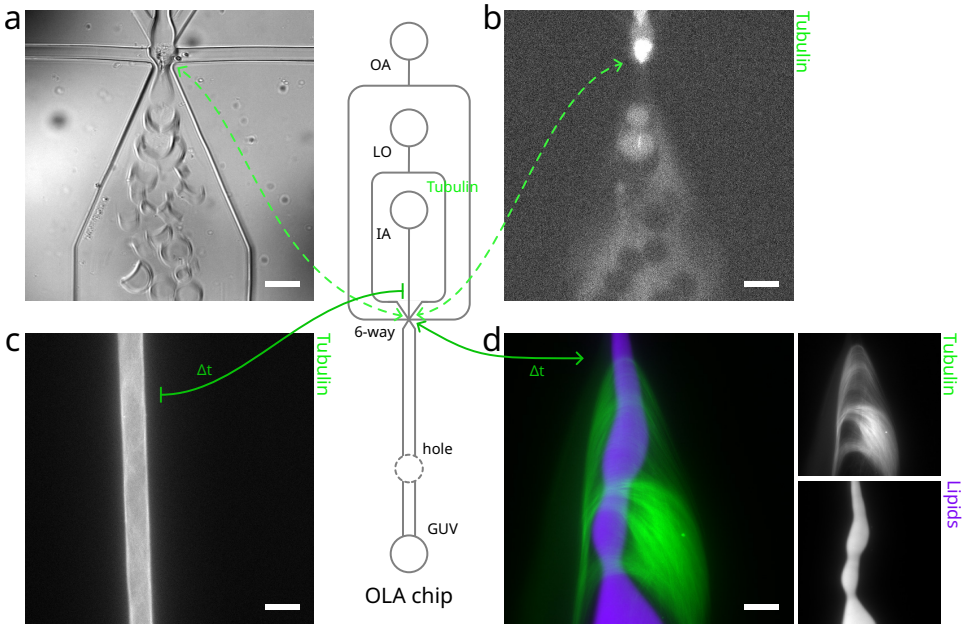

Figure 4.5: **Tubulin encapsulation issues with OLA.** (centre) Overview of the OLA microfluidic chip. (a) Early in the experiment, GUVs are formed at the T-junction (bright field) and burst immediately. (b) Bursting of GUVs leads to spreading of tubulin (40 µM, with MT seeds) in the post T-junction channel. After a while, (c) a filamentous signal was seen in the IA channel (pre T-junction), indicating the presence of MTs, and (d) GUV formation was interrupted (post T-junction) with the LO solution just flowing as an uninterrupted stream, while dense long MT filaments appear growing stuck to the post T-junction channel. Scale bar — 40 µm.

dsGUV

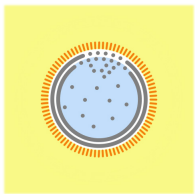

GUV assembly in dsGUV.

After trying different methods from the two most common types of vesicle formation techniques, i.e. swelling and emulsion transfer based, we explored dsGUV formation, a technique with a fundamentally different underlying membrane formation mechanism, based on SUV fusion. Knowing that tubulin is exhibiting issues with lipid membranes and GUV formation, we designed experimental assays using different modes and variations of dsGUV, to dissect and explore the effect of tubulin. We used tubulin with MT seeds to promote polymerization, and we used two different surfactants for stabilizing droplets — Click Tri-block surfactant (CTS) and Click Di-block surfactant (CDS, or dsPos). We tested five different lipid compositions (Tab. 4.3) to optimize tubulin compatibility with lipids and surfactants. For dsGUV formation, we first used a microfluidic chip variant with double inlet (see Fig. 4.S5(d)) to sheath the tubulin mix with another aqueous solution and delay tubulin contact with the oil-water interface or lipids. Next, to completely separate the processes

of membrane of vesicle formation and tubulin encapsulation, we pre-formed empty dsGUVs and later introduced tubulin by using a pico-injection technique (Sec. 4.2.2).

With the double inlet experiments, dsGUVs with pH-sensitive lipids had the best initial coverage over the droplet interface (Fig. 4.6(a)). The lipids covered almost the entire interface, but the droplets with an apparent high concentration of tubulin had a lower signal of lipids at the cortex. Since every droplet was made exactly the same, they should all have the same concentration of tubulin. And for tubulin, there is theoretically nowhere else to go other than being in the droplet lumen. Since the oil used for dsGUV formation is fluorinated (HFE 7500), this makes it super-hydrophobic and lipo-phobic too. Yet, some droplets did not have a tubulin signal, and we observed a weak lipid signal in oil. The dsGUVs with negative lipids were the worst. The lipid coverage was partial, and lots of lipid signal in oil. All the tubulin was at the droplet interface (Fig. 4.S5(a)). The dsGUVs were not stable and appeared coalesced. Following incubation at 37 °C for 5 min, the tubulin showed signs of polymerization. The dsGUVs with pH-sensitive lipids had lots of MTs and bundles (Fig. 4.6(b)). The lipid aggregates appeared at the interface and the lipid signal in the oil increased. We observed a network of MTs throughout the lumen of dsGUVs (Fig. 4.6(c)). However, we also found a weak tubulin signal at the dsGUV interface, co-localising with the lipid signal. The dsGUVs with neutral (w/ PEG) (Fig. 4.S5(b)) and charged (Fig. 4.S5(c)) lipids also showed lots of tubulin polymerization. The dsGUVs were not stable and coalesced overnight. The lipid coverage for neutral (w/ PEG) lipids was very patchy, while charged lipids had complete coverage at the interface.

For ideal complete lipid coverage on the inside of dsGUVs, overnight (O/N) incubation (at 4 °C) is recommended. Hence, the tubulin encapsulated with GTP (2 mM) was supplemented with GMPCPP (1 mM) for O/N incubation of dsGUVs. Next day, after incubation at 37 °C for 5 min, all the pH-sensitive dsGUVs had the tubulin at the droplet interface and showed no signs of polymerization (Fig. 4.6(d)). The lipid coverage for most of the dsGUVs was complete and the lipid signal in oil did not increased much overnight. Tubulin and lipid shells like two different phase separated domains were observed (Fig. 4.6(e)). Similar tubulin shells and tiny lipid patches were seen on dsGUVs with charged lipids (Fig. 4.S5(e)). However, a few MT bundles were also seen, indicating that the tubulin was still functional even after overnight cold incubation. To see if the lipid shell actually corresponds to the membrane of a vesicle, the dsGUVs were released using PFO to obtain GUVs. Very few GUVs (or GUV-like spherical objects) survived after the release. This was indicative of lack of lipid membrane. The 3D spherical objects seen had a complete tubulin shell and the lipid aggregates decorating the surface (Figs. 4.6(f) & 4.S8). We checked if there was any fluidity to the surface, any remnant traces of membrane. The FRAP analysis of a surface of this object, showed no recovery. The tubulin shell was solidified, while the lipid aggregates tend to fluctuate as if tethered to the surface of the tubulin shell (Fig. 4.S5(f)). This tubulin shell was a non-functional, yet a fascinating observation. This can be the first observation of tubulin proteinosome. The double inlet dsGUV experiments with different lipids and their effects on tubulin polymer-

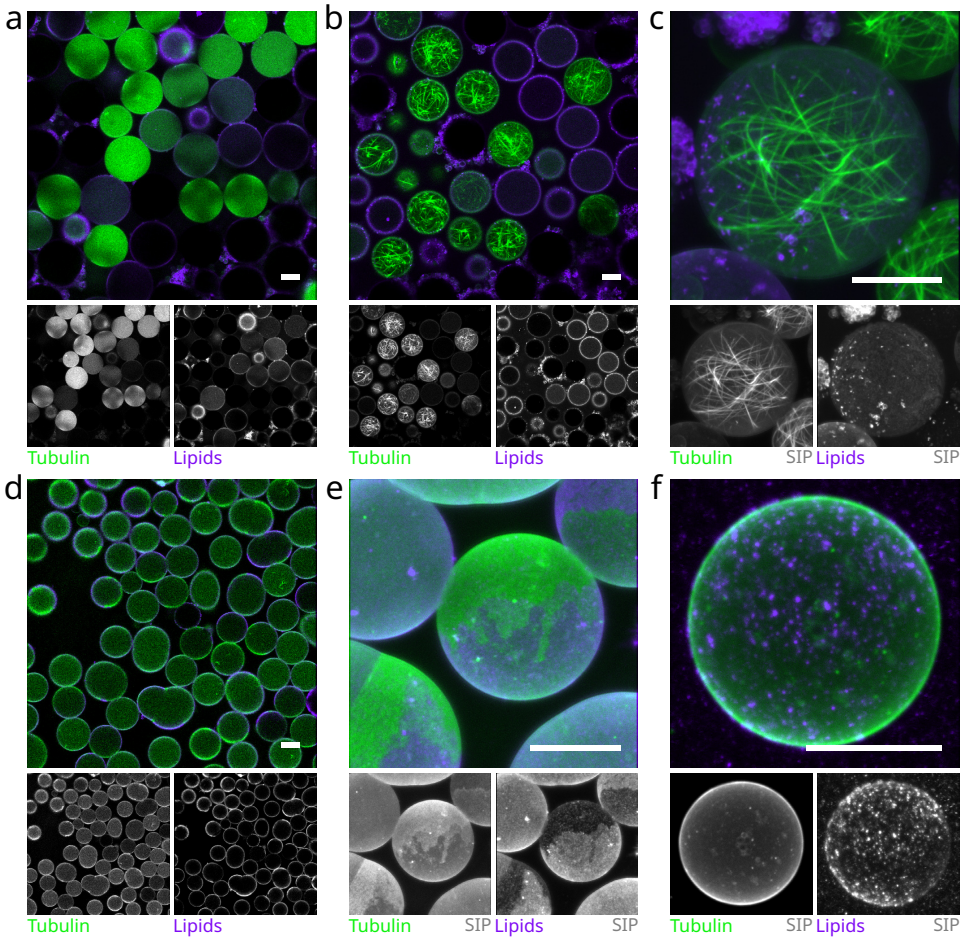

Figure 4.6: **Tubulin encapsulation with dsGUV — double inlet approach.** dsGUVs are formed with tubulin (40 µM, with MT seeds) and pH-sensitive lipids using dsGUV method (with double inlet microfluidic chip (see Fig. 4.S5(d))). (a) dsGUVs just after formation. (b) dsGUVs after 5 min incubation at 37 °C. MT polymerization is seen inside dsGUVs. Amount MT polymerization appear inversely proportional to amount of lipids present at the dsGUVs. Furthermore, lipid signal in background (SOS) increases compared to initial timepoint. (c) Standard-deviation Intensity Z-Projection (SIP) of a dsGUV showing a network of MTs, along with the presence of both tubulin and lipids at the dsGUV cortex. (d) dsGUVs (tubulin with GMPCPP 1 mM) after overnight (O/N) incubation (for optimal GUV formation) and 5 min at 37 °C (for promoting tubulin polymerization). No tubulin polymerization is seen and a patchy lipid signal. (e) SIP of a dsGUV (O/N) showing phase separation of tubulin and lipid into two domains along the dsGUV cortex. (f) GUVs are released from dsGUVs (O/N) using PFO solution. Very few GUVs survive. SIP of a GUV showing a complete tubulin cortex decorated in lipid aggregates, instead of a lipid membrane. See Fig. 4.S8 for a 3D movie. Scale bar — 20 µm.

ization was summarized in Tab. 4.1. Tubulin polymerization worked in most of the cases, but the lipid membranes did not form or were not stable enough to make vesicles.

Name	Double inlet			
	Lipid coverage	Tubulin polymerization	dsGUV stability	Contents in SOS
Neutral	Complete	-	Good	tubulin, lipids
Neutral (w/ PEG)	Exclusive (if tubulin), aggregates	very few MTs, bundles	Good	-
Negative	Patchy (if tubulin)	at cortex	Merging (if tubulin)	lipids
Charged	Exclusive (if tubulin), aggregates; Patchy (O/N)	many MTs, bundles	Good; Merging (O/N)	-
pH-sensitive	Exclusive (if tubulin), aggregates; Patchy (O/N)	many MTs, bundles	Good; Merging (O/N)	lipids

Table 4.1: **Overview of dsGUV double inlet experiments.** GUV release from dsGUVs was only attempted for charged and pH-sensitive lipids, considering O/N yield and tubulin polymerization.

Next, we decoupled vesicle formation and tubulin polymerization using pico-injection. 'Empty' dsGUVs with just MRB80 buffer were formed and incubated for few (∼2–3 h) hours for enough lipid coverage. Later, tubulin was pico-injected inside the dsGUVs. Some smaller droplets with only tubulin signal can be artefacts of leaky pico-injection, but they cannot for dsGUV due to lack of lipids. The dsGUVs with neutral (w/ PEG) lipids had the best complete lipid coverage (Fig. 4.7(a)). Followed by pH-sensitive lipid dsGUVs with complete coverage with a few aggregates (Fig. 4.S6(d)) and charged lipid dsGUVs with partial coverage (Fig. 4.S6(a)). The dsGUVs with neutral lipids also had a partial coverage, but some lipid signal in the oil. Finally, dsGUVs with negative lipids had no lipid coverage, and all the lipids were in the oil.

After the pico-injection of tubulin in dsGUVs and incubation at 37 °C for 5 min, the dsGUVs with neutral (/w PEG) lipids showed a mutually exclusive patten of tubulin and lipid signal (Fig. 4.7(b)). The dsGUVs with tubulin signal did not have any lipid signal and vice versa. This suggested that the dsGUVs which got injected with tubulin, lost their lipids. The oil background showed signals of both the tubulin and lipids. It was very interesting to see tubulin also going into the fluorinated oil. Some dsGUVs with neutral (w/ PEG) lipids showed a few MTs (Fig. 4.7(c)). The dsGUVs were stable after pico-injection. The dsGUVs with charged lipids (Fig. 4.S6(b)) and pH-sensitive lipids (Fig. 4.S6(e)) both showed similar mutually exclusive pattern of tubulin and lipids signals. Both dsGUVs showed some lipid aggregates at the interface, and all the lipids were in oil. While the dsGUVs of pH-sensitive lipids were stable after pico-injection, the charged dsGUVs started coalescing. This can be indicative of poor lipid coverage and maybe tubulin also affecting the surfactant by destabilizing the oil-water droplet interface. On the contrary, the dsGUVs with charged lipid shows high signs of tubulin polymerization, lots of MT bundles were seen (Fig. 4.S6(c)). And the pH-sensitive lipid dsGUVs had suboptimal tubulin polymerization (Fig. 4.S6(f)). Some MTs and filamentous structures are seen but also

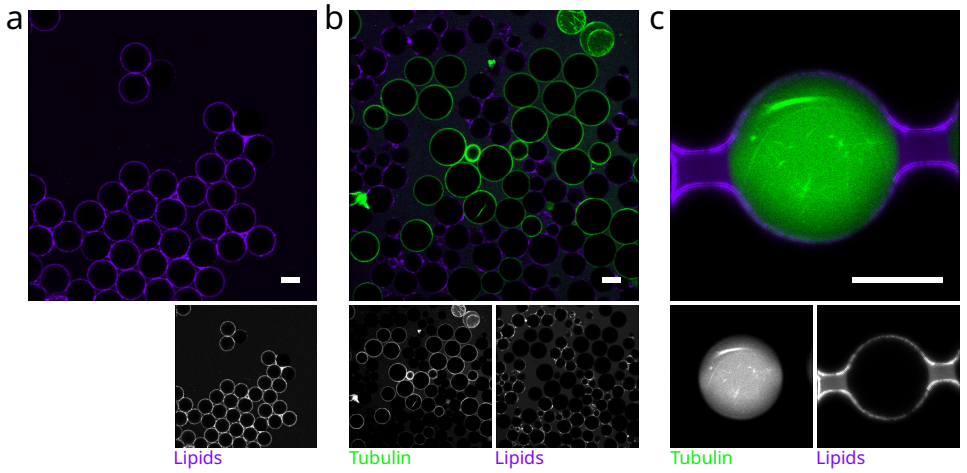

Figure 4.7: **dsGUVs and tubulin encapsulation with pico-injection.** dsGUVs are formed with neutral (w/ PEG) lipids. Tubulin (40 µM, with MT seeds) is inserted into the dsGUVs using pico-injection. (a) dsGUVs just after formation. (b) dsGUVs just after the pico-injection of tubulin. Very few dsGUVs with tubulin in lumen and MT polymerization. Tubulin and lipid at the dsGUV cortex are mutually exclusive. In addition, background (SOS) shows presence of both tubulin and lipid signal. (c) dsGUV (in a microfluidic trap) showing MT polymerization inside and no lipids present at the cortex, instead, transferring from IAS to SOS. Scale bar — 20 µm.

some signs of tubulin aggregation. We skipped injecting tubulin in dsGUVs with negative lipids due to poor vesicle quality. No attempts of releasing GUVs from dsGUVs for any lipid type were made due to the poor lipid signal at the interface and prevalence of tubulin signal, indicative of tubulin shells similar to those observed with double inlet dsGUVs. The pico-injection of dsGUV experiments with different lipids and their effects on tubulin polymerization is summarized in Tab. 4.2.

All the dsGUVs experiments reported were performed using CTS and Krytox as surfactants. The dsGUVs experiments with CDS (or dsPOS) surfactant failed severely with just MRB80 buffer too. All the lipids used to end up going in the oil instead of forming a membrane at the droplet interface. The CDS surfactant synthesis needs to be optimized for obtaining dsGUVs with MRB80 buffer.

4.2.3 Visualizing tubulin-membrane interactions

It is becoming increasingly evident that tubulin is interfering with the lipid membranes and also possibly interacting. Therefore, we decided to visualize the results of the interaction of tubulin with lipid membranes in a simpler and more controlled environment than GUVs. We need a simple assay to have a clear interpretation, so we limit the use to two minimal components, the lipids, and the protein (tubulin), and study their interaction. Such scenarios commonly use variations of supported lipid

Name	Before injection		
	Lipid coverage	dsGUV stability	Contents in SO
Neutral	Partial	Good	lipids
Neutral (w/ PEG)	Complete	Good	-
Charged	Partial	Good	-
Negative	-	-	lipids
pH-sensitive	Complete	Good	-

Name	After injection			
	Lipid coverage	dsGUV stability	Contents in SO	Tubulin polymerization
Neutral	Exclusive (if tubulin)	Good	lipids	MTs
Neutral (w/ PEG)	Exclusive (if tubulin)	Good	tubulin, lipids	few MTs
Charged	Exclusive (if tubulin)	Merging	lipids	MT bundles, at cortex
Negative	-	-	-	-
pH-sensitive	Exclusive (if tubulin)	Good	lipids	MTs, bundles, at cortex

Table 4.2: **Overview of dsGUV and pico-injection experiments.**

bilayers (SLBs) to characterize membrane properties, drug testing and membrane pores properties (see review [416]).

FsLB

We use, free-standing lipid bilayer (FsLB), a variant of SLB. They are usually formed at a water/oil interface along support structures within microchannels. The primary advantage over SLB is that the molecule (protein) can interact with both lipid leaflet, insert, or pass through the membrane in case of FsLB. Conventionally, FsLB are constructed in parallel orientation of imaging plane to study the molecules [417], but we were interested in visualizing both the membrane and the molecule. Therefore we created FsLBs perpendicular to the imaging plane based on Yahyazadeh Shourabi et al. [418] (and [419]). The microfluidic chip contains two channels, one for membrane formation, with support pillars and the other for replacing solutions (for detailed chip design see Fig. 4.S7). The positive mould of microfluidic design was fabricated on a silicon wafer, followed by making a negative mould with PDMS. Eventually the device was cast with UV photopolymerized thiolene resin, Norland Optical Adhesive 81 (NOA81)[12]. The organic phase containing lipids was flowed in the main channel, immediately followed by an aqueous solution. Both these solutions consecutively pass over the support pillars, creating lipid monolayers at the water-organic phase interface (Fig. 4.8(a)). The pillars separate the channel into two halves, and the monolayers from the two halves come close together (Fig. 4.8(b).i). The organic phase starts to drain away (Fig. 4.8(b).ii). The monolayers get very close to each other and trap a thin layer of organic phase in between (Fig. 4.8(b).iii). Eventually, the monolayers zip together to form a FsLB (Fig. 4.8(b).iv) in between the pillars. Over time, the organic phase was completely pushed out of the monolayers towards

[12]NOA was used instead of usual PDMS for casting device, since the organic phase like chloroform get absorbed into the PDMS and swell and change microchannel dimensions.

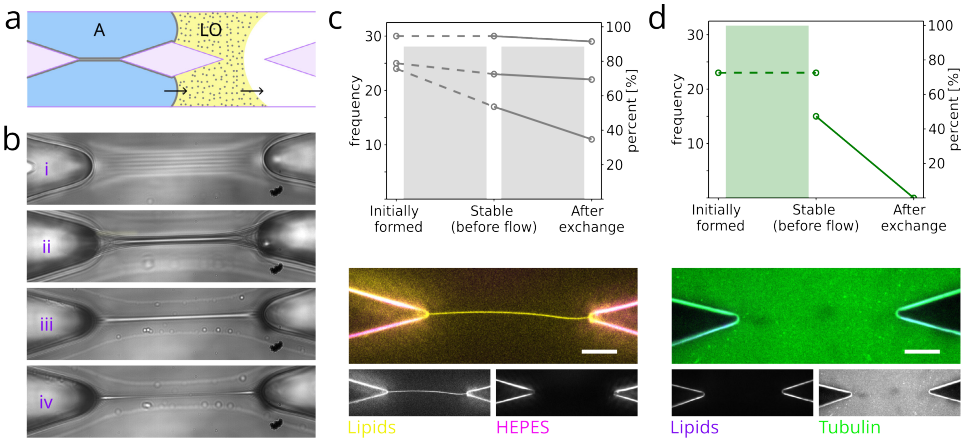

Figure 4.8: **Tubulin destroys the FsLB.** (a) Schematic showing FsLB formation in a microfluidic chip (see Fig. 4.S7). First, the lipid organic (LO) solution flows past pillars. And it is followed by an aqueous (A) solution. The lipid monolayer at the AS and LOS interface coats the pillars. And in-between the pillars, monolayers come in contact with each other after the drainage of organic phase and zip to form a free-standing lipid bilayer (FsLB) membrane. (b) Formation of FsLB, (i) monolayers approaching, (ii) organic phase draining — monolayers about to touch, (iii) monolayers just touched, organic phase trapped (bright signal), and (iv) spontaneous zipping — formation of bilayer, organic phase pushed out towards pillars. Complete removal of organic phase takes some time (∼0.5–2 h). See Fig. 4.S9 for a movie. (c)(d) Membrane survival assay (MSA) with replacement solutions, (c) HEPES buffer and (d) tubulin (20 µM). (top) Number of FsLB — initially formed, stable over time (before AS replacement), and survived (after AS replacement). And as percent (bars), after each stage. (bottom) FsLB in between support pillars in case of (c) HEPES buffer replacement, while only 2 membranes in case of (d) tubulin. NOA81 pillars exhibit auto-fluorescence. (In tubulin MSA, due to a trapped air bubble, only 23 FsLBs were formed and only ∼15 FsLBs were accessible to tubulin after buffer replacement.) Scale bar — 100 µm.

the pillars, FsLB become solvent free (Fig. 4.S9). Once the FsLBs are stabilized, the aqueous solution in the main channel can be exchanged[13] by flowing in protein solution from the exchange channel. The protein diffuse towards the membrane and starts interacting and affecting the membrane.

The FsLB device was tested with a membrane survival assay (MSA). As a control, the membranes with DOPC lipids and HEPES buffer. We observed, 88.61 % of initially formed FsLBs stabilize and survive over time (∼2 h). Solution exchange was performed with just HEPES buffer as a negative control, to test the effect of flow and solution replacement on membrane survival. We observed, 88.57 % of the stabilized FsLBs survive the buffer exchange. We performed similar MSA with tubulin. We tried making membranes with DOPC lipids and MRB80 buffer, but noticed that the absurdly long membranes (∼1000 µm) generated across different parts of

[13] Exchange typically take 170 s at 2.5 µL/s

the main channel. These membranes were super stable over time. Typically, such long membranes should not form at first place, and definitely should rupture due to instabilities and fluctuations in the fluid flow. Given all the previous issues with MRB80, we had expected a low survival rate for initially formed membranes, but on the contrary, MRB80 seems to stabilise the membrane. So we just created membranes with HEPES buffer again[14]. And in HEPES, 100 % of FsLBs stabilize. Now, we replace the HEPES buffer with tubulin in MRB80. Within ∼15–30 min, we see almost all[15] the membranes are lost. 0 % of stabilized FsLBs survive the tubulin replacement. This clearly demonstrate that tubulin destroys the lipid membrane, and is incompatible for vesicle encapsulation.

4.3 Discussion

4.3.1 Tubulin in solution

To get a better understanding of how proteins, specifically tubulin, affect the aqueous solution and eventually the yield of vesicles, we continued studying the physical properties of protein solutions. The contact angle measurement for hydrophobicity did not reveal any major effect, but showed a nominal (slight) trend — hydrophobicity increases with ionic strength of the buffer and with increasing concentrations of proteins. In Chapter 3, we showed that tubulin not only affects bulk properties like viscosity but also surface properties like interfacial tension. Hydrophobicity is also a surface phenomenon (with three surfaces involved), some increase in contact angle was expected. Most proteins have some tendency to populate the water-air or water-oil interface [364]. While the interfacial tension decrease is not that significant with proteins alone, it has been shown for actin that it forms a thin film at the air-water (or oil-water) interfaces [365, 366]. We speculate that a similar phenomenon occurrs in the case of tubulin. Only in the presence of a true amphipathic surfactant molecule like a lipid, the effect of protein adsorption at the interface is amplified (Fig. 3.4(b)), making it behave like a strongly amphipathic protein. This not just prevents formation of pure lipid membranes, but also the drastically reduces the surface tension of tubulin solutions[16]. Furthermore, tubulin is unable to polymerize with the additive like OptiPrep™ used in emulsion transfer-based vesicle formation methods like cDICE and eDICE, as density contrast agent. Critically analysis of the effects of different additives used in different vesicle formation methods (OptiPrep™ in cDICE [277]; glycerol, poloxamer 188 in OLA [301]) on protein function is necessary and caution should be excercised when developing new and improved methods.

4.3.2 Tubulin in vesicles

In the past, simple single filament reconstitution of MTs in vesicles has been accomplished. Most of these reconstitutions were based on swelling and freeze-fusion

[14] Due to a trapped air bubble in a part of the channel, only 23 FsLBs were formed correctly.

[15] Due to a trapped air bubble in a part of the channel, HEPES buffer was not completely replaced from certain parts of the channel and tubulin could only reach ∼15 FsLBs.

[16] Even interfering with pendant drop tensiometry measurements as the surface tension is no longer sufficient to hold the pendant drop at the needle tip (see Ch. 3 Fig. 3.4(b)).

approaches [258–260, 405, 406]. As discussed in the Chapter 2, swelling-based methods are considered not ideal compared to newer emulsion-based methods for complex protein reconstitutions, as the encapsulation efficiency is not very high and protein stoichiometry cannot be maintained. Electroformation [273], despite being considered as the best method for clean vesicle formation, is not suitable for protein encapsulation. Nonetheless, we still gave swelling based methods a try, with gel- and bead-assisted swelling, and did not see enough vesicles and not enough tubulin encapsulated to promote nucleation inside upon increasing temperature. Comparing to previous attempts to tubulin encapsulation, we had different lipid composition, mainly contained neutral DOPC. Up to 30–40 n% negatively charged DOPS was used along with DOPC in case of fusion [259, 405] and swelling-based methods [260]. And also very high concentrations[17] of saturated and charged lipids, DPPG or Cardiolipin (CL) with DPPC or DMPC (1000:1) were used with swelling-based methods [258, 406]. With these experiments, yield of vesicles is not mentioned (as usually described in recent literatures) to compare with our outcome. Observing ∼10–20 vesicles per experiment is not very high throughput or successful. While the effect of lipids type on vesicle formation is expected, not seeing any tubulin polymerization in our experiments is quite surprising.

cDICE and eDICE

With cDICE, we see decrease in the yield of the vesicle even with MRB80 buffer and a further significant decrease upon addition of tubulin. With both cDICE and eDICE, the quality of vesicles is lower. We observed lipid aggregates as well as aggregation of tubulin into unphysiological 3D structures. The quality of vesicle membranes is known to be affected by buffers and proteins. Apart from the previous attempts at simple MT encapsulation in vesicles, some recent work has reported encapsulation of complex tubulin protein mixes using an emulsion transfer based method, cDICE [286, 350, 420]. Keber et al. [350] and Sciortino et al. [420] show deformation of vesicles due to active nematic system of MTs and kinesin. In both cases GMPCPP stabilized[18] MTs were encapsulated, either in Egg-PC [350] or DOPC vesicles [420]. We mostly just used DOPC in our tubulin encapsulations with cDICE. Sciortino et al. [420] has also modified the cDICE protocol by using a larger chamber[19] without further explanation. Gavriljuk et al. [286] show dynamic MT polymerization by encapsulating tubulin with Egg-PC lipids, using original cDICE protocol [271]. While this is the only example of dynamic MT encapsulation[20], the method description regarding cDICE lacks details. Interestingly, no optimization was required for tubulin encapsulation. Also, the values of sucrose-glucose iso-osmotic density gradient in

[17] 10 mM or 50 mg vs 50 µg i.e. $\sim 10^3\times$ more

[18] GMPCPP — slow hydrolysable analogue of GTP; no need for free tubulin monomers

[19] original chamber [271] — diameter 35 mm, height 8 mm vs modified chamber [421] — diameter 70 mm, height 2 mm

[20] [personal communications] Thomas Surrey (Centre for Genomic Regulation, Barcelona, Spain) mentioned, attempts of encapsulating a dynamic MT system in vesicles (using cDICE, in collaboration with Andreas R. Bausch) results in 'dead', inactive system within minutes.

inner and outer buffers do not make sense[21]. This could indicate that successful tubulin encapsulation in vesicles with cDICE needs some optimization, that are not clearly and explicitly described in the literature[22]. More complicated cytoskeletal reconstitution, like Cytostatic-factor-arrested (CSF) Xenopus laevis egg extracts in vesicles using inverted emulsion, is shown [422]. Again, the MTs in the extracts were stabilized with taxol. No demonstration of dynamic frog egg extracts are found in the literature[23].

OLA AND DSGUV

Encapsulation of tubulin in vesicles with OLA seemed promising, as at least tubulin shows signs of rapid polymerization, probably due to the presence of a high concentration of crowding agents. However, the vesicles are not stable, likely due to the tubulin interactions with the lipids.

Tubulin encapsulation in vesicles using dsGUV method distinctly revealed the competition of tubulin against the lipids at the membrane. With both double inlet and pico-injection approach, it is clear that lipids are readily replaced at the droplet interface if and only if tubulin is present in the vesicle. The dsGUV have interesting biochemical environment, the fluorinated oil is neither favourable for hydrophobic lipids nor hydrophilic proteins (tubulin), and yet we see the replaced lipids exchanged into the fluorinated oil. Even at times, some of the tubulin is exchanged. It should be noted that rhodamine-labelled tubulin was used, and rhodamine-dyes are known to interact with Krytox[24] and partition to the oil phase [306]. This presence of lipids and protein in the fluorinated oil cannot be explained, we can only speculate, even though unfavourable, the exchange occurs through not so strong enough surfactant effect of CTS[25]. The lipid composition also affects the outcome, with just neutral and negative not able to form membrane in MRB80 buffer. It would be interesting to test how lipid compositions from the literature like Egg-PC or saturated lipids work in presence of BRB80 buffer and tubulin. The tubulin replacing the lipids at the interface forms a solid shell, a ball of tubulin (Fig. 4.S8). Such protein films at the lipid-air interface have been shown for actin [365, 366]. This can be an example of a tubulin thin-film. What is more interesting is that even with partial tubulin being lost at the interface, we still see signs of tubulin polymerization inside the vesicles. Empirically, it is known that the tubulin encapsulated in water-in-oil droplets requires more than twice the tubulin concentration for polymerization compared to *in vitro* bulk experiments [228, 237, 423]. Some reasons speculated for

[21] while 300 mM sucrose and 80 mM glucose in inner buffer, and 380 mM glucose in outer buffer, make sense in terms of concentration balance, it does not take into account the osmolality change due to high ionic BRB80 (inner) buffer compared to outer aqueous buffer.

[22] [personal communications] Alfredo Sciortino [420] describes the use of less ionic strength buffer like 'Tic-Tac', results in better yield compared to BRB80 buffer. Also, different oxygen scavenging system also affect the yield and protein lifetime. And some of the optimizations are empirical.

[23] [personal communications] Matthew C. Good (University of Pennsylvania, USA) mentioned, attempts of encapsulating whole frog egg extracts in vesicles (using microfluidic double emulsion) results in spontaneous bursting of vesicles.

[24] Rhodamine-6G partitioning assay was used to titrate Krytox concentration in dsGUV protocol.

[25] Other surfactants can be tested to prevent lipid exchange into the oil.

this, include decreased monomer availability in 3D confinement and partial loss of tubulin at the water-oil interface or even in the oil phase[26,27]. It should be noted that both in case of double inlet and pico-injection, the tubulin concentration gets diluted. And in case of pico-injection, with injection of only up to ∼10–25 %v tubulin, the encapsulated tubulin concentration[28] gets diluted, and we still see polymerization in presence of MT seeds. This helps explain some of the previously mentioned droplet encapsulation related issues. So monomer availability is not an issue in 3D confinement, and definitely some of the tubulin is getting lost in the oil phase.

4.3.3 Tubulin-membrane interactions

Finally, the membrane survival assay with tubulin using FsLB, clearly demonstrates the unfavourable tubulin interactions even with pre-formed stable lipid bilayer, that destroys the lipid membrane. We speculate that tubulin forms rings on the lipid bilayer and creates holes in the membrane[29]. Tubulin is surprisingly found attached to the membrane in liver [424], T-cells [425], and neuronal cells [426]. During tubulin purification from brain tissue with the common cold-warm cycling purification protocol, the yield of tubulin is only ∼70 %, with the rest being membrane bound and ∼10 % of it being non-recoverable [427]. This fraction is called as 'plasma membrane tubulin', Wolff [428] (review) summarizes and explains all the possible cases for presence of tubulin at the membrane. Experimentally, tubulin has been shown to have preference towards phase separated lipids domains on DPPC and DOPC membranes [368]. Tubulin has a different preference for different phospholipids [429] and coarse-grained molecular dynamic simulations, reveal preference of tubulin dimer polymerization site towards DOPE over DOPC [369].

This indicates purified native tubulin is fundamentally incompatible with the lipid membrane and destroys it, rupturing the vesicles. Still, given a few successful examples of tubulin encapsulation in vesicles, we suspect the following reason for our failed attempts, which needs to be further tested. We hypothesize that specifically the free tubulin dimers affect the membrane (of specific composition and state), and vesicle formation in the absence of free dimers (with pre-formed stabilized MTs) should therefore be further tested. It should also be noted that, although unlikely, we cannot exclude that commercially purified (lyophilized) tubulin (Cytoskeleton, Inc.), contains an unknown chemical reagent (cryoprotectant) affecting the lipid bilayer.

4.4 Conclusion

Tubulin encapsulation is challenging. A couple of groups have shown successful encapsulation of complex tubulin organization in vesicles [286, 350, 420, 430], with Gavriljuk et al. [286] being the only one with dynamic MTs. Even in giant polymer-lipid hybrid vesicles, with synthetic membranes, tubulin hardly polymerizes [431].

[26] Detection of proteins, especially at low concentrations, in oil is challenging.

[27] [personal communications] Thomas Surrey (Centre for Genomic Regulation, Barcelona, Spain) also discussed possibilities of tubulin adsorption at the oil-water interface and exchange in oil due the hydrophobic patches on tubulin dimer, and also due to high hydrophobicity of the commonly used dye for tubulin labelling — TAMRA/Rhodamine.

[28] 40 µM tubulin ∼4–5 x diluted to ∼8–10 µM

[29] Based on very preliminary AFM results of tubulin interactions with SLB (not shown).

A single vesicle production ideally produces millions of vesicles, if not, a few thousands survive eventually, but with tubulin, barely a few tens of vesicles are reported. In cells, tubulin interaction with the membrane is potentially regulated by MAPs. Tubulin concentration is also tightly regulated throughout the cell cycle, possibly to minimize free tubulin in the cytoplasm and its interaction with other proteins and lipid membrane. As opposed to high concentrations used *in vitro* reconstitutions to overcome nucleation and polymerization barrier. Stathmin is one such potential MAP, it negatively regulates MT-dynamics by sequestering tubulin [432], and has been shown to regulate spindle during mitosis [433]. Each molecule of stathmin can bind to two tubulin heterodimers forming a trimeric T_2S-complex [434, 435], effectively reducing the free dimers avialable in the cytoplasm for polymerization[30]. Interestingly, the only example of a complex dynamic tubulin encapsulation also involved a stathmin-based MT-regulator gradient [286]. It would be interesting to attempt to encapsulate in-house purified tubulin using cDICE, ideally unlabeled (or visualized with a less-hydrophobic dye, other than rhodamine), in order to replicate the previously reported old conditions used in case of simple swelling-based tubulin encapsulations [258–260, 405, 406], and try lipid compositions with membrane-mimicking egg-PC or saturated lipids (e.g. DPPC). And another approach can be to increase the complexity of tubulin encapsulation, to minimize the membrane interaction, such as by assembling an actin cortex.

4.5 Material and Methods

4.5.1 Materials

CHEMICALS See Sec. 2.6 for a detailed list of chemicals. Chemicals were purchased from Merck (Merck Life Science), unless otherwise stated: Guanosine 5'-triphosphate sodium salt hydrate (GTP, G8877 Sigma), Potassium chloride (KCl, P9333 Sigma), Guanosine-5'-[(α,β)-methyleno]triphosphate, Sodium salt (GMPCPP, NU-405 Jena Bioscience GmbH), PLL(20)-g[3.5]-PEG(2)/PEG(3.4)-biotin(20 %) (PLL-PEG-biotin Susos AG), PLL(20)-g[3.5]-PEG(2)/PEG(3.5)-RGD (PLL-PEG Susos AG), NeutrAvidin®(Neutravidin, A2666 Invitrogen™, Thermo), Poly(ethylene glycol) (PEG-6000, 81255 Sigma), Poly(ethylene glycol) (PEG-35 000, 94646 Sigma), Paclitaxel (Taxol, T7402 Sigma), 4-(2-Hydroxyethyl)piperazine-1-ethanesulfonic acid, N-(2-Hydroxyethyl)piperazine-N'-(2-ethanesulfonic acid) (HEPES, H3375 Sigma) .

LIPIDS See Sec. 2.6 for a detailed list of lipids. All lipids were purchased from Avanti Research (Merck Life Science): N-(4-carboxybenzyl)-N,N-dimethyl-2,3-bis(oleoyloxy)propan-1-aminium (DOBAQ, 850310C), Egg PC (840051C), 1,2-di-(9Z-octadecenoyl)-sn-glycero-3-phospho-(1'racglycerol) (sodium salt) (DOPG, 840475C) .

[30] Stathmin, a oncoprotein 18 (OP18) class of protein, can be phosphorylated on up to 4 residues (pStathmin) upon extermal stimuli, which inactivates its inhibitory effect, allowing for tubulin polymerization.

BUFFERS AND PROTEINS See Sec. 2.6 for more details about buffers. And Sec. 2.6 for more details related to protein purification.

HEPES buffer was composed of 10 mM HEPES (pH 7.4 adjusted with KOH solution), 150 mM KCl, and 0.5 mg mL^{-1} BSA. Buffer was filter sterilized (Whatman™ 0.2 µm) and stored at 4 °C.

All lyophilized porcine brain tubulin was purchased from Cytoskeleton Inc. (Tebu-Bio): Tubulin (>99 % pure) (tubulin, T240), Tubulin (rhodamine) (TL590M), Tubulin (HiLyte 647) (TL670M), Tubulin (HiLyte 488) (TL488M), Tubulin (biotin) (TL333P) . Tubulin was resuspended in MRB80, aliquoted, snap-frozen and stored at −80 °C.

All protein mixes were made on ice (4 °C), unless otherwise stated.

EB3 — mCherry-EB3 [436] was purified in-house from *E. coli*, and was a kind gift from Michel Steinmetz (Laboratory of Molecular Research, Paul Scherrer Institute, Switzerland) and Anna Akhmanova (Department of Biology, Utrecht University, the Netherlands).

Centrosomes — Centrosomes were isolated from human lymphoblastic KE37 cells using sucrose density gradient method [234, 437]. See Sec. 5.4 for more details.

bTubAB — *Prosthecobacter dejongeii* bacterial tubulins A and B (bTubA and bTubB) were co-expressed and purified as described in Díaz-Celis et al. [438] except that vectors were overexpressed in OverExpress C41(DE3) Chemical Component Cells (Immunosource). See [439, §2] for more details.

4.5.2 Methods

Contact angle measurement

The contact angle measurements were performed using a drop shape analyser (DSA30S Kruss, Germany) and analysed with Dropen (v3, MATLAB) software [440]. A 7.2 µL droplet of aqueous solution was dropped on a silicon wafer using an automated dosing system from a hanging glass syringe with needle diameter of 1 mm (Hamilton). The image was acquired after the drop has fallen and equilibrated on the surface (∼5 s).

Microtubule dynamics assay

Microtubule dynamics assay was performed based on protocol described in [441]. GMPCPP-stablized MT seeds (70 % tubulin, 18 % biotin-tubulin, and 12 % 647-tubulin or 488-tubulin) were prepared based on the protocol described in [442].

Dynamics mix — A 20 µL protein mix of 0.5 mg mL^{-1} κ-casein, 50 mM KCl, 1 mM GTP, 1 x OX, 30 µM tubulin (10 % rhodamine-tubulin), and 50 mM glucose was made in MRB80. cDICE IA solution mix — A 40 µL protein mix of 1 mM Trolox, 0.1 mg mL^{-1} κ-casein, 50 mM KCl, 3 mM GTP, 1 x OX, 40 µM tubulin (2.5 % labelled), 18.5 %w/v OptiPrep™, and 50 mM glucose was made in MRB80. Both mixes were centrifuged in an air driven ultracentrifuge (Airfuge®, Beckman) with fixed angle rotor (A-100/18) at 30 psig for 5 min.

The flow chambers were assembled and functionalized with sequential 10 min incubations of 0.2 mg mL^{-1} PLL-PEG-biotin, 0.5 mg mL^{-1} Neutravidin, and 0.5 mg mL^{-1}

κ-casein. MT seeds (~100–300 x diluted) were attached via biotin-Neutravidin interactions with 10 min incubation. The protein mixes were added to the flow chambers and the flow chambers were sealed with vacuum grease. MTs were imaged immediately in TIRF mode at 30 °C.

Swelling

PROTEIN MIX Bead swelling — A 20 µL protein mix of 1 mM Trolox, 0.5 mg mL^{-1} κ-casein, 50 mM KCl, 3 mM GTP, 1 x OX, 40 µM tubulin (2.5 % labelled), 200 x diluted MT seeds, and 50 mM glucose was made in MRB80.

Gel swelling — A 20 µL protein mix of 1 mM Trolox, 0.5 mg mL^{-1} κ-casein, 50 mM KCl, 3 mM GTP, 1 x OX, 50 µM tubulin (2 % labelled), 7.5 %v/v glycerol, and 50 mM glucose was made in MRB80.

LIPID SUBSTRATE Lipid-coated beads and lipid-coated coverslips were made as described in Sec. 2.6.

FORMATION Both bead-based and gel-based swelled GUVs were formed as described in Sec. 2.6. The samples were heated to 34 °C to induce tubulin polymerization.

cDICE and eDICE

PROTEIN MIX Effect of proteins — A 40 µL protein mix of 1 mM Trolox, 0.5 mg mL^{-1} κ-casein, 50 mM KCl, 1 x OX, 1 µM SspB-mCh, 18.5 %w/v OptiPrep™, and 50 mM glucose was made in MRB80. A 20 µL protein mix of 1 mM Trolox, 0.5 mg mL^{-1} κ-casein, 50 mM KCl, 3 mM GTP, 1 x OX, 35 µM tubulin (1.5 % labelled), 18.5 %w/v OptiPrep™, and 50 mM glucose was made in MRB80 (default tubulin mix).

Tubulin polymerization troubleshooting — Various similar tubulin protein mixes (as described above) were made while troubleshooting tubulin polymerization in GUVs made with cDICE and eDICE. The changes in protein mix composition are described in Tab. 4.S1.

Bacterial tubulin — A 40 µL protein mix of 1 mM Trolox, 1 mg mL^{-1} κ-casein, 50 mM KCl, 1 x OX, 2.5 µM GTP, 6.6 µM bTubAB (10 % labelled), 18.5 %w/v OptiPrep™, and 50 mM glucose was made in MRB80.

LO DISPERSION LO dispersion were made as described in Sec. 2.6. **Tubulin polymerization troubleshooting mixes** — Various similar LO dispersion were made while troubleshooting tubulin polymerization in GUVs made with cDICE and eDICE. The changes in lipid composition are described in Tab. 4.S1.

Bacterial tubulin mix — LO dispersion of 50.775 n% DOPC, 11.5 n% DOPG, 35.6 n% DOPE, 2.1 n% Cardiolipin, and 0.025 n% Cy5-PE was made as described in Sec. 2.6.

FORMATION cDICE and eDICE -based GUVs were formed as described in Sec. 2.6. The samples were heated to 22–34 °C to induce tubulin polymerization.

OLA

PROTEIN MIX A 80 µL mix (IA) of 0.5 mg mL^{-1} κ-casein, 1 x OX, 3 mM GTP, 40 µM tubulin (5 % labelled), 160 x diluted MT seeds, 15 % glycerol, 5 mM dextran (6000 MW) and 50 mM glucose (added at last) was made in MRB80 (5 x).

LIPID-OCTANOL SOLUTION LO solution was made as described in Sec. 2.6.
FORMATION GUVs were formed as described in Sec. 2.6.

dsGUV

PROTEIN MIX A 90–150 µL protein mix of 0.5 mg mL^{-1} κ-casein, 1 x OX, 1 %v/v PEG-6000, 3 mM GTP (2 mM GTP and 1 mM GMPCPP for overnight dsGUVs), 40 µM tubulin (5 % labelled), 90 x diluted MT seeds, and 50 mM glucose was made in MRB80.
SO DISPERSION SO and LA (SUVs containing) solutions were made as described in Sec. 2.6. LA solutions with SUVs of different lipid composition were made while troubleshooting tubulin polymerization in dsGUVs. The changes in lipid composition are described in Tab. 4.3.

Name	Composition [n%]
Neutral	100% DOPC
Neutral (w/ PEG)	96% DOPC, 4% PEG2000-PE
Negative	96% DOPS, 4% PEG2000-PE
Charged	66% DOPC, 30% DOPS, 4% PEG2000-PE
pH-sensitive	40% DOPC, 30% DOBAQ, 20% DOPS, 6% DOPE, 4% PEG2000-PE

Table 4.3: **Lipid composition for dsGUV.** All lipid mixes contain additional 0.5 n% Atto488-DOPE (adjusted in DOPC n%) for visualization.

FORMATION dsGUVs and GUVs were formed as described in Sec. 2.6. Samples made for releasing GUVs from dsGUVs were incubated on rollers in the cold room (overnight) and later released using PFO solution. Some samples were heated for 37 °C, 5 min to induce tubulin polymerization.
PICO-INJECTION dsGUVs were formed as described above and in Sec. 2.6. Pico-injection was performed as described in Sec. 2.6.

FsLB

AQUEOUS PHASE **Formation** — HEPES buffer.

Replacement — A 200 µL mix of 0.5 mg mL^{-1} κ-casein, and 20 µM tubulin (5 % labelled) was made in MRB80.
ORGANIC PHASE Lipid mix (10 mg mL^{-1}, ∼100 µL) of 99.975 n% DOPC, and 0.025 n% Cy5-PE was made in chloroform.
FORMATION FsLBs were formed based on the protocol described in [418, 419, 443]. The microfluidic device was connected to the two syringe pumps (NE-300 ProSense) with tubing. The tubing was held in placed on device inlets with a custom holder. The custom holder consisted of two acrylic strips, sandwiching the FsLB device with silicon spacers, held together with nuts and bolts. The first syringe (S1) was filled with HEPES buffer, and lipid solution was injected at the tip of the tubing just before connecting to the device. The other syringe (S2) was filled with MRB80 buffer,

and replacement (tubulin) mix was pulled from the tip of the tubing just before connecting to the device. First, S2 solution was flown (4.5 µL min^{-1}) until it reached the opening of the connecting (resistance) channel (Fig. 4.S7), then the flow was stopped. Then S1 solution was flown (9.5 µL min^{-1}) until it reached the pillars in the membrane channel, then S1 (4.5 µL min^{-1}) and S2 (0.5 µL min^{-1}) flows were reduced until all the chloroform was flushed out. Both S1 and S2 flows were stopped. Membranes were allowed to stabilize for 2 h. Then HEPES from the membrane channel was replaced with protein (tubulin) mix by flowing S2 (0.2 µL min^{-1}, ∼30 min or 2.5 µL s^{-1}, ∼3 min). During the beginning of replacement, the outlet of the replacement channel was sealed with a UV glue (7004631 Bison). Within ∼30 min, the replaced reagents diffuse towards the membrane and start interacting.

The master chip mould was made with SU-8 on a silicon wafer (as described in [418, 443]). Minor PDMS (negative mould) was made with PDMS (as described in Sec. 2.6). The PDMS mould was silanized with Trichloro(1H,1H,2H,2H-perfluorooctyl)silane (448931 Sigma) (2 h, under vacuum). The microfluidic FsLB device was made by casting optical glue (NOA81 Norland) on to the PDMS mould and topping it with a glass slide. The cast was cured by UV exposure (UVL-36 Promed, 4 x 9 W) for 5 min. Later the PDMS mould was removed, and inlet/outlets were drilled. The FsLB device was closed with a coverslip (with NOA81 spin-coated, and partially cured for 60 s). Finally, NOA81 in FsLB device was completely cured by UV exposure for 10 min and baking at 85 °C for 8 h on a hot plate.

Samples were observed on a light microscope (AE31E Motic).

4.6 Acknowledgements

We thank Eli van der Sluis for purifying proteins. We thank Roland Kieffer and Nils Klughammer for information regarding contact angle measurements. We thank the following people for discussions regarding troubleshooting tubulin encapsulation — Christophe Danelon and Elisa Godino (Bead swelling); Gijsje Koenderink, Lucia Baldauf, Lennard van Buren, Iris Lambert and Renu Maan (cDICE). We thank Martina Iacona for help with making the FsLB devices and control MSA data.

4.7 Supplementary Information

4.7.1 Supplementary Figures

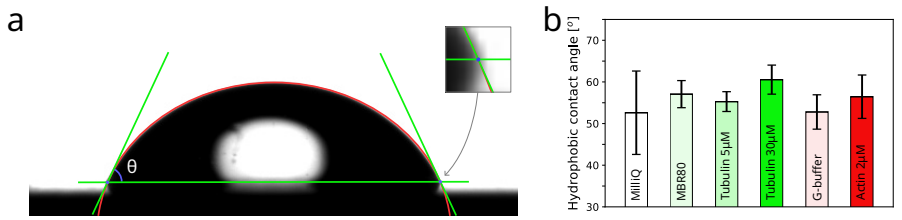

Figure 4.S1: **Hydrophobicity of aqueous solutions.** (a) Contact angle θ determination of fluid drop (tubulin 30 μM in MRB80) in contact with a silicon wafer using Dropen (v3) [444]. Zoom insert, showing manually determined contact point. (b) Hydrophobic angle measurements for different buffers — MRB80 and G-buffer, protein solutions — tubulin (5 μM and 30 μM) and actin (2 μM), along with water (milliQ) using contact drop method.

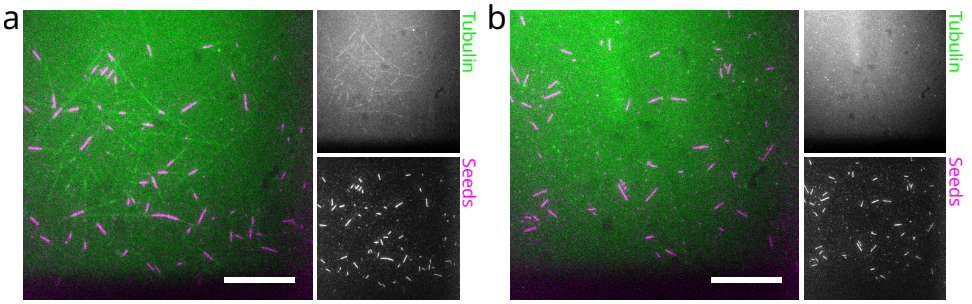

Figure 4.S2: **OptiPrep inhibits MT dynamics.** *In vitro* microtubule dynamics assay with, (a) dynamics mix (tubulin 30 μM) and (b) cDICE IAS mix (tubulin 40 μM with 18.5 %v/v OptiPrep™). Microtubules grow from the seeds in dynamics mix, while tubulin does not polymerize in presence of OptiPrep. Scale bar — 20 μm.

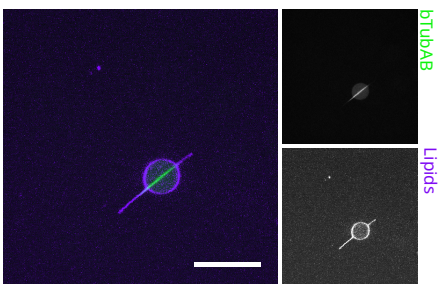

Figure 4.S3: **Bacterial tubulin polymerization in GUVs.** Bacterial tubulin encapsulation with cDICE, polymerizes with bTubAB (10 μM), GTP (2.5 mM), and OptiPrep™ (18.5 %v/v) in MRB80. Filaments deform the GUVs. Scale bar — 20 μm.

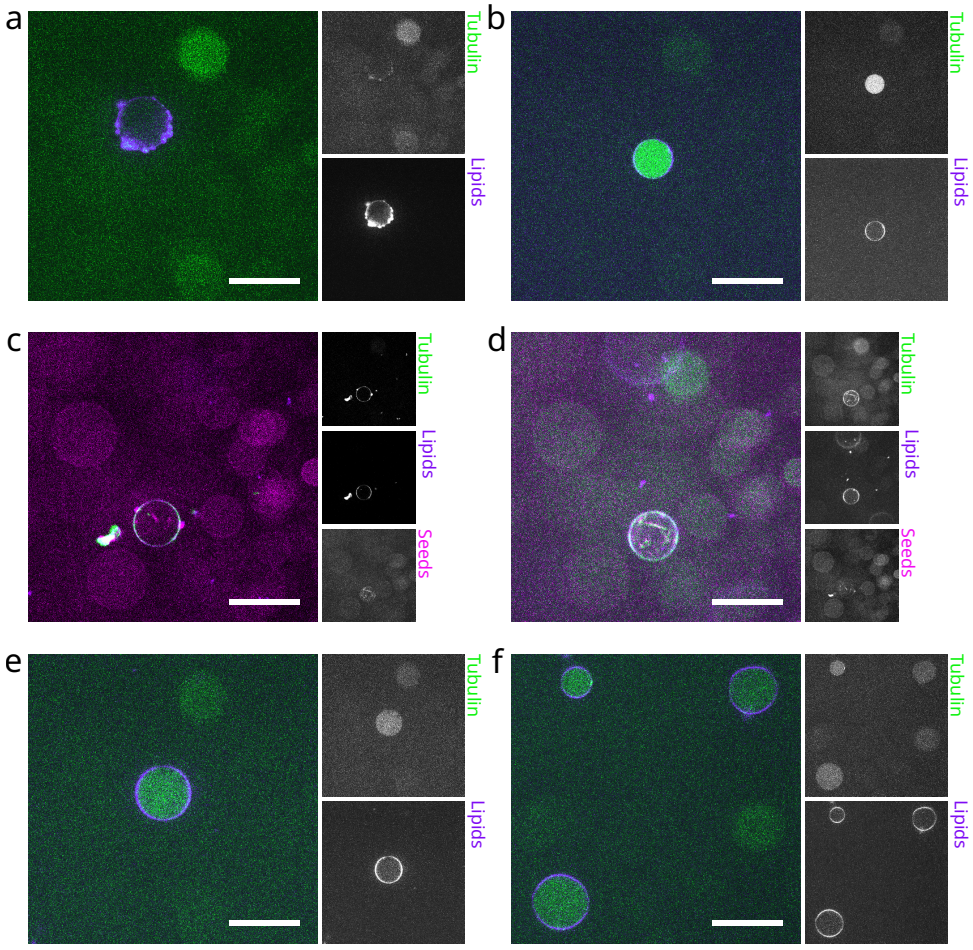

Figure 4.S4: **No tubulin polymerization in GUVs.** Tubulin encapsulation with cDICE showing no polymerization even in presence of following reagents, known for aiding polymerization, (a) Taxol (20 µM), with tubulin (50 µM) and Sucrose (1.75 %w/v) (b) Centrosomes (10 %v/v), with tubulin (40 µM) and Sucrose (1.75 %w/v) (c) Taxol (100 µM), with tubulin (40 µM), MT seeds, and OptiPrep™ (18.5 %v/v) (d) GMPCPP (1 mM), with tubulin (40 µM), MT seeds, and OptiPrep™ (18.5 %v/v) (e) PEG 6000 (1.5 %w/v), with tubulin (35 µM), MT seeds, and OptiPrep™ (18.5 %v/v) (f) PEG 35000 (1 %w/v), with tubulin (35 µM), MT seeds, and OptiPrep™ (18.5 %v/v). Images shown are representative of GUVs with various different tubulin artefacts. GUV yield was very low. Scale bar — 20 µm.

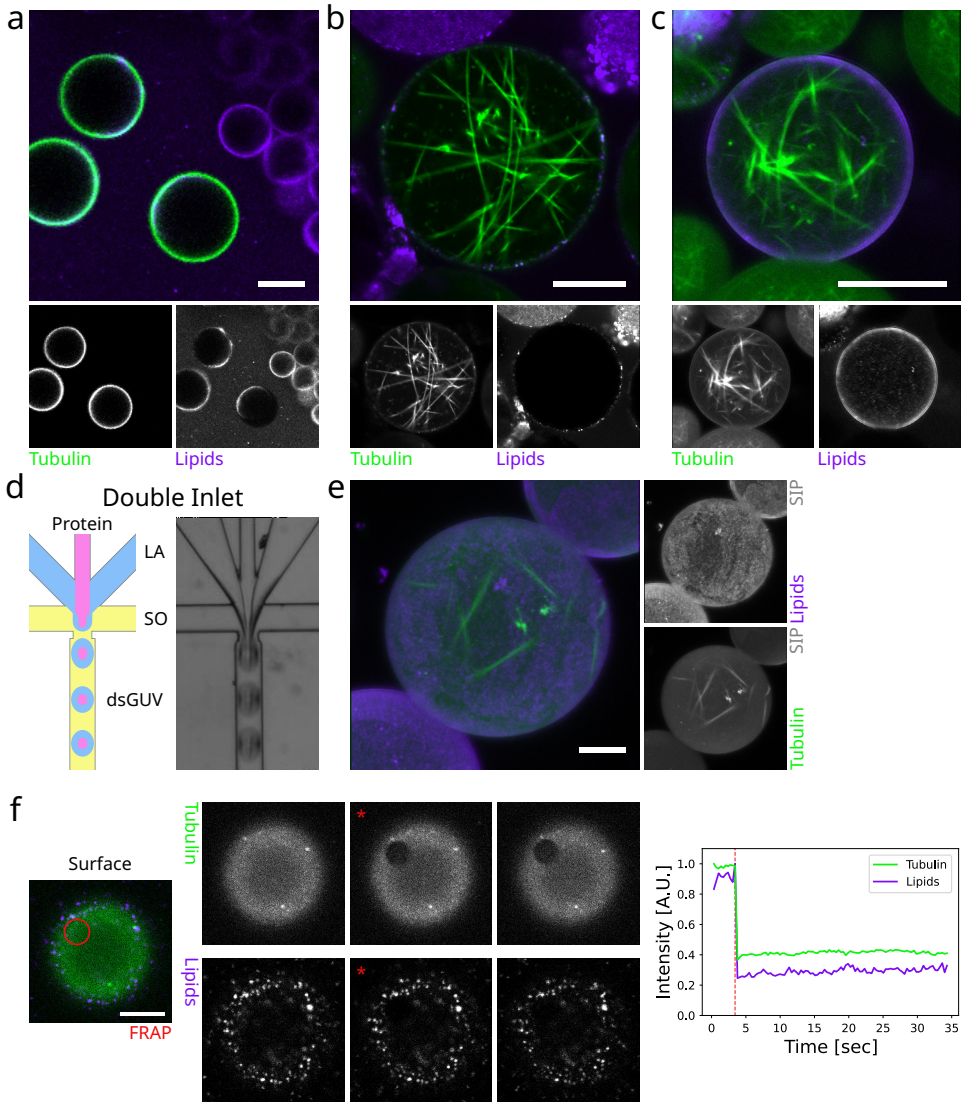

Figure 4.S5: **Tubulin encapsulation with dsGUV — double inlet approach.** dsGUVs are formed with tubulin (40 µM, with MT seeds) and different lipids using dsGUV method (with double inlet microfluidic chip). (a) dsGUVs with negative lipids just after formation. Tubulin already at the cortex and incomplete lipid coverage. (b) A dsGUV with neutral (w/ PEG) lipids after 5 min incubation at 37 °C. MT polymerization is seen inside dsGUV. Lipid coverage is not optimal. (c) A dsGUV with charged lipids after 5 min incubation at 37 °C. MT polymerization is seen inside dsGUV. Lipid coverage is optimal. (d) 6-way junction from a double inlet microfluidic chip. Protein solution is sheathed by lipid aqueous (LA) solution before it gets encapsulated by surfactant oil (SO) solution to form dsGUV droplets, as shown in (left) schematic and (right) bright field image. (e) Standard-deviation Intensity Z-Projection (SIP) of a dsGUV (tubulin with GMPCPP 1 mM) after overnight (O/N) incubation and later 5 min at 37 °C, showing few MT bundles and tubulin and lipid at the dsGUV cortex. (f) FRAP analysis of a surface of a GUV are released from dsGUVs (with pH-sensitive lipids, O/N, Fig. 4.6(d)) using PFO solution. The surface shows a tubulin cortex decorated in lipid aggregates, none recovers after photobleaching. Scale bar — 20 µm.

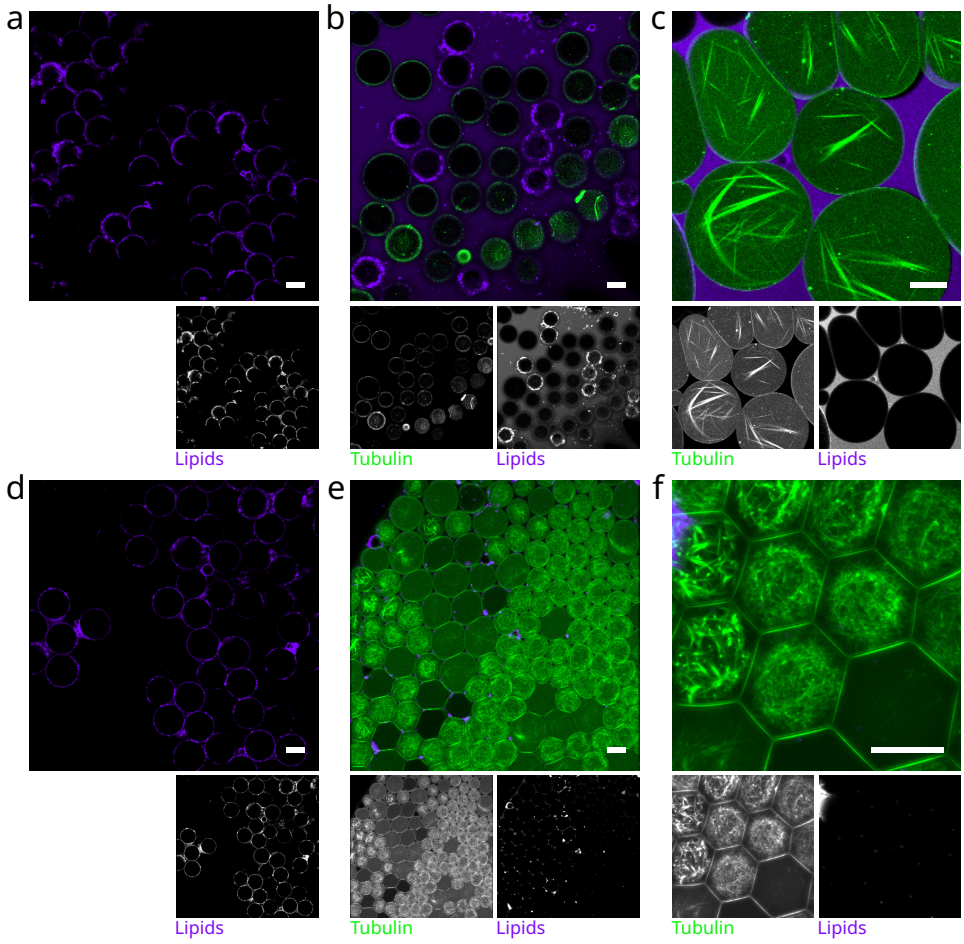

Figure 4.S6: **dsGUVs and tubulin encapsulation with pico-injection.** dsGUVs are formed with (a)(b)(c) charged and (d)(e)(f) pH-sensitive lipids. Tubulin (40 µM, with MT seeds) is inserted into the dsGUVs using pico-injection. (a) dsGUVs just after formation. Lipid coverage is not optimal. (b) dsGUVs just after the pico-injection of tubulin. Very few dsGUVs with tubulin in lumen and MT polymerization. Tubulin and lipid at the dsGUV cortex are mutually exclusive. In addition, background (SOS) shows presence of lipid signal. (c) dsGUVs showing MT polymerization inside and no lipids present at the cortex, instead, transferring from IAS to SOS. (d) dsGUVs just after formation. (e) dsGUVs just after the pico-injection of tubulin. Many dsGUVs with tubulin in lumen and MT polymerization. Almost no lipid coverage. (f) dsGUVs showing some MT polymerization inside, but mostly aggregated bundles and no lipids present at the cortex. Scale bar — 20 µm.

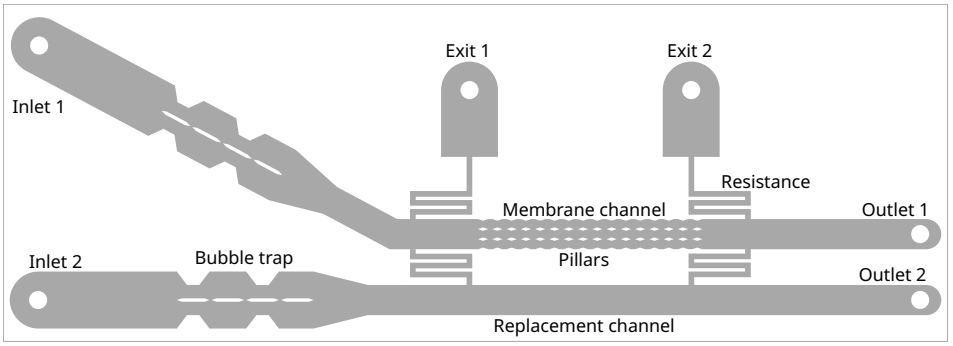

Figure 4.S7: **Microfluidic chip design for FsLB formation.** Detailed scaled design for free-standing lipid bilayer (FsLB) membrane formation ([418]). Two primary channels for membranes and replacement solution, with inlet, bubble trap, and outlet. Membrane channel has two rows of 16 pillars each (alternatively spaced 75 µm and 120 µm apart) providing support contacts for possible 30 independent FsLBs in total. The replacement channel connects the membrane channel before and after with a serpentine, flow dampening resistance channels. On the other side, the membrane channel has two exits, also connected with resistance channels, mirroring the replacement channel entry and exit points, for stabilizing the fluid flow pressure during replacement if required.

4.7.2 Supplementary Tables

Tubulin [µM]	Other	GUV yield	Tubulin polymerization
	18.5 %v/v OptiPrep™		
SspB	-	High	-
40	-	Ok	few aggregates
35	0.002% PEG-2000 DOPE	Low	few aggregates
35	1% PEG-2000 DOPE	Ok (lipid aggregates)	many aggregates
30 seeds	1.5 %w/v PEG-6000	Low	-
30 seeds	1 %v/v PEG-35000	Low	-
40 seeds	30% DOPS	Ok	-
40	1 mM GMPCPP	Ok	few aggregates
40 seeds	1 mM GMPCPP	Ok	few MTs, aggregates, at cortex
40 seeds	20 µM Taxol	Ok	few aggregates, at cortex
40	10 %v/v Centrosomes, 30%DOPS	Ok (lipid aggregates)	at cortex
44	10 %v/v Centrosomes	Ok	few aggregates, at cortex
	1.75 %w/v Sucrose		
SspB	-	High	-
40	-	Ok	-
105	200 nM EB3	Ok	-
105	20 µM Taxol	Low (lipid aggregates)	-
40	10 %v/v Centrosomes	Ok	-
5	1 mM GMPCPP, EggPC	Low (lipid aggregates)	few aggregates
5	1 mM GMPCPP	Low	many aggregates

Table 4.S1: **Tubulin encapsulation conditions with cDICE.** Some interesting conditions tried for GUV formation during optimization of tubulin encapsulation with cDICE (in comparison with SspB (0.5–2 µM) encapsulation for reference). Conditions mentioned here are deviation from the default conditions mentioned in the methods section. The GUV yield and tubulin polymerisation are general interpretation, as experimental outcomes had some variations.

4.7.3 Supplementary Movies

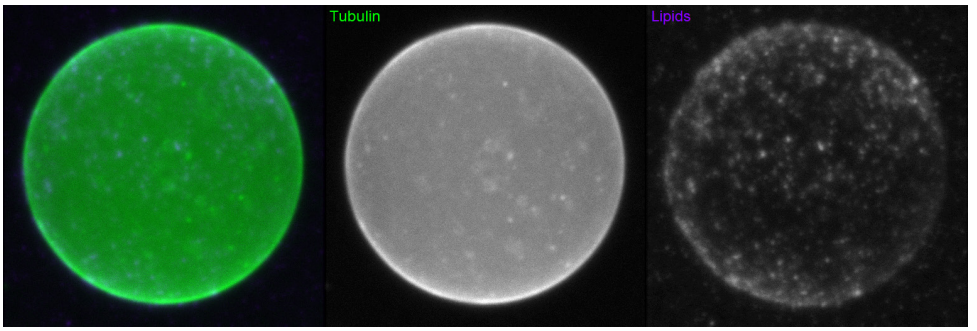

Figure 4.S8: **Tubulin shell.** GUV (Fig. 4.6(f)) released from dsGUV shows a shell made of tubulin, decorated with lipid aggregates. Images are 3D projected. [ ]

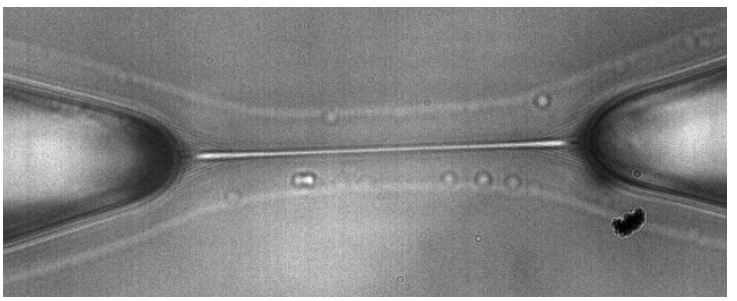

Figure 4.S9: **FsLB formation.** Formation of FsLB between two pillars (Fig. 4.8(b)). [reduced, low-res]

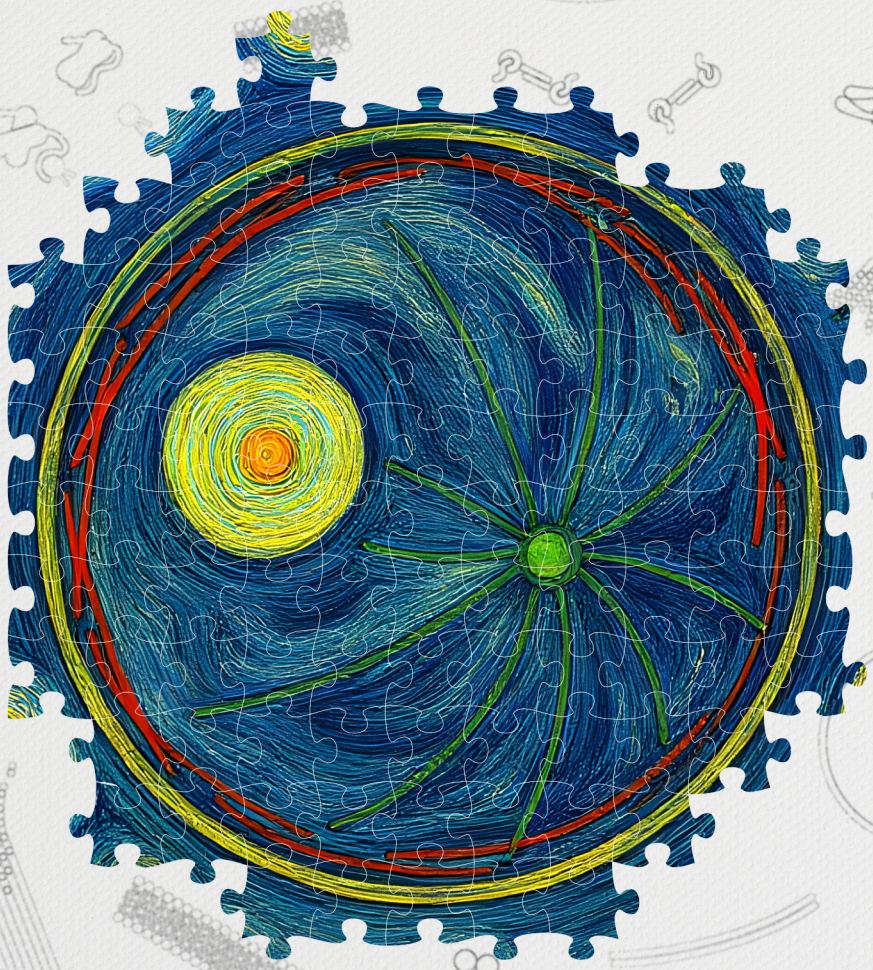

Minimal aster positioning in droplets

One step at a time.
Layer upon layer.

The beauty of the cell lies in its complexity. But that also makes it challenging to study. Hence, individual cellular processes or proteins are investigated in isolation within the cell or outside the cell. In vitro reconstitutions involve interactions of a few proteins in a limited pseudo or bulk 3D geometry. And 3D cell-like reconstitutions are limited to a couple of proteins at max, involved in only one cellular process. Bottom-up approaches need to increase the complexity of reconstitution while maintaining a minimal system to gain a better understanding of cellular functioning. We, therefore, build up the complexity by incorporating an increasing number of components from across different cellular processes. Here, in this chapter, we managed to combine major cellular components like microtubule asters and actin cortex, and microtubule asters and nucleus (mimic). We also discuss options for external and orthogonal tools to mimic complex cellular networks and gain precise control over the reconstituted system.

This chapter includes experiments with bead and aster positioning, performed by Gaspard Waage (under supervision of Yash Jawale), and experiments with actin cortex and aster positioning, performed with Marcos Arribas Perez (Gijsje Koenderink lab, TUD, Netherlands).

5.1 Introduction

Cells are made up of many different components that work together to sustain life. Dissecting the cell, we quickly find some of the largest components, like the cytoskeletal microtubule network present across the cell, the actin network predominantly present at the cell cortex, the nucleus generally occupying the cell centre, and then some smaller yet many, fragmented components, like endoplasmic reticulum, and cargo vesicles spread across the cell. These components are regulated and coordinated to ensure proper functioning of the cell. The cytoskeleton plays an important role in many cellular processes like cell shape regulation, development and polarity establishment, intracellular transport, fertilization, cell migration, and cell division (Fig. 5.1).

In these processes, actin and microtubule crosstalk is important, MT tips act as nucleation points for actin and also guide actin filaments, while actin network provides support for MTs (review [127]). Forces generated by MT pushing and pulling, actin flows, and actin-MT interactions are responsible for controlling the position of centrosomes (review [445]). Actin is responsible for asymmetrical positioning of spindle in oocytes (review [446]) and embryos. Microtubules control the nuclear and pro-nuclear positioning in oocytes and embryos (review [166]), and help position the spindle at the cell centre (reviews [189, 447]). The cytoplasm with its viscoelasticity properties due to macromolecular crowding ensure a proper maintenance of spindle positioning (review [448]). Regulation of MTs by MAPs and a force balance between the pushing and pulling MTs is required for a proper spindle assembly and segregation (reviews [449, 450]). In order to build a functional synthetic cell, we

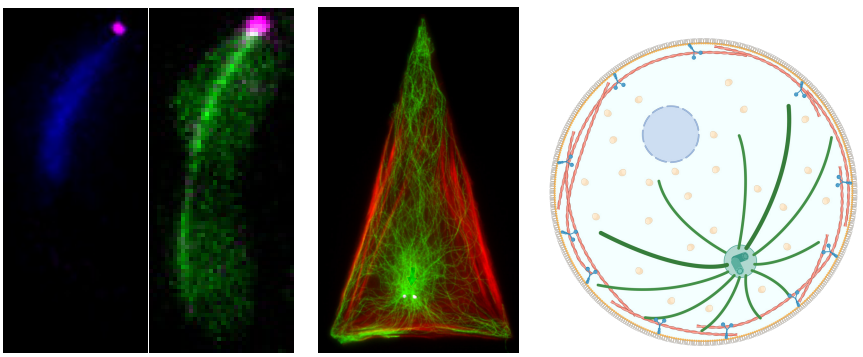

Figure 5.1: **Cytoskeleton in cellular processes.** (left) Nucleus (H2B) attached to spindle pole body (Sfi1) exhibiting horsetail oscillations due to dynamic MTs (α2-tubulin) pulled by polar cortical dynein (Dhc1), during meiosis (prophase) in *Schizosaccharomyces pombe* zygote. Movies adapted from [451] and [452] respectively. [ ] (middle) Centrosome (anti-γ-tubulin; 2 dots) is positioned off-centred by MT aster (anti-tubulin) in actin-inner zone (Phalloidin) of mouse embryonic fibroblasts (p150-glued dominant-negative) cytoplasts (i.e. enucleated cells). Image adapted from [453]. (right) Schematic representation of building complexity for aster positioning in W/O droplet (lipids), in presence of other components like nucleus (bead), actin cortex, motors (dynein), and cargo vesicles. (Image created with BioRender.com)

need to identify and understand its components. *In vivo* experiments provide a qualitative overview of individual components and bulk or single molecule *in vitro* experiments provide a quantitative perspective, but no clear understanding of a process at cellular level is obtained. More complex *in vitro* reconstitutions of these processes with minimal system in 3D cell-like confinements help to provide a complete picture. Higher order cytoskeletal organization, such as asters assembly and positioning, has been demonstrated in water-in-oil droplets, by encapsulating tubulin with MAPs centrosomes or crosslinking motor proteins like kinesin (review [454]). Most of these studies use MT and cross-linking motor protein, kinesin, to assemble acentrosomal asters [237, 238] or centrosomes with tubulin to assembly centrosomal asters and dynein at the cortex, to position the asters in the W/O droplets [235, 455]. Simple cytoskeletal crosstalk and co-organization has also been reconstituted in W/O droplets, by co-encapsulating tubulin and actin filaments [239].

In vitro reconstitutions are tricky, re-encapsulating proteins purified from cells into a minimal 3D container has its challenges. Attempts of the cytoskeleton encapsulation in droplets up until now are limited to two major cytoskeletal components at a time — MTs and kinesin, MTs and dynein, and MTs and actin filaments. Complexity of the encapsulation increases non-linearly with addition of extra new components. Here, we establish a minimal assay to reconstitute basic cytoskeletal systems within droplets. We extend this system by introducing two additional components (Fig. 5.1): a nucleus-mimicking bead and an actin-cortex. The bead represents a nucleus by occupying physical volume within the droplet, while the actin cortex is assembled using branched nucleators and crosslinkers. This allows us to study aster positioning in the presence of a nucleus-like object, mimicking cellular processes such as nuclear and pro-nuclear positioning, as well as polarization. The subsequent addition of an actin cortex makes the assay more cell-like and enables exploration of further processes like cell migration. Altogether, these assays provide a foundation for studying more complex cytoskeletal processes in a controlled environment, independent of cellular redundancies.

Orthogonal control over complexity

Although working with minimal *in vitro* reconstitutions simplifies the interactions to observe and account for, it also limits the degree of complexity that can be achieved. Cells have a redundant network of up- and down- stream pathways to regulate proteins in a complex spatio-temporal manner. Reconstituting even a single pathway needs addition of multiple extra proteins. Non-biological alternatives can be used to substitute these pathways. Chemical induced dimerization (CID) systems[1] were discovered and developed (see reviews [456, 457]) to target membrane oligomerisation, organelles targetting, and gene expression regulation. Another widely used way to control biological systems is with light. Many small chemical molecules[2], like nucleotides and secondary messengers have been modified, mostly caged (trigger release or activate upon illumination), to create rapid global or precise local con-

[1] FKBP — FRB, DHFR — MTX, ABA — PYL1 & ABI1, GA_3 — GAI & GID1

[2] ATP, GTP, cAMP, cGMP; Ca_{2+}, IP_3

centration changes with temporal control [458]. Recent development has extended caging other molecules[3] like peptides, enzymes, mRNA and DNA, and neurotransmitters (see review [459]). These systems often have limitations, such as limited spatio-temporal control, irreversibility and limited exchange with environment.

Optogenetics enables better spatio-temporal control as it is protein based (i.e. genetically encoded, close system) and are fast and reversible. Optogenetic tools are being used in vivo to regulate cellular pathways (see reviews [460, 461]) like gene transcription, cell motility, organelle positioning, and GTPase signaling. Various cytoskeleton related optogenetic tools have also been developed to regulate microtubule growth, severing, plus-end disassembly, crosslinking with F-actin, and modify PTMs (see review [462]). Optogentic tools also have wide applicability in synthetic cell research, as they provide fast and precise control in encapsulated systems too. Only external light is required to trigger the system. Many types of ontogenetic switches[4] are identified and engineered to perform diverse actions[5] and respond to a wide spectrum of light[6]. Optobase[7] is a comprehensive online database that provides overview and latest trends of molecular optogentic tools [463]. We will explore one such opto-switch, iLID[8]-SspB [240], which offers reliable spatiotemporal control, in Sec. 6.1.

5.2 Results

Here, we introduce bead, as a nucleus mimic, in the presence of a single aster to study the aster positioning in cellular processes like cell polarization, pro-nuclear migration, and cell migration. We also organize actin filaments into 3D actin cortex around the droplet, to investigate how positioning of a single aster is affected. This is equivalent to cellular processes like cell shape reorganization, cell migration, and cell division. These additional components will help build up the complexity towards understanding the cytoskeleton related cellular processes like nuclear positioning and role of actin cortex in MT network organization in our minimal *in vitro* assay, and provide quantitative insights at system level, free from the effects of redundant cellular pathways.

5.2.1 Variations in centrosome purification

The centrosomes are microtubule organising centres (MTOC), and play an important role in the cytoskeleton of the cell [464]. Asters are just a radial collection of MTs growing from the centrosomes. So, centrosomes are essential for *in vitro* reconstitution and studying of aster positioning in droplets. We used two different methods for

[3] DMNPE-caged DNA, Bhc-caged mRNA; BNPA-cofilin, NVOC-actin; caged amino acids (CpAAs), cgY, CpSer; MNI-Glu, NP-EGTA

[4] Domains: UV receptors, Cryptochromes, BLUF, LOV, Phytochromes

[5] Actions: Homodimerization, Heterodimerization, Oligomerization, Dissociation, Shielding, Photocleavage

[6] Wavelength: 300–750 nm

[7] www.optobase.org

[8] iLID — improved Light Induced Dimerization

purification of centrosomes — the traditional, sucrose density gradient (SDG) based centrifugation [234, 437], and a more recent, Centrosome Affinity Capture (CAPture) based pull-down [465].

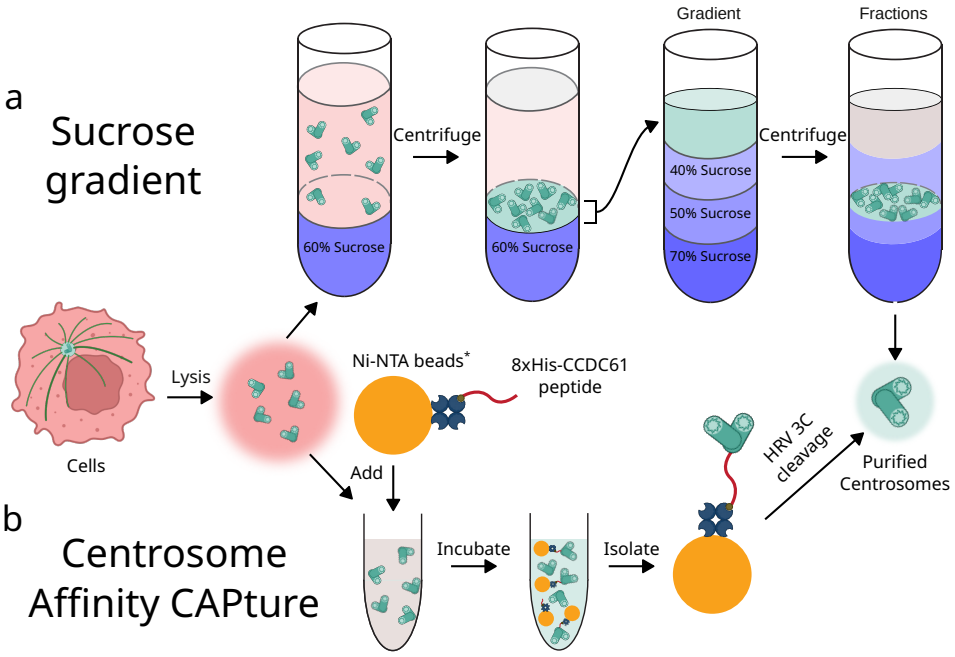

Figure 5.2: **Methods for centrosome purification.** (a) Sucrose density gradient (SDG) [437] — Cells are grown, and lysed. The centrosomes from lysate are first concentrated on 60 % sucrose cushion. The concentrated centrosomes are further separated on a discontinuous 40 %, 50 % and 70 % sucrose gradient. The centrosomes are collected in fractions by punching a hole in the bottom of the gradient tube. (b) Centrosome Affinity Capture (CAPture) [465] — Cells are grown and lysed. The lysate is incubated with 8xHis -tagged CCDC61 peptide attached to Ni-NTA magnetic beads. The centrosomes are pull-down with a magnet and the isolated centrosomes are eluted with HRV 3C cleavage. (Images adapted from [466] and partially created with BioRender.com)

There are significant differences in the quality of centrosomes, i.e. the number and the length of the MTs nucleated from the centrosomes, across different batches of purification. Also, getting a high enough concentration of centrosomes required for sufficient encapsulation of a single or double aster in droplets is difficult.

Sucrose density gradient purification

In SDG, centrosomes are purified from cell lysate with a series of centrifugations, as shown in Fig. 5.2(a). First, centrosomes are concentrated on a 60 % sucrose cush-

ion. Then the concentrated centrosomes are passed through a discontinuous 40 %, 50 % and 70 % sucrose gradient. The centrosomes are collected from the bottom of the gradient tube in fractions. These fractions are tested in a flow cell to identify the fractions with most concentration of the centrosomes. The aster grown from the SDG centrosomes show difference in quality. While most of the centrosomes have a good number (∼100) of MTs, a few of them have very few (≤10) MTs (Fig. 5.3(a)). Along with these asters, the flow cell has regions of MT mesh (Fig. 5.S1(a)). These are spontaneously nucleated MTs but clustered, without any radial organization. The majority of the asters with many MTs are seen in scattered (or damaged) state, the MTs appear radially originating around a central point, but no clear centre, centrioles, can be observed. The asters (∼100 µm) seem huge compared to average eukaryotic cells (∼10–20 µm), an order of magnitude difference. There are few asters in compact (or intact) state, the MTs are fewer and shorter compared to the scattered state aster, but a clear centre can be identified (Fig. 5.3(b)). Experiments in this work with aster positioning are performed using SDG centrosomes only. The fluorescently labelled CAPture peptide can be used as marker (for centrioles and peri-centriolar matrix (PCM) around the centrosomes) too, if added to the lysate during the purification. The CAPture peptide shows a blob (≲10 µm) at the centre in case of scattered centrosomes, and a bright spot in case of compact centrosome (Fig. 5.3(b)). This indicates that the PCM is scattered (hence, the scattered state centrosome) or damaged, as opposed to typical (≲1–3 µm) [467]. It can also explain the presence of MT mesh regions, nucleating with the help of MAPs from damaged PCM.

Centrosome Affinity Capture purification

The CAPture is pull-down based centrosome purification, as shown in Fig. 5.2(b). The cell lysate is incubated with 8xHis-HRV3C-mStayGold-3xFLAG-Avi-CCD61$^{334\text{-}366}$ peptide attached to Ni-NTA magnetic Dynabeads™. The centrosomes are pull-down with a magnet and the isolated centrosomes are eluted from the beads with HRV 3C cleavage. The coiled-coil-domain-containing protein 61 (CCD61)'s low-complexity region, shown to interact with many centrosome proteins, especially Ninein, which localizes with CEP170 attached the minus end of centrioles [465]. The centrosomes purified with CAPture have been shown to have many more proteins in PCM compared to SDG purification [465].

The CAPture centrosomes show a compact state (Fig. 5.3(c)), compared to most of the scattered state SDG centrosomes (Fig. 5.3(b)). The CAPture peptide appears as a single spot (less bright due to possibly single copy of fluorescent CAPture peptide), at the centre of the centrosomes. The tubulin enrichment is seen around the CAPture spot in compact state. Despite the assumed intact PCM in compact state and high tubulin enrichment, the number and length of MTs is lower. The CAPture centrosomes, purified over a gravity column with Ni-NTA Sepharose resin (as a simpler alternative method), show similar compact state (Fig. 5.S1(b)).

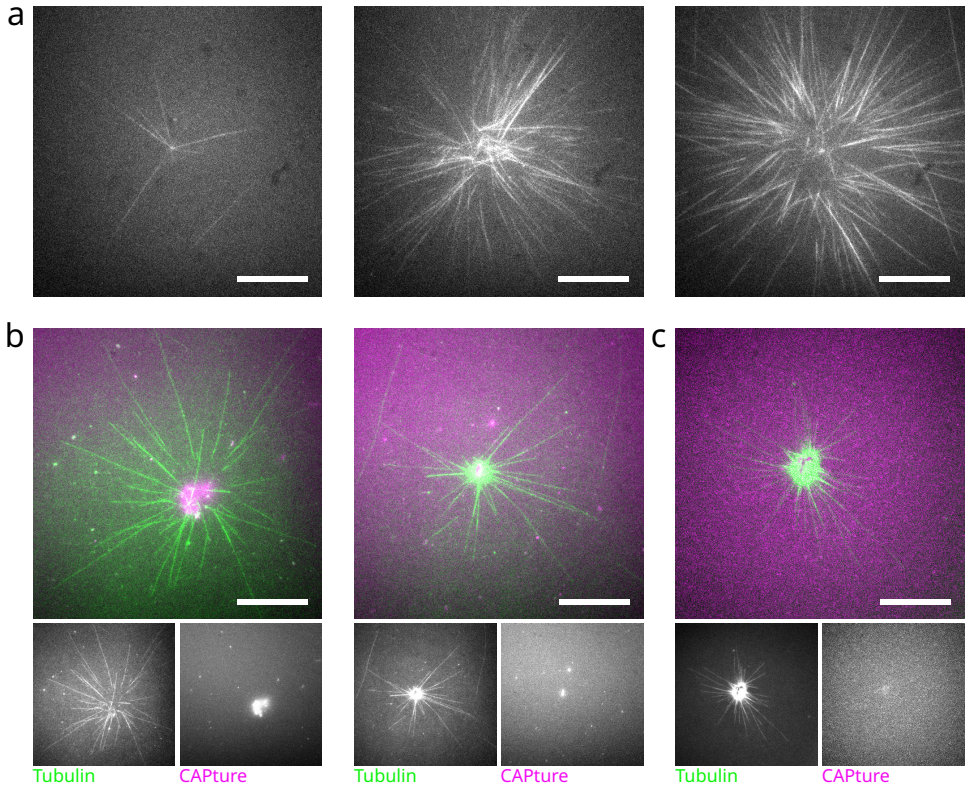

Figure 5.3: **Variation in asters grown from purified centrosomes.** (a) Centrosomes purified with sucrose gradient vary in the quality (number of MTs nucleated). (left—right) few, short MTs to many, long MTs. (b) Sucrose gradient purified centrosomes show two types — (left) most commonly in scattered state, (right) few in compact state, with identifiable centre. The same is corroborated with CAPture peptide, a proxy for PCM, blob (left) versus puncta (right). Tubulin localisation is also seen around the puncta. Number and length of MTs is less in compact state compared to scattered state. (c) CAPture purified centrosomes only show compact state (as described earlier). All images shown are brightness and contrast enhanced. Scale bar — 20 µm.

5.2.2 Asters in presence of Nucleus-mimic beads

Asters can grow large, covering almost the entire cytoplasm of a cell. They have to co-exist with the largest organelle of the cell, the nucleus. Therefore, two of the largest structures inside the cell are confined in a limited volume of the cell. So, aster positioning cannot be considered in isolation, as it is influenced by other organelles [468]. This plays an important role in cellular processes like pro-nuclear migration and differentiation. In cells, centrosomes and nucleus are connected through linker of nucleoskeleton and cytoskeleton (LINC) complexes [469, 470]. Here, we reconstitute a minimal *in vitro* system to co-encapsulate an unlinked aster and a nucleus-mimic bead in droplets (Fig. 5.4(a)) to study how each affects the other's

positioning.

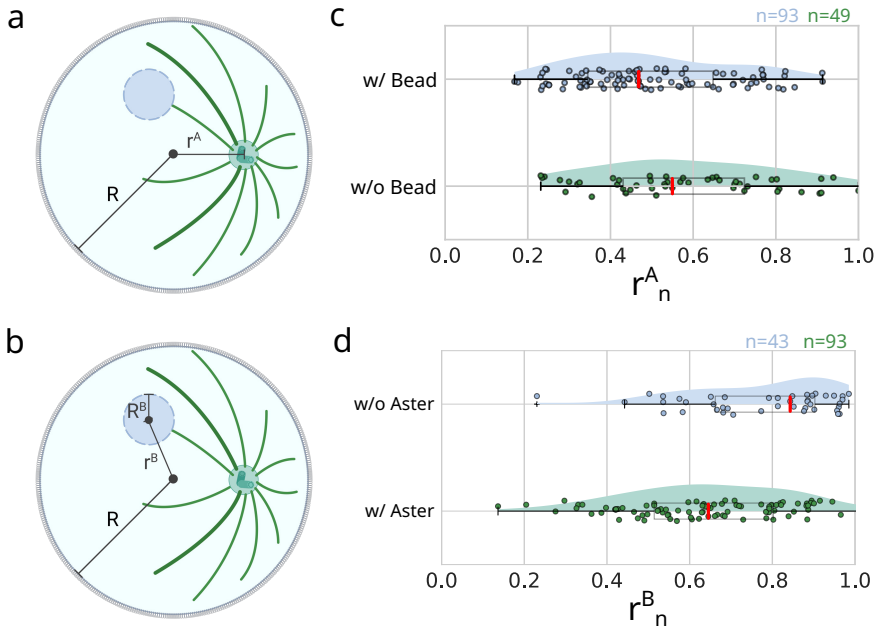

Figure 5.4: **Aster and bead centering.** (a) Schematic of MT aster positioning affected by presence of bead in droplets. r^A is aster-centre distance and R is the radius of the droplet. (b) Schematic of bead positioning affected by presence of MT aster in droplets. r^B is bead-centre distance, R^B is the radius of the bead, and R is the radius of the droplet. (Image created with BioRender.com) (c) Quantification of $r^A_n = r^A/R$, in presence and absence of bead. (d) Quantification of $r^B_n = r^B/(R - R^B)$, in presence and absence of aster. (c)(d) Box plot (black) with quartiles, and violin plot (shaded regions) with probability density.

Co-encapsulated aster and beads centres in droplets

Co-encapsulation of centrosome asters and beads in droplets required fine-tuning conditions. We have used polystyrene beads[9] as to mimic the nucleus. These beads are denser than water and need addition of 12.1 %w/v sucrose to results in zero buoyancy environment for beads (Fig. 5.S3(a)). This is exclusive of the sucrose coming from SDG purified centrosomes. Up concentration of beads to 25 x was needed to statistically achieve one bead per droplet. We classify the droplets with — only aster (aster without bead), only bead (bead without aster), and both (aster with bead; bead with aster). We analysed the - aster-centre distance r^A, bead-centre distance r^B, diameter of the droplet D, and radius of the bead R^B. The centre of aster is manually quantified, while all other parameters are obtained with automated image

[9]The 4.5–10 µm diameter beads are suitable for achieving ∼15 % nuclear volume in ∼20 µm droplets (Fig. 5.S2(a)).

analysis. We determine normalised distances of aster $r_n^A = r^A/R$ (Fig. 5.4(a)), and bead $r_n^B = r^B/\left(R - R^B\right)$ (Fig. 5.4(b)), correcting for maximum bead distance r^B due to radius of the bead R^B. We observe, aster centering r_n^A is 0.47 and 0.55 in presence of and absence of bead respectively (Fig. 5.4(c)). This shows that the aster centres more in presence of bead. And for bead centering r_n^B is 0.65 and 0.84 in presence of and absence of aster respectively (Fig. 5.4(d)). This indicated bead positions closer to the centre in presence of aster. Both the aster and the bead position themselves away from the centre in independent cases, but when together, both prefer to position closer to the centre of the droplet. It makes sense for the asters to position closer to centre due to nuclear-occlusion effect of the bead (∼5–15 %v) (Fig. 5.S2(a)). But it is not intuitive for the beads to position closer to centre in presence of an aster.

Aster and bead co-localise together

Next, we wanted to check aster and bead's relative positioning with respect to each other, do they co-localise? We also analysed — aster-bead distance d^{AB} (this is the distance from centre of the aster to the surface of the bead) and determined the normalised aster-bead distance $d_n^{AB} = d^{AB}/\left(D - 2R^B\right)$ (Fig. 5.5(a)), correcting for the maximum aster-bead distance d^{AB} due to the diameter of the bead. We also assessed if the bead was in 5 %v around the aster centre. We observed 55 % of the beads co-localise around the 5 %v of aster centre ($d_n^{AB} \leq 0.37$) (Fig. 5.5(b)). There was no extreme separation between aster and bead, even when bead in not within the 5 %v of the aster (Fig. 5.5(c)). The data also showed a subset of population, almost 30 % of aster-bead pairs have $d_n^{AB} \leq 0.1$ distance, indicating very close proximity. We further investigated the cause-effect of this proximity.

Co-localisation affects aster positioning

The position of aster and bead are measured in 3D from the centre of the droplet, but the aster-bead distance d_n^{AB} simplifies this as 2D distance between two points, ignoring the centre. So we defined a parameter which considers all three points, an angle θ. This is defined as the angle formed between the aster centre — droplet centre — bead centre (Fig. 5.6(a)). A bi-modal distribution was observed with θ. The aster and bead either form a very low angle (<15°), or a high angle (>60°) (Fig. 5.6(b)). Re-categorizing aster bead distance d_n^{AB} in angle sub-classes shows extreme co-localisation for low angle and normal distribution for high angle (Fig. 5.6(c)). Almost all the low angle cases have $d_n^{AB} \leq 0.1$ and all the beads fall within 5 %v of the aster centre. Representative low angle and high angle aster bead co-localisation are shown in Fig. 5.6(d). This provides a clear picture for better understanding the aster positioning with respect to the co-localization. For low angle, it is pretty much intuitive that with such close proximity of aster and bead, it appears like aster and bead (or nucleus mimic) are somehow linked, and high angle are geometrically very unlikely. And in case of high angle, there is no relation with the angle θ and aster bead distance d_n^{AB}. We also observed the aster centering (r_n^A) of 0.61 and 0.45 for low and high angle respectively (Fig. 5.S3(b)). Aster centres more in case of high

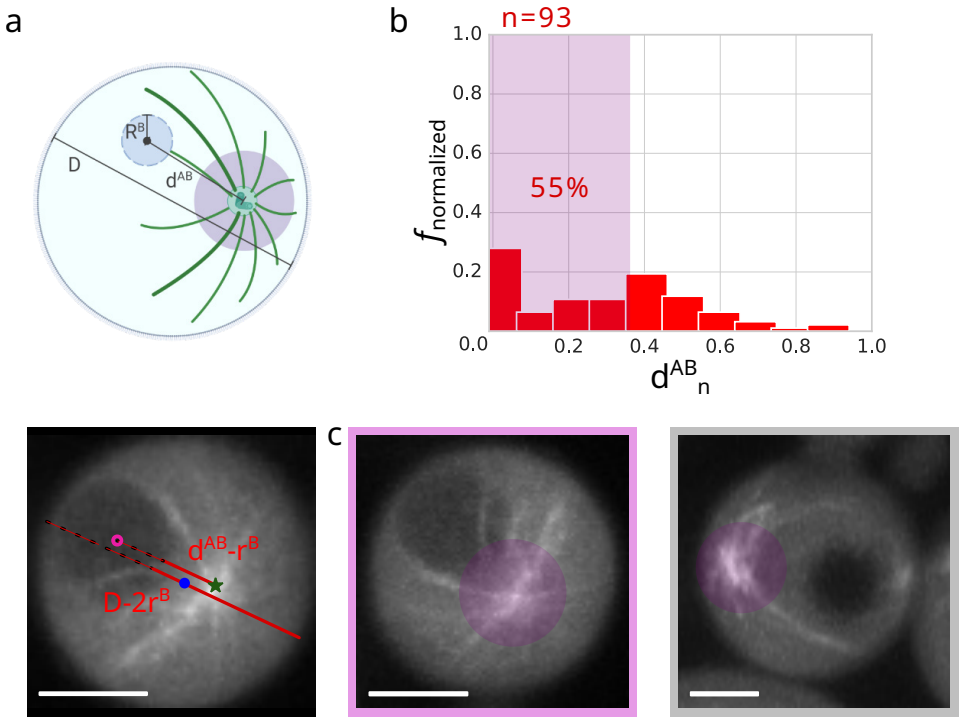

Figure 5.5: **Aster and bead co-localisation.** (a) (top) Schematic of MT aster — bead positioning relative to each other. d^{AB} is aster-bead (aster centre to bead's surface) distance, R^B is the radius of the droplet, and D is the diameter of the droplet. The purple sphere around the aster centre represents 5 % of droplet volume. (Image created with BioRender.com) (bottom) Aster (white) and bead (black, void) co-encapsulated in droplet. centre of droplet (•), aster centre (⋆), and centre of bead (∘). The image is the sum of maximum intensity projection (for aster) and median intensity projection (for bead) of 3D Z-stack. (see Fig. 5.S5 for a 3D projection example.) (b) Quantification of $d^{AB}_n = d^{AB} \big/ \left(D - 2R^B\right)$. Histogram binned with $\sqrt{n} + 1$, frequency f_n is sum normalised. The purple region indicates 5 %v around aster centre. (c) Image Z-projection, showing cases of — (left) bead within 5 %v of aster, (right) bead outside of 5 %v of aster. Scale bar — 6 µm.

angle, where it is free from bead. For the low angle cases, with proximal positioning of the aster and bead, the aster is pushed away from the centre and the bead centers itself.

5.2.3 Asters in presence of Actin cortex

Just as centrosomes are essential for aster formation in cellular cytoskeleton, the position of these asters with respect to the cell is also important for various cellular processes like cell migration, and cell division. MTs from the aster interact with the actin cortex at cell periphery. It is shown that the actin cortex or even actomy-

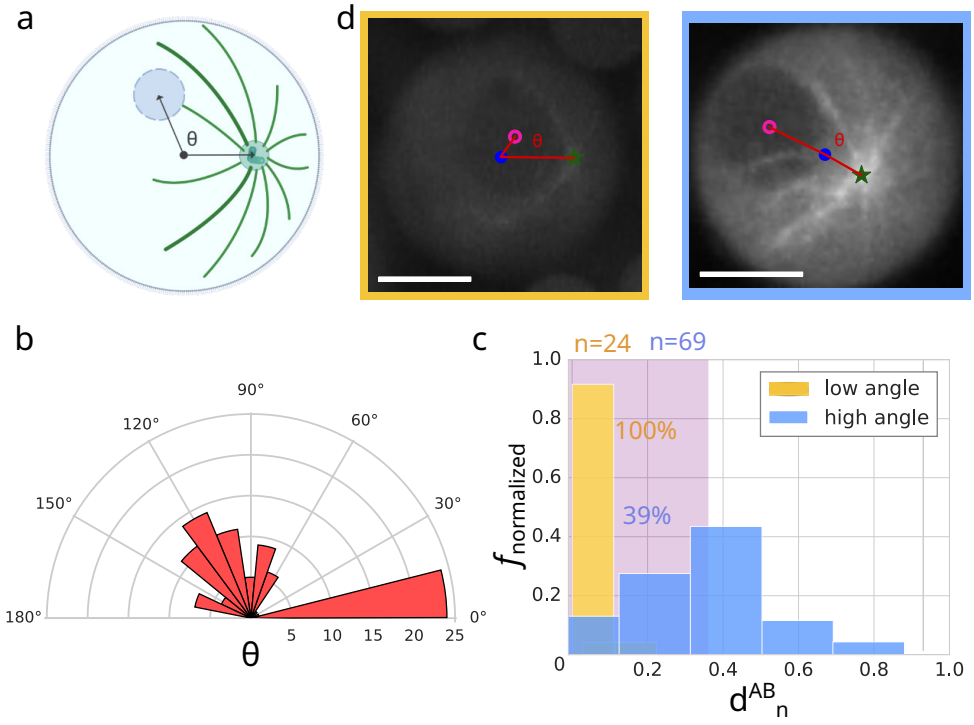

Figure 5.6: **Bead affects aster positioning.** (a) Schematic of MT aster — droplet centre — bead angle. θ is the angle formed in 3D with centres of aster, droplet, and bead. (Image created with BioRender.com) (b) Quantification of θ. Circular histogram binned with $\sqrt{n}$, and absolute frequency. Bi-modal distribution seen with low angle (<15°) and high angle (<15°). (c) Quantification of θ with angle classification. Histogram binned with $\sqrt{(n_1 + n_2)}$, frequency f_n is sum normalised. The purple region indicates 5 %v around aster centre. (d) Image Z-projection (maximum+median), showing cases of — (left) low angle (<15°) and (right) high angle (<15°). Key — centre of droplet (•), aster centre (⋆), and centre of bead (∘). Scale bar — 6 µm.

osin network can control centrosome positioning in cells [453, 471, 472]. Similar effects on aster positioning have been observed with *in vitro* reconstitution of artificial centrosomes in micro-wells [473]. Actin cortex formation in cells is a complex process, and replicating the exact mechanism *in vitro* remains challenging. To address this, we designed a simplified, minimal actin cortex. This can be assembled either as a meshwork of branched actin filaments generated by the Arp2/3 complex and its activator VCA anchored to the dropet interface, or by attaching actin filaments to the cortex and crosslinking them using α-actinin. In this work, we try to take the reconstitution closer to *in vivo* conditions, by combining purified centrosomes, an actin cortex, and 3D spherical confinement (Fig. 5.7(d)). This minimal system enables investigation of actin cortex's influence on aster positioning, as observed in

various cellular processes.

Assembling actin cortex

We have tried different approaches to assembly actin cortices in droplets. First, a branched actin cortex is reconstituted using actin (8 µM), 10xHis-VCA (5 µM) and Arp2/3 (50 nM) in F-buffer. A uniform, continuous actin signal is seen at the droplet interface (Fig. 5.7(a)) and maximum intensity projection (MIP) of the droplet shows a smooth, uniform actin cortex assembled inside the droplet (appears as a continuous actin cortex Fig. 5.7(c)). The FRAP analysis of actin cortex, showed rapid recovery (Fig. 5.S4), indicating the presence of active actin nucleation and polymerization in a dynamic cortex. Second, an crosslinked actin cortex is reconstituted using actin (8 µM), and α-actinin (1.6 µM) in F-buffer. Actin bundles are seen inside the droplet lumen and at the droplet interface (Fig. 5.7(b)) and MIP of the droplet shows actin bundles throughout the droplet, while the one lining the interface forms a crude meshed cortex (appears as a bundled actin cortex Fig. 5.7(e)). The actin cortex assembled with VCA and Arp2/3 resembles the *in vivo* actin cortex more than the crosslinked actin bundle cortex assembled with α-actinin. So, we focused on working further with VCA and Arp2/3 for cortex assembly. We also checked the VCA localisation at the interface (Fig. 5.7(f)) and also tested lowering actin concentration (4 µM) for cortex assembly in droplets. While actin is ideally polymerized in F-buffer, eventually working with tubulin, the protein needs to polymerize in tubulin conditions too. For this reason, we tested actin cortex assembly in presence of MRB80 buffer and PEG-6000 (1 %w/v, a crowding agent aiding tubulin polymerization in droplets). An actin cortex is seen using actin (8 µM), VCA (5 µM), Arp2/3 (50 nM), and PEG-6000 (1 %w/v) in MRB80 buffer (Fig. 5.7(g)). A dynamic actin cortex assembly is possible in droplets under tubulin polymerizing conditions, too. The presence of PEG-6000 starts to bundle the actin filaments at the interface, therefore the cortex is not continuous any more, but it becomes patchy although still more homogeneous than the crosslinked actin-bundle mesh cortex made with α-actinin.

Optimizing actin and tubulin co-polymerization

Next, we increase the complexity of *in vitro* reconstitution by combining actin and tubulin polymerization. Tubulin is known to be sensitive to the buffer conditions, deviations from the ideal MRB80 or BRB80 buffer, like changes in salt concentration and pH, affects the tubulin polymerization. While some changes stabilize tubulin, most reduce severely the growth rate. Buffer exchange to BRB80 is required for experiments of motor proteins, MAPs with dynamic MTs, or alternatively these experiments are performed with Taxol stabilized MTs. *In vitro* assays involving actin and tubulin are also known to use Tic-Tac buffer [473] but we did not find the buffer conditions working in our hands. Instead, we focused on optimizing actin and tubulin polymerization in MRB80 buffer for droplets.

As a simple initial test, we tried polymerising actin and tubulin together without any optimizations. Droplets encapsulating tubulin (40 µM) with MT seeds, and actin (2 µM) did not show any MTs and a homogeneous actin signal all over the lumen

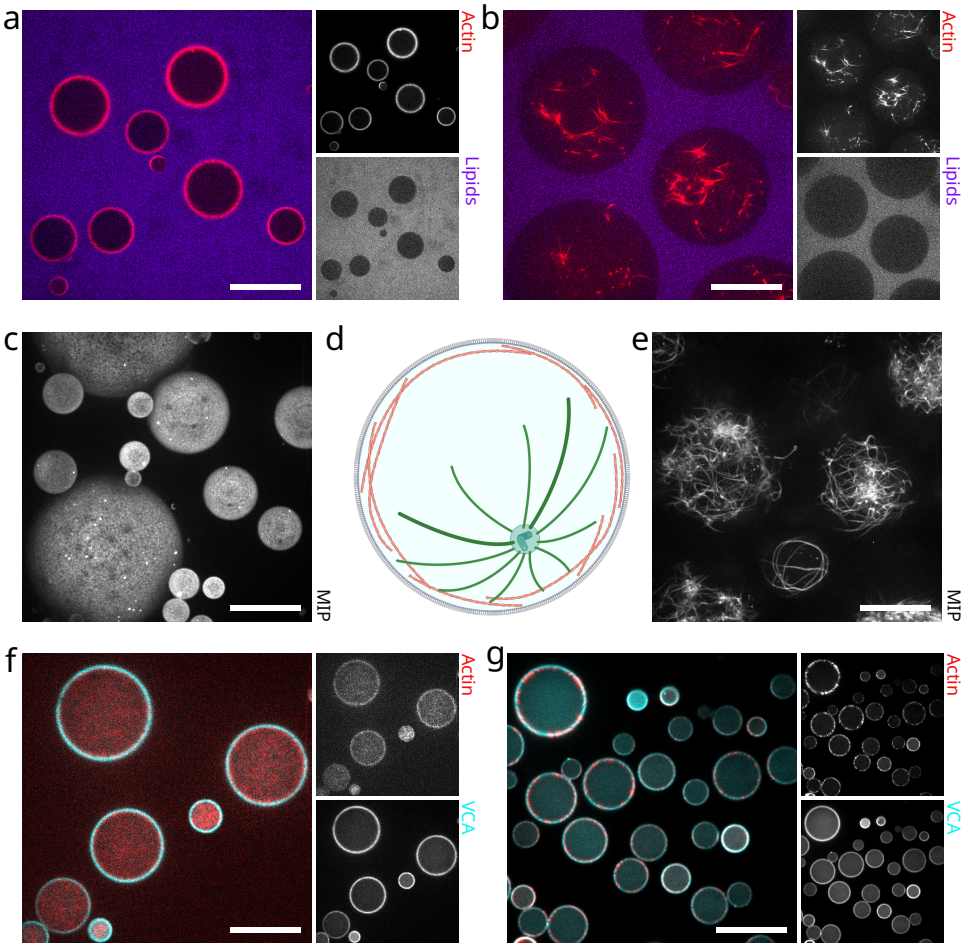

Figure 5.7: **Assembling actin cortex in droplets.** (a) Branched (continuous) actin cortex formed with actin (8 µM), 10xHis-VCA (5 µM), Arp2/3 (50 nM) in F-buffer at lipids along oil-water interface of droplet. (b) Crosslinked (bundled) cortex formed with actin (8 µM, biotinylated), α-actinin (1.6 µM) in F-buffer at lipids along oil-water interface of droplet, along with actin-bundles in the droplet lumen. (c) Maximum intensity projection (MIP) of branched actin cortex. Smooth, uniform cortex is seen. (see Fig. 5.S6 for a cropped 3D projection.) (d) Schematic of actin cortex formed at the interface of droplet with either lipid attached His-VCA (branched actin cortex) or biotin-actin (crosslinked actin cortex). MT aster positioning is affected by MT interactions with actin cortex. (Image created with BioRender.com) (e) Maximum intensity projection (MIP) of crosslinked actin cortex. Cross-linked actin-bundles lining the lipids at the interface forms the crude meshed cortex. (see Fig. 5.S6 for a 3D projection.) (f) Branched actin cortex formed with actin (4 µM), 10xHis-VCA (2.5 µM), Arp2/3 (25 nM) in F-buffer at lipids along oil-water interface of droplet. (g) Patchy actin cortex formed with actin (8 µM), 10xHis-VCA (5 µM), Arp2/3 (50 nM) in MRB80 buffer at lipids along oil-water interface of droplet. Scale bar — 20 µm.

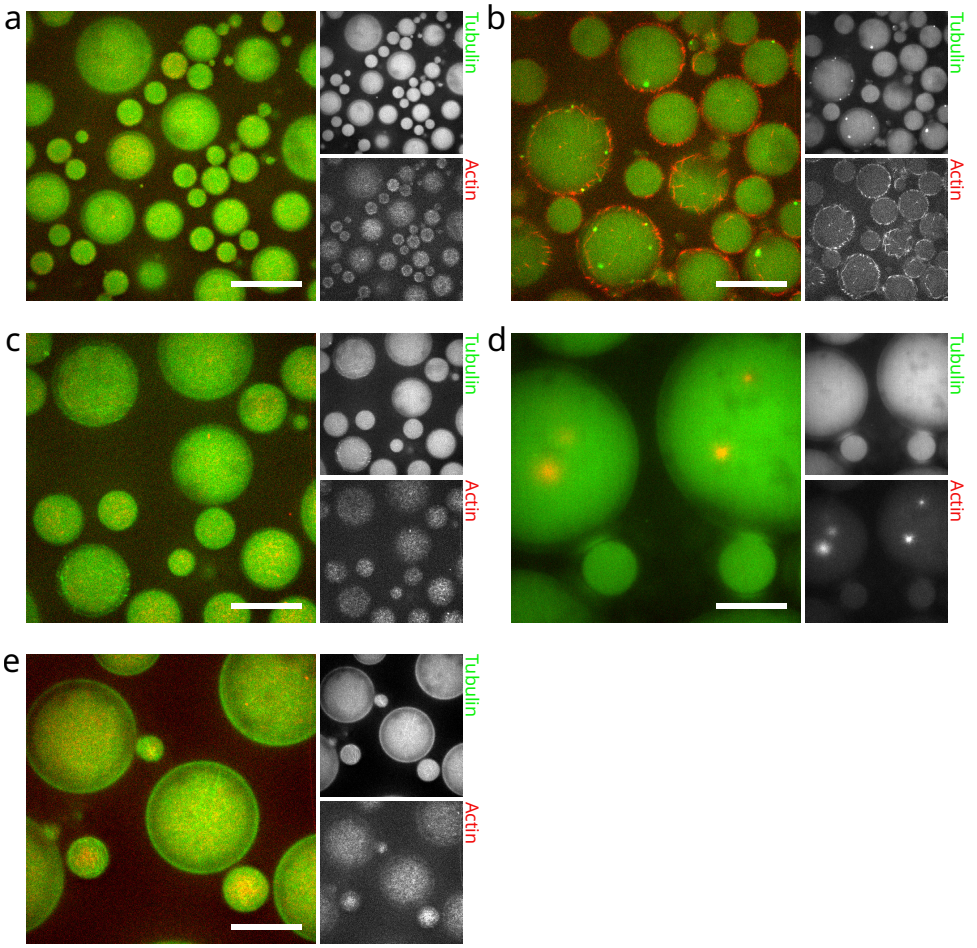

Figure 5.8: **Optimizing actin and tubulin co-polymerization in droplets.** Various different conditions for optimizing actin and tubulin co-polymerization in droplets. (a) No tubulin polymerization, and actin polymerization seen with tubulin (40 µM), MT seeds, and actin (2 µM, in F-buffer). (b) No tubulin polymerization, and actin polymerization and bundling seen with tubulin (40 µM), MT seeds, actin (2 µM), and PEG-6000 (1 %w/v). (c) Tubulin polymerization seen with tubulin (40 µM), MT seeds, pre-polymerized phalloidin stabilized actin (4 µM), and PEG-6000 (1 %w/v). (d) No tubulin polymerization, and no actin polymerization along with actin accumulation at centrosomes seen with tubulin (40 µM), centrosomes, actin (4 µM), VCA, and Arp2/3. (e) Tubulin polymerization, and actin polymerization seen with separate pre-incubation of tubulin (40 µM), and centrosomes at 37 °C for 5 min, and actin (4 µM in MRB80 buffer), VCA, and Arp2/3 at RT for 30 min. During acquisition, the slide is heated with an Objective heater around ∼30 °C. Scale bar — 20 µm.

(Fig. 5.8(a)). We next added PEG-6000 (1 %w/v) to aid tubulin polymerization. With tubulin (40 µM), MT seeds, actin (2 µM), and PEG-6000 (1 %w/v), we still did not see any MTs, while the F-actin starts to bundle and is pushed to the cortex (Fig. 5.8(b)). Considering stock protein concentrations, the final reaction mix had ∼30 %v/v F-buffer compared to MRB80 buffer. No tubulin polymerization observed in presence of F-buffer, so we decided to remove F-buffer. Actin was pre-polymerized and stabilized with phalloidin. The actin filaments were pelleted and resuspended in MRB80 buffer. Then with tubulin (40 µM), MT seeds, actin filaments (4 µM), and PEG-6000 (1 %w/v), we start seeing individual MTs inside the droplet (Fig. 5.8(c)). No presence of F-buffer clearly helps with tubulin polymerization. But, active actin filaments are required for dynamic actin cortex. So, during the preparation of reaction mixes, we diluted stocks of actin and actin-associated proteins (VCA and Arp2/3) with 5 x concentrated MRB80 buffer, while adjusting the concentration of KCl to 50 mM to promote actin polymerization. This step is essential to bring back the MRB80 buffer, PIPES levels to ∼99 % and bring down F-buffer, Tris-Cl levels to ∼6 %.

Next, we tried this buffer conditions with centrosomes instead of MT seeds, to see MT aster with actin cortex. With tubulin (40 µM), centrosomes, actin (4 µM), VCA, and Arp2/3, we see no MTs, no aster, not even any actin filaments. Surprisingly, almost all the G-actin was seen accumulated at the centrosomes (Fig. 5.8(d)) and prevent MT polymerization. Actin signal is not like a protein aggregate or blob, but corresponds to the shape of a very tiny aster, small filamentous structures seen radiating outwards. Previously, it has been shown that actin and Arp2/3 accumulate at the centrosome's PCM condensate and control the nucleation dynamics of MTs from centrosomes [474, 475]. We suspected a similar scenario in our droplet reconstitutions. To prevent actin accumulation, which prevents both MT growth by blocking centrosomes and formation of actin cortex, we incubate the actin mix (at RT for 30 min) and tubulin mix (at 37 °C for 5 min) separately before combining into the final reaction mix for droplet production. So with separate pre-incubation of tubulin (40 µM), and centrosomes, and actin (4 µM in MRB80 buffer), VCA, and Arp2/3, we start seeing actin and tubulin polymerization (Fig. 5.8(e)). We observed a fuzzy actin signal in the droplet lumen, suggesting the presence of numerous F-actin filaments, but potentially still not enough to trigger actin cortex formation. Also, many MTs were seen floating in the lumen. We think, separate pre-incubation allows centrosomes to start nucleating MTs and for actin to reach equilibrium with G-actin and F-actin. This also helps later after mixing, as there is reduced free G-actin to accumulate at centrosome. The optimizations for co-encapsulation of dynamic actin and tubulin in droplets are summarized in Tab. 5.1.

In vitro reconstitutions have constant challenge for optimizing protein's functions and minimizing reaction volumes to save precious purified proteins. Further in more complex reconstitutions, as the number of proteins and reagents start to increase (≳10), the minimum reaction volume (≳10 µL) needs to be increased to keep up with minimum error-free pipette-able volume[10]. Whereas, especially for encapsulations, even a 0.5 µL of reaction mix is enough for making droplets[11]. The strategic intro-

[10] A ∼0.5–1 µL is resonable with a 0.2–2.5 µL pipette

[11] This leaves the rest of 95 % reaction mix as waste. Even imaging 100× droplets (with an average

Issue	Fix
No polymerization	add PEG & MT seeds
Still no polymerization	replace G-buffer
Actin accumulation at centrosomes	separate pre-incubation

Table 5.1: **Optimizing actin and tubulin co-polymerization conditions.** Summary of different solutions to the issues with co-polymerization of dynamic actin and tubulin in droplets.

duction of additional components — either in the pre-mix or via a channel mix — while maintaining minimal reaction volume becomes an optimization problem.

The concentrations of actin and tubulin were optimized for optimal protein functions i.e. formation of actin cortex and MT aster with minimum volumes possible, also to have some free room in the reaction mix to further increase the complexity of the reconstitution by addition of more proteins in the future work. In Fig. 5.8(e), we have seen actin cortex and MTs with tubulin (40 µM) and actin (4 µM). We titrated 20–40 µM tubulin against 8–4 µM actin, with constant ratio of actin:VCA:Arp2/3 and centrosomes (∼5.5–11.25 %v/v) proportional to tubulin concentration, and constant PEG-6000 (1 %w/v). Actin polymerization is seen in all the conditions. Consistently, formation of branched actin cortex with a few actin bundles (due to PEG-6000) along the cortex, is seen with actin ≥5 µM (Figs. 5.9(a)-5.9(d)). MTs and even asters, are seen with tubulin ≥25 µM (Figs. 5.9(b)-5.9(e)). The higher the concentration, the better the actin cortex and asters are observed; therfore, a minimum of 5 µM actin and 30 µM tubulin should be ideal. This also leaves some room in the reaction mix for addition of more proteins later. More experiments are needed to collect enough data to examine the effect of actin cortex on aster positioning and compared it with the simple aster positioning (Ch. 6, [250]). With an attempt to reduce PEG-6000 to 0.5 %w/v, no tubulin polymerization is seen (Fig. 5.9(f)). Polyethylene glycol (PEG) is known to help tubulin polymerization by stabilizing MT filaments [476, 477]. Hence, a minimum of PEG-6000 1 %w/v is required for tubulin polymerization in droplets.

5.3 Discussion

Aster positioning is an integrated part of various cellular processes like cellular and pro-nuclear migration, cell division, and differentiation. While a lot of work on *in vitro* aster positioning has been performed [130, 136, 237, 478], it has been carried out in isolation with tubulin, motors, and MAPs only. Some *in vitro* studies have tried to investigate the role of microtubules with actin and other polarity proteins [239, 473, 479]. But the interactions and crosstalk with other non tubulin cytoskeleton components is lacking. Also, the interaction with various other cellular organelles like nucleus, Golgi body, endoplasmic reticulum or mitochondria is largely neglected. Here we take a step towards expanding the complexity of the tubulin reconstitution by adding other components like nucleus mimic, and actin cortex.

radius of 10 µm is ∼4.2 pL only) is like imaging only $^1/_{1000}$ of the 0.5 µL

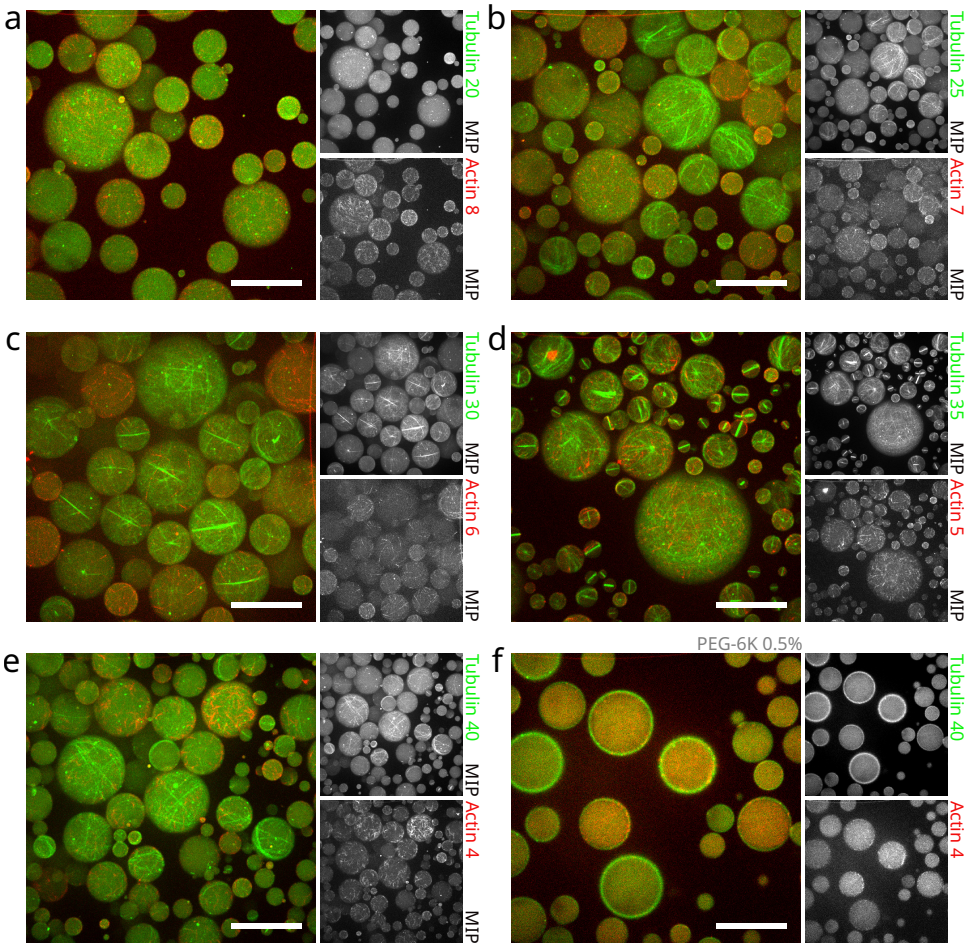

Figure 5.9: **Optimizing actin and tubulin co-polymerization concentration.** Titrating actin and tubulin concentrations for finding respective minimum optimal co-polymerization conditions in droplets. All conditions include — tubulin, centrosomes (∼5.5–11.25 %v/v), actin, VCA, Arp2/3, and PEG-6000 (1 %w/v). (a) Tubulin (20 µM), actin (8 µM) (b) Tubulin (25 µM), actin (7 µM) (c) Tubulin (30 µM), actin (6 µM) (d) Tubulin (35 µM), actin (5 µM) (see Fig. 5.S8 for a cropped 3D projection.) (e) Tubulin (40 µM), actin (4 µM) (f) Tubulin (40 µM), actin (4 µM), PEG 6000 (0.5 %w/v). Actin polymerization can be seen with ≥5 µM and tubulin polymerization can be seen with ≥25 µM. No tubulin polymerization seen in case with PEG-6000 (0.5 %w/v). Images are maximum intensity projection (MIP) for all conditions, except (f). During acquisition, the slide is heated with Objective heater around ∼30 °C. Scale bar — 20 µm.

5.3.1 Search for consistent quality aster generators

Asters are usually assembled from MTOCs, like centrosomes. However, centrosomes are difficult to work with. They are a complex of about more than a hundred proteins and are particularly difficult to purify. We used the SDG [234, 437], a commonly used method in the literature to purify centrosomes. We show variation in the quality of centrosomes purified (Fig. 5.3(a)), and this changes with different batches of centrosome purification. Hence, it is recommended to work with large batches of cells ($\geq 3 \times 10^9$) to obtain a purification batch with good and large quality of centrosomes enough for many experiments. This ensures consistent centrosome quality across the different experimental conditions. We also find that the quality of centrosomes in a batch largely depends on the state of the cell in the starting culture. The concentration of centrosomes in collected fractions is also sensitive to the size of the punch hole in the gradient tube and the flow rate from the hole. A smaller hole size correlates with a higher concentration of centrosome fraction, but can take hours for fraction collection. Testing the centrosome in bulk show the majority of them in a scattered state, without a distinct centre and long MTs. This is in contrast with the centrosomes purified with CAPture [465], a recent method for simpler pull-down based purification. CAPture centrosomes appear compact compared to SDG centrosomes. The CAPture peptide, an indirect marker for PCM, also reveals differences. SDG centrosomes show a blob, while CAPture centrosomes have a single bright spot. This indicates possibility of damage to PCM during ultra centrifugation. In contrast, the scattered SDG centrosome have many and longer MTs compared to the compact CAPture centrosomes. The CAPture method claim to give centrosomes of better quality compared to SGD. This claim is based on measurments of the number of PCM proteins using mass spectrometry, immunostaining with centriolar and PCM markers and electron microscopy to verify the structure of the centrioles. But a true test for quality of centrosomes for *in vitro* reconstitutions should be their ability to nucleate MTs and form asters.

Attempts are made to replace centrosomes, with artificial MTOCs like beads coated with nucleator MAPs like Aurora-A kinase [480] or with stable MT seeds [473]. This has success in generating radial MT structures resembling asters, but it comes with a different set of problems like sinking of beads [481, §4].

5.3.2 Presence of large objects affects aster positioning

Centrosomes[12] are typically located at the center of the cell. Their (aster) positioning is a well-studied phenomenon. We introduced another component, nucleus-mimic, to study its effect in the aster positioning. While nucleus purification methods exist [483], they seem equally if not more complicated compared to centrosome purification. We have worked with beads as an easy and crude substitute for nucleus. It has own advantages and disadvantages. Beads are solid incompressible objects, usually heavier than the buffer, and their surface is biologically inactive compared to real nucleus. Beads are more stable and their concentration and size are easier to

[12] Centrosome, something that occupies a central position in the cell; discovered by Heidenhain and term coined by Boveri [482].

control and quantify compared to purified cell nuclei. Considering these simplifications, we show that large objects like nucleus mimic beads affects aster positioning.

We find both aster and the bead centres to a greater extent in presence of each other compared to independent individual positioning. Also, the aster and the bead tend to co-localise together in proximity. This is interesting, as in cells, asters usually are linked to the nucleus with LINC complexes [469, 470]. However, we find this *in vitro* reconstitutions, even without any active linking between aster and bead, in about half of the droplets. In one-third of the droplets, the aster is almost in contact with the bead surface, and in the rest of droplets aster bead distance is normally distributed. But the aster positioning in case of proximity positioned aster-beads pairs is further away from droplet centre. We think this is largely dependent on the MT pushing forces (F^{MT}) and initial positions of aster and bead during droplet formation. With having just a few static time points from the dynamic process of aster positioning in the presence of large objects like nucleus, we would like to speculate on the underlying mechanism. In case of low angle initialization, the aster starts close to the bead, in-between the bead and the droplet cortex (Fig. 5.10(a)). The MTs growing in the direction of the bead are likely to slip off the curve surface of the bead, pivot at the centrosome and grow aside the bead (Fig. 5.10(c)). So they do not contribute the pushing forces against the bead. And in case where centrosome is almost touching the bead ($d_n^{AB} \leq 0.1$), we think MTs from that side of centrosome are not able to grow due to lack of access to tubulin dimers. And for MTs from the centrosome growing towards the cortex can generate forces against the cortex. The pushing force of an individual MTs (∼5–10 pN) [131] is not enough to displace (push) the bead (∼4.5–6 µm). These MTs are likely to buckle and pivot to relieve the stress (Fig. 5.10(d)). The MTs growing from the side encounter the cortex, bend, slide, and eventually start pushing the aster more towards the cortex, i.e. away from the centre of the droplet (Fig. 5.10(e)). In case of high angle initialization, the aster and bead are far away from each other (Fig. 5.10(b)). The MT from the aster start growing and pushing against the cortex. This results in movement of the aster towards the droplet centre. The aster MTs grow longer and eventually encounter the bead. In a similar way, they slip off the bead, pivot and grow around the bead. And thus cannot generate enough pushing force to displace the bead (Fig. 5.10(c)). The MTs growing around the bead hit the cortex on the opposite side and buckle along with sliding down the smooth droplet cortex to prevent further stress buildup. This buckling and sliding configuration of the MTs engulf the bead and bring it closer to the center (Fig. 5.10(f)) [13]. The forces depend on the MT properties like rigidity, catastrophe rate, and also the number of MTs present. While more time points of this dynamic aster-bead positioning is desired for better understanding, simulations can help bridge the missing gap and provide quantitative estimates of stress and forces in the MTs. We have based our speculations based on similar simulations of centrosome positioning by MT network [484]. It is believed that the centrosome is being positioned in the cell [485], but recently it was shown in some cases that the cell boundary rearranges around the centrosome and not the other

[13] This speculative model of minimal system reminds of an old primitive, Heidenhain's rubber model (based on Van Beneden's theory) of mitosis [482].

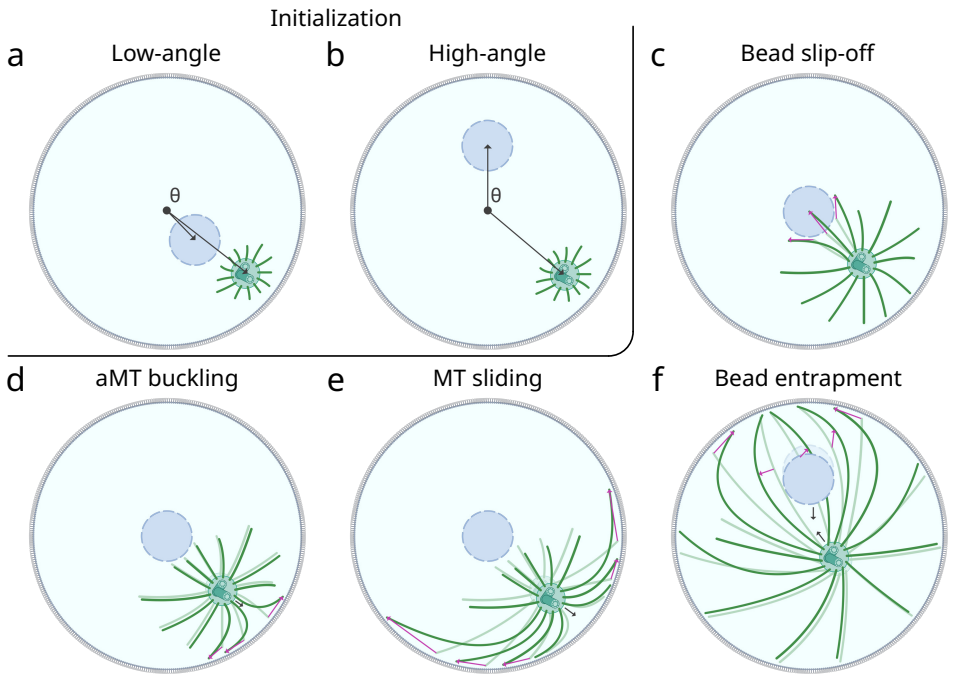

Figure 5.10: **Cases during aster positioning in presence of bead.** Aster-bead initialization scenarios, (a) low angle and (b) high angle initialization. Different cases during aster positioning in presence of bead, which can change force balance. (c) MTs slide off the curve surface of the bead, unable to generate pushing forces. (d) Due to not enough pushing force to displace the bead, MTs at the cortex buckle and pivot, and in the process, pull the aster slightly towards the cortex. (e) MTs growing orthogonally to the aster-bead axis, undergo following phases on encountering the cortex: initial bending, subsequent sliding, and continued growth. These interactions progressively generate forces that push the aster towards the cortex. (f) MTs growing around the bead, undergo following transition on encountering the cortex: they buckle and slide along the cortex. This generates spring-like centripetal forces that move the aster toward the cell center, at the same time pull the bead to a more central position. The black arrows represent the displacement of the objects, while the magenta arrows track the changes in the MT conformations. (Images created with BioRender.com)

way around [472]. Such considerations should also be taken into account for better understanding, since current simulations typically consider the outer shell as a fixed frame of reference. And the bead, also being relatively immovable for pushing MTs in a viscous environment, will not result in proper MT force balance. Presence of a force generator like dynein at the cortex can change force balance, and can displace the nucleus [486, 487]. It will be intersting to incorporate dynein in our *in vitro* aster

positioning assay in presence of a bead.

5.3.3 Integrating actin and tubulin systems in 3D reconstitutions

We incorporated a new cellular component, dynamic actin cortex, in the droplets by multiple ways. Different actin cortices were assembled with the help of either, VCA and Arp2/3 or α-actinin. Actin cortex assembled with VCA and Arp2/3, had smooth and uniform coverage at the droplet cortex. While the actin cortex assembled with α-actinin, resulted more in a shell formed with a network of actin bundles. *In vitro* co-encapsulation of actin and tubulin is difficult, especially in closed 3D environments. Also, to maintain conditions conducive to polymerization of both actin and tubulin is not easy. Tubulin does not polymerize in presence of even a fraction of actin buffer, G-buffer. Even addition of nucleators (MT seeds) and crowding agents (PEG) does not promote tubulin polymerization in the presence of G-buffer. Polymerization can be rescued by replacing the G-buffer with MRB80 buffer. Also, actin accumulates in the centrosomes, possibly phase separates into the LLPS droplet of centrosome and its PCM proteins. This also blocks new nucleation of MTs from the centrosomes. A separate incubation of actin and tubulin mixes before encapsulation into droplets, allows for the nucleation of new MTs from centrosomes (early aster) and potentially accelerates formation of actin-cortex. Finally, optimizing the concentration of actin and tubulin helps in co-encapsulation of both dynamic actin and dynamic microtubules in the droplets.

Actin plays an important role in various cellular processes involving aster positioning. Hence, *in vitro* studies of dynamics of tubulin and tubulin-related processes, along with actin, is necessary. Previous attempts of *in vitro* reconstitutions of both actin and tubulin have limitations, either stabilized actin was used [239] or encapsulation were performed in non-spherical containers, cylindrical wells [473]. Here, we increased the number of active components and complexity of the *in vitro* reconstitutions. While the optimizations have been performed, the work is in preliminary stage of proof-of-concept. This will take us a step closer towards reconstituting a sophisticated and dynamic actin-tubulin system in more cell-like containers, 3D droplets. It will enable mimicking and testing underlying mechanism of cellular processes like asymmetric cell division, cell migration or polarity establishment.

5.4 Material and Methods

5.4.1 Materials

Chemicals See Secs. 2.6 & 4.5 for a detailed list of chemicals. Chemicals were purchased from Merck (Merck Life Science), unless otherwise stated: RPMI-1640 Medium (8758 Sigma), Methyl-[5-(2-thienylcarbonyl)-1H-benzimidazol-2-yl]-carbamate (nocodazole, 487928 Sigma), Cytochalasin B (250233 Sigma), β-mercaptoethanol (M6250 Sigma), Phenylmethanesulfonyl fluoride (PMSF, P7626 Sigma), protease inhibitor (P8340 Sigma), DNAse1 (600032 Aligent), phosphatase inhibitor (PhosSTOP™

, PHOSS-RO Roche), cOmplete™ EDTA-free Protease Inhibitor Cocktail (COEDTAF-RO Roche), Pefabloc® SC (PEFBSC-RO Roche), Methyl cellulose (methyl-cellulose M0512 Sigma), Tween®20 (P9416 Sigma), Polybead®Microspheres 4.5 µm (17135-5 Polysciences), Polybead®Microspheres 6 µm (07312-5 Polysciences), Polybead®Microsphere 10 µm (17136-5 Polysciences), Tris base (H5131 Promega), ATP (adenosine 5'-triphosphate) solution (ATP, R0441 Thermo), DL-Dithiothreitol (DTT, 10197777001 Roche), Protocatechuic acid (PCA, 03930590), Protocatechuate 3,4-Dioxygenase from *Pseudomonas sp.* (PCD, P8279 Sigma) .

LIPIDS See Sec. 2.6 for a detailed list of lipids. All lipids were purchased from Avanti Research (Merck Life Science): 1,2-dioleoyl-sn-glycero-3-phosphoethanolamine-N-(lissamine rhodamine B sulfonyl) (ammonium salt) (Rhod-PE, 810150C), 1,2-di-(9Z-octadecenoyl)-sn-glycero-3-[(N-(5-amino-1-carboxypentyl)iminodiacetic acid)succinyl] (nickel salt) (DGS-NTA(Ni) 790404C), 1,2-dioleoyl-sn-glycero-3-phosphoethanolamine-N-(cap biotinyl) (sodium salt) (Biotin-PE, 870273C) .

BUFFERS AND PROTEINS See Secs. 2.6 & 4.5 for more details about buffers. And Sec. 2.6 for more details related to protein purification.

G-buffer was composed of 20 mM Tris (pH 7.8 adjusted with HCl), 0.2 mM $CaCl_2$, and 5 mM DTT. Buffer was filter sterilized (Whatman™ 0.2 µm) and stored at 4 °C. F-buffer was made from G-buffer by adding 50 M KCl, 2 mM $MgCl_2$.

All lyophilized rabbit skeletal muscle actin was purchased from Hypermol (HYPERMOL EK, Germany): Actin (rabbit skeletal muscle alpha actin) (8101), ATTO647-Actin (alpha skeletal muscle actin, rabbit) (A647-actin, 8158), Biotin-Actin (alpha-actin, rabbit skeletal muscle) (biotin-actin, 8109) . Actin was resuspended in G-buffer (with 0.2 mM ATP), aliquoted, snap-frozen and stored at −80 °C.

All protein mixes were made on ice (4 °C), unless otherwise stated.

Centrosomes — Centrosomes were isolated from human lymphoblastic KE37 cells. Cells were grown in RPMI-1640 medium at 37 °C and 5 % CO_2 in 3 L spinner flask. Around 10^9 cells (1 L, 10^6 cells/mL) are required.

SDG [234, 437] — All steps were performed at 4 °C. Cells were treated with nocodazole (1 mM, 200 µL) and Cytochalasin D (5 mM, 200 µL) for 1 h at 37 °C. Cells were washed (1200 rpm/280 g, 8 min) in TBS (1 X), TBS (0.1 X, 8 % sucrose) and resuspended in TBS (0.1 X, 8 % sucrose, 20 mL). Lysis buffer (80 mL, 1 mM HEPES pH 7.2, 0.5 % NP-40, 0.5 mM $MgCl_2$, 0.1 % β-mercaptoethanol, 1 mM PMSF, and protease inhibitors 1 X (Roche tablet)) was added and slowly mixed by inverting the tube (10 times, 5 min). The lysate was centrifuged (3500 rpm/2500 g, 10 min) and the supernatant was filtered through a nylon mesh. HEPES concentration was adjusted to 10 mM. The supernantant was treated with DNAse1 (1 µg mL^{-1}, 30 min). CAPture peptide can be added during the DNAse1 treatment to label the centrosomes. Centrosomes were concentrated by sedimentation (7500 rpm/10 400 g, 30 min) on a sucrose cushion (60 %, 12 mL) and the top $^2/_3{}^{rd}$ of solution was removed. Finally, centrosomes were purified by ultracentrifugation (25 000 rpm, 1 h, SW28 on Beckman) on a discontinuous sucrose gradient (40 %, 50 % and 70 %, 3 mL each). Purified centrosome fractions were collected by perforating a tube at the bottom with a needle (21G) and manually collecting (14 500 µL) fractions. Fractions were tested

using centrosome dynamics assay, and ones with higher yield were flash frozen and stored at –150 °C.

CAPture [465] — All steps were performed at 4 °C. Cells were washed (800 rpm, 5 min) in TBS (1 X), TBS (0.1 X, 8 % sucrose) and resuspended in TBS (0.1 X, 8 % sucrose, 3 mL). Lysis buffer (30 mL, 50 mM Tris-HCl pH 8, 300 mM NaCl, 0.2 % NP-40, 10 % glycerol, phosphatase inhibitors 1 X (Roche tablet), and protease inhibitors 1 X (Roche tablet)) was added and slowly mixed by inverting the tube (10 times, 10 min). The lysate was centrifuged (2000 rpm, 10 min) and the supernatant was filtered through a nylon mesh. The supernantant was treated with DNAse1 (1 µg mL^{-1}, 60 min). CAPture peptide coated beads were added to the lysate and mixed on a rotating wheel (12 rpm, 2 h). The mixture was transferred to a gravity column and washed with BRB80 buffer. Bead slurry was resuspended in BRB80 (800 µL) and transferred to in a microcentrifuge tube. Centrosomes were released from the beads by cleavage with homemade 3C enzyme (1 h). The sample was centrifuged (500 g, 30 s), and centrosome supernatant was flash frozen and stored at –150 °C.

CAPture peptide — For affinity purification of centrosomes analogous to the CAPture method that employs a biotinylated CCDC61 peptide [465], we created a histidine-tagged fusion construct (pED135) consisting of His_8-3C-$mStayGold^{E138D/C174I}$-$FLAG_3$-Avi-$CCDC61^{334-366}$. The protein was expressed at room temperature in Overnight Express™ Instant TB Medium (Novagen 71491) and purified using cOmplete™ His-Tag Purification Resin. Unlike the CAPture peptide, we did not biotinylate the fusion protein and instead employed the (unremoved) histidine-tag for immobilization.

pED135 | His 3C mStayGold $FLAG_3$ Avi CCDC61

```
  1 MGHHHHHHHH DYDIPTTLEV LFQGPMASTP FKFQLKGTIN
 41 GKSFTVEGEG EGNSHEGSHK GKYVCTSGKL PMSWAALGTS
 81 FGYGMKYYTK YPSGLKNWFH EVMPEGFTYD RHIQYKGDGS
121 IHAKHQHFMK NGTYHNIVEF TGQDFKENSP VLTGDMNVSL
161 PNDVQHIPRD DGVECPVTLL YPLLSDKSKC VEAHQNTIIK
201 PLHNQPAPDV PYHWIRKQYT QSKDDTEERD HIIQSETLEA
241 HLAAADYKDH DGDYKDHDID YKDDDDKGLN DIFEAQKIEW
281 HEGSPSPTGG RALRFDPTAF VKAKERKQRE IQMKQQ
```

CAPture peptide-bead complex — Sepharose beads (TALON) were used instead of Dyanbeads [465]. Beads (20 mg mL^{-1}, 100 µL) were washed (TBS-N 20 mL, lysis buffer 10 mL) on a gravity column and resuspended in lysis buffer (800 µL). CAPture peptide (21 µM, 100 µL) was added to the beads. The tube was incubated on rotor (12 rpm, 1.5 h). The CAPture-bead complex was freshly prepared prior to the centrosome purification.

VCA-His — The VCA domain (amino acids 400–501 of murine N-Wasp) with a 10xHis-tag [488] was purified from modified pCoofy1 (43974), received from Kristina Ganzinger (AMOLF, the Netherlands). The protein was expressed in BL21 (DE3) cells. Overnight grown cultures with 50 mg mL^{-1} Kanamycin at 37 °C. The cultures were diluted 1:400 and protein was expressed with 0.5 mM IPTG at an absorbance of 0.6–0.8 OD600 overnight at 17 °C. Cells were collected with centrifuging at 4000 g for 10 min at 4 °C. Cells were resuspended in lysis buffer (Tris 20 mM (pH8.0), NaCl

200 mM, EDTA 1 mM, Glycerol 5 %, Triton X-100 0.1 %, DTT 1 mM and cOmplete™ protease inhibitor). Cells were lysed using sonicator for 3.5 min (30 s on, 59 s off, 30 % power). The lysate was centrifuged at 15 000 g for 15 min at 4 °C, and again at 18 000 g for 30 min at 4 °C. The supernatant was loaded onto a HisTrap™ FF crude nickel column (GE Healthcare 95056-136) and washed (Tris 20 mM (pH8.0), NaCl 200 mM, EDTA 1 mM, glycerol 5 %, Imidazole 20 mM, DTT 1 mM) and eluted (Tris 20 mM (pH8.0), NaCl 200 mM, EDTA 1 mM, glycerol 5 %, Imidazole 300 mM, DTT 1 mM). Fractions were run over 4–15 % SDS-PAGE gel (Bio-Rad 4561086) and were pooled accordingly. Fractions were loaded over Mono Q 4.6/100 PE column (GE Healthcare 17517901) and washed (Tris 20 mM (pH8.0) and DTT 1 mM) and eluted (Tris 20 mM (pH8.0), NaCl 1 M, and DTT 1 mM). Peak fractions were pooled, analysed over 4–15 % SDS-PAGE gel and fractions were pooled accordingly. Pooled fractions were dialysed (Tris 20 mM (pH8.0), EDTA 0.5 mM, glycerol 5 %, DTT 1 mM) overnight at 4 °C. Finally VCA was concentrated as required and labelled with Alexa Fluor® 647 as described in Sonal et al. [488].

Arp2/3 — Arp2/3 was purchased from Hypermol (8413).

α-actinin — α-actinin 4 [489] was purified from a pET-30a(+) (EMD) derivative, as a 6xHis-tagged protein, and purified as described in [490]. The protein was expressed in BL21 (DE3) Rosetta. Overnight grown cultures with 50 mg mL^{-1} Kanamycin and 50 mg mL^{-1} Chloramphenicol at 4 °C. The cultures were diluted 1:1000 and protein was expressed with 0.5 mM IPTG at an absorbance of 0.6–0.8 OD600 overnight at 16 °C. Cells were collected with centrifuging at 4000 g for 10 min at 4 °C. Cells were resuspended in lysis buffer(HEPES 20 mM, NaCl 20 mM, 5 mg mL^{-1} Lysozyme, Pefabloc® SC 0.1 mM and cOmplete™ protease inhibitor). Cells were lysed using sonicator for 3.5 min (30 s on, 59 s off, 30 % power). The lysate was centrifuged at 1 000 000 g for 30 min at 4 °C. The supernatant was loaded onto a HisTrap™ FF crude nickel column and washed (HEPES 20 mM, NaCl 500 mM, Imidazole 25 mM) and eluted (HEPES 20 mM, NaCl 500 mM, Imidazole 500 mM). Fractions were analysed on 4–15 % SDS-PAGE gel and were pooled accordingly. Pooled fractions were loaded over a Superdex™ 200 Increase 10/300 GL column (Cytiva 28990944) with gel filtration buffer (HEPES 20 mM, NaCl 150 mM, DTT 10 mM). Protein was concentrated as required.

IMAGE ACQUISITION AND ANALYSIS Image acquisition was performed as described in Sec. 2.6. The samples were heated to 34 °C to induce tubulin polymerization. For 3D confocal imaging of droplets, Z-stacks were acquired with 0.2 µm (0.1–1 µm). Projections were created using ImageJ (FIJI) built-in plugins — Z project and 3D project.

5.4.2 Methods

Centrosome nucleation assay

Centrosomes were thawed in warm water (37 °C) to activate the centrosomes [235]. The activity of centrosomes was tested in flow chambers. Centrosomes (2 µL, diluted in warm MRB80) were adhered on a clean glass surface by 10 min incubation. The surface was blocked with sequential 10 min incubations of 0.2 mg mL^{-1} PLL-PEG-

biotin, 0.5 mg mL^{-1} κ-casein with intermediate MRB80 washes. A 20 µL protein mix (per centrosome fraction) of 0.5 mg mL^{-1} κ-casein, 50 mM KCl, 0.1 % methylcellulose, 3 mM GTP, 1 x OX, 27.5 µM tubulin (9 % rhodamine-tubulin), and 50 mM glucose was made in MRB80. The protein mixes were added to the flow chambers and the flow chambers were sealed with vacuum grease. MTs were imaged immediately in TIRF mode at 30 °C.

Aster and bead in droplets

Protein mix Due to small reaction volume, volumes of individual components become very small (∼0.5 µL), so the protein mix was split into pre-mix and main mix. Pre-mix was made in bulk to reduce pipetting volume errors. A pre-mix of 0.3 mg mL^{-1} κ-casein, 0.016 % Tween 20, 3 mM GTP, 1 x OX, and 50 mM glucose was made. A 20 µL protein mix with 4.52 µL pre-mix, 40 µM tubulin (3 % rhodamine-tubulin, stock 200 µM), 0.4 % PEG-6000, 10 %v beads (25 X stock), and 20 %v centrosomes was made in MRB80. The mix was airfuged before addition of beads and centrosomes. After addition of centrosomes, the mix was maintained at room temperature (to prevent cold shock to centrosomes).

Lipid-in-oil (LO) dispersion LO dispersion of 99.9 n% DOPC, and 0.01 n% Cy5-PE was made as described in Sec. 2.6.

Formation Droplets were formed by dragging method as described in Sec. 2.6. The samples were heated to 30 °C to induce tubulin polymerization.

Optimizations Crowding — Tubulin polymerization inside droplets is difficult compared to bulk *in vitro* experiments. A PEG-6000 concentration of 0.4 % (from 0 %, 0.2 %, 0.4 %, 0.6 %, 0.8 %, 1.0 % and 1.2 %) was found to be optimal for tubulin concentration of 40 µM (from 25 µM, 30 µM, 35 µM, 40 µM and 45 µM). This ensured high enough tubulin concentration to promote nucleation and minimum crowding with PEG to prevent bundling.

Bead passivation — Polystyrene beads of diameter 4.5 µm, 6 µm and 10 µm were used to mimic a cell nucleus (see Fig. 5.S3(a)). Beads were washed (15 000 g, 15 min) with MRB80 and resuspended with 40 mg mL^{-1} BSA in MRB80, left to incubate on rollers (overnight, cold room). BSA gets adsorbed on the bead surface and passivates it, this prevents tubulin from sticking to the bead surface. Beads were again washed (15 000 g, 15 min) with MRB80 and now resuspended with 1 mg mL^{-1} BSA in MRB80. During this resuspension, bead concentration was increased (to 25 x by pelleting). And free BSA in solution prevents dissociation of BSA from the bead surface.

One each per droplet — Just as centrosome concentration was limiting to encapsulate at least one centrosome per droplet, bead concentration was also limiting. The beads were up concentrated and 25 x (from 0 %, 0.2 %, 0.4 %, 0.6 %, 0.8 %, 1.0 % and 1.2 %) was found to be optimal to statistically encapsulate one centrosome per droplet.

Image and data analysis — Positions of aster centers in droplets were manually annotated in 3D in ImageJ (FIJI). Positions of bead and droplet centers were calculated as following, custom ImageJ macros calculates the 2D center and radius of bead and droplet at each Z-slice. Macro performed following image operations —

Gaussian blur (to reduce noise and smoothening), *Binary*, *Hole fill* (to create solid close shapes), *Watershed* (to detect objects, with conditional erosion (to separate fused objects)), *Edge detection*, and *Circular Hough* transform (to determine the radius and 2D center). 3D center of beads and droplets were determined with a custom python script. Random points in 3D were assigned based on the 2D centers and radius from each Z-slice. These points are fitted to the equation of a sphere in 3D with linear regression using the least square fitting, with residuals calculated as,

$$(\delta x)^2 = \sum_{i=1}^{n} (x_i - x_0)^2 + (y_i - y_0)^2 + (z_i - z_0)^2 - r^2$$

where, (x_i, y_i, z_i) are coordinates of the points in 3D, and (x_0, y_0, z_0) and r are coordinates of center and radius of the object. The size distribution of detected bead radius matches with the CV 10 % of the manufacturer (Polysciences Polybeads®) for 4.5 µm diameter beads (Fig. 5.S2(b)).

Aster and actin cortex in droplets

Protein mix Due to small reaction volume, volumes of individual components become very small (∼0.5 µL), so the protein mix was split into multiple parts.

Actin cortex only mix — A 25 x pre-mix of 1 mM DTT, 1 mM ATP, 1 mM PCA, and 0.05 µM PCD was made in G-buffer. Branched cortex mix with 1 x pre-mix, 8 µM actin (10 % actin-647), 50 nM Arp2/3, and 5 µM His-VCA was made in F-buffer. Cross-linked cortex mix with 1 x pre-mix, 8 µM actin (10 % actin-647, 4 % actin-biotin), 1.6 µM α-actinin, and 0.8 µM Neutravidin (after 30 min) was made in F-buffer.

VCA visualization in branched cortex mix — The same 25 x pre-mix of 1 mM DTT, 1 mM ATP, 1 mM PCA, and 0.05 µM PCD was made in G-buffer. VCA-G-buffer mix with 1 x pre-mix, 4 µM actin (10 % actin-647), 25 nM Arp2/3, and 2.5 µM His-VCA was made in F-buffer. VCA-MRB80 mix with 1 x pre-mix, 8 µM actin (10 % actin-647), 50 nM Arp2/3, 5 µM His-VCA, and 50 mM KCl was made in MRB80.

Actin and tubulin co-polymerization mix — The same 25 x pre-mix of 1 mM DTT, 1 mM ATP, 1 mM PCA, and 0.05 µM PCD was made in G-buffer. Actin mix with 2 µL MRB80 (5 x), 0–50 mM KCl, 0.4 µL pre-mix, 4–8 µM actin (10 % actin-647), 25–50 nM Arp2/3, and 2.5–5 µM His-VCA was made in MRB80. Tubulin mix of 20–40 µM tubulin (10 % rhodamine-tubulin), 1 mM GTP, 5–10 % centrosomes, and 0.5–1 % PEG-6000 was made in MRB80. Actin mix was incubated at room temperature for 30 min and tubulin mix was incubated in a 37 °C water bath for 5 min. Actin and tubulin (final co-polymerization) mixes were made by mixing actin and tubulin mixes in contrasting concentration ranges.

Optimization mixes — Different mixes tried during optimizing actin and tubulin co-polymerization were based on the above-mentioned co-polymerization mix. Changes include, MT seeds in tubulin mix and actin mix in G-buffer; MT seeds and PEG-6000 in tubulin mix and actin mix in MRB80; PEG-6000 in tubulin mix and stabilized actin; centrosomes in tubulin mix; and separate actin and tubulin mixes pre-incubation.

Lipid-in-oil (LO) dispersion DOPC based LO dispersion were made as described in Sec. 2.6. Functional and fluorescent lipids were incorporated (at the expense of

DOPC) based on the requirement of the experiments, **branched cortex** — 10 n% DGS-NTA(Ni), and 1 n% AF488-PE; **crosslinked cortex** — 10 n% biotin-PE, and 1 n% AF488-PE; **VCA visualization** — 10 n% DGS-NTA(Ni), and 1 n% Rhod-PE; and **actin and tubulin co-polymerization** — 10 n% DGS-NTA(Ni), and 1 n% AF488-PE.
FORMATION Droplets were formed by dragging method as described in Sec. 2.6. The samples were heated to 30 °C to induce tubulin polymerization.

5.5 Acknowledgements

We thank Esengül Yildirim, Eli van der Sluis, and Jeffrey den Haan for purifying proteins. We thank Kristina Ganzinger for providing VCA plasmid.

5.6 Supplementary Information

5.6.1 Supplementary Figures

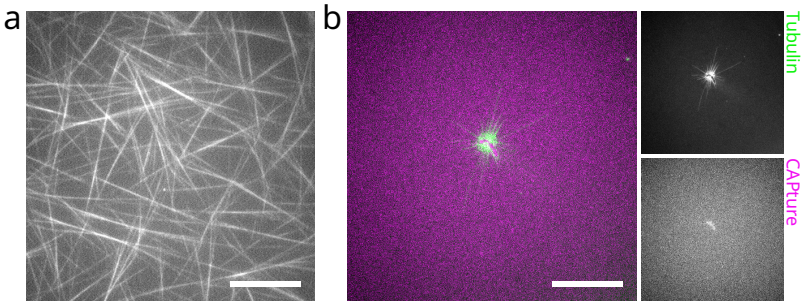

Figure 5.S1: **Asters grown from purified centrosomes** (a) Mesh of spontaneously nucleated MTs in the flow cell with SDG centrosome sample. (b) CAPture purified centrosomes with Ni-NTA Sepharose resin show compact state. Scale bar — 20 µm.

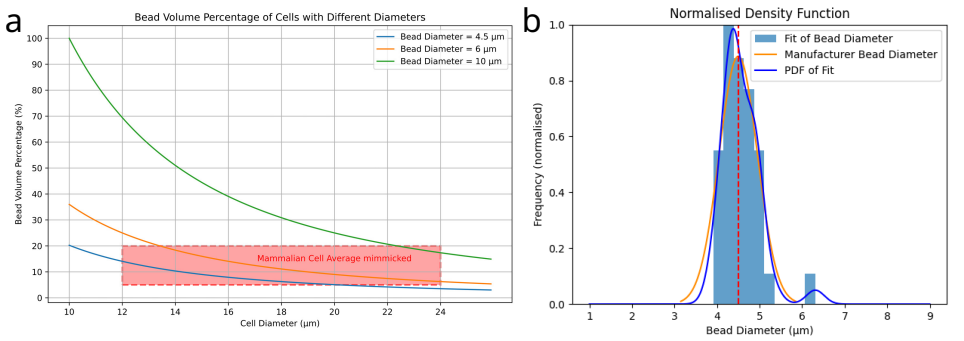

Figure 5.S2: **Bead size quantification for nucleus mimicking.** (a) Plot of bead volume (% of droplet volume) against droplet diameter for 4.5 µm, 6 µm and 10 µm diameter beads. Overlay (shaded red region) covers spectrum nuclear volume and cell diameter of most common cultured mammalian cells [491]. (b) Verification of analysed bead diameters with reference bead diameters. Histogram of analysed bead diameter with max normalised frequency and PDF fit (blue). Manufacturer bead reference [492] diameter - mean 4.5 µm (red dotted line), distribution CV 10 % (orange). The analysed and reference distribution coincide.

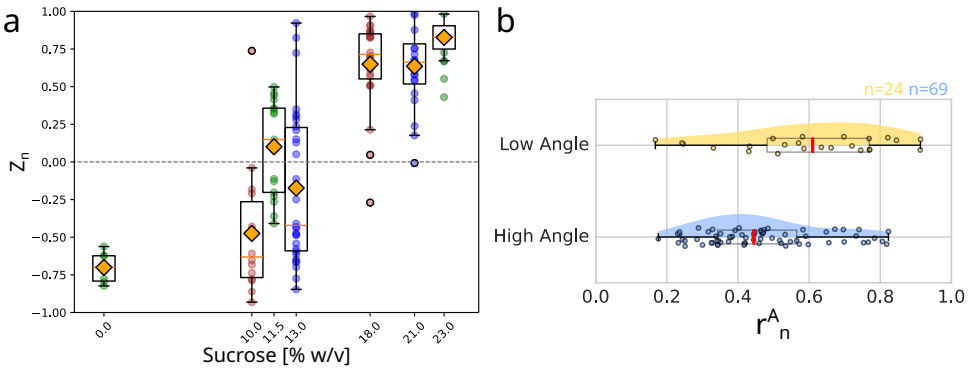

Figure 5.S3: **Quantifcations.** (a) Estimating ideal sucrose concentration. Box plots with mean (yellow diamonds) with normalised Z distance from droplet centre against sucrose concentration in reaction mix for different bead sizes - 4.5 µm, 6 µm, and 10 µm. 12.1 %w/v sucrose results in zero buoyancy on beads. (b) Quantification of r^A in presence of bead, cases — low angle and high angle. Box plot (black) with quartiles, and violin plot (shaded regions) with probability density.

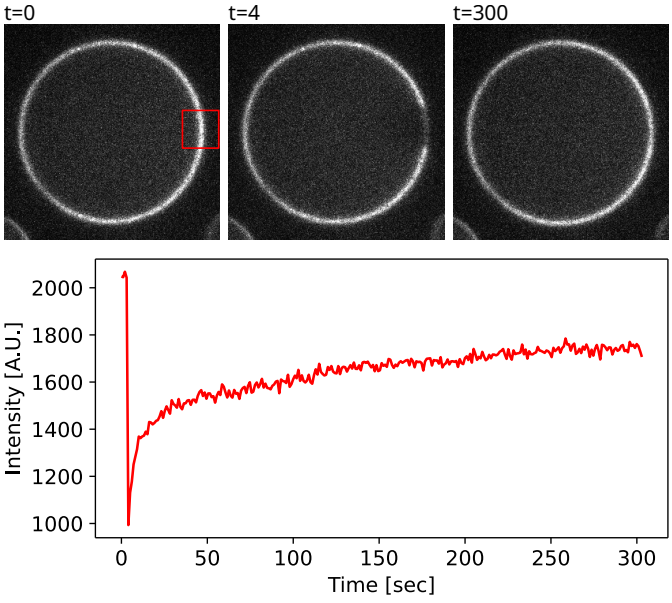

Figure 5.S4: **Dynamic actin cortex.** FRAP curve shows recovers of bleached actin cortex (Fig. 5.7(a)) at the droplet interface. The recovery is rapid but not 100%, but still indicative of active actin cortex made of dynamic actin filaments. The image montage shown above includes the — initial, FRAP-, and last time points.

5.6.2 Supplementary Movies

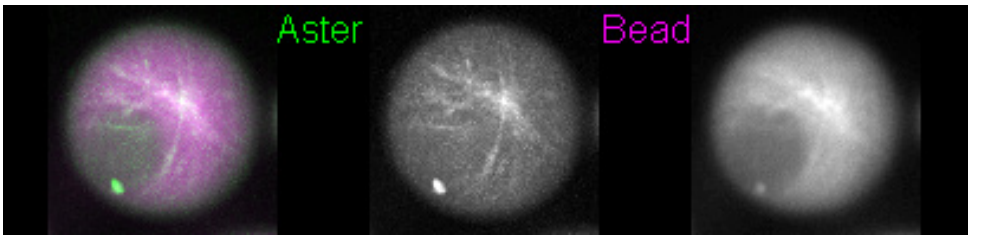

Figure 5.S5: **Aster and bead positioning.** Positioning of aster and bead in a droplet (pseudo-channels — maximum and mean 3D projections respectively). [ ]

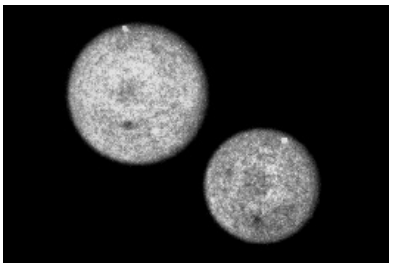

Figure 5.S6: **Actin cortex.** Branched (continuous) actin cortex in droplet (crop Fig. 5.7(c) maximum 3D projection). [ ]

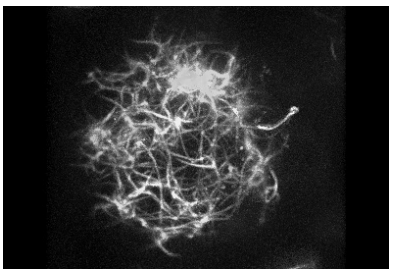

Figure 5.S7: **Actin cortex.** Crosslinked (bundled) actin cortex in droplet (Fig. 5.7(e) maximum 3D projection). [ ]

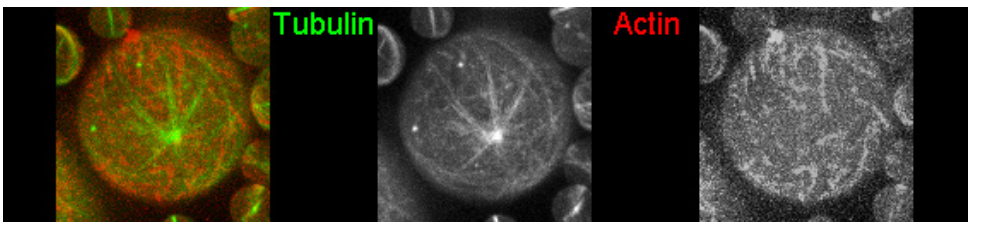

Figure 5.S8: **Co-polymerization in droplet.** Co-polymerized tubulin and actin in droplets, affect the aster positioning due to actin cortex at the interface (crop Fig. 5.9(d)). [ ]

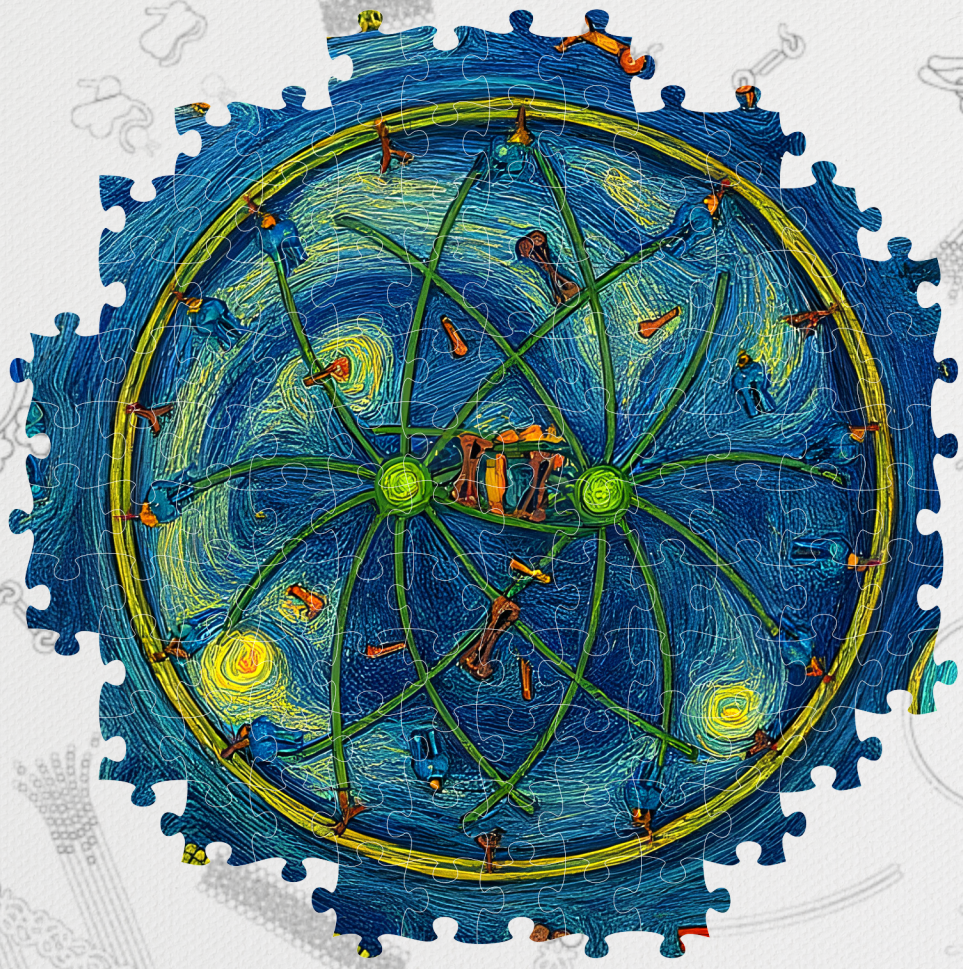

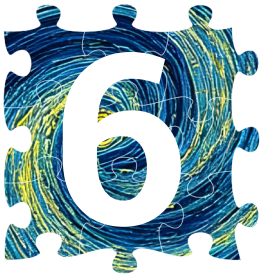

Minimal mitotic spindle positioning in droplets

Like two peas in a pod.
Piecing together.
One-up.

The mitotic spindle is one of the most complicated pieces of the cell. It is a result of a delicate and coordinated force balance. With imitation being the sincerest form of flattery, even a replication of spindle organization from isolated components in a minimal in vitro reconstitution will not only help appreciate the spindle but also help gain quantitative insights into its working. Here, we design a system for asymmetric spindle positioning to mimic the C. elegans embryo first cell division. We first re-build a minimal mitotic spindle and compare our results. We observe metaphase-like organization with just two asters and crosslinker Ase1. Next, we introduce an opto-switch for spatio-temporal regulation of dynein, the cortical pulling force generator. We observed poor photo-activation in droplets and insufficient light-induced MT transport.

A part of this chapter reproduces and compares the minimal aster positioning from Roth et al. [250] (on bioRxiv). And a revised manuscript, Reconstitution of basic mitotic spindles in cell-like confinement. Sophie Roth, Ioana C. Gârlea, https://orcid.org/0000-0003-2988-2628Mathijs Vleugel, Yash K. Jawale, Bela M. Mulder, Marileen Dogterom., is in revision at *Communications Biology*.

6.1 Introduction

Cell division is one of the important cell process, that helps to propagate life. The spindle plays an important role in cell division, it is responsible for segregation of genetic material, chromosomes. Reconstituting an *in vitro* minimal spindle will help better understanding its functioning. As discussed in Sec. 1.1.2, the spindle is a dynamic bipolar structure build from MTs and MAPs, and their interactions with other cellular organelles and cell boundary (Fig. 6.1(b)) [172, 173, 176, 493, 494]. MTs from the asters growing against the cell cortex generate length-dependent pushing forces [130, 131, 134, 495]. MTs also interact with the dynein at the cortex to generate pulling forces by MT shrinkage [136]. Bipolar spindle assembly also requires antiparallel MTs from the two asters to interact and make interpolar MTs, which regulate the spindle length during the cell division [496–500]. These antiparallel MT interactions are facilitated by kinesin-5, which generate outward pushing forces [201, 501–509], and MAP65 (Ase1), a diffusive crosslinker, which generates friction and tends to decrease the antiparallel overlap [206, 510–512]. It can generate enough forces to oppose kinesin MT sliding activity [204]. The spindle is a result of the

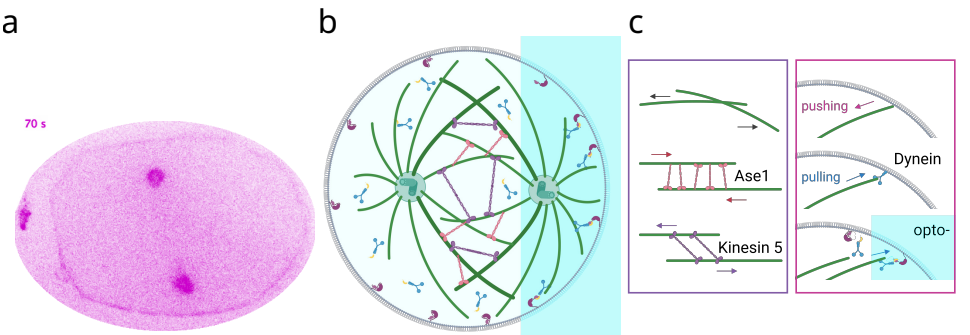

Figure 6.1: **Controlling spindle positioning with light.** (a) Artificially induced transverse positioning of the spindle by local recruitment of LIN-5-ePDZ (dynein adaptor) using photo activation and its subsequent rotation back to the anterior-posterior orientation, during *C. elegans* embryo first cell division. Movie adapted from [163]. [ ] (b) Schematic representation for asymmetric positioning of minimal spindle in W/O droplet (lipids), with MT asters, motors like dynein, Kinesin5, and MAP Ase1. Blue laser is used to trigger the spatiotemporal activation. Dynein is recruited to the cortex via photo-activated iLID-SspB, generating an asymmetric distribution. This results in asymmetric positioning of the minimal spindle. [ ] (c) Force generating components in the minimal spindle. In the midplane, MTs originated from opposite asters interact, generating steric repulsive forces [513], and antiparallel MTs experience attractive forces from crosslinkers (Ase1) [204], and repulsive forces due to Kinesin5 [201]. At the cortex, MTs growing against the membrane, generate pushing forces [26], and MTs interacting with cortical dynein are subjected to pulling forces [136]. This cortical pulling force can be regulated with opto-switches (iLID-SspB). [163]. (Images created with BioRender.com)

overall force balance between these pulling and pushing forces (Fig. 6.1(c)). Spindle positioning and orientation is also influenced by cell shape and size [494, 514–517].

As discussed in Sec. 1.2, the top down approach provides qualitative insights into the overall cellular process, and bottom-up reconstitutions provide more quantitative insights into the individual components involved. In Sec. 5.1, we developed a basic assay to reconstitute cytoskeletal systems in droplets. Here, we will build on the assay to reconstitute a minimal mitotic spindle to get a better understanding of the process. The aim is to replicate the asymmetric positioning of the spindle during the first cell division of *C. elegans* embryo. We first start with rebuilding the minimal spindle, similar to 3D *in vitro* reconstitutions as described in Roth et al. [250]. For this, we assemble different stages of the spindle, single aster and double aster positioning, and compare them with earlier experiments. As a next step, we try to position the spindle asymmetrically, as in worm embryo, where more dynein (force generators) is present on the posterior side compared to anterior, which results in displacement of spindle towards the posterior side (see Sec. 1.3.2). We increase the complexity of the reconstitution by introducing the orthogonal spatiotemporal regulation tools (as described in Sec. 5.1).

A similar approach has been demonstrated in *C. elegans* embryo, to perturb spindle positioning by modifying the dynein localization at the cortex using an opto-switch (Fig. 6.1(a)) [163]. We used iLID, an LOV based opto-switch, to spatially and temporally control the recruitment of dynein at the cortex. It acts as a substitute to the complex up-stream pathways present in the cell, that regulate the asymmetric distribution of dynein at the cell cortex. In our 3D *in vitro* reconstitution, upon photo-activation in one half of the droplet, we expect asymmetric dynein recruitment on that side of cortex, increasing the cortical pulling forces and resulting in asymmetric positioning of the minimal spindle (Fig. 6.1(b)).

6.2 Results

6.2.1 Re-building a minimal spindle

We reconstituted different stages of spindle in W/O droplets, in order to build the minimal spindle. We compared our results with the minimal spindle by Roth et al. [250]. Asters were formed from MTs growing from centrosomes encapsulated in droplets. Encapsulation yielded droplets containing centrosomes ranging from 0 to 2+[1] due to the centrosomes' limiting concentration. The asters in droplets were categorised intro three regimes, based on the relative lengths of the MTs with respect to the size of the droplets, where MT lengths were shorter (1), approximately equal (2), and longer (3) than the radius R of the droplet.

Single aster positioning

Positioning of a single aster was quantified as $r_n = r^A/R$ (Fig. 6.2(a)), where r^A is the distance of the aster to the centre of the droplet, and R is the radius of the droplet. An aster was considered centred if it localized within the central 5 % volume of the droplet, corresponding to $r_n \leq 0.36$. For regime 1, asters tend to diffuse around in

[1] In a limiting case, a Poisson distribution is expected, which can be right-shifted by increasing the volume fraction of centrosomes in the reaction mix.

the droplets, as average MT lengths are shorter. For regime 2, we saw the asters centre in the droplets (Fig. 6.2(b)), somewhat similar to the 9 % observed in Roth et al. [250] (Fig. 6.S1(a)). Here, the aster should not have freedom to move around, as the MTs should just be in contact with the cortex. But for regime 3, we saw the asters at the droplet periphery (Fig. 6.2(b)), just like the 100 % observed in Roth et al. [250] (Fig. 6.S1(b)). Aster centering was only possible for MT lengths of approximately equal to the radius of the droplet. If MTs grow longer, they exert the pushing force, causing them to buckle and eventually achieve a peripheral position, to straighten the rigid MTs, relaxing the buckling strain. This was in accordance with previously published predictions [191].

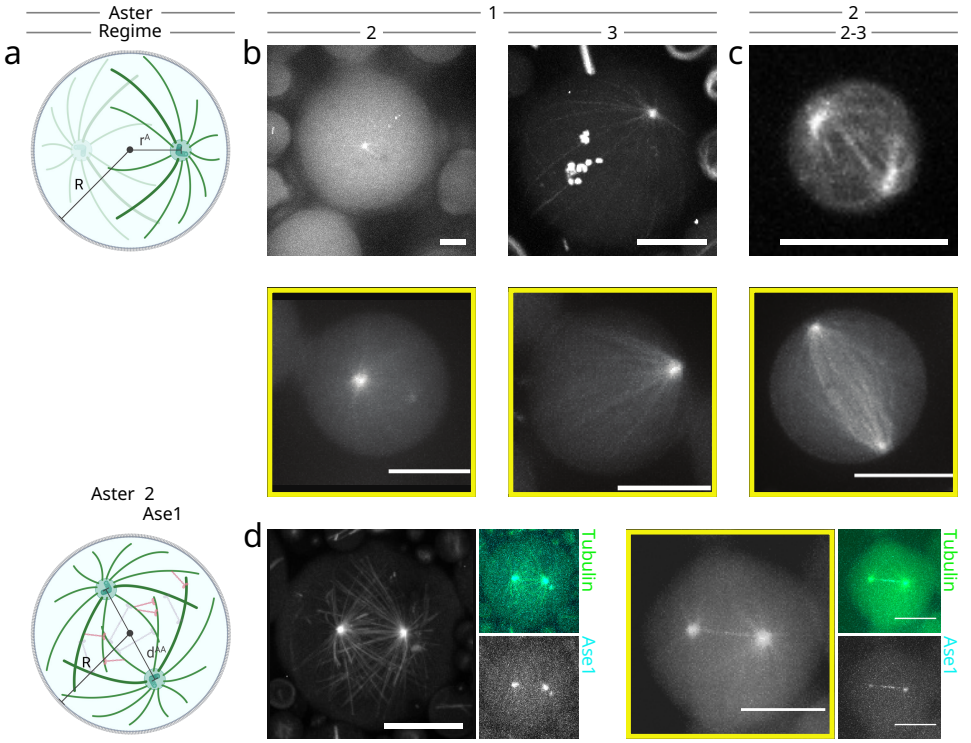

Figure 6.2: **Rebuilding the minimal spindle components.** (a) Schematic representing steps of building a minimal spindle in W/O droplet (lipids), (top) single and double aster positioning, quantified using $r_n = r^A/R$, and (bottom) effect of interaction of MAPs Ase1 with double asters, quantified using $d_n = d^{AA}/2R$. (Images created with BioRender.com) (b) Comparing pushing forces in single aster positioning (regime 2 (Tubulin 25 µM) and 3 (Tubulin 30 µM)). (c) Comparing pushing forces in double aster positioning (regime 2-3 (Tubulin 25 µM)). (d) Comparing effect of Ase1 (36 nM) on double aster positioning (Tubulin 20 µM). Images are maximum intensity projection (MIP) of confocal Z-stack. (see Fig. 6.S3 for a 3D projection.) Yellow boxes represent the reference images used for comparison from previous minimal spindle reconstitution by Roth et al. [250]. Scale bar — 10 µm.

Double aster positioning

Positioning of double asters was quantified in terms of aster separation, as $d_n = d^{AA}/2R$ (Fig. 6.2(a)), where d^{AA} is the inter-aster distance (between the centres of the two asters), and R is the radius of the droplet. For regime 1, asters tend to remain fairly in the centre of the droplets. For regime2-3, we saw the asters more towards the droplet periphery ($d_n > 0.8$) on diametrically opposite ends (Fig. 6.2(c)), like the 67 % observed in Roth et al. [250] (Fig. 6.S1(c)). The asters position away from each other due to separation dependent steric repulsive force between them. Density of MTs decreases going away from the aster centre core region, and also as the MT length increases, MT bending force decreases. This prevents asters from getting too close to each other.

Aster-aster attraction with crosslinker

The effect of MAPs was tested in the presence of double asters, and quantified with $d_n = d^{AA}/2R$ (Fig. 6.2(a)). To create interpolar connection between the asters via antiparallel MT bundling, we introduced a diffusive cross-linker Ase1 [518]. In the presence of 36 nM Ase1, we saw the interpolar MTs forming connections and the asters were still oriented on diametrically opposite ends, but the inter-aster distance decreased (Figs. 6.2(d) & 6.S3). Fewer asters pairs locate at the periphery, like the 11 % observed in Roth et al. [250] (Fig. 6.S1(d)). Ase1 with its crosslinking and diffusive nature, decreases the aster separation and overcomes the aster-aster repulsive forces.

We could have replicated the aster positioning experiments in the presence of cortical dynein, and kinesin-5 from Roth et al. [250], but we wanted to implement spatiotemporal recruitment instead of just uniform binding.

6.2.2 Opto-genetic control

Optogenetic switch provide a way to control the recruitment of proteins in a spatial and temporal manner. Some of the commonly used opto-switches are derived from phototropins, first discovered in *Arabidopsis* [519]. Phototropins are light-activated kinases (and receptors) that binds flavin mononucleotide (FMN) and responds to blue light. These have two LOV (light, oxygen, or voltage) domains [520], specialized PAS superfamily domains with an extra helix at the C-terminal, called Jα. Upon blue light illumination, the non-covalent LOV2-FMN complex is temporarily converted into a covalent flavin-cystine(C^{39}) adduct, and leads to conformational change in LOV2 domain [521–523]. Since the Jα helix is present under the LOV domain, close to the FMN cofactor, the conformational change propagates to Jα helix and undocks it from the LOV2 domain. This reversible undocking of Jα helix upon photoactivation is exploited in LOV based ontogenetic applications (see review [524]). In these tools[2], peptides binding to the protein of interests are typically appended to

[2]Switches: LOVTRAP, LID, TULIP

the Jα helix, and remain sterically blocked in the dark state (Fig. 6.3(a)). Upon illumination, Jα helix undocks from LOV2, and the peptide is available for binding to its binding partner.

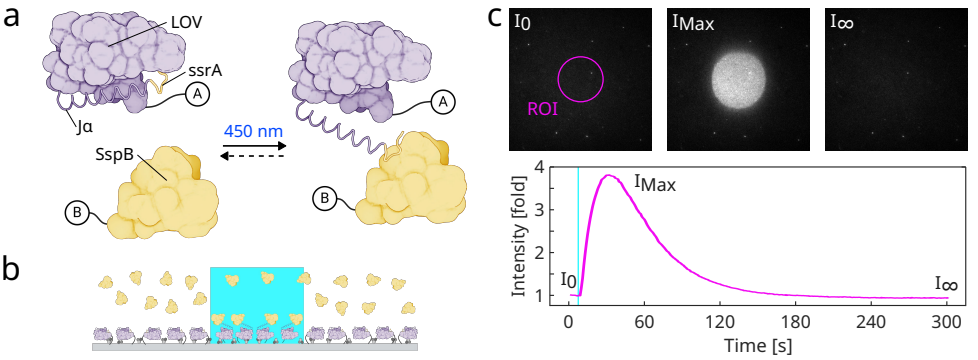

Figure 6.3: **Light-induced heterodimerization with iLID.** (a) Schematic of a photoswitch, improved light-inducible dimer system (iLID). The SsrA peptide is attached to C-terminal Jα helix of the second photosensitive LOV domain of phototropin 1 from *Avena sativa*. In the dark, SsrA peptide is sterically blocked. Upon activation with 450 nm blue light, LOV domain undergoes conformational change, the helix undocks and the SsrA peptide is available for binding to its binding partner SspB (nano variant). This conformation change is reversible. Other protein-of-interests can be attached to the iLID and SspB (e.g. 'A' — LactC2 peptide and 'B' — mCherry) to create light inducible heterodimerization protein pairs. (b) Schematic of flow chamber assay, glass surface is coated with iLID and passivated with κ-casein, SspB is flowed in. SspB binds to iLID upon selective illumination with 488 nm laser. (Images created with BioRender.com) (c) Spatio-temporal control on iLID-SspB binding (biotin-iLID-YFP and $SspB_{nano}$-mCherry). (top) [Spatial] A circular ROI is illuminated once with a flash of 488 nm laser. TIRF Image montage of SspB intensities, representing time points — I_0 pre-activation, I_{Max} maximum (following a fast activation), and I_∞ steady state (following a slower deactivation). (bottom) [Temporal] Corresponding SspB binding dynamics. Intensity of SspB is normalized with averaged pre-activation ROI intensity to obtain a fold increase.

Spatio-temporal regulation

We use an improved light-inducible dimer (iLID) system. iLID are variants of oLID [525], tuned for tighter and higher photoactivation, based on predictive point-mutation analysis and phage-display screening. In this system, the bacterial SsrA peptide is attached to the C-terminal Jα helix of LOV2 domains of phototropin 1 from *Avena sativa* [240]. The SsrA peptide is sterically blocked in the dark state of iLID, as the end of Jα helix is in close contact with LOV domain (Fig. 6.3(a)). Following the activation with blue light (450 nm), the Jα helix undocks and partially unfolds, allowing the SsrA peptide to bind its natural binding partner, SspB. The SsrA-SspB binding is reversible, LOV domain slowly decays into the inactive (dark) sate in absence of light. We have used SspB nano with K_d of 132 nM and 4.7 µM with light and dark

state of iLID respectively [240].

We tested the photo-activation of iLID on a glass surface in a flow chamber assay (Fig. 6.3(b)). The acid Piranha cleaned glass is coated with PLL-PEG-biotin and Neutravidin, and passivated with κ-casein. Later incubated with biotin-iLID and the excess is washed away. $SspB_{nano}$-mCherry is flowed in, and the chamber is sealed. A central circular region (ROI) of the field of view (FOV) is illuminated with a flash of a blue (488 nm) laser. This results in activation of iLID in the ROI and SspB is quickly recruited on the glass surface, with I_{Max} ∼4 x fold increase in SspB intensity (compared/normalized with pre-activation SspB intensity in the ROI) (Fig. 6.3(c)). We also see a slight in activation of iLID outside the ROI. After just a flash of blue light, in the absence of light, the iLID goes back to dark (inactive) state and SspB intensity overtime (I_∞) in the ROI fall back to pre-activation levels (I_0) (Fig. 6.3(c)). The iLID can be hold in an active state for longer periods of time, with constant illumination, but illumination with high laser power can permanently switch some fraction of iLID [526, §6]. The preliminary dissociation rate, k_{off} ∼0.038 s^{-1} matches the reported value for SsrA-$SspB_{nano}$ binding (0.037 s^{-1}) [526, §6]. This provides a way for recruiting proteins in a spatial (by controlling the illumination region) and temporal (by controlling the illumination frequency) manner using light.

Activation issues in Droplets

Increasing the dimensionality, from 2D glass surface to 3D sphere, we encapsulated iLID opto-system in W/O droplets. Droplets are generated by pipetting, LactC2-YFP-iLID (1 µM) and $SspB_{nano}$-mCherry (1 µM) solution with a lipid-oil (DOPS 30 n%, Span 80 0.7 %v/v) solution. LactC2 tag binds to the negatively charged lipids like DOPS. LactC2-YFP-iLID is seen bound to DOPS lipid monolayer at the droplet cortex. While the $SspB_{nano}$-mCherry is in the lumen (Fig. 6.4(a)). Upon illumination with a flash of blue light, the $SspB_{nano}$-mCherry however, is still in the lumen, and no increase in SspB intensity is seen at the cortex (Fig. 6.4(b)). The iLID at the cortex is unable to bind and recruit SspB to cortex inside droplets.

Optical control on dynein

Having demonstrated the spatiotemporal control of recruitment of proteins with opto-switch iLID on a glass surface, we tested the recruitment of opto-dynein (SspB-mCh-dynein). Upon illumination by blue light, iLID-biotin (attached to the surface) recruits the opto-dynein, and MTs start gliding (Fig. 6.5(a)).

MTs were enriched near the coverslip with addition of methycellulose (MECE) [527]. In presence of regular (direct surface bound) dynein, MTs moved directionally on the coverslip (Fig. 6.5(c)), while in absence of dynein, MTs just diffused around (Fig. 6.5(b)). With opto-dynein, in absence of illumination, MTs seemed bound to the surface, and showed some non-directional, diffusive motion (Fig. 6.5(d)). Upon illumination with blue light, opto-dynein binds to the surface, but only a few MTs show limited directional motion (Fig. 6.5(e)). Observed speed and efficiency of opto-dynein is not optimal. Since opto-dynein is present in the solution, prior to photo-activation, it can bind to the floating MTs and already walk towards the minus end.

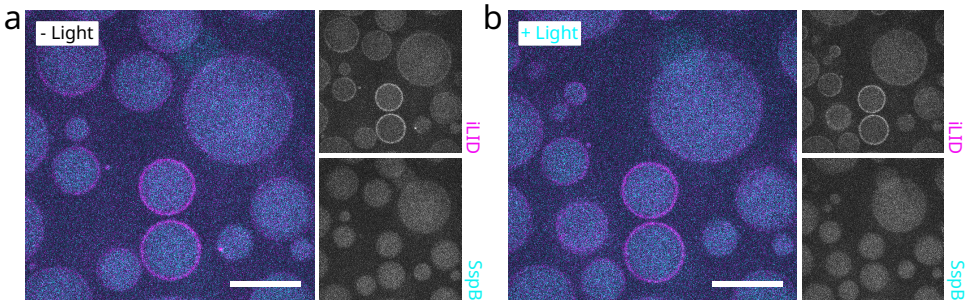

Figure 6.4: **Photo-activation in droplets.** Encapsulating LactC2-YFP-iLID and $SspB_{nano}$-mCherry in W/O droplets. (a) Pre-activation. iLID is at the cortex (LactC2 tag targets DOPS lipids at the interface) and SspB is in the lumen. (a) After 488 nm activation, SspB is still in the lumen. No signs of recruitment to iLID at the cortex. iLID-SspB has activation and binding issues on lipid monolayer at the droplet W/O interface. Scale bar — 20 µm.

This dynein (from budding yeast) is super processive ([138]) and can accumulate on at the minus end. This can result in traffic jam formation for MT gliding [528, 529].

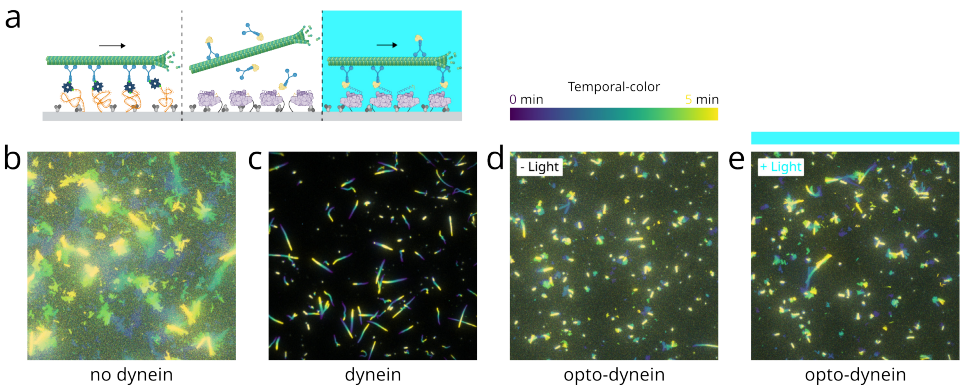

Figure 6.5: **Photo-activated gliding assay.** (a) Schematic of MT gliding assay(s), glass surface passivated with BSA, PLL-PEG-biotin, and neutravidin. Surface is incubated with dynein-biotin-GFP (for classical gliding assay), and iLID-biotin (for opto-gliding assay). SspB-mCh-dynein (2 nM) is present in opto-gliding assay. (Images created with BioRender.com) Following are temporal color-coded maximum intensity projections of MT displacement during, (b) no motor, (c) dynein-biotin-GFP (attached to the surface), and with SspB-mCh-dynein during (d) dark, and (e) photo-activated state. Dynein binds to the surface upon illumination with 488 nm laser. Image scale — 81.92 µm.

6.3 Discussion

Crucial to achieving asymmetric spindle positioning *in vitro* reconstitution requires two foundations, first a minimal spindle, and second an ability for an external spatiotemporal regulation. The following discussion summarizes our efforts on both the fronts.

6.3.1 Reproducing the minimal spindle

We were able to reproduce the basic parts required for the assembly of the minimal spindle, as described by Roth et al. [250]. We found similar single and double aster positioning, in absence of dynein. Longer MTs position the asters peripherally to minimize the bending and pushing forces experienced by them. In the presence of two asters and no MAPs, they acquire peripheral position by repelling each other to the cortex. It has been proposed that pushing from MTs of opposite asters can separate centrosomes during prophase [530]. We think this strong aster-aster repulsive forces are dependent of density and mean length of MTs. We also saw overcoming of aster-aster repulsive forces due to attractive forces in the antiparallel mid-spindle MTs created by addition of Ase1.

Bipolar spindle organization is usually explained with the classic push-pull model [190], in which separation of centrosomes is driven by opposing activity of motors in the MT overlap. Our results might not be able to show spindle dynamics, like aster separation, due to the absence of the activity of cortical dynein and kinesin-5. But to an extent it resembles a bipolar spindle like organization. The *in vitro* reconstituted minimal spindle, helps dissect the role of individual components in the spindle organization and positioning (Fig. 6.6). Growing MTs causes aster separation, organizing into an anaphase-like spindle, while balancing repulsive forces with crosslinking MAPs, results in a more metaphase-like spindle organization. It will be interesting to test the spindle organization in presence of all the MAPs, dynein, kinesin-5, and Ase1 together. Also interesting would be to further increase the complexity of spindle with asymmetric dynein localization for asymmetric spindle positioning.

6.3.2 Suboptimal spatiotemporal control

Having control over the recruitment of proteins at the cortex allows for increased complexity in the reconstitution. However, proteins recruitment to the cortex is regulated by *in vivo* signaling pathways. Using optogenetic switches, the need for these complex pathways can be eliminated. In our reconstitution of iLID opto-system in droplets, we did not see any sign of activation and recruitment of SspB to iLID. Previous attempts by Vendel [481, §5] at encapsulating iLID opto-sytem in W/O droplets faced similar issues. The recruitment of iLID to the cortex varied from batch to batch, also further affecting the activation and recruitment of SspB. Tuning the membrane recruitment anchor of iLID and insertion of linkers of varying length also did not improve the iLID's photo-activation at the droplet cortex[3].

[3] [personal communications] Anne Doerr, Christophe Danelon lab (Delft University of Technology, Delft, Netherlands) mentioned, trying different tags, -biotin and -His, and addition of linkers with different

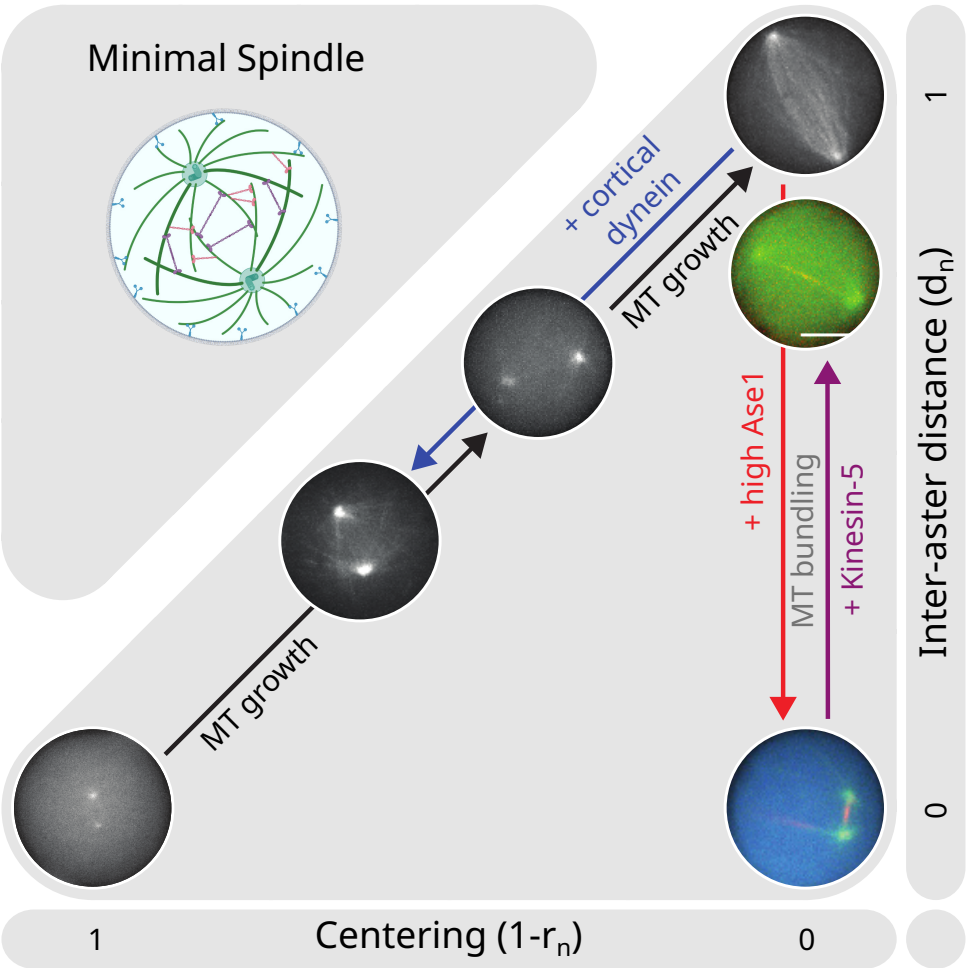

Figure 6.6: **Schematic diagram of spindle configurations.** Schematic based on from Roth et al. [250].

We tested photo-activation of iLID on a supported lipid bilayer (SLB) (Fig. 6.S2(a)) in a flow chamber assay, instead of bare glass surface or the lipid monolayer of droplets. LactC2-YFP-iLID is attached to the SLB (DOPS) on the glass surface, and $SspB_{nano}$-mCherry (0.1 µM) is flowed in. A regional illumination with flash of blue light, results in activation of iLID, and rapid SspB recruitment is observed (Fig. 6.S2(b)). Thus, the lack of response to photo-activation in droplets suggests that there maybe a problem with the lipid monolayer at the oil-water interface. A

length, to create space and separate iLID away from the oil-water interface, did not improve iLID's response to illumination.

single layer of lipids may not be enough to prevent iLID protein (and it's hydrophobic regions and amphipathic Jα helix) from interacting with the hydrophobic oil. Hence, no spatio-temporal control can be achieved in droplets. Opto-control in droplets remains challenging.

We also tested photo-activation of opto-dynein for spatiotemporally regulated MT movement, and it did not enable significant MT transport, as compared to just surface bound dynein. Previous attempts by Kok [526, §5] at inducing MT gliding with opto-control on dynein recruitment observed similar inefficiency, while opto-control with iLID for MT gliding has been demonstrated for kinesin [531]. Alternative opto-switch like PhyB-PIF, shown to create opto-bidirectional transport [532], can be tried to solve the photo-activation related issues. The issues of no photo-activation in droplets, and suboptimal MT gliding by opto-dynein needs to be addressed, for a successful asymmetric positioning of the minimal spindle *in vitro* reconstituted droplets.

6.4 Material and Methods

6.4.1 Materials

Chemicals See Secs. 2.6, 4.5 & 5.4 for a detailed list of chemicals.

Lipids See Secs. 2.6 & 5.4 for a detailed list of lipids.

Buffers and proteins See Secs. 2.6 & 5.4 for more details about buffers. And Sec. 2.6 for more details related to protein purification.

Ase1 — Ase1 was a kind gift from Marcel Janson (Wageningen University & Research, the Netherlands).

Kinesin5 — Kinesin5 was a kind gift from Zdeněk Lánský (Institute of Biotechnology, Czech Academy of Sciences, Czech Republic).

Biotin-YFP-iLID and **biotin-iLID** — Biotinylated variants of iLID (with YFP) were purified in-house as described in Guntas et al. [240], see [526, §5] for more details.

Biotin-GFP-dynein — Biotin-GFP-dynein is based on *Saccharomyces cerevisiae* GST-dynein331 construct by Reck-Peterson et al. [138], and was purified in-house from yeast, and biotinylated on SNAP tag as described in [138, 228, 533]. The GST tag artifically dimerizes the truncated monomeric dynein.

SspB-mCh-dynein — The SspB-mCh-dynein construct is a derivative of strain RPY1084 (*P_{GAL1}-ZZ-TEV-GFP-3xHA-SNAP-GST-DYN1$_{331kDa}$-HALO-KanR*) [534] that was expressed and purified accordingly [138]. For the creation of strain EDY2411 (*P_{GAL1}-ZZ-3C-SspB^{nano}-mCherry-3xHA-SNAP-GST-DYN1$_{331kDa}$-HALO-KanR*) the TEV-GFP region from RPY1084 was replaced by *3C-SspB^{nano}-mCherry*. Cloning strategies and amino acid sequence are given below.

EDY2411 | ZZ 3C SspB^{nano} L mCherry 3xHA SNAP GST Dynein331 Halo[4]

```
  1 MCMAGLAQHD EAVDNKFNKE QQNAFYEILH LPNLNEEQRN
 41 AFIQSLKDDP SQSANLLAEA KKLNDAQAPK VDNKFNKEQQ
```

[4] An old variant of Halo, DhaA tag.

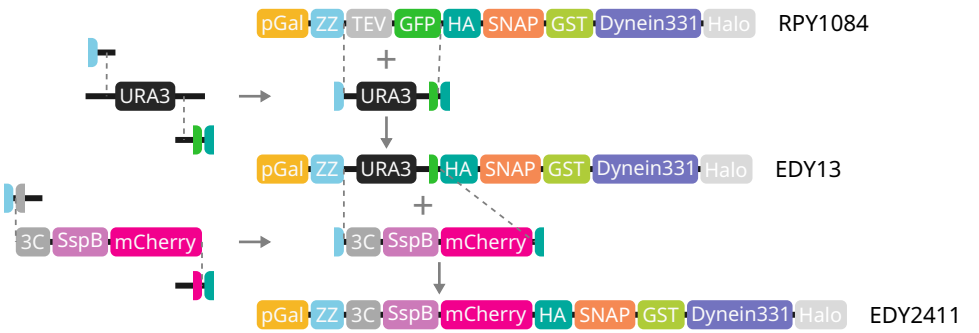


```
  81 NAFYEILHLP NLNEEQRNAF IQSLKDDPSQ SANLLAEAKK
 121 LNDAQAPKVD ANSAGKSTLE VLFQGPLGSM DLSGLTLQEF
 161 SSPKRPKLLR EYYDWLVDNS FTPYLVVDAT YLGVNVPVEY
 201 VKDGQIVLNL SASATGNLQL TNDFIQFNAR FKGVSRELYI
 241 PMGAALAIYA RENGDGVMFE PEEIYDELNI GPWGGGGSKL
 281 VSKGEEDNMA IIKEFMRFKV HMEGSVNGHE FEIEGEGEGR
 321 PYEGTQTAKL KVTKGGPLPF AWDILSPQFM YGSKAYVKHP
 361 ADIPDYLKLS FPEGFKWERV MNFEDGGVVT VTQDSSLQDG
 401 EFIYKVKLRG TNFPSDGPVM QKKTMGWEAS SERMYPEDGA
 441 LKGEIKQRLK LKDGGHYDAE VKTTYKAKKP VQLPGAYNVN
 481 IKLDITSHNE DYTIVEQYER AEGRHSTGGM DELYKSRYPY
 521 DVPDYAGYPY DVPDYAGSYP YDVPDYAMDK DCEMKRTTLD
 561 SPLGKLELSG CEQGLHRIIF LGKGTSAADA VEVPAPAAVL
 601 GGPEPLMQAT AWLNAYFHQP EAIEEFPVPA LHHPVFQQES
 641 FTRQVLWKLL KVVKFGEVIS YSHLAALAGN PAATAAVKTA
 681 LSGNPVPILI PCHRVVQGDL DVGGYEGGLA VKEWLLAHEG
 721 HRLGKPGLGG SMSPILGYWK IKGLVQPTRL LLEYLEEKYE
 761 EHLYERDEGD KWRNKKFELG LEFPNLPYYI DGDVKLTQSM
 801 AIIRYIADKH NMLGGCPKER AEISMLEGAV LDIRYGVSRI
 841 AYSKDFETLK VDFLSKLPEM LKMFEDRLCH KTYLNGDHVT
 881 HPDFMLYDAL DVVLYMDPMC LDAFPKLVCF KKRIEAIPQI
 921 DKYLKSSKYI AWPLQGWQAT FGGGDHPPKS D---Dynein
 961 331------- GSMGSEIGTG FPFDPHYVEV LGERMHYVDV
1001 GPRDGTPVLF LHGNPTSSYL WRNIIPHVAP SHRCIAPDLI
1041 GMGKSDKPDL DYFFDDHVRY LDAFIEALGL EEVVLVIHDW
1081 GSALGFHWAK RNPERVKGIA CMEFIRPIPT WDEWPEFARE
1121 TFQAFRTADV GRELIIDQNA FIEGALPMGV VRPLTEVEMD
1161 HYREPFLKPV DREPLWRFPN ELPIAGEPAN IVALVEAYMN
1201 WLHQSPVPKL LFWGTPGVLI PPAEAARLAE SLPNCKTVDI
1241 GPGLFLLQED NPDLIGSEIA RWLPGLAG*
```

Dynein331

```
Linker AAA1 AAA2 AAA3 AAA4 Lis1 site MT site AAA5 AAA6
  1 DQLTHVVEEV KTYDLVWRSI KNLWEDVQRT FETPWCRVDV
```

```
  41 LLLQSDLANF LRRADELPRA VKQFEMYKSL FSQVNMLTSV
  81 NKILVELKDG ALKPRHWNMI FRDIGKRQIQ KNLLDKLEFS
 121 LKDVMVLNLT LNEILLTKII ERAQKEFVIE KSLNRIKKFW
 161 KEAQYEVIEH SSGLKLVREW DVLEQACKED LEELVSMKAS
 201 NYYKIFEQDC LDLESKLTKL SEIQVNWVEV QFYWLDLYGI
 241 LGENLDIQNF LPLETSKFKS LTSEYKMITT RAFQLDTTIE
 281 VIHIPNFDTT LKLTIDSLKM IKSSLSTFLE RQRRQFPRFY
 321 FLGNDDLLKI IGSGKHHDQV SKFMKKMFGS IESIIFFEDS
 361 ITGVRSVEGE VLNLNEKIEL KDSIQAQEWL NILDTEIKLS
 401 VFTQFRDCLG QLKDGTDIEV VVSKYIFQAI LLSAQVMWTE
 441 LVEKCLQTNE FSKYWKEVDM KIKGLLDKLN KSSDNVKKKI
 481 EALLVEYLHF NNVIGQLKNC STKEEARLLW AKVQKFYQKN
 521 DTLDDLNSVF ISQSGYLLQY KFEYIGIPER LIYTPLLLVG
 561 FATLTDSLHQ KYGGCFFGPA GTGKTETVKA FGQNLGRVVV
 601 VFNCDDSFDY QVLSRLLVGI TQIGAWGCFD EFNRLDEKVL
 641 SAVSANIQQI QNGLQVGKSH ITLLEEETPL SPHTAVFITL
 681 NPGYNGRSEL PENLKKSFRE FSMKSPQSGT IAEMILQIMG
 721 FEDSKSLASK IVHFLELLSS KCSSMNHYHF GLRTLKGVLR
 761 NCSPLVSEFG EGEKTVVESL KRVILPSLGD TDELVFKDEL
 801 SKIFDSAGTP LNSKAIVQCL KDAGQRSGFS MSEEFLKKCM
 841 QFYYMQKTQQ ALILVGKAGC GKTATWKTVI DAMAIFDGHA
 881 NVVYVIDTKV LTKESLYGSM LKATLEWRDG LFTSILRRVN
 921 DDITGTFKNS RIWVVFDSDL DPEYVEAMNS VLDDNKILTL
 961 PNGERLPIPP NFRILFETDN LDHTTPATIT RCGLLWFSTD
1001 VCSISSKIDH LLNKSYEALD NKLSMFELDK LKDLISDSFD
1041 MASLTNIFTC SNDLVHILGV RTFNKLETAV QLAVHLISSY
1081 RQWFQNLDDK SLKDVITLLI KRSLLYALAG DSTGESQRAF
1121 IQTINTYFGH DSQELSDYST IVIANDKLSF SSFCSEIPSV
1161 SLEAHEVMRP DIVIPTIDTI KHEKIFYDLL NSKRGIILCG
1201 PPGSGKTMIM NNALRNSSLY DVVGINFSKD TTTEHILSAL
1241 HRHTNYVTTS KGLTLLPKSD IKNLVLFCDE INLPKLDKYG
1281 SQNVVLFLRQ LMEKQGFWKT PENKWVTIER IHIVGACNPP
1321 TDPGRIPMSE RFTRHAAILY LGYPSGKSLS QIYEIYYKAI
1361 FKLVPEFRSY TEPFARASVH LYNECKARYS TGLQSHYLFS
1401 PRELTRLVRG VYTAINTGPR QTLRSLIRLW AYEAWRIFAD
1441 RLVGVKEKNS FEQLLYETVD KYLPNQDLGN ISSTSLLFSG
1481 LLSLDFKEVN KTDLVNFIEE RFKTFCDEEL EVPMVIHESM
1521 VDHILRIDRA LKQVQGHMML IGASRTGKTI LTRFVAWLNG
1561 LKIVQPKIHR HSNLSDFDMI LKKAISDCSL KESRTCLIID
1601 ESNILETAFL ERMNTLLANA DIPDLFQGEE YDKLLNNLRN
1641 KTRSLGLLLD TEQELYDWFV GEIAKNLHVV FTICDPTNNK
1681 SSAMISSPAL FNRCIINWMG DWDTKTMSQV ANNMVDVVPM
1721 EFTDFIVPEV NKELVFTEPI QTIRDAVVNI LIHFDRNFYQ
1761 KMKVGVNPRS PGYFIDGLRA LVKLVTAKYQ DLQENQRFVN
1801 VGLEKLNESV LKVNELNKTL SKKSTELTEK EKEARSTLDK
```

```
1841 MLMEQNESER KQEATEEIKK ILKVQEEDIR KRKEVVMKSI
1881 QDIEPTILEA QRGVKNIKKQ QLTEIRSMVN PPSGVKIVME
1921 AVCAILGYQF SNWRDIQQFI RKDDFIHNIV HYDTTLHMKP
1961 QIRKYMEEEF LSDPNFTYET INRASKACGP LYQWVNAQIN
2001 FSKVLENVDP LRQEMKRIEF ESLKTKANLL AAEEMTQDLE
2041 ASIEVSKQKY SLLIRDVEAI KTEMSNVQAN LDRSISLVKS
2081 LTFEKERWLN TTKQFSKTSQ ELIGNCIISS IYETYFGHLN
2121 ERERGDMLVI LKRLLGKFAV KYDVNYRFID YLVTLDEKMK
2161 WLECGLDKND YFLENMSIVM NSQDAVPFLL DPSSHMITVI
2201 SNYYGNKTVL LSFLEEGFVK RLENAVRFGS VVIIQDGEFF
2241 DPIISRLISR EFNHAGNRVT VEIGDHEVDV SGDFKLFIHS
2281 CDPSGDIPIF LRSRVRLVHF VTNKESIETR IFDITLTEEN
2321 AEMQRKREDL IKLNTEYRLK LKNLEKRLLE ELNNSQGNML
2361 ENDELMVTLN NLKKEAMNIE KKLSESEEFF PQFDNLVEEY
2401 SIIGKHSVKI FSMLEKFGQF HWFYGISIGQ FLSCFKRVFI
2441 KKSRETRAAR TRVDEILWLL YQEVYCQFST ALDKKFKMIM
2481 AMTMFCLYKF DIESEQYKEA VLTMIGVLSE SSDGVPKLTV
2521 DTNDDLRYLW DYVTTKSYIS ALNWFKNEFF VDEWNIADVV
2561 ANSENNYFTM ASERDVDGTF KLIELAKASK ESLKIIPLGS
2601 IENLNYAQEE ISKSKIEGGW ILLQNIQMSL SWVKTYLHKH
2641 VEETKAAEEH EKFKMFMTCH LTGDKLPAPL LQRTDRVVYE
2681 DIPGILDTVK DLWGSQFFTG KISGVWSVYC TFLLSWFHAL
2721 ITARTRLVPH GFSKKYYFND CDFQFASVYL ENVLATNSTN
2761 NIPWAQVRDH IATIVYGGKI DEEKDLEVVA KLCAHVFCGS
2801 DNLQIVPGVR IPQPLLQQSE EEERARLTAI LSNTIEPADS
2841 LSSWLQLPRE SILDYERLQA KEVASSTEQL LQEM
```

IMAGE ACQUISITION AND ANALYSIS Image acquisition was performed as described in Sec. 2.6. The samples were heated to 34 °C to induce tubulin polymerization. For 3D confocal imaging of droplets, Z-stacks were acquired with 0.2 µm (0.1–1 µm). Z-stack and temporal-color projections were created using ImageJ (FIJI) built-in plugins — Z project, 3D project and Temporal-color code.

6.4.2 Methods

Asters in droplets

PROTEIN MIX Due to small reaction volume, volumes of individual components become very small (∼0.5 µL), so protein mix was split into pre-mix and main mix. Pre-mix was made in bulk to reduce pipetting volume errors. A pre-mix of 0.5 mg mL^{-1} κ-casein, 0.016 % Tween 20, 1 x OX, and 50 mM glucose was made. A 10 µL protein mix with 2.26 µL pre-mix, 3 mM GTP, 20–30 µM tubulin (10 % rhodamine-tubulin, stock 200 µM), 1 % PEG-6000 (optional), and 10 %v centrosomes was made in MRB80. The mix was airfuged (5 min, 30 psi) before addition of centrosomes. After addition of centrosomes, the mix was maintained at room temperature (to prevent cold shock to centrosomes).

LIPID-IN-OIL (LO) DISPERSION LO dispersion of 99.95 n% DOPC, and 0.05 n% Cy5-PE was made as described in Sec. 2.6.
FORMATION Droplets were formed by dragging method as described in Sec. 2.6. The samples were heated to 30 °C to induce tubulin polymerization.

Opto-genetic activation

ON GLASS The protocol is similar to MT dynamics assay (see Sec. 4.5). **iLID mix** — A 20 µL protein mix of 0.5 mg mL^{-1} κ-casein, 0.1 % methyl-cellulose, 50 mM KCl, 1 x OX, 50 mM glucose, and 100 nM SspB-mCh was made in MRB80.

The flow chambers were assembled and functionalized with sequential 10 min incubations of 0.2 mg mL^{-1} PLL-PEG-biotin, 2 µL biotin-iLID (diluted with MRB80 to 10 µL), and 0.5 mg mL^{-1} κ-casein. The iLID mix was added to the flow chamber and the flow chamber was sealed with vacuum grease. The sample was imaged in TIRF mode and photo-activation was performed with a pulse of 488 nm laser.

IN DROPLETS **Protein mix** — A pre-mix of 4 mg mL^{-1} κ-casein, 0.1 % Tween 20, and 4 mg mL^{-1} BSA was made. A 15 µL protein mix with 5.33 µL pre-mix, 1 x OX, 50 mM glucose, 1 µM LactC2-YFP-iLID, 1 µM SspB-mCh, and 50 mM KCl was made in MRB80. The mix was airfuged.

LO dispersion — LO dispersion of 54.5 n% DOPC, 30 n% DOPS, 15 n% Cardiolipin, and 0.5 n% Cy5-PE was made as described in Sec. 2.6.

Formation — Droplets were formed by dragging method as described in Sec. 2.6. The sample was imaged in confocal mode and photo-activation was performed with the pulse of 488 nm laser.

ON SLB **Protein mix** — A pre-mix of 0.5 mg mL^{-1} κ-casein, 0.1 % methyl-cellulose, 50 mM KCl, and 1 x OX was made. A 30 µL protein mix with 7.1 µL pre-mix, 1 µM SspB-mCh, and 50 mM glucose was made in MRB80. The mix was airfuged.

SUVs — SUVs with 39.5 n% DOPC, 40 n% DOPS, 20 n% biotin-PE, and 0.5 n% Cy5-PE were made in H-buffer (150 mM, 10 mM HEPES pH 7.4) using extrusion as described in Sec. 2.6.

Formation — The flow chambers were assembled and functionalized with 10 min incubations of 20 µL SUVs and washed with MRB80. The protein mix was added to the flow chamber and the flow chamber was sealed with vacuum grease. The sample was imaged in TIRF mode and photo-activation was performed with the pulse of 488 nm laser.

GLIDING ASSAY The protocol is similar to MT dynamics assay (see Sec. 4.5) and [526, §5].

Classic gliding assay mix — A 20 µL protein mix of 0.3 mg mL^{-1} κ-casein, 0.1 % methyl-cellulose, 2 x OX, 100 mM glucose, and 2 mM ATP was made in MRB80.

Opto-gliding assay mix — A 15 µL protein mix of 0.5 mg mL^{-1} κ-casein, 0.1 % methyl-cellulose, 50 mM KCl, 1 x OX, 50 mM glucose, 2 mM ATP, and 2 nM SspB-mCh-dynein was made in MRB80.

The flow chambers were assembled and functionalized with sequential 10 min incubations of 0.2 mg mL^{-1} PLL-PEG-biotin, dynein-biotin-GFP (diluted 100 x), and 0.5 mg mL^{-1} κ-casein (for classic gliding assay) and 0.2 mg mL^{-1} PLL-PEG-biotin, 2 µL biotin-iLID (diluted to 10 µL), and 0.5 mg mL^{-1} κ-casein (for opto-gliding assay).

The mixes were airfuged (5 min, 30 psi), MT seeds (0.2–1 µL, diluted 300 x) added to the flow chamber and the flow chamber was sealed with vacuum grease. The sample was imaged in TIRF mode, samples were heated to 30 °C and photo-activation was performed with a pulse of 488 nm laser.

6.5 Acknowledgements

We thank Esengül Yildirim, and Eli van der Sluis for purifying proteins. We thank Samantha Reck-Peterson for providing dynein construct, Marcel Janson for providing Ase1 protein, and Zdeněk Lánský for providing Kinesin5 protein.

6.6 Supplementary Information

6.6.1 Supplementary Figures

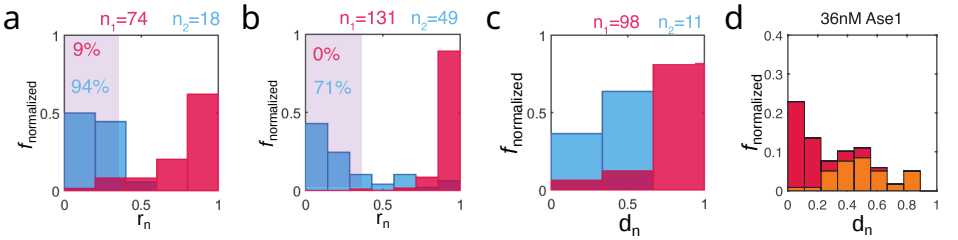

Figure 6.S1: **Aster positioning statistics.** Data reproduced from Roth et al. [250]. Quantification of aster position. (a) Single aster, regime 2 (Fig. 6.2(b)) (b) Single aster, regime 3 (Fig. 6.2(b)) (c) Double aster, regime 2-3 (Fig. 6.2(c)) (d) Double aster, Ase1 (Fig. 6.2(d)). Red histograms represent the Fig. 6.2 yellow boxes data.

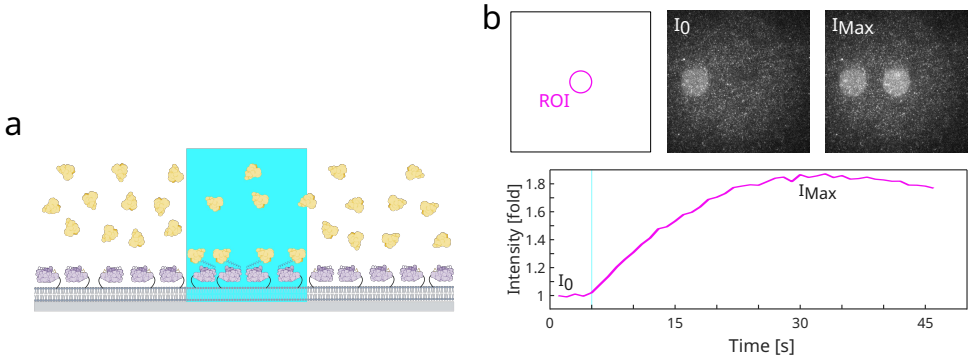

Figure 6.S2: **Photo-activation on SLB.** (a) Schematic of flow chamber assay, glass surface coated with supported lipid bilayer (SLB). LactC2-YFP-iLID and $SspB_{nano}$-mCherry is flowed in. SspB binds to iLID upon selective illumination with 488 nm laser. (Image created with BioRender.com) (b) Spatio-temporal control on iLID-SspB binding (LactC2-YFP-iLID and $SspB_{nano}$-mCherry) on SLB. (top) A circular ROI is illuminated once with a flash of 488 nm laser in field-of-view (FOV). TIRF Image montage of SspB intensities, representing time points — I_0 pre-activation, I_{Max} maximum (following a fast activation). (bottom) Corresponding SspB binding dynamics. Intensity of SspB is normalized with averaged pre-activation ROI intensity to obtain a fold increase. iLID-SspB show activation and binding on SLB.

6.6.2 Supplementary Movies

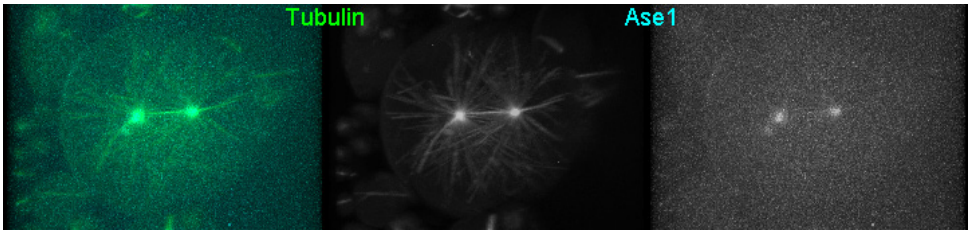

Figure 6.S3: **Asters in droplet.** Aster positioning in presence of Ase1 (from Fig. 6.2(d)). [ ]

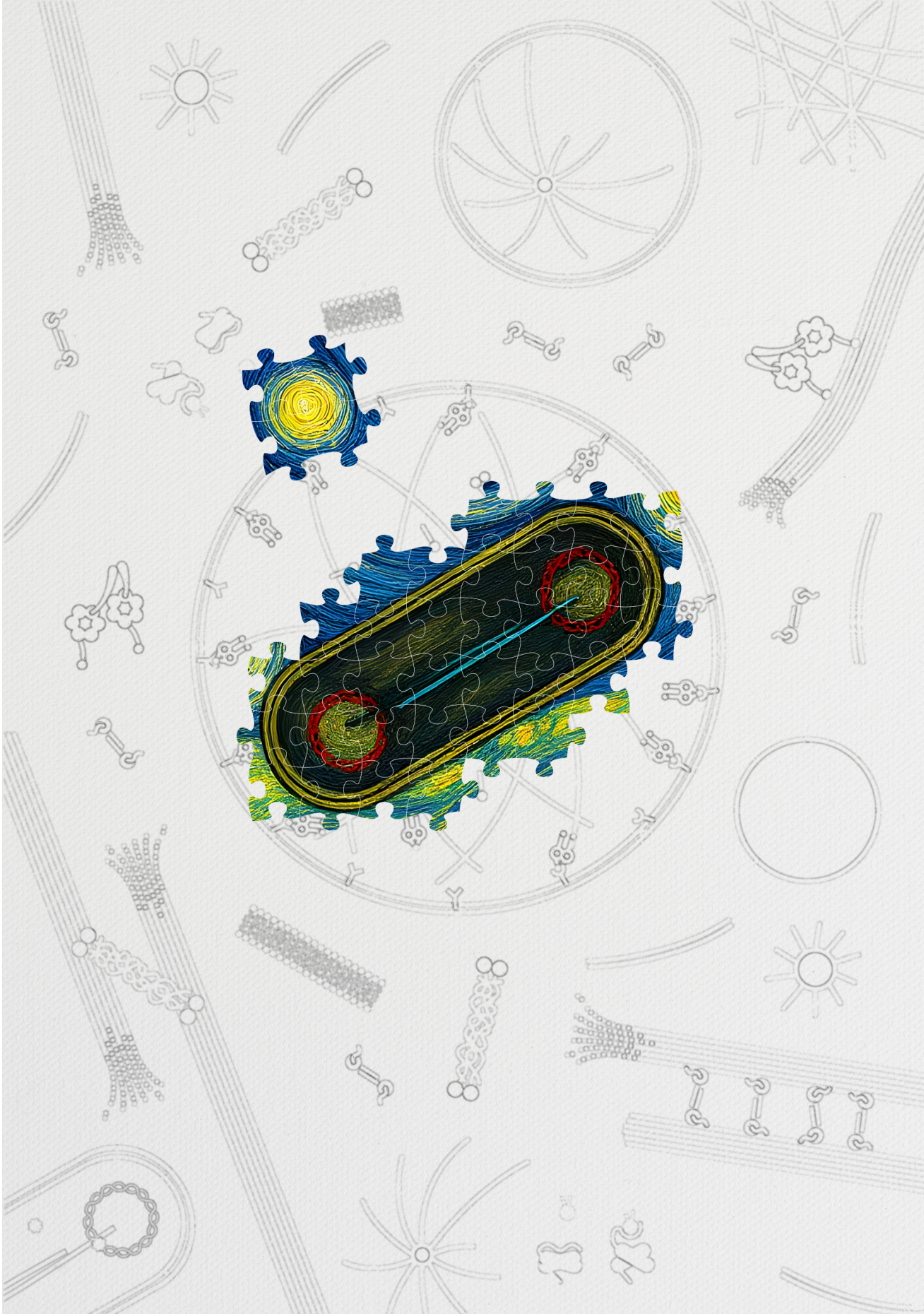

Opto-ParMRC system for Synthetic cell

Less is More.
Reinvent the wheel.
Knock off.

Inheriting equal genetic information during cell division is important. It governs the life and cell cycle. Cells have sophisticated machinery to ensure proper segregation of DNA. The more evolved a cell is, the more complicated its mechanism becomes. A synthetic cell needs a minimal DNA segregation system. Here, we adapted a simple par system from E. coli low copy number plasmid R1 for this purpose. To regulate it with the synthetic cell cycle, we introduced a spatiotemporal control on the adaptor molecule with opto-switch, iLID. We mimic the ParMRC system for DNA segregation in a minimal in vitro setting. While the components of our opto-ParR system function as we intended under photo-activation, the system reconstituted as a whole is not light responsive yet in our preliminary work. Further optimizations are required to enable opto-genetic regulation.

This chapter includes segregation experiments performed by Koen van Gent (under supervision of Yash Jawale and Reza Amini Hounejani), and opto-switches designed together with Eli van der Sluis and Beatriz Orozco Monroy.

7.1 Introduction

The initial synthetic cell will be a bare minimum of what a eukaryotic cell, or even a bacterial cell, can do. It needs to perform the basic functions, mimicking the cellular processes required to sustain life, like maintain metabolism, propagate genetic information, and divide (see Sec. 1.4). In this chapter, we focus on designing a DNA segregation module, required before the cell division in a synthetic cell. We saw, building a minimal eukaryotic spindle, even *in vitro*, is a daunting task (Ch. 6). And so a synthetic cell needs something minimal and even more simple than the minimal mitotic spindle. Also, the components of the synthetic cell must meet basic requirements like, ability to be expressed in a cell-free expression systems (PURE, TXTL), ability to be encapsulated in an artificial cell-like container (vesicles), and be part of an active and dynamic system, that can adapt and be regulated in coordination with other components.

Bacteria are much simpler compared to eukaryotic cells. Their cellular processes have less complexity. The bacterial chromosome, nucleoid, segregates during or after replication, which involves several protein complexes that regulate the unfolding and folding (entropic processes), distributing the origin of replication (ori), and eventually the chromosome (Fig. 7.1(a)). The bacterial chromosome is still a large genome compared to the future genome of the first synthetic cell (by at least an order of magnitude large). So, similar mechanisms are not essential. However, bacteria do have other smaller genetic material also, i.e. plasmids. Most of the high copy number plasmids get distributed by passive processes (diffusion) where exact allocation in daughter cells is not needed (Fig. 7.1(b)). But in the low copy number plasmids, where equal allocation or even the single copy needs to be distributed in each daughter cell, segregation occurs via special partitioning (*par*) systems (Fig. 7.1(c)). Such active plasmid partition gene cassettes were first identified in low copy number P1 and F plasmids in *E. coli* [535–537].

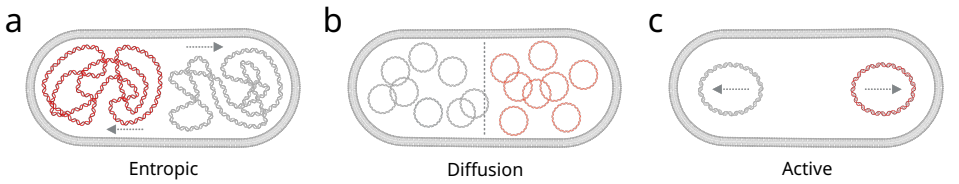

Figure 7.1: **Bacterial DNA segregation.** Different segregation mechanisms for original and replicated bacterial DNA, (a) entropic, (b) passive, and (c) active. (Images created with BioRender.com) [ ]

7.1.1 Segrosome

Segrosome is a nucleoprotein complex formed at the centromere-like DNA site on the plasmid, along with two proteins, a centromere-binding adaptor protein (CBP), the link between the DNA and a motor protein, usually an ATPase, which actively pushes or pulls the DNA to drive the segregation (Fig. 7.3) (see [538–540]). The multiple centromere sites present in the form of tandem repeats, recruit the adaptor proteins to form nucleoprotein complexes, and assemble into a higher-order partitioning complex. This partition complex recruits the motor protein to form a segro-

some, and trigger DNA separation. These *par* systems have been mainly classified in two groups, NTPase, type I (Walker A-type ATPase; P-loop), and type II (cytomotive, actin-like ATPase) [541]. Recently, additional type III (cytomotive, tubulin-like GTPase) have been discovered [542], and also type IV (DNA binders) [543] has been proposed. The type I systems can be classified further into type Ia and Ib, depending on the position of the centromere-like site in the operon, downstream and upstream respectively.

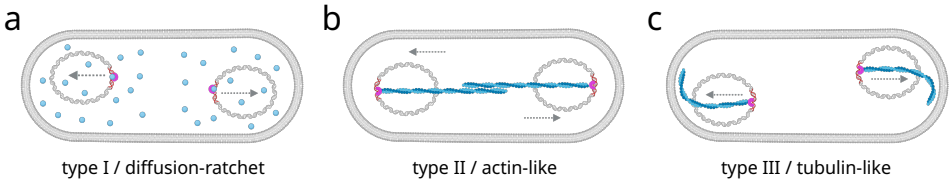

Figure 7.2: **Bacterial DNA segregation.** Major types of active DNA segregation mechanisms (centromere-like site, adaptor protein, and motor protein), (a) type I (diffusion ratchet) e.g. ParABS, (b) type II (actin-like) ParMRC, and (c) type III (tubulin-like) TubZRC. (Images created with BioRender.com) [ ]

Examples of **type I** systems are ParABS (R1 plasmid), SopABC (F plasmid) (type Ia) [535–537], and ParFG*H* (TP228 plasmid) (type Ib) (Fig. 7.2(a)) [544, 545]. The centromere sites have asymmetrically positioned inverted repeats [546, 547]. The type Ia CBPs have dual role, regulate not only partition but also transcription [548–550]. They have three domains [551], N-terminal, central (with a DNA-binding helix-turn-helix (HTH) motif), and C-terminal. The central domain interacts with the DNA (also bridges with other adaptors), while N- and C- terminals are unstructured and help spread out the centromere sites. In comparison, type Ib CBPs are smaller and only have two domains, an unstructured N-terminal and C-terminal (ribbon-helix-helix (RHH)) DNA-binding motif [544, 552], and can form dimers. An example of **type II** system is ParMRC (pSK41, R1 plasmid) (Fig. 7.2(b)). The tandem repeats of centromere sites can be continuous [553] or in two groups [554]. The type II CBPs are similar to type Ib CBPs, with two domains, an N-terminal RHH motif for DNA binding, and a C-terminal domain for motor protein interaction. The segrosome binds to the growing end of ParM filaments, which make an antiparallel bundle, pushing the plasmids at the cell poles [555] (Fig. 7.3). An example of **type III** system is TubZRC (pBToxis, pBsph plasmids) (Fig. 7.2(c)). The centromere sites can be in multiple blocks [556]. The CBP has HTH DNA binding motif with an additional wing shape [557]. In contrast to type II system, it follows a pulling mechanism, where segrosome tracks the shrinking minus end of TubZ filament [558]. Also, extra protein TubY is found, with HTH DNA binding motif and a long coiled-coil domain, which is speculated to regulated TubZ assembly [559]. Lastly, examples of an uncharacterised suggestive **type IV** system are single gene based *par* systems (pSK1 (orf245), R388 plasmids) [543, 560], where a pilot-fish segregation mechanism is proposed.

7.1.2 ParMRC

The ParMRC system is one of the best known systems for bacterial DNA segregation (see [562, 563]). The ParMRC locus was first discovered on a large, low-copy number, multiple-resistance R1 plasmid in *E. coli* [564]. It is extensively studied with cytology [554, 565], biochemical assays [553, 566–568], live cell imaging [569], and X-ray and electron microscopy [555, 570–572], thus well characterised (Fig. 7.3). Most importantly, it has been successfully reconstituted in *in vitro* assays [573, 574]. Hence, with only three components (only two proteins) in the partitioning system, it is a leading candidate for DNA segregation using a minimal spindle in synthetic cells. Recent studies have demonstrated its feasibility and proof-of-principle application for synthetic cell with 3D *in vitro* reconstitutions in containers [575, 576]. In this chapter, we investigate the application of the ParMRC system as minimal spindle for synthetic cells.

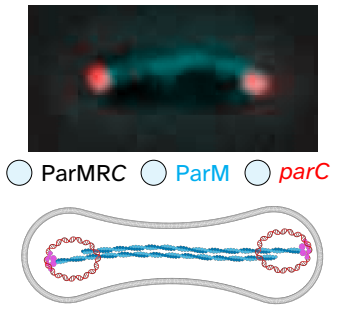

Figure 7.3: **ParMRC.** (top) Segregation of *par*$^+$ plasmids by ParM filaments in *E. coli* MC1000 cells. Image adapted from [561]. (bottom) A minimal segrosome of a synthetic cell, with ParMRC segrosome, antiparallel ParM spindle segregating plasmids via ParR attachment at *parC*. [ ]

Structure and function

ParMRC DNA segregation system consists of *parC*, a centromere-like DNA region, ParR, an adaptor protein, and ParM, an actin-like motor protein.

parC

The centromere-like *parC* locus on R1 plasmid (100 kb) is discontinuous, present as two clusters of five 11 bp iterons, around the either side of the 39 bp promoter site (Fig. 7.4) [554, 577].

ParR

The ParR[1], like type II CBPs, has two domains, ParR^N (1–53 aa), and ParR^C (54–117 aa) (Fig. 7.4). The β strand in ParR^N domain, from two monomers combine to form an antiparallel sheet, that interacts with the major groove in the *parC* DNA sites. While the two α helices from each monomer come together to form a tight dimer [553, 567]. The three α helices from ParR^C domain stabilizes the dimerization of the N-terminal domain [567], and the unstructured C-terminal tail (ParR$^{C\text{-}p}$, 101–117 aa) interacts with the ParM filament end [568] through the hydrophobic pocket in ParM monomers [555].

ParM

The ParM proteins assemble into filaments, hydrolyse ATP, and generate pushing forces through polymerization to segregate the DNA, hence defined as cytomotive filaments [578]. The ParM protein has two domains, I and II. The monomer is an ATPase, and shows conformational changes (∼25° domain closure) depending on the state of nucleotide bound (ATP, ADP, AMPPNP) [579]. Also, the conformational

[1] ParR (117 aa) from pJSC1 plasmid.

state of a ParM protein on filament form is different from monomeric form [555, 571]. The conformational changes from monomeric to filament form, promote the ATP hydrolysis [561, 580]. While the ParM is held in the filament through longitudinal lattice contacts, the ATP hydrolysis in filament form disrupts these contacts, and makes the filament unstable. ParM filaments have a left-handed twist, two-start helix with two protofilaments [555, 570, 572], and has barbed and pointed ends like actin. ParM also has actin-like fold, but the assembled ParM filaments are different from actin (right-handed helix) [579]. ParM has rapid spontaneous nucleation, kinetically apolar[2], and exhibits dynamic instability[3] [574], compared to actin's slow nucleation, polarized growth, and treadmilling. The dynamic instability of ParM can be attributed to the presence of ATP caps at both ends[4].

Figure 7.4: **ParMRC structure.** (top) Structure of 11 bp centromere-like *parC* DNA region, and ParM filament (PDB 4A6J, 10 monomers, molecular surface with cartoon representation of 1 monomer) (bottom, scale 3 x) Structure of ParR dimer, showing $ParR^{N}$ (with RHH motif), and $ParR^{C}$ domains, along with $ParR^{C\text{-}p}$ peptide. Dimer folded using Alphafold server [581], and C-terminal tail modelled using MODELLER [582]. Model images rendered using ChimeraX [404].

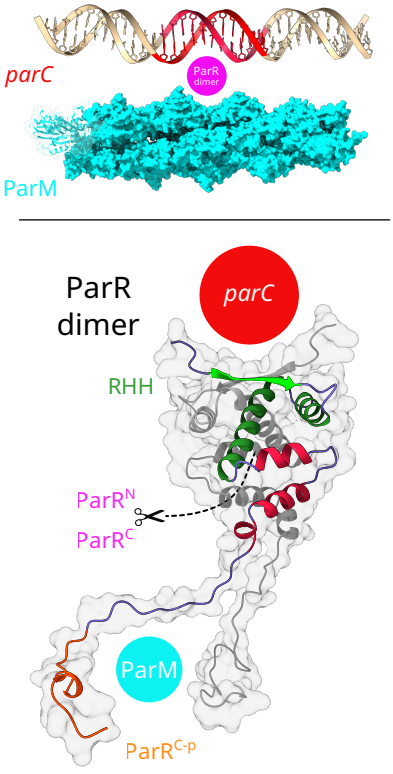

ParRC

The ParR dimers bind to the *parC* iterons, and form a lockwasher-like super-helical structure (right-handed helix, ⌀ 15–18 nm) with multiple ParRC nucleoprotein complex (one dimer per *parC* interon) [567]. The negatively charged *parC* DNA wraps on the ParR dimers, due to its positively charged surface, and the promoter region is confined to form a ring [568]. The ParRC complex also lowers the critical nucleation concentration of ParM filament formation [555].

ParMRC

The ParM filaments are dynamically unstable. They undergo cycles of growth and shrinkage to search the cell for ParRC complexes, the search-and-capture mechanism [574]. The ParRC complex captures the barbed end of the ParM, increasing its growth rate, and binding also prevents the ParM disassembly [555]. The opposite handed helical nature of structures of ParM and ParR is suspected to make a stable cap at the end. The ParRC bound end grows

[2] Symmetrical bidirectional elongation from both ends.
[3] Ability to spontaneously switch between growing and shrinking phase, like MTs [40].
[4] Just like the GTP cap on the plus end of MTs, responsible for their dynamic instability.

with insertional polymerization [561, 573]. Two ParR*C* bound ParM filaments form an antiparallel spindle, which segregate the DNA. And the disassembly of the pointed end is inhibited by lateral support from binding of other ParR*C* bound ParM filament from the ParMRC spindle [555].

Control

Interestingly, *in vivo* ParMR*C* system is asynchronous, each bipolar antiparallel spindle segregates a different plasmid sisters [571]. It is also not coordinated with the bacterial cell cycle. But eventually all plasmid sisters are segregated before cell division, and the bacterium manages to survive[5]. Even though plasmids are accessory genome in bacteria, but for the synthetic cell it will serve as core genome. So it is absolutely necessary to properly segregate the (likely singular copy of) DNA plasmids. Thus, the DNA segregation needs to be coordinated with the synthetic cell cycle.

Spatiotemporal control

We currently plan to externally regulate the DNA segregation spatiotemporally using opto-switches, for the (independent) DNA segregation module designed for synthetic cell. As discussed in Sec. 5.1, optogenetics is a powerful tool, that enables fast and reversible spatio-temporal control. We will be using the opto-switch, iLID-SspB for this purpose (characterised in Sec. 6.2.2) [240]. Eventually, in the synthetic cell, the DNA segregation will be coordinated and integrated with other synthetic cellular processes like DNA replication and cell division using other approaches.

The ParR protein can be split into its two domains (Fig. 7.4). And $ParR^{N}$ domain alone has been shown to be capable of binding the *parC* sites [553]. Also, the $ParR^{C\text{-}p}$ has been shown to interact with the ParM [568]. With this, we fused the iLID-SspB pair with the two ParR domains, to create a series of opto-ParR constructs, based on structural information of ParR dimer, knowledge of iLID fusions proteins, and logical reasoning. Of the many designs (Tab. 7.1), the following design pair, $ParR^{N}$-iLID and SspB-$ParR^{C}$, seems effective (Fig. 7.8(a),Fig. 7.S2). The fusion protein iLID-$ParR^{N}$ has the $ParR^{N}$ domain (for DNA binding), a leucine zipper motif (to help create a higher order structure, forced dimerization of dimers), YFP (for visualization), and the iLID (for opto-control)[6]. Each of the two $ParR^{N}$ domains in this construct forms a natural dimer with an extra copy of $ParR^{N}$ domain. The resulting $ParR^{N}$-iLID dimer has 4 $ParR^{N}$ domains, capable of binding 2 *parC* sites. While the fusion protein SspB-$ParR^{C}$ has SspB (for SsrA binding in iLID), a leucine zipper (to stabilize the $ParR^{C}$ intra-domain dimerising interactions), $ParR^{C}$ (for ParM interactions), and an additional copy of $ParR^{C\text{-}p}$ (to boost the ParM interactions). The resulting SspB-$ParR^{C}$ dimer has 4 copies of $ParR^{C\text{-}p}$ peptides for enhanced ParM interactions.

These opto-ParR constructs should enable the light-controlled plasmid DNA segregation. The $ParR^{N}$ dimer is already bound to the *parC* DNA, and the SspB-$ParR^{C}$

[5] Forestalls to trigger the post-segregational killing (PSK) or plasmid addiction, which is activated if accessory plasmids are not present in the newly formed daughter cells [583].

[6] The light spectrum for iLID activation overlaps with YFP excitation.

dimer is interacting with the ParM filaments. Upon blue light illumination, the ParR^{N}-iLID and SspB-ParR^{C} should interact, and form the ParRC complex, which stabilizes the ParM filament and will promote bipolar spindle formation. Additionally, the ParRC complex will aid insertional polymerization at the ends, further accelerating the DNA segregation. Upon successful DNA segregation, the light illumination can be stopped, causing the ParRC complex to fall apart and destabilize the spindle.

7.2 Results

7.2.1 Building a synthetic cell spindle

The ParMRC system is shown to form a bipolar spindle, *in vivo* [569] and *in vitro* [574], to segregate the DNA. So, we first tested the ParMRC system for basic *in vitro* characterization like its dynamic properties, encapsulation in vesicles, and cell-free expression.

in vitro reconstitution of ParMRC system

ParM forms dynamic filaments. To test the ParM kinetics, we performed a series of polymerization assays with 1–5 μM ParM and 2–10 mM ATP. We saw ParM filaments polymerizing instantaneously. They were small (∼1–3 μm) and dynamic. This made it difficult to observe them, as they tend to diffuse a lot, even in presence of methylcellulose[7] (0.8 %w/v). Even with 5 μM ParM and 10 mM ATP, they were small and tended to bundle. We switched to AMP-PNP[8] for all further experiments, to get longer and stable filaments that are easy to observe. With 2.5 μM ParM and 2.5 mM AMP-PNP, we saw longer filaments, that diffuse a lot less, but then grew longer overtime and tend to bundle (<10 min). With 2.5 mM AMP-PNP, we saw no polymerization at 0.4 μM ParM and filaments at 0.8 mM ParM (Fig. 7.S1). This is in accordance with previous reported critical concentration of 0.6 μM for ParM in presence AMP-PNP [555, 573].

Next, we reconstituted the ParM spindle, to check separation (Fig. 7.5(a)). With 2.5 μM ParM, 30 nM ParR, and 2.5 mM AMP-PNP, we saw the ParM filaments' search-and-capture of ParR (Fig. 7.S5). ParR binds to the tip of the ParM filament and the complex of ParR proteins was further capable to recruit multiple ParM filaments, resulting in an aster-like structure. Earlier, these aster like structures were observed in presence of ParR and beads coated with *parC* [573]. We encountered them even in absence of *parC*. ParM filaments from neighbouring asters interact to form an antiparallel bundle, corresponding to a bipolar spindle. In these bundles, we saw ParR segregating as the ParM filament grew by insertional polymerization at the capped ends (Fig. 7.5(b), Fig. 7.S4). We saw similar spindle formation with wild type ParMRC system at 5 μM ParM, 300 nM ParR, 750 nM *parC*, and 4 mM AMP-PNP. The ParRC complex separation was observed on the bipolar ParM spindle (Fig. 7.5(c), Fig. 7.S3). This suggests that ParR alone is able to lower the nucleation barrier for

[7] Methylcellulose, a macromolecular crowding agent that forms a mesh, which pushes the filaments towards the glass surface.

[8] AMP-PNP is a very slowly hydrolysable variant of ATP.

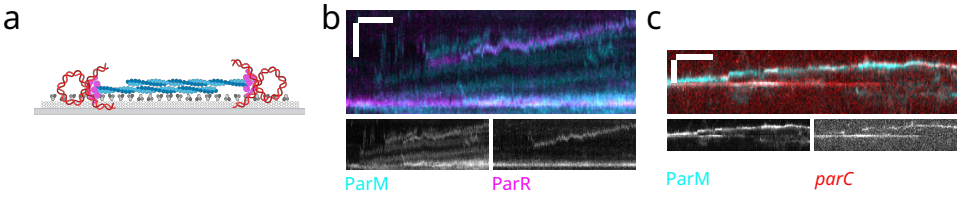

Figure 7.5: **ParMRC dynamics.** (a) Schematic of dynamics assay, glass surface passivated with BSA. ParM spindle segregates ParRC (ParR and *parC*) complex. (Image created with BioRender.com) (b) Kymograph showing spindle separation. ParM (2.5 µM), and ParR (30 nM) with 2.5 mM AMP-PNP is flown in. (see Fig. 7.S4 for a video) (c) Kymograph showing spindle separation. ParM (5 µM), ParR (300 nM), *parC* (750 nM) with ATP (4 mM) is flown in. (see Fig. 7.S3 for a video) Scale bar - 3 µm (vertical), time - 30 s (horizontal).

ParM filaments, whether can it also increase the growth rate of the capped end like ParRC complex remains to be investigated.

Encapsulation of ParM

The components of the segregation system of the synthetic cell should be compatible with vesicles. ParM is the main motor (cytomotive) protein that forms the spindle, capable of generating pushing forces. So we formed vesicles, and encapsulated 2.5 µM ParM, and 3 mM AMP. ParM readily polymerized, and ParM filaments can be seen diffusing around in vesicles (Fig. 7.6). Recently ParM, along with other components also have been demonstrated to be encapsulated in water-in-oil droplets [575], and in vesicles [576].

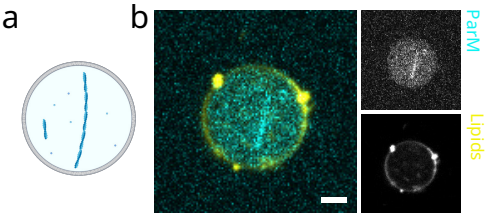

Figure 7.6: **ParM encapsulation.** (a) Schematic of ParM filament encapsulated in GUV, formed with eDICE. (Image created with BioRender.com) (b) A GUV with ParM filament (2.5 µM, AMP 3 mM). Scale bar - 3 µm.

PURE expression of iLID

One of the most important requirements for the components of the synthetic cell is the ability to be expressed in a cell-free environment. We tested the expression of opto-ParMRC components *in vitro* transcription and translation system, PURE [225, 584].

ParM and ParR has been already demonstrated to be expressed in PURE[9].

[9] [unpublished data, personal communications] Christophe Danelon (Toulouse Biotechnology Institute, Toulouse, France) mentioned, expressing ParM and ParR in PURExpress2.0. Expressed ParM can form filaments. While for *de novo* expression of ParM in vesicles with PURE (and additional ribosomes

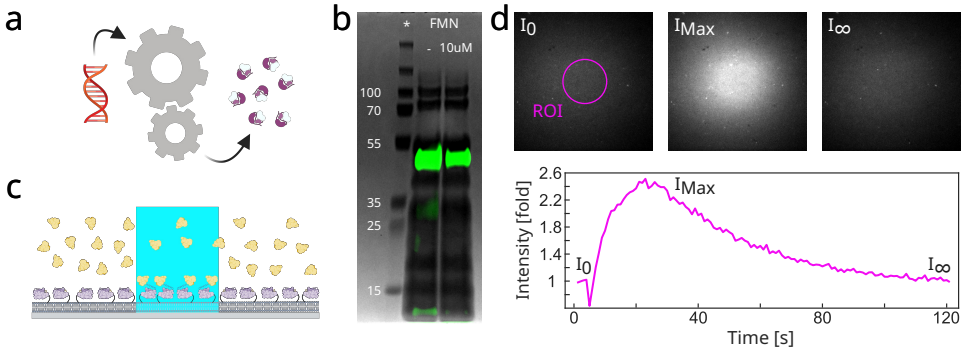

Figure 7.7: **PURE expressed iLID.** (a) Schematic of PURE, depicting DNA being transcribed and translated into iLID. (Image created with BioRender.com) (b) Translation products on a 4–12 % gradient polyacrylamide gel, imaged in bright field and fluorescence. Lanes — ladder (in kDa), LactC2-iLID without and with riboflavin (FMN 10 µM). LactC2-iLID (38.2 kDa) signal also seen in fluorescence due to incorporated GreenLys. (c) Schematic of flow chamber assay, glass surface coated with supported lipid bilayer (SLB). LactC2-iLID and $SspB_{nano}$-mCherry is flowed in. SspB binds to iLID upon selective illumination with 488 nm laser. (Image created with BioRender.com) (d) Spatio-temporal control on iLID-SspB binding (LactC2-iLID and $SspB_{nano}$-mCherry) on SLB. (top) A circular ROI is illuminated once with a flash of 488 nm laser in field-of-view (FOV). TIRF Image montage of SspB intensities, representing time points — I_0 pre-activation, I_{Max} maximum (following a fast activation, along with diffusion), and I_∞ steady state (following a slower deactivation). (bottom) Corresponding SspB binding dynamics. Intensity of SspB is normalized with averaged pre-activation ROI intensity to obtain a fold increase. iLID-SspB show activation and binding on SLB.

So, we next tested the expression of iLID (Fig. 7.7(a)), the new component required for introducing optical control over segregation, in PURE. Linear DNA with LactC2-iLID was PCR amplified for PURE expression. The 5 nM DNA was incubated in PURExpress2.0 mix with and without riboflavin (FMN)[10] and the transcription products show presence of a band (in between 35–55 kDa), corresponding to LactC2-iLID (38.2 kDa) (Fig. 7.7(b)). Expression of iLID in PURE is independent of FMN, as expected, and also its addition does not interfere with functioning of the PURE enzymes. Next, we tested if the PURE expressed iLID is functionally active (ie. light responsive), in an photo-activation assay on an SLB (Fig. 7.7(c)). Upon a flash illumination with blue light, we saw PURE expressed iLID rapidly recruit SspB in the activation region (Fig. 7.7(d)). Some iLID diffused out of the region due to diffusion on SLB and followed by a gradual deactivation. This shows that the opto-switch, iLID, can be expressed in functional form with PURE. But PURE expression of $ParR^N$-iLID needs to be evaluated.

as crowding agents), filamentous structures (ParM filaments/bundles not yet confirmed) can be seen deforming the vesicles, only after long times (>6 h).

[10] Flavin mononucleotide (FMN), a chromophore cofactor required in the core of the LOV domain of the iLID protein, for the light responsive functioning [240].

7.2.2 Opto-control on ParMRC

Having *in vitro* reconstituted the basic ParMRC segregation system, with aster separation, we next wanted to implement the optical control on segregation. We design the ParR^{N}-iLID and SspB-ParR^{C} constructs, by splitting ParR into ParR^{N} and ParR^{C} domains, and fusing them with opto-switch iLID-SspB pair (Fig. 7.8(a)). Upon illumination, these constructs form a ParR mimicking structure, enabling ParMRC complex and spindle formation, and DNA segregation (see Sec. 7.1.2).

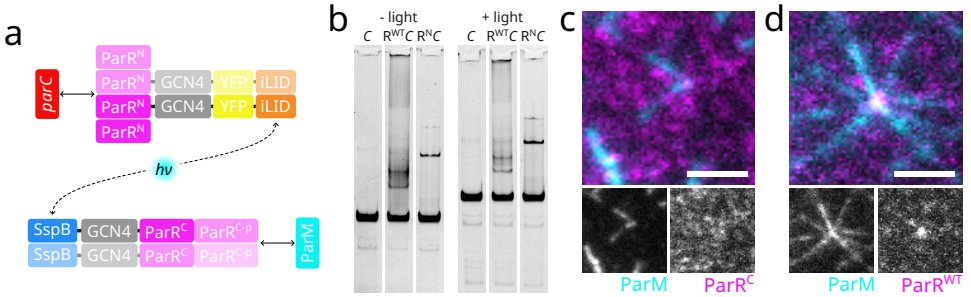

Figure 7.8: **Activity of opto-ParR constructs.** (a) Schematic of opto-ParR constructs. ParR^{N}-iLID fusion protein, with ParR^{N} domain, leucine zipper motif (GCN4), YFP, and iLID. An extra copy of ParR^{N} domain forms a natural dimer with ParR^{N} on the fusion protein, and the fusion protein force dimerizes due to GCN4. The resulting ParR^{N}-iLID dimer interacts with *parC*. SspB-ParR^{C} fusion protein, has SspB, leucine zipper (GCN4), ParR^{C}, and ParR$^{C\text{-}p}$. The fusion protein force dimerizes due to GCN4. The resulting SspB-ParR^{C} dimer interacts with ParM filament. Upon illumination, the ParR^{N}-iLID and SspB-ParR^{C} interact and form the opto-ParRC complex. (b) An EMSA on 6 % polyacrylamide gel, showing *parC* binding response of ParR^{N}-iLID, in absence and presence of photo-activation. Lanes — negative control (1.5 nM *parC*), ParR (76 nM, 1.5 nM *parC*), and ParR^{N}-iLID (76 nM, 1.5 nM *parC*). (See Fig. 7.S2 for activity of other constructs from Tab. 7.1.) (c) (d) Formation higher-order structures with (c) ParM (2.5 µM), and SspB-ParR^{C} $_{AF488}$ (300 nM) (see Fig. 7.S5 for a video) and (d) ParM (2.5 µM), and ParR (300 nM) (see Fig. 7.S4 for a video). Scale bar - 3 µm.

We first tested the interactions of ParR^{N}-iLID with *parC* DNA using Electrophoretic Mobility Shift Assay (EMSA). The ParR (wild type) shows the largest shift, with most of the ParRC stuck in the well, with some smear indicative of partial binding (some sites out of 10). The ParR^{N}-iLID also showed a significant shift with a clean band, suggesting partial but consistent binding (Fig. 7.8(b)). This binding to the *parC* DNA was not affected by photo-activation of iLID, as expected.

Next, we tested the other half, SspB-ParR^{C} interaction with ParM filaments in a dynamic assay. The ParR (wild type) forms aster of ParM fiaments (as described above) (Fig. 7.8(d), Fig. 7.S4). SspB-ParR^{C} too formed a higher order structure, with a few filaments interacting at the tip (Fig. 7.8(c)). This suggests decreased binding of SspB-ParR^{C} to ParM compared to ParR (wild type), but still effective enough to interact with one or more ParM filaments.

We also tested all the components, both ParR^{N}-iLID and SspB-ParR^{C} with ParM and *parC*, of opto-ParMRC together in dynamic assay. But our preliminary results

were inconclusive and showing signs of modest constitutive binding, independent photo-activation. The design of opto-ParR constructs needs further fine-tuning.

7.3 Discussion

Adapting a system to a new purpose is a two-step process, first understand and rebuild the system, and later modify it accordingly. In this chapter, we first rebuild an *in vitro* minimal spindle, encoded by the well-known R1 plasmid from *E. coli*. Then we tried to redesign it to be controlled by light, for coordination with the cell cycle of the synthetic cell.

7.3.1 Reproducing the ParMRC spindle

We were able to reproduce the DNA segregation with *in vitro* reconstituted ParMRC, as reported in Garner et al. [573]. There ParMRC spindle was assembled with the help of micro-beads coated with *parC* DNA [573], and similar strategies have been used to assembly the ParMRC spindle for synthetic cell purpose too [575, 576]. The use of *parC* coated beads helps with observing and tracking the DNA. However, this approach promotes formation of thick ParM bundles, even ParM bands [573]. These conditions are far from cell physiology. Cell solely contains doublets, pure two anti-parallel filament ParM spindles, maybe a few with a few filaments [571]. Here, we tried to lower the ParM bundling by decreasing ParM concentration, and stabilizing them with AMPPNP, to obtain single filaments like in cells, but it does make it hard to observed them overtime. But in the process, we loose the dynamic instability of the filaments, making the search-and-capture mechanism inefficient. This study represents a preliminary proof-of-concept for ParM-based DNA segregation. Additional work is required to optimize the system under physiologically relevant conditions, such as protein and ATP concentrations.

7.3.2 Optimizing the opto-control

Having a controlled cell division is important for the cells, let alone for the synthetic cell, as it is minimal, with no redundancy check points or stress response mechanisms. Hence, we introduced an opto-switch for controlling the DNA segregation in ParMRC system by regulating the ParR and ParRC complex assembly. Our individual components of opto-ParR system work as expected but, our current whole system together is not light responsive. The SspB-ParR^{C} being able to form aster-like structures can also contribute to the problem. The assembly of higher order structure on ParM tip should be mediated by oligomerisation of ParR^{N}-iLID-par*C* nucleoprotein complex, only upon photo-activation.

The opto-ParR system needs to be further optimized. We propose the following new constructs, based on set of three new strategies (Fig. 7.9). In type 1, construct a regulates the DNA binding. The LOV domain can be strategically inserted in the ParR in-between the two domains, such that it will make the ParR dimer and DNA binding pocket light responsive. Upon illumination, the conformational change from

LOV will disrupt the interlocking of β strands, and dimers will also fall apart. This will distrupt the ParR's binding to the *parC*.

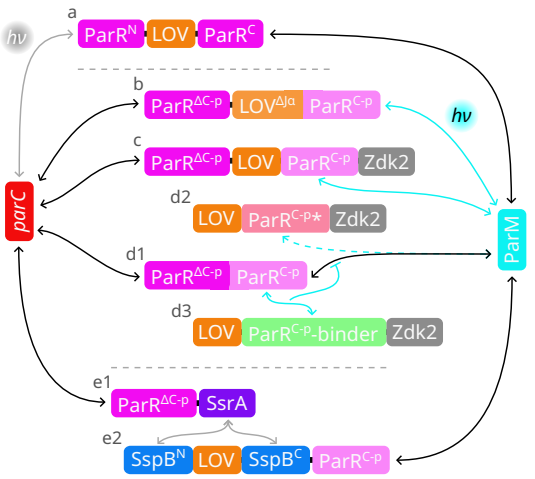

Figure 7.9: **Opto-ParR constructs.** Schematic of 3 types of proposed opto-ParR constructs. (a) targets binding to *parC*, (b-d) target binding to ParM, and (e) targets interaction of ParR domains. Arrows represent the nature of protein interactions — black are constitutive, cyan are active under blue light, gray are active in dark, and flat arrow represent inhibitory effect.

In type 2, constructs b - d control the filament binding. For regulating the ParM binding, the ParR$^{C\text{-}p}$ can be targeted. In construct b, the ParR$^{C\text{-}p}$ is fused with the LOV domain, replacing the Jα helix in LOV with ParR$^{C\text{-}p}$, and the LOV domain is connected with (the rest of the) ParR$^{\Delta C\text{-}p}$. The ParR$^{\Delta C\text{-}p}$ can bind to *parC*, however the ParR$^{C\text{-}p}$ peptide is only accessible upon illumination. This will make the binding of ParR to ParM light responsive. Some mutations might be needed to ensure tight packing of the peptide in the LOV pocket. Constructs c, d2, and d3 are based on a Z-lock mechanism [585]. In a Z-lock construct, the protien-of-interest (PoI) is inserted in-between LOV and (one of the) Zdk domain. In dark/lock state, Zdk binds back on LOV, trapping the PoI. Thus PoI is sterically blocked from interacting with its binding partner. Upon illumination, the conformational change in LOV distrupts Zdk's binding and unlocks PoI, making it available for interactions. In construct c, the ParR$^{C\text{-}p}$ is the PoI, and the Z-lock system is connected with (the rest of the) ParR$^{\Delta C\text{-}p}$. Thus ParR$^{C\text{-}p}$ peptide will only be able to interact with ParM upon illumination.

Construct d1 is wild-type ParR i.e. ParR$^{\Delta C\text{-}p}$ connected with the ParR$^{C\text{-}p}$. In construct d2, the ParR$^{C\text{-}p}$*, a mutant[11] of ParR$^{C\text{-}p}$, is the PoI in Z-lock system. The ParR$^{C\text{-}p}$* peptide can only interact under illumination. Thus construct d2 will compete with wt-ParR (d1) for binding to ParM. The concentrations and the binding affinities of d2 and d1 should be tuned in such a way that under illumination even with low-binding but high concentrations the d2 will compete out the d1, and prevents the wt-ParR's interactions with the ParM. Under dark, with low-binding and negligible concentrations of d2, wt-ParR system with work normally. Thus d1 - d2 construct pair will create a light responsive system. In construct d3, an anti-ParR$^{C\text{-}p}$ binding peptide, an synthetically designed[12] peptide, is the PoI in Z-lock system.

The anti-ParR$^{C\text{-}p}$ binding peptide can only bind with ParR$^{C\text{-}p}$ peptide under illumination. The concentrations and the binding affinities of d3 and d1 should be tuned in such a way that under illumination even with low-binding but high concentrations the d3 will bind to and deplete out the d1, and thus reducing the available pool of wt-ParR for interacting with the ParM. Thus d1 - d3 construct pair will create a light responsive system.

In type 3, constructs e control assembly of the ParR domains. While the ParR$^{\Delta C\text{-}p}$ can bind to the *parC*, and the ParR$^{C\text{-}p}$ can bind the ParM, their interaction with each other is light responsive. The construct e1 has SsrA tag connected with the ParR$^{\Delta C\text{-}p}$. While the construct e2 has SspB(LOV2) chimera connected to the ParR$^{C\text{-}p}$ peptide. The LOV2 domain is strategically inserted in the SspB (based on 3D topology map), such that upon illumination, the conformational change in LOV break off the SspB structure. This distrupts its ability to bind to SsrA tag. Only in the dark state, e2 can interact with e1, connecting the two ParR parts, and thus assembling the adaptor protein (ParR) required for connecting the *parC* DNA to the ParM filament. This design is based on PhoBIT1 system (photo-inducible binary interaction tools, a light-OFF switch) [586] and is more like the two-part opto-ParR strategy previously we tested in this chapter.

We remain hopeful, that some of these new approaches will enable spatiotemporal opto-ParR control. They simplify the design down to a single component (except one, e), as opposed to the previous two parts. Also, some of them allow for the use of wild type ParR. This will help retain the shape and structure (without the presence of sterically bulky iLID and SspB domains), designed through natural evolution, to assemble into the lockwasher-like ParR*C* segrosome complex. And thus the synthetic cell can have the opto-ParMR*C* based DNA segregation module.

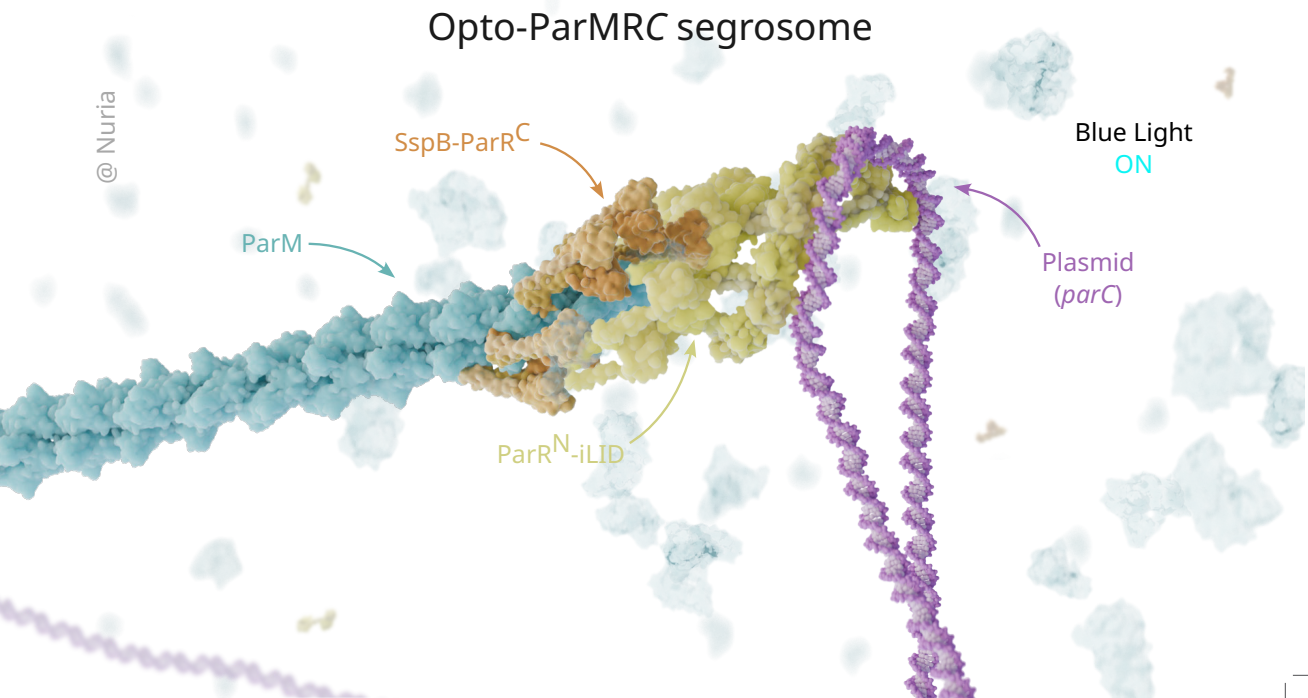

7.4 Material and Methods

7.4.1 Materials

CHEMICALS See Secs. 2.6 & 4.5 for a detailed list of chemicals. Chemicals were purchased from Merck (Merck Life Science), unless otherwise stated: Adenosine 5'-(β,γ-imido)triphosphate lithium salt hydrate (AMP-PNP, 10102547001 Roche), PURE-frex® 2.0 (PF201 GeneFrontier Corporation, China), Riboflavin-5'-phosphate sodium salt dihydrate (FMN, 11491918 Thermo), FluoroTect™ $Green_{Lys}$ (L5001 Promega), RNase A (A7973 Promega).

LIPIDS See Sec. 2.6 for a detailed list of lipids.

BUFFERS AND PROTEINS See Secs. 2.6 & 4.5 for more details about buffers. And Sec. 2.6 for more details related to protein purification.

F-buffer[13] was composed of 30 mM Tris (pH 7.5 adjusted with HCl), 100 mM KCl, 1 mM DTT, and 2 mM $MgCl_2$. Buffer was filter sterilized (Whatman™ 0.2 µm) and stored at 4 °C.

All protein mixes were made on ice (4 °C), unless otherwise stated.

LactC2-iLID — For expression in the PURE system, the C2-L_2-iLID region from modified pMAL-c5X (pED48, see Sec. 2.6) was amplified by PCR using a forward primer (Ed194) containing a T7 promoter, a lac operator, a ribosome binding site and an in-frame N-terminal T7-tag (residues MASMTGGQQMG), and a reverse primer annealing to the 3' end of iLID (Ed195).

```
Ed194 | T7 promoter lac operator RBS T7 tag
  1 TAATACGACT CACTATAGGG GAATTGTGAG CGGATAACAA
 41 TTCCCCTCTA GAAATAATTT TGTTTAACTT TAAGAAGGAG
 81 ATATACATAT GGCTAGCATG ACTGGTGGAC AGCAAATGGG
121 TTGCACTGAA CCCCTAGGCC TGAAG
Ed195
  1 TTAAAAGTAA TTTTCGTCGT TCGC
```

parC — For visualization of *parC* DNA, a 418 bp stretch containing ten *parC* repeats was amplified by PCR from a fragment of the R1 plasmid [588] cloned into pUC57 (kindly provided by Christophe Danelon, Toulouse Biotechnology Institute, France), by using two primers (Ed136 and Ed137) labelled at their 5' end with Atto-647N.

Ed136

[11] A mutant of $ParR^{C\text{-}p}$ peptide should be generate such that it has higher dissociation constant (K_d) than the original peptide. This mutant can be made with a combination of approaches like, evaluating binding affinities of peptide variants with single of multiple point-mutations using Molecular Dynamics simulations, and/or experimentally generating and testing direct- or point- mutation library of the peptide.

[12] Computationally design the anti-$ParR^{C\text{-}p}$ binding peptide with slightly higher dissociation constant (K_d), using the new Rosetta-DL tools (based on RoseTTA-Fold [587]), and evaluating the binding affinities using Molecular Dynamics simulations.

[13] Actin also has a buffer with similar name, F-buffer.

```
  1 CCGACCGTGG AATACCGCAG CCGT
Ed137
  1 CATTTATAAA ACTCCTTATG GTGT
```

ParM — The actin-like protein ParM (originating from plasmid R1 [588]) was expressed from plasmid pJSC1 [568] in *Escherichia coli* C41/DE3 [589, 590], purified essentially according to [574], labelled with Alexa Fluor™ 568 C5-Maleimide (ThermoFisher A20341) according the manufacturer's instructions (∼31 % efficiency) and stored at −80 °C in buffer F.

ParR and derivatives — Wildtype ParR (originating from plasmid R1 [588]) was expressed as a ParR-intein-CBD fusion protein from plasmid pTXB1-ParR (kindly provided by Prof. Jan Löwe, MRC Cambridge, UK) and purified using chitin Sepharose (New England Biolabs S6651S) according to the manufacturer's instructions. The resulting tag-free ParR was labelled for 30 min at room temperature with 0.1 mM Alexa Fluor™ 488 C5 Maleimide (ThermoFisher A10254), and separated from free label by gel filtration (Superdex S200) in 50 mM Tris (pH 7.0), 100 mM KCl, 1 mM $MgCl_2$.

Several ParR fusion proteins were constructed for optogenetic studies, the earliest version of which contains two fused 'tandem' N-terminal fragments of ParR (residues 2-53) that are covalently linked by a 23-residue long sequence, similarly to the naturally occurring tandem RHH protein AvtR [591]. In addition, it contains a GCN4-derived leucine zipper for dimerization, and an iLID domain for light-dependent recruitment of SspB-fusion proteins [240]. It was expressed from pED64 in *Escherichia coli* ER2566 cells [592] and purified using Talon resin (ThermoFisher) via an amino-terminal His8-tag that was subsequently removed by treatment with homemade HRV 3C protease. Several derivatives of plasmid pED64 were constructed (see Tab. 7.1), that either lacked the leucine zipper (pED78 and pED84), included a YFP domain (pED77, pED78, pED82, and pED84), or contained an unfused $ParR^N$ tandem (pED80, pED82, and pED84). The latter two 'bicistronic' $ParR^N$ constructs were created by introducing a stop codon at the end of the first $ParR^N$ coding region, and replacing the flexible linker for 20 noncoding nucleotides containing a ribosome binding site. The final buffer used for size exclusion chromatography and storage was 20 mM HEPES/NaOH (pH 7.5, room temperature), 200 mM NaCl, 5 %w/v glycerol.

Table 7.1: **ParR derivative constructs.** Several derivatives of plasmid pED64 for different $ParR^N$ fusion proteins.

Plasmid	$ParR^N$	LZ	YFP
pED64	Tandem	+	-
pED77	Tandem	+	+
pED78	Tandem	-	+
pED80	Unfused	+	-
pED82	Unfused	+	+
pED84	Unfused	-	+

The fusion protein that we refer to as '$SspB\text{-}ParR^C$' is expressed as a dimeric fu-

sion protein of MBP, SspB, a GCN4-derived leucine zipper, the C-terminal fragment of ParR (residues 54-117), a Twin-Strep-tag (not used for purification), and a second stretch of the ParM-binding C-terminal peptide of ParR (residues 101-117) [555]. It was expressed from pED65 in *Escherichia coli* ER2566, purified using amylose resin (New England Biolabs E8021S), MBP-tag cleaved off by 3C protease, and labelled with Alexa Fluor™ 488 (ThermoFisher) according the manufacturer's instructions and stored at −80 °C in the same buffer as ParR^{N}-iLID.

Key | ParR^{N} L LZ iLID YFP

pED64

```
  1 MGHHHHHHHH DYDIPTTLEV LFQGPMDKRR TIAFKLNPDV
 41 NQTDKIVCDT LDSIPQGERS RLNRAALTAG LALYRQDSGG
 81 GATAGAGGAG GPAGLINPGG MDKRRTIAFK LNPDVNQTDK
121 IVCDTLDSIP QGERSRLNRA ALTAGLALYR QDGMKQLEDK
161 VEELLSKNYH LENEVARLKK LVGEGSGEFL ATTLERIEKN
201 FVITDPRLPD NPIIFASDSF LQLTEYSREE ILGRNCRFLQ
241 GPETDRATVR KIRDAIDNQT EVTVQLINYT KSGKKFWNVF
281 HLQPMRDYKG DVQYFIGVQL DGTERLHGAA EREAVMLIKK
321 TAFQIAEAAN DENYF
```

pED77

```
  1 MGHHHHHHHH DYDIPTTLEV LFQGPMDKRR TIAFKLNPDV
 41 NQTDKIVCDT LDSIPQGERS RLNRAALTAG LALYRQDSGG
 81 GATAGAGGAG GPAGLINPGG MDKRRTIAFK LNPDVNQTDK
121 IVCDTLDSIP QGERSRLNRA ALTAGLALYR QDGMKQLEDK
161 VEELLSKNYH LENEVARLKK LVGEGGMVSK GEELFTGVVP
201 ILVELDGDVN GHKFSVSGEG EGDATYGKLT LKFICTTGKL
241 PVPWPTLVTT FGYGLQCFAR YPDHMKQHDF FKSAMPEGYV
281 QERTIFFKDD GNYKTRAEVK FEGDTLVNRI ELKGIDFKED
321 GNILGHKLEY NYNSHNVYIM ADKQKNGIKV NFKIRHNIED
361 GSVQLADHYQ QNTPIGDGPV LLPDNHYLSY QSKLSKDPNE
401 KRDHMVLLEF VTAAGITLGM DELYKSGLRS GSGEFLATTL
441 ERIEKNFVIT DPRLPDNPII FASDSFLQLT EYSREEILGR
481 NCRFLQGPET DRATVRKIRD AIDNQTEVTV QLINYTKSGK
521 KFWNVFHLQP MRDYKGDVQY FIGVQLDGTE RLHGAAEREA
561 VMLIKKTAFQ IAEAANDENY F
```

pED78

```
  1 MGHHHHHHHH DYDIPTTLEV LFQGPMDKRR TIAFKLNPDV
 41 NQTDKIVCDT LDSIPQGERS RLNRAALTAG LALYRQDSGG
 81 GATAGAGGAG GPAGLINPGG MDKRRTIAFK LNPDVNQTDK
121 IVCDTLDSIP QGERSRLNRA ALTAGLALYR QDGMKQLEDK
161 GGMVSKGEEL FTGVVPILVE LDGDVNGHKF SVSGEGEGDA
201 TYGKLTLKFI CTTGKLPVPW PTLVTTFGYG LQCFARYPDH
241 MKQHDFFKSA MPEGYVQERT IFFKDDGNYK TRAEVKFEGD
281 TLVNRIELKG IDFKEDGNIL GHKLEYNYNS HNVYIMADKQ
321 KNGIKVNFKI RHNIEDGSVQ LADHYQQNTP IGDGPVLLPD
```

```
361 NHYLSYQSKL SKDPNEKRDH MVLLEFVTAA GITLGMDELY
401 KSGLRSGSGE FLATTLERIE KNFVITDPRL PDNPIIFASD
441 SFLQLTEYSR EEILGRNCRF LQGPETDRAT VRKIRDAIDN
481 QTEVTVQLIN YTKSGKKFWN VFHLQPMRDY KGDVQYFIGV
521 QLDGTERLHG AAEREAVMLI KKTAFQIAEA ANDENYF
pED80
  1 MGHHHHHHHH DYDIPTTLEV LFQGPMDKRR TIAFKLNPDV
 41 NQTDKIVCDT LDSIPQGERS RLNRAALTAG LALYRQD
  1 MDKRRTIAFK LNPDVNQTDK IVCDTLDSIP QGERSRLNRA
 41 ALTAGLALYR QDGMKQLEDK VEELLSKNYH LENEVARLKK
 81 LVGEGSGEFL ATTLERIEKN FVITDPRLPD NPIIFASDSF
121 LQLTEYSREE ILGRNCRFLQ GPETDRATVR KIRDAIDNQT
161 EVTVQLINYT KSGKKFWNVF HLQPMRDYKG DVQYFIGVQL
201 DGTERLHGAA EREAVMLIKK TAFQIAEAAN DENYF
pED82
  1 MGHHHHHHHH DYDIPTTLEV LFQGPMDKRR TIAFKLNPDV
 41 NQTDKIVCDT LDSIPQGERS RLNRAALTAG LALYRQD
  1 MDKRRTIAFK LNPDVNQTDK IVCDTLDSIP QGERSRLNRA
 41 ALTAGLALYR QDGMKQLEDK VEELLSKNYH LENEVARLKK
 81 LVGEGGMVSK GEELFTGVVP ILVELDGDVN GHKFSVSGEG
121 EGDATYGKLT LKFICTTGKL PVPWPTLVTT FGYGLQCFAR
161 YPDHMKQHDF FKSAMPEGYV QERTIFFKDD GNYKTRAEVK
201 FEGDTLVNRI ELKGIDFKED GNILGHKLEY NYNSHNVYIM
241 ADKQKNGIKV NFKIRHNIED GSVQLADHYQ QNTPIGDGPV
281 LLPDNHYLSY QSKLSKDPNE KRDHMVLLEF VTAAGITLGM
321 DELYKSGLRS GSGEFLATTL ERIEKNFVIT DPRLPDNPII
361 FASDSFLQLT EYSREEILGR NCRFLQGPET DRATVRKIRD
401 AIDNQTEVTV QLINYTKSGK KFWNVFHLQP MRDYKGDVQY
441 FIGVQLDGTE RLHGAAEREA VMLIKKTAFQ IAEAANDENY
481 F
pED84
  1 MGHHHHHHHH DYDIPTTLEV LFQGPMDKRR TIAFKLNPDV
 41 NQTDKIVCDT LDSIPQGERS RLNRAALTAG LALYRQD
  1 MDKRRTIAFK LNPDVNQTDK IVCDTLDSIP QGERSRLNRA
 41 ALTAGLALYR QDGMKQLEDK GGMVSKGEEL FTGVVPILVE
 81 LDGDVNGHKF SVSGEGEGDA TYGKLTLKFI CTTGKLPVPW
121 PTLVTTFGYG LQCFARYPDH MKQHDFFKSA MPEGYVQERT
161 IFFKDDGNYK TRAEVKFEGD TLVNRIELKG IDFKEDGNIL
201 GHKLEYNYNS HNVYIMADKQ KNGIKVNFKI RHNIEDGSVQ
241 LADHYQQNTP IGDGPVLLPD NHYLSYQSKL SKDPNEKRDH
281 MVLLEFVTAA GITLGMDELY KSGLRSGSGE FLATTLERIE
321 KNFVITDPRL PDNPIIFASD SFLQLTEYSR EEILGRNCRF
361 LQGPETDRAT VRKIRDAIDN QTEVTVQLIN YTKSGKKFWN
401 VFHLQPMRDY KGDVQYFIGV QLDGTERLHG AAEREAVMLI
441 KKTAFQI
```

SAMPLE PREPARATION Samples were prepared as described in Sec. 2.6. Coverslips were either cleaned in acid Piranha or silanized. Coverslips were Oxygen plasma treated (50 W, 3 min, Plasma Prep III SPI), followed by silanization with either Dimethyloctadecyl[3-(trimethoxysilyl)propyl]ammonium chloride (DMOAP, 435694 Sigma) or Trichloroethylene (TCE, 251402 Sigma) (2 %v/v, 20 min). Coverslips were washed with isopropyl alcohol (IPA), deionised water, and dried under an N_2 gas stream.

IMAGE ACQUISITION AND ANALYSIS Image acquisition was performed as described in Sec. 2.6. Samples were also observed on a Nikon ECLIPSE Ti2 inverted microscope with ring-TIRF unit (iLas 2 GATACA Systems, Paris) with 405 nm (100 mW), 488 nm (150 mW), 561 nm (150 mW), 642 nm (140 mW) laser lines and a quad filter cube (TRF89901 Chroma), a EM-CCD camera (iXon Ultra 888 Oxford Instruments), and 100 x objective (CFI APO TIRF 100XC oil 1.49 NA, Nikon). The final magnification was 7.8125 pixel/µm.

7.4.2 Methods

Dynamics assay

The protocol is similar to the MT dynamics assay (see Sec. 4.5) and [555, 574].
ParMRC mix — A 20 µL protein mix of 6 mg mL^{-1} BSA, 0.8 % methyl-cellulose, 1 x OX, 50 mM glucose, 0.4–5 µM ParM (3.1 % Alexa Fluor®568-ParM), 30–300 nM ParR (Cy5 labelled, optional), 0–750 pM *parC* (ATTO 647 -N labelled, optional), and 2–10 mM ATP or 2.5 mM AMP-PNP was made in F-buffer.

The flow chambers were assembled and functionalized with 10 min incubations of 5 mg mL^{-1} BSA. The mix was added in the flow chamber and the flow chamber was sealed with vacuum grease. The sample was imaged in TIRF mode, and photoactivation was performed with a pulse of 488 nm laser, whenever required.

Encapsulation

PROTEIN MIX A 40 µL protein mix of 2 mg mL^{-1} BSA, 1 x OX, 2.5 µM ParM (10 % Alexa Fluor®568), 3 mM AMP-PNP, 1.75 %w/v Sucrose, and 50 mM glucose was made in F-buffer.

LO DISPERSION LO dispersion were made as described in Sec. 2.6. LO dispersion of 99.875 n% DOPC, 0.1 n% PEG-2k-PE, and 0.025 n% Cy5-PE was made as described in Sec. 2.6.

FORMATION GUVs were formed with eDICE, as described in Sec. 2.6.

iLID expression

PURE EXPRESSION PURExpress® 2.0 was utilized as per supplier instructions. The 20 µL reaction mix of 10 µL solution I (buffer), 2 µL solution II (enzymes), 1 µL solution III (ribosomes), 1 µL FluoroTect™ $Green_{Lys}$ (5 x diluted), 5 nM LactC2-iLID DNA template, and 0–10 µM FMN was made in deionised water. Protein expression was

performed in PCR tubes, 5–24 h at 37 °C on the thermocycler. The sample was treated with 0.3 µL RNase A for 30 min at 37 °C.

DETECTION Sample was denatured in SDS loading buffer (with 10 mM DTT) for 10 min at 90 °C. Samples were loaded and run on a 4–12 % gradient NuPAGE™ gel (10338442 Invitrogen) at 200 V for 20 min. Gel was imaged on a gel imager (Typhoon Amersham Biosciences).

ACTIVITY ON SLB A pre-mix of 13 mg mL^{-1} κ-casein, 0.1 % methyl-cellulose, 50 mM KCl, and 1 x OX was made. A 13 µL protein mix of 0.384 mg mL^{-1} κ-casein, 1 µL Trolox, 10 µL PURE expressed LactC2-iLID, and 1 µM SspB-mCh was made in deionised water.

SUVs and SLB formation was performed as described in Sec. 6.4.

OPTO-PARR ACTIVITY

PARR^{N}-ILID Electrophoretic Mobility Shift Assay — The 8.8 µL reaction mixes of 1.5 nM *parC* with no ParR, or either 76 nM ParR or 76 nM ParR^{N}-iLID were made in F-buffer, and incubated in absence and presence of blue LED lamp (5730 LED 456 nm, 30 W; FL-30 SMD, Eurolite) for 25 min. Subsequently, 1.2 µL glycerol (30 %), and 2 µL gel loading dye was added. The dark and exposed samples were loaded and run on 6 % Novex™ TBE gels (12005735 Invitrogen) at 100 V for 90 min. Gels were imaged on a gel imager (Typhoon Amersham Biosciences).

SSPB-PARR^{C} SspB-ParR^{C} mix — A 20 µL protein mix of 6 mg mL^{-1} BSA, 0.8 % methyl-cellulose, 1 x OX, 50 mM glucose, 2.5 µM ParM (3.1 % Alexa Fluor®568-ParM), 300 nM SspB-ParR^{C} (Alexa Fluor®488), and 2.5 mM AMP-PNP was made in F-buffer.

The activity was tested in dynamic assay (as described above).

7.5 Acknowledgements

We thank Eli van der Sluis and Anne Doerr for purifying proteins. We thank Christophe Danelon for providing ParMRC related material and discussion regarding PURE expression, and Céline Cleij for help with PURE expression. We thank Jan Löwe for providing ParR plasmid. We thank Seraphine Wegner for suggestions regarding opto-genetic constructs.

7.6 Supplementary Information

7.6.1 Supplementary Figures

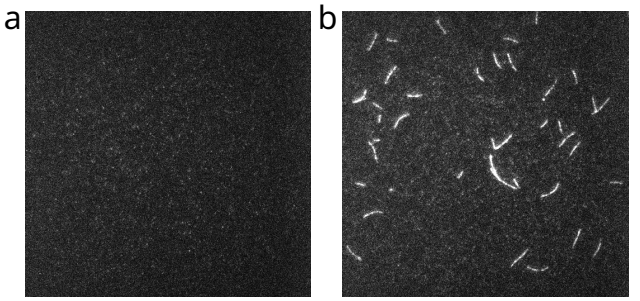

Figure 7.S1: **ParM polymerization.** Critical concentration of ParM is 0.6 µM with 2.5 mM AMP-PNP. (a) No filaments with 0.4 µM ParM, and (b) filaments 0.8 µM ParM.

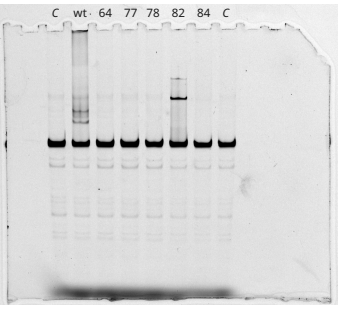

Figure 7.S2: **Activity of ParR^{N} constructs.** An EMSA on 6 % polyacrylamide gel, showing *parC* binding response of various ParR^{N}-iLID (Tab. 7.1), in presence of photo-activation. Lanes — '*C*' (*parC* only), 'wt' (wild type ParR), ParR^{N} constructs, and '*C*'. Concentrations — 76 nM ParR^{N} constructs, 1.5 nM *parC* each.

7.6.2 Supplementary Movies

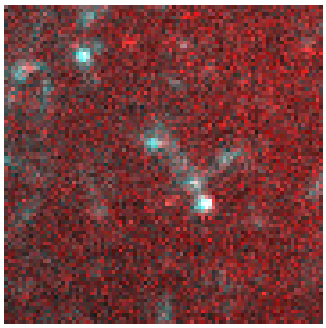

Figure 7.S3: **ParMRC dynamics.** The *parC* is seen segregating via elongating ParM spindle (from Fig. 7.5(c)). [| reduced]

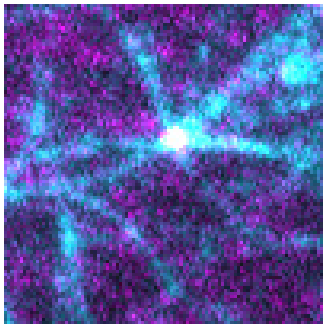

Figure 7.S4: **ParMR dynamics.** ParR assembles ParM filaments into asters and is also seen segregating via elongating ParM spindle (from Fig. 7.8(d) and Fig. 7.5(b)). [| reduced]

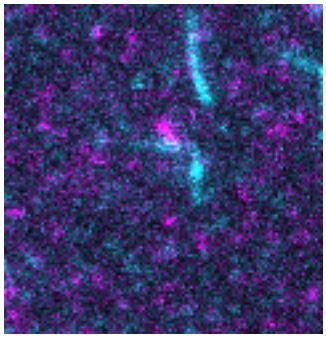

Figure 7.S5: **ParMR^{N} dynamics.** ParR^{N} searches for ParM filaments and captures them, assembling them into asters (from Fig. 7.8(c)). [| reduced]

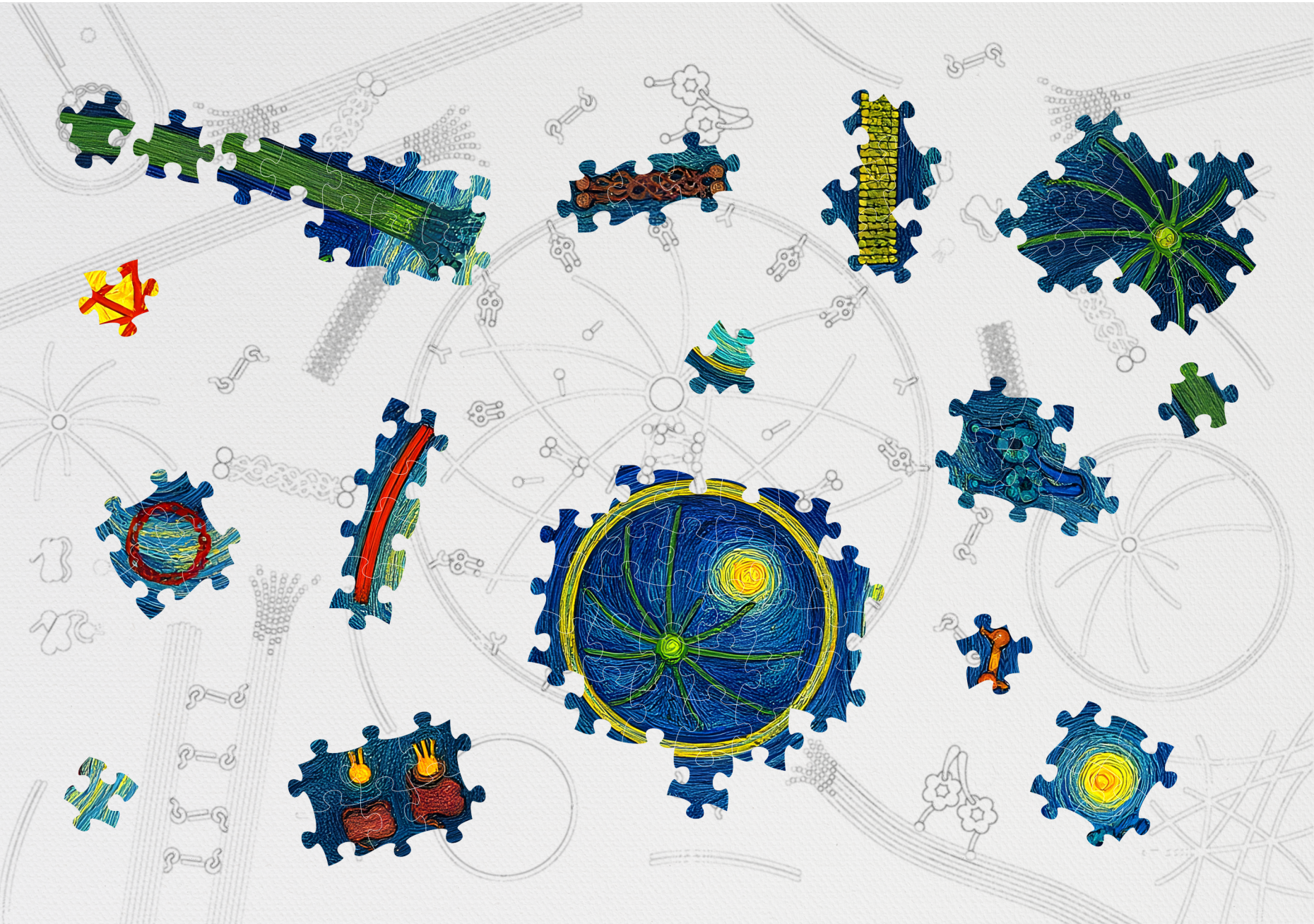

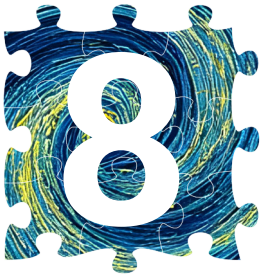

Discussion and Outlook

Hindsight is 20/20.
Between a rock and a hard place.
On the horizon.
Time will tell.

Building things from scratch improves our understanding of the mechanisms underlying their working. Building a synthetic cell is an ambitious task, but it could potentially provide us with a better understanding of life and its origins. So far, we have focused on cell division, understanding the asymmetric spindle positioning in in vitro reconstituted systems of C. elegans embryos' first cell division. We also increased the complexity of reconstitutions by introducing new components. We then designed a minimal synthetic spindle for DNA segregation in synthetic cells and presented our preliminary work. In this chapter, we discuss the major challenges encountered during this process. We summarize our findings and suggest future directions for both systems.

This chapter includes lipid phase seperation experiments performed by Luca Chicoş (under supervision of Yash Jawale), and opto-switches designed together with Beatriz Orozco Monroy, and Eli van der Sluis.

Introduction

We discussed the various complex and coordinated functions performed by a cell as the fundamental unit of life. Most of these cellular processes are executed through the cytoskeleton, especially microtubules (MTs, Chapter 1). Our focus was on MT-related nucleus and aster positioning. Out of the two approaches used to study these processes, we used bottom-up *in vitro* reconstitutions. For this, we explored different techniques of droplet and vesicle formation to create *in vitro* 3D cell-like containers (Chapter 2). We found that no one method suits all the needs, and the choice of methods depends on the requirement of this system. We investigated one of the methods, cDICE, to understand vesicle formation (Chapter 3). It was observed that tubulin encapsulation in vesicles is a problem with most of the methods (Chapter 4). Therefore, went back to using droplets for MT-based encapsulation and increased the complexity of MT-based reconstitution with introduction of new components like a bead (a nucleus mimic) and actin cortex (Chapter 5). We attempted to assemble a basic mitotic spindle with an optogenetic tool to create an asymmetric spindle positioning system inspired by the first cell division in a *C. elegans* embryo (Chapter 6). While the basic biophysical interactions — the pulling and pushing forces worked as expected, controlling the biochemical interactions — protein-(non-)protein interactions, in a minimal environment, whether it be vesicles or droplets and not the cell, was challenging. Fundamental insights into the mechanisms underlying various eukaryotic cellular functions are important for understanding the cell physiology and disease state, and a synthetic cell with reduced redundancies and cross-interactions across cellular processes could be an interesting tool to learn about life. So, we (as a part of BaSyC[1]) started designing a minimal ParMRC-based DNA-segregation spindle for synthetic cells (Chapter 7). Synthetic cells have a potential to be a simple and well-characterized system that can be used to rapidly develop robust real-world applications.

8.1 Challenges

Some of the challenges we faced during this work are described in the following subsections. These challenges posed severe limitations on the scope of the work to assemble an asymmetric spindle positioning (Sec. 1.3.2) and warrant further investigation. Overcoming these challenges could potentially advance the work and the overall field of *in vitro* 3D cytoskeletal reconstitutions.

Centrosome variability

As our work is focused on reconstituting MT-based aster positioning system, MTOCs are a major component of the reconstitution. MTOCs are required to generate several MTs that form the aster, generate pushing forces and provide tracks, for motors to generate pulling forces and MAPs to regulate their dynamics. We have used centrosomes, the natural and most potent MTOC of the cell. Given that MTOCs are purified from cells, we see batch-to-batch variation in quantity and concentration

[1] BaSyC — Building a Synthetic Cell consortium, the Netherlands

of centrosomes. The quality of the centrosomes is observed to vary with different purification protocols (Sec. 5.2.1). This makes the development of reliable and reproducible experiments challenging.

The current sucrose density gradient (SDG)-based centrifugation protocol [234, 437] is based on Bornens & Moudjou [234] from the 90 s. Centrosome purification needs to be optimized and standardized. There is a need for development of a new centrosome purification protocol, particularly for *in vitro* work, where purification yields higher concentration and centrosomes are still viable in their principal activity of MT nucleation. The quality of centrosomes should not only be assessed by using immunostaining and electron microscopy, but also using *in vitro* nucleation assay.

A recent method, centrosome affinity capture (CAPture)-based pull-down [465], has provided an alternative, but still has limited applications *in vitro*. Alternatives for centrosomes as MTOCs have also been developed. These artificial MTOCs include coating micron-sized beads with nucleator MAPs like Aurora-A kinase (from *Xenopus* egg extracts) [480] or with stable MT seeds [473]. Although these artificial MTOCs can successfully nucleate an aster-like structures, the process is hampered by beads sinking in 3D reconstitutions [481, §4]. Similarly, we are additionally exploring creation of artificial MTOCs, but this time accounting for the limitations we experienced previously. Our plan will involve coating nano-beads[2] with nucleator MAPs like CLASP2[3,4] CLASP has been shown to nucleate MTs in a non-centrosomal manner [593].

Tubulin and lipids incompatibility

This work hinges around tubulin encapsulation as well, given that we are focused on reconstituting 3D aster positioning systems. While there are different types of containers, vesicles are more cell-like, as compared to the droplets. Considering the advantages (and disadvantages) of vesicles over droplets (see Sec. 2.2), tubulin encapsulation in vesicles is preferred. However, we learned in Ch. 3, how the presence of even the tubulin buffer, MRB80, can negatively affect vesicle formation by altering the physical properties of the solution and lipid adsorption dynamics required for the formation of lipid layers in cDICE for GUV formation. This effect intensifies, becomes adverse in the presence of tubulin. The yield of vesicles is drastically reduced. These effects are predictable, given how complicated it is to work with tubulin (Sec. 4.1), but dynamic tubulin encapsulation in vesicles was not found feasible under current conditions (Sec. 4.3). Despite employing various vesicle formation strategies, we did not obtain any vesicles containing functionally active tubulin and in general, there were very few vesicles (Sec. 4.2.2). With a more direct observation in MSA with FsLB, it became clear that the presence of tubulin disrupts the lipid membrane (Sec. 4.2.3).

[2] ∼100–200 nm nano-sized beads are buoyant enough to not sink well during experimental timeframe (∼2–5 h), and still would have surface area enough to nucleate many MTs (≥100) to form an aster-like structure.

[3] Cytoplasmic Linker Associated Protein 2

[4] [personal communications] Anna Akhmanova (Utrecht University, Utrecht, the Netherlands) suggested the use of CLASP2 as a potent single-MAP based MT nucleator, and has kindly gifted a CLASP2 protein sample.

All the observations are indicative of some form of incompatibility between tubulin and lipid membranes. Tubulin is known to stick to membranes [428] but preliminary results from AFM[5], with tubulin on SLB show the presence of some form of tubulin rings, which appear to have formed holes in SLB[6]. Further studies are needed to decode the underlying mechanism. While coarse-grained molecular dynamics has demonstrated the preference of tubulin dimer polymerization site towards lipids [369], all-atom molecular dynamics or even quantum molecular dynamics (allowing for better interactions, and protein conformational changes like unfolding) simulation may provide better quantitative insights.

Opto-switch incompatibility

In minimal *in vitro* reconstitution, the system needs to be simplified and complex pathways need to be substituted. Also, constantly increasing the reconstitution complexity by addition of more components in the mix requires innovative and orthogonal ways to retain control over them. Opto-genetics is one such tool which provides the ability to have spatio-temporal control over protein functionality (Sec. 5.1). We tested opto-switch, iLID-SspB pair, a reversible light induced dimerizing system, with the motivation to recruit dynein asymmetrically on the cortex for asymmetric spindle positioning. Initial tests on glass surface show ideal reversible photo activation with spatio temporal control. However, testing inside droplets had almost no activation (Sec. 6.2.2). Similar photo activation issues have been encountered previously [481, §5].

[5] Atomic Force Microscopy
[6] Unpublished, data not shown.

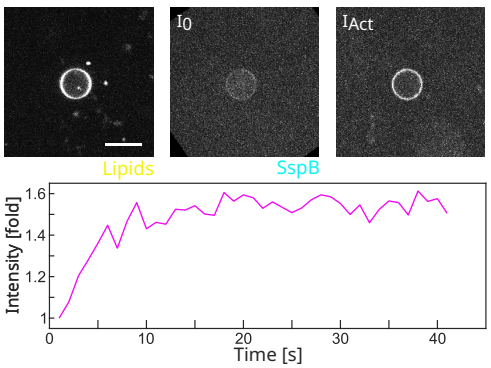

Figure 8.1: **Photo-activation in GUVs.** Photo-activation on LactC2-YFP-iLID and $SspB_{nano}$-mCherry in GUVs. (top) Image showing intensity of iLID recruited at the membrane of the GUV. Follows, image montage of SspB intensities at the cortex, representing time points — I_0 pre-activation, I_{Act} maximum (following a continuous activation). (bottom) Corresponding SspB binding dynamics. Intensity of SspB is normalized with averaged pre-activation ROI intensity to obtain a fold increase. iLID-SspB show activation and binding at GUV cortex. Scale bar — 20 µm.

In our previous experiments, we have consistently observed better photo activation on SLBs (Sec. 6.3), which has a bilayer of lipids as compared to a monolayer (loaded with surfactants) of droplets. So, we tested photo activation in vesicles. SspB binds to the iLID localized on the GUV membrane, upon photo activation (Fig. 8.1). This shows that opto-switch, iLID-SspB pair, can be used to trigger spatio temporal regulation of proteins in GUVs.

While other opto-switches[7] like VVD (Magnets) or CRY2-CIB1 can be tested to check if there is an issue specific to iLID-SspB, functionality in GUVs (more cell-like) over droplets is preferred.

8.2 Minimal mitotic spindle

8.2.1 Discussion

A spindle is one of the most intricate mechanical structure inside the cell, critical balancing pulling and pushing forces, governed by the law of biophysics. Many efforts have been made to recapture its properties and aesthetics, to understand it more precisely. In our quest for reconstituting an *in vitro* 3D asymmetric spindle position-

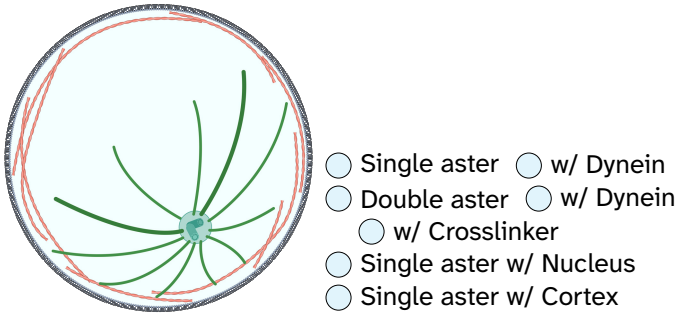

Figure 8.2: **Building up complexity.** Summary of building complexity towards reconstituting aster positioning systems. (Images created with BioRender.com) [| click on interactive buttons]

ing system, we first tested the encapsulation of tubulin in containers (Sec. 4.2.2). We also introduced, optimized, and characterized other cytoskeletal (actin) and non-cytoskeletal (nucleus-mimic, opto-switch) components (Secs. 5.2 & 6.2). This allowed us to build up the complexity of the minimal reconstitutions, mimicking a fully functional cellular process. We were able to assemble single aster positioning with dynein, nucleus and actin cortex, and double aster positioning with dynein, and kinesin5 and Ase1 (Fig. 8.2). Our current efforts to assemble an asymmetric spindle positioning system are stalled due to the following conundrum[8]. Opto-switch does not seem to work in droplets, but works in vesicles; on the other hand, tubulin encapsulation appears to be feasible only in droplets. Opto-switches are essential for fabricating asymmetric dynein localization at the cortex (a prerequisite for asymmetric spindle positioning), tubulin only can make the asters, and containers are mandatory, to provide a boundary for force generation. Either of the issues needs to

[7] see heterodimers at OptoBase
[8] Catch-22

be solved. A potential solution is to substitute opto-switches with CID[9] systems. Recent developments have led to creation of reversible CID systems, such as HaloTag-eDHFR with azoMTX [594]. Ideally, minimal spindle reconstitutions should be done in vesicles.

8.2.2 Outlook

Here, we describe things that to explored to potentially increase the complexity of *in vitro* 3D aster-based reconstitutions.

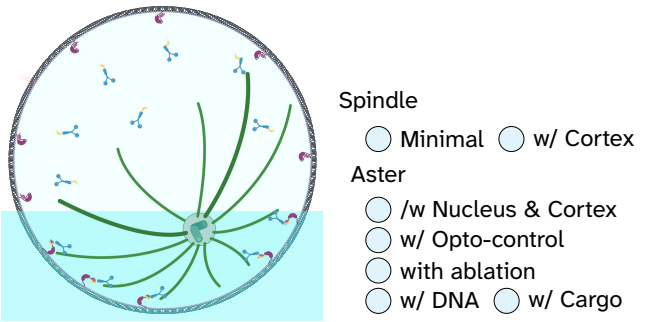

Figure 8.3: **Increasing complexity.** Possible ways to further increase the complexity towards reconstituting aster positioning systems. (Images created with BioRender.com) [| click on interactive buttons]

With previously well-characterized components, we can assemble a bipolar spindle with motors (dynein, kinesin5) and MAPs Ase1 together, and aster positioning with nucleus and actin cortex together (Fig. 8.3), with new components: aster positioning with cargo transport (for cytoplasmic pulling) [139] and nucleotide (ATP, GTP) regeneration systems, and Ndc80 (proxy for kinetochores, chromosomes-mimics with rods) [595] and anillin (actin-MT crosslinker responsible for cytokinetic ring alignment) [596] localization at mid-plane in two aster system. The aster positioning system could also be tested to quantify forces with physical manipulations [172] like shape and size changes, laser ablation, micro-needle, and magnetic tweezers.

Laser ablation

Laser ablation [597] is a technique that uses femtosecond pulse laser to precisely dissect subcellular structures like MTs. These cuts can be used to perturb the spindle, disrupt the force balance, and observe the resulting movements to infer the underlying mechanism. Ablation experiments in *C. elegans* embryos have shown the role of cortical pulling in asymmetric spindle positioning [194, 598] and pronuclear centration [598]. In Xenopus eggs extracts, these experiments helped reveal MT flux and polarity in spindles [599]. Here, we show our preliminary attempts at using laser ablation to sever MTs

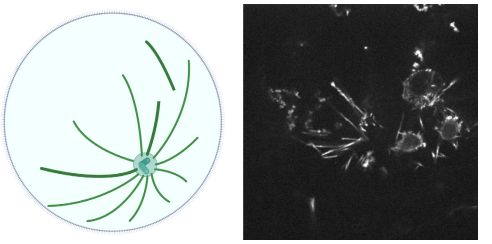

Figure 8.4: **Aster ablation.** Ablating MT aster in droplet, with a laser. [ ]

[9] chemically induced dimerization

in 3D *in vitro* constitutions. Ablating the centrosome of the aster inside a droplet shows dispersion of MTs centering the aster with pushing forces (Fig. 8.4). These laser ablation experiments will also help understand the force balance in *in vitro* reconstituted minimal spindle systems.

Lipid domains

A cell membrane is not just a physical boundary or confinement for contains the contents of the cell. It is as complex as the cell itself and plays an important role in cell function regulation. Membrane is described in the fluid mosaic model [600] as two leaflets (layers) containing a sea of lipid molecules and proteins. Lipids in the membrane have three phases, solid gel (G, S_o or L_β), liquid-ordered (L_o), and liquid-disordered or liquid-crystalline (L_d or L_α). These are temperature sensitive, above melting temperature (T_m), phases shift to L_d. Lipids in L_d (and L_o) phase exhibit high mobility and fast lateral diffusion ($L_d > L_o \gg S_o$) [601]. The L_o phase is also known as lipid rafts (domains) and has physiological functions [602]. Domains are caused by phase separation of lipids into mostly L_d-L_o phases (Fig. 8.4(a)). A ternary mixture of lipids is required for liquid-liquid phase separation (LLPS), with a sterol (cholesterol) being mandatory [603]. Ratio or composition of ternary mixture is difficult to predict, and needs to be experimentally determined [293, 604].

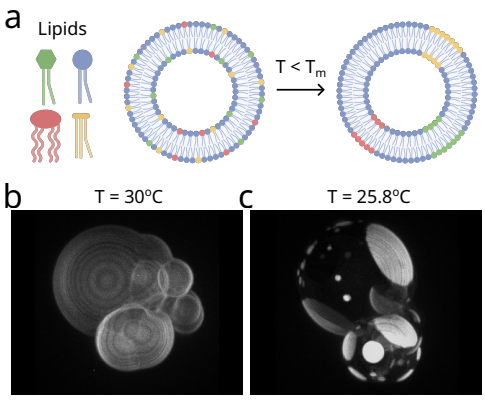

Figure 8.5: **LLPS.** (a) (left) Lipid types with different head and tails. (right) Schematic of lipid liquid-liquid phase separation on GUVs below melting temperature (T_m). (Image created with BioRender.com) (b) GUV at T =30 °C. (c) GUV at T =25.8 °C [ ]

These lipid domains can be used in *in vitro* constitutions for targeted recruitment of proteins, such as dynein for asymmetric spindle positioning. The sole use of opto-switch is not enough for localized membranes, since the activated protein can rapidly (<1 min) diffuse out of the photo-activated region-of-interest (~10 µm) on the membrane. The domain nature of rafts and reduced lateral mobility of lipids can help contain the protein to a limited region of the membrane. In principle, the protein can be directly attached to the domain. In our attempts, LLPS was observed on GUVs (Figs. 8.4(b) & 8.4(c)) with DOPC:DPPC:Chol (35:35:30) lipid mixture on lower temperature ($T < T_m$). For our ideal experiment of 3D *in vitro* reconstitution of asymmetric spindle positioning, in microfluidic traps (for shape symmetry-breaking), a ternary lipid mixture of DiPhyPS:DPPC:Chol (70:20:10-20:60:20) is suitable[10]. The L_o domains will align with walls of the trap and L_d domains at the two ends can,

[10] [personal communications] Sarah Keller (University of Washington, Seattle USA) helped to identify the LLPS experimental conditions suitable for our experiment.

act as (anterior-posterior) poles. And dynein can be recruited to either pole (with LactC2-tag targeting to DxPS (DiPhyPs) lipids concentrated in L_d domains).

Simulations

Similar to *in vivo* and *in vitro* experiments and the way their findings complement each other, *in silico* experiments are also valuable. ALthough results from *in silico* models and simulations are considered as predictions only until they are verified with or match either *in vivo* or *in vitro* results, they can help speculate and test theories. Cytosim[11] is one such tool, commonly used for simulating cytoskeleton-based scenarios [605]. Simulations have helped to explain cellular processes by testing hypotheses. For example, the MT pushing forces dominate centrosome positioning in confinement [484]. In fission yeast, the nuclear centering caused by MT dynamics requires a length-dependent catastrophe [606]. And in a *C. elegans* embryos, the anaphase spindle oscillation is controlled by MT dynamics [607]. We have also setup *in vitro* aster positioning simulations to validate our data and models (Fig. 8.6). Furthermore, simulations can potentially scan the parameter-space of different protein concentrations used in reconstitution and help reduce or identify ideal conditions to test in *in vitro* experiments.

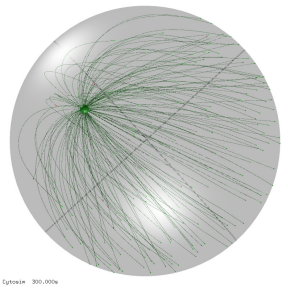

Figure 8.6: **Spindle simulation.** Simulating aster (and spindle) positioning scenarios with different components using Cytosim [605]. [ ]

Lastly, in the context of spindle assembly and positioning mechanisms — typically explained by the push-pull model — I propose viewing the spindle through the lens of tensegrity as well [608]. Although the tensegrity model has been proposed for the whole cell [609, 610], I suggest that the spindle itself can also be considered a tensegrity structure, with microtubules (MTs) acting as compression elements, and the membrane (at a large scale), together with motors and MAPs (at a smaller scale), serving as tension elements that enable remodelling. While the push-pull model explains localized force generation within the spindle, a tensegrity-based perspective offers a complementary framework for understanding how these forces are globally integrated and balanced — potentially explaining transitions between distinct spindle architectures during different stages of cell division.

8.3 Synthetic cell spindle

8.3.1 Discussion

Synthetic cell holds a great promise for the future of our understanding of life (Sec. 1.4). Reconstituting a cell from scratch, with known and well characterized components, provides better control for designing real-world biotech applications. We focused on designing a minimal DNA segregation spindle for the cell division module of the

[11] Cytosim, a Langevin-Brownian dynamics simulator.

synthetic cell. It is based on ParMRC system from *E. coli*. We introduced spatiotemporal control on DNA segregation using an opto-switch (Ch. 7). It involves controlling the ParMRC complex formation. Regulation is currently being achieved by splitting ParR N- and C- terminus domains and fusing them with iLID-SspB pair respectively. ParR will assemble only upon photo-activation by light, allowing spindle formation and subsequent segregation of DNA (Fig. 8.7). The Opto-ParMRC system needs further optimization, as the ParMRC complex formation is not completely light responsive yet (Sec. 7.2.1). This aspect remains under active investigation.

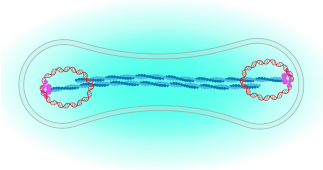

Figure 8.7: **Opto-ParMRC.** ParMRC based minimal spindle for synthetic cell with optogenetic spatiotemporal control, regulated with cell cycle. (Images created with BioRender.com) [ ]

8.3.2 Outlook

The following aspects need to be investigated to streamline opto-switch based spatiotemporal control of DNA segregation and assess the feasibility of integrating the modules into the synthetic cell cycle.

Single component Opto-ParR

As discussed in Sec. 7.3, the single component (only iLID based) strategy to make opto-ParR has advantages over the two component (iLID-SspB based). However, the approach to target ParR dimer's ability to bind to *parC* DNA is challenging owing to the need for ParMRC complex to attain its characteristic semicircular ring conformation. The presence of bulky iLID protein may still create stearic hindrance, even though the strategy to target ParR dimer's ability to bind to the ParM filament appears to be superior. This is because: first, the bulky iLID protein will either be positioned away from the *parC* binding domain or may even be absent, leaving ParR as wild type. Conceptually, this may allow for promoting ParM filament depolymerization once the DNA segregation has been achieved, as reversible unbinding of ParR (i.e. falling off of ParRC) from ParM filament tip may destabilize it. This could eventually help later during cytokinesis, as no ParM filament would be present in the fission plane, preventing cell division.

Module integration

Chapter 7 describes a module for DNA segregation in synthetic cells, but it represents only one "module" of the broader framework. A synthetic cell is required to perform other cellular processes (modules) as well, in a coordinated manner [611]. The following are some modules developed in isolation in the BaSyC research consortium that can be used to put together a possible synthetic cell cycle.

First, compatibility with these other modules needs to be tested, and optimized for. A synthetic cell consistently needs energy for its metabolism and other cellu-

lar processes. Module with ArcA, ArcB, ArcC1, and ArcD2[12] genes can constantly regenerate ATP within the system [612]. Synthetic cell needs to produce new proteins to sustain its cellular machinery. Proteins can be synthesized using PURE[13] systems [584]. Synthetic cell needs to grow, increase its membrane. A module with pGEMM7 gene cassette[14] can be used to produce PE and PG lipids for membrane growth [613]. On achieving sufficient growth, the synthetic cell needs to replicate its DNA. A module based on titration of DnaA levels [614] can trigger DNA replication initiation using a φ29 system [615]. Once replicated, DNA can be segregated by our Opto-ParMRC module. After DNA segregation, cell division needs to be initiated. A module, based on FtsZ-FtsA genes, can assemble and begin constriction of the liposome [616]. The division needs to take place in the middle of the cell. A module of MinDE genes can regulate the positioning of the FtsZ ring and even deform vesicles [617]. Complete cytokinesis is required for the daughter cell formation. A module based on DynaminA can scission the membrane at the neck formation from FtsZ ring constriction [618].

Second, these modules need to function in a coordinated manner, need a spatiotemporal regulation in accordance with the synthetic cell cycle [611]. For example, cell division should not be triggered before DNA replication. While *in vitro* reconstitution with a single module involving limited number of proteins is already technically demanding, incorporating (∼20–25) proteins across multiple modules from different species presents a significantly greater challenge. Achieving optimal functionality in a single container would mark a significant milestone, as the integration of them into a spatiotemporal cycle remains challenging. Evolutionary processes have employed generous time and resources, with countless attempts to design, create and evolve the cell, compared to our limited time, resources, and attempts to create even one minimal synthetic cell, despite its known and tried and tested natural design. Working on first principles, full understanding of certain components must be sacrificed, as was previously done. For example, ribosomes cannot be expressed and assembled functionally *in vitro*, and the synthetic cell requires a constant external supply of basic resources. Similarly, eventually for module integration, the idea of building a synthetic cell (BaSyC)[15] from scratch with known components, calls for a combination of evolution (natural) and AI[16] (synthetic) black-box[17] optimizations to evolve life from non-life (evolf)[18].

BaSyC eVolf

[12] Arginine deiminase (ArcA), ornithine transcarbamoylase (ArcB), carbamate kinase (ArcC1), and the arginine/ornithine antiporter ArcD2.
[13] IVTT systems — PURExpress, PUREfrex and PUREfrex2.0
[14] Seven genes — *plsB*, *plsC*, *cdsA*, *pssA*, *psd*, *pgsa*, and *pgpa*
[15] BaSyC — Building a Synthetic Cell consortium, the Netherlands
[16] artificial intelligence
[17] A system without any knowledge of its internal working.
[18] evolf — Evolving life from non-life consortium, the Netherlands

@ Nuria

8.4 Material and Methods

8.4.1 Materials

Chemicals See Sec. 2.6 for a detailed list of chemicals.

Lipids See Sec. 2.6 for a detailed list of lipids. All lipids were purchased from Avanti Research (Merck Life Science): 1,2-dihexadecanoyl-sn-glycero-3-phosphocholine (DPPC (T_m 41 °C), 850355C), cholest-5-en-3β-ol (Chol, 700100P).

8.4.2 Methods

Opto-genetic activation in GUVs

Protein mix Effect of proteins — A 40 µL protein mix of 1 mM Trolox, 0.5 mg mL^{-1} κ-casein, 50 mM KCl, 1 x OX, 2 µM SspB-mCh, 2 µM LactC2-YFP-iLID, 18.5 %w/v OptiPrep™, and 50 mM glucose was made in MRB80.

LO dispersion LO dispersion were made as described in Sec. 2.6. LO dispersion of 68.75 n% DOPC, 30 n% DOPS, 1 n% biotin-PE, and 0.25 n% Cy5-PE was made as described in Sec. 2.6.

Formation GUVs were formed with cDICE as described in Sec. 2.6. The sample was imaged in confocal mode and photo-activation was performed with a pulse of 488 nm laser.

Aster ablation in droplet

Protein mix A pre-mix of 0.3 mg mL^{-1} κ-casein, 0.016 % Tween 20, 1 x OX, 50 mM glucose, and 2 µM Atto488 (NHS ester) dye was made. A 20 µL protein mix with 8.61 µL pre-mix, 25 µM tubulin (10 % rhodamine-tubulin, stock 100 µM), 3 mM GTP, ∼1.56 µL sucrose (70 %w/v stock), and 10 %v centrosomes was made in MRB80. The mix was airfuged before the addition of centrosomes. After adding of centrosomes, the mix was maintained at room temperature (to prevent cold shock to centrosomes).
Lipid-in-oil (LO) dispersion LO dispersion of 69.99 n% DOPC, 30 n% DOPS, and 0.01 n% Cy5-PE was made as described in Sec. 2.6.
Formation Droplets were formed by pipetting method as described in Sec. 2.6. The sample was heated to 30 °C to induce tubulin polymerization. The sample was ablated with 355 nm (400 ps, 2 kW) UV pulse laser (iLas 3 GATACA Systems, Paris).

LLPS

Swelling mix A 300 µL swelling mix containing sucrose was made in MRB80. Osmolality was adjusted to 284 mOsm.
Lipid substrate Lipid solution (1 mg mL^{-1}) of 35 n% DOPC, 35 n% DPPC, 30 n% Chol, and ∼0.002 n% Cy5-PE was made in chloroform. Lipid-coated coverslips were made as described in Sec. 2.6.
Formation The gel-based swelled GUVs were formed as described in Sec. 2.6. The coverslips were heated to 60 °C (T_M>41 °C) on a hot plate, during swelling for 20 min. And the collected GUVs were also incubated at 41 °C for 10–15 min to melt the lipids, before imaging.

Cytosim

The simulation was executed in Cytosim, a Langevin-Brownian dynamics simulator downloaded from f-nedelec/cytosim GitLab repository. A 10 min simulation with 1 aster, and 250 MTs/aster in a 3D cell (⌀ 30 µm), was run on Intel machine (6th gen Core i3) running Linux (Ubuntu 22.04) with 8 GB memory. Runs lasted ∼4 h.

8.5 Data availability

All data used in the dissertation are available as a collection via 4TU.ResearchData at DOI: 10.4121/1647ae32-1a2d-4c18-8ad8-3e81ba87ac6a [324], which includes source data for the images and plots for all the chapters.

8.6 Acknowledgements

We thank Esengül Yildirim, and Eli van der Sluis for purifying proteins. We thank Sarah Keller for a discussion regarding LLPS.

Bibliography

1. Jones, E. M. *"Where is everybody?": An account of Fermi's question* https://web.archive.org/web/20070629 10311-ms.pdf. Mar. 1985 (cit. on p. 2).
2. Shklovskii, I. S. & Sagan, C. *Intelligent life in the universe* 901257032 (San Francisco : Holden-Day, 1966) (cit. on p. 2).
3. Hart, M. H. Explanation for the Absence of Extraterrestrials on Earth. *Quarterly Journal of the Royal Astronomical Society* **16,** 128–135 (1975) (cit. on p. 2).
4. Trifonov, E. N. Vocabulary of Definitions of Life Suggests a Definition. *Journal of Biomolecular Structure and Dynamics* **29,** 259–266. doi:10.1080/073911011010524992 (Oct. 2011) (cit. on p. 2).
5. Luisi, P. L. About Various Definitions of Life. *Origins of Life and Evolution of the Biosphere* **28,** 613–622. doi:10.1023/a:1006517315105 (1998) (cit. on p. 2).
6. Horowitz, N. H. & Miller, S. L. in *Progress in the Chemistry of Organic Natural Products* 423–459 (Springer Vienna, 1962). ISBN:9783709171554. doi:10.1007/978-3-7091-7153-0_10 (cit. on p. 2).
7. Johnson, G. *The Living World* ISBN:9781259694042 (McGraw-Hill Education, 17th Feb. 2017) (cit. on p. 2).
8. Bohr, N. Light and Life*. *Nature* **131,** 457–459. doi:10.1038/131457a0 (Apr. 1933) (cit. on p. 2).
9. Schrödinger, E. *What is Life?* ISBN:9780521427081 (Cambridge University Press, 31st Jan. 1992) (cit. on p. 2).
10. Le Mercier, P., Bolleman, J., de Castro, E., Gasteiger, E., Bansal, P., Auchincloss, A. H., Boutet, E., Breuza, L., Casals-Casas, C., Estreicher, A., Feuermann, M., Lieberherr, D., Rivoire, C., Pedruzzi, I., Redaschi, N. & Bridge, A. SwissBioPics—an interactive library of cell images for the visualization of subcellular location data. *Database* **2022.** doi:10.1093/database/baac026 (1st Jan. 2022) (cit. on pp. 2, 15).
11. Pollard, T. D. & Goldman, R. D. *The Cytoskeleton* ISBN:9781621820161 (Cold Spring Harbor Laboratory Press, 2017) (cit. on p. 2).
12. Hou, X., Chen, Y., Carrillo, N. D., Cryns, V. L., Anderson, R. A., Sun, J., Wang, S. & Chen, M. Phosphoinositide signaling at the cytoskeleton in the regulation of cell dynamics. *Cell Death amp; Disease* **16.** doi:10.1038/s41419-025-07616-x (14th Apr. 2025) (cit. on p. 2).
13. Alberts, B., Johnson, A., Lewis, J., Morgan, D., Raff, M., Roberts, K. & Walter, P. *Molecular Biology of the Cell* ISBN:9780815344322 (Garland Science, 18th Nov. 2014) (cit. on p. 2).

14. Pollard, T. D. Actin and Actin-Binding Proteins. *Cold Spring Harbor Perspectives in Biology* **8,** a018226. doi:10.1101/cshperspect.a018226 (17th Mar. 2016) (cit. on pp. 2, 9).

15. Dominguez, R. & Holmes, K. C. Actin Structure and Function. *Annual Review of Biophysics* **40,** 169–186. doi:10.1146/annurev-biophys-042910-155359 (9th June 2011) (cit. on p. 2).

16. Etienne-Manneville, S. Cytoplasmic Intermediate Filaments in Cell Biology. *Annual Review of Cell and Developmental Biology* **34,** 1–28. doi:10.1146/annurev-cellbio-100617-062534 (6th Oct. 2018) (cit. on pp. 2, 8).

17. Herrmann, H. & Aebi, U. Intermediate Filaments: Structure and Assembly. *Cold Spring Harbor Perspectives in Biology* **8,** a018242. doi:10.1101/cshperspect.a018242 (Nov. 2016) (cit. on pp. 2, 8).

18. Goodson, H. V. & Jonasson, E. M. Microtubules and Microtubule-Associated Proteins. *Cold Spring Harbor Perspectives in Biology* **10,** a022608. doi:10.1101/cshperspect.a022608 (June 2018) (cit. on pp. 2, 9).

19. Desai, A. & Mitchison, T. J. MICROTUBULE POLYMERIZATION DYNAMICS. *Annual Review of Cell and Developmental Biology* **13,** 83–117. doi:10.1146/annurev.cellbio.13.1.83 (Nov. 1997) (cit. on p. 2).

20. Ludueña, R. F., Shooter, E. M. & Wilson, L. Structure of the tubulin dimer. *Journal of Biological Chemistry* **252,** 7006–7014. doi:10.1016/s0021-9258(19)66927-9 (Oct. 1977) (cit. on p. 3).

21. Tilney, L. G., Bryan, J., Bush, D. J., Fujiwara, K., Mooseker, M. S., Murphy, D. B. & Snyder, D. H. MICROTUBULES: EVIDENCE FOR 13 PROTOFILAMENTS. *The Journal of Cell Biology* **59,** 267–275. doi:10.1083/jcb.59.2.267 (1st Nov. 1973) (cit. on p. 3).

22. Zhang, R., LaFrance, B. & Nogales, E. Separating the effects of nucleotide and EB binding on microtubule structure. *Proceedings of the National Academy of Sciences* **115.** doi:10.1073/pnas.1802637115 (June 2018) (cit. on p. 3).

23. Kamimura, S., Fujita, Y., Wada, Y., Yagi, T. & Iwamoto, H. Xray fiber diffraction analysis shows dynamic changes in axial tubulin repeats in native microtubules depending on paclitaxel content, temperature and GTPhydrolysis. *Cytoskeleton* **73,** 131–144. doi:10.1002/cm.21283 (Mar. 2016) (cit. on p. 3).

24. LaFrance, B. J., Roostalu, J., Henkin, G., Greber, B. J., Zhang, R., Normanno, D., McCollum, C. O., Surrey, T. & Nogales, E. Structural transitions in the GTP cap visualized by cryo-electron microscopy of catalytically inactive microtubules. *Proceedings of the National Academy of Sciences* **119.** doi:10.1073/pnas.2114994119 (Jan. 2022) (cit. on p. 3).

25. Gittes, F., Mickey, B., Nettleton, J. & Howard, J. Flexural rigidity of microtubules and actin filaments measured from thermal fluctuations in shape. *The Journal of cell biology* **120,** 923–934. doi:10.1083/jcb.120.4.923 (15th Feb. 1993) (cit. on pp. 3, 7).

26. Dogterom, M. & Yurke, B. Measurement of the Force-Velocity Relation for Growing Microtubules. *Science* **278,** 856–860. doi:10.1126/science.278.5339.856 (31st Oct. 1997) (cit. on pp. 3, 10, 12, 158).

27. Janson, M. E. & Dogterom, M. A bending mode analysis for growing microtubules: evidence for a velocity-dependent rigidity. *Biophysical journal* **87,** 2723–36. doi:10.1529/biophysj.103.038877 (Oct. 2004) (cit. on p. 3).

28. Chaaban, S. & Brouhard, G. J. A microtubule bestiary: structural diversity in tubulin polymers. *Molecular Biology of the Cell* **28** (ed Bement, W.) 2924–2931. doi:10.1091/mbc.e16-05-0271 (Nov. 2017) (cit. on p. 3).

29. Evans, L., Mitchison, T. & Kirschner, M. Influence of the centrosome on the structure of nucleated microtubules. *The Journal of cell biology* **100,** 1185–1191. doi:10.1083/jcb.100.4.1185 (1st Apr. 1985) (cit. on p. 3).

30. Mandelkow, E. M., Schultheiss, R., Rapp, R., Müller, M. & Mandelkow, E. On the surface lattice of microtubules: helix starts, protofilament number, seam, and handedness. *The Journal of cell biology* **102,** 1067–1073. doi:10.1083/jcb.102.3.1067 (1st Mar. 1986) (cit. on p. 3).

31. Chrétien, D. & Wade, R. H. New data on the microtubule surface lattice. *Biology of the Cell* **71,** 161–174. doi:10.1016/0248-4900(91)90062-r (Jan. 1991) (cit. on p. 3).

32. Lewis, S. A., Tian, G., Vainberg, I. E. & Cowan, N. J. Chaperonin-mediated folding of actin and tubulin. *The Journal of cell biology* **132,** 1–4. doi:10.1083/jcb.132.1.1 (1st Jan. 1996) (cit. on p. 3).

33. Lewis, S. A., Tian, G. & Cowan, N. J. The α- and β-tubulin folding pathways. *Trends in Cell Biology* **7,** 479–484. doi:10.1016/s0962-8924(97)01168-9 (Dec. 1997) (cit. on p. 3).

34. Minoura, I., Hachikubo, Y., Yamakita, Y., Takazaki, H., Ayukawa, R., Uchimura, S. & Muto, E. Overexpression, purification, and functional analysis of recombinant human tubulin dimer. *FEBS Letters* **587,** 3450–3455. doi:10.1016/j.febslet.2013.08.032 (7th Sept. 2013) (cit. on p. 3).

35. Ti, S.-C., Wieczorek, M. & Kapoor, T. M. Purification of Affinity Tag-free Recombinant Tubulin from Insect Cells. *STAR Protocols* **1,** 100011. doi:10.1016/j.xpro.2019.100011 (June 2020) (cit. on p. 3).

36. David-Pfeuty, T., Erickson, H. P. & Pantaloni, D. Guanosinetriphosphatase activity of tubulin associated with microtubule assembly. *Proceedings of the National Academy of Sciences* **74,** 5372–5376. doi:10.1073/pnas.74.12.5372 (Dec. 1977) (cit. on p. 3).

37. Spiegelman, B. M., Penningroth, S. M. & Kirschner, M. W. Turnover of tubulin and the N site GTP in chinese hamster ovary cells. *Cell* **12,** 587–600. doi:10.1016/0092-8674(77)90259-8 (Nov. 1977) (cit. on p. 3).

38. Weisenberg, R. C., Broisy, G. G. & Taylor, E. W. Colchicine-binding protein of mammalian brain and its relation to microtubules. *Biochemistry* **7,** 4466–4479. doi:10.1021/bi00852a043 (1st Dec. 1968) (cit. on p. 3).

39. Community, B. O. *Blender - a 3D modelling and rendering package* Blender Foundation (Stichting Blender Foundation, Amsterdam, 2018) (cit. on p. 4).

40. Mitchison, T. & Kirschner, M. Dynamic instability of microtubule growth. *Nature* **312,** 237–242. doi:10.1038/312237a0 (Nov. 1984) (cit. on pp. 3, 92, 179).

41. Mitchison, T. & Kirschner, M. Microtubule assembly nucleated by isolated centrosomes. *Nature* **312,** 232–237. doi:10.1038/312232a0 (Nov. 1984) (cit. on p. 3).

42. Detrich III, H. W., Parker, S. K., Williams Jr., R. C., Nogales, E. & Downing, K. H. Cold Adaptation of Microtubule Assembly and Dynamics. *Journal of Biological Chemistry* **275,** 37038–37047. doi:10.1074/jbc.m005699200 (Nov. 2000) (cit. on p. 3).

43. Troman, L., de Gaulejac, E., Biswas, A., Stiens, J., Kuropka, B., Moores, C. A. & Reber, S. Mechanistic basis of temperature adaptation in microtubule dynamics across frog species. *Current Biology* **35,** 612–628.e6. doi:10.1016/j.cub.2024.12.022 (Feb. 2025) (cit. on p. 3).

44. Fygenson, D. K., Braun, E. & Libchaber, A. Phase diagram of microtubules. *Physical Review E* **50,** 1579–1588. doi:10.1103/physreve.50.1579 (1st Aug. 1994) (cit. on p. 3).

45. Walker, R. A., O'Brien, E. T., Pryer, N. K., Soboeiro, M. F., Voter, W. A., Erickson, H. P. & Salmon, E. D. Dynamic instability of individual microtubules analyzed by video light microscopy: rate constants and transition frequencies. *The Journal of cell biology* **107,** 1437–1448. doi:10.1083/jcb.107.4.1437 (1st Oct. 1988) (cit. on p. 3).

46. Mandelkow, E. M., Mandelkow, E. & Milligan, R. A. Microtubule dynamics and microtubule caps: a time-resolved cryo-electron microscopy study. *The Journal of cell biology* **114,** 977–991. doi:10.1083/jcb.114.5.977 (1st Sept. 1991) (cit. on p. 3).

47. Melki, R., Carlier, M. F., Pantaloni, D. & Timasheff, S. N. Cold depolymerization of microtubules to double rings: geometric stabilization of assemblies. *Biochemistry* **28,** 9143–9152. doi:10.1021/bi00449a028 (14th Nov. 1989) (cit. on pp. 3, 4).

48. Alushin, G. M., Lander, G. C., Kellogg, E. H., Zhang, R., Baker, D. & Nogales, E. High-resolution microtubule structures reveal the structural transitions in αβ-tubulin upon GTP hydrolysis. *Cell* **157,** 1117–29. doi:10.1016/j.cell.2014.03.053 (22nd May 2014) (cit. on p. 4).

49. Kamimura, S., Fujita, Y., Wada, Y., Yagi, T. & Iwamoto, H. X-ray fiber diffraction analysis shows dynamic changes in axial tubulin repeats in native microtubules depending on paclitaxel content, temperature and GTP-hydrolysis. *Cytoskeleton* **73,** 131–144. doi:10.1002/cm.21283 (Mar. 2016) (cit. on p. 4).

50. Müller-Reichert, T., Chrétien, D., Severin, F. & Hyman, A. A. Structural changes at microtubule ends accompanying GTP hydrolysis: Information from a slowly hydrolyzable analogue of GTP, guanylyl (α,β)methylenediphosphonate. *Proceedings of the National Academy of Sciences* **95,** 3661–3666. doi:10.1073/pnas.95.7.3661 (31st Mar. 1998) (cit. on p. 4).

51. Jánosi, I. M., Chrétien, D. & Flyvbjerg, H. Modeling elastic properties of microtubule tips and walls. *European Biophysics Journal* **27,** 501–513. doi:10.1007/s002490050160 (21st Aug. 1998) (cit. on p. 4).

52. Howard, W. D. & Timasheff, S. N. GDP state of tubulin: stabilization of double rings. *Biochemistry* **25,** 8292–8300. doi:10.1021/bi00373a025 (16th Dec. 1986) (cit. on p. 4).

53. Carlier, M. F., Didry, D. & Pantaloni, D. Microtubule elongation and guanosine 5'-triphosphate hydrolysis. Role of guanine nucleotides in microtubule dynamics. *Biochemistry* **26,** 4428–4437. doi:10.1021/bi00388a036 (14th July 1987) (cit. on p. 4).

54. Carlier, M. F. & Pantaloni, D. Kinetic analysis of guanosine 5'-triphosphate hydrolysis associated with tubulin polymerization. *Biochemistry* **20,** 1918–1924. doi:10.1021/bi00510a030 (31st Mar. 1981) (cit. on p. 4).

55. Roostalu, J., Thomas, C., Cade, N. I., Kunzelmann, S., Taylor, I. A. & Surrey, T. The speed of GTP hydrolysis determines GTP cap size and controls microtubule stability. *eLife* **9.** doi:10.7554/elife.51992 (13th Feb. 2020) (cit. on p. 5).

56. Maurer, S. P., Fourniol, F. J., Bohner, G., Moores, C. A. & Surrey, T. EBs Recognize a Nucleotide-Dependent Structural Cap at Growing Microtubule Ends. *Cell* **149,** 371–382. doi:10.1016/j.cell.2012.02.049 (Apr. 2012) (cit. on p. 5).

57. Zanic, M., Stear, J. H., Hyman, A. A. & Howard, J. EB1 Recognizes the Nucleotide State of Tubulin in the Microtubule Lattice. *PLoS ONE* **4** (ed May, R. C.) e7585. doi:10.1371/journal.pone.0007585 (23rd Oct. 2009) (cit. on p. 5).

58. Caplow, M. & Shanks, J. Evidence that a single monolayer tubulin-GTP cap is both necessary and sufficient to stabilize microtubules. *Molecular Biology of the Cell* **7,** 663–675. doi:10.1091/mbc.7.4.663 (Apr. 1996) (cit. on p. 5).

59. Drechsel, D. N. & Kirschner, M. W. The minimum GTP cap required to stabilize microtubules. *Current Biology* **4,** 1053–1061. doi:10.1016/s0960-9822(00)00243-8 (Dec. 1994) (cit. on p. 5).

60. Kok, M., Huber, F., Kalisch, S.-M. & Dogterom, M. EB3-informed dynamics of the microtubule stabilizing cap during stalled growth. *Biophysical Journal*. doi:10.1016/j.bpj.2024.11.3314 (Nov. 2024) (cit. on pp. 5, 17).

61. Voter, W. A., O'Brien, E. T. & Erickson, H. P. Dilution-induced disassembly of microtubules: Relation to dynamic instability and the GTP cap. *Cell Motility* **18,** 55–62. doi:10.1002/cm.970180106 (Jan. 1991) (cit. on p. 5).

62. Seetapun, D., Castle, B. T., McIntyre, A. J., Tran, P. T. & Odde, D. J. Estimating the Microtubule GTP Cap Size In Vivo. *Current Biology* **22,** 1681–1687. doi:10.1016/j.cub.2012.06.068 (Sept. 2012) (cit. on p. 5).

63. Duellberg, C., Cade, N. I., Holmes, D. & Surrey, T. The size of the EB cap determines instantaneous microtubule stability. *eLife* **5.** doi:10.7554/elife.13470 (6th Apr. 2016) (cit. on p. 5).

64. Maurer, S. P., Bieling, P., Cope, J., Hoenger, A. & Surrey, T. GTPγS microtubules mimic the growing microtubule end structure recognized by end-binding proteins (EBs). *Proceedings of the National Academy of Sciences* **108,** 3988–3993. doi:10.1073/pnas.1014758108 (22nd Feb. 2011) (cit. on p. 5).

65. Hyman, A. A., Salser, S., Drechsel, D. N., Unwin, N. & Mitchison, T. J. Role of GTP hydrolysis in microtubule dynamics: information from a slowly hydrolyzable analogue, GMPCPP. *Molecular Biology of the Cell* **3,** 1155–1167. doi:10.1091/mbc.3.10.1155 (Oct. 1992) (cit. on pp. 5, 6).

66. SCHIFF, P. B., FANT, J. & HORWITZ, S. B. Promotion of microtubule assembly in vitro by taxol. *Nature* **277,** 665–667. doi:10.1038/277665a0 (Feb. 1979) (cit. on pp. 5, 6).

67. Al-Bassam, J. & Chang, F. Regulation of microtubule dynamics by TOG-domain proteins XMAP215/Dis1 and CLASP. *Trends in Cell Biology* **21,** 604–614. doi:10.1016/j.tcb.2011.06.007 (Oct. 2011) (cit. on pp. 5, 7).

68. Nogales, E., Grayer Wolf, S., Khan, I. A., Ludueña, R. F. & Downing, K. H. Structure of tubulin at 6.5 Å and location of the taxol-binding site. *Nature* **375,** 424–427. doi:10.1038/375424a0 (June 1995) (cit. on p. 5).

69. Kellogg, E. H., Hejab, N. M., Howes, S., Northcote, P., Miller, J. H., Díaz, J. F., Downing, K. H. & Nogales, E. Insights into the Distinct Mechanisms of Action of Taxane and Non-Taxane Microtubule Stabilizers from Cryo-EM Structures. *Journal of Molecular Biology* **429,** 633–646. doi:10.1016/j.jmb.2017.01.001 (Mar. 2017) (cit. on p. 5).

70. Jordan, M. A. & Wilson, L. Microtubules as a target for anticancer drugs. *Nature Reviews Cancer* **4,** 253–265. doi:10.1038/nrc1317 (Apr. 2004) (cit. on p. 5).

71. Findeisen, P., Mühlhausen, S., Dempewolf, S., Hertzog, J., Zietlow, A., Carlomagno, T. & Kollmar, M. Six Subgroups and Extensive Recent Duplications Characterize the Evolution of the Eukaryotic Tubulin Protein Family. *Genome Biology and Evolution* **6,** 2274–2288. doi:10.1093/gbe/evu187 (27th Aug. 2014) (cit. on p. 5).

72. Ludueña, R. F. & Banerjee, A. in *The Role of Microtubules in Cell Biology, Neurobiology, and Oncology* 123–175 (Humana Press, 2008). ISBN:9781588292940. doi:10.1007/978-1-59745-336-3_6 (cit. on p. 5).

73. Cleveland, D. W., Lopata, M. A., MacDonald, R. J., Cowan, N. J., Rutter, W. J. & Kirschner, M. W. Number and evolutionary conservation of α- and β-tubulin and cytoplasmic β- and γ-actin genes using specific cloned cDNA probes. *Cell* **20,** 95–105. doi:10.1016/0092-8674(80)90238-x (May 1980) (cit. on p. 5).

74. Committee, H. G. N. *Gene group: Tubulins (TUB)* https://www.genenames.org/data/genegroup/#!/group/778 (cit. on p. 5).

75. Turk, E., Wills, A. A., Kwon, T., Sedzinski, J., Wallingford, J. B. & Stearns, T. Zeta-Tubulin Is a Member of a Conserved Tubulin Module and Is a Component of the Centriolar Basal Foot in Multiciliated Cells. *Current Biology* **25,** 2177–2183. doi:10.1016/j.cub.2015.06.063 (Aug. 2015) (cit. on p. 5).

76. Sackett, D. L. in *Proteins: Structure, Function, and Engineering* 255–302 (Springer US, 1995). ISBN:9781489917294. doi:10.1007/978-1-4899-1727-0_9 (cit. on p. 5).

77. Nogales, E., Wolf, S. G. & Downing, K. H. Structure of the αβ tubulin dimer by electron crystallography. *Nature* **391,** 199–203. doi:10.1038/34465 (8th Jan. 1998) (cit. on pp. 5, 92).

78. Janke, C. & Magiera, M. M. The tubulin code and its role in controlling microtubule properties and functions. *Nature Reviews Molecular Cell Biology* **21,** 307–326. doi:10.1038/s41580-020-0214-3 (27th Feb. 2020) (cit. on p. 5).

79. Roll-Mecak, A. Intrinsically disordered tubulin tails: complex tuners of microtubule functions? *Seminars in Cell & Developmental Biology* **37,** 11–19. doi:10.1016/j.semcdb.2014.09.026 (Jan. 2015) (cit. on p. 5).

80. Verhey, K. J. & Gaertig, J. The Tubulin Code. *Cell Cycle* **6,** 2152–2160. doi:10.4161/cc.6.17.4633 (Sept. 2007) (cit. on p. 6).

81. Kuchnir Fygenson, D., Flyvbjerg, H., Sneppen, K., Libchaber, A. & Leibler, S. Spontaneous nucleation of microtubules. *Physical Review E* **51,** 5058–5063. doi:10.1103/physreve.51.5058 (1st May 1995) (cit. on p. 6).

82. Caudron, N., Arnal, I., Buhler, E., Job, D. & Valiron, O. Microtubule Nucleation from Stable Tubulin Oligomers. *Journal of Biological Chemistry* **277,** 50973–50979. doi:10.1074/jbc.m209753200 (Dec. 2002) (cit. on p. 6).

83. Voter, W. A. & Erickson, H. P. The kinetics of microtubule assembly. Evidence for a two-stage nucleation mechanism. *Journal of Biological Chemistry* **259,** 10430–10438. doi:10.1016/s0021-9258(18)90982-8 (Aug. 1984) (cit. on p. 6).

84. Oosawa, F. *Thermodynamics of the polymerization of protein* ISBN:012527050X (Academic Press, London, 1975) (cit. on pp. 6, 7).

85. Tobacman, L. S. & Korn, E. D. The kinetics of actin nucleation and polymerization. *Journal of Biological Chemistry* **258,** 3207–3214. doi:10.1016/s0021-9258(18)32850-3 (Mar. 1983) (cit. on pp. 6, 7).

86. Wieczorek, M., Bechstedt, S., Chaaban, S. & Brouhard, G. J. Microtubule-associated proteins control the kinetics of microtubule nucleation. *Nature Cell Biology* **17,** 907–916. doi:10.1038/ncb3188 (22nd June 2015) (cit. on pp. 6, 7).

87. Flyvbjerg, H., Jobs, E. & Leibler, S. Kinetics of self-assembling microtubules: an "inverse problem" in biochemistry. *Proceedings of the National Academy of Sciences* **93,** 5975–5979. doi:10.1073/pnas.93.12.5975 (11th June 1996) (cit. on p. 6).

88. Rice, L. M., Moritz, M. & Agard, D. A. Microtubules form by progressively faster tubulin accretion, not by nucleation-elongation. *Journal of Cell Biology* **220.** doi:10.1083/jcb.202012079 (18th Mar. 2021) (cit. on p. 6).

89. Verde, F., Dogterom, M., Stelzer, E., Karsenti, E. & Leibler, S. Control of microtubule dynamics and length by cyclin A- and cyclin B-dependent kinases in Xenopus egg extracts. *The Journal of cell biology* **118,** 1097–1108. doi:10.1083/jcb.118.5.1097 (1st Sept. 1992) (cit. on p. 6).

90. Dogterom, M. & Leibler, S. Physical aspects of the growth and regulation of microtubule structures. *Physical Review Letters* **70,** 1347–1350. doi:10.1103/physrevlett.70.1347 (1st Mar. 1993) (cit. on p. 6).

91. VanBuren, V., Cassimeris, L. & Odde, D. J. Mechanochemical Model of Microtubule Structure and Self-Assembly Kinetics. *Biophysical Journal* **89,** 2911–2926. doi:10.1529/biophysj.105.060913 (Nov. 2005) (cit. on p. 6).

92. Alexandrova, V. V., Anisimov, M. N., Zaitsev, A. V., Mustyatsa, V. V., Popov, V. V., Ataullakhanov, F. I. & Gudimchuk, N. B. Theory of tip structure-dependent microtubule catastrophes and damage-induced microtubule rescues. *Proceedings of the National Academy of Sciences* **119.** doi:10.1073/pnas.2208294119 (7th Nov. 2022) (cit. on p. 6).

93. Gudimchuk, N. B., Alexandrova, V. V., Ulyanov, E. V., Fedorov, V. A., Kholina, E. G. & Kovalenko, I. B. Modeling Microtubule Dynamics on Lomonosov-2 Supercomputer of Moscow State University: From Atomistic to Cellular Scale Simulations. *Supercomputing Frontiers and Innovations* **11,** 107–116. doi:10.14529/jsfi240307 (Sept. 2024) (cit. on p. 6).

94. Keates, R. A. Effects of glycerol on microtubule polymerization kinetics. *Biochemical and Biophysical Research Communications* **97,** 1163–1169. doi:10.1016/0006-291x(80)91497-7 (Dec. 1980) (cit. on p. 6).

95. Roostalu, J. & Surrey, T. Microtubule nucleation: beyond the template. *Nature Reviews Molecular Cell Biology* **18,** 702–710. doi:10.1038/nrm.2017.75 (23rd Aug. 2017) (cit. on p. 6).

96. Zheng, Y., Wong, M. L., Alberts, B. & Mitchison, T. Nucleation of microtubule assembly by a γ-tubulin-containing ring complex. *Nature* **378,** 578–583. doi:10.1038/378578a0 (Dec. 1995) (cit. on p. 6).

97. Moritz, M., Braunfeld, M. B., Sedat, J. W., Alberts, B. & Agard, D. A. Microtubule nucleation by γ-tubulin-containing rings in the centrosome. *Nature* **378,** 638–640. doi:10.1038/378638a0 (7th Dec. 1995) (cit. on p. 6).

98. Lin, T.-c., Neuner, A. & Schiebel, E. Targeting of γ-tubulin complexes to microtubule organizing centers: conservation and divergence. *Trends in Cell Biology* **25,** 296–307. doi:10.1016/j.tcb.2014.12.002 (May 2015) (cit. on p. 6).

99. Petry, S., Groen, A. C., Ishihara, K., Mitchison, T. J. & Vale, R. D. Branching Microtubule Nucleation in Xenopus Egg Extracts Mediated by Augmin and TPX2. *Cell* **152,** 768–777. doi:10.1016/j.cell.2012.12.044 (Feb. 2013) (cit. on p. 6).

100. Brito, C., Serna, M., Guerra, P., Llorca, O. & Surrey, T. Transition of human γ-tubulin ring complex into a closed conformation during microtubule nucleation. *Science* **383,** 870–876. doi:10.1126/science.adk6160 (23rd Feb. 2024) (cit. on p. 6).

101. Vermeulen, B. J., Böhler, A., Gao, Q., Neuner, A., Župa, E., Chu, Z., Würtz, M., Jäkle, U., Gruss, O. J., Pfeffer, S. & Schiebel, E. γ-TuRC asymmetry induces local protofilament mismatch at the RanGTP-stimulated microtubule minus end. *The EMBO Journal* **43,** 2062–2085. doi:10.1038/s44318-024-00087-4 (10th Apr. 2024) (cit. on p. 6).

102. Aher, A., Urnavicius, L., Xue, A., Neselu, K. & Kapoor, T. M. Structure of the γ-tubulin ring complex-capped microtubule. *Nature Structural & Molecular Biology* **31,** 1124–1133. doi:10.1038/s41594-024-01264-z (12th Apr. 2024) (cit. on p. 6).

103. Rai, D., Song, Y., Hua, S., Stecker, K., Monster, J. L., Yin, V., Stucchi, R., Xu, Y., Zhang, Y., Chen, F., Katrukha, E. A., Altelaar, M., Heck, A. J. R., Wieczorek, M., Jiang, K. & Akhmanova, A. CAMSAPs and nucleation-promoting factors control microtubule release from γ-TuRC. *Nature Cell Biology* **26,** 404–420. doi:10.1038/s41556-024-01366-2 (29th Feb. 2024) (cit. on p. 6).

104. Tournebize, R., Popov, A., Kinoshita, K., Ashford, A. J., Rybina, S., Pozniakovsky, A., Mayer, T. U., Walczak, C. E., Karsenti, E. & Hyman, A. A. Control of microtubule dynamics by the antagonistic activities of XMAP215 and XKCM1 in Xenopus egg extracts. *Nature Cell Biology* **2,** 13–19. doi:10.1038/71330 (29th Nov. 1999) (cit. on p. 7).

105. Popov, A. V., Severin, F. & Karsenti, E. XMAP215 Is Required for the Microtubule-Nucleating Activity of Centrosomes. *Current Biology* **12,** 1326–1330. doi:10.1016/s0960-9822(02)01033-3 (Aug. 2002) (cit. on p. 7).

106. Ghosh, S., Hentrich, C. & Surrey, T. Micropattern-Controlled Local Microtubule Nucleation, Transport, and Mesoscale Organization. *ACS Chemical Biology* **8,** 673–678. doi:10.1021/cb300583p (14th Jan. 2013) (cit. on p. 7).

107. Roostalu, J., Cade, N. I. & Surrey, T. Complementary activities of TPX2 and chTOG constitute an efficient importin-regulated microtubule nucleation module. *Nature Cell Biology* **17,** 1422–1434. doi:10.1038/ncb3241 (28th Sept. 2015) (cit. on p. 7).

108. Hanson, J. & Lowy, J. The structure of F-actin and of actin filaments isolated from muscle. *Journal of Molecular Biology* **6,** 46–IN5. doi:10.1016/s0022-2836(63)80081-9 (Jan. 1963) (cit. on p. 7).

109. Huxley, H. Electron microscope studies on the structure of natural and synthetic protein filaments from striated muscle. *Journal of Molecular Biology* **7,** 281–IN30. doi:10.1016/s0022-2836(63)80008-x (Sept. 1963) (cit. on p. 7).

110. Fujii, T., Iwane, A. H., Yanagida, T. & Namba, K. Direct visualization of secondary structures of F-actin by electron cryomicroscopy. *Nature* **467,** 724–728. doi:10.1038/nature09372 (15th Sept. 2010) (cit. on p. 7).

111. Herman, I. M. Actin isoforms. *Current Opinion in Cell Biology* **5,** 48–55. doi:10.1016/s0955-0674(05)80007-9 (Feb. 1993) (cit. on p. 7).

112. Vandekerckhove, J. & Weber, K. At least six different actins are expressed in a higher mammal: An analysis based on the amino acid sequence of the amino-terminal tryptic peptide. *Journal of Molecular Biology* **126,** 783–802. doi:10.1016/0022-2836(78)90020-7 (Dec. 1978) (cit. on p. 7).

113. Pardee, J. D. & Spudich, J. A. in *Methods in Cell Biology* 271–289 (Elsevier, 1982). doi:10.1016/s0091-679x(08)60661-5 (cit. on p. 7).

114. Oda, T., Iwasa, M., Aihara, T., Maéda, Y. & Narita, A. The nature of the globular- to fibrous-actin transition. *Nature* **457,** 441–445. doi:10.1038/nature07685 (22nd Jan. 2009) (cit. on p. 7).

115. Pollard, T. D., Blanchoin, L. & Mullins, R. D. Molecular Mechanisms Controlling Actin Filament Dynamics in Nonmuscle Cells. *Annual Review of Biophysics and Biomolecular Structure* **29,** 545–576. doi:10.1146/annurev.biophys.29.1.545 (June 2000) (cit. on p. 8).

116. Wegner, A. Head to tail polymerization of actin. *Journal of Molecular Biology* **108,** 139–150. doi:10.1016/s0022-2836(76)80100-3 (Nov. 1976) (cit. on p. 8).

117. Lengsfeld, A. M., Löw, I., Wieland, T., Dancker, P. & Hasselbach, W. Interaction of Phalloidin with Actin. *Proceedings of the National Academy of Sciences* **71,** 2803–2807. doi:10.1073/pnas.71.7.2803 (July 1974) (cit. on p. 8).

118. Yarmola, E. G., Somasundaram, T., Boring, T. A., Spector, I. & Bubb, M. R. Actin-Latrunculin A Structure and Function. *Journal of Biological Chemistry* **275,** 28120–28127. doi:10.1074/jbc.m004253200 (Sept. 2000) (cit. on p. 8).

119. Mullins, R. D., Heuser, J. A. & Pollard, T. D. The interaction of Arp2/3 complex with actin: Nucleation, high affinity pointed end capping, and formation of branching networks of filaments. *Proceedings of the National Academy of Sciences* **95,** 6181–6186. doi:10.1073/pnas.95.11.6181 (26th May 1998) (cit. on p. 8).

120. Peter, A. & Stick, R. Evolutionary aspects in intermediate filament proteins. *Current Opinion in Cell Biology* **32,** 48–55. doi:10.1016/j.ceb.2014.12.009 (Feb. 2015) (cit. on p. 8).

121. Bodakuntla, S., Jijumon, A., Villablanca, C., Gonzalez-Billault, C. & Janke, C. Microtubule-Associated Proteins: Structuring the Cytoskeleton. *Trends in Cell Biology* **29,** 804–819. doi:10.1016/j.tcb.2019.07.004 (Oct. 2019) (cit. on p. 9).

122. Akhmanova, A. & Steinmetz, M. O. Control of microtubule organization and dynamics: two ends in the limelight. *Nature Reviews Molecular Cell Biology* **16,** 711–726. doi:10.1038/nrm4084 (12th Nov. 2015) (cit. on p. 9).

123. Roll-Mecak, A. & McNally, F. J. Microtubule-severing enzymes. *Current Opinion in Cell Biology* **22,** 96–103. doi:10.1016/j.ceb.2009.11.001 (Feb. 2010) (cit. on p. 9).

124. Walczak, C. E. & Shaw, S. L. A MAP for Bundling Microtubules. *Cell* **142,** 364–367. doi:10.1016/j.cell.2010.07.023 (Aug. 2010) (cit. on p. 9).

125. Dehmelt, L. & Halpain, S. The MAP2/Tau family of microtubule-associated proteins. *Genome Biology* **6,** 204. doi:10.1186/gb-2004-6-1-204 (2004) (cit. on p. 9).

126. Sweeney, H. L. & Holzbaur, E. L. Motor Proteins. *Cold Spring Harbor Perspectives in Biology* **10,** a021931. doi:10.1101/cshperspect.a021931 (May 2018) (cit. on p. 9).

127. Dogterom, M. & Koenderink, G. H. Actin-microtubule crosstalk in cell biology. *Nature Reviews Molecular Cell Biology* **20,** 38–54. doi:10.1038/s41580-018-0067-1 (15th Oct. 2018) (cit. on pp. 9, 12, 126).

128. Seetharaman, S. & Etienne-Manneville, S. Cytoskeletal Crosstalk in Cell Migration. *Trends in Cell Biology* **30,** 720–735. doi:10.1016/j.tcb.2020.06.004 (Sept. 2020) (cit. on p. 9).

129. Wu, H.-Y., Nazockdast, E., Shelley, M. J. & Needleman, D. J. Forces positioning the mitotic spindle: Theories, and now experiments. *BioEssays* **39.** doi:10.1002/bies.201600212 (27th Dec. 2016) (cit. on p. 10).

130. Holy, T. E., Dogterom, M., Yurke, B. & Leibler, S. Assembly and positioning of microtubule asters in microfabricated chambers. *Proceedings of the National Academy of Sciences of the United States of America* **94,** 6228–31. doi:10.1073/pnas.94.12.6228 (10th June 1997) (cit. on pp. 10, 140, 158).

131. Janson, M. E., de Dood, M. E. & Dogterom, M. Dynamic instability of microtubules is regulated by force. *The Journal of Cell Biology* **161,** 1029–1034. doi:10.1083/jcb.200301147 (23rd June 2003) (cit. on pp. 10, 17, 143, 158).

132. Kolomeisky, A. B. & Fisher, M. E. Force-Velocity Relation for Growing Microtubules. *Biophysical Journal* **80,** 149–154. doi:10.1016/s0006-3495(01)76002-x (Jan. 2001) (cit. on p. 10).

133. Mogilner, A. & Oster, G. Cell motility driven by actin polymerization. *Biophysical Journal* **71,** 3030–3045. doi:10.1016/s0006-3495(96)79496-1 (Dec. 1996) (cit. on p. 10).

134. Dogterom, M., Kerssemakers, J. W., Romet-Lemonne, G. & Janson, M. E. Force generation by dynamic microtubules. *Current Opinion in Cell Biology* **17,** 67–74. doi:10.1016/j.ceb.2004.12.011 (Feb. 2005) (cit. on pp. 10, 12, 158).

135. Howard, J. Elastic and damping forces generated by confined arrays of dynamic microtubules. *Physical Biology* **3,** 54–66. doi:10.1088/1478-3975/3/1/006 (28th Feb. 2006) (cit. on pp. 10, 12).

136. Laan, L., Pavin, N., Husson, J., Romet-Lemonne, G., van Duijn, M., López, M. P., Vale, R. D., Jülicher, F., Reck-Peterson, S. L. & Dogterom, M. Cortical Dynein Controls Microtubule Dynamics to Generate Pulling Forces that Position Microtubule Asters. *Cell* **148,** 502–514. doi:10.1016/j.cell.2012.01.007 (Feb. 2012) (cit. on pp. 10, 13, 17, 140, 158).

137. Gennerich, A., Carter, A. P., Reck-Peterson, S. L. & Vale, R. D. Force-induced bidirectional stepping of cytoplasmic dynein. *Cell* **131,** 952–65. doi:10.1016/j.cell.2007.10.016 (30th Nov. 2007) (cit. on p. 10).

138. Reck-Peterson, S. L., Yildiz, A., Carter, A. P., Gennerich, A., Zhang, N. & Vale, R. D. Single-Molecule Analysis of Dynein Processivity and Stepping Behavior. *Cell* **126,** 335–348. doi:10.1016/j.cell.2006.05.046 (July 2006) (cit. on pp. 10, 17, 164, 167).

139. Palenzuela, H., Lacroix, B., Sallé, J., Minami, K., Shima, T., Jegou, A., Romet-Lemonne, G. & Minc, N. In Vitro Reconstitution of Dynein Force Exertion in a Bulk Viscous Medium. *Current Biology* **30,** 4534–4540.e7. doi:10.1016/j.cub.2020.08.078 (Nov. 2020) (cit. on pp. 10, 202).

140. Rai, A. K., Rai, A., Ramaiya, A. J., Jha, R. & Mallik, R. Molecular Adaptations Allow Dynein to Generate Large Collective Forces inside Cells. *Cell* **152,** 172–182. doi:10.1016/j.cell.2012.11.044 (Jan. 2013) (cit. on p. 10).

141. Lüdecke, A., Seidel, A.-M., Braun, M., Lansky, Z. & Diez, S. Diffusive tail anchorage determines velocity and force produced by kinesin-14 between crosslinked microtubules. *Nature Communications* **9.** doi:10.1038/s41467-018-04656-0 (June 2018) (cit. on p. 10).

142. Bugiel, M., Mitra, A., Girardo, S., Diez, S. & Schäffer, E. Measuring Microtubule Supertwist and Defects by Three-Dimensional-Force-Clamp Tracking of Single Kinesin-1 Motors. *Nano Letters* **18,** 1290–1295. doi:10.1021/acs.nanolett.7b04971 (Feb. 2018) (cit. on p. 10).

143. Ramaiya, A., Roy, B., Bugiel, M. & Schäffer, E. Kinesin rotates unidirectionally and generates torque while walking on microtubules. *Proceedings of the National Academy of Sciences* **114,** 10894–10899. doi:10.1073/pnas.1706985114 (Sept. 2017) (cit. on p. 10).

144. Mitra, A., Meißner, L., Gandhimathi, R., Renger, R., Ruhnow, F. & Diez, S. Kinesin-14 motors drive a right-handed helical motion of antiparallel microtubules around each other. *Nature Communications* **11.** doi:10.1038/s41467-020-16328-z (May 2020) (cit. on p. 10).

145. Pyrpassopoulos, S., Arpağ, G., Feeser, E. A., Shuman, H., Tüzel, E. & Ostap, E. M. Force Generation by Membrane-Associated Myosin-I. *Scientific Reports* **6.** doi:10.1038/srep25524 (May 2016) (cit. on p. 10).

146. Tyska, M. J., Dupuis, D. E., Guilford, W. H., Patlak, J. B., Waller, G. S., Trybus, K. M., Warshaw, D. M. & Lowey, S. Two heads of myosin are better than one for generating force and motion. *Proceedings of the National Academy of Sciences* **96,** 4402–4407. doi:10.1073/pnas.96.8.4402 (Apr. 1999) (cit. on p. 10).

147. Buonfiglio, V., Pertici, I., Marcello, M., Morotti, I., Caremani, M., Reconditi, M., Linari, M., Fanelli, D., Lombardi, V. & Bianco, P. Force and kinetics of fast and slow muscle myosin determined with a synthetic sarcomere–like nanomachine. *Communications Biology* **7.** doi:10.1038/s42003-024-06033-8 (Mar. 2024) (cit. on p. 10).

148. Sosa, B. A., Rothballer, A., Kutay, U. & Schwartz, T. U. LINC Complexes Form by Binding of Three KASH Peptides to Domain Interfaces of Trimeric SUN Proteins. *Cell* **149,** 1035–1047. doi:10.1016/j.cell.2012.03.046 (May 2012) (cit. on p. 10).

149. Wu, J., Kent, I. A., Shekhar, N., Chancellor, T., Mendonca, A., Dickinson, R. B. & Lele, T. P. Actomyosin Pulls to Advance the Nucleus in a Migrating Tissue Cell. *Biophysical Journal* **106,** 7–15. doi:10.1016/j.bpj.2013.11.4489 (Jan. 2014) (cit. on p. 10).

150. Hagan, I. M. & Hyams, J. S. The use of cell division cycle mutants to investigate the control of microtubule distribution in the fission yeast *Schizosaccharomyces pombe*. *Journal of Cell Science* **89,** 343–357. doi:10.1242/jcs.89.3.343 (1st Mar. 1988) (cit. on p. 10).

151. Höög, J. L., Schwartz, C., Noon, A. T., O'Toole, E. T., Mastronarde, D. N., McIntosh, J. R. & Antony, C. Organization of Interphase Microtubules in Fission Yeast Analyzed by Electron Tomography. *Developmental Cell* **12,** 349–361. doi:10.1016/j.devcel.2007.01.020 (Mar. 2007) (cit. on p. 10).

152. Tolic□-Nørrelykke, I. M., Sacconi, L., Stringari, C., Raabe, I. & Pavone, F. S. Nuclear and Division-Plane Positioning Revealed by Optical Micromanipulation. *Current Biology* **15,** 1212–1216. doi:10.1016/j.cub.2005.05.052 (July 2005) (cit. on p. 10).

153. Tran, P., Doye, V., Chang, F. & Inoue, S. Microtubule-dependent nuclear positioning and nuclear-dependent septum positioning in the fission yeast Saccharomyces pombe. *The Biological Bulletin* **199,** 205–206. doi:10.2307/1542900 (Oct. 2000) (cit. on p. 10).

154. Yeh, E., Skibbens, R. V., Cheng, J. W., Salmon, E. D. & Bloom, K. Spindle dynamics and cell cycle regulation of dynein in the budding yeast, Saccharomyces cerevisiae. *The Journal of cell biology* **130,** 687–700. doi:10.1083/jcb.130.3.687 (1st Aug. 1995) (cit. on p. 11).

155. Markus, S. M. & Lee, W.-L. Regulated Offloading of Cytoplasmic Dynein from Microtubule Plus Ends to the Cortex. *Developmental Cell* **20,** 639–651. doi:10.1016/j.devcel.2011.04.011 (May 2011) (cit. on p. 11).

156. Ding, D.-Q., Chikashige, Y., Haraguchi, T. & Hiraoka, Y. Oscillatory nuclear movement in fission yeast meiotic prophase is driven by astral microtubules, as revealed by continuous observation of chromosomes and microtubules in living cells. *Journal of Cell Science* **111,** 701–712. doi:10.1242/jcs.111.6.701 (15th Mar. 1998) (cit. on p. 11).

157. Varshney, N. & Sanyal, K. Nuclear migration in budding yeasts: position before division. *Current Genetics* **65,** 1341–1346. doi:10.1007/s00294-019-01000-x (31st May 2019) (cit. on p. 11).

158. Garzon-Coral, C., Fantana, H. A. & Howard, J. A force-generating machinery maintains the spindle at the cell center during mitosis. *Science* **352,** 1124–1127. doi:10.1126/science.aad9745 (27th May 2016) (cit. on pp. 11, 13).

159. HAMAGUCHI, M. S. & HIRAMOTO, Y. Analysis of the Role of Astral Rays in Pronuclear Migration in Sand Dollar Eggs by the Colcemid-UV Method. *Development, Growth & Differentiation* **28,** 143–156. doi:10.1111/j.1440-169x.1986.00143.x (Apr. 1986) (cit. on p. 11).

160. Gönczy, P., Pichler, S., Kirkham, M. & Hyman, A. A. Cytoplasmic Dynein Is Required for Distinct Aspects of Mtoc Positioning, Including Centrosome Separation, in the One Cell Stage *Caenorhabditis elegans* Embryo. *The Journal of Cell Biology* **147,** 135–150. doi:10.1083/jcb.147.1.135 (4th Oct. 1999) (cit. on pp. 11, 13).

161. Malone, C. J., Misner, L., Le Bot, N., Tsai, M.-C., Campbell, J. M., Ahringer, J. & White, J. G. The C. elegans Hook Protein, ZYG-12, Mediates the Essential Attachment between the Centrosome and Nucleus. *Cell* **115,** 825–836. doi:10.1016/s0092-8674(03)00985-1 (Dec. 2003) (cit. on p. 11).

162. Reinsch, S. & Gönczy, P. Mechanisms of nuclear positioning. *Journal of Cell Science* **111,** 2283–2295. doi:10.1242/jcs.111.16.2283 (15th Aug. 1998) (cit. on p. 11).

163. Fielmich, L.-E., Schmidt, R., Dickinson, D. J., Goldstein, B., Akhmanova, A. & van den Heuvel, S. Optogenetic dissection of mitotic spindle positioning in vivo. *eLife* **7.** doi:10.7554/elife.38198 (15th Aug. 2018) (cit. on pp. 11, 19, 158, 159).

164. Schmidt, R. *Genetic and optogenetic analysis of cell cleavage plane positioning* PhD thesis (2020). ISBN:978-90-393-7238-8 (cit. on p. 11).

165. Delattre, M. & Goehring, N. W. in *Current Topics in Developmental Biology* 269–308 (Elsevier, 2021). ISBN:9780128161777. doi:10.1016/bs.ctdb.2020.12.006 (cit. on p. 11).

166. Deshpande, O. & Telley, I. A. Nuclear positioning during development: Pushing, pulling and flowing. *Seminars in Cell & Developmental Biology* **120,** 10–21. doi:10.1016/j.semcdb.2021.09.020 (Dec. 2021) (cit. on pp. 11, 126).

167. Kellogg, D. R., Mitchison, T. J. & Alberts, B. M. Behaviour of microtubules and actin filaments in living*Drosophila*embryos. *Development* **103,** 675–686. doi:10.1242/dev.103.4.675 (1st Aug. 1988) (cit. on p. 11).

168. Telley, I. A., Gáspár, I., Ephrussi, A. & Surrey, T. Aster migration determines the length scale of nuclear separation in the *Drosophila* syncytial embryo. *Journal of Cell Biology* **197,** 887–895. doi:10.1083/jcb.201204019 (18th June 2012) (cit. on p. 12).

169. Karr, T. L. & Alberts, B. M. Organization of the cytoskeleton in early Drosophila embryos. *The Journal of cell biology* **102,** 1494–1509. doi:10.1083/jcb.102.4.1494 (1st Apr. 1986) (cit. on p. 12).

170. Karsenti, E. & Vernos, I. The Mitotic Spindle: A Self-Made Machine. *Science* **294,** 543–547. doi:10.1126/science.1063488 (19th Oct. 2001) (cit. on p. 12).

171. Hertwig, O. *Das Problem der Befruchtung und der Isotropie des Eies, eine Theorie der Vererbung* urn:nbn:de:kobv:11-712722 (Verlag von Gustav Fischer, Jena, 1884) (cit. on p. 12).

172. Dumont, S. & Mitchison, T. J. Force and Length in the Mitotic Spindle. *Current Biology* **19,** R749–R761. doi:10.1016/j.cub.2009.07.028 (Sept. 2009) (cit. on pp. 12, 158, 202).

173. Scholey, J. M., Brust-Mascher, I. & Mogilner, A. Cell division. *Nature* **422,** 746–752. doi:10.1038/nature01599 (Apr. 2003) (cit. on pp. 12, 158).

174. Mitchison, T. J. & Salmon, E. D. Mitosis: a history of division. *Nature Cell Biology* **3,** E17–E21. doi:10.1038/35050656 (Jan. 2001) (cit. on p. 12).

175. Wittmann, T., Hyman, A. & Desai, A. The spindle: a dynamic assembly of microtubules and motors. *Nature Cell Biology* **3,** E28–E34. doi:10.1038/35050669 (Jan. 2001) (cit. on p. 12).

176. Walczak, C. E. & Heald, R. in *International Review of Cytology* 111–158 (Elsevier, 2008). doi:10.1016/s0074-7696(07)65003-7 (cit. on pp. 12, 158).

177. Rieder, C. L. & Salmon, E. The vertebrate cell kinetochore and its roles during mitosis. *Trends in Cell Biology* **8,** 310–318. doi:10.1016/s0962-8924(98)01299-9 (Aug. 1998) (cit. on p. 12).

178. Hill, T. L. Theoretical problems related to the attachment of microtubules to kinetochores. *Proceedings of the National Academy of Sciences* **82,** 4404–4408. doi:10.1073/pnas.82.13.4404 (July 1985) (cit. on p. 12).

179. Volkov, V. A., Huis in 't Veld, P. J., Dogterom, M. & Musacchio, A. Multivalency of NDC80 in the outer kinetochore is essential to track shortening microtubules and generate forces. *eLife* **7.** doi:10.7554/elife.36764 (9th Apr. 2018) (cit. on p. 12).

180. Lyczak, R., Gomes, J.-E. & Bowerman, B. Heads or Tails. *Developmental Cell* **3,** 157–166. doi:10.1016/s1534-5807(02)00226-5 (Aug. 2002) (cit. on p. 12).

181. Kapoor, T. M., Mayer, T. U., Coughlin, M. L. & Mitchison, T. J. Probing spindle assembly mechanisms with monastrol, a small molecule inhibitor of the mitotic kinesin, Eg5. *The Journal of cell biology* **150,** 975–88. doi:10.1083/jcb.150.5.975 (4th Sept. 2000) (cit. on p. 12).

182. Jiang, W., Jimenez, G., Wells, N. J., Hope, T. J., Wahl, G. M., Hunter, T. & Fukunaga, R. PRC1. *Molecular Cell* **2,** 877–885. doi:10.1016/s1097-2765(00)80302-0 (Dec. 1998) (cit. on p. 12).

183. Glotzer, M. The 3Ms of central spindle assembly: microtubules, motors and MAPs. *Nature Reviews Molecular Cell Biology* **10,** 9–20. doi:10.1038/nrm2609 (Jan. 2009) (cit. on p. 12).

184. Kline-Smith, S. L. & Walczak, C. E. Mitotic Spindle Assembly and Chromosome Segregation. *Molecular Cell* **15,** 317–327. doi:10.1016/j.molcel.2004.07.012 (Aug. 2004) (cit. on p. 12).

185. Minc, N., Burgess, D. & Chang, F. Influence of cell geometry on division-plane positioning. *Cell* **144,** 414–26. doi:10.1016/j.cell.2011.01.016 (4th Feb. 2011) (cit. on p. 12).

186. Pearson, C. G. & Bloom, K. Dynamic Microtubules Lead the Way for Spindle Positioning. *Nature Reviews Molecular Cell Biology* **5,** 481–492. doi:10.1038/nrm1402 (June 2004) (cit. on p. 13).

187. Roegiers, F. & Jan, Y. N. Asymmetric cell division. *Current Opinion in Cell Biology* **16,** 195–205. doi:10.1016/j.ceb.2004.02.010 (Apr. 2004) (cit. on p. 13).

188. Pelletier, J. F., Field, C. M., Fürthauer, S., Sonnett, M. & Mitchison, T. J. Co-movement of astral microtubules, organelles and F-actin by dynein and actomyosin forces in frog egg cytoplasm. *eLife* **9.** doi:10.7554/elife.60047 (7th Dec. 2020) (cit. on p. 13).

189. Wühr, M., Dumont, S., Groen, A. C., Needleman, D. J. & Mitchison, T. J. How does a millimeter-sized cell find its center? *Cell Cycle* **8,** 1115–1121. doi:10.4161/cc.8.8.8150 (15th Apr. 2009) (cit. on pp. 13, 126).

190. MCINTOSH, J. R., HEPLER, P. K. & WIE, D. G. V. Model for Mitosis. *Nature* **224,** 659–663. doi:10.1038/224659a0 (Nov. 1969) (cit. on pp. 13, 165).

191. Ma, R., Laan, L., Dogterom, M., Pavin, N. & Jülicher, F. General theory for the mechanics of confined microtubule asters. *New Journal of Physics* **16,** 013018. doi:10.1088/1367-2630/16/1/013018 (15th Jan. 2014) (cit. on pp. 13, 160).

192. Rose, L. & Gonczy, P. Polarity establishment, asymmetric division and segregation of fate determinants in early C. elegans embryos. *WormBook,* 1–43. doi:10.1895/wormbook.1.30.2 (30th Dec. 2014) (cit. on p. 13).

193. Cheng, N. N., Kirby, C. M. & Kemphues, K. J. Control of cleavage spindle orientation in Caenorhabditis elegans: the role of the genes par-2 and par-3. *Genetics* **139,** 549–559. doi:10.1093/genetics/139.2.549 (1st Feb. 1995) (cit. on p. 13).

194. Grill, S. W., Gönczy, P., Stelzer, E. H. K. & Hyman, A. A. Polarity controls forces governing asymmetric spindle positioning in the Caenorhabditis elegans embryo. *Nature* **409,** 630–633. doi:10.1038/35054572 (Feb. 2001) (cit. on pp. 13, 202).

195. Grill, S. W., Howard, J., Schäffer, E., Stelzer, E. H. K. & Hyman, A. A. The Distribution of Active Force Generators Controls Mitotic Spindle Position. *Science* **301,** 518–521. doi:10.1126/science.1086560 (25th July 2003) (cit. on p. 13).

196. Srinivasan, D. G., Fisk, R. M., Xu, H. & van den Heuvel, S. A complex of LIN-5 and GPR proteins regulates G protein signaling and spindle function in*C. elegans*. *Genes & Development* **17,** 1225–1239. doi:10.1101/gad.1081203 (2nd May 2003) (cit. on p. 13).

197. Nguyen-Ngoc, T., Afshar, K. & Gönczy, P. Coupling of cortical dynein and Gα proteins mediates spindle positioning in Caenorhabditis elegans. *Nature Cell Biology* **9,** 1294–1302. doi:10.1038/ncb1649 (5th Oct. 2007) (cit. on p. 13).

198. Kotak, S., Busso, C. & Gönczy, P. Cortical dynein is critical for proper spindle positioning in human cells. *Journal of Cell Biology* **199,** 97–110. doi:10.1083/jcb.201203166 (1st Oct. 2012) (cit. on p. 13).

199. Hendricks, A. G., Lazarus, J. E., Perlson, E., Gardner, M. K., Odde, D. J., Goldman, Y. E. & Holzbaur, E. L. Dynein Tethers and Stabilizes Dynamic Microtubule Plus Ends. *Current Biology* **22,** 632–637. doi:10.1016/j.cub.2012.02.023 (Apr. 2012) (cit. on p. 13).

200. Farhadifar, R., Baer, C. F., Valfort, A.-C., Andersen, E. C., Müller-Reichert, T., Delattre, M. & Needleman, D. J. Scaling, Selection, and Evolutionary Dynamics of the Mitotic Spindle. *Current Biology* **25,** 732–740. doi:10.1016/j.cub.2014.12.060 (Mar. 2015) (cit. on p. 13).

201. Kapitein, L. C., Peterman, E. J. G., Kwok, B. H., Kim, J. H., Kapoor, T. M. & Schmidt, C. F. The bipolar mitotic kinesin Eg5 moves on both microtubules that it crosslinks. *Nature* **435,** 114–118. doi:10.1038/nature03503 (May 2005) (cit. on pp. 13, 158).

202. Fink, G., Hajdo, L., Skowronek, K. J., Reuther, C., Kasprzak, A. A. & Diez, S. The mitotic kinesin-14 Ncd drives directional microtubule-microtubule sliding. *Nature Cell Biology* **11,** 717–723. doi:10.1038/ncb1877 (10th May 2009) (cit. on p. 13).

203. Scholey, J. E., Nithianantham, S., Scholey, J. M. & Al-Bassam, J. Structural basis for the assembly of the mitotic motor Kinesin-5 into bipolar tetramers. *eLife* **3.** doi:10.7554/elife.02217 (8th Apr. 2014) (cit. on p. 13).

204. Lansky, Z., Braun, M., Lüdecke, A., Schlierf, M., ten Wolde, P. R., Janson, M. E. & Diez, S. Diffusible Crosslinkers Generate Directed Forces in Microtubule Networks. *Cell* **160,** 1159–1168. doi:10.1016/j.cell.2015.01.051 (Mar. 2015) (cit. on pp. 13, 158).

205. Forth, S., Hsia, K.-C., Shimamoto, Y. & Kapoor, T. M. Asymmetric Friction of Nonmotor MAPs Can Lead to Their Directional Motion in Active Microtubule Networks. *Cell* **157,** 420–432. doi:10.1016/j.cell.2014.02.018 (Apr. 2014) (cit. on p. 13).

206. Braun, M., Lansky, Z., Fink, G., Ruhnow, F., Diez, S. & Janson, M. E. Adaptive braking by Ase1 prevents overlapping microtubules from sliding completely apart. *Nature Cell Biology* **13,** 1259–1264. doi:10.1038/ncb2323 (4th Sept. 2011) (cit. on pp. 13, 158).

207. Valfort, A.-C., Launay, C., Sémon, M. & Delattre, M. Evolution of mitotic spindle behavior during the first asymmetric embryonic division of nematodes. *PLOS Biology* **16** (ed Basto, R.) e2005099. doi:10.1371/journal.pbio.2005099 (22nd Jan. 2018) (cit. on p. 13).

208. Khatri, D., Brugière, T., Athale, C. A. & Delattre, M. Evolutionary divergence of anaphase spindle mechanics in nematode embryos constrained by antagonistic pulling and viscous forces. *Molecular Biology of the Cell* **33** (ed Mogilner, A.) doi:10.1091/mbc.e21-10-0532 (15th May 2022) (cit. on p. 13).

209. Oriola, D., Needleman, D. J. & Brugués, J. The Physics of the Metaphase Spindle. *Annual Review of Biophysics* **47,** 655–673. doi:10.1146/annurev-biophys-060414-034107 (20th May 2018) (cit. on p. 14).

210. Da Silva, R. G. L., Schweizer, J., Kamenova, K., Au, L., Blasimme, A. & Vayena, E. Organizational change of synthetic biology research: Emerging initiatives advancing a bottom-up approach. *Current Research in Biotechnology* **7,** 100188. doi:10.1016/j.crbiot.2024.100188 (2024) (cit. on p. 14).

211. Schwille, P. Jump-starting life? Fundamental aspects of synthetic biology. *Journal of Cell Biology* **210,** 687–690. doi:10.1083/jcb.201506125 (31st Aug. 2015) (cit. on pp. 14, 15).

212. Xu, X., Meier, F., Blount, B. A., Pretorius, I. S., Ellis, T., Paulsen, I. T. & Williams, T. C. Trimming the genomic fat: minimising and re-functionalising genomes using synthetic biology. *Nature Communications* **14.** doi:10.1038/s41467-023-37748-7 (8th Apr. 2023) (cit. on p. 14).

213. Hashimoto, M., Ichimura, T., Mizoguchi, H., Tanaka, K., Fujimitsu, K., Keyamura, K., Ote, T., Yamakawa, T., Yamazaki, Y., Mori, H., Katayama, T. & Kato, J.-i. Cell size and nucleoid organization of engineered *Escherichia coli* cells with a reduced genome. *Molecular Microbiology* **55,** 137–149. doi:10.1111/j.1365-2958.2004.04386.x (25th Nov. 2004) (cit. on p. 15).

214. Iwadate, Y., Honda, H., Sato, H., Hashimoto, M. & Kato, J.-i. Oxidative stress sensitivity of engineered Escherichia coli cells with a reduced genome. *FEMS Microbiology Letters* **322,** 25–33. doi:10.1111/j.1574-6968.2011.02331.x (29th June 2011) (cit. on p. 15).

215. Gibson, D. G., Glass, J. I., Lartigue, C., Noskov, V. N., Chuang, R.-Y., Algire, M. A., Benders, G. A., Montague, M. G., Ma, L., Moodie, M. M., Merryman, C., Vashee, S., Krishnakumar, R., Assad-Garcia, N., Andrews-Pfannkoch, C., Denisova, E. A., Young, L., Qi, Z.-Q., Segall-Shapiro, T. H., Calvey, C. H., Parmar, P. P., Hutchison III, C. A., Smith, H. O. & Venter, J. C. Creation of a Bacterial Cell Controlled by a Chemically Synthesized Genome. *Science* **329,** 52–56. doi:10.1126/science.1190719 (2nd July 2010) (cit. on p. 15).

216. Pelletier, J. F., Sun, L., Wise, K. S., Assad-Garcia, N., Karas, B. J., Deerinck, T. J., Ellisman, M. H., Mershin, A., Gershenfeld, N., Chuang, R.-Y., Glass, J. I. & Strychalski, E. A. Genetic requirements for cell division in a genomically minimal cell. *Cell* **184,** 2430–2440.e16. doi:10.1016/j.cell.2021.03.008 (Apr. 2021) (cit. on p. 15).

217. Forster, A. C. & Church, G. M. Towards synthesis of a minimal cell. *Molecular Systems Biology* **2.** doi:10.1038/msb4100090 (Jan. 2006) (cit. on pp. 15, 20).

218. Szostak, J. W., Bartel, D. P. & Luisi, P. L. Synthesizing life. *Nature* **409,** 387–390. doi:10.1038/35053176 (Jan. 2001) (cit. on p. 15).

219. Schwille, P. Bottom-Up Synthetic Biology: Engineering in a Tinkerer's World. *Science* **333,** 1252–1254. doi:10.1126/science.1211701 (2nd Sept. 2011) (cit. on p. 15).

220. Phillips, R., Kondev, J., Theriot, J. & Garcia, H. *Physical Biology of the Cell* ISBN:9780429168833 (CRC Press LLC, 2012) (cit. on p. 16).

221. Lombard, J., López-García, P. & Moreira, D. The early evolution of lipid membranes and the three domains of life. *Nature Reviews Microbiology* **10,** 507–515. doi:10.1038/nrmicro2815 (11th June 2012) (cit. on p. 16).

222. Rideau, E., Dimova, R., Schwille, P., Wurm, F. R. & Landfester, K. Liposomes and polymersomes: a comparative review towards cell mimicking. *Chemical Society Reviews* **47,** 8572–8610. doi:10.1039/c8cs00162f (2018) (cit. on p. 16).

223. Spoelstra, W. K., Deshpande, S. & Dekker, C. Tailoring the appearance: what will synthetic cells look like? *Current Opinion in Biotechnology* **51,** 47–56. doi:10.1016/j.copbio.2017.11.005 (June 2018) (cit. on p. 16).

224. Knight, T. *Draft Standard for Biobrick Biological Parts* BBF RFC 10. May 2007. doi:10.17487/RFC9405 (cit. on p. 16).

225. Shimizu, Y., Inoue, A., Tomari, Y., Suzuki, T., Yokogawa, T., Nishikawa, K. & Ueda, T. Cell-free translation reconstituted with purified components. *Nature Biotechnology* **19,** 751–755. doi:10.1038/90802 (Aug. 2001) (cit. on pp. 16, 182).

226. Nandagopal, N. & Elowitz, M. B. Synthetic Biology: Integrated Gene Circuits. *Science* **333,** 1244–1248. doi:10.1126/science.1207084 (2nd Sept. 2011) (cit. on p. 16).

227. Gallup, O., Ming, H. & Ellis, T. Ten future challenges for synthetic biology. *Engineering Biology* **5,** 51–59. doi:10.1049/enb2.12011 (2nd Aug. 2021) (cit. on p. 16).

228. Roth, S., Laan, L. & Dogterom, M. in *Methods in Enzymology* 205–230 (Elsevier, 2014). doi:10.1016/b978-0-12-397924-7.00012-1 (cit. on pp. 17, 32, 109, 167).

229. Romet-Lemonne, G., VanDuijn, M. & Dogterom, M. Three-Dimensional Control of Protein Patterning in Microfabricated Devices. *Nano Letters* **5,** 2350–2354. doi:10.1021/nl0507111 (26th Oct. 2005) (cit. on p. 17).

230. Baclayon, M., Kalisch, S.-M., Hendel, E., Laan, L., Husson, J., Munteanu, E. L. & Dogterom, M. in *Methods in Molecular Biology* 411–435 (Springer New York, 15th Nov. 2016). ISBN:9781493964192. doi:10.1007/978-1-4939-6421-5_16 (cit. on p. 17).

231. Laan, L., Husson, J., Munteanu, E. L., Kerssemakers, J. W. J. & Dogterom, M. Force-generation and dynamic instability of microtubule bundles. *Proceedings of the National Academy of Sciences* **105,** 8920–8925. doi:10.1073/pnas.0710311105 (July 2008) (cit. on p. 17).

232. Taberner, N., Weber, G., You, C., Dries, R., Piehler, J. & Dogterom, M. in *Methods in Cell Biology* 69–90 (Elsevier, 2014). doi:10.1016/b978-0-12-417136-7.00005-7 (cit. on p. 17).

233. Grishchuk, E. L., Molodtsov, M. I., Ataullakhanov, F. I. & McIntosh, J. R. Force production by disassembling microtubules. *Nature* **438,** 384–388. doi:10.1038/nature04132 (Nov. 2005) (cit. on p. 17).

234. Bornens, M. & Moudjou, M. in *Methods in Cell Biology* 13–34 (Elsevier, 1998). doi:10.1016/s0091-679x(08)61973-1 (cit. on pp. 17, 112, 129, 142, 146, 199).

235. Vleugel, M., Roth, S., Groenendijk, C. F. & Dogterom, M. Reconstitution of Basic Mitotic Spindles in Spherical Emulsion Droplets. *Journal of Visualized Experiments.* doi:10.3791/54278-v (13th Aug. 2016) (cit. on pp. 17, 18, 31, 32, 50, 127, 148).

236. Ndlec, F. J., Surrey, T., Maggs, A. C. & Leibler, S. Self-organization of microtubules and motors. *Nature* **389,** 305–308. doi:10.1038/38532 (Sept. 1997) (cit. on p. 18).

237. Juniper, M. P. N., Weiss, M., Platzman, I., Spatz, J. P. & Surrey, T. Spherical network contraction forms microtubule asters in confinement. *Soft Matter* **14,** 901–909. doi:10.1039/c7sm01718a (2018) (cit. on pp. 18, 109, 127, 140).

238. Baumann, H. & Surrey, T. Motor-mediated Cortical versus Astral Microtubule Organization in Lipid-monolayered Droplets. *Journal of Biological Chemistry* **289,** 22524–22535. doi:10.1074/jbc.m114.582015 (Aug. 2014) (cit. on pp. 18, 31, 127).

239. Vendel, K. J. A., Alkemade, C., Andrea, N., Koenderink, G. H. & Dogterom, M. in *Methods in Molecular Biology* 53–75 (Springer US, 27th Dec. 2019). ISBN:9781071602188. doi:10.1007/978-1-0716-0219-5_5 (cit. on pp. 18, 31, 32, 50, 80, 127, 140, 145).

240. Guntas, G., Hallett, R. A., Zimmerman, S. P., Williams, T., Yumerefendi, H., Bear, J. E. & Kuhlman, B. Engineering an improved light-induced dimer (iLID) for controlling the localization and activity of signaling proteins. *Proceedings of the National Academy of Sciences* **112,** 112–117. doi:10.1073/pnas.1417910112 (22nd Dec. 2014) (cit. on pp. 19, 48, 49, 128, 162, 163, 167, 180, 183, 189).

241. Van Bergeijk, P., Adrian, M., Hoogenraad, C. C. & Kapitein, L. C. Optogenetic control of organelle transport and positioning. *Nature* **518,** 111–114. doi:10.1038/nature14128 (7th Jan. 2015) (cit. on p. 19).

242. Virchow, R. *Die cellularpathologie in ihrer begründung auf physiologische und pathologische gewebelehre* (Berlin, A. Hirschwald, Pathologischen institute zu Berlin, Feb. 1858) (cit. on p. 19).

243. Wöhler, F. Ueber künstliche Bildung des Harnstoffs. *Annalen der Physik* **88,** 253–256. doi:10.1002/andp.18280880206 (Jan. 1828) (cit. on p. 19).

244. Miller, S. L. A Production of Amino Acids Under Possible Primitive Earth Conditions. *Science* **117,** 528–529. doi:10.1126/science.117.3046.528 (15th May 1953) (cit. on p. 19).

245. Miller, S. L. & Urey, H. C. Organic Compound Synthesis on the Primitive Earth. *Science* **130,** 245–251. doi:10.1126/science.130.3370.245 (31st July 1959) (cit. on p. 19).

246. Oparin, A. I. *The Origin of Life* ISBN:9780486602134 (Dover Publications, 1965) (cit. on p. 19).

247. Haldane, J. B. S. *The origins of life* first. ASIN : B019ZDQTIO (Penguin Books, 1954) (cit. on p. 19).

248. Luisi, P. L. *The Emergence of Life* ISBN:9780521821179 (Cambridge Press, 13th July 2006) (cit. on p. 19).

249. Ganti, T. *The Principles of Life* (eds Szathmary, E. & Griesemer, J.) 18th Sept. 2003. doi:10.1093/acprof:oso/9780198507260.001.0001 (cit. on p. 20).

250. Roth, S., Gârlea, I. C., Vleugel, M., Mulder, B. M. & Dogterom, M. *Reconstitution of basic mitotic spindles in cell-like confinement* 16th Sept. 2019. doi:10.1101/770602 (cit. on pp. 21, 140, 157, 159–161, 165, 166, 172).

251. *BaSyC - Building a Synthetic Cell* NWO Gravitation grant 024.003.019. https://www.basyc.nl/ (cit. on pp. 26, 64).

252. *European Synthetic Cell Initiative (SynCellEU)* https://syntheticcell.eu/ (cit. on p. 26).

253. *Build-A-Cell* NSF #1901145. https://www.buildacell.org/ (cit. on p. 26).

254. *MaxSynBio* https://www.maxsynbio.mpg.de/home (cit. on p. 26).

255. *fabriCELL* https://www.imperial.ac.uk/a-z-research/fabricell/ (cit. on p. 26).

256. Rawicz, W., Olbrich, K., McIntosh, T., Needham, D. & Evans, E. Effect of Chain Length and Unsaturation on Elasticity of Lipid Bilayers. *Biophysical Journal* **79,** 328–339. doi:10.1016/s0006-3495(00)76295-3 (July 2000) (cit. on p. 26).

257. Needham, D. & Nunn, R. Elastic deformation and failure of lipid bilayer membranes containing cholesterol. *Biophysical Journal* **58,** 997–1009. doi:10.1016/s0006-3495(90)82444-9 (Oct. 1990) (cit. on p. 26).

258. Hotani, H. Dynamic features of microtubules as visualized by dark-field microscopy. *Advances in Biophysics* **26,** 135–156. doi:10.1016/0065-227x(90)90010-q (1990) (cit. on pp. 26, 93, 108, 111).

259. Fygenson, D. K., Marko, J. F. & Libchaber, A. Mechanics of Microtubule-Based Membrane Extension. *Physical Review Letters* **79,** 4497–4500. doi:10.1103/physrevlett.79.4497 (1st Dec. 1997) (cit. on pp. 26, 93, 108, 111).

260. Emsellem, V., Cardoso, O. & Tabeling, P. Vesicle deformation by microtubules: A phase diagram. *Physical Review E* **58,** 4807–4810. doi:10.1103/physreve.58.4807 (1st Oct. 1998) (cit. on pp. 26, 93, 108, 111).

261. Good, M. C., Vahey, M. D., Skandarajah, A., Fletcher, D. A. & Heald, R. Cytoplasmic Volume Modulates Spindle Size During Embryogenesis. *Science* **342,** 856–860. doi:10.1126/science.1243147 (15th Nov. 2013) (cit. on p. 26).

262. Hazel, J., Krutkramelis, K., Mooney, P., Tomschik, M., Gerow, K., Oakey, J. & Gatlin, J. C. Changes in Cytoplasmic Volume Are Sufficient to Drive Spindle Scaling. *Science* **342,** 853–856. doi:10.1126/science.1243110 (15th Nov. 2013) (cit. on p. 26).

263. Dimova, R. & Marques, C. M. *The Giant Vesicle Book* ISBN:9781498752176 (CRC Press, 2019) (cit. on pp. 26, 64).

264. Zhang, G. & Sun, J. Lipid in Chips: A Brief Review of Liposomes Formation by Microfluidics. *International Journal of Nanomedicine* **Volume 16,** 7391–7416. doi:10.2147/ijn.s331639 (Nov. 2021) (cit. on p. 26).

265. Van de Cauter, L., van Buren, L., Koenderink, G. H. & Ganzinger, K. A. Exploring Giant Unilamellar Vesicle Production for Artificial Cells — Current Challenges and Future Directions. *Small Methods* **7.** doi:10.1002/smtd.202300416 (18th July 2023) (cit. on pp. 26, 64).

266. Nair, K. S. & Bajaj, H. Advances in giant unilamellar vesicle preparation techniques and applications. *Advances in Colloid and Interface Science* **318,** 102935. doi:10.1016/j.cis.2023.102935 (Aug. 2023) (cit. on p. 26).

267. Harayama, T. & Riezman, H. Understanding the diversity of membrane lipid composition. *Nature Reviews Molecular Cell Biology* **19,** 281–296. doi:10.1038/nrm.2017.138 (7th Feb. 2018) (cit. on p. 26).

268. Politova, N. I., Tcholakova, S., Tsibranska, S., Denkov, N. D. & Muelheims, K. Coalescence stability of water-in-oil drops: Effects of drop size and surfactant concentration. *Colloids and Surfaces A: Physicochemical and Engineering Aspects* **531,** 32–39. doi:10.1016/j.colsurfa.2017.07.085 (Oct. 2017) (cit. on p. 26).

269. Elani, Y., Gee, A., Law, R. V. & Ces, O. Engineering multi-compartment vesicle networks. *Chemical Science* **4,** 3332. doi:10.1039/c3sc51164b (2013) (cit. on p. 27).

270. Pautot, S., Frisken, B. J. & Weitz, D. A. Production of Unilamellar Vesicles Using an Inverted Emulsion. *Langmuir* **19,** 2870–2879. doi:10.1021/la026100v (19th Feb. 2003) (cit. on p. 27).

271. Abkarian, M., Loiseau, E. & Massiera, G. Continuous droplet interface crossing encapsulation (cDICE) for high throughput monodisperse vesicle design. *Soft Matter* **7,** 4610. doi:10.1039/c1sm05239j (2011) (cit. on pp. 27, 36, 37, 53, 59, 64–66, 68, 73–76, 94–96, 108).

272. Yandrapalli, N., Petit, J., Bäumchen, O. & Robinson, T. Surfactant-free production of biomimetic giant unilamellar vesicles using PDMS-based microfluidics. *Communications Chemistry* **4.** doi:10.1038/s42004-021-00530-1 (29th June 2021) (cit. on pp. 27, 39).

273. Angelova, M. I. & Dimitrov, D. S. Liposome electroformation. *Faraday Discussions of the Chemical Society* **81,** 303. doi:10.1039/dc9868100303 (1986) (cit. on pp. 28, 64, 108).

274. Dao, T., Fauquignon, M., Fernandes, F., Ibarboure, E., Vax, A., Prieto, M. & Le Meins, J. Membrane properties of giant polymer and lipid vesicles obtained by electroformation and pva gel-assisted hydration methods. *Colloids and Surfaces A: Physicochemical and Engineering Aspects* **533,** 347–353. doi:10.1016/j.colsurfa.2017.09.005 (Nov. 2017) (cit. on p. 28).

275. Pott, T., Bouvrais, H. & Méléard, P. Giant unilamellar vesicle formation under physiologically relevant conditions. *Chemistry and Physics of Lipids* **154,** 115–119. doi:10.1016/j.chemphyslip.2008.03.008 (Aug. 2008) (cit. on p. 29).

276. Weakly, H. M., Wilson, K. J., Goetz, G. J., Pruitt, E. L., Li, A., Xu, L. & Keller, S. L. Several common methods of making vesicles (except an emulsion method) capture intended lipid ratios. *Biophysical Journal*. doi:10.1016/j.bpj.2024.08.019 (Aug. 2024) (cit. on p. 29).

277. Van de Cauter, L., Fanalista, F., van Buren, L., De Franceschi, N., Godino, E., Bouw, S., Danelon, C., Dekker, C., Koenderink, G. H. & Ganzinger, K. A. Optimized cDICE for Efficient Reconstitution of Biological Systems in Giant Unilamellar Vesicles. *ACS Synthetic Biology* **10,** 1690–1702. doi:10.1021/acssynbio.1c00068 (29th June 2021) (cit. on pp. 29, 36, 37, 53, 59, 64, 65, 68, 70, 73, 75, 77, 79, 82, 83, 94, 96, 107).

278. Blosser, M. C., Horst, B. G. & Keller, S. L. cDICE method produces giant lipid vesicles under physiological conditions of charged lipids and ionic solutions. *Soft Matter* **12,** 7364–7371. doi:10.1039/c6sm00868b (2016) (cit. on pp. 30, 34, 64).

279. Weiss, M., Frohnmayer, J. P., Benk, L. T., Haller, B., Janiesch, J.-W., Heitkamp, T., Börsch, M., Lira, R. B., Dimova, R., Lipowsky, R., Bodenschatz, E., Baret, J.-C., Vidakovic-Koch, T., Sundmacher, K., Platzman, I. & Spatz, J. P. Sequential bottom-up assembly of mechanically stabilized synthetic cells by microfluidics. *Nature Materials* **17,** 89–96. doi:10.1038/nmat5005 (16th Oct. 2017) (cit. on pp. 30, 41, 43, 55, 56).

280. Göpfrich, K., Haller, B., Staufer, O., Dreher, Y., Mersdorf, U., Platzman, I. & Spatz, J. P. One-Pot Assembly of Complex Giant Unilamellar Vesicle-Based Synthetic Cells. *ACS Synthetic Biology* **8,** 937–947. doi:10.1021/acssynbio.9b00034 (1st May 2019) (cit. on pp. 30, 41).

281. Pick, U. Liposomes with a large trapping capacity prepared by freezing and thawing of sonicated phospholipid mixtures. *Archives of Biochemistry and Biophysics* **212,** 186–194. doi:10.1016/0003-9861(81)90358-1 (Nov. 1981) (cit. on p. 30).

282. Jørgensen, I. L., Kemmer, G. C. & Pomorski, T. G. Membrane protein reconstitution into giant unilamellar vesicles: a review on current techniques. *European Biophysics Journal* **46,** 103–119. doi:10.1007/s00249-016-1155-9 (20th July 2016) (cit. on p. 30).

283. Pinot, M., Steiner, V., Dehapiot, B., Yoo, B.-K., Chesnel, F., Blanchoin, L., Kervrann, C. & Gueroui, Z. Confinement induces actin flow in a meiotic cytoplasm. *Proceedings of the National Academy of Sciences* **109,** 11705–11710. doi:10.1073/pnas.1121583109 (2nd July 2012) (cit. on p. 31).

284. Maan, R., Loiseau, E. & Bausch, A. R. Adhesion of Active Cytoskeletal Vesicles. *Biophysical Journal* **115,** 2395–2402. doi:10.1016/j.bpj.2018.10.013 (Dec. 2018) (cit. on p. 33).

285. Litschel, T., Ramm, B., Maas, R., Heymann, M. & Schwille, P. Beating Vesicles: Encapsulated Protein Oscillations Cause Dynamic Membrane Deformations. *Angewandte Chemie International Edition* **57,** 16286–16290. doi:10.1002/anie.201808750 (20th Nov. 2018) (cit. on pp. 33, 34, 64).

286. Gavriljuk, K., Scocozza, B., Ghasemalizadeh, F., Seidel, H., Nandan, A. P., Campos-Medina, M., Schmick, M., Koseska, A. & Bastiaens, P. I. H. A self-organized synthetic morphogenic liposome responds with shape changes to local light cues. *Nature Communications* **12.** doi:10.1038/s41467-021-21679-2 (9th Mar. 2021) (cit. on pp. 33, 93, 108, 110, 111).

287. Wubshet, N. H., Bashirzadeh, Y. & Liu, A. P. Fascin-induced actin protrusions are suppressed by dendritic networks in giant unilamellar vesicles. *Molecular Biology of the Cell* **32** (ed Discher, D.) 1634–1640. doi:10.1091/mbc.e21-02-0080 (19th Aug. 2021) (cit. on p. 33).

288. Baldauf, L., Frey, F., Arribas Perez, M., Idema, T. & Koenderink, G. H. Branched actin cortices reconstituted in vesicles sense membrane curvature. *Biophysical Journal* **122,** 2311–2324. doi:10.1016/j.bpj.2023.02.018 (June 2023) (cit. on pp. 33, 36, 37, 54, 75, 79, 85, 94).

289. Schaich, M., Sobota, D., Sleath, H., Cama, J. & Keyser, U. F. Characterization of lipid composition and diffusivity in OLA generated vesicles. *Biochimica et Biophysica Acta (BBA) - Biomembranes* **1862,** 183359. doi:10.1016/j.bbamem.2020.183359 (Sept. 2020) (cit. on p. 34).

290. Dürre, K. & Bausch, A. R. Formation of phase separated vesicles by double layer cDICE. *Soft Matter* **15,** 9676–9681. doi:10.1039/c8sm02491j (2019) (cit. on p. 34).

291. Pautot, S., Frisken, B. J. & Weitz, D. A. Engineering asymmetric vesicles. *Proceedings of the National Academy of Sciences* **100,** 10718–10721. doi:10.1073/pnas.1931005100 (8th Sept. 2003) (cit. on p. 34).

292. Lu, L., Doak, W. J., Schertzer, J. W. & Chiarot, P. R. Membrane mechanical properties of synthetic asymmetric phospholipid vesicles. *Soft Matter* **12,** 7521–7528. doi:10.1039/c6sm01349j (2016) (cit. on p. 34).

293. Veatch, S. L. & Keller, S. L. Separation of Liquid Phases in Giant Vesicles of Ternary Mixtures of Phospholipids and Cholesterol. *Biophysical Journal* **85,** 3074–3083. doi:10.1016/s0006-3495(03)74726-2 (Nov. 2003) (cit. on pp. 34, 203).

294. Schoenmakers, L. L. J., den Uijl, M. J., Postma, J. L., van den Akker, T. A. P., Huck, W. T. S. & Driessen, A. J. M. SecYEG-mediated translocation in a model synthetic cell. *Synthetic Biology* **9.** doi:10.1093/synbio/ysae007 (1st Jan. 2024) (cit. on p. 34).

295. Weinberger, A., Tsai, F.-C., Koenderink, G. H., Schmidt, T. F., Itri, R., Meier, W., Schmatko, T., Schröder, A. & Marques, C. Gel-Assisted Formation of Giant Unilamellar Vesicles. *Biophysical Journal* **105,** 154–164. doi:10.1016/j.bpj.2013.05.024 (July 2013) (cit. on pp. 34, 52, 64).

296. Yamabe, K., Kato, Y., Onishi, H. & Machida, Y. In vitro characteristics of liposomes and double liposomes prepared using a novel glass beads method. *Journal of Controlled Release* **90,** 71–79. doi:10.1016/s0168-3659(03)00159-7 (June 2003) (cit. on pp. 34, 51).

297. Blanken, D., van Nies, P. & Danelon, C. Quantitative imaging of gene-expressing liposomes reveals rare favorable phenotypes. *Physical Biology* **16,** 045002. doi:10.1088/1478-3975/ab0c62 (12th Apr. 2019) (cit. on pp. 34, 51).

298. Tsumoto, K., Matsuo, H., Tomita, M. & Yoshimura, T. Efficient formation of giant liposomes through the gentle hydration of phosphatidylcholine films doped with sugar. *Colloids and Surfaces B: Biointerfaces* **68,** 98–105. doi:10.1016/j.colsurfb.2008.09.023 (Jan. 2009) (cit. on p. 34).

299. Loiseau, E. *Approche biomimétique de la vaso-occlusion dans la drépanocytose: production de vésicules et microfluidique* Doctoral thesis (Université Montpellier II - Sciences et Techniques du Languedoc, 2011). tel: 00681260 (cit. on p. 36).

300. Bashirzadeh, Y., Wubshet, N., Litschel, T., Schwille, P. & Liu, A. P. Rapid Encapsulation of Reconstituted Cytoskeleton Inside Giant Unilamellar Vesicles. *Journal of Visualized Experiments*. doi:10.3791/63332 (10th Nov. 2021) (cit. on pp. 36, 37, 54, 59).

301. Deshpande, S., Caspi, Y., Meijering, A. E. C. & Dekker, C. Octanol-assisted liposome assembly on chip. *Nature Communications* **7.** doi:10.1038/ncomms10447 (22nd Jan. 2016) (cit. on pp. 37, 54, 64, 107).

302. Morita, M., Onoe, H., Yanagisawa, M., Ito, H., Ichikawa, M., Fujiwara, K., Saito, H. & Takinoue, M. Droplet-Shooting and Size-Filtration (DSSF) Method for Synthesis of Cell-Sized Liposomes with Controlled Lipid Compositions. *ChemBioChem* **16,** 2029–2035. doi:10.1002/cbic.201500354 (17th Aug. 2015) (cit. on pp. 39, 40, 55).

303. Venero, O. M., Sato, W., Heili, J. M., Deich, C. & Adamala, K. P. in *Methods in Molecular Biology* 227–235 (Springer US, 2022). ISBN:9781071619971. doi:10.1007/978-1-0716-1998-8_14 (cit. on pp. 39–41, 59).

304. Chen, Z., Liao, P., Zhang, F., Jiang, M., Zhu, Y. & Huang, Y. Centrifugal micro-channel array droplet generation for highly parallel digital PCR. *Lab on a Chip* **17,** 235–240. doi:10.1039/c6lc01305h (2017) (cit. on pp. 39, 40, 55).

305. Shin, D.-C., Morimoto, Y. & Takeuchi, S. *Generation of Monodisperse Droplets from Tens of μL Sample Volume using Centrifuge-Based Microfluidic Device* in *2019 IEEE 32nd International Conference on Micro Electro Mechanical Systems (MEMS)* (IEEE, Jan. 2019). doi:10.1109/memsys.2019.8870638 (cit. on p. 41).

306. Haller, B., Göpfrich, K., Schröter, M., Janiesch, J.-W., Platzman, I. & Spatz, J. P. Charge-controlled microfluidic formation of lipid-based single- and multicompartment systems. *Lab on a Chip* **18,** 2665–2674. doi:10.1039/c8lc00582f (2018) (cit. on pp. 41, 109).

307. Waeterschoot, J., Gosselé, W., Alizadeh Zeinabad, H., Lammertyn, J., Koos, E. & Casadevall i Solvas, X. Formation of Giant Unilamellar Vesicles Assisted by Fluorinated Nanoparticles. *Advanced Science* **10.** doi:10.1002/advs.202302461 (9th Oct. 2023) (cit. on p. 42).

308. Abate, A. R., Hung, T., Mary, P., Agresti, J. J. & Weitz, D. A. High-throughput injection with microfluidics using picoinjectors. *Proceedings of the National Academy of Sciences* **107,** 19163–19166. doi:10.1073/pnas.1006888107 (20th Oct. 2010) (cit. on pp. 42, 43, 56).

309. Fanalista, F., Birnie, A., Maan, R., Burla, F., Charles, K., Pawlik, G., Deshpande, S., Koenderink, G. H., Dogterom, M. & Dekker, C. Shape and Size Control of Artificial Cells for Bottom-Up Biology. *ACS Nano* **13,** 5439–5450. doi:10.1021/acsnano.9b00220 (10th May 2019) (cit. on pp. 42, 44, 56).

310. Heinrich, V. & Rawicz, W. Automated, High-Resolution Micropipet Aspiration Reveals New Insight into the Physical Properties of Fluid Membranes. *Langmuir* **21,** 1962–1971. doi:10.1021/la047801q (27th Jan. 2005) (cit. on p. 42).

311. Deng, N.-N., Vibhute, M. A., Zheng, L., Zhao, H., Yelleswarapu, M. & Huck, W. T. S. Macromolecularly Crowded Protocells from Reversibly Shrinking Monodisperse Liposomes. *Journal of the American Chemical Society* **140,** 7399–7402. doi:10.1021/jacs.8b03123 (5th June 2018) (cit. on p. 42).

312. Dreher, Y., Jahnke, K., Bobkova, E., Spatz, J. P. & Göpfrich, K. Division and Regrowth of Phase-Separated Giant Unilamellar Vesicles**. *Angewandte Chemie International Edition* **60,** 10661–10669. doi:10.1002/anie.202014174 (24th Mar. 2021) (cit. on p. 43).

313. Christopher, G. F., Bergstein, J., End, N. B., Poon, M., Nguyen, C. & Anna, S. L. Coalescence and splitting of confined droplets at microfluidic junctions. *Lab on a Chip* **9,** 1102. doi:10.1039/b813062k (2009) (cit. on p. 43).

314. Deshpande, S., Spoelstra, W. K., van Doorn, M., Kerssemakers, J. & Dekker, C. Mechanical Division of Cell-Sized Liposomes. *ACS Nano* **12,** 2560–2568. doi:10.1021/acsnano.7b08411 (18th Feb. 2018) (cit. on p. 43).

315. Wang, W., Yang, C. & Li, C. M. On-demand microfluidic droplet trapping and fusion for on-chip static droplet assays. *Lab on a Chip* **9,** 1504. doi:10.1039/b903468d (2009) (cit. on p. 43).

316. Litschel, T. & Schwille, P. Protein Reconstitution Inside Giant Unilamellar Vesicles. *Annual Review of Biophysics* **50,** 525–548. doi:10.1146/annurev-biophys-100620-114132 (6th May 2021) (cit. on p. 46).

317. Zacharias, D. A., Violin, J. D., Newton, A. C. & Tsien, R. Y. Partitioning of Lipid-Modified Monomeric GFPs into Membrane Microdomains of Live Cells. *Science* **296,** 913–916. doi:10.1126/science.1068539 (3rd May 2002) (cit. on p. 48).

318. Schmidt, H. G. Safe Piranhas: A Review of Methods and Protocols. *ACS Chemical Health & Safety* **29,** 54–61. doi:10.1021/acs.chas.1c00094 (29th Dec. 2021) (cit. on p. 49).

319. Schindelin, J., Arganda-Carreras, I., Frise, E., Kaynig, V., Longair, M., Pietzsch, T., Preibisch, S., Rueden, C., Saalfeld, S., Schmid, B., Tinevez, J.-Y., White, D. J., Hartenstein, V., Eliceiri, K., Tomancak, P. & Cardona, A. Fiji: an open-source platform for biological-image analysis. *Nature Methods* **9,** 676–682. doi:10.1038/nmeth.2019 (28th June 2012) (cit. on pp. 50, 78).

320. Laermer, F., Franssila, S., Sainiemi, L. & Kolari, K. in *Handbook of Silicon Based MEMS Materials and Technologies* 417–446 (Elsevier, 2020). ISBN:9780128177860. doi:10.1016/b978-0-12-817786-0.00016-5 (cit. on p. 51).

321. Chen, C., Ganar, K. A. & Deshpande, S. On-Chip Octanol-Assisted Liposome Assembly for Bioengineering. *Journal of Visualized Experiments*. doi:10.3791/65032 (17th Mar. 2023) (cit. on p. 54).

322. Johnson, J. M., Ha, T., Chu, S. & Boxer, S. G. Early Steps of Supported Bilayer Formation Probed by Single Vesicle Fluorescence Assays. *Biophysical Journal* **83,** 3371–3379. doi:10.1016/s0006-3495(02)75337-x (Dec. 2002) (cit. on p. 55).

323. Platzman, I., Janiesch, J.-W. & Spatz, J. P. Synthesis of Nanostructured and Biofunctionalized Water-in-Oil Droplets as Tools for Homing T Cells. *Journal of the American Chemical Society* **135,** 3339–3342. doi:10.1021/ja311588c (25th Feb. 2013) (cit. on p. 55).

324. Jawale, Y. *Building Minimal Spindles: Reconstituting spindle positioning in synthetic cells (Collection)* Collection (4TU.ResearchData, Sept. 2025). doi:10.4121/1647ae32-1a2d-4c18-8ad8-3e81ba87ac6a (cit. on pp. 57, 208).

325. Van de Cauter, L., Jawale, Y. K., Tam, D., Baldauf, L., van Buren, L., Koenderink, G. H., Dogterom, M. & Ganzinger, K. A. High-Speed Imaging of Giant Unilamellar Vesicle Formation in cDICE. *ACS Omega* **9,** 42278–42288. doi:10.1021/acsomega.4c04825 (25th Sept. 2024) (cit. on p. 63).

326. Ganzinger, K. A. & Schwille, P. More from less - bottom-up reconstitution of cell biology. *Journal of Cell Science* **132.** doi:10.1242/jcs.227488 (Feb. 2019) (cit. on p. 64).

327. Walde, P., Cosentino, K., Engel, H. & Stano, P. Giant Vesicles: Preparations and Applications. *ChemBioChem* **11,** 848–865. doi:10.1002/cbic.201000010 (Apr. 2010) (cit. on p. 64).

328. Reeves, J. P. & Dowben, R. M. Formation and properties of thin-walled phospholipid vesicles. *Journal of Cellular Physiology* **73,** 49–60. doi:10.1002/jcp.1040730108 (Feb. 1969) (cit. on p. 64).

329. Dimova, R. Giant Vesicles and Their Use in Assays for Assessing Membrane Phase State, Curvature, Mechanics, and Electrical Properties. *Annual Review of Biophysics* **48,** 93–119. doi:10.1146/annurev-biophys-052118-115342 (May 2019) (cit. on p. 64).

330. Papahadjopoulos, D. & Kimelberg, H. K. Phospholipid vesicles (liposomes) as models for biological membranes: Their properties and interactions with cholesterol and proteins. *Progress in Surface Science* **4,** 141–232. doi:10.1016/s0079-6816(74)80006-7 (Jan. 1974) (cit. on p. 64).

331. Mulla, Y., Aufderhorst-Roberts, A. & Koenderink, G. H. Shaping up synthetic cells. *Physical Biology* **15,** 041001. doi:10.1088/1478-3975/aab923 (Apr. 2018) (cit. on p. 64).

332. Gaut, N. J. & Adamala, K. P. Reconstituting Natural Cell Elements in Synthetic Cells. *Advanced Biology* **5.** doi:10.1002/adbi.202000188 (Feb. 2021) (cit. on p. 64).

333. Sercombe, L., Veerati, T., Moheimani, F., Wu, S. Y., Sood, A. K. & Hua, S. Advances and Challenges of Liposome Assisted Drug Delivery. *Frontiers in Pharmacology* **6.** doi:10.3389/fphar.2015.00286 (Dec. 2015) (cit. on p. 64).

334. Allen, T. M. & Cullis, P. R. Liposomal drug delivery systems: From concept to clinical applications. *Advanced Drug Delivery Reviews* **65,** 36–48. doi:10.1016/j.addr.2012.09.037 (Jan. 2013) (cit. on p. 64).

335. Montes, L.-R., Alonso, A., Goñi, F. M. & Bagatolli, L. A. Giant Unilamellar Vesicles Electroformed from Native Membranes and Organic Lipid Mixtures under Physiological Conditions. *Biophysical Journal* **93,** 3548–3554. doi:10.1529/biophysj.107.116228 (Nov. 2007) (cit. on p. 64).

336. Breton, M., Amirkavei, M. & Mir, L. M. Optimization of the Electroformation of Giant Unilamellar Vesicles (GUVs) with Unsaturated Phospholipids. *The Journal of Membrane Biology* **248,** 827–835. doi:10.1007/s00232-015-9828-3 (4th Aug. 2015) (cit. on p. 64).

337. Dimova, R., Aranda, S., Bezlyepkina, N., Nikolov, V., Riske, K. A. & Lipowsky, R. A practical guide to giant vesicles. Probing the membrane nanoregime via optical microscopy. *Journal of Physics: Condensed Matter* **18,** S1151–S1176. doi:10.1088/0953-8984/18/28/s04 (28th June 2006) (cit. on p. 64).

338. Horger, K. S., Estes, D. J., Capone, R. & Mayer, M. Films of Agarose Enable Rapid Formation of Giant Liposomes in Solutions of Physiologic Ionic Strength. *Journal of the American Chemical Society* **131,** 1810–1819. doi:10.1021/ja805625u (20th Jan. 2009) (cit. on p. 64).

339. López Mora, N., Hansen, J. S., Gao, Y., Ronald, A. A., Kieltyka, R., Malmstadt, N. & Kros, A. Preparation of size tunable giant vesicles from cross-linked dextran(ethylene glycol) hydrogels. *Chem. Commun.* **50,** 1953–1955. doi:10.1039/c3cc49144g (2014) (cit. on p. 64).

340. Schultze, J., Vagias, A., Ye, L., Prantl, E., Breising, V., Best, A., Koynov, K., Marques, C. M. & Butt, H.-J. Preparation of Monodisperse Giant Unilamellar Anchored Vesicles Using Micropatterned Hydrogel Substrates. *ACS Omega* **4,** 9393–9399. doi:10.1021/acsomega.9b00912 (29th May 2019) (cit. on p. 64).

341. Hu, P. C., Li, S. & Malmstadt, N. Microfluidic Fabrication of Asymmetric Giant Lipid Vesicles. *ACS Applied Materials & Interfaces* **3,** 1434–1440. doi:10.1021/am101191d (11th Apr. 2011) (cit. on p. 64).

342. Ito, H., Yamanaka, T., Kato, S., Hamada, T., Takagi, M., Ichikawa, M. & Yoshikawa, K. Dynamical formation of lipid bilayer vesicles from lipid-coated droplets across a planar monolayer at an oil/water interface. *Soft Matter* **9,** 9539. doi:10.1039/c3sm51766g (2013) (cit. on p. 64).

343. Van Swaay, D. & deMello, A. Microfluidic methods for forming liposomes. *Lab on a Chip* **13,** 752. doi:10.1039/c2lc41121k (2013) (cit. on p. 64).

344. Funakoshi, K., Suzuki, H. & Takeuchi, S. Formation of Giant Lipid Vesiclelike Compartments from a Planar Lipid Membrane by a Pulsed Jet Flow. *Journal of the American Chemical Society* **129,** 12608–12609. doi:10.1021/ja074029f (1st Oct. 2007) (cit. on p. 64).

345. Stachowiak, J. C., Richmond, D. L., Li, T. H., Liu, A. P., Parekh, S. H. & Fletcher, D. A. Unilamellar vesicle formation and encapsulation by microfluidic jetting. *Proceedings of the National Academy of Sciences* **105,** 4697–4702. doi:10.1073/pnas.0710875105 (25th Mar. 2008) (cit. on p. 64).

346. Richmond, D. L., Schmid, E. M., Martens, S., Stachowiak, J. C., Liska, N. & Fletcher, D. A. Forming giant vesicles with controlled membrane composition, asymmetry, and contents. *Proceedings of the National Academy of Sciences* **108,** 9431–9436. doi:10.1073/pnas.1016410108 (18th May 2011) (cit. on p. 64).

347. Beltramo, P. J., Scheidegger, L. & Vermant, J. Toward Realistic Large-Area Cell Membrane Mimics: Excluding Oil, Controlling Composition, and Including Ion Channels. *Langmuir* **34,** 5880–5888. doi:10.1021/acs.langmuir.8b00837 (1st May 2018) (cit. on p. 64).

348. Ardham, V. R., Zoni, V., Adamowicz, S., Campomanes, P. & Vanni, S. Accurate Estimation of Membrane Capacitance from Atomistic Molecular Dynamics Simulations of Zwitterionic Lipid Bilayers. *The Journal of Physical Chemistry B* **124,** 8278–8286. doi:10.1021/acs.jpcb.0c03145 (28th Aug. 2020) (cit. on p. 64).

349. Deek, J., Maan, R., Loiseau, E. & Bausch, A. R. Reconstitution of composite actin and keratin networks in vesicles. *Soft Matter* **14,** 1897–1902. doi:10.1039/c7sm00819h (2018) (cit. on p. 64).

350. Keber, F. C., Loiseau, E., Sanchez, T., DeCamp, S. J., Giomi, L., Bowick, M. J., Marchetti, M. C., Dogic, Z. & Bausch, A. R. Topology and dynamics of active nematic vesicles. *Science* **345,** 1135–1139. doi:10.1126/science.1254784 (5th Sept. 2014) (cit. on pp. 64, 108, 110).

351. Litschel, T., Ganzinger, K. A., Movinkel, T., Heymann, M., Robinson, T., Mutschler, H. & Schwille, P. Freeze-thaw cycles induce content exchange between cell-sized lipid vesicles. *New Journal of Physics* **20,** 055008. doi:10.1088/1367-2630/aabb96 (18th May 2018) (cit. on p. 64).

352. Umbanhowar, P. B., Prasad, V. & Weitz, D. A. Monodisperse Emulsion Generation via Drop Break Off in a Coflowing Stream. *Langmuir* **16,** 347–351. doi:10.1021/la990101e (14th Oct. 1999) (cit. on pp. 66, 68, 69).

353. Barkley, D. & Henderson, R. D. Three-dimensional Floquet stability analysis of the wake of a circular cylinder. *Journal of Fluid Mechanics* **322,** 215–241. doi:10.1017/s0022112096002777 (10th Sept. 1996) (cit. on p. 68).

354. Stone, H. A. Dynamics of Drop Deformation and Breakup in Viscous Fluids. *Annual Review of Fluid Mechanics* **26,** 65–102. doi:10.1146/annurev.fl.26.010194.000433 (Jan. 1994) (cit. on p. 70).

355. Janssen, P. J. A. & Anderson, P. D. Boundary-integral method for drop deformation between parallel plates. *Physics of Fluids* **19.** doi:10.1063/1.2715621 (1st Apr. 2007) (cit. on p. 70).

356. Komrakova, A., Shardt, O., Eskin, D. & Derksen, J. Lattice Boltzmann simulations of drop deformation and breakup in shear flow. *International Journal of Multiphase Flow* **59,** 24–43. doi:10.1016/j.ijmultiphaseflow.2013.10.009 (Feb. 2014) (cit. on p. 70).

357. May, S. & Maher, J. Capillary-wave relaxation for a meniscus between miscible liquids. *Physical Review Letters* **67,** 2013–2016. doi:10.1103/physrevlett.67.2013 (Oct. 1991) (cit. on p. 70).

358. Ganzinger, K. A., Merino-Salomón, A., García-Soriano, D. A., Butterfield, A. N., Litschel, T., Siedler, F. & Schwille, P. FtsZ Reorganization Facilitates Deformation of Giant Vesicles in Microfluidic Traps**. *Angewandte Chemie International Edition* **59,** 21372–21376. doi:10.1002/anie.202001928 (17th Sept. 2020) (cit. on pp. 70, 93).

359. Loiseau, E., Schneider, J. A. M., Keber, F. C., Pelzl, C., Massiera, G., Salbreux, G. & Bausch, A. R. Shape remodeling and blebbing of active cytoskeletal vesicles. *Science Advances* **2.** doi:10.1126/sciadv.1500465 (Apr. 2016) (cit. on pp. 70, 93).

360. Tjahjadi, M., Stone, H. A. & Ottino, J. M. Satellite and subsatellite formation in capillary breakup. *Journal of Fluid Mechanics* **243,** 297. doi:10.1017/s0022112092002738 (Oct. 1992) (cit. on p. 72).

361. NOTZ, P. K. & BASARAN, O. A. Dynamics and breakup of a contracting liquid filament. *Journal of Fluid Mechanics* **512.** doi:10.1017/s0022112004009759 (23rd July 2004) (cit. on p. 72).

362. Berry, J. D., Neeson, M. J., Dagastine, R. R., Chan, D. Y. & Tabor, R. F. Measurement of surface and interfacial tension using pendant drop tensiometry. *Journal of Colloid and Interface Science* **454,** 226–237. doi:10.1016/j.jcis.2015.05.012 (Sept. 2015) (cit. on p. 72).

363. Baldursdottir, S. G., Fullerton, M. S., Nielsen, S. H. & Jorgensen, L. Adsorption of proteins at the oil/water interface—Observation of protein adsorption by interfacial shear stress measurements. *Colloids and Surfaces B: Biointerfaces* **79,** 41–46. doi:10.1016/j.colsurfb.2010.03.020 (Aug. 2010) (cit. on p. 72).

364. Mitropoulos, V., Mütze, A. & Fischer, P. Mechanical properties of protein adsorption layers at the air/water and oil/water interface: A comparison in light of the thermodynamical stability of proteins. *Advances in Colloid and Interface Science* **206,** 195–206. doi:10.1016/j.cis.2013.11.004 (Apr. 2014) (cit. on pp. 72, 107).

365. Gicquaud, C., Chauvet, J.-P. & Tancrède, P. Surface film pressure of actin: interactions with lipids in mixed monolayers. *Biochemical and Biophysical Research Communications* **308,** 995–1000. doi:10.1016/s0006-291x(03)01505-5 (Sept. 2003) (cit. on pp. 72, 73, 107, 109).

366. Gicquaud, C., Chauvet, J.-P., Grenier, G., Tancrède, P. & Coulombe, G. Adsorption of actin at the air-water interface: A monolayer study. *Biopolymers* **70,** 289–296. doi:10.1002/bip.10475 (29th Sept. 2003) (cit. on pp. 72, 107, 109).

367. Schroer, C. F. E., Baldauf, L., van Buren, L., Wassenaar, T. A., Melo, M. N., Koenderink, G. H. & Marrink, S. J. Charge-dependent interactions of monomeric and filamentous actin with lipid bilayers. *Proceedings of the National Academy of Sciences* **117,** 5861–5872. doi:10.1073/pnas.1914884117 (2nd Mar. 2020) (cit. on p. 72).

368. Klausner, R., Kumar, N., Weinstein, J., Blumenthal, R. & Flavin, M. Interaction of tubulin with phospholipid vesicles. I. Association with vesicles at the phase transition. *Journal of Biological Chemistry* **256,** 5879–5885. doi:10.1016/s0021-9258(19)69290-2 (June 1981) (cit. on pp. 72, 110).

369. Hoogerheide, D. P., Noskov, S. Y., Jacobs, D., Bergdoll, L., Silin, V., Worcester, D. L., Abramson, J., Nanda, H., Rostovtseva, T. K. & Bezrukov, S. M. Structural features and lipid binding domain of tubulin on biomimetic mitochondrial membranes. *Proceedings of the National Academy of Sciences* **114.** doi:10.1073/pnas.1619806114 (18th Apr. 2017) (cit. on pp. 72, 93, 110, 200).

370. Magnaudet, J. & Mercier, M. J. Particles, Drops, and Bubbles Moving Across Sharp Interfaces and Stratified Layers. *Annual Review of Fluid Mechanics* **52,** 61–91. doi:10.1146/annurev-fluid-010719-060139 (5th Jan. 2020) (cit. on p. 75).

371. Amador, G. J., van Dijk, D., Kieffer, R., Aubin-Tam, M.-E. & Tam, D. Hydrodynamic shear dissipation and transmission in lipid bilayers. *Proceedings of the National Academy of Sciences* **118.** doi:10.1073/pnas.2100156118 (21st May 2021) (cit. on p. 75).

372. Christopher, G. F., Noharuddin, N. N., Taylor, J. A. & Anna, S. L. Experimental observations of the squeezing-to-dripping transition in T-shaped microfluidic junctions. *Physical Review E* **78.** doi:10.1103/physreve.78.036317 (18th Sept. 2008) (cit. on p. 76).

373. DE MENECH, M., GARSTECKI, P., JOUSSE, F. & STONE, H. A. Transition from squeezing to dripping in a microfluidic T-shaped junction. *Journal of Fluid Mechanics* **595,** 141–161. doi:10.1017/s0022112007009100x (8th Jan. 2008) (cit. on p. 76).

374. Van de Cauter, L., Jawale, Y. K., Tam, D., Baldauf, L., van Buren, L., Koenderink, G. H., Dogterom, M. & Ganzinger, K. A. *High-Speed Imaging of Giant Unilamellar Vesicle Formation in cDICE (Dataset)* Dataset (4TU.ResearchData, Sept. 2025). doi:10.4121/f86cd528-8bcc-4e76-b530-4e272516e4ec (cit. on p. 79).

375. Tcholakova, S., Denkov, N. D. & Danner, T. Role of Surfactant Type and Concentration for the Mean Drop Size during Emulsification in Turbulent Flow. *Langmuir* **20,** 7444–7458. doi:10.1021/la049335a (1st Aug. 2004) (cit. on p. 80).

376. Wells, W. A. The discovery of tubulin. *The Journal of Cell Biology* **169,** 552–552. doi:10.1083/jcb1694fta1 (23rd May 2005) (cit. on p. 92).

377. Borisy, G. G. & Taylor, E. W. THE MECHANISM OF ACTION OF COLCHICINE. *The Journal of Cell Biology* **34,** 525–533. doi:10.1083/jcb.34.2.525 (1st Aug. 1967) (cit. on p. 92).

378. MOHRI, H. Amino-acid Composition of “Tubulin” constituting Microtubules of Sperm Flagella. *Nature* **217,** 1053–1054. doi:10.1038/2171053a0 (Mar. 1968) (cit. on p. 92).

379. Satir, P. STUDIES ON CILIA. *The Journal of Cell Biology* **39,** 77–94. doi:10.1083/jcb.39.1.77 (1st Oct. 1968) (cit. on p. 92).

380. Wells, W. A. Microtubules get a name. *The Journal of Cell Biology* **168,** 852–853. doi:10.1083/jcb1686fta1 (14th Mar. 2005) (cit. on p. 92).

381. Ledbetter, M. C. & Porter, K. R. A "MICROTUBULE" IN PLANT CELL FINE STRUCTURE. *The Journal of Cell Biology* **19,** 239–250. doi:10.1083/jcb.19.1.239 (1st Oct. 1963) (cit. on p. 92).

382. Kirschner, M. Beyond self-assembly: From microtubules to morphogenesis. *Cell* **45,** 329–342. doi:10.1016/0092-8674(86)90318-1 (May 1986) (cit. on p. 92).

383. Wells, W. A. Microtubules get dynamic. *The Journal of Cell Biology* **172,** 643–643. doi:10.1083/jcb.1725fta1 (27th Feb. 2006) (cit. on p. 92).

384. Tilney, L. G. & Porter, K. R. STUDIES ON THE MICROTUBULES IN HELIOZOA. *The Journal of Cell Biology* **34,** 327–343. doi:10.1083/jcb.34.1.327 (1st July 1967) (cit. on p. 92).

385. Bordas, J., Mandelkow, E.-M. & Mandelkow, E. Stages of tubulin assembly and disassembly studied by time-resolved synchrotron X-ray scattering. *Journal of Molecular Biology* **164,** 89–135. doi:10.1016/0022-2836(83)90089-x (Feb. 1983) (cit. on p. 92).

386. Wu, R., Guzman-Sepulveda, J., Kalra, A., Tuszynski, J. & Dogariu, A. Thermal hysteresis in microtubule assembly/disassembly dynamics: The aging-induced degradation of tubulin dimers. *Biochemistry and Biophysics Reports* **29,** 101199. doi:10.1016/j.bbrep.2021.101199 (Mar. 2022) (cit. on p. 92).

387. Johnson, K. A. & Borisy, G. G. The equilibrium assembly of microtubules in vitro. *Society of General Physiologists series* **30,** 119–41 (1975) (cit. on p. 92).

388. Weisenberg, R. C. Microtubule Formation in vitro in Solutions Containing Low Calcium Concentrations. *Science* **177,** 1104–1105. doi:10.1126/science.177.4054.1104 (22nd Sept. 1972) (cit. on p. 92).

389. Olmsted, J. B. & Borisy, G. G. Ionic and nucleotide requirements for microtubule polymerization in vitro. *Biochemistry* **14,** 2996–3005. doi:10.1021/bi00684a032 (1st July 1975) (cit. on p. 92).

390. Karecla, P., Hirst, E. & Bayley, P. Polymorphism of tubulin assembly *in vitro*. *Journal of Cell Science* **94,** 479–488. doi:10.1242/jcs.94.3.479 (1st Nov. 1989) (cit. on p. 92).

391. Erickson, H. P. Assembly of microtubules from preformed, ring-shaped protofilaments and 6-s tubulin. *Journal of Supramolecular Structure* **2,** 393–411. doi:10.1002/jss.400020228 (Jan. 1974) (cit. on p. 92).

392. Baker, T. & Amos, L. Structure of the tubulin dimer in zinc-induced sheets. *Journal of Molecular Biology* **123,** 89–106. doi:10.1016/0022-2836(78)90378-9 (July 1978) (cit. on p. 92).

393. WAXMAN, P. G., DEL CAMPO, A. A., LOWE, M. C. & HAMEL, E. Induction of Polymerization of Purified Tubulin by Sulfonate Buffers. *European Journal of Biochemistry* **120,** 129–136. doi:10.1111/j.1432-1033.1981.tb05679.x (Nov. 1981) (cit. on p. 92).

394. Gaskin, F., Cantor, C. R. & Shelanski, M. L. Turbidimetric studies of the in vitro assembly and disassembly of porcine neurotubules. *Journal of Molecular Biology* **89,** 737–755. doi:10.1016/0022-2836(74)90048-5 (Nov. 1974) (cit. on p. 92).

395. Guo, W., Ale, T. A., Sun, S., Sanchez, J. E. & Li, L. A Comprehensive Study on the Electrostatic Properties of Tubulin-Tubulin Complexes in Microtubules. *Cells* **12,** 238. doi:10.3390/cells12020238 (5th Jan. 2023) (cit. on p. 92).

396. Caplow, M. & Fee, L. Dissociation of the tubulin dimer is extremely slow, thermodynamically very unfavorable, and reversible in the absence of an energy source. *Molecular biology of the cell* **13,** 2120–31. doi:10.1091/mbc.e01-10-0089 (June 2002) (cit. on p. 92).

397. Tuszyński, J., Brown, J., Crawford, E., Carpenter, E., Nip, M., Dixon, J. & Satarić, M. Molecular dynamics simulations of tubulin structure and calculations of electrostatic properties of microtubules. *Mathematical and Computer Modelling* **41,** 1055–1070. doi:10.1016/j.mcm.2005.05.002 (May 2005) (cit. on p. 92).

398. Barahona, I., Soares, H., Cyrne, L., Penque, D., Denoulet, P. & Rodrigues-Pousada, C. Sequence of one α- and two β-tubulin genes of Tetrahymena pyriformis. *Journal of Molecular Biology* **202,** 365–382. doi:10.1016/0022-2836(88)90271-9 (Aug. 1988) (cit. on p. 92).

399. Sackett, D., Knutson, J. & Wolff, J. Hydrophobic surfaces of tubulin probed by time-resolved and steady-state fluorescence of nile red. *Journal of Biological Chemistry* **265,** 14899–14906. doi:10.1016/s0021-9258(18)77201-3 (Sept. 1990) (cit. on p. 92).

400. Kotani, S., Kawai, G., Yokoyama, S. & Murofushi, H. Interaction mechanism between microtubule-associated proteins and microtubules. A proton nuclear magnetic resonance analysis on the binding of synthetic peptide to tubulin. *Biochemistry* **29,** 10049–10054. doi:10.1021/bi00495a006 (1st Oct. 1990) (cit. on p. 92).

401. Jurrus, E., Engel, D., Star, K., Monson, K., Brandi, J., Felberg, L. E., Brookes, D. H., Wilson, L., Chen, J., Liles, K., Chun, M., Li, P., Gohara, D. W., Dolinsky, T., Konecny, R., Koes, D. R., Nielsen, J. E., Head-Gordon, T., Geng, W., Krasny, R., Wei, G.-W., Holst, M. J., McCammon, J. A. & Baker, N. A. Improvements to the APBS biomolecular solvation software suite. *Protein Science* **27,** 112–128. doi:10.1002/pro.3280 (24th Oct. 2017) (cit. on p. 93).

402. Kyte, J. & Doolittle, R. F. A simple method for displaying the hydropathic character of a protein. *Journal of molecular biology* **157,** 105–32. doi:10.1016/0022-2836(82)90515-0 (5th May 1982) (cit. on p. 93).

403. Jämbeck, J. P. M. & Lyubartsev, A. P. An Extension and Further Validation of an All-Atomistic Force Field for Biological Membranes. *Journal of Chemical Theory and Computation* **8,** 2938–2948. doi:10.1021/ct300342n (10th July 2012) (cit. on p. 93).

404. Pettersen, E. F., Goddard, T. D., Huang, C. C., Meng, E. C., Couch, G. S., Croll, T. I., Morris, J. H. & Ferrin, T. E. UCSF ChimeraX: Structure visualization for researchers, educators, and developers. *Protein Science* **30,** 70–82. doi:10.1002/pro.3943 (22nd Oct. 2020) (cit. on pp. 93, 179).

405. Kuchnir Fygenson, D., Elbaum, M., Shraiman, B. & Libchaber, A. Microtubules and vesicles under controlled tension. *Physical Review E* **55,** 850–859. doi:10.1103/physreve.55.850 (1st Jan. 1997) (cit. on pp. 93, 108, 111).

406. Kaneko, T., Itoh, T. J. & Hotani, H. Morphological transformation of liposomes caused by assembly of encapsulated tubulin and determination of shape by microtubule-associated proteins (MAPs) 1 1Edited by M. F. Moody. *Journal of Molecular Biology* **284,** 1671–1681. doi:10.1006/jmbi.1998.2251 (Dec. 1998) (cit. on pp. 93, 108, 111).

407. Hayashi, M., Nishiyama, M., Kazayama, Y., Toyota, T., Harada, Y. & Takiguchi, K. Reversible Morphological Control of Tubulin-Encapsulating Giant Liposomes by Hydrostatic Pressure. *Langmuir* **32,** 3794–3802. doi:10.1021/acs.langmuir.6b00799 (6th Apr. 2016) (cit. on p. 93).

408. Young, T. III. An essay on the cohesion of fluids. *Philosophical Transactions of the Royal Society of London* **95,** 65–87. doi:10.1098/rstl.1805.0005 (31st Dec. 1805) (cit. on p. 94).

409. Law, K.-Y. Definitions for Hydrophilicity, Hydrophobicity, and Superhydrophobicity: Getting the Basics Right. *The Journal of Physical Chemistry Letters* **5,** 686–688. doi:10.1021/jz402762h (20th Feb. 2014) (cit. on p. 94).

410. Vogler, E. A. Structure and reactivity of water at biomaterial surfaces. *Advances in Colloid and Interface Science* **74,** 69–117. doi:10.1016/s0001-8686(97)00040-7 (Feb. 1998) (cit. on p. 94).

411. Graham, J. M. Isolation of Nuclei and Nuclear Membranes From Animal Tissues. *Current Protocols in Cell Biology* **12.** doi:10.1002/0471143030.cb0310s12 (Oct. 2001) (cit. on p. 94).

412. Baldauf, L. *Rebuilding Cytokinesis One Molecule at a Time* PhD thesis (2022). doi:10.4233/UUID:412A4272-9EC2-4ABA-852D-981E392D64D0 (cit. on p. 95).

413. Kattan, J. *Biosynthesis of protein filaments for the creation of a minimal cell* PhD thesis (2020). doi:10.4233/UUID:724F70A9-EFD9-4598-9A24-064AA77DB509 (cit. on p. 96).

414. Xie, S., Li, J., Sun, S., Chen, W., Cheng, H., Song, Y., Li, Y., Liu, M., Zhu, X., Liang, X. & Zhou, J. TUBright: A Peptide Probe for Imaging Microtubules. *Analytical Chemistry* **94,** 11168–11174. doi:10.1021/acs.analchem.2c01285 (2nd Aug. 2022) (cit. on p. 98).

415. Kattan, J., Doerr, A., Dogterom, M. & Danelon, C. Shaping Liposomes by Cell-Free Expressed Bacterial Microtubules. *ACS Synthetic Biology* **10,** 2447–2455. doi:10.1021/acssynbio.1c00278 (29th Sept. 2021) (cit. on p. 99).

416. Fernandes, E., Cardoso, V. F., Lanceros-Méndez, S. & Lúcio, M. Lipid Microfluidic Biomimetic Models for Drug Screening: A Comprehensive Review. *Advanced Functional Materials* **34.** doi:10.1002/adfm.202315166 (16th Feb. 2024) (cit. on p. 105).

417. Beltramo, P. J., Van Hooghten, R. & Vermant, J. Millimeter-area, free standing, phospholipid bilayers. *Soft Matter* **12,** 4324–4331. doi:10.1039/c6sm00250a (2016) (cit. on p. 105).

418. Yahyazadeh Shourabi, A., Iacona, M. & Aubin-Tam, M.-E. Microfluidic system for efficient molecular delivery to artificial cell membranes. *Lab on a Chip* **25,** 1842–1853. doi:10.1039/d4lc00930d (2025) (cit. on pp. 105, 114, 115, 120).

419. Dols-Perez, A., Marin, V., Amador, G. J., Kieffer, R., Tam, D. & Aubin-Tam, M.-E. Artificial Cell Membranes Interfaced with Optical Tweezers: A Versatile Microfluidics Platform for Nanomanipulation and Mechanical Characterization. *ACS Applied Materials & Interfaces* **11,** 33620–33627. doi:10.1021/acsami.9b09983 (26th Aug. 2019) (cit. on pp. 105, 114).

420. Sciortino, A., Faizi, H. A., Uplap, S., Frechette, L., Peterson, M. S. E., Vlahovska, P., Baskaran, A., Hagan, M. F. & Bausch, A. R. *Active membrane deformations of a minimal synthetic cell* 18th Dec. 2023. doi:10.1101/2023.12.18.571643 (cit. on pp. 108–110).

421. Hsu, C.-P., Sciortino, A., de la Trobe, Y. A. & Bausch, A. R. Activity-induced polar patterns of filaments gliding on a sphere. *Nature Communications* **13.** doi:10.1038/s41467-022-30128-7 (11th May 2022) (cit. on p. 108).

422. Pinot, M., Chesnel, F., Kubiak, J., Arnal, I., Nedelec, F. & Gueroui, Z. Effects of Confinement on the Self-Organization of Microtubules and Motors. *Current Biology* **19,** 954–960. doi:10.1016/j.cub.2009.04.027 (June 2009) (cit. on p. 109).

423. Bermudez, J. G., Deiters, A. & Good, M. C. Patterning Microtubule Network Organization Reshapes Cell-Like Compartments. *ACS Synthetic Biology* **10,** 1338–1350. doi:10.1021/acssynbio.0c00575 (14th May 2021) (cit. on p. 109).

424. Bernier-Valentin, F., Aunis, D. & Rousset, B. Evidence for tubulin-binding sites on cellular membranes: plasma membranes, mitochondrial membranes, and secretory granule membranes. *The Journal of cell biology* **97,** 209–216. doi:10.1083/jcb.97.1.209 (1st July 1983) (cit. on p. 110).

425. Von Haller, P. D., Donohoe, S., Goodlett, D. R., Aebersold, R. & Watts, J. D. Mass spectrometric characterization of proteins extracted from Jurkat T cell detergent-resistant membrane domains. *Proteomics* **1,** 1010–21. doi:10.1002/1615-9861(200108)1:8{\textless}1010::AID-PROT1010{\textgreater}3.0.CO;2-L (Aug. 2001) (cit. on p. 110).

426. Palestini, P., Pitto, M., Tedeschi, G., Ferraretto, A., Parenti, M., Brunner, J. & Masserini, M. Tubulin Anchoring to Glycolipid-enriched, Detergent-resistant Domains of the Neuronal Plasma Membrane. *Journal of Biological Chemistry* **275,** 9978–9985. doi:10.1074/jbc.275.14.9978 (Apr. 2000) (cit. on p. 110).

427. Beltramo, D. M., Nuñez, M., Alonso, A. d. C. & Barra, H. S. The relationship of hydrophobic tubulin with membranes in neural tissue. *Molecular and Cellular Biochemistry* **141,** 57–63. doi:10.1007/bf00935591 (1994) (cit. on p. 110).

428. Wolff, J. Plasma membrane tubulin. *Biochimica et Biophysica Acta (BBA) - Biomembranes* **1788,** 1415–1433. doi:10.1016/j.bbamem.2009.03.013 (July 2009) (cit. on pp. 110, 200).

429. Hargreaves, A. J. & McLean, W. The characterization of phospholipids associated with microtubules, purified tubulin and microtubule associated proteins in vitro. *International Journal of Biochemistry* **20,** 1133–1138. doi:10.1016/0020-711x(88)90259-5 (Jan. 1988) (cit. on p. 110).

430. Sciortino, A., Faizi, H. A., Fedosov, D. A., Frechette, L., Vlahovska, P. M., Gompper, G. & Bausch, A. R. Active membrane deformations of a minimal synthetic cell. *Nature Physics*. doi:10.1038/s41567-025-02839-3 (24th Mar. 2025) (cit. on p. 110).

431. De Dios Andres, P., Akter, M., Ryberg, C., Städler, B. & Liu, A. P. Distinct Network Morphologies from In Situ Polymerization of Microtubules in Giant Polymer-Lipid Hybrid Vesicles. *Advanced Biology*. doi:10.1002/adbi.202400601 (12th Mar. 2025) (cit. on p. 110).

432. Andersen, S. S. Spindle assembly and the art of regulating microtubule dynamics by MAPs and Stathmin/Op18. *Trends in Cell Biology* **10,** 261–267. doi:10.1016/s0962-8924(00)01786-4 (July 2000) (cit. on p. 111).

433. Andersen, S. S. L., Ashford, A. J., Tournebize, R., Gavet, O., Sobel, A., Hyman, A. A. & Karsenti, E. Mitotic chromatin regulates phosphorylation of Stathmin/Op18. *Nature* **389,** 640–643. doi:10.1038/39382 (Oct. 1997) (cit. on p. 111).

434. Jourdain, L., Curmi, P., Sobel, A., Pantaloni, D. & Carlier, M.-F. Stathmin: A Tubulin-Sequestering Protein Which Forms a Ternary T_2S Complex with Two Tubulin Molecules. *Biochemistry* **36,** 10817–10821. doi:10.1021/bi971491b (1st Sept. 1997) (cit. on p. 111).

435. Gigant, B., Curmi, P. A., Martin-Barbey, C., Charbaut, E., Lachkar, S., Lebeau, L., Siavoshian, S., Sobel, A. & Knossow, M. The 4 Å X-Ray Structure of a Tubulin:Stathmin-like Domain Complex. *Cell* **102,** 809–816. doi:10.1016/s0092-8674(00)00069-6 (Sept. 2000) (cit. on p. 111).

436. Komarova, Y., De Groot, C. O., Grigoriev, I., Gouveia, S. M., Munteanu, E. L., Schober, J. M., Honnappa, S., Buey, R. M., Hoogenraad, C. C., Dogterom, M., Borisy, G. G., Steinmetz, M. O. & Akhmanova, A. Mammalian end binding proteins control persistent microtubule growth. *Journal of Cell Biology* **184,** 691–706. doi:10.1083/jcb.200807179 (2nd Mar. 2009) (cit. on p. 112).

437. Gogendeau, D., Guichard, P. & Tassin, A.-M. in *Methods in Cell Biology* 171–189 (Elsevier, 2015). doi:10.1016/bs.mcb.2015.03.004 (cit. on pp. 112, 129, 142, 146, 199).

438. Díaz-Celis, C., Risca, V. I., Hurtado, F., Polka, J. K., Hansen, S. D., Maturana, D., Lagos, R., Mullins, R. D. & Monasterio, O. Bacterial Tubulins A and B Exhibit Polarized Growth, Mixed-Polarity Bundling, and Destabilization by GTP Hydrolysis. *Journal of Bacteriology* **199** (ed de Boer, P. A. J.) doi:10.1128/jb.00211-17 (Oct. 2017) (cit. on p. 112).

439. Amini Hounejani, R. *Bacterial cytoskeletal filaments: Towards a DNA segregation system for a synthetic cell* PhD thesis (2023). doi:10.4233/UUID:79DE9E6E-8201-499B-8D41-7C52AE450257 (cit. on p. 112).

440. Akbari, R. *Dropen_V01* 4th May 2021. doi:10.17632/WZCHZBM58P.3 (cit. on p. 112).

441. Bieling, P., Laan, L., Schek, H., Munteanu, E. L., Sandblad, L., Dogterom, M., Brunner, D. & Surrey, T. Reconstitution of a microtubule plus-end tracking system in vitro. *Nature* **450,** 1100–1105. doi:10.1038/nature06386 (Dec. 2007) (cit. on p. 112).

442. Mohan, R., Katrukha, E. A., Doodhi, H., Smal, I., Meijering, E., Kapitein, L. C., Steinmetz, M. O. & Akhmanova, A. End-binding proteins sensitize microtubules to the action of microtubule-targeting agents. *Proceedings of the National Academy of Sciences* **110,** 8900–8905. doi:10.1073/pnas.1300395110 (14th May 2013) (cit. on p. 112).

443. Yahyazadeh Shourabi, A., Kieffer, R., de Jong, D., Tam, D. & Aubin-Tam, M.-E. Mechanical characterization of freestanding lipid bilayers with temperature-controlled phase. *Soft Matter* **20,** 8524–8537. doi:10.1039/d4sm00706a (2024) (cit. on pp. 114, 115).

444. Akbari, R. & Antonini, C. Contact angle measurements: From existing methods to an open-source tool. *Advances in Colloid and Interface Science* **294,** 102470. doi:10.1016/j.cis.2021.102470 (Aug. 2021) (cit. on p. 116).

445. Burakov, A. V. & Nadezhdina, E. S. Centering and Shifting of Centrosomes in Cells. *Cells* **9,** 1351. doi:10.3390/cells9061351 (29th May 2020) (cit. on p. 126).

446. Almonacid, M., Terret, M.-É. & Verlhac, M.-H. Actin-based spindle positioning: new insights from female gametes. *Journal of Cell Science*. doi:10.1242/jcs.142711 (1st Jan. 2014) (cit. on p. 126).

447. Tolić-Nørrelykke, I. M. Push-me-pull-you: how microtubules organize the cell interior. *European Biophysics Journal* **37,** 1271–1278. doi:10.1007/s00249-008-0321-0 (11th Apr. 2008) (cit. on p. 126).

448. Bai, L. & Mitchison, T. J. Spring-like behavior of cytoplasm holds the mitotic spindle in place. *Proceedings of the National Academy of Sciences* **119.** doi:10.1073/pnas.2203036119 (24th Mar. 2022) (cit. on p. 126).

449. Goshima, G. & Scholey, J. M. Control of Mitotic Spindle Length. *Annual Review of Cell and Developmental Biology* **26,** 21–57. doi:10.1146/annurev-cellbio-100109-104006 (10th Nov. 2010) (cit. on p. 126).

450. Pavin, N. & Tolić, I. M. Self-Organization and Forces in the Mitotic Spindle. *Annual Review of Biophysics* **45,** 279–298. doi:10.1146/annurev-biophys-062215-010934 (5th July 2016) (cit. on p. 126).

451. Fujita, I., Kimura, A. & Yamashita, A. A force balance model for a cell size-dependent meiotic nuclear oscillation in fission yeast. *EMBO reports* **24.** doi:10.15252/embr.202255770 (9th Jan. 2023) (cit. on p. 126).

452. Vogel, S. K., Pavin, N., Maghelli, N., Jülicher, F. & Tolić-Nørrelykke, I. M. Self-Organization of Dynein Motors Generates Meiotic Nuclear Oscillations. *PLoS Biology* **7** (ed Schliwa, M.) e1000087. doi:10.1371/journal.pbio.1000087 (21st Apr. 2009) (cit. on p. 126).

453. Jimenez, A. J., Schaeffer, A., De Pascalis, C., Letort, G., Vianay, B., Bornens, M., Piel, M., Blanchoin, L. & Théry, M. Acto-myosin network geometry defines centrosome position. *Current Biology* **31,** 1206–1220.e5. doi:10.1016/j.cub.2021.01.002 (Mar. 2021) (cit. on pp. 126, 135).

454. Dogterom, M. & Surrey, T. Microtubule organization in vitro. *Current Opinion in Cell Biology* **25,** 23–29. doi:10.1016/j.ceb.2012.12.002 (Feb. 2013) (cit. on p. 127).

455. Laan, L., Roth, S. & Dogterom, M. End-on microtubule-dynein interactions and pulling-based positioning of microtubule organizing centers. *Cell Cycle* **11,** 3750–3757. doi:10.4161/cc.21753 (16th Aug. 2012) (cit. on p. 127).

456. Fegan, A., White, B., Carlson, J. C. T. & Wagner, C. R. Chemically Controlled Protein Assembly: Techniques and Applications. *Chemical Reviews* **110,** 3315–3336. doi:10.1021/cr8002888 (30th Mar. 2010) (cit. on p. 127).

457. DeRose, R., Miyamoto, T. & Inoue, T. Manipulating signaling at will: chemically-inducible dimerization (CID) techniques resolve problems in cell biology. *Pflügers Archiv - European Journal of Physiology* **465,** 409–417. doi:10.1007/s00424-012-1208-6 (9th Jan. 2013) (cit. on p. 127).

458. Lester, H. A. & Nerbonne, J. M. Physiological and Pharmacological Manipulations with Light Flashes. *Annual Review of Biophysics and Bioengineering* **11,** 151–175. doi:10.1146/annurev.bb.11.060182.001055 (June 1982) (cit. on p. 128).

459. Ellis-Davies, G. C. R. Caged compounds: photorelease technology for control of cellular chemistry and physiology. *Nature Methods* **4,** 619–628. doi:10.1038/nmeth1072 (30th July 2007) (cit. on p. 128).

460. Zhang, K. & Cui, B. Optogenetic control of intracellular signaling pathways. *Trends in Biotechnology* **33,** 92–100. doi:10.1016/j.tibtech.2014.11.007 (Feb. 2015) (cit. on p. 128).

461. Manoilov, K. Y., Verkhusha, V. V. & Shcherbakova, D. M. A guide to the optogenetic regulation of endogenous molecules. *Nature Methods* **18,** 1027–1037. doi:10.1038/s41592-021-01240-1 (26th Aug. 2021) (cit. on p. 128).

462. Lian, Y.-L. & Lin, Y.-C. The emerging tools for precisely manipulating microtubules. *Current Opinion in Cell Biology* **88,** 102360. doi:10.1016/j.ceb.2024.102360 (June 2024) (cit. on p. 128).

463. Kolar, K., Knobloch, C., Stork, H., Žnidarič, M. & Weber, W. OptoBase: A Web Platform for Molecular Optogenetics. *ACS Synthetic Biology* **7,** 1825–1828. doi:10.1021/acssynbio.8b00120 (18th June 2018) (cit. on p. 128).

464. Bornens, M. The Centrosome in Cells and Organisms. *Science* **335,** 422–426. doi:10.1126/science.1209037 (27th Jan. 2012) (cit. on p. 128).

465. Carden, S., Vitiello, E., Rosa e Silva, I., Holder, J., Quarantotti, V., Kishore, K., Roamio Franklin, V. N., D'Santos, C., Ochi, T., van Breugel, M. & Gergely, F. Proteomic profiling of centrosomes across multiple mammalian cell and tissue types by an affinity capture method. *Developmental Cell* **58,** 2393–2410.e9. doi:10.1016/j.devcel.2023.09.008 (Nov. 2023) (cit. on pp. 129, 130, 142, 147, 199).

466. Hung, H.-F., Hehnly, H. & Doxsey, S. in *Methods in Cell Biology* 47–58 (Elsevier, 2015). doi:10.1016/bs.mcb.2015.03.024 (cit. on p. 129).

467. Woodruff, J. B., Wueseke, O. & Hyman, A. A. Pericentriolar material structure and dynamics. *Philosophical Transactions of the Royal Society B: Biological Sciences* **369,** 20130459. doi:10.1098/rstb.2013.0459 (5th Sept. 2014) (cit. on p. 130).

468. Barker, A. R., McIntosh, K. V. & Dawe, H. R. Centrosome positioning in non-dividing cells. *Protoplasma* **253,** 1007–1021. doi:10.1007/s00709-015-0883-5 (30th Aug. 2015) (cit. on p. 131).

469. Chang, W., Antoku, S., Östlund, C., Worman, H. J. & Gundersen, G. G. Linker of nucleoskeleton and cytoskeleton (LINC) complex-mediated actin-dependent nuclear positioning orients centrosomes in migrating myoblasts. *Nucleus* **6,** 77–88. doi:10.1080/19491034.2015.1004947 (2nd Jan. 2015) (cit. on pp. 131, 143).

470. Burakov, A. V. & Nadezhdina, E. S. Association of nucleus and centrosome: magnet or velcro? *Cell Biology International* **37,** 95–104. doi:10.1002/cbin.10016 (2nd Jan. 2013) (cit. on pp. 131, 143).

471. Orii, R. & Tanimoto, H. Structural response of microtubule and actin cytoskeletons to direct intracellular load. *Journal of Cell Biology* **224.** doi:10.1083/jcb.202403136 (15th Nov. 2024) (cit. on p. 135).

472. Schaeffer, A., Buracco, S., Gazzola, M., Gelin, M., Vianay, B., de Pascalis, C., Blanchoin, L. & Théry, M. Microtubule-driven cell shape changes and actomyosin flow synergize to position the centrosome. *Journal of Cell Biology* **224.** doi:10.1083/jcb.202405126 (17th Apr. 2025) (cit. on pp. 135, 144).

473. Yamamoto, S., Gaillard, J., Vianay, B., Guerin, C., Orhant-Prioux, M., Blanchoin, L. & Théry, M. Actin network architecture can ensure robust centering or sensitive decentering of the centrosome. *The EMBO Journal* **41.** doi:10.15252/embj.2022111631 (2nd Aug. 2022) (cit. on pp. 135, 136, 140, 142, 145, 199).

474. Inoue, D., Obino, D., Pineau, J., Farina, F., Gaillard, J., Guerin, C., Blanchoin, L., Lennon-Duménil, A.-M. & Théry, M. Actin filaments regulate microtubule growth at the centrosome. *The EMBO Journal* **38.** doi:10.15252/embj.201899630 (22nd Mar. 2019) (cit. on p. 139).

475. Farina, F., Gaillard, J., Guérin, C., Couté, Y., Sillibourne, J., Blanchoin, L. & Théry, M. The centrosome is an actin-organizing centre. *Nature Cell Biology* **18,** 65–75. doi:10.1038/ncb3285 (14th Dec. 2015) (cit. on p. 139).

476. HERZOG, W. & WEBER, K. Microtubule Formation by Pure Brain Tubulin in vitro. The Influence of Dextran and Poly(ethylene glycol). *European Journal of Biochemistry* **91,** 249–254. doi:10.1111/j.1432-1033.1978.tb20959.x (Nov. 1978) (cit. on p. 140).

477. Maan, R., Reese, L., Volkov, V. A., King, M. R., van der Sluis, E. O., Andrea, N., Evers, W. H., Jakobi, A. J. & Dogterom, M. Multivalent interactions facilitate motor-dependent protein accumulation at growing microtubule plus-ends. *Nature Cell Biology* **25,** 68–78. doi:10.1038/s41556-022-01037-0 (19th Dec. 2022) (cit. on p. 140).

478. Baumann, H. & Surrey, T. in *Methods in Cell Biology* 39–55 (Elsevier, 2015). doi:10.1016/bs.mcb.2015.01.015 (cit. on p. 140).

479. Taberner, N., Lof, A., Roth, S., Lamers, D., Zeijlemaker, H. & Dogterom, M. in *Methods in Cell Biology* 1–22 (Elsevier, 2015). doi:10.1016/bs.mcb.2015.02.008 (cit. on p. 140).

480. Tsai, M.-Y. & Zheng, Y. Aurora A Kinase-Coated Beads Function as Microtubule-Organizing Centers and Enhance RanGTP-Induced Spindle Assembly. *Current Biology* **15,** 2156–2163. doi:10.1016/j.cub.2005.10.054 (Dec. 2005) (cit. on pp. 142, 199).

481. Vendel, K. *On the role of microtubules in cell polarity* PhD thesis (2020). doi:10.4233/UUID:34F174D5-F8AD-4BF2-86F7-47660A84FE64 (cit. on pp. 142, 165, 199, 200).

482. Wilson, E. B. *The cell in development and heredity* third (New York : Macmillan, 1925) (cit. on pp. 142, 143).

483. Ma, J. & Weake, V. M. Affinity-based Isolation of Tagged Nuclei from Drosophila Tissues for Gene Expression Analysis. *Journal of Visualized Experiments*. doi:10.3791/51418 (25th Mar. 2014) (cit. on p. 142).

484. Letort, G., Nedelec, F., Blanchoin, L. & Théry, M. Centrosome centering and decentering by microtubule network rearrangement. *Molecular Biology of the Cell* **27** (ed Mogilner, A.) 2833–2843. doi:10.1091/mbc.e16-06-0395 (15th Sept. 2016) (cit. on pp. 143, 204).

485. Burakov, A., Nadezhdina, E., Slepchenko, B. & Rodionov, V. Centrosome positioning in interphase cells. *The Journal of Cell Biology* **162,** 963–969. doi:10.1083/jcb.200305082 (15th Sept. 2003) (cit. on p. 143).

486. Yi, J., Wu, X., Chung, A. H., Chen, J. K., Kapoor, T. M. & Hammer, J. A. Centrosome repositioning in T cells is biphasic and driven by microtubule end-on capture-shrinkage. *Journal of Cell Biology* **202,** 779–792. doi:10.1083/jcb.201301004 (26th Aug. 2013) (cit. on p. 144).

487. Gros, O. J., Damstra, H. G. J., Kapitein, L. C., Akhmanova, A. & Berger, F. Dynein self-organizes while translocating the centrosome in T-cells. *Molecular Biology of the Cell* **32** (ed Mogilner, A.) 855–868. doi:10.1091/mbc.e20-10-0668 (19th Apr. 2021) (cit. on p. 144).

488. Sonal, Ganzinger, K. A., Vogel, S. K., Mücksch, J., Blumhardt, P. & Schwille, P. Myosin-II activity generates a dynamic steady state with continuous actin turnover in a minimal actin cortex. *Journal of Cell Science* **132.** doi:10.1242/jcs.219899 (11th Dec. 2018) (cit. on pp. 147, 148).

489. Tang, V. W. & Brieher, W. M. α-Actinin-4/FSGS1 is required for Arp2/3-dependent actin assembly at the adherens junction. *Journal of Cell Biology* **196,** 115–130. doi:10.1083/jcb.201103116 (9th Jan. 2012) (cit. on p. 148).

490. Mulla, Y., Avellaneda, M. J., Roland, A., Baldauf, L., Jung, W., Kim, T., Tans, S. J. & Koenderink, G. H. Weak catch bonds make strong networks. *Nature Materials* **21,** 1019–1023. doi:10.1038/s41563-022-01288-0 (25th Aug. 2022) (cit. on p. 148).

491. Milo, R. & Phillips, R. *Cell Biology by the Numbers* ISBN:9781317230694. doi:10.1201/9780429258770 (Garland Science, 7th Dec. 2015) (cit. on p. 152).

492. *Polybead® Microspheres TECHNICAL DATA SHEET 788* (cit. on p. 152).

493. Compton, D. A. Spindle Assembly in Animal Cells. *Annual Review of Biochemistry* **69,** 95–114. doi:10.1146/annurev.biochem.69.1.95 (June 2000) (cit. on p. 158).

494. Dema, A., van Haren, J. & Wittmann, T. Optogenetic EB1 inactivation shortens metaphase spindles by disrupting cortical force-producing interactions with astral microtubules. *Current Biology* **32,** 1197–1205.e4. doi:10.1016/j.cub.2022.01.017 (Mar. 2022) (cit. on p. 158).

495. Faivre-Moskalenko, C. & Dogterom, M. Dynamics of microtubule asters in microfabricated chambers: The role of catastrophes. *Proceedings of the National Academy of Sciences* **99,** 16788–16793. doi:10.1073/pnas.252407099 (16th Dec. 2002) (cit. on p. 158).

496. Ferenz, N. P., Paul, R., Fagerstrom, C., Mogilner, A. & Wadsworth, P. Dynein Antagonizes Eg5 by Crosslinking and Sliding Antiparallel Microtubules. *Current Biology* **19,** 1833–1838. doi:10.1016/j.cub.2009.09.025 (Nov. 2009) (cit. on p. 158).

497. Mitchison, T. J., Maddox, P., Gaetz, J., Groen, A., Shirasu, M., Desai, A., Salmon, E. D. & Kapoor, T. M. Roles of Polymerization Dynamics, Opposed Motors, and a Tensile Element in Governing the Length of*Xenopus*Extract Meiotic Spindles. *Molecular Biology of the Cell* **16,** 3064–3076. doi:10.1091/mbc.e05-02-0174 (June 2005) (cit. on p. 158).

498. Sharp, D. J., Yu, K. R., Sisson, J. C., Sullivan, W. & Scholey, J. M. Antagonistic microtubule-sliding motors position mitotic centrosomes in Drosophila early embryos. *Nature Cell Biology* **1,** 51–54. doi:10.1038/9025 (May 1999) (cit. on p. 158).

499. Tanenbaum, M. E., Macůrek, L., Galjart, N. & Medema, R. H. Dynein, Lis1 and CLIP-170 counteract Eg5-dependent centrosome separation during bipolar spindle assembly. *The EMBO Journal* **27,** 3235–3245. doi:10.1038/emboj.2008.242 (20th Nov. 2008) (cit. on p. 158).

500. Tanenbaum, M. E., Macůrek, L., Janssen, A., Geers, E. F., Alvarez-Fernández, M. & Medema, R. H. Kif15 Cooperates with Eg5 to Promote Bipolar Spindle Assembly. *Current Biology* **19,** 1703–1711. doi:10.1016/j.cub.2009.08.027 (Nov. 2009) (cit. on p. 158).

501. Ferenz, N. P., Gable, A. & Wadsworth, P. Mitotic functions of kinesin-5. *Seminars in Cell & Developmental Biology* **21,** 255–259. doi:10.1016/j.semcdb.2010.01.019 (May 2010) (cit. on p. 158).

502. Kapoor, T. M. & Mitchison, T. J. Eg5 is static in bipolar spindles relative to tubulin. *The Journal of Cell Biology* **154,** 1125–1134. doi:10.1083/jcb.200106011 (17th Sept. 2001) (cit. on p. 158).

503. Kashina, A. S., Scholey, J. M., Leszyk, J. D. & Saxton, W. M. An essential bipolar mitotic motor. *Nature* **384,** 225–225. doi:10.1038/384225a0 (Nov. 1996) (cit. on p. 158).

504. Kashina, A., Rogers, G. & Scholey, J. The bimC family of kinesins: essential bipolar mitotic motors driving centrosome separation. *Biochimica et Biophysica Acta (BBA) - Molecular Cell Research* **1357,** 257–271. doi:10.1016/s0167-4889(97)00037-2 (July 1997) (cit. on p. 158).

505. Kwok, B. H., Yang, J. G. & Kapoor, T. M. The Rate of Bipolar Spindle Assembly Depends on the Microtubule-Gliding Velocity of the Mitotic Kinesin Eg5. *Current Biology* **14,** 1783–1788. doi:10.1016/j.cub.2004.09.052 (Oct. 2004) (cit. on p. 158).

506. Sawin, K. E., LeGuellec, K., Philippe, M. & Mitchison, T. J. Mitotic spindle organization by a plus-end-directed microtubule motor. *Nature* **359,** 540–543. doi:10.1038/359540a0 (Oct. 1992) (cit. on p. 158).

507. Scholey, J. M. Kinesin-5 in Drosophila embryo mitosis: Sliding filament or spindle matrix mechanism? *Cell Motility* **66,** 500–508. doi:10.1002/cm.20349 (16th Mar. 2009) (cit. on p. 158).

508. Sharp, D. J., McDonald, K. L., Brown, H. M., Matthies, H. J., Walczak, C., Vale, R. D., Mitchison, T. J. & Scholey, J. M. The Bipolar Kinesin, KLP61F, Cross-links Microtubules within Interpolar Microtubule Bundles of *Drosophila* Embryonic Mitotic Spindles. *The Journal of Cell Biology* **144,** 125–138. doi:10.1083/jcb.144.1.125 (11th Jan. 1999) (cit. on p. 158).

509. Van den Wildenberg, S. M., Tao, L., Kapitein, L. C., Schmidt, C. F., Scholey, J. M. & Peterman, E. J. The Homotetrameric Kinesin-5 KLP61F Preferentially Crosslinks Microtubules into Antiparallel Orientations. *Current Biology* **18,** 1860–1864. doi:10.1016/j.cub.2008.10.026 (Dec. 2008) (cit. on p. 158).

510. Gaska, I., Armstrong, M. E., Alfieri, A. & Forth, S. The Mitotic Crosslinking Protein PRC1 Acts Like a Mechanical Dashpot to Resist Microtubule Sliding. *Developmental Cell* **54,** 367–378.e5. doi:10.1016/j.devcel.2020.06.017 (Aug. 2020) (cit. on p. 158).

511. Jagrić, M., Risteski, P., Martinčić, J., Milas, A. & Tolić, I. M. Optogenetic control of PRC1 reveals its role in chromosome alignment on the spindle by overlap length-dependent forces. *eLife* **10.** doi:10.7554/elife.61170 (22nd Jan. 2021) (cit. on p. 158).

512. Wierenga, H. & Wolde, P. R. t. Diffusible Cross-linkers Cause Superexponential Friction Forces. *Physical Review Letters* **125.** doi:10.1103/physrevlett.125.078101 (12th Aug. 2020) (cit. on p. 158).

513. Blackwell, R., Edelmaier, C., Sweezy-Schindler, O., Lamson, A., Gergely, Z. R., O'Toole, E., Crapo, A., Hough, L. E., McIntosh, J. R., Glaser, M. A. & Betterton, M. D. Physical determinants of bipolar mitotic spindle assembly and stability in fission yeast. *Science Advances* **3.** doi:10.1126/sciadv.1601603 (6th Jan. 2017) (cit. on p. 158).

514. Bouvrais, H., Chesneau, L., Le Cunff, Y., Fairbrass, D., Soler, N., Pastezeur, S., Pécot, T., Kervrann, C. & Pécréaux, J. The coordination of spindle-positioning forces during the asymmetric division of the *Caenorhabditis elegans* zygote. *EMBO reports* **22.** doi:10.15252/embr.202050770 (26th Apr. 2021) (cit. on p. 158).

515. Lancaster, O. M., Le Berre, M., Dimitracopoulos, A., Bonazzi, D., Zlotek-Zlotkiewicz, E., Picone, R., Duke, T., Piel, M. & Baum, B. Mitotic Rounding Alters Cell Geometry to Ensure Efficient Bipolar Spindle Formation. *Developmental Cell* **25,** 270–283. doi:10.1016/j.devcel.2013.03.014 (May 2013) (cit. on p. 158).

516. Lázaro-Diéguez, F., Ispolatov, I. & Müsch, A. Cell shape impacts on the positioning of the mitotic spindle with respect to the substratum. *Molecular Biology of the Cell* **26** (ed Marshall, W.) 1286–1295. doi:10.1091/mbc.e14-08-1330 (Apr. 2015) (cit. on p. 158).

517. O'Connell, C. B. & Wang, Y.-l. Mammalian Spindle Orientation and Position Respond to Changes in Cell Shape in a Dynein-dependent Fashion. *Molecular Biology of the Cell* **11** (ed McIntosh, J. R.) 1765–1774. doi:10.1091/mbc.11.5.1765 (May 2000) (cit. on p. 158).

518. Loïodice, I., Staub, J., Setty, T. G., Nguyen, N.-P. T., Paoletti, A. & Tran, P. T. Ase1p Organizes Antiparallel Microtubule Arrays during Interphase and Mitosis in Fission Yeast. *Molecular Biology of the Cell* **16,** 1756–1768. doi:10.1091/mbc.e04-10-0899 (Apr. 2005) (cit. on p. 161).

519. Huala, E., Oeller, P. W., Liscum, E., Han, I.-S., Larsen, E. & Briggs, W. R. *Arabidopsis* NPH1: A Protein Kinase with a Putative Redox-Sensing Domain. *Science* **278,** 2120–2123. doi:10.1126/science.278.5346.2120 (19th Dec. 1997) (cit. on p. 161).

520. Christie, J. M., Salomon, M., Nozue, K., Wada, M. & Briggs, W. R. LOV (light, oxygen, or voltage) domains of the blue-light photoreceptor phototropin (nph1): Binding sites for the chromophore flavin mononucleotide. *Proceedings of the National Academy of Sciences* **96,** 8779–8783. doi:10.1073/pnas.96.15.8779 (20th July 1999) (cit. on p. 161).

521. Harper, S. M., Neil, L. C. & Gardner, K. H. Structural Basis of a Phototropin Light Switch. *Science* **301,** 1541–1544. doi:10.1126/science.1086810 (12th Sept. 2003) (cit. on p. 161).

522. Salomon, M., Eisenreich, W., Dürr, H., Schleicher, E., Knieb, E., Massey, V., Rüdiger, W., Müller, F., Bacher, A. & Richter, G. An optomechanical transducer in the blue light receptor phototropin from *Avena sativa*. *Proceedings of the National Academy of Sciences* **98,** 12357–12361. doi:10.1073/pnas.221455298 (16th Oct. 2001) (cit. on p. 161).

523. Swartz, T. E., Corchnoy, S. B., Christie, J. M., Lewis, J. W., Szundi, I., Briggs, W. R. & Bogomolni, R. A. The Photocycle of a Flavin-binding Domain of the Blue Light Photoreceptor Phototropin. *Journal of Biological Chemistry* **276,** 36493–36500. doi:10.1074/jbc.m103114200 (Sept. 2001) (cit. on p. 161).

524. Pudasaini, A., El-Arab, K. K. & Zoltowski, B. D. LOV-based optogenetic devices: light-driven modules to impart photoregulated control of cellular signaling. *Frontiers in Molecular Biosciences* **2.** doi:10.3389/fmolb.2015.00018 (12th May 2015) (cit. on p. 161).

525. Lungu, O. I., Hallett, R. A., Choi, E. J., Aiken, M. J., Hahn, K. M. & Kuhlman, B. Designing Photoswitchable Peptides Using the AsLOV2 Domain. *Chemistry & Biology* **19,** 507–517. doi:10.1016/j.chembiol.2012.02.006 (Apr. 2012) (cit. on p. 162).

526. Kok, M. *The dynamics of microtubule stability: A reconstitution of regulated microtubule assembly under force* PhD thesis (2019). doi:10.4233/UUID:5CB3DD60-78AB-4272-A820-7A754C2CC6A0 (cit. on pp. 163, 167, 171).

527. Uyeda, T. Q., Kron, S. J. & Spudich, J. A. Myosin step size. *Journal of Molecular Biology* **214,** 699–710. doi:10.1016/0022-2836(90)90287-v (Aug. 1990) (cit. on p. 163).

528. Ciandrini, L., Neri, I., Walter, J. C., Dauloudet, O. & Parmeggiani, A. Motor protein traffic regulation by supply-demand balance of resources. *Physical Biology* **11,** 056006. doi:10.1088/1478-3975/11/5/056006 (10th Sept. 2014) (cit. on p. 164).

529. Leduc, C., Padberg-Gehle, K., Varga, V., Helbing, D., Diez, S. & Howard, J. Molecular crowding creates traffic jams of kinesin motors on microtubules. *Proceedings of the National Academy of Sciences* **109,** 6100–6105. doi:10.1073/pnas.1107281109 (19th Mar. 2012) (cit. on p. 164).

530. Cytrynbaum, E., Scholey, J. & Mogilner, A. A Force Balance Model of Early Spindle Pole Separation in Drosophila Embryos. *Biophysical Journal* **84,** 757–769. doi:10.1016/s0006-3495(03)74895-4 (Feb. 2003) (cit. on p. 165).

531. Tas, R. P., Chen, C.-Y., Katrukha, E. A., Vleugel, M., Kok, M., Dogterom, M., Akhmanova, A. & Kapitein, L. C. Guided by Light: Optical Control of Microtubule Gliding Assays. *Nano Letters* **18,** 7524–7528. doi:10.1021/acs.nanolett.8b03011 (19th Nov. 2018) (cit. on p. 167).

532. Adrian, M., Nijenhuis, W., Hoogstraaten, R. I., Willems, J. & Kapitein, L. C. A Phytochrome-Derived Photoswitch for Intracellular Transport. *ACS Synthetic Biology* **6,** 1248–1256. doi:10.1021/acssynbio.6b00333 (30th Mar. 2017) (cit. on p. 167).

533. Laan, L. *Force generation at microtubule ends: An in vitro approach to cortical interactions* PhD thesis (2009). ISBN:9789077209332 (cit. on p. 167).

534. Derr, N. D., Goodman, B. S., Jungmann, R., Leschziner, A. E., Shih, W. M. & Reck-Peterson, S. L. Tug-of-War in Motor Protein Ensembles Revealed with a Programmable DNA Origami Scaffold. *Science* **338,** 662–665. doi:10.1126/science.1226734 (2nd Nov. 2012) (cit. on p. 167).

535. Ogura, T. & Hiraga, S. Partition mechanism of F plasmid: Two plasmid gene-encoded products and a cis-acting region are involved in partition. *Cell* **32,** 351–360. doi:10.1016/0092-8674(83)90454-3 (Feb. 1983) (cit. on pp. 176, 177).

536. Austin, S. & Abeles, A. Partition of unit-copy miniplasmids to daughter cells: I. P1 and F miniplasmids contain discrete, interchangeable sequences sufficient to promote equipartition. *Journal of Molecular Biology* **169,** 353–372. doi:10.1016/s0022-2836(83)80055-2 (Sept. 1983) (cit. on pp. 176, 177).

537. Austin, S. & Abeles, A. Partition of unit-copy miniplasmids to daughter cells: II. The partition region of miniplasmid P1 encodes an essential protein and a centromere-like site at which it acts. *Journal of Molecular Biology* **169,** 373–387. doi:10.1016/s0022-2836(83)80056-4 (Sept. 1983) (cit. on pp. 176, 177).

538. Oliva, M. A. Segrosome Complex Formation during DNA Trafficking in Bacterial Cell Division. *Frontiers in Molecular Biosciences* **3.** doi:10.3389/fmolb.2016.00051 (9th Sept. 2016) (cit. on p. 176).

539. Hayes, F. & Barillà, D. The bacterial segrosome: a dynamic nucleoprotein machine for DNA trafficking and segregation. *Nature Reviews Microbiology* **4,** 133–143. doi:10.1038/nrmicro1342 (Feb. 2006) (cit. on p. 176).

540. Schumacher, M. A. Structural biology of plasmid partition: uncovering the molecular mechanisms of DNA segregation. *Biochemical Journal* **412,** 1–18. doi:10.1042/bj20080359 (25th Apr. 2008) (cit. on p. 176).

541. Gerdes, K., Møller-Jensen, J. & Jensen, R. B. Plasmid and chromosome partitioning: surprises from phylogeny. *Molecular Microbiology* **37,** 455–466. doi:10.1046/j.1365-2958.2000.01975.x (Aug. 2000) (cit. on p. 177).

542. Larsen, R. A., Cusumano, C., Fujioka, A., Lim-Fong, G., Patterson, P. & Pogliano, J. Treadmilling of a prokaryotic tubulin-like protein, TubZ, required for plasmid stability in *Bacillus thuringiensis*. *Genes amp; Development* **21,** 1340–1352. doi:10.1101/gad.1546107 (17th May 2007) (cit. on p. 177).

543. Guynet, C. & de la Cruz, F. Plasmid segregation without partition. *Mobile Genetic Elements* **1,** 236–241. doi:10.4161/mge.1.3.18229 (Sept. 2011) (cit. on p. 177).

544. Golovanov, A. P., Barillà, D., Golovanova, M., Hayes, F. & Lian, L.-Y. ParG, a protein required for active partition of bacterial plasmids, has a dimeric ribbon-helix-helix structure. *Molecular Microbiology* **50,** 1141–1153. doi:10.1046/j.1365-2958.2003.03750.x (13th Oct. 2003) (cit. on p. 177).

545. Schumacher, M. A., Ye, Q., Barge, M. T., Zampini, M., Barillà, D. & Hayes, F. Structural Mechanism of ATP-induced Polymerization of the Partition Factor ParF. *Journal of Biological Chemistry* **287,** 26146–26154. doi:10.1074/jbc.m112.373696 (July 2012) (cit. on p. 177).

546. Davis, M. A. & Austin, S. J. Recognition of the P1 plasmid centromere analog involves binding of the ParB protein and is modified by a specific host factor. *The EMBO Journal* **7,** 1881–1888. doi:10.1002/j.1460-2075.1988.tb03021.x (June 1988) (cit. on p. 177).

547. Funnell, B. E. Participation of Escherichia coli integration host factor in the P1 plasmid partition system. *Proceedings of the National Academy of Sciences* **85,** 6657–6661. doi:10.1073/pnas.85.18.6657 (Sept. 1988) (cit. on p. 177).

548. Surtees, J. A. & Funnell, B. E. in *Current Topics in Developmental Biology* 145–180 (Elsevier, 2003). doi:10.1016/s0070-2153(03)01010-x (cit. on p. 177).

549. Davis, M. A., Radnedge, L., Martin, K. A., Hayes, F., Youngren, B. & Austin, S. J. The P1 ParA protein and its ATPase activity play a direct role in the segregation of plasmid copies to daughter cells. *Molecular Microbiology* **21,** 1029–1036. doi:10.1046/j.1365-2958.1996.721423.x (Sept. 1996) (cit. on p. 177).

550. Davey, M. & Funnell, B. E. The P1 plasmid partition protein ParA. A role for ATP in site-specific DNA binding. *Journal of Biological Chemistry* **269,** 29908–29913. doi:10.1016/s0021-9258(18)43967-1 (Nov. 1994) (cit. on p. 177).

551. Schumacher, M. A., Piro, K. M. & Xu, W. Insight into F plasmid DNA segregation revealed by structures of SopB and SopB-DNA complexes. *Nucleic Acids Research* **38,** 4514–4526. doi:10.1093/nar/gkq161 (4th June 2010) (cit. on p. 177).

552. Murayama, K., Orth, P., de la Hoz, A. B., Alonso, J. C. & Saenger, W. Crystal structure of ω transcriptional repressor encoded by Streptococcus pyogenes plasmid pSM19035 at 1.5 Å resolution 1 1Edited by R. Huber. *Journal of Molecular Biology* **314,** 789–796. doi:10.1006/jmbi.2001.5157 (Dec. 2001) (cit. on p. 177).

553. Schumacher, M. A., Glover, T. C., Brzoska, A. J., Jensen, S. O., Dunham, T. D., Skurray, R. A. & Firth, N. Segrosome structure revealed by a complex of ParR with centromere DNA. *Nature* **450,** 1268–1271. doi:10.1038/nature06392 (Dec. 2007) (cit. on pp. 177, 178, 180).

554. Dam, M. & Gerdes, K. Partitioning of plasmid R1 Ten direct repeats flanking the parA promoter constitute a centromere-like partition site parC, that expresses incompatibility. *Journal of Molecular Biology* **236,** 1289–1298. doi:10.1016/0022-2836(94)90058-2 (Mar. 1994) (cit. on pp. 177, 178).

555. Gayathri, P., Fujii, T., Møller-Jensen, J., van den Ent, F., Namba, K. & Löwe, J. A Bipolar Spindle of Antiparallel ParM Filaments Drives Bacterial Plasmid Segregation. *Science* **338,** 1334–1337. doi:10.1126/science.1229091 (7th Dec. 2012) (cit. on pp. 177–181, 190, 192).

556. Aylett, C. H. S. & Löwe, J. Superstructure of the centromeric complex of TubZR*C* plasmid partitioning systems. *Proceedings of the National Academy of Sciences* **109,** 16522–16527. doi:10.1073/pnas.1210899109 (25th Sept. 2012) (cit. on p. 177).

557. Ni, L., Xu, W., Kumaraswami, M. & Schumacher, M. A. Plasmid protein TubR uses a distinct mode of HTH-DNA binding and recruits the prokaryotic tubulin homolog TubZ to effect DNA partition. *Proceedings of the National Academy of Sciences* **107,** 11763–11768. doi:10.1073/pnas.1003817107 (4th June 2010) (cit. on p. 177).

558. Fink, G. & Löwe, J. Reconstitution of a prokaryotic minus end-tracking system using TubRC centromeric complexes and tubulin-like protein TubZ filaments. *Proceedings of the National Academy of Sciences* **112.** doi:10.1073/pnas.1423746112 (30th Mar. 2015) (cit. on p. 177).

559. Oliva, M. A., Martin-Galiano, A. J., Sakaguchi, Y. & Andreu, J. M. Tubulin homolog TubZ in a phage-encoded partition system. *Proceedings of the National Academy of Sciences* **109,** 7711–7716. doi:10.1073/pnas.1121546109 (26th Apr. 2012) (cit. on p. 177).

560. Simpson, A. E., Skurray, R. A. & Firth, N. A Single Gene on the Staphylococcal Multiresistance Plasmid pSK1 Encodes a Novel Partitioning System. *Journal of Bacteriology* **185,** 2143–2152. doi:10.1128/jb.185.7.2143-2152.2003 (Apr. 2003) (cit. on p. 177).

561. Møller-Jensen, J., Borch, J., Dam, M., Jensen, R. B., Roepstorff, P. & Gerdes, K. Bacterial Mitosis. *Molecular Cell* **12,** 1477–1487. doi:10.1016/s1097-2765(03)00451-9 (Dec. 2003) (cit. on pp. 178–180).

562. Gayathri, P. & Harne, S. in *Subcellular Biochemistry* 299–321 (Springer International Publishing, 2017). ISBN:9783319530451. doi:10.1007/978-3-319-53047-5_10 (cit. on p. 178).

563. Salje, J., Gayathri, P. & Löwe, J. The ParMRC system: molecular mechanisms of plasmid segregation by actin-like filaments. *Nature Reviews Microbiology* **8,** 683–692. doi:10.1038/nrmicro2425 (16th Sept. 2010) (cit. on p. 178).

564. Gerdes, K., Larsen, J. E. & Molin, S. Stable inheritance of plasmid R1 requires two different loci. *Journal of bacteriology* **161,** 292–8. doi:10.1128/jb.161.1.292-298.1985 (Jan. 1985) (cit. on p. 178).

565. Gerdes, K. & Molin, S. Partitioning of plasmid R1. *Journal of Molecular Biology* **190,** 269–279. doi:10.1016/0022-2836(86)90001-x (Aug. 1986) (cit. on p. 178).

566. Jensen, R. B. & Gerdes, K. Partitioning of plasmid R1. The ParM protein exhibits ATPase activity and interacts with the centromere-like ParR-parC complex. *Journal of Molecular Biology* **269,** 505–513. doi:10.1006/jmbi.1997.1061 (June 1997) (cit. on p. 178).

567. Møller-Jensen, J., Ringgaard, S., Mercogliano, C. P., Gerdes, K. & Löwe, J. Structural analysis of the ParR/parC plasmid partition complex. *The EMBO Journal* **26,** 4413–4422. doi:10.1038/sj.emboj.7601864 (27th Sept. 2007) (cit. on pp. 178, 179).

568. Salje, J. & Löwe, J. Bacterial actin: architecture of the ParMRC plasmid DNA partitioning complex. *The EMBO Journal* **27,** 2230–2238. doi:10.1038/emboj.2008.152 (24th July 2008) (cit. on pp. 178–180, 189).

569. Campbell, C. S. & Mullins, R. D. In vivo visualization of type II plasmid segregation: bacterial actin filaments pushing plasmids. *The Journal of Cell Biology* **179,** 1059–1066. doi:10.1083/jcb.200708206 (26th Nov. 2007) (cit. on pp. 178, 181).

570. Popp, D., Narita, A., Oda, T., Fujisawa, T., Matsuo, H., Nitanai, Y., Iwasa, M., Maeda, K., Onishi, H. & Maéda, Y. Molecular structure of the ParM polymer and the mechanism leading to its nucleotide-driven dynamic instability. *The EMBO Journal* **27,** 570–579. doi:10.1038/sj.emboj.7601978 (10th Jan. 2008) (cit. on pp. 178, 179).

571. Bharat, T. A. M., Murshudov, G. N., Sachse, C. & Löwe, J. Structures of actin-like ParM filaments show architecture of plasmid-segregating spindles. *Nature* **523,** 106–110. doi:10.1038/nature14356 (27th Apr. 2015) (cit. on pp. 178–180, 185).

572. Orlova, A., Garner, E. C., Galkin, V. E., Heuser, J., Mullins, R. D. & Egelman, E. H. The structure of bacterial ParM filaments. *Nature structural molecular biology* **14,** 921–6. doi:10.1038/nsmb1300 (Oct. 2007) (cit. on pp. 178, 179).

573. Garner, E. C., Campbell, C. S., Weibel, D. B. & Mullins, R. D. Reconstitution of DNA Segregation Driven by Assembly of a Prokaryotic Actin Homolog. *Science* **315,** 1270–1274. doi:10.1126/science.1138527 (2nd Mar. 2007) (cit. on pp. 178, 180, 181, 185).

574. Garner, E. C., Campbell, C. S. & Mullins, R. D. Dynamic Instability in a DNA-Segregating Prokaryotic Actin Homolog. *Science* **306,** 1021–1025. doi:10.1126/science.1101313 (5th Nov. 2004) (cit. on pp. 178, 179, 181, 189, 192).

575. Hürtgen, D., Mascarenhas, J., Heymann, M., Murray, S. M., Schwille, P. & Sourjik, V. Reconstitution and Coupling of DNA Replication and Segregation in a Biomimetic System. *ChemBioChem* **20,** 2633–2642. doi:10.1002/cbic.201900299 (28th Aug. 2019) (cit. on pp. 178, 182, 185).

576. Zhao, J. & Han, X. Investigation of artificial cells containing the Par system for bacterial plasmid segregation and inheritance mimicry. *Nature Communications* **15.** doi:10.1038/s41467-024-49412-9 (10th June 2024) (cit. on pp. 178, 182, 185).

577. Breüner, A., Jensen, R. B., Dam, M., Pedersen, S. & Gerdes, K. The centromere-like *parC* locus of plasmid R1. *Molecular Microbiology* **20,** 581–592. doi:10.1046/j.1365-2958.1996.5351063.x (May 1996) (cit. on p. 178).

578. Löwe, J. & Amos, L. A. Evolution of cytomotive filaments: The cytoskeleton from prokaryotes to eukaryotes. *The International Journal of Biochemistry amp; Cell Biology* **41,** 323–329. doi:10.1016/j.biocel.2008.08.010 (Feb. 2009) (cit. on p. 178).

579. Van den Ent, F. F-actin-like filaments formed by plasmid segregation protein ParM. *The EMBO Journal* **21,** 6935–6943. doi:10.1093/emboj/cdf672 (16th Dec. 2002) (cit. on pp. 178, 179).

580. Gayathri, P., Fujii, T., Namba, K. & Löwe, J. Structure of the ParM filament at 8.5Å resolution. *Journal of Structural Biology* **184,** 33–42. doi:10.1016/j.jsb.2013.02.010 (Oct. 2013) (cit. on p. 179).

581. Abramson, J., Adler, J., Dunger, J., Evans, R., Green, T., Pritzel, A., Ronneberger, O., Willmore, L., Ballard, A. J., Bambrick, J., Bodenstein, S. W., Evans, D. A., Hung, C.-C., O'Neill, M., Reiman, D., Tunyasuvunakool, K., Wu, Z., Žemgulytė, A., Arvaniti, E., Beattie, C., Bertolli, O., Bridgland, A., Cherepanov, A., Congreve, M., Cowen-Rivers, A. I., Cowie, A., Figurnov, M., Fuchs, F. B., Gladman, H., Jain, R., Khan, Y. A., Low, C. M. R., Perlin, K., Potapenko, A., Savy, P., Singh, S., Stecula, A., Thillaisundaram, A., Tong, C., Yakneen, S., Zhong, E. D., Zielinski, M., Žídek, A., Bapst, V., Kohli, P., Jaderberg, M., Hassabis, D. & Jumper, J. M. Accurate structure prediction of biomolecular interactions with AlphaFold 3. *Nature* **630,** 493–500. doi:10.1038/s41586-024-07487-w (8th May 2024) (cit. on p. 179).

582. Šali, A. & Blundell, T. L. Comparative Protein Modelling by Satisfaction of Spatial Restraints. *Journal of Molecular Biology* **234,** 779–815. doi:10.1006/jmbi.1993.1626 (Dec. 1993) (cit. on p. 179).

583. Jensen, R. B. & Gerdes, K. Programmed cell death in bacteria: proteic plasmid stabilization systems. *Molecular Microbiology* **17,** 205–210. doi:10.1111/j.1365-2958.1995.mmi_17020205.x (July 1995) (cit. on p. 180).

584. Doerr, A., de Reus, E., van Nies, P., van der Haar, M., Wei, K., Kattan, J., Wahl, A. & Danelon, C. Modelling cell-free RNA and protein synthesis with minimal systems. *Physical Biology* **16,** 025001. doi:10.1088/1478-3975/aaf33d (9th Jan. 2019) (cit. on pp. 182, 206).

585. Stone, O. J., Pankow, N., Liu, B., Sharma, V. P., Eddy, R. J., Wang, H., Putz, A. T., Teets, F. D., Kuhlman, B., Condeelis, J. S. & Hahn, K. M. Optogenetic control of cofilin and αTAT in living cells using Z-lock. *Nature Chemical Biology* **15,** 1183–1190. doi:10.1038/s41589-019-0405-4 (18th Nov. 2019) (cit. on p. 186).

586. Lee, Y.-T., Guo, L., Lan, T.-H., Nonomura, T., Liu, G., Ma, G., Wang, R., Huang, Y. & Zhou, Y. Engineering of photo-inducible binary interaction tools for biomedical applications. *Nature Communications* **16.** doi:10.1038/s41467-025-61710-4 (July 2025) (cit. on p. 187).

587. Baek, M., DiMaio, F., Anishchenko, I., Dauparas, J., Ovchinnikov, S., Lee, G. R., Wang, J., Cong, Q., Kinch, L. N., Schaeffer, R. D., Millán, C., Park, H., Adams, C., Glassman, C. R., DeGiovanni, A., Pereira, J. H., Rodrigues, A. V., van Dijk, A. A., Ebrecht, A. C., Opperman, D. J., Sagmeister, T., Buhlheller, C., Pavkov-Keller, T., Rathinaswamy, M. K., Dalwadi, U., Yip, C. K., Burke, J. E., Garcia, K. C., Grishin, N. V., Adams, P. D., Read, R. J. & Baker, D. Accurate prediction of protein structures and interactions using a three-track neural network. *Science* **373,** 871–876. doi:10.1126/science.abj8754 (20th Aug. 2021) (cit. on p. 188).

588. Cox, K. E. & Schildbach, J. F. Sequence of the R1 plasmid and comparison to F and R100. *Plasmid* **91,** 53–60. doi:10.1016/j.plasmid.2017.03.007 (May 2017) (cit. on pp. 188, 189).

589. Miroux, B. & Walker, J. E. Over-production of Proteins inEscherichia coli: Mutant Hosts that Allow Synthesis of some Membrane Proteins and Globular Proteins at High Levels. *Journal of Molecular Biology* **260,** 289–298. doi:10.1006/jmbi.1996.0399 (July 1996) (cit. on p. 189).

590. Schlegel, S., Genevaux, P. & de Gier, J.-W. De-convoluting the Genetic Adaptations of E. coli C41(DE3) in Real Time Reveals How Alleviating Protein Production Stress Improves Yields. *Cell Reports* **10,** 1758–1766. doi:10.1016/j.celrep.2015.02.029 (Mar. 2015) (cit. on p. 189).

591. Peixeiro, N., Keller, J., Collinet, B., Leulliot, N., Campanacci, V., Cortez, D., Cambillau, C., Nitta, K. R., Vincentelli, R., Forterre, P., Prangishvili, D., Sezonov, G. & van Tilbeurgh, H. Structure and Function of AvtR, a Novel Transcriptional Regulator from a Hyperthermophilic Archaeal Lipothrixvirus. *Journal of Virology* **87,** 124–136. doi:10.1128/jvi.01306-12 (Jan. 2013) (cit. on p. 189).

592. Zhou, L., Yu, H., Wang, K., Chen, T., Ma, Y., Huang, Y., Li, J., Liu, L., Li, Y., Kong, Z., Zheng, Q., Wang, Y., Gu, Y., Xia, N. & Li, S. Genome re-sequencing and reannotation of the Escherichia coli ER2566 strain and transcriptome sequencing under overexpression conditions. *BMC Genomics* **21.** doi:10.1186/s12864-020-06818-1 (16th June 2020) (cit. on p. 189).

593. Efimov, A., Kharitonov, A., Efimova, N., Loncarek, J., Miller, P. M., Andreyeva, N., Gleeson, P., Galjart, N., Maia, A. R., McLeod, I. X., Yates III, J. R., Maiato, H., Khodjakov, A., Akhmanova, A. & Kaverina, I. Asymmetric CLASP-Dependent Nucleation of Noncentrosomal Microtubules at the trans-Golgi Network. *Developmental Cell* **12,** 917–930. doi:10.1016/j.devcel.2007.04.002 (June 2007) (cit. on p. 199).

594. Mashita, T., Kowada, T., Yamamoto, H., Hamaguchi, S., Sato, T., Matsui, T. & Mizukami, S. Quantitative control of subcellular protein localization with a photochromic dimerizer. *Nature Chemical Biology* **20,** 1461–1470. doi:10.1038/s41589-024-01654-w (18th June 2024) (cit. on p. 202).

595. Maiato, H., DeLuca, J., Salmon, E. D. & Earnshaw, W. C. The dynamic kinetochore-microtubule interface. *Journal of Cell Science* **117,** 5461–5477. doi:10.1242/jcs.01536 (1st Nov. 2004) (cit. on p. 202).

596. Gregory, S. L., Ebrahimi, S., Milverton, J., Jones, W. M., Bejsovec, A. & Saint, R. Cell Division Requires a Direct Link between Microtubule-Bound RacGAP and Anillin in the Contractile Ring. *Current Biology* **18,** 25–29. doi:10.1016/j.cub.2007.11.050 (Jan. 2008) (cit. on p. 202).

597. Bessis, M. & Nomarski, G. IRRADIATION ULTRA-VIOLETTE DES ORGANITES CELLULAIRES AVEC OBSERVATION CONTINUE EN CONTRASTE DE PHASE. *The Journal of Cell Biology* **8,** 777–791. doi:10.1083/jcb.8.3.777 (1st Dec. 1960) (cit. on p. 202).

598. Wu, H.-Y., Kabacaoğlu, G., Nazockdast, E., Chang, H.-C., Shelley, M. J. & Needleman, D. J. Laser ablation and fluid flows reveal the mechanism behind spindle and centrosome positioning. *Nature Physics* **20,** 157–168. doi:10.1038/s41567-023-02223-z (2nd Nov. 2023) (cit. on p. 202).

599. Brugués, J., Nuzzo, V., Mazur, E. & Needleman, D. J. Nucleation and Transport Organize Microtubules in Metaphase Spindles. *Cell* **149,** 554–564. doi:10.1016/j.cell.2012.03.027 (Apr. 2012) (cit. on p. 202).

600. Singer, S. J. & Nicolson, G. L. The Fluid Mosaic Model of the Structure of Cell Membranes. *Science* **175,** 720–731. doi:10.1126/science.175.4023.720 (18th Feb. 1972) (cit. on p. 203).

601. Hjort Ipsen, J., Karlström, G., Mourtisen, O., Wennerström, H. & Zuckermann, M. Phase equilibria in the phosphatidylcholine-cholesterol system. *Biochimica et Biophysica Acta (BBA) - Biomembranes* **905,** 162–172. doi:10.1016/0005-2736(87)90020-4 (Nov. 1987) (cit. on p. 203).

602. Simons, K. & Toomre, D. Lipid rafts and signal transduction. *Nature Reviews Molecular Cell Biology* **1,** 31–39. doi:10.1038/35036052 (Oct. 2000) (cit. on p. 203).

603. Veatch, S. L. & Keller, S. L. Seeing spots: Complex phase behavior in simple membranes. *Biochimica et Biophysica Acta (BBA) - Molecular Cell Research* **1746,** 172–185. doi:10.1016/j.bbamcr.2005.06.010 (Dec. 2005) (cit. on p. 203).

604. Blosser, M. C., Starr, J. B., Turtle, C. W., Ashcraft, J. & Keller, S. L. Minimal Effect of Lipid Charge on Membrane Miscibility Phase Behavior in Three Ternary Systems. *Biophysical Journal* **104,** 2629–2638. doi:10.1016/j.bpj.2013.04.055 (June 2013) (cit. on p. 203).

605. Nedelec, F. & Foethke, D. Collective Langevin dynamics of flexible cytoskeletal fibers. *New Journal of Physics* **9,** 427–427. doi:10.1088/1367-2630/9/11/427 (30th Nov. 2007) (cit. on p. 204).

606. Foethke, D., Makushok, T., Brunner, D. & Nédélec, F. Force- and length-dependent catastrophe activities explain interphase microtubule organization in fission yeast. *Molecular Systems Biology* **5.** doi:10.1038/msb.2008.76 (Jan. 2009) (cit. on p. 204).

607. Kozlowski, C., Srayko, M. & Nedelec, F. Cortical Microtubule Contacts Position the Spindle in C. elegans Embryos. *Cell* **129,** 499–510. doi:10.1016/j.cell.2007.03.027 (May 2007) (cit. on p. 204).

608. Buckminster Fuller, R. in (ed Frankfurter, A. M.) fourth, 112–127 (The Art Foundation Press, New York, 1961) (cit. on p. 204).

609. Ingber, D. E., Wang, N. & Stamenović, D. Tensegrity, cellular biophysics, and the mechanics of living systems. *Reports on Progress in Physics* **77,** 046603. doi:10.1088/0034-4885/77/4/046603 (1st Apr. 2014) (cit. on p. 204).

610. Ingber, D. E. Cellular tensegrity: defining new rules of biological design that govern the cytoskeleton. *Journal of Cell Science* **104,** 613–627. doi:10.1242/jcs.104.3.613 (1st Mar. 1993) (cit. on p. 204).

611. Olivi, L., Berger, M., Creyghton, R. N. P., De Franceschi, N., Dekker, C., Mulder, B. M., Claassens, N. J., ten Wolde, P. R. & van der Oost, J. Towards a synthetic cell cycle. *Nature Communications* **12.** doi:10.1038/s41467-021-24772-8 (26th July 2021) (cit. on pp. 205, 206).

612. Pols, T., Sikkema, H. R., Gaastra, B. F., Frallicciardi, J., Śmigiel, W. M., Singh, S. & Poolman, B. A synthetic metabolic network for physicochemical homeostasis. *Nature Communications* **10.** doi:10.1038/s41467-019-12287-2 (18th Sept. 2019) (cit. on p. 206).

613. Blanken, D., Foschepoth, D., Serrão, A. C. & Danelon, C. Genetically controlled membrane synthesis in liposomes. *Nature Communications* **11.** doi:10.1038/s41467-020-17863-5 (28th Aug. 2020) (cit. on p. 206).

614. Berger, M. & Wolde, P. R. t. Robust replication initiation from coupled homeostatic mechanisms. *Nature Communications* **13.** doi:10.1038/s41467-022-33886-6 (7th Nov. 2022) (cit. on p. 206).

615. Van Nies, P., Westerlaken, I., Blanken, D., Salas, M., Mencía, M. & Danelon, C. Self-replication of DNA by its encoded proteins in liposome-based synthetic cells. *Nature Communications* **9.** doi:10.1038/s41467-018-03926-1 (20th Apr. 2018) (cit. on p. 206).

616. Godino, E. & Danelon, C. GeneDirected FtsZ Ring Assembly Generates Constricted Liposomes with Stable Membrane Necks. *Advanced Biology* **7.** doi:10.1002/adbi.202200172 (2nd Jan. 2023) (cit. on p. 206).

617. Godino, E., López, J. N., Foschepoth, D., Cleij, C., Doerr, A., Castellà, C. F. & Danelon, C. De novo synthesized Min proteins drive oscillatory liposome deformation and regulate FtsA-FtsZ cytoskeletal patterns. *Nature Communications* **10.** doi:10.1038/s41467-019-12932-w (31st Oct. 2019) (cit. on p. 206).

618. De Franceschi, N., Barth, R., Meindlhumer, S., Fragasso, A. & Dekker, C. Dynamin A as a one-component division machinery for synthetic cells. *Nature Nanotechnology* **19,** 70–76. doi:10.1038/s41565-023-01510-3 (5th Oct. 2023) (cit. on p. 206).

Curriculum Vitæ

Yash Kiran Jawale

02-07-1995 Born in Jalgaon, India.

Education

2010–2011 SSC
Maharashtra State Board, India

2012–2013 HSC
Maharashtra State Board, India

2013–2018 BS-MS
Indian Institute of Science Education and Research Pune, India
Thesis: Role of External Forcing in Directional Instability of Microtubule Transport
Promotor: Prof. dr. Chaitanya Athale

2020–2025 PhD. Biophysics
Delft University of Technology
Thesis: Building Minimal Spindles: Reconstituting spindle positioning in synthetic cells
Promotor: Prof. dr. Marileen Dogterom
Promotor: Dr. ir. Liedewij Laan

Awards

2013–2018 Innovation in Science Pursuit for Inspired Research scholarship, Govt. of India

List of Publications

3. **Jawale, Y. K.**, Schröeter, M., De Lora, J., Yahyazadeh Shourabi, A., Chen, C., De Franceschi, N., Dekker, C., Deshpande, S., Aubin-Tam, M.-E., Spatz, J. P. & Dogterom, M. Tubulin interactions affect lipid membrane formation and disrupt liposomes. (in preparation)

2. Roth, S., Gârlea, I. C., Vleugel, M., **Jawale, Y. K.**, Mulder, B. M. & Dogterom, M. Reconstitution of basic mitotic spindles in cell-like confinement. *Communications Biology*. (under review)

1. Van de Cauter, L.‡, **Jawale, Y. K.**‡, Tam, D., Baldauf, L., van Buren, L., Koenderink, G. H., Dogterom, M. & Ganzinger, K. A. High-Speed Imaging of Giant Unilamellar Vesicle Formation in cDICE. *ACS Omega* **9,** 42278–42288. issn: 2470-1343. doi:10.1021/acsomega.4c04825 (25th Sept. 2024)

Other

2. Nair, A.‡, **Jawale, Y.**‡, Dubey, S. R., Dharmadhikari, S. & Zadey, S. Workforce problems at rural public health-centres in India: a WISN retrospective analysis and national-level modelling study. *Human Resources for Health* **19.** issn: 1478-4491. doi:10.1186/s12960-021-00687-9 (Jan. 2022)

1. Chaphalkar, A. R.‡, **Jawale, Y. K.**‡, Khatri, D. & Athale, C. A. Quantifying Intracellular Particle Flows by DIC Object Tracking. *Biophysical Journal* **120,** 393–401. issn: 0006-3495. doi:10.1016/j.bpj.2020.12.013 (Feb. 2021)

‡Equal contributions

Acknowledgements

I often find myself struggling to articulate my thoughts in ways that are immediately clear to others — a challenge I continue to work on. What follows is my (perhaps not-so-clear) attempt at expressing gratitude to those who have been patient and supportive throughout. The reflections are shaped by my own perspective, and I hope any inaccuracies will be received with understanding. This section occasionally borrows from fictional characters and cultural references for style and metaphor. Any resemblance to real people — living, supervising, or otherwise — is entirely coincidental... and hopefully taken as a compliment.

My mission, should I have chosen to accept it — and clearly, I did — was to assemble a spindle and position it asymmetrically. I was quietly ushered into the BaSyC Fall meeting 2019 (tucked in the back of A1.100), to get a brief of the project, where I saw fellow agents and received current progress updates on the WP3: Cell Division. *As always, should I have created a blunder, the president of the KNAW (then, chair of BN) would disavow all knowledge of my actions. And this mission would self-destruct at Go/No-Go*. Having only heard you before, I finally met M in person thanks to a last-minute chance to join the group meeting — a day before my official start (because of course, it was a Wednesday). Being a BaSyC recruit meant *I got a license to encapsulate*. From that moment on, no messing around with purified tubulin.

To **Marileen**, our very own M. Though our 1-on-1 meetings were just 30 min each week, they were consistent — no small feat, considering how many hats you wear. They were insightful, often ran over the next slot, and always left me with more ideas to try (and experiments to troubleshoot) than any one week could hold. Thank you for the conversations and feedback that kept this mission alive, and for steering me through the labyrinth of academica. Your motivation nudged a pessimistic me toward a more pragmatic path. All things considered, this PhD journey has been about as ideal as one can hope for — at least within the limits of controllable conditions. *Let's just hope it doesn't make me an optimist. I'd probably ruin my own life somewhere along the way*.

Then came winter — snow falling again after a long wait — and with it, the real-life Long Night: COVID. It was an interesting time — working in shift, virtual group meetings and even some game nights. Thanks to then-and-now MDo group members. **Anne**, thank you for being the ultimate kickstart guide for just about everything lab-

[0] Hallucinated from — *Mission: Impossible*, *James Bond*, *Fleabag*, *Game of Thrones*, *Despicable Me*, *Cinderella*, *Superman*, *Twitter*, *John Wick*, *The Matrix*, *Finding Nemo*, *The Office*, *Parks and Recreation*, *The Lord of the Rings*, *Seasome street*, *Star Wars*, *Doctor Who*, *Disney*, *Black Mirror*, *Indiana Jones*, *Iron Man*, *Shape of You*, *The Godfather*, *The Simpsons*, *Scrubs*, *Community*, *South Park*, *Taylor Swift*, *Rick and Morty* and many more that could not be accommodated.

related: protocols, proteins, experiments, microscope, scheduling, meetings, and more. Honestly, the only upside to COVID was that it delayed your departure — giving me just a bit more time to learn from you. **Eli**, the crazy chimera creator (C^3), our own *Dr. Nefario*. Always ready to entertain even my most absurd protein assembly construct ideas — and somehow turning them into actual, purified reality. **Esengül** (Essie), the iGEM queen, our very own lab fairy godmother. Always ready to help, grant 'wishes', give hope — whether lab-related or otherwise. Ever available, be it for ~~gossip~~ chit-chat or going around BN for 'shopping'. As someone once said, *"Even miracles take a little time"*. That said, centrosomes remains her only known kryptonite. **Vladimir**, the admired go-to guy in the lab for advice, troubleshooting and references. A serious critic of my work from day-zero, not impressed during the presentation. Couldn't meet with the busy-bee that day. Who knows — I might have ended up working with tweezers instead! *I once saw him pull a microtubule with a tweezer... with an IR tweezer. He's not exactly Reviewer 2 — he's the one you send to review Reviewer 2*. **Renu** — the lab elder, part mentor, part reality check. The one who doesn't just teach you experiments, but also makes sure you confront the real-world truths of doing a PhD. Thank you for introducing me to the world of droplets, microfluidics... and uncomfortable truths. *It was never supposed to be easy — just honest*. **Ilina**, the local/in-lab actin expert. Much like treadmilling actin, your presence kept things balanced and dynamic—quietly sustaining momentum and helping the lab keep moving forward. **Reza** — the Prince of Office (& Lab & Persia & Habibi). *"Theres a lot of beauty in ordinary things. Isn't that kind of the point?"* Nah, iPad. Thank you for nudging me out of the work bubble — from that early COVID-era bike ride to Delftse Hout, to BN borrels and game nights. You made sure it wasn't just about surviving the PhD, but actually living through it. **Ali** — the no nonsense guy and office buddy. Thanks for hosting countless delicious BBQs — just meat, smoke, fire, and results. Conferences, intercontinental travel, and academic chaos — *I think we were quite ready for another adventure*. **Nemo** — the Silicon Sorcerer and the Cookie Monster. Thank you for being the trusted supplier of silicon chips, and co-conspirator on many noble (but unfinished) side-projects. *"Do. Or do not. There is no try."* You also stood guard over of all things open-source and data-safe — from Git commits to open hardware sanity. *"Cookie!" Om nom nom nom nom*. What is a friend, if not someone you'd share your last cookie with — or your Git history? (Well... maybe not by Dutch social standards. Give it 10+ years.) **Sinda** — the ~~drug~~ seed dealer from Paris. Keeper of all tubulin PTM knowledge, always ready with a fresh aliquot. *The girl who travels* (across labs): ever curious, slightly mysterious. Whether it's PTMs or Parisian wisdom, *you somehow always arrive where the action is — just in time, no TARDIS needed*. **Beatriz** (Bea), the master of Light, PURE, AlphaFold, MD simulations and more. Yet somehow, I used the *'Force'* to get you work on ParMR*C* — a true Jedi mind trick. **Vincent** — the paranoid, aristocratic Seigneur du Château Chemist, with just a hint of madness. Always ready to set the lab on fire (figuratively... we hope). Let's hope the lipid chaos doesn't trigger your OCD/ADHD — *though somehow, I'm still the one you think is unpredictable*. **Roland** — The 'R' is the new 'Q'. Always ready to help — 'we can build that' — whether its building a custom cDICE microscope setup, modifying the SD-TIRF setup, setting up IRM,

or fixing the ever-breaking down MetaMorph (as soon as possible). From a custom slide heater to 3D printed parts, your wizardry kept the microscopes running — and the experiments alive. **Ashmiani** (Ash) — basically a Disney NPC, but in a lab coat. Thanks for keeping the lab alive with musical hums, good vibes, and just the right amount of sparkle. **Olga** — the in-house philosopher. Your reflections on the public perception of the synthetic cell — and its philosophical implications — were always refreshing, and sparked wonderfully long discussions. *If a synthetic cell can move, grow, and replicate… what does that make the original?* Thank you for reminding us that science isn't just about what life is made of — but what it means.

To the new ones, **Birgit** — If anyone can catch a MAP-covered MT mid-mischief in amorphous ice, it's you. All hail CLEM. Like a molecular archaeologist, you chase fluorescent clues buried in the frozen unknown. *MTs belong on a grid*. **Yuchang** — an emerging encapsulation expert. Here's hoping you can encapsulate and integrate whatever wild Opto-ParMRC contraption Bea dreams up next. After all, *sometimes you gotta to run before you can walk*. **Prashali** — It's a nano (small) world after all. Hi to a fellow IISER(-Pune)ite! May you find your project — hopefully something MT-related. You're the last hope for continuing the MT legacy in the lab. **Joris** — a calm, level-headed presence (a perfect counterbalance to Vincent's boundless energy). *May the PURE-FtsZ Force be with your GUVs for a successful division.* **Lisa** — Always cheerful and full of good energy. *Make those GUVs fall in love with the shape of MreB*. To the previous ones, **Kim** — Always helpful and patient. Thank you for guiding me through the 'simple reliable' world of MetaMorph and all its image acquisition possibilities. The light-sensitive dyneins remain… a work in progress. **Celine** — Ever organized and efficient. Thanks for your support with the many conference, course, and workshop applications — and for later with a helping hand in lab management, too. **Maurits** — From whom I took over the office desk (and a few dynein dilemmas). Thanks for the practical tips. Your handover made the transition smooth (mostly). **Louis** — From whom I inherited the lab bench. Thanks for handing over a well-maintained state of organized chaos (unofficially disapproved by Essie, the lab manager). I hope I've at least preserved it — if not taken it to new heights.

To the sabbatical visitors, **Tomohiro** (Tomo) — Helpful, kind, and always approachable during your year with us (and even later). Sharing a bench with you was like having a *sabbatical sensei* — always something to learn. It was a great opportunity to work alongside you, and learn from your experience. Thanks for continuing to show up in the *Zoom* window, even from afar. *Distance means so little when the bench/office was once shared.* **Sarah** — Insightful and precise, our temporary lipid alchemist. Your visit brought clarity and excitement, especially for someone struggling to navigate the lipid world. I appreciated the chance to learn from you, explore experimental directions that might've otherwise stayed buried. *"It's not magic, it's science… but with lipids."*

To the BEP students, It's always nice to have someone to explore your ideas — whether it's mandane optimization or venturing into wild, uncharted spin-offs. *"Make them an offer they can't refuse."* That's how you recruit students, right Nemo & Vincent? *D'oh!* If I may be allowed the comparison — you were kind of like my own *Minions* (with fewer explosions). It was a fun and rewarding experience supervising

you, and I hope you also took something meaningful away from it too. *"I can't do this all on my own. I'm no Superman."* Thanks to: **Thibaud** — for tackling cDICE optimizations and making a strong first attempt at high-speed imaging; **Koen** — for kickstarting the (opto-)ParMRC project, which has now has grown beyond a single PhD project; **Gaspard** — for establishing the bead in droplets assay; **Quint** — for pushing that idea even further; **Luca** — for navigating and making sense of the unexplored domain of lipid phase separation in our lab. And to **Catalina** — even though you weren't my student, it was a pleasure sharing the office with you for more than a year. Thanks for the good company.

To the collaborators, Science is, and has always been, a collaborative adventure. Thank you for your invitation, openness, discussions, and for hosting me in your labs. Every journey into the unknown — temporal or experimental — is better with curious companions asking the right questions. Thank you for helping me navigate this one. **Kristina** and **Lori** — Imaging vesicle formation at such high speed brought its own temporal distortions. Thanks also to **Daniel** for diving into the theory of fluid dynamics — It took some wrangling, but we got it over the line and into print. (*"Time is relative, but reviewers are eternal."*) **Jacqueline** and **Martin** (Spatz lab) — Learning a new GUV technique was exciting, but seeing pico-injection in action? That was pure sci-fi. A moment where the GUV felt larger on the inside — full of unexpected possibilities. **Siddharth** and **Chang** — Thank you for giving tubulin encapsulation a go with OLA. A solid first attempt — and there's still more ground to cover. **Marcos** and **Gijsje** — Exploring actin-MT crosstalk in droplets with you felt like a detective case: *"It was a study in droplets."* The game's afoot, and Dr. Arribas Perez was right there in the thick of it. **Arash** and **Marie-Eve** — Thank you for trying to untangle the mysteries of tubulin-lipid interaction in microfluidics. It was reassuring to discover I'm not the only one haunted by the quirks of working with lipids! In the end, it's all about teamwork — solving one problem, then the next, together. But in case of GUVs, well... it was simply: *"Pop! Pop!" "Oh my God, they killed Liposomes!"*

I've been fortunate to interact with many PIs throughout this journey. From sharing the lab with the *in vitro* **Bio-softies** during COVID, to tight collaborations with **Anna**'s lab — sharing protocols, proteins, and catching up at Synergy/NWO-XL meetings every couple of months — it truly felt like working with a sister labs. A special shout-out to **Dipti** (*'didi'*). **Liedewij**, it was a great opportunity to have someone who had worked on the foundations of this project as a co-promoter. I wish we'd had more chances to interact. TA-ing for **Dimphna** and Gijsje's *Physical Biology of the Cell* course, alongside **Christos**, and others was both fun and full of learning. Thanks also to **Arjen**, as an advisor, for the occasional chats about the oddities of academic life — always helpful in their own way. And to **Martin**, for being the friendly and accessible department boss. Time passed, styles changed, and the department evolved — sometimes visibly so, just next door. As did the facial hair on both sides of the office wall. BN has come a long way. The same is true regarding the thesis committee — I've had opportunity to interact with many of you in way or another. With **Thomas** and **Allen**, it all began at the Lorentz Center workshop in Leiden (my first in-person event after COVID restrictions lifted), and continued through regular encounters at the EMBO Microtubule and SynCell meetings — and nearly every

other conference in the field. It was always a pleasure to discuss my work with you. I also had the chance to meet Thomas even earlier, during my Master's. **Gayathri**, from attending your courses during my Master's to now working on a topic you've helped shaped significantly, the arc has been both fun and inspiring. There were also moments of interaction with **Marvin** during BN forums, and with **Pascale** through BaSyC meetings. Thank you to Thomas, Allen, Gayathri, Marvin, Gijsje, Liedewij, and Pascale for taking the time to review my thesis. I hope it made for an interesting read.

Thanks to fellow colleagues on this journey — in both work and beyond. The **cDICE troubleshooting club** — Lucia, Lennard, Gerard, and Iris, led by Gijsje — was a collective effort in perseverance, sharing problems, tweaks, and occasional victories to keep the cDICE spinning. **Lucia**, in the end, I couldn't get the GUVs to listen to tubulin. To my fellow **BaSyC** (*"basic"*) colleagues — Roman, Sabrina, Ana, Vadim, Federico, and many others — thank you for the discussions and company during BaSyC events. To the **BN nanoworld crew** — Federico (F), Nicola, Jeffrey, Bert, Brian, Justas, Elisa, Céline, Margreet, Wiel, Jan, Anthony, Anders, Nynke, Roland (K), Theo, Alok, Michal, Jaco, Adja, and others — thanks for your help in one way or another throughout this journey. **BN LAN party** legends — Nemo, Reza, Arash, Roland (K), Ramon, Jan, and Steve — it was a blast mining and shooting (in Minecraft and CS:GO, of course). Thanks to the GK, MEA, LL, and ChD lab members for company during BN social events, *Quo Vadis*, game nights, and more. **Dimitri** — hardware wizard and go-to guy for custom parts. Together with Roland, the two of you were the unofficial R&D team. Having access to an in-house workshop (and now 3D printers!) was an underrated superpower for research. Finally, none of this work would've gone as smoothly without the tireless support of the **BN secretariat**. Thanks to Esther, Valentina, (Marty), Heleen, and others — from paperwork to room bookings and scheduling chaos, you kept everything running. *"As they say — it takes a village to build a cell."*

I've never seen myself as much of a traveler, yet collaborations and conferences carried me to places I never expected—Heidelberg, Texel, Paris, Hokkaido, Dubrovnik, Boston, Barcelona, Minnesota, Toulouse, and more—sometimes solo, sometimes in good company. Working on microtubules, a trip to Heidelberg is practically a rite of passage. Between the classic DB delays and great company — first with Ali & Ilina, then Sinda & Beatriz — it became a recurring landmark on the map. *"All tubulin protofilaments lead to Heidelberg"*. The iGEM Jamboree with Essie and SynCell conferences with the BaSyC folks were highlights as well. The Naito MT meeting in Japan with Ali was special — especially thanks to Tomo, whose warm hospitality transformed it into a truly memorable experience. And of course, the MDo game nights, outings and our biennial 'lab trips' to France were consistently fun — turning work into something a lot more adventure than agenda. Thanks for making this journey more than just research... it's been an odyssey.

A word for **tubulin** — the integral thread running through my PhD. Ever fascinating, always mysterious, and never quite predictable. *It's not easy being green, huh? "Look what you made me do" — could I have tried any more encapsulation techniques? In the game of encapsulation, you either win... or you try again. To en-*

capsulation and beyond. "Wubba Lubba Dub Dub." That's enough. *"I'm not superstitious, but working with tubulin has made me a little stitious.* Despite everything, tubulin — you've been oddly rewarding company. A wonderfully quirky, stubborn, and endlessly fascinating protein to study. Thanks for keeping things interesting.

To the **friends** — Siddhesh, Sanket, Swapnil(s), Harsh (bavdi / HG42) and others from the **IISER Pune Marathi gang** — thank you for the fun, the memories, and everything in between. Special thanks to Sanket for the weekend getaways in and around Amsterdam — much-needed pit stops along the winding road of PhD life. To the proof-reading crew — Lucia, Marcos, Beatriz, Reza, Eli, Sid — led by Anushree, *the crown jewel* — thank you for making this document far more readable than it started out. It was long (too long), and one can always find more to fix. Perfection maybe a myth, but your time and effort made it a whole lot better. To Parth — the only person I knew outside BN in all of Delft, and that too from the university — thank you for being my designated "I know someone here" card. To the three neighbours — whose names I may not even know — for being part of the backdrop to this journey. And finally, if you find yourself missing from this acknowledgements section — let's just say it wasn't because I forgot you, but because I'm respecting your privacy. (That's my story, and I'm sticking to it.)

To **my family** — my parents and sister — the source of my motivation and perseverance. *Thank you* for your unwavering support throughout life and this PhD journey — each in your own way, trying to understand and support me and my path (in academia). Sometimes, silence and simplicity carry the deepest gratitude. A heartfelt thank you!

Though I'm not one for many words, here I am — having poured them all into this thesis. Thank you for reading it to the end.

Grateful, Dankbaar, कृतज्ञ
— Yash Yawale